ÉCOLE DOCTORALE *Énergie, Matériaux, Sciences de la Terre et de l'Univers*

Institut des Sciences de la Terre d'Orléans / School of Earth Sciences and Engineering

THÈSE EN COTUTELLE INTERNATIONALE présentée par :

Jiashuo LIU

soutenue le : 9 décembre 2025

pour obtenir le grade de :
Docteur de Université d'Orléans
et de l'Université de Nanjing

Discipline / Spécialité : Sciences de l'Univers

Early Mesozoic lithospheric rheology of the Cathaysia Block, South China: Insights from deformation, metamorphism, magmatism and geodynamic modelling

THÈSE dirigée par :

M. RAIMBOURG Hugues	Professeur, Université d'Orléans, France
M. WANG Bo	Professeur, Nanjing University, China

RAPPORTEURS :

M. KUO Li-Wei	Professeur, National Central University, China
M. LI Jianhua	Professeur, Chinese Academy of Geological Sciences, China

---

JURY :

M. LIN Wei (Président du jury)	Professeur, Institute of Geology and Geophysics, China
M. AUGIER Romain	Associate Professeur, Université d'Orléans, France
M. GERYA Taras	Professeur, ETH Zürich, Switzerland
M. KUO Li-Wei	Professeur, National Central University, China
M. LI Jianhua	Professeur, Chinese Academy of Geological Sciences, China
M. RAIMBOURG Hugues	Professeur, Université d'Orléans, France
M. SHU Liangshu	Professeur, Nanjing University, China
M. WANG Bo	Professeur, Nanjing University, China

INVITÉS :

M. CHEN Yan	Professeur, Université d'Orléans, France

Acknowledgments

轻舟已过万重山 Since the first look with Nanjing University in the mid-summer of 2017, it has been eight years. The following year, I was fortunate enough to be admitted to this century-old university and had the honor of being a master student under the supervision of Prof. WANG Bo. During the past several years, I was fortunate to study abroad, i.e., as an exchange master student under the supervision of Associate Prof. AUGIER Romain in Université d’Orléans from the February to July of 2020 supported by the Institut des Sciences de la Terre d'Orléans and Loiret region government, as a joint-PhD student under the supervision of Prof. RAIMBOURG Hugues in Université d’Orléans from December 2022 to November 2024 supported by the China Scholarship Council, and as an academic visitor under the supervision of Prof. GERYA Taras in ETH Zürich from September to December 2023 supported by the Institut des Sciences de la Terre d'Orléans. Since the winter of 2019, COVID-19 has slowed the world down. As I stand at the end of this amazing journey and look back, I must be honest—it has been long and hard for me, yet deeply enriching, not just for scientific knowledge but for life itself. Here, as I reflect on my PhD journey, I have lots of thanks to say. I appreciate the countless supports. These pages are dedicated to all the kind people who have illuminated my academic career and life.

桃李不言 下自成蹊 First of all, I would like to extend my sincerest gratitude to my Chinese supervisor, Prof. WANG Bo from Nanjing University. I will never forget the first time I met him at the School of Earth Sciences and Engineering in the mid-summer of 2017. He had just returned from a field trip with undergraduates, yet without even pausing to drink water or change his clothes, he enthusiastically gave us an introduction to structural geology. I will always cherish the memory of our first field trip in Xinjiang in September of 2018, where he kindly reminded me to have breakfast on time, just like a caring father. Nor can I forget the countless discussions in his office, where he patiently taught me how to do research, think critically, and work efficiently.

I learned a lot from him, for science, for life, for man. All his time, energy, ideas, support, and funding are greatly appreciated. I am grateful for his support in pursuing my studies in France and Switzerland.

亦师亦友 亦导亦伴 I am profoundly thankful to my French supervisor, Prof. RAIMBOURG Hugues from Université d'Orléans. I often drop by his office without an appointment, and I thank him for taking the time to patiently answer my questions. I greatly appreciate his patience in teaching me the method of data processing, his knowledge of the Raman thermometer, and his constructive suggestions on my thesis. I was deeply impressed by his exceptional work efficiency. I would like to sincerely thank Associate Prof. AUGIER Romain from Université d'Orléans. I sincerely thank him for being my initiating mentor on the RSCM. Even facing the Covid-19 pandemic at that time, we persisted in discussing online and overcame the difficulties to return to the laboratory. I am deeply grateful for his concern when I was restricted to the dormitory during the French confinement in 2020. I sincerely appreciate Prof. GERYA Taras from ETH Zürich. He awoke my interest in geodynamic numerical modelling and introduced me to this academic field. His modelling courses are insightful and inspiring, and they make me benefit a lot. I sincerely appreciate those who guided me as both teachers and friends. They created an open environment for free academic discussions.

春风化雨 润物无声 Special appreciation is expressed to Prof. CHEN Yan from Université d'Orléans. During my twice study trips in France, I greatly appreciate his help in my academic and personal life. I can still vividly recall how he tirelessly assisted me with accommodation and bank procedures during my first arrival in France. When I returned for my second study trip in France, his support in daily life continued to be invaluable. His attitude towards science and his passion for geology profoundly inspired me. The numerous discussions with him, ranging from my thesis to his research experiences and life insights, greatly enlightened me. I would also like to express my gratitude to Prof. SHU Liangshu from Nanjing University. I sincerely thank him for providing me with a position as a teaching assistant during my master, which significantly enhanced my disciplinary skills. I am particularly grateful that, despite his advanced age, his tirelessly accompany and guidance in three field investigations in South China, which significantly enhanced my fieldwork competencies and improved my professional skills.

山水一程 三生有幸 During my doctoral studies, I met many excellent teachers and I am grateful for their help in my study and life. I thank FAURE Michel, GUMIAUX Charles and SORET Mathieu from ISTO, COCHELIN Bryan and GUILLOU-FROTTIER Laurent from the BRGM, CANIZARES Aurélien from the CEMHTI, for their time on the discussions of my scientific questions, the constructive suggestions on the thesis and the guidance in experimental work. I thank DE-SIGOYER Julia from Université Grenoble Alpes, SERINYEL Zeynep and AUBRY Olivier from Université d'Orléans, for their follow-up on both my research progress and doctoral life their constructive feedback. I thank ROUILLIER Marie-France and GAUDEFROY Olivier from ISTO, for their help on the administrative procedures in Orléans. I thank DUDOK DE WIT Thierry, LANDAIS Frederique and GRELET Veronique from Université d'Orléans, for their time and help on enrollment of my PhD. I thank BALAZS Attila and BOLLIGER Monika from ETH Zürich, for their help on the administrative procedures in Zürich. I thank XU Zhiqin, JIA Dong, ZHU Wenbin, LI Yongxiang, WANG Qin, LI Guangwei, GE Rongfeng, HUANG Zhouchuan, WANG Shengli from Nanjing University and LIN Wei, SONG Yuhuan, CHU Yang, WEI Wei from the IGGCAS, for their help, teaching and suggestions for my PhD study. I thank ZHANG Wenlan, HU Huan, WU Bing, PAN Yuguan, YUAN Yanjuan, WANG Yaxiao and TANG Xiaoqian, ZHAO Dandan, SHAN Taisong, JIN Xin from Nanjing University, for their guidance in experimental work and assistance with administrative procedures in Nanjing, respectively.

愿岁并谢 与长友兮 I am truly fortunate and I am grateful that I have a group of like-minded and mutually supportive friends and colleagues throughout my PhD journey. They are: RAJIČ Kristijan, ALAOUI Khadija, QIU Huabiao, GAO Pengyuan,

XU Yating and JIA Li from ISTO, ROQUE Anthony, ZHANG Zheng, SUN Tingwei, WANG Pengcheng and XUE Chaoyang from CNRS, XIE Yuan, GAO Wensheng, HUANG Luyuan, ZHOU Xin, ZHU Xiaoxi, TIAN Jiacheng and Gray Timothy from ETH Zürich, ZHANG Wenbo, LIU Tanjie, HUANG Meiyun and SHI Kaihui from IGGCAS, WU Xuejin from NIGPAS, XU Shihua, SHEN Boheng, REN Jun, ZHOU Teng, GAO Guohui, LIU Xinyu, MA Anlin, QIU Erkang, WU Hailin, ZHENG Bihai, ZHOU Zhongbiao, YAN Chaolei and SUN Junjun from Nanjing University. I thank everyone in our structural group in Nanjing University: LIU Hongsheng, ZHONG Linglin, ZHU Xin, HE Zhiyuan, FANG Ting, Guzalnur Wali, ZHU Xiaoyan, ZHOU Yong, CAO Shengnan, NI Xinghua, SUN Zhaochen, GAN Haonan, LI Yingying, DENG Ju, SONG Fang, LU Shenghua, CAO Tingting, CHEN Yiyi, SUN Yuxin, HE Xiaoke, LI Haoxiang, JIA Guoqing, JI Shang, ZHU Ji and Sylvain. I thank all the roommates in office A407: ZHANG Yong, HUANG Renbo, FAN Xiaogen, HU Jing, YANG Shuang, ZHONG Cheng, ZHANG Li, ZHAO Jiabin, GOU Yiren, LIU Jun, ZHU Xiaoyu, DAI Jun, GE Jiacheng, LI Wei, MA Haitao, WEN Die, XU Qi and ZHOU Di.

春晖寸草 山高海深 I would like to express my deepest gratitude to my family, my grandfather, my father, my mother, and my brother. Thanks for their endless understanding, unconditional love, unwavering support and consistent encouragement. Thank you for everything you have done for me! I would not be where I am today without you.

乍见之欢 久处砰然 I would like to express my heartfelt gratitude to my beloved partner, Ms. HAN Rongrong, for her unwavering support and companionship over the past six years. During the 700 days of separation amid the COVID-19 pandemic, the 1,000 nights spent under foreign skies, and the journeys spanning 30,000 kilometers for meeting, I thank her understanding and encouragement. I thank her for the quiet moments of swallowing loneliness alone, and the bedside lamp she kept burning for me. Her smiles over video calls, her greetings transcending time zones, became my

sustaining strength. I am profoundly grateful for her love, understanding and patience throughout this journey.

道阻且长 行则将至 Finally thanks to myself, for my own persisting in this journey, despite some doubts, hesitations and wavering.

Where of what's past is prologue.

--The Tempest

by William Shakespeare

凡是过往，皆为序章！

--朱生豪 译

Contents

Résumé

L'une des prémisses fondamentales de la tectonique des plaques est celle des plaques lithosphériques rigides. Ces plaques se déplacent comme des blocs rigides les unes par rapport aux autres, avec la déformation, le métamorphisme et le magmatisme concentrés à leurs limites. Cependant, les plaques lithosphériques sont des corps visco-élastiques plutôt que parfaitement rigides. Cela implique probablement une lithosphère rhéologiquement hétérogène composée de multiples sous-blocs, plutôt qu'une plaque homogène. En réponse aux contraintes dans l'intérieur de la Terre, la rhéologie de la lithosphère est la clé pour décrypter l'évolution et les processus géodynamiques de la lithosphère continentale. Le Bloc de la Chine du Sud, un bloc continental majeur du continent de l'Asie de l'Est, a connu une histoire tectonique longue et complexe. Depuis le Méso-/Néo-Protérozoïque, son évolution a été influencée par l'assemblage et la fragmentation des supercontinents, ainsi que par les processus de subduction et de fermeture des océans Paléo-Chine du Sud, Proto-Téthys, Paléo-Téthys et Paléo-Pacifique. En tant que composante principale du Bloc de la Chine du Sud, le bloc du Cathaysia joue un rôle clé dans la compréhension de l'évolution tectonique du Bloc de Chine du Sud et du continent est-asiatique. Un effort considérable et des recherches fructueuses ont été menés sur son magmatisme, son métamorphisme et son évolution tectonique. Cependant, des controverses subsistent concernant ses propriétés rhéologiques et le contexte géodynamique. La déformation pervasive et le magmatisme distribué de manière plane au sein du bloc du Cathaysia en font un laboratoire idéal pour examiner la rhéologie et la rigidité de la plaque lithosphérique. Cette thèse présente une étude à l'échelle du bloc et multidisciplinaire sur la déformation, le métamorphisme, l'état thermique crustal et le contexte géodynamique du bloc du Cathaysia durant le Mésozoïque inférieur. Premièrement, le métamorphisme de haute température induit par le magmatisme et l'écoulement de la croûte moyenne dans le massif de Yunkai au sud du bloc du Cathaysia ont été révélés par la géologie structurale, la géochronologie multi-minérale et l'estimation P-T. Deuxièmement, la lithosphère multi-blocs du bloc de Cathaysia au Mésozoïque inférieur et son hétérogénéité thermique crustale ont été reconnues par des investigations de terrain et thermiques à l'échelle du bloc. Troisièmement, le contexte géodynamique du bloc de Cathaysia au Mésozoïque inférieur a été révélé par des investigations géologiques et de modélisation numérique dynamique. Les principaux résultats conduisent aux conclusions suivantes : (1) Le magmatisme intracontinental répandu au sein du bloc Cathaysia au Mésozoïque inférieur a induit un métamorphisme local de haute température et un écoulement de la croûte moyenne. Ce métamorphisme dans le massif de Yunkai a atteint 6.8–7.0 kbar et 780–810 ℃. (2) Le bloc de Cathaysia présente une hétérogénéité de déformation, de métamorphisme et d'état thermique crustal durant le Mésozoïque inférieur. Le massif de Yunkai présente une déformation plus intensive, un grade de métamorphisme plus élevé et une température plus haute par rapport aux massifs de Wuyi et Nanling. (3) Le bloc de Cathaysia ne peut pas être considéré comme un bloc rigide durant le Mésozoïque inférieur; au contraire, il présente des caractéristiques de sous-blocs composites avec une rhéologie hétérogène. (4) Les zones structurelles préexistantes sont des canaux potentiellement importants pour le transport de chaleur. (5) La déformation, le métamorphisme et l'état thermique crustal du bloc de Cathaysia au Mésozoïque inférieur sont des concéquences de l'interaction entre les multiples blocs, en particulier le long de la ceinture de la Paléo-Téthys. La force motrice principale des réactions géologiques et de leur hétérogénéité au sein du bloc de Cathaysia provient de la collision avec le bloc de l'Indochine.

Mots clés: Rhéologie lithosphérique, État thermique crustal, Déformation et métamorphisme, Modélisation géodynamique, Mésozoïque inférieur, Chine du Sud

Abstract

One of the fundamental premises of plate tectonics is that of rigid lithospheric plates. These plates move as rigid blocks with respect to each other, with deformation, metamorphism, and magmatism concentrated at their boundaries. However, the lithospheric plates are visco-elastic rather than perfectly rigid bodies. This probably implies a rheologically heterogeneous lithosphere comprising multiple sub-blocks, rather than a homogeneous plate. As a response to the stress in the interior of the Earth, the rheology of the lithosphere is the key to decipher the evolution and geodynamic processes of the continental lithosphere. The South China Block, a major continental block of the East Asian Continent, has undergone a long and complex tectonic history. Since the Meso-/Neo-Proterozoic, its evolution has been influenced by the assembly and break-up of the supercontinents, as well as by the consumption and closure progress of the Paleo-South China, Proto-Tethys, Paleo-Tethys and Paleo-Pacific oceans. As the main component of the South China Block, the Cathaysia block plays a key role in understanding the tectonic evolution of the South China Block and the East Asian Continent. A considerable effort and fruitful research have been conducted on its magmatism, metamorphism and tectonic evolution. However, there are still controversies about rheological properties and the dynamic background. The pervasive deformation and planar distributed magmatism within the Cathaysia Block make it an ideal laboratory for examining the rheology and rigidity of the lithospheric plate. This thesis presents a block-scale and multi-disciplinary study on deformation, metamorphism, crustal thermal state and dynamic background of the Cathaysia Block during the Early Mesozoic. Firstly, the magma-induced high-temperature metamorphism and mid-crustal flow in the Yunkai Massif to the south of the Cathaysia Block have been revealed by structural geology, multi-mineral geochronology and P-T estimation. Secondly, the multi-block lithosphere of the Early Mesozoic Cathaysia Block and its crustal thermal heterogeneity were recognized by the block-scale field and thermal investigations. Thirdly, the Early Mesozoic dynamic background of the

Cathaysia Block was revealed by comprehensive studies of geological investigation and dynamic numerical modelling. The main results lead to the following conclusions: (1) The Early Mesozoic widespread intracontinental magmatism within the Cathaysia induced the local high-temperature metamorphism and mid-crustal flow. This metamorphism in the Yunkai Massif reached 6.8–7.0 kbar and 780–810 ℃. (2) The Cathaysia Block exhibits a heterogeneity of deformation, metamorphism and crustal thermal state during the Early Mesozoic. The Yunkai Massif exhibits a more intense deformation, a higher grade of metamorphism and a higher temperature with respect to the Wuyi and Nanling massifs. (3) The Cathaysia Block cannot be considered as a rigid block during the Early Mesozoic; in contrast, it exhibits characteristics of composite sub-blocks with a heterogeneous rheology. (4) The pre-existing structural zones are an important potential channel for heat transportation. (5) The Early Mesozoic deformation, metamorphism and crustal thermal state of the Cathaysia Block are the results of the interaction between the multiple blocks, especially along the Paleo-Tethys Belt. The main driving force of the geological responses and their heterogeneity within the Cathaysia Block is from the collision with the Indochina Block.

Keywords: Lithospheric rheology, Crustal thermal state, Deformation and metamorphism, Geodynamic modelling, Early Mesozoic, South China

Résumé étendu en français

L'une des prémisses fondamentales de la tectonique des plaques indique que les plaques lithosphériques sont rigides, cela signifie que lors de déplacement d'une plaque plaques lithosphère par rapport aux autres, la déformation, le métamorphisme et le magmatisme se localisent essentiellement au niveau des ceintures mobiles en bordure. Cependant, la ceinture mobile pourrait présenter une largeur non négligeable et la déformation pourrait être plus diffuse à l'intérieur de la plaque. De plus, les plaques possèdent une propriété visco-élastique plutôt qu'une rigidité parfaite. Il est important de noter que la cause fondamentale sur la différence entre la déformation diffuse et étendue à l'intérieur de la plaque et la déformation localisée le long de limites des plaques concerne principalement de la rhéologie intrinsèque de la lithosphère continentale. En réponse à la dynamique l'intérieur de la Terre, la rhéologie de la lithosphère est la clé pour décrypter l'évolution et les processus géodynamiques de la lithosphère continentale.

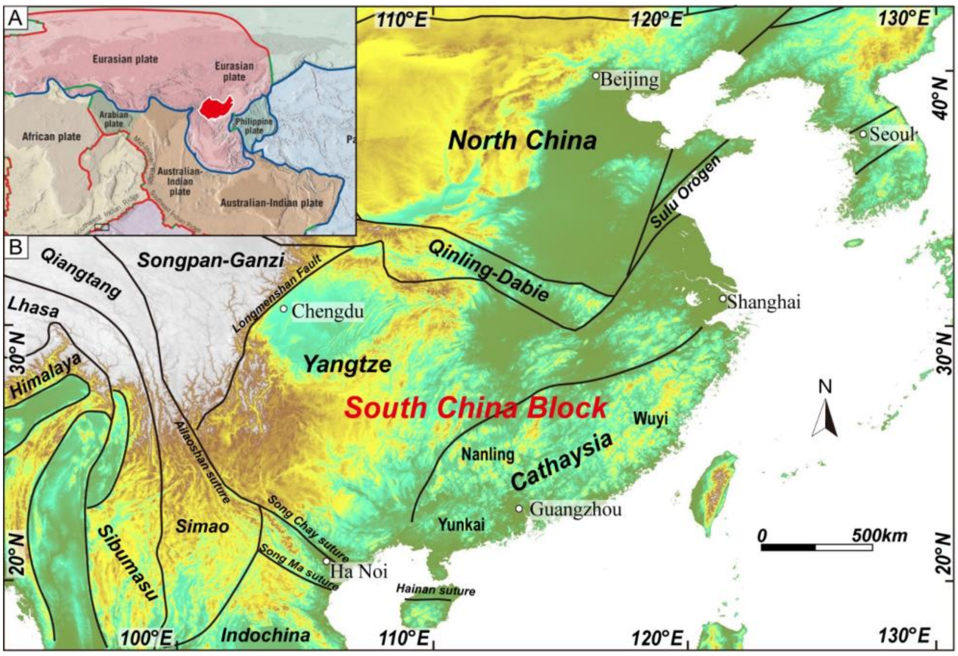

Figure 1. Cadre tectonique simplifié du Bloc de Chine du Sud. (A) Localisation du Bloc de Chine du Sud en Asie orientale (modifié d'après Tarbuck EJ et al., 2017). (B) Cadre tectonique de l'Asie orientale, montrant le Bloc de Chine du Sud et les blocs adjacents (modifié d'après Li JH et al., 2017b).

Le Bloc de Chine du Sud, une unité continentale majeure de l'Asie orientale (Fig. 1A), a eu une histoire tectonique longue et complexe. Depuis le Méso/Néoprotérozoïque, son évolution peut être tracée par l'assemblage et la fragmentation des blocs et supercontinents, ainsi que les fermetures des océans Paléo-Chine du Sud, Proto-Téthys, Paléo-Téthys et Paléo-Pacifique. En tant que composante principale du Bloc de Chine du Sud (Fig. 1B), le Bloc de Cathaysia présente des comportements distincts du craton rigide de Yangtsé, notamment une déformation pervasive et un magmatisme distribué de manière planaire à l'échelle du bloc, cela présente en fait un laboratoire idéal pour étudier sa rhéologie et sa rigidité à l'échelle lithosphérique. L'étude de la rhéologie lithosphérique du Bloc de Cathaysia peut nous aider à comprendre les caractéristiques de rigidité de la plaque du Bloc de Chine du Sud, révéler son évolution tectonique, et approfondir la compréhension de la déformation intracontinentale et de la géodynamique continentale.

Même si des efforts considérables et des avancements fructueux ont été menés par les chercheurs prédécesseurs sur la déformation et la cinématique, le magmatisme, le métamorphisme, la métallogénie et l'évolution tectonique du Bloc de Cathaysia. nombreuses controverses restent en débat et des questions fondamentales demeurent sans réponse dans ces domaines.

(1) L'homogénéité et la rigidité du Bloc de Cathaysia au Mésozoïque inférieur sont peu connues. L'investigations géologique et l'atténuation extrêmement faible des ondes sismique Lg montrent que le Bloc de Cathaysia ne possède pas un socle unifié et cohérent, présentant une forte hétérogénéité crustale. La déformation, le magmatisme et le métamorphisme au Mésozoïque inférieur étaient distribués de manière planaire au sein du Bloc de Cathaysia, plutôt que de présenter des structures linéaires ou de déformation et magmatisme distribués le long de marges du bloc. De plus, le magmatisme et le métamorphisme du Mésozoïque du Bloc de Cathaysia sont caractérisé par des intrusions fortement peralumineuses et de haute température, respectivement, sans une distribution spatio-temporelle régulière. Ces caractéristiques

indiquent que le Bloc de Cathaysia présente un comportement rhéologique distinct par rapport à un bloc rigide classique. Jusqu’à maintenant, peu d’études a été menée sur la propriété rhéologique du Bloc de Cathaysia au Mésozoïque inférieur.

(2) Les caractéristiques de la déformation et du métamorphisme au Mésozoïque inférieur dans le Massif de Yunkai restent disputées. Des études antérieures ont documenté différentes déformations et cinématiques au Massif de Yunkai durant le Mésozoïque inférieur, telles qu'un chevauchement vers le Nord/Nord-Est, une transpression sénestre d'orientation NE, et une extension régionale NE-SO. De plus, différentes opinions contradictoires ont été proposées concernant les âges de métamorphisme à l'Est du Massif de Yunkai, notamment au Néoprotérozoïque, au Paléozoïque inférieur et au Mésozoïque inférieur. Par ailleurs, les conditions métamorphiques en pression-température des migmatites et leur relation avec les intrusions granitiques ne sont pas claires, malgré certaines températures estimées à partir de la fraction de fusion et de inclusion du Ti-dans-la-biotite.

(3) L'état thermique crustal du Bloc de Cathaysia au Mésozoïque inférieur n'a pas encore été révélé en détail. L'état thermique est un facteur crucial pour évaluer la rhéologie lithosphérique. Bien que de nombreuses études sur l'état thermique et le flux de chaleur du Bloc de Cathaysia aient fourni une vision significative sur les caractéristiques géothermiques, celle-ci en effet concerne l'état thermique actuel lié aux processus géodynamique depuis le Mésozoïque supérieur. Des tentatives ont été menénes pour explorer l'état thermique du Bloc de Cathaysia au Mésozoïque inférieur en estimant la température à partir de la déformation, de thermomètres minéraux et de thermochronomètres. Cependant, les études antérieures étaient limitées à des observations ponctuelles, manquant de résolution suffisante pour élucider la variation spatiale de la température.

(4) L'influence des structures héritées/préexistantes sur l'état thermique crustal du Bloc de Cathaysia est inconnue. La connaissance sur l'héritage structural peut aider à comprendre l'hétérogénéité de la déformation, du métamorphisme et de la rhéologie de

la lithosphère continentale. Des études antérieures ont révélé l'influence des structures préexistantes sur la mise en place de magma et la forme de plutons, ainsi que sur la minéralisation, cependant, aucune étude a été réalisée sur la relation entre les structures préexistantes et l'état thermique crustal.

(5) Le contexte géodynamique du Bloc de Cathaysia au Mésozoïque inférieur reste toujours en débat. Sur la base des observations de la déformation, du métamorphisme et du magmatisme, différents modèles tectoniques du Bloc de Cathaysia au Mésozoïque inférieur ont été proposés, tels que la subduction classique de la plaque océanique de Paléo-Téthys vers le sud suivie la collision entre les blocs de l'indochine et de Chine du Sud, la subduction vers l'ouest de la plaque océanique de Paléo-Pacifique, ou bien l'interaction multi-plaques entre le Bloc de Cathaysia et les blocs adjacents.

Compte tenu des problématiques mentionnées ci-dessus, la recherche de cette thèse se concentre sur l'étude des propriétés rhéologiques de la lithosphère du Bloc de Cathaysia au Mésozoïque inférieur, ce qui peut fournir une nouvelle perspective pour comprendre la relation entre la déformation, le métamorphisme et l'état thermique du Bloc de Cathaysia.

Premièrement, des études de la déformation et du métamorphisme du Massif de Yunkai au sud du Bloc de Cathaysia ont été réalisées en géologie structurale, géochronologie multi-minérale et estimation des conditions métamorphiques en Pression-Température (P-T). Ensuite, la répartition de la déformation régionale et du métamorphisme au Mésozoïque inférieur du Bloc de Cathaysia a été reconnue par des investigations structurales et thermiques à l'échelle du bloc. Enfin, le contexte géodynamique du Bloc de Cathaysia au Mésozoïque inférieur a été démontré.

Basé sur de différentes approches, y compris des études de la déformation, du métamorphisme, de l'état thermique crustal et la modélisation numérique dynamique du Bloc de Cathaysia au Mésozoïque inférieur, les résultats de cette thèse révèlent la hétérogénéités en rhéologie et à l'échelle lithosphérique du Bloc de Cathaysia avec les 3 massifs distincts, ceci nous a rapporté nouvelle compréhension approfondie des réponses tectoniques intracontinentales et de la géodynamique continentale. Les principaux résultats et conclusions issus de cette thèse sont les suivants:

(1) Écoulement méso-crustal induit par le magmatisme et le métamorphisme à haute température au massif de Yunkai

Les investigations structurale de terrain et microscopique au laboratoire ont révélé trois phases principales de la déformations, à savoir : un écoulement magmatique NE-SO en faciès amphibolite (D1), un cisaillement décrochant dextre NE-SO dans en faciès schiste vert (D2) et un écoulement magmatique vertical (D3). Parmi ces trois phases, la déformation D1 est accompagnée par la mise en place du magma et de la migmatisation. Les styles de déformation sont cohérents avec une structure en dôme. Les études pétrologiques sur les assemblages minéraux et les profils de composition de grenat ont identifié trois stades de métamorphisme: prograde, pic et rétrograde. Les calculs de pseudosections P-T ont révélé que les conditions du pic métamorphique étaient de 6,8-7,0 kbar et 780-810 °C, suivi d'un stade rétrograde de refroidissement et décompression à 3,2-4,2 kbar et 595-615 °C, ce qui suggère un métamorphisme de haute température au niveau de la croûte moyenne. Les protolithes des roches métamorphiques sont des grauwackes métamorphiques du Silurien et des roches magmatiques associées. Les données géochronologiques multi-minérales indiquent que la déformation a duré au moins jusqu'à 237 Ma, que le magma s'est mis en place et a cristallisé entre 254 et 237 Ma, et que le métamorphisme de haute température s'est produit entre 241 et 238 Ma.

Considérant 1) les caractéristiques de la fusion partielle syn-déformation in situ, 2) les intrusions granitiques dans le bloc de Cathaysia dépassent volumétriquement largement les roches métamorphiques de haut grade, 3) les roches métamorphiques de haut grade se localisent toujours près de grandes intrusions granitiques, 4) les granites étaient en contact intrusif avec les migmatites, 5) outre le granite de type S, il existe un faible volume de granites de type I et de type A qui ne peut pas être dérivé de la fusion partielle de roches supracrustales, 6) la température du magmatisme est d'environ 800 °C, proche de la limite supérieure de la température métamorphique, 7) les granites

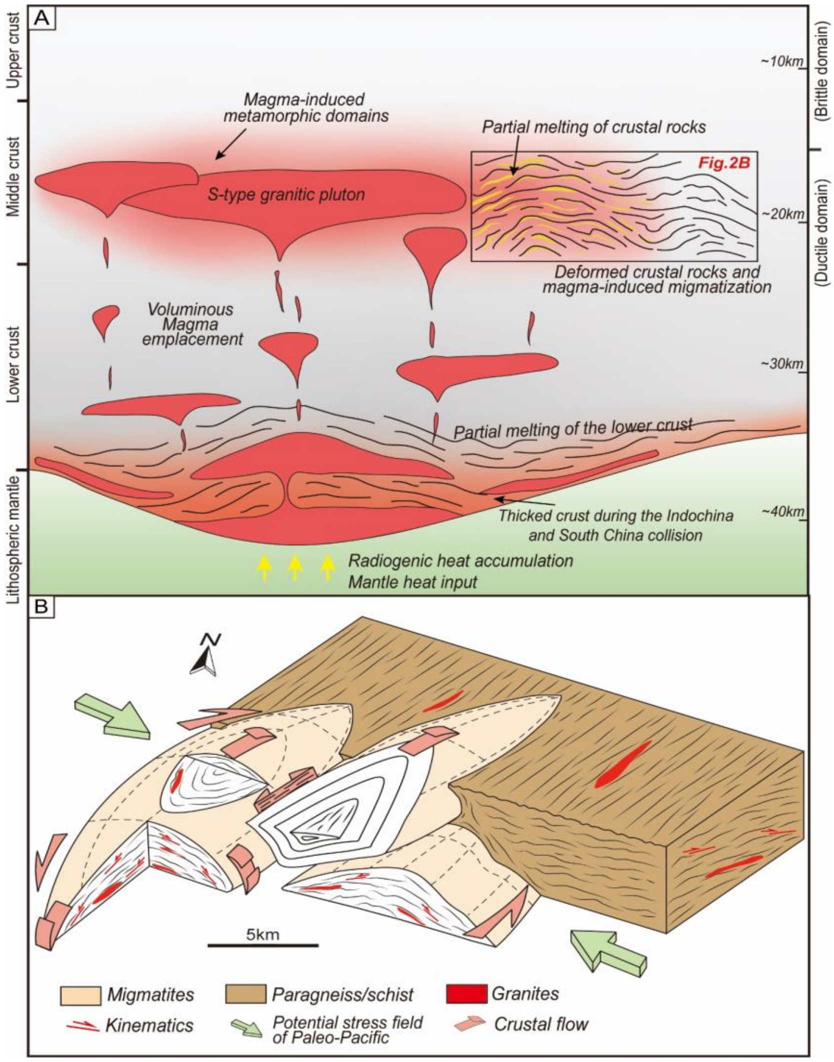

Figure 2. *Modèle préliminaire pour la migmatisation et la répartition des contraintes du dôme.*

présentent une source plus complexe basée sur l'isotope Nd, l'âge modèle Nd et l'isotope O, 8) une différence d'environ 10 Ma révélée par les données géochronologiques compilées entre le magmatisme à haute température et le métamorphisme. La haute température induite par le magma métamorphisme a été identifiés (Fig. 2) et le grand volume de granites peralumineux régionaux est probablement responsable de ce métamorphisme local de haute température et de la migmatisation. La fusion partielle, survenue de la croûte inférieure épaissie, a généré d'important volume de magma peralumineux à l'échelle régionale. La migration ascendante et la mise en place de ce magma au niveaux de la croûte moyenne ont conduit à la formation de plutons granitiques, déclenchant une fusion partielle additionnelle sur de roches encaissantes et un métamorphisme de haute température. Cette fusion partielle induite par le magma et ce métamorphisme de haute température ont significativement réduit la résistance crustale et favorisé la localisation de la déformation. Finalement, un écoulement à la croûte moyenne d'une orientation NE-SO s'est développé dans une croûte affaiblie mécaniquement sous le régime de contraintes régional.

(2) Hétérogénéité de l'intensité de la déformation et du degré métamorphique à travers le Bloc de Cathaysia

Les investigations de terrain révèlent des variations significatives de l'intensité de la déformation à travers les différents massifs du Bloc de Cathaysia. Généralement, le Massif de Yunkai présente une déformation plus intense, suivi du Massif de Wuyi, tandis que le Massif de Nanling ne montre aucune déformation ductile. De plus, les roches du Paléozoïque inférieur et supérieur présentent la même intensité de déformation au centre du Massif de Yunkai et à la bordure du Massif de Wuyi. D'ailleurs, les roches du Paléozoïque supérieur au-dessus de la discordance ne sont pas déformées ductilement, tandis que les roches du Paléozoïque inférieur en dessous de la discordance présentent une faible déformation ductile avec un clivage slatetifié et une schistosité. Parallèlement, deux orientations structurales prédominantes peuvent être identifiées, i.e., les structures d'orientation NO-SE et celles d'orientation NNE-SSO (Figs. 3A-B), suggérant deux directions de raccourcissement. Les structures plus anciennes d'orientation NO-SE ont été ultérieurement surimprimées par les structures d'orientation NE-SO (Fig. 3C). Une tendance significative émerge à l'échelle du Bloc de Cathaysia, où l'intensité de la déformation diminue du Sud vers le Nord et augmente d'Ouest en Est (Fig. 3D). De plus, les domaines proches des failles majeures présentent une déformation intense.

Comparable à la variation de l'intensité de la déformation, le Bloc de Cathaysia présente de degrés variables du métamorphisme régional à travers les différents massifs. Les massifs de Yunkai et Wuyi présentent un métamorphisme régional de haut degré, suivi du Massif de Nanling. Les roches anté-dévoniennes ont été impliquées dans le métamorphisme régional, tandis que le métamorphisme régional du Paléozoïque supérieur n'est survenu qu'au centre du Massif de Yunkai et à la bordure orientale du Massif de Wuyi. Presque toutes les roches mésozoïques n'ont pas été impliquées dans le métamorphisme régional. Le degré du métamorphisme montre également une similaire tendance à diminuer du Sud vers le Nord et à augmenter d'Ouest en Est. De plus, les roches situées dans l'auréole de métamorphisme de contact de grands plutons ont présenté un degré de métamorphisme plus élevé, voire une migmatisation.

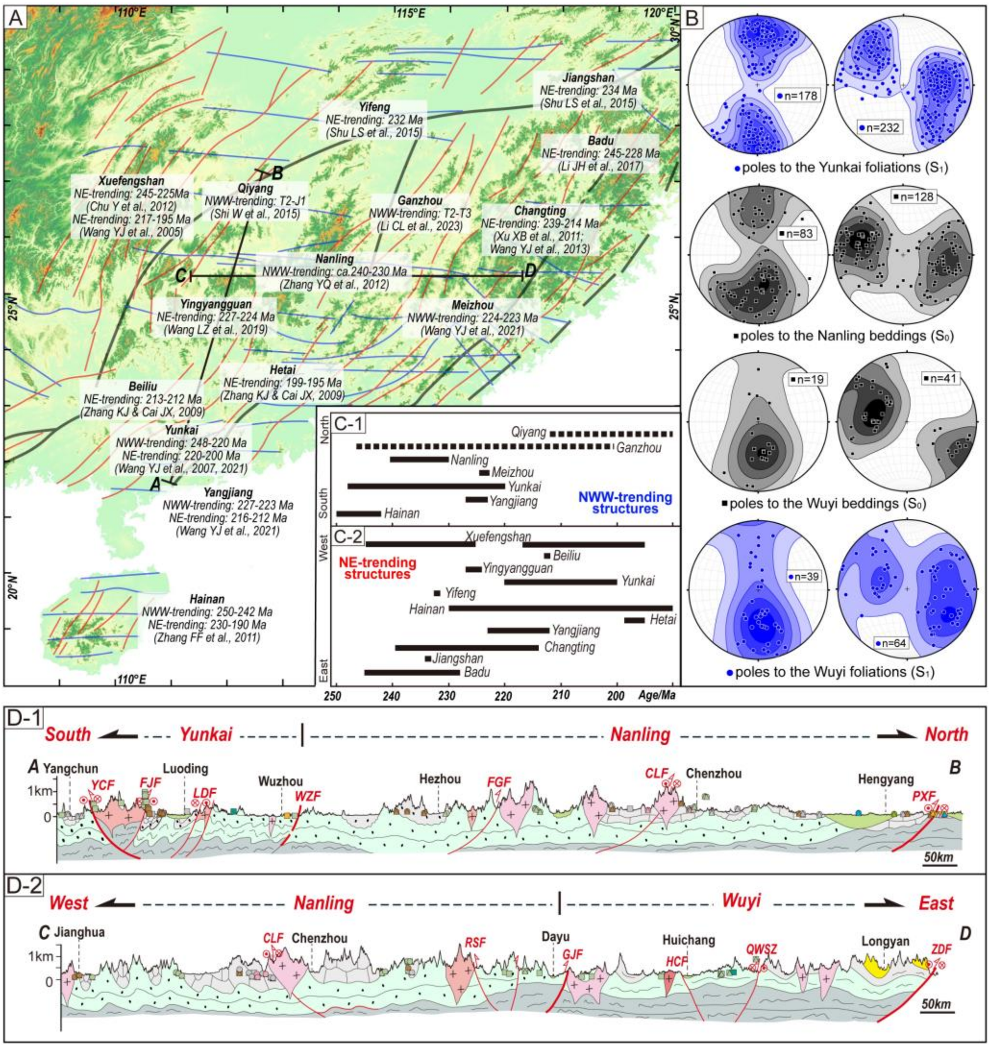

Figure 3. *Schémas structuraux du Bloc de Cathaysia. (A) des structures représentatives du Mésozoïque inférieur dans différentes directions. (B) Statistiques des occurrences des stratifications (en noir) et des foliations (en bleu) dans différents massifs. (C) Statistiques des structures à tendance NO et NE en fonction de leurs âges et de leurs emplacements. (D) Schémas structuraux de Yunkai à Nanling et de Nanling à Wuyi.*

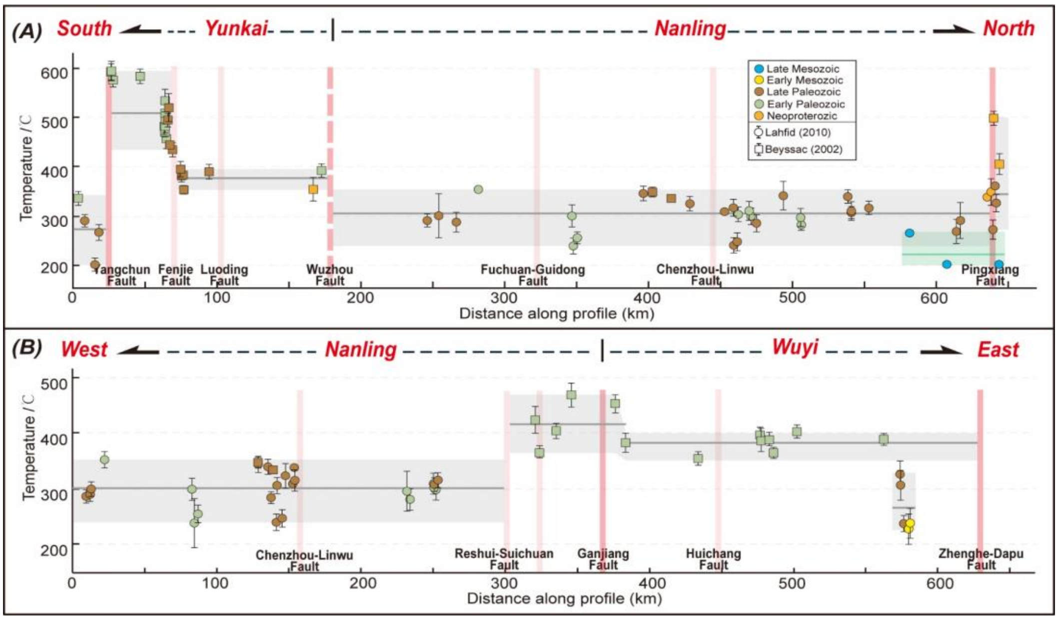

Figure 4. *Variation spatiale des températures RSCM le long des profils de Yunkai-Nanling (A) et Nanling-Wuyi (B).*

(3) Hétérogénéité thermique aux échelles crustale et lithosphèrique avec multiple blocs du Bloc de Cathaysia au Mésozoïque inférieur

La spectroscopie Raman de matière carbonée (RSCM) est un nouveau géothermomètre permettant de décrypter l'état thermique des anciennes ceintures orogéniques, qui peut enregistrer la température la plus élevée sur la base du degré d'organisation de la matière carbonée. Elle offre un outil rapide et quantitatif et nous permet d'explorer la croûte à l'échelle d'un bloc. Selon l'étude par RSCM, les trois massifs présentent une hétérogénéité spatiale significative de la températures du Mésozoïque inférieur. Le Massif de Yunkai a enregistré les températures les plus élevées, suivi des massifs de Wuyi et de Nanling (Fig. 4). La température moyenne du Sud du Massif de Yunkai atteignait à ~509 ± 54 °C, tandis qu'au Nord, elle diminuait à ~376 ± 18 °C. Le Massif de Wuyi a enregistré une température moyenne de ~383 ± 18 °C dans le socle anté-dévonien et de ~266 ± 46 °C dans le bassin permien-triasique. Le Massif de Nanling présente une température moyenne de ~304 ± 33 °C. De plus, la température moyenne le long de la faille majeure de Ganjiang, entre les massifs de Nanling et de Wuyi, augmente jusqu'à ~416 ± 41 °C. D'après les données disponibles sur les estimations pression-température (P-T), ainsi que les analyses des écarts de température et de l'épaisseur des strates de plusieurs bassins, le gradient paléo-géothermique le plus élevé a été observé au Massif de Yunkai (~40−75 °C/km), suivi du Massif de Wuyi (~33−52 °C/km), tandis que le plus faible a été enregistré au Massif de Nanling (~21−38 °C/km).

Ces reconstructions de l'état thermique et du gradient thermique du Bloc de Cathaysia au Mésozoïque inférieur reflètent des discontinuités structures à m'échelle lithosphériques et des propriétés rhéologiques différentielles à travers les trois massifs. Le Massif de Yunkai, proche de l'orogène indosinien, est plus chaud que les massifs de Nanling et de Wuyi, suggérant une rhéologie affaiblie et une rigidité réduite. En revanche, le Massif de Nanling se caractérise comme un massif plus rigide avec une basse température et un faible gradient thermique.

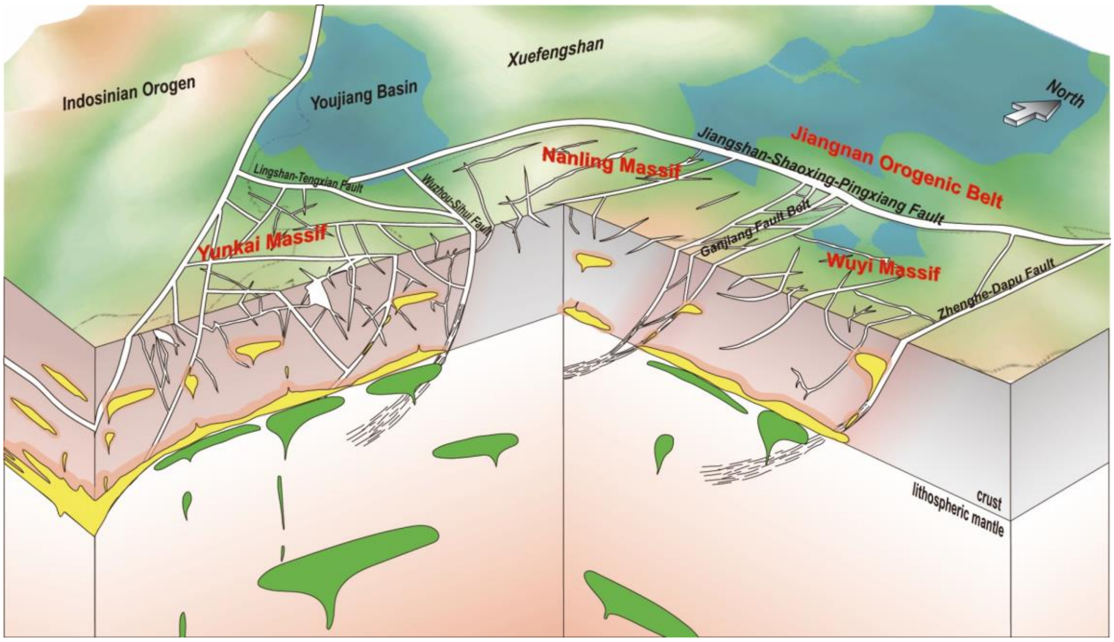

Figure 5. *Un modèle conceptuel illustrant les propriétés multi-blocs du bloc de Cathaysia et l'état thermique hétérogène et la rigidité relative entre les trois massifs.*

Le Bloc de Cathaysia ne peut pas être considéré comme un bloc rigide pendant le Mésozoïque inférieur; il présentait plutôt des caractéristiques de sous-blocs composites avec une rhéologie hétérogène (Fig. 5). Cette hétérogénéité en rhéologie se reflète dans les variations de déformation, de métamorphisme et d'état thermique crustal. Par exemple, le Nanling était dominé par des structures fragiles avec de faibles paléo-températures, tandis que le Massif de Yunkai se caractérise par une déformation ductile intensive et de hautes températures.

(4) Les structures préexistantes ont servi de conduits potentiels pour le transfert thermique

Une augmentation prononcée de la température s'est produite près de certaines failles majeures, en particulier le long de la faille de Ganjiang qui sépare les massifs de Nanling et de Wuyi, où des anomalies thermiques allant jusqu'à ~100 °C ont été observées. Cette faille a été identifiée comme une faille trans-crustale sur l'image magnétotellurique, abritant de nombreuses failles secondaires. Le réseau de failles étendu représente la localisation de la déformation pendant l'interaction tectonique entre les massifs relativement rigides de Nanling et de Wuyi. Ces failles ont servi de conduits potentiels pour le transfert thermique en profondeur au Mésozoïque inférieur, favorisant la migration ascendante de la chaleur et entraînant une anomalie thermique positive.

De plus, de multiples gisements de tungstène-étain d'âge jurassiques se sont développés le long de la faille majeure de Ganjiang, suggérant une autre réactivation pendant le Mésozoïque supérieur. Le réseau de failles secondaires au sein de cette faille majeure a probablement également fourni un conduit pour les fluides minéralisateurs jurassiques, resultant en distribution groupée des gisements jurassiques dans cette région.

(5) Contexte géodynamique du Bloc de Cathaysia au Mésozoïque inférieur

Pendant le Mésozoïque inférieur le Bloc de Cathaysia était entouré de plusieurs blocs et impliqué dans une transition tectonique de domaines de la fermeture de l'Océans Paléo-Téthys à la subduction de l'Océans Paléo-Pacifique (Fig. 6). Au Permien vers ~310−258 Ma (e.g., Carter A et al., 2001; Li YJ et al., 2016; Wang YJ et al., 2018; Wang Y et al., 2022; Lin W et al., 2024), la subduction de l'Océan Paléo-Téthys a non seulement conduit à sa fermeture mais aussi à la collision entre le Bloc de l'Indochine et le Bloc de Chine du Sud vers ~258−240 Ma (e.g., Faure M et al., 2014, 2016a; Li YJ et al., 2016; Wang YJ et al., 2018; Gao W et al., 2022), resultant en un épaississement crustal atteignant jusqu'à ~60 km. Durant ce processus, les roches supracrustales ont été enfouies à de profondeurs dépassant 20 km, correspondant à des pressions excédant de 7 kbar. En raison de l'accumulation de chaleur radioactive et de l'apport thermique mantellique, la croûte épaissie a partiellement fondu, et le magma produit par cette fusion partielle a migré vers le haut en formant des intrusions granitiques. La zone de transition entre les domaines ductile et fragile a constitué la principale barrière mécanique durant l'ascension magmatique (Vigneresse JL, 1995; Burchardt S, 2009), l'arrêtant à de profondeurs croûte moyenne. Tant l'accumulation thermique des intrusions magmatiques au sein de la croûte que la chaleur radioactive provenant de la croûte épaissie ont contribué à de températures relativement élevées, dépassant le solidus des roches supracrustales profondément enfouies, et ont produit une fusion partielle et des migmatites en dôme dans la croûte moyenne vers ~240 Ma.

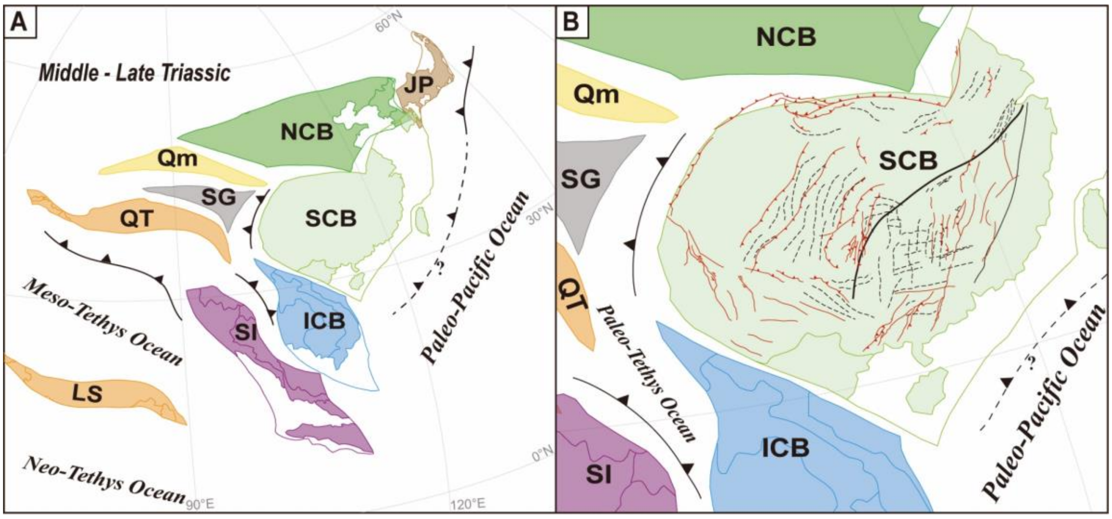

Figure 6. *(A) Cartes de reconstruction du Trias moyen à supérieur de la Chine du Sud et de ses blocs adjacents (modifiées d'après Scotese C, 2016). (B) Les structures (failles et plis) du Trias moyen à supérieur au sein du bloc de Chine du Sud en réponse à l'interaction entre les blocs adjacents.*

Parallèlement, les collisions du bloc de Chine du Nord avec Le Bloc de Chine du

Sud vers ~246−220 Ma et du Bloc de Qiangtang avec Le Bloc de Chine du Sud vers ~235−230 Ma ont probablement provoqué des réponses plus marquées au sein de la lithosphère du Bloc de Cathaysia. Par exemple, la réactivation de la chaine orogénique néoprotérozoïque de Jiangnan, l'augmentation du gradient géothermique du centre du Massif de Nanling vers la chaine orogénique de Jiangnan, ainsi que le métamorphisme de haute température identifié au Nord du Massif de Wuyi et l'Est de la chaine orogénique de Jiangnan.

Concernant les structures d'orientation NE, elles sont probablement de conséquence de la subduction et la fermeture de l'océan Paléo-Téthys situé au Nord-Ouest du bloc de Chine du Sud. La force motrice s'est propagée à travers le craton rigide de Yangtsé et a produit la déformation d'orientation NE au niveau des zones intracontinentales préexistantes en faiblesse de la déformation, telles que la chaine orogénique de Jiangnan (Xuefengshan) et la zone de Badu. Ensuite, la contrainte accumulée continue de s'étendre à l'intérieur du Bloc de Cathaysia.

La décompression résultant de l'effondrement post-collision de l'orogène indosinien vers ~240−200 Ma a facilité la fusion partielle, entraînant une diminution significative de la résistance rhéologique crustale. La présence de la plaque Paléo-Pacifique au Sud-Est a contraint l'extrusion latérale de l'écoulement crustal. Sous le champ de contraintes combinées, la croûte moyenne-inférieure à faible viscosité a flué horizontalement dans la direction NE-SO. La partition des déformations a montré différents modes de déformation selon les localisations, à savoir un écoulement horizontal au cœur du dôme et un décrochement avec l’écoulement vertical au niveau de la bordure. Une exhumation et un refroidissement rapides se sont produits dans le Sud du Bloc de Cathaysia pendant ~240−215 Ma.

La déformation, le métamorphisme et l'état thermique crustal du Bloc de Cathaysia au Mésozoïque inférieur résultent de l'interaction entre les multiples blocs, particulièrement le long de la marge de la Paléo-Téthys. La force motrice principale provient de la collision avec le Bloc de l'Indochine.

Mots clés: Rhéologie lithosphérique, État thermique crustal, Déformation et métamorphisme, Modélisation géodynamique, Mésozoïque inférieur, Chine du Sud.

Chapter 1. General introduction

1.1 Plate rigidity and lithospheric rheology

The theory of *Plate Tectonics* has been considered as a fundamental principle in the field of solid earth science since the 1960s (McKenzie DP and Parker RL, 1967; Le Pichon X, 1968; Morgan WJ, 1968). It is a brand-new concept and framework for describing and predicting the lithosphere's behavior and interpreting the planet's evolution. The fundamental premises of the plate tectonics theory are rigid lithospheric plates, persistent plate margins, and horizontal differential movement (Le Pichon X et al., 1973; Zheng YF, 2021). It was considered that the major deformation, metamorphism and magmatism were concentrated at the narrow mobile belts——plate boundaries (Fig. 1.1), the massive deformation cannot be absorbed in the interior of the plate, thus intraplate deformation was neglected (McKenzie DP and Parker RL, 1967; Morgan WJ, 1968; Le Pichon X et al., 1973).

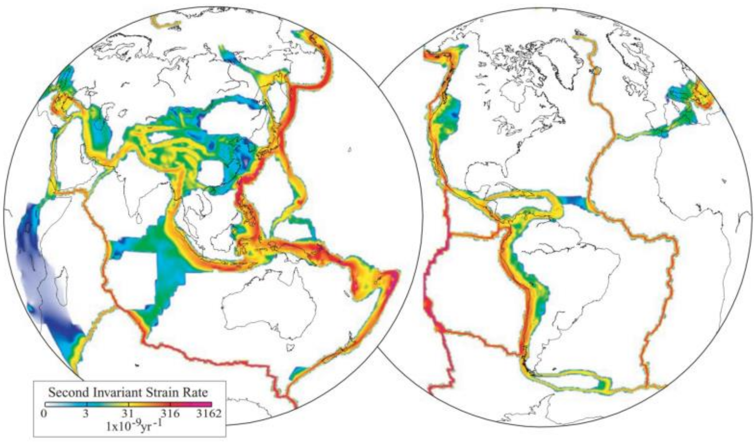

Figure 1.1. *The global second invariant strain rate field (Kreemer C et al., 2003), showing the deformation along the rigid plate boundaries.*

However, as Le Pichon X et al. (1973) mentioned in the book *Plate Tectonics*, the limitations of the definition are that 1) the mobile belt has a non-negligible width and may be more diffusive in the interior of the plate, and 2) the plates have a property of visco-elasticity rather than perfect rigidity. More recent studies found that some plates escape the initial definition of plate tectonics due to pervasive deformation and sometimes widespread distributed magmatism. Currently, the intracontinental orogenesis around the world are Neoproterozoic Petermann Orogen and Paleozoic Alice Springs Orogen in Central Australia (e.g., Lambeck K, 1983; Scrimgeour and Close, 1999; Aitken AR et al., 2009; McLaren S et al., 2009; Raimondo T et al., 2014), Early Paleozoic South China intracontinental orogen in East Asia (e.g., Faure M et al., 2009; Charvet J et al., 2010; Shu LS, 2012; Shu LS et al., 2015), Late Mesozoic Pyrenees Orogen in Europe (e.g., Boillot G and Capdevila R, 1977; Ford M and Vergés J, 2021), Cenozoic Tian Shan and Altai Orogens in Central Asia (e.g., Molnar P and Tapponnier P, 1975; Cunningham D, 2005; Yin A, 2010; Chen HL et al., 2022; Li W et al., 2022), Late Mesozoic Laramide Orogen in North America (e.g., Livaccari RF et al., 1981; Marshak S et al., 2003) and Atlas Orogen in North Africa (e.g., Gomez F et al., 1996; Gomez F et al., 2000; Bracène R and Frizon de Lamotte D, 2002). It is worth noting that the fundamental reason for the difference between the wide pervasive deformation within the plate and the narrow deformation belt along the plate boundaries mainly lies in the complex intrinsic rheological properties of the continental lithosphere (Ranalli G, 1995; Burov E and Yamato P, 2008; Zhang JJ et al., 2019).

Rheology is the study of the flow and deformation of matter in response to stress (Reiner M, 1958). *Lithospheric rheology* is the response of the lithosphere to stress within the Earth. It governs the deformation of the rocks and can be studied from the perspectives of time, temperature, stress, strain and other parameters (Ranalli G, 1997; Liu SW et al., 2007; Bürgmann R and Dresen G, 2008). After a long period of evolution, the rheological properties of the continental lithosphere display strong lateral heterogeneity and vertical stratification, the variation of the thermal gradient and the stratification of the lithosphere (Ranalli G and Murphy DC, 1987; Vauchez A et al., 1998). Currently, three representative rheological profiles of the continental lithosphere were proposed: jelly sandwich model, crème brûlée model (Jackson J, 2002) and banana split model (Afonso JC and Ranalli G, 2004; Burov EB and Watts AB, 2006; Bürgmann R and Dresen G, 2008). The heterogeneous rheology of the continental lithosphere determines the different rheological behaviors of the continental materials under various stress and physicochemical conditions. It also strongly controls the reactivation of the crust, as well as the locations and the kinematics of the orogenic belts. The rheology plays a decisive role in the formation and evolution of continental plates and orogenic belts, and can explain the tectonics at different scales involved in different branches of earth sciences (Cunningham D and Zhang J, 2021). If the lithosphere is composed of the strong crust and lithospheric mantle, its deformation, metamorphism and magmatism will be mainly concentrated at the plate margins, forming a linear and narrow cold orogenic belt which is dominated by the lateral motions, such as the Andes orogenic belt. In contrast, a planar and wide hot orogenic belt will be developed if the lithosphere is composed of weak crust and lithospheric mantle, and this hot orogenic belt will be dominated by the vertical flow and lack of strain localization, such as the Precambrian Yavapai of the Southwestern United States (Fig. 1.2; Cagnard F et al., 2006; Chardon D et al., 2009; Gapais D et al., 2009).

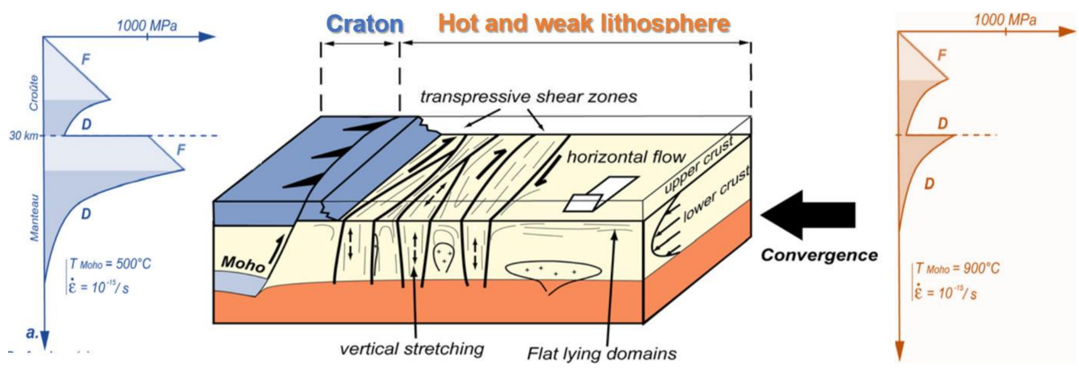

Figure 1.2. *Two types of rheological profile and their possible effects on the behaviors of continental lithosphere (modified after Gapais D et al., 2005).*

However, the rheology of the lithosphere is governed by a multitude of factors and it varies as a function of a number of constitutive and environmental aspects (Bürgmann R and Dresen G, 2008), for example, the crust structure (e.g., Wang LS et al., 2000; Jin S et al., 2022), rock assemblages, melt fraction (e.g., Chen Z et al., 2017), inherited structures (e.g., Shu LS et al., 2015; Heron PJ and Pysklywec RN, 2016), temperature structure (e.g., Goes S et al., 2020; Yang P and Liu SW, 2024), etc. The different crustal layering structure and petrological assemblages can result in different rheological profiles of the lithosphere (Ranalli G and Murphy DC, 1987). When the melt fraction exceeds 25%, the strength of the rock rapidly decreases to less than 10% of its original value (Lejeune A-M and Richet P, 1995; Rosenberg CL and Handy MR, 2005; Chen Z et al., 2017; Chiaraluce L et al., 2017), and the accumulation of the melt causes the crustal failure and facilitates large-scale plastic flow deformation within the lithosphere (Hollister LS and Crawford ML, 1986; Brown M, 2001, 2007). The pre-existing sutures and fault zones, as well as deformation belts, play a critical role in the later event. These inherited structures significantly influence strain distribution and the migration of melts and heat (Heron PJ and Pysklywec RN, 2016; Balázs A et al., 2017; Xue L et al., 2024). High heat flow or geothermal gradient can notably soften the crustal rocks and reduce the strength of the lithosphere. The decreasing rigidity of the softened lithosphere with more plastic behavior affects the deformation pattern and strain distribution, and then controls the geodynamic evolution of the orogenic belt (Goes S et al., 2020; Sun YY et al., 2022; Xu JS and Zeng XF, 2022; Sun YJ et al., 2025).

1.2 Scientific questions

The South China Block (SCB) was formed through the collision and amalgamation of the Yangtze and Cathaysia blocks during the Neoproterozoic, resulting in the sandwiched Jiangnan Orogenic Belt (Yao JL et al., 2014; Xia Y et al., 2018; Shu LS et al., 2019, 2021). Hereafter, it experienced a long-term polyphase tectonic evolution. Following the amalgamation between the Yangtze and Cathaysia blocks, intracontinental rifting and bimodal volcanism developed at the Late Neoproterozoic. Affected by the Proto-Tethys Ocean, Paleo-Tethys Ocean and Paleo-Pacific Ocean, the SCB witnessed the Early Paleozoic intracontinental orogeny (Charvet J et al., 2010; Wang YJ et al., 2012, 2013; Shu LS et al., 2015), Early Mesozoic intracontinental reworking (Wang YJ et al., 2007a, 2021; Lin W et al., 2008; Chu Y et al., 2012a, 2012b; Shu LS et al., 2015; Cochelin B et al., 2022; Li JH et al., 2022b) and Late Mesozoic multi-phase lithospheric compression and extension, as well as the basin-and-range tectonics (Zhou XM et al., 2006; Li ZX and Li XH, 2007; Li ZX et al., 2012; Wei W et al., 2015; Li JH et al., 2018, 2024; Li SZ et al., 2019). The studies on the tectonic framework, deformation pattern and geodynamic evolution of the SCB, can shed light on the tectonic evolution of the East Asian Continent. As an important part of the SCB, the Cathaysia Block displays distinct deformation behaviors with respect to the Yangtze Block, and creates conditions to explore the deformation pattern, tectonic events and strain distribution of multi-stage structures. It can help us to reveal its tectonic evolution and geodynamic characteristics, recognize intracontinental deformation, and, consequently, understand the rheological properties and plate rigidity characteristics of the continental lithosphere of the SCB.

The predecessors have done a lot of work on the deformation pattern and kinematic, magmatism, metamorphism, metallogeny and tectonic evolution of the Cathaysia Block and have obtained fruitful results. However, there are still some issues that need to be addressed:

1.2.1 What were the characteristics of the Early Mesozoic deformation and metamorphism in the Yunkai Massif?

Previous studies have documented the Early Mesozoic structural deformation pattern in the Yunkai Massif (Fig. 1.3). Wang YJ et al. (2007a, 2021) revealed Early Triassic top-to-north dextral thrusting and Late Triassic NE-trending sinistral transpression, occurring under the amphibolite-facies and greenschist-facies conditions. The grade of deformation decreases northward (Fig. 1.3A). Lin W et al. (2008) reported the Early Paleozoic top-to-the-northwest extension under the amphibolite-facies condition, Early Mesozoic top-to-the-northeast thrusting under the conditions from amphibolite-facies to greenschist-facies, and Late Mesozoic compression and normal fault (Fig. 1.3B). Faure M et al. (2016b) emphasized a 100 km-scale basement nappe overthrusting northward onto the Late Paleozoic sedimentary rocks (Fig. 1.3C). Although the above studies generally recorded a northward thrust during the Early

Mesozoic, Cochelin B et al. (2022) recently found an Early Mesozoic deep crustal NE-SW lateral flow in the Yunkai Massif (Fig. 1.3D), suggesting the structural pattern of the Yunkai Massif needs further discussion.

A great volume of high-grade metamorphic rocks (e.g., granitic gneiss, paragneiss, granulite) and migmatites were developed in the Yunkai Massif. The precise timing constraints on the high-grade metamorphism play a crucial role in understanding the partial melting and upward emplacement of melts, and the evolution of orogenic belts. An Early Mesozoic high-temperature metamorphism (>850 °C) was reported based on the studies of the charnockite and granulite enclaves (Zhao L et al., 2010, 2012; Jiao SJ et al., 2013, 2015). At the center of the Yunkai Massif, Early Paleozoic charnockite and high-pressure pelitic granulites and gneisses (7.8−9.5 kbar / 840−870 °C) were reported (Li C et al., 2020a, 2025).

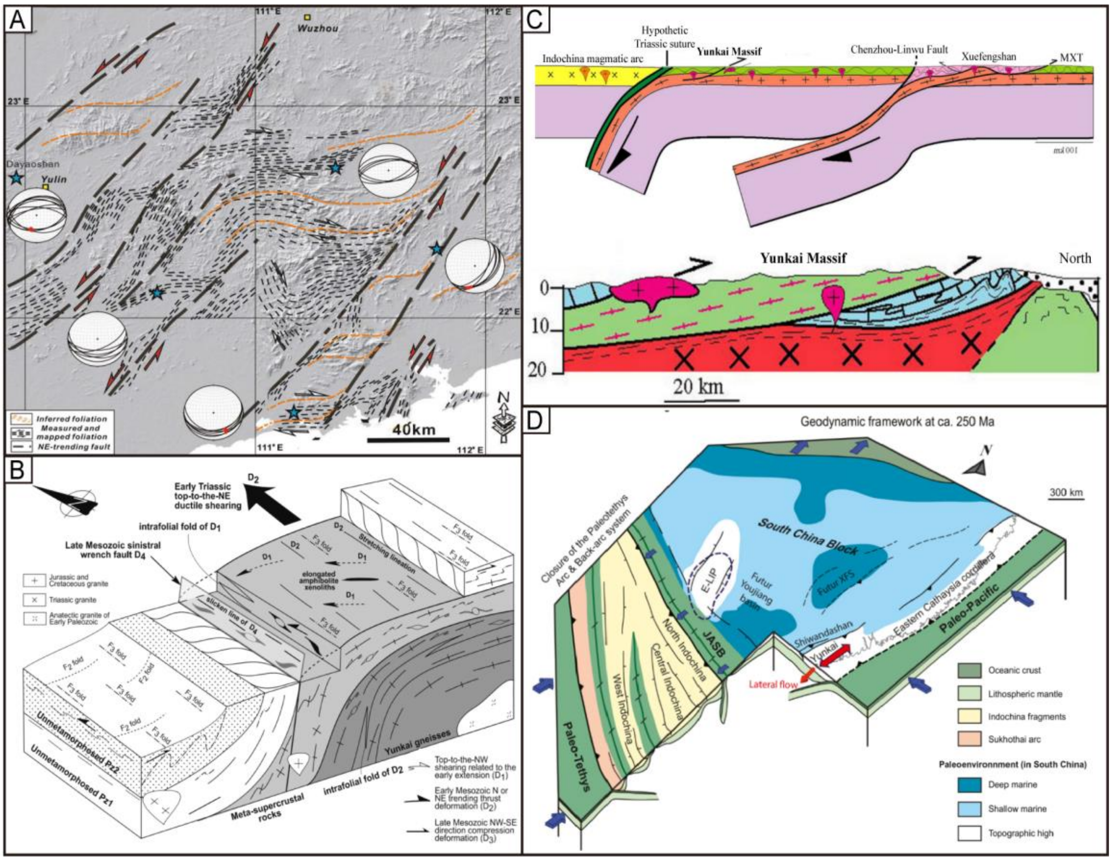

Figure 1.3. *Structural deformation pattern in the Yunkai Massif (modified after Lin W et al., 2008; Faure M et al., 2016b; Wang YJ et al., 2021; Cochelin B et al., 2022).*

Despite advances in the metamorphic petrology in the western and central parts of the Yunkai Massif, the precise timing, pressure-temperature conditions of the migmatites to the east of Yunkai, and their relationship with the granitic intrusions remain a subject of ongoing debate. Existing geochronological data yield discrepant ages for the high-grade metamorphism, for example, Neoproterozoic (Chen Z et al., 2021), Early Paleozoic (Zhou DY and Xu XS, 2017; Zhang JH et al., 2019, 2023) and Early Mesozoic (Ke XZ et al., 2018; Wang XD et al., 2020). Most of the researchers emphasized the Early Paleozoic Orogeny and high-temperature metamorphism, however, the effect of the Early Mesozoic event has been substantially underestimated in previous studies. In addition, people focus more on geochronology and metamorphic temperature. For example, Wang XD et al. (2020) calculated the Ti saturation temperature of biotite at 650−700°C, and Zhang JH et al. (2017) estimated the temperature at 630−705 °C based on the melt fraction. However, relatively limited attention has been paid to the petrological metamorphic pressure-temperature conditions and the genetic relationship between migmatites and granites.

1.2.2 How was the Cathaysia Block's homogeneity and rigidity during the Early Mesozoic?

The closure of the Paleo-South China Ocean at 900−850 Ma triggered the collision and amalgamation of the Yangtze and Cathaysia blocks, culminating in the final assembly of a unified SCB, Proto-South China Continental (Shu LS et al., 2021) at ca. 850−800 Ma (Yao JL et al., 2014; Zhang YZ et al., 2015; Zhao GC, 2015a; Xia Y et al., 2018). The SCB experienced a second-stage breakup at ~825 Ma, resulting in the formation of the three massifs: Nanling (located at the central and southern Jiangxi province and southern Hunan province), Wuyi (located at the southern Zhejiang province, Fujian province and northern Guangdong province) and Yunkai (located at the eastern Guangxi province and western Guangdong province; Fig. 1.4). These massifs were bounded by rift systems and oceanic troughs, where thick sequences of Early Sinian to Late Ordovician clastic sediments were deposited (Shu LS, 2006; Shu

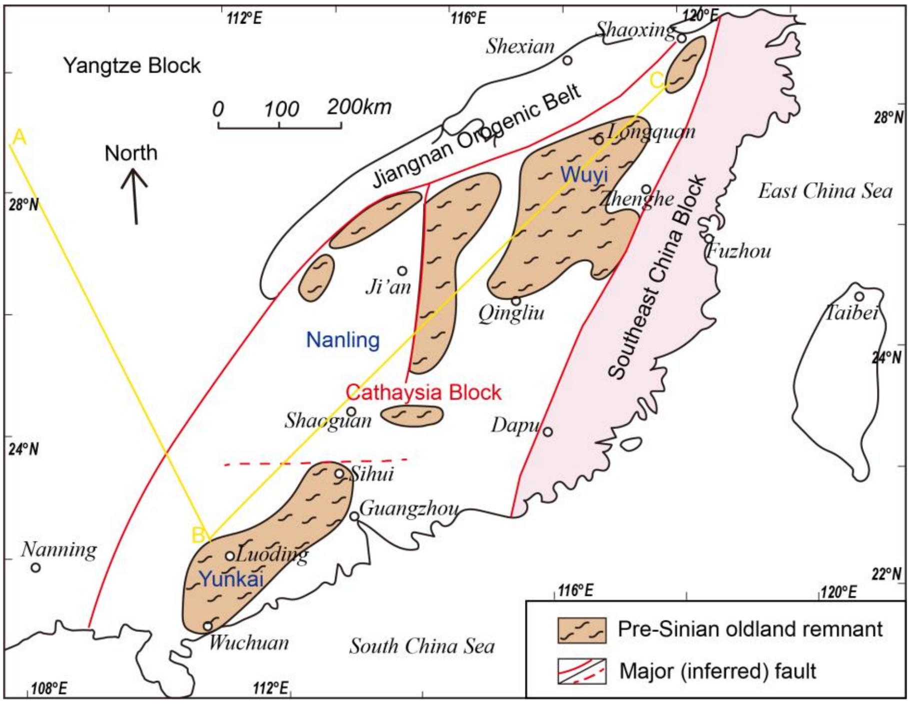

Figure 1.4. *Distribution of the Pre-Sinian oldland remnant within the Cathaysia Block (modified after Shu LS, 2006). The yellow line is the section presented in Figure 1.5.*

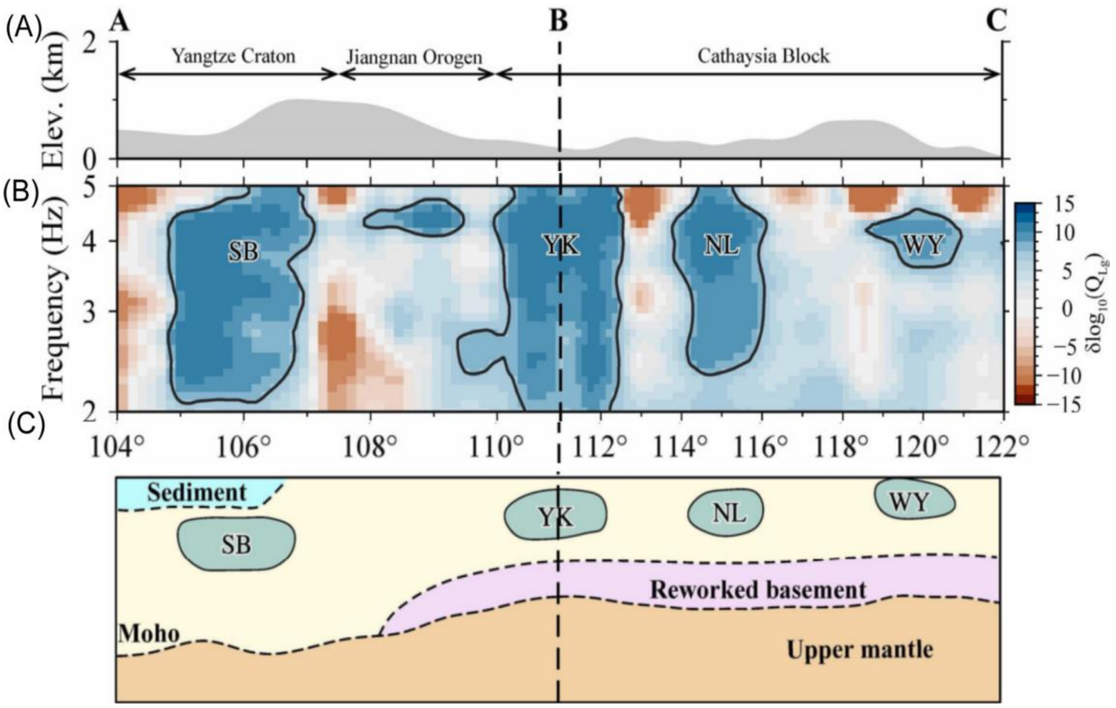

Figure 1.5. *Cross-section along potential ancient continental remnant in the South China Block (modified after Shen L et al., 2023), including topography (A), percentage Q_{Lg} perturbations versus frequency between 2.0 and 5.0 Hz (B) and inferred ancient continental remnant (C).*

LS et al., 2021). Afterwards, they evolved together and experienced the Early Paleozoic intracontinental orogen, Early Mesozoic reworking and Late Mesozoic Paleo-Pacific subduction. However, the field investigation revealed that the Wuyi Massif exposed the most extensive outcrops of Precambrian basement rocks, followed by the Yunkai Massif, while the Nanling Massif displays the least exposure of basement strata. The latest geophysical data found the extremely weak Lg attenuation within the Cathaysia Block, corresponding to the Wuyi, Nanling and Yunkai massifs, respectively (Fig. 1.5; Shen L et al., 2023). This novel discovery reflects the distribution of the core of the ancient continent. The above findings demonstrate that the Cathaysia Block lacks a unified, coherent basement, exhibiting a pronounced heterogeneity in basement distribution.

Regional unconformity between the Early Mesozoic and Late Mesozoic was developed within the Cathaysia Block. The pre-Triassic strata displayed intense and pervasive deformation, dominated by thrust and fold, ductile shearing zones and crustal shortening. The Early Mesozoic deformation and metamorphism were extensively distributed within the Cathaysia Block, rather than exhibiting a linear or zonal pattern along block margins (Shu LS, 2012; Wang YJ et al., 2013, 2021; Zhang GW et al., 2013; Song MJ et al., 2017; Shu LS et al., 2021). A detailed investigation into the Early Mesozoic magmatism was conducted in previous studies. People found that Early Mesozoic magmatism within the Cathaysia Block lacks distinct spatiotemporal migration regularity, neither along the SE-NW or the SW-NE cross-sections (Wang YJ et al., 2013). In contrast, the magmatism displays a planar distribution in a block scale rather than along a linear and narrow magmatic belt (Gao P et al., 2017; Liu JX et al., 2020). Furthermore, the statistics of the Early Mesozoic magmatism revealed that they are strongly peraluminous with A/CNK > 1.1, covering an area exceeding 15,200 km^2 and accounting for 72% of the total granites from this period (Sun T, 2006; Zhou XM et al., 2006), representing typical granites sourced from the crustal partial melting.

Similar to the magmatism, the Early Mesozoic metamorphism also displays the planar distribution without any significant spatiotemporal migration regularity. Notably, it is dominated by the high-temperature metamorphism, with migmatization somewhere, for example, the migmatite in Xinyi, Yangjiang and Zengcheng (Zhou HW et al., 1997; Yu JH et al., 2008; Wang YJ et al., 2013; Cochelin B et al., 2022).

The Cathaysia Block exhibited pervasive penetrative deformation, planar distributed strongly peraluminous magmatism and high-temperature metamorphism during the Early Mesozoic, indicating rheological behavior distinct from typical rigid blocks. Currently, the studies on the Early Mesozoic rheological properties of Cathaysia remain limited. To advance our understanding of the Cathaysia Block's unique rheological behavior during the Early Mesozoic, it is necessary to largely investigate its rheological properties and understand the mechanistic constraints on these parameters exerting on deformation styles, stress partitioning, and long-term geodynamic evolution.

1.2.3 How was the Early Mesozoic crustal thermal state of the Cathaysia Block?

Thermal state is the crucial factor to assess lithospheric rheology. The pattern and distribution of the deformation during the orogenesis and crustal seismic velocity structure are significantly controlled by the thermal state (Fossen H et al., 2017; Shen WS et al., 2020; Vlaha DR et al., 2024). A hot and weak lithosphere is dominated by dispersive deformation and vertical crustal flow. In contrast, a cold and strong lithosphere is characterized by linear or banded deformations and strain localization (Cagnard F et al., 2006; Chardon D et al., 2009). The Cathaysia Block experienced multi-stage orogenies and developed pervasive deformation and planar distributed magmatism during the Early Mesozoic, making it an ideal laboratory for examining the rheology and rigidity of this lithosphere plate. In addition, the Cathaysia Block exhibits signs of heterogeneity in the geophysical fields, e.g., Lg wave attenuation, the ratio of the Vp/Vs, and the crustal radial anisotropy (Guo LH et al., 2019; Li TZ et al., 2023; Shen L et al., 2023).

The modern lithospheric thermal state can be constrained by direct and indirect methods (Goes S et al., 2020). For example, heat flow measurements from the surface or drillholes (Mareschal J et al., 2000; Lewis TJ et al., 2003), petrology of mantle xenolith (Canil D and Russell JK, 2022; Zieman L et al., 2023), seismic wave (Shen WS et al., 2020; Waszek L et al., 2021), magnetic observation (Sánchez MA et al., 2019) and thermal isostasy (Artemieva IM, 2019). Fruitful studies on the thermal state and heat flow of the Cathaysia Block have provided significant insights into the geothermal characteristics. For instance, Hu SB et al. (2000) reported a present-day high heat flow of 52−97 mW/m^2 of Cathaysia based on the measurements within drill holes. Yang P and Liu SW (2024) proposed a hot and weak lithosphere of Cathaysia by integrating the heat flow, xenoliths and Pn seismic velocity data. However, they are the present-day thermal state related to the geodynamic processes since the Late Mesozoic. The constraints on the paleo-thermal state are indispensable for understanding the lithospheric rheology and tectonic evolution during geological history.

Due to the long-term complex geological processes involved and the scarcity of direct observational data, studying the thermal state of ancient orogenic belts remains challenging. Even so, the potential for unraveling by the metamorphic petrology, thermo-chronology and numerical modelling remains (Perchuk AL et al., 2018; Petroccia A et al., 2022; Wu HL et al., 2023). The Early Mesozoic thermal state of Cathaysia has been attempted to be explored by estimating the temperature of the quartz dynamic recrystallization (Cochelin B et al., 2022), mineral thermometer (Zhao L et al., 2012) and thermo-chronometers (Tao N et al., 2019). The temperature can be estimated based on the dynamic recrystallization of the quartz, i.e., bulging (BLG), subgrain rotation (SGR) and grain boundary migration (GBM), which were determined by the temperature. In addition, both the mineral thermometer within the metamorphic rocks and the several closure temperatures of the multi-geochronology can also provide constraints on the temperature. However, previous studies were limited to the observation at isolated positions, lacking sufficient resolution to elucidate spatial variations.

1.2.4 What were the influences of inherited/pre-existing structures on subsequent crustal thermal state in the Cathaysia Block?

The pre-existing structures developed during the previous tectonic events preferentially reactivated during the subsequent orogeny, they will significantly control the locations of the strain localization, the distribution of the deformation and metamorphism, as well as the emplacement of the magmatism (Butler RWH et al., 2006; Balázs A et al., 2017). The localizing deformation preferentially developed along the pre-existing structures, resulting in the heterogeneous distribution of shear zones and metamorphic facies. Mostly Archean shear zones were reactivated during the subsequent orogeny (Prasannakumar V and McCaig A, 2016; Bhowmick S and Mondal TK, 2020). The pre-existing structures acting as fluid channels can enhance connectivity and permeability and facilitate the migration of mineral-forming elements and fluids. The world-class ore deposits are spatially correlated with crustal-scale fault reactivation (Groves DI et al., 2018), for example, the gold deposits in Peru (Wiemer D et al., 2022). Additionally, the pre-existing major fault zones are the potential heat channels creating sustained thermal anomalies (Kebede H et al., 2022). Thus, structural inheritance can help to understand the heterogeneity of the deformation and metamorphism and rheology of the continental lithosphere.

The Cathaysia Block has a long geological history, including the Neoproterozoic collision and rifting, and the Early Paleozoic intracontinental orogeny (Yu JH et al., 2007; Charvet J et al., 2010; Wang YJ et al., 2013; Shu LS et al., 2021). Many of the structures developed during that time became a part of the inherited structures and were reactivated during the Early Mesozoic and subsequent events. The previous research revealed that these pre-Mesozoic inherited structures control the emplacement and shape of the subsequent magma, for example, the Guposhan-Huashan pluton in the Nanling Massif, the Shibei Pluton in the Wuyi Massif (Feng ZH et al., 2011; Liu HS et al., 2020). The close spatial relationship between the faults and the deposits in the Nanling Massif reveals that the pre-existing faults provided a favorable condition for

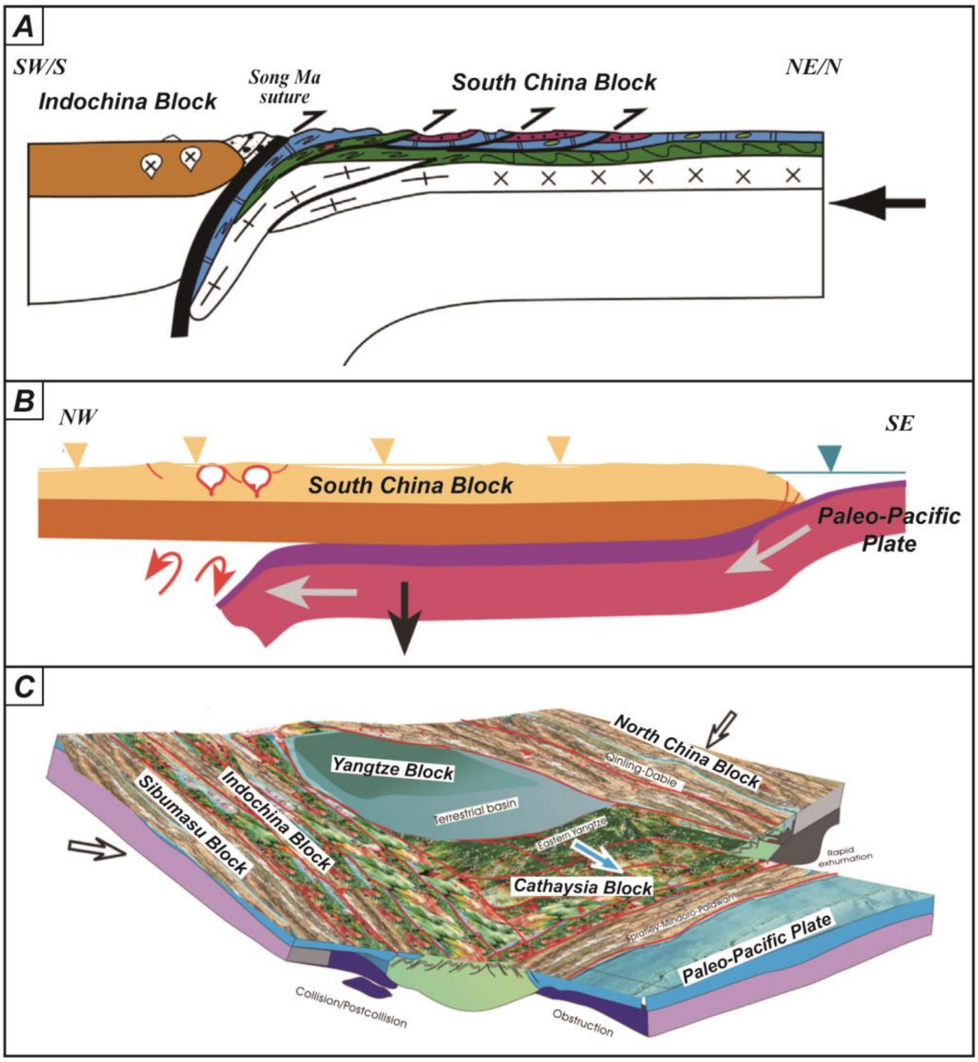

Figure 1.6. *Examples of the different geodynamic models of the Early Mesozoic South China Block. (A) The southward subduction model of the Paleo-Tethys Ocean (modified after Faure M et al., 2014). (B) The flat-slab subduction model of the Paleo-Pacific Plate (modified after Li ZX and Li XH, 2007). (C) The multi-block-confined intracontinental orogenesis model (modified after Wang YJ et al., 2013).*

the transportation, aggregation and mineralization of ore-forming fluids (Peng N et al., 2023). However, there is no further report about the effect on the crustal thermal state.

1.2.5 What was the Early Mesozoic geodynamic background of the Cathaysia Block?

It is worth noting that the orogeny in South China dominantly occurred in the interior of the block. The deformation was pervasive, and the metamorphism and magmatism were planar distributed, especially in the Early Paleozoic and Early Mesozoic (Zhou XM et al., 2006; Li ZX and Li XH, 2007; Wang YJ et al., 2013; Liu JX et al., 2020). Based on observations on the characteristics of deformation, metamorphism and magmatism, different tectonic models of the Early Mesozoic Cathaysia Block were proposed in previous studies (Fig. 1.6). The traditional subduction model suggests that the southward subduction Paleo-Tethys Ocean beneath the Indochina Block (ICB) and the subsequent ICB-SCB collision are attributed to the deformation behaviors in the Cathaysia Block (Faure M et al., 2014; Wang Y et al., 2022; Lin W et al., 2024). Alternatively, the Paleo-Pacific Ocean subduction model emphasized a driving force from the southeast. These researchers argued for a westward flat subduction beneath the SCB based on the magmatism distribution, deformation pattern and the newly discovered arc volcanism in the South China Sea margin (Li ZX and Li XH, 2007; Li CL et al., 2021; Xu F et al., 2022). Moreover, a multi-plate model has recently been proposed. This model argues that the interactions between the SCB and its surrounding plates result in the intracontinental reworking (Wang YJ et al., 2013, 2021).

Given the above controversies of the geodynamic models, further investigations and discussions into the tectonic setting are essential to clarify the geodynamic mechanisms of the behaviors of the Cathaysia Block.

1.3 Research focuses

Considering the above questions, this thesis focuses on the rheological properties of the lithosphere of the Early Mesozoic Cathaysia Block, which can provide a new perspective to understand the relationship among the deformation, metamorphism and thermal state of the Cathaysia Block, and provide clues for its tectonic evolution.

First, the Yunkai Massif serves as an ideal representative area for investigating the characteristics of deformation and metamorphism. Located to the southwest of the Cathaysia Block, it exhibits extensive intracontinental magmatic, metamorphic and deformation zones. Moreover, the Yunkai Massif is located at the intersection of the Paleo-Tethys and Paleo-Pacific tectonic domains, making it a critical window for studying the transition from Paleo-Tethys to Paleo-Pacific tectonic systems. The widespread exposure of the granitoids and migmatites within the Yunkai Massif provides critical insights into the mechanical behavior of the middle to lower crust.

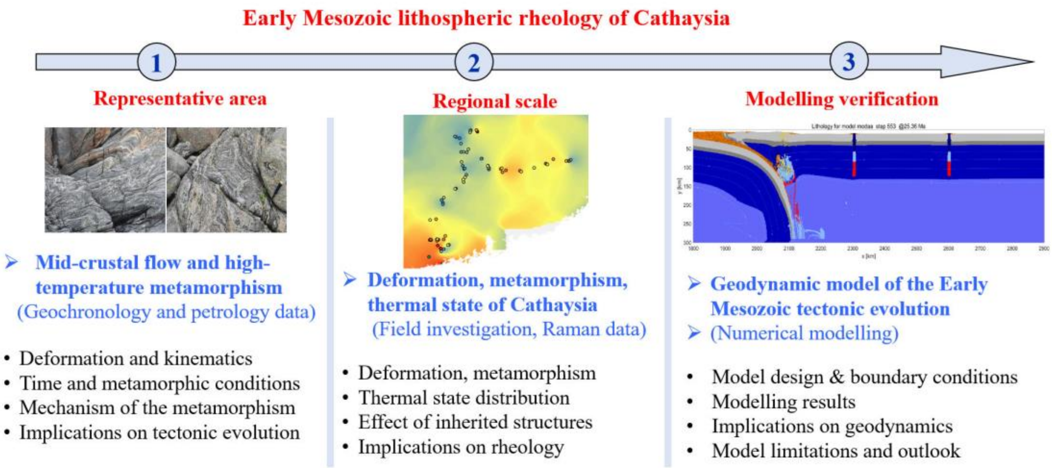

Figure 1.7. *Diagram of the research strategy and research contents.*

Then, in a broader block scale, we further examine the distribution regularity of the deformation, metamorphism and crustal thermal state within the Cathaysia Block. The heat is a primary controlling factor on the lithospheric rheology, while the deformation and metamorphism can provide additional constraints on the crustal thermal state. Furthermore, the thermal state can help to identify the potential thermal anomaly and assess the influence of the inherited structures.

Finally, the geodynamic modelling provides further validation to complement the geological observations. Integrating deformation, metamorphism, thermal state and geodynamic model enables a more comprehensive understanding of the Early Mesozoic geodynamic background of the Cathaysia Block (Fig. 1.7).

1.4 Research content

According to the above research strategy, the research content of this thesis includes the following four principal parts:

(1) Study on the deformation and metamorphism in the Yunkai Massif. The aim is

to reveal the deformation pattern, metamorphic condition and timing in the Yunkai Massif. The detailed work is on: i) the field structural investigation, aiming to determine the episode and style of the deformation in the Yunkai Massif; ii) the metamorphic petrological study and phase equilibria modelling, aiming to reveal the metamorphic stage and the P-T condition; iii) the multi-mineral (zircon, monazite, apatite and garnet) geochronology, aiming to determine the timing of the deformation, metamorphism and magmatism, as well as the effect of the deformation on the age record. This work was presented in Chapter 4 of this thesis.

(2) Study on the deformation and metamorphism in the Cathaysia Block. The aim is to reveal the regularity of the distribution and the grade of the deformation and metamorphism in the block scale. It is achieved by regional structural investigation and the compilation of the published data. This work was presented in Sections 5.2, 5.3 and 5.4 of this thesis.

(3) Study on the crustal thermal state of the Cathaysia Block. The aim is to reveal the regularity of the paleo-temperature variation and the paleo-geothermal gradients, as well as some potential thermal anomalies. The detailed work is on: i) the Raman temperature calculation, aiming to provide a new dataset and reveal the paleo-temperature and gradient of the Cathaysia Block; ii) the temperature estimation of the quartz dynamic recrystallization, aiming to provide further validation for the paleo-temperature and link the Raman temperature with the deformation; iii) the compilation of the published vitrinite reflection data, aiming to provide some validation for the Raman temperature. This work was presented in Section 5.5 of this thesis.

(4) Study on the geodynamic modelling. The aim is to validate the observations on the deformation, metamorphism and crustal thermal state, and help to understand the Early Mesozoic geodynamic background of the Cathaysia Block. This work was presented in Chapter 6 of this thesis.

Chapter 2. Regional geological background

2.1 Geological and tectonic framework

The SCB is situated at the southeast corner of the Eurasia Plate, which is the convergence center of the Philippine Plate, Indian Plate and Eurasia Plate nowadays (Fig. 2.1A). It is separated from the North China Block by the Qinling-Dabie ultra-high pressure metamorphic belt and Sulu Orogen to the north (Fig. 2.1B; Zhang KJ, 1997; Faure M et al., 2001; Dong YP et al., 2011). They are formed due to the subduction and closure of the northern branch of the eastern Paleo-Tethys Ocean (Mianlue Ocean) from Permian to Early Triassic, followed by the northern subduction of the SCB beneath the North China Block at ca. 240−225Ma (Dong YP et al., 2011; Wu YB and Zheng YF, 2013). To the northwest, the SCB is bounded by the Longmenshan Fault and separated from the Songpan-Ganzi and Qiangtang Blocks. Due to the closure of the northern branch of the eastern Paleo-Tethys Ocean at the Middle Triassic, Songpan-Ganzi Basin was filled by approximately 10−15km thick Middle to Upper Triassic flysch rocks (Nie SY et al., 1994; She ZB et al., 2006; Jian X et al., 2019; Song PP et al., 2020). To the south, the SCB subducted beneath the ICB along the Ailaoshan−Song Ma−Song Chay−Hainan suture zone, following the subduction and closure of the south branch of the eastern Paleo-Tethys Ocean at ca. 250−230 Ma (Findlay RH and Trinh PT, 1997; Wang EC and Meng QR, 2009; Zhang RY et al., 2013; Faure M et al., 2014).

The SCB is composed of the Yangtze Block in the northwest and the Cathaysia Block in the southeast (Fig. 2.2). They were separated by the Paleo-South China Ocean during the Neoproterozoic, which was characterized by the ophiolite suites extending 1500km along the Jiangshan-Shaoxing-Pingxiang-Longsheng belt (Guo LZ et al., 1989; Shu LS et al., 1991, 2019; Zhang SB et al., 2012; Yao JL et al., 2016). The closure of the Paleo-South China Ocean and the subsequent collision between the Yangtze Block and Cathaysia Block welded the SCB and formed the Jiangnan Orogenic Belt (Yao JL et al., 2014; Zhao GC, 2015b; Yan CL et al., 2019; Wang YY et al., 2022; Zhang FQ et al., 2025). The estimation of the final amalgamation was generally accepted to have

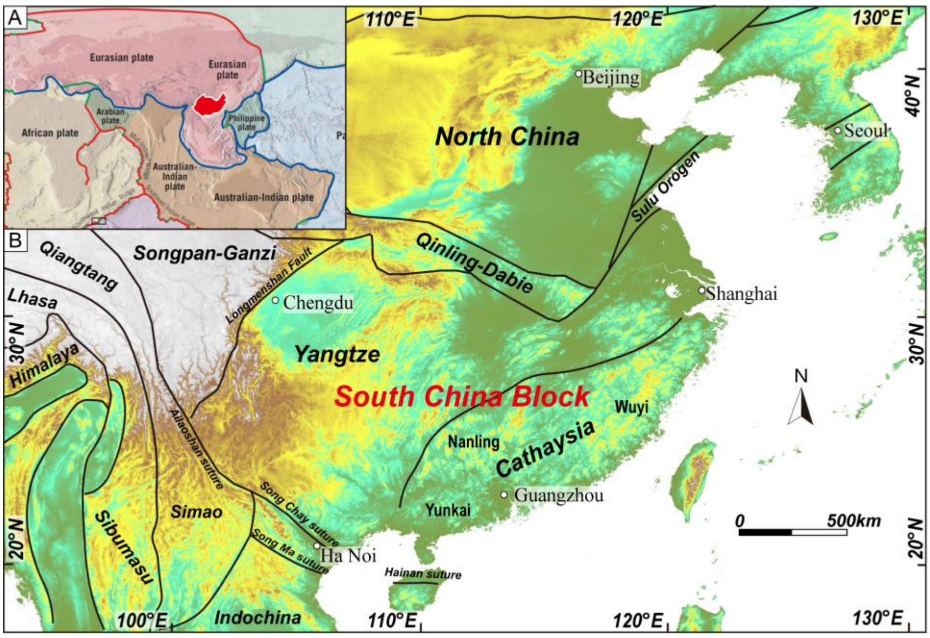

Figure 2.1. *Simplified tectonic framework of the South China Block. (A) The location of the South China Block in East Asia (modified after Tarbuck EJ et al., 2017). (B) The tectonic framework of East Asia, showing the South China Block and its surrounding blocks (modified after Li JH et al., 2017b).*

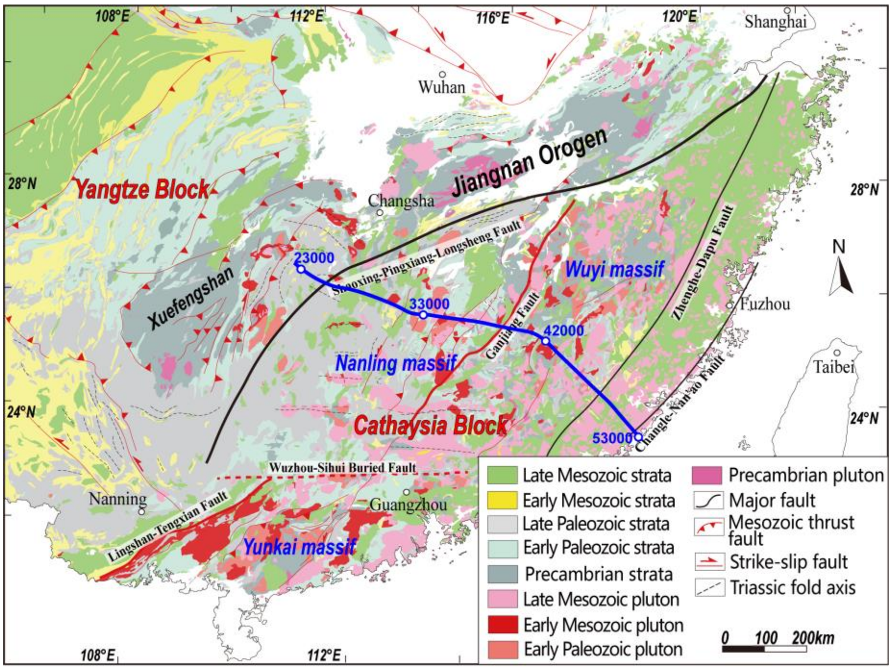

Figure 2.2. *Geological map of the South China Block (modified after China Geological Survey, 2020) shows the locations of the Yunkai, Wuyi and Nanling massifs. Blue line is the seismic profile in Figure 2.3.*

occurred during the Neoproterozoic at 850−800Ma (Yao JL et al., 2014; Zhang YZ et al., 2015; Zhao GC, 2015a; Sun JJ et al., 2018; Xia Y et al., 2018; Li QW and Zhao JH, 2020), although the time of the final assembly remains controversial. For example, some people consider the Jiangnan Orogen as a Grenvillian-aged orogen and proposed the final collision occurred at 1000−880Ma (Li ZX et al., 2007; Li XH et al., 2009a), some people proposed a Late Neoproterozoic (~635Ma, Zhang FQ et al., 2025), or even the Early Paleozoic amalgamation between Yangtze-West Cathaysia and East Cathaysia (Lin SF and Beakhouse GP, 2013; Lin SF et al., 2024).

2.2 Geological units in the Cathaysia Block and their characteristics

During the late 1980s, the researcher proposed the multiple terranes/massifs within the Cathaysia Block (Guo LZ et al., 1989). So far, the Cathaysia Block in South China has been widely recognized as comprising three major massifs, i.e., the Wuyi, Yunkai and Nanling massifs (Deng P et al., 2002; Shu LS, 2006, 2012; Yu JH et al., 2006, 2010; Shu LS et al., 2021; Shen L et al., 2023; Li JY et al., 2024). Several large-scale boundary faults define the tectonic units and control the distribution of the Mesozoic−Cenozoic sediments basin and plutons (Shu LS et al., 2004, 2006).

As the northern parts of the Cathaysia Block, the northern boundary of the Wuyi Massif is the Jiangshan-Shaoxing-Pingxiang-Longsheng Fault (Fig. 2.2; Shu LS et al., 2021). To the west, the boundary between the Wuyi and Nanling massifs is situated at the Ganjiang Fault Belt (Deng P et al., 2003; Liang X and Wu GY, 2006; Shu LS et al., 2021). To the east of the Wuyi Massif, it was separated from the Eastern Coastal Volcanic Belt by the Zhenghe-Dapu Fault (Cawood PA et al., 2020; Dong SW et al., 2020; Li TZ et al., 2023; Han S et al., 2025). The western boundary of the Nanling Massif is the Pingxiang-Longsheng-Guilin Fault (Shu LS et al., 2006, 2021; Guo LH and Gao R, 2018; Wang YD et al., 2021). However, some people argued for different locations of the boundaries, i.e., the Chenzhou-Linwu Fault (Wang YJ et al., 2003; Zhang ZJ et al., 2013; Li TZ et al., 2023) and Shizong-Mile-Luodian Fault (Ren JS, 1989; Zhao JH et al., 2011). The Yunkai Massif is situated to the southmost of the

Cathaysia Block. In the previous studies, its western and eastern boundaries were considered as the NE-trending Bobai-Wuzhou Fault and Wuchuan-Yangchun-Sihui shear zone (Shao JG et al., 1995; Wang YJ et al., 2007a; Lin W et al., 2008; Liu SF et al., 2018). To the north, the Yunkai Massif was separated from the Nanling Massif by the Wuzhou-Sihui Buried Fault (Shu LS et al., 2006).

2.2.1 Boundary Faults

These boundary faults, namely Jiangshan–Shaoxing–Pingxiang–Longsheng Fault, Zhenghe–Dapu Fault, Ganjiang Fault, Wuchuan–Yangchun–Sihui Fault, Bobai–Wuzhou Fault, and Wuzhou–Sihui Buried Fault (Fig. 2.2), were considered as the previous rifting valley or the deep-sea trough formed during the Neoproterozoic rifting of the Proto-South China Continent (Shu LS, 2006). They generally strike in NE and NNE directions, except for the Wuzhou-Sihui Buried Fault, which corresponds to the southern boundary of the Fogang-Xinfengjiang batholith and strikes in East/West (Fig. 2.2; Shu LS, 2006). The lengths of them exceeds 400 km and most have the width ranging from ~25−50km, and some individual one has a length reaching more than 1000 km, such as Jiangshan–Shaoxing–Pingxiang–Longsheng Fault, or a width more than 100 km with numerous second-level faults developed, such as Ganjiang Fault (Fig. 2.2; BGMRGD, 1988; Huang HL and Zheng JY, 2001; Shu LS and Zhou XM, 2002; Deng P et al., 2003; Nie TC and Zhu GL, 2004; Liang X and Wu GY, 2006; Shu LS et al., 2006; Bi BT et al., 2022).

Except for Wuzhou-Sihui Buried Fault which deep structure has not been revealed by the deep geophysical field (Shu LS, 2006), geophysical data (e.g., gravity, magnetic, and crustal thickness anomalies) consistently reveal the anomaly belts along these fault zones and suggest the transcrustal faults, forming major boundaries between different geophysical domains (BGMRGD, 1988; Hu KM, 2001; Deng P et al., 2003; Liang X and Wu GY, 2006; Guo LH and Gao R, 2018; Xu S et al., 2019; Yan JY et al., 2019; Dong SW et al., 2020; Bi BT et al., 2022; Han S et al., 2025; Wei YH et al., 2025). Significant differences of the crustal thickness can be observed on their two sides, for example, the Zhenghe-Dapu Fault caused a ~4-5 km difference in the crustal thickness (Dong SW et al., 2020; Han S et al., 2025). Geochemical anomalies, such as enrichment in Cu, Pb, Zn, Au, Ag, and Hg elements, as well as variations in Hf isotopes, also reveal these fault zones, highlighting their role in controlling polymetallic mineralization (Hu KM, 2001; Nie TC and Zhu GL, 2004; Cai HT et al., 2021; Zhang ZY et al., 2023).

Tectonically, these faults initiated during the Neoproterozoic and have been repeatedly reactivated through the Phanerozoic events (e.g., Nie TC and Zhu GL, 2004; Shu LS, 2006). For example, the Jiangshan-Shaoxing-Pingxiang-Longsheng Fault was reactivated by the Early Paleozoic (ca. 460–390 Ma) northward thrusting deformation and metamorphism, Early Mesozoic (ca. 234−232 Ma) sinistral ductile shearing, and Late Mesozoic compressional to extensional deformation (Hu KM, 2001; Zhang FF et al., 2012; Shu LS et al., 2015; Sun HS et al., 2018). Zhenghe-Dapu Fault, Ganjiang Fault and Wuchuan-Yangchun-Sihui Fault mostly behaved as large-scale sinistral striking-slip faults during the Early Paleozoic, Early Mesozoic and Late Mesozoic reactivation (Shui T et al., 1993; Shu LS et al., 1999; Deng P et al., 2003; Nie TC and Zhu GL, 2004; Wang YJ et al., 2007a; Lin W et al., 2008).

Their long-lived activity profoundly influenced regional geological evolution, controlling the distribution of sedimentary strata, magmatic rocks, and Cenozoic basins (Hu KM, 2001; Shu LS et al., 2006). Typically, magmatic rocks and mineralization zones are concentrated along or on one side of these faults, for example, the Late Mesozoic magmatic rocks were absent at the western part of the Ganjiang Fault (Shu LS et al., 2004) and the Cretaceous magmatic activities were confined to the southeastern Zhenghe-Dapu Fault (Shu LS and Zhou XM, 2002; Shu LS et al., 2004; Zhang YQ et al., 2021). In addition, some faults control the Late Mesozoic half-graben basin (e.g., Ganjiang Fault and Ganzhou Basin; Shu LS et al., 2004). The orientations of some basins were often influenced by the faults, for example, the NE-striking basins southeast of the Zhenghe-Dapu Fault versus E-W- and NE-striking basins to the northwest (Shu LS et al., 2004).

In general, these deep and major faults acted as tectonic boundaries and channels for magmatic and hydrothermal activities, exerting a first-order control on the crustal architecture and metallogenic framework of the Cathaysia Block.

2.2.2 Wuyi Massif

So far, no outcrops of the Archean basement have been found in the Cathaysia Block, which is only recorded by the detrital zircons with an age of 2.73−2.38 Ma (Yao JL et al., 2011; Li XH et al., 2014; Wang TT et al., 2020; Li SL et al., 2021). The Cathaysia Block is composed of Proterozoic basement and Neoproterozoic to Cenozoic sedimentary cover. The Proterozoic basement is dispersed into three massifs. The oldest basement is the Paleoproterozoic Badu Group, which is sporadically exposed in the northern Wuyi Massif (the southwest of Zhejiang Province and the northern Fujian Province) (BGMRJX, 1984; Shu LS, 2012). Badu Group is composed of the biotite granulite, biotite schist, quartz schist, plagioclase amphibolite and migmatite (BGMRFJ, 1985; BGMRZJ, 1989; Hu X et al., 1991). The age of the metamorphic/crystallized basement is at 1.93−1.77 Ga, corresponding to the Columbia supercontinent cycle (Hu X et al., 1991; Li XH et al., 1998; Shen WZ et al., 2000; Yu JH et al., 2009, 2012; Zhao L et al., 2014, 2015). The Mesoproterozoic rocks are rarely exposed in the Cathaysia Block (Yu JH et al., 2006; Shu LS et al., 2021), and only a few meta-volcanic rocks outcrop in the Le'an-Yujiang-Yiyang area in the northern Wuyi Massif (Zhang BT and Hum GR, 2006; He JR et al., 2008). The Neoproterozoic basement rocks include the Chencai Group (southern Zhejiang Province), the Mayuan Group (northwestern Fujian Province) and the Shenshan Group (central-southern Jiangxi Province) in the northern Wuyi Massif (BGMRJX, 1984; BGMRFJ, 1985; BGMRZJ, 1989). The representative rocks are the amphibolite-facies plagioclase gneiss, plagioclase amphibolite, granulite, marble, biotite quartz schist and phyllite, accompanied by local migmatization.

Since the Sinian, the three massifs within the Cathaysia Block experienced the same evolution and have almost similar sedimentary environments (Shu LS, 2006, 2012; Shu LS et al., 2008b, 2020, 2021; Zheng HR and Hu ZQ, 2010; Wang YJ et al., 2013;

Zhang GW et al., 2013). The Phanerozoic rocks are widespread within the Cathaysia Block. The Sinian to Ordovician is a shallow marine to semi-deep marine facies environment and is composed of continuously sandstone-mudstone rhythmic layers, carbonaceous shale and a few limestone and siliceous rocks (Shu LS et al., 2008b). All these rocks exhibit a greenschist-facies metamorphism during the subsequent orogenic events (Song MJ, 2017). They are unconformably overlain by the Middle Devonian conglomerate and sandstone, due to the Early Paleozoic event and the absence of the Silurian (Shu LS, 2006; Zheng HR and Hu ZQ, 2010).

During the Late Paleozoic to Early Triassic, the sedimentary environment in the Cathaysia Block evolved from terrestrial to shallow marine carbonate platform facies (Zheng HR and Hu ZQ, 2010). The Devonian is characterized by the terrestrial clastic rocks (i.e., conglomerate, sandstone, siltstone, mudstone) and some carbonate rocks in the upper layers (Shu LS, 2012; Shu LS et al., 2020). The Cathaysia evolved into platform facies and epicontinental shallow marine facies since the Carboniferous (Shu LS, 2012). It is represented by the regional sediments of the carbonate rocks, except for the Upper Permian, which is the terrestrial clastic rocks due to the marine regression (Zheng HR and Hu ZQ, 2010; Shu LS, 2012).

The Middle Triassic is absent due to the Early Mesozoic orogenic event, and the Upper Triassic unconformably overlies the previous strata. Since then, the Cathaysia Block ended the marine facies environments and evolved into terrestrial river/lake environments (Zheng HR and Hu ZQ, 2010). The Late Mesozoic strata consist of terrestrial clastic rocks and volcanic rocks (BGMRJX, 1984; BGMRFJ, 1985; BGMRGX, 1985; BGMRGD, 1988; BGMRZJ, 1989).

2.2.3 Yunkai Massif

The Archean to Mesoproterozoic rocks are not exposed in the Yunkai Massif. Only some records from the inherited zircon gave information about that period (Yu JH et al., 2006). The oldest exposed basement in the Yunkai Massif is the Gaozhou Complex in the center of the Yunkai Massif and the Yunkai Group in the surroundings (BGMRGX, 1985; BGMRGD, 1988; Zhou HW et al., 1997; Wan YS et al., 2010). The Gaozhou Complex is composed of amphibolite facies (locally granulite facies) paragneiss, schist, quartzite, marble and associated migmatites (Chen CH et al., 2012). The Yunkai Group consists of greenschist–amphibolite facies schist, phyllite, slate and a small number of paragneiss, amphibolite and marble (Wan YS et al., 2010). Both are unconformably overlain by the Phanerozoic rocks (Zhong ZQ et al., 1996; Zhou HW et al., 1997). The Phanerozoic sedimentary environments and the sedimentary series are almost the same of the Wuyi Massif, which was described in Section 2.2.2.

2.2.4 Nanling Massif

Similar to the Yunkai Massif, the Archean to Mesoproterozoic rocks are not exposed in the Nanling Massif (Shu LS et al., 2006; Yu JH et al., 2006). The exposed Neoproterozoic basement rocks are composed of the greenschist-facies metamorphic sedimentary and volcanic clastic rocks, including the meta-conglomerate, meta-sandstone, slate, sericite phyllite, schist, metamorphosed volcanic breccia and tuff, and carbonate rocks (Qin XF et al., 2015; Tian Y et al., 2020; Wang LZ et al., 2020). They are represented by the Yingyangguan Group and Sibao Group in northern Guangxi Province, and the Lengjiaxi Group in Hunan Province (BGMRGX, 1985; BGMRGD, 1988; BGMRHN, 1988; Zhou HW et al., 1997; Tian Y et al., 2020). Overlying this sequence, the area developed a set of glacial tillites, siliceous rocks, sandstone and siltstone (Xu XB et al., 2021). The Phanerozoic strata are dominantly Early Paleozoic marine facies clastic rocks, a small amount of the Late Triassic to Middle Jurassic marine-continental transitional, and Cretaceous terrestrial volcanic clastic rocks (Shu LS et al., 2006; Xu XB et al., 2021). Their sedimentary environments are similar to those of the Wuyi Massif, which was described in Section 2.2.2.

2.3 Deep crustal and lithospheric structures

Numerous geophysical investigations, which are represented by the *SinoProbe* project, have been conducted in South China. These comprehensive studies have yielded fruitful results and have significantly advanced our understanding of the deep crustal and lithospheric structures of the SCB.

2.3.1 Earthquake data and seismic reflection profiles

The distributions of the earthquake data since 1965 show that the earthquakes within the Cathaysia Block are mainly in Wuyi, Yunkai, Youjiang Basin and the Southeastern Coast Belt, while a few are situated at the Nanling Massif (Di QY et al., 2021). The magnitudes of the earthquakes are relatively low (M*s*<5.0) and occurred at a depth of 20km or even shallower. The accumulation of the strain at the weak zones or the pre-existing fault can easily reach the shear strength and trigger earthquakes. The greater number of earthquakes in the Wuyi and Yunkai massifs with respect to the Nanling Massif suggests higher levels of strain accumulation and greater crustal activity there.

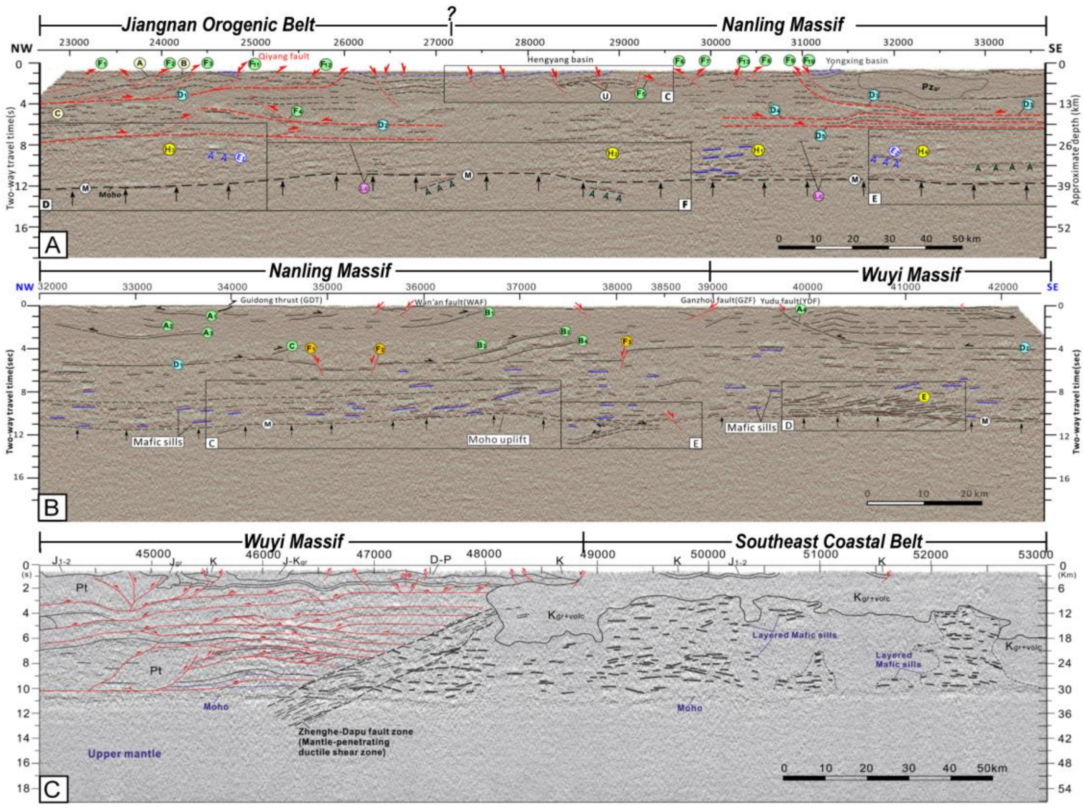

Figure 2.3. *The seismic reflection profiles from SINOPROBE across central South China (modified from Dong SW et al., 2020, 2023; Li JH et al., 2022a). The profile location is shown in Figure 2.2.*

The seismic reflection profiles reveal crustal vertical heterogeneity of the Cathaysia Block (Fig. 2.3). The upper crust is characterized by the weak and low-angle reflections, suggesting the pre-existing thrust faults and the Cretaceous normal faults and extensional basins (Dong SW et al., 2020, 2023). The middle crust has several flat décollement faults with the thrusting systems, which were reworked by the subsequent normal faults (Dong SW et al., 2020, 2023; Li JH et al., 2022a). The lower crust is characterized by sub-horizontal reflections, which reflect the ductile flow. The mantle shear zone can be observed somewhere below the Moho surface (Dong SW et al., 2020, 2023; Li JH et al., 2022a). The seismic reflection profiles also revealed the lateral variation of the crustal architecture showing that more structures were developed in the Jiangnan Orogenic Belt and Wuyi Massif with respect to the Nanling Massif, which reflected the stronger lithosphere strength in the Nanling Massif (Fig. 2.3).

2.3.2 Seismic velocity structure and tomography

The Cathaysia Block has a high shear wave velocity even at different depths (Fig. 2.4). At depths of 4 km and 10 km, the Yunkai and Wuyi massifs exhibit a higher shear wave velocity (>3.2 km/s and >3.6 km/s, respectively) than that of the Nanling Massif (Fig. 2.4A; Guo Z et al., 2018). At a depth of 16-28 km, the velocity is different, and it seems homogenous within the Cathaysia Block (Fig. 2.4B). The differences occurred again at a depth of 34 km, with only the western Nanling massif and Ganjiang Fault showing the relatively low velocity (Fig. 2.4C; Guo Z et al., 2018). The high velocity (>4.4 km/s) occurred in the whole Cathaysia Block beneath 40km (Fig. 2.4D). The shear wave tomography revealed a low-velocity anomaly beneath the Cathaysia Block at a depth of 50−200 km (Shan B et al., 2017).

In the planar view, the P-wave is a heterogeneous distribution. At a depth of 13−123 km, the local high-velocity is situated beneath the northern part of the Cathaysia Block (Figs. 2.4E and F; Wang XR et al., 2018). The mantle Vp model shows that a low-velocity anomaly is beneath the Cathaysia Block at a depth of 150−400 km (Figs. 2.4G and H; Wang XR et al., 2018; Zhang HJ et al., 2023). Different from the structures

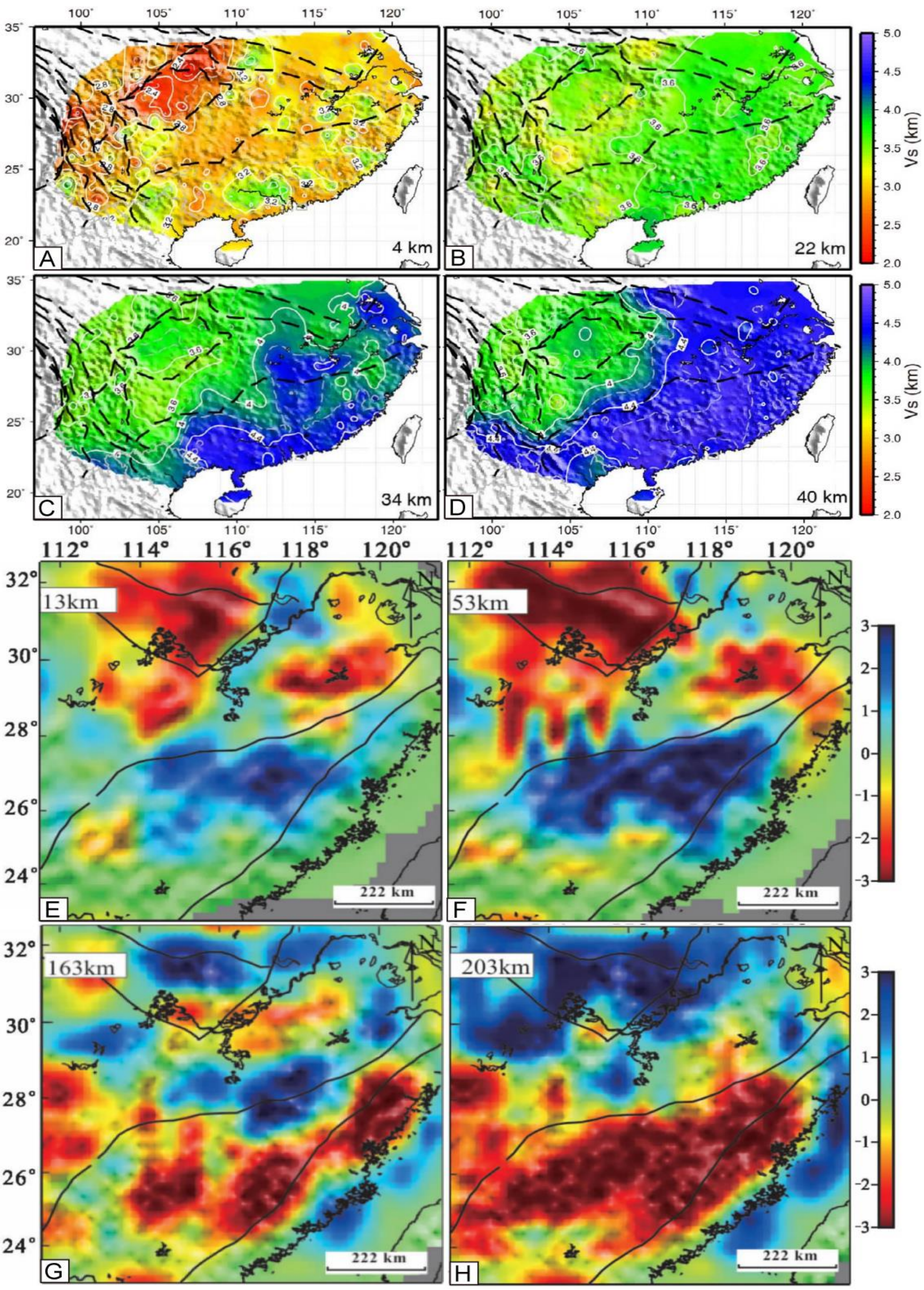

Figure 2.4. *Maps of shear wave velocity and P wave velocity distribution at different depths within the Cathaysia Block (modified from Guo Z et al., 2018; Wang XR et al., 2018).*

that include a high-velocity anomaly at shallow depths and a low-velocity anomaly at deeper levels, the Jiangshan-Shaoxing-Pingxiang Fault and Zhenghe-Dapu Fault exhibit the low-velocity anomaly from the upper crust to the mantle (Wang XR et al., 2018).

The Cathaysia Block has a relatively low Vp/Vs ratio. The Wuyi and Nanling massifs show a higher Vp/Vs ratio (1.70−1.73), the Vp/Vs ratio of the Yunkai Massif and the Jiangnan Orogenic Belt is lower than 1.70, while the Southeastern Coastal Belt has a Vp/Vs ratio higher than 1.73 (He C et al., 2013; Guo Z et al., 2018; Li JH et al., 2023). The observed variations in the velocity structures across three massifs within the Cathaysia Block revealed both the lateral and vertical heterogeneity of the crustal architecture. The high-velocity anomalies in the shallow crust beneath the Wuyi and Yunkai massifs are likely associated with ancient continental remnants, while the low-velocity anomalies in the Nanling Massif were attributed to the sedimentary covers (Wang XR et al., 2018). In addition, the low-velocity anomalies in the deep indicated the mantle flow beneath the Cathaysia Block caused by the subduction of the Paleo-Pacific Ocean.

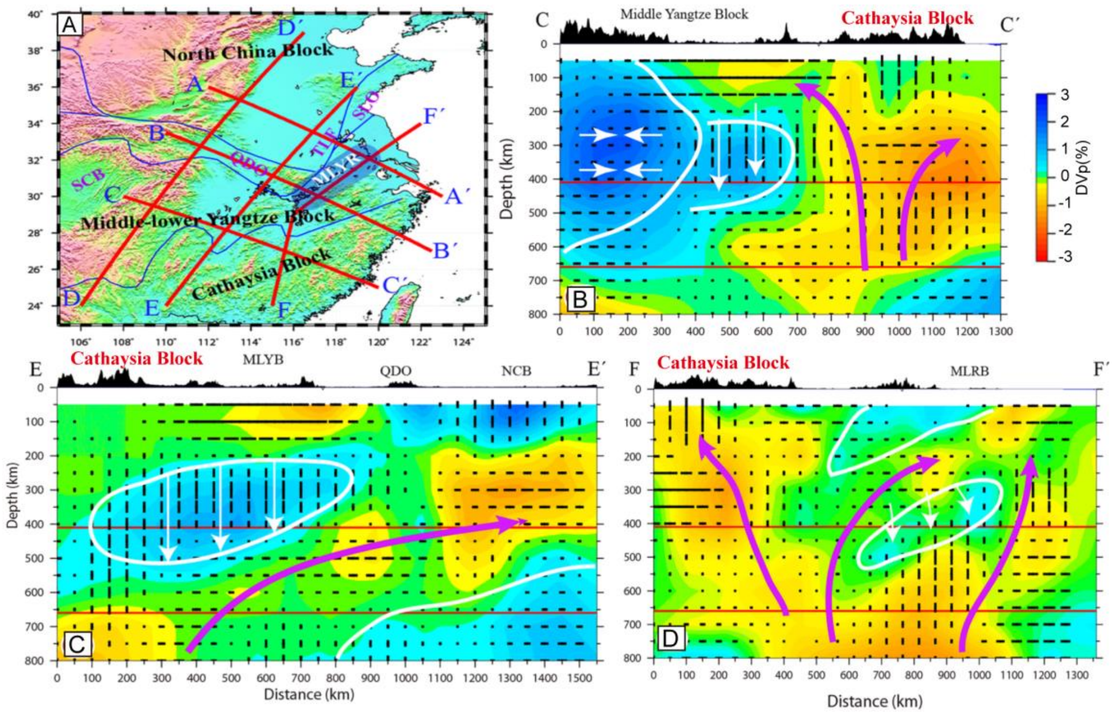

Figure 2.5. *Vertical cross-sections of Vp radial anisotropy (RAN) tomography along the profiles CC', EE' and FF'. The horizontal and vertical black bars represent positive and negative RANs, respectively (modified from Jiang GM et al., 2021).*

2.3.3 Seismic velocity anisotropy

In a vertical cross-section view, the Cathaysia Block displays a negative radial anisotropy at the depths of 50−200 km and 410−660 km, representing a preferred vertical orientation (Fig. 2.5; Jiang GM et al., 2021). Between 200−410 km depth, positive radial anisotropy is observed beneath the Cathaysia Block, reflecting the horizontal preferred orientation (Fig. 2.5; Jiang GM et al., 2021). In the planar view, the azimuthal anisotropy shows a predominantly north-south fast-axis orientation at depths shallower than 410 km. At 500 km depth, the southern Cathaysia Block exhibits an east-west fast-axis trend, which shifts to the SE-trending orientation below 600 km (Jiang GM et al., 2021). In addition, the crustal anisotropy divided the block into three zones, i.e., Yunkai, Nanling and southern Wuyi, northern Wuyi (Li MK et al., 2023).

The seismic velocity anisotropy revealed an upwelling thermal flow obliquely from the uppermost lower mantle to the bottom of the lithosphere beneath the Cathaysia Block and then moving horizontally northward (Jiang GM et al., 2021).

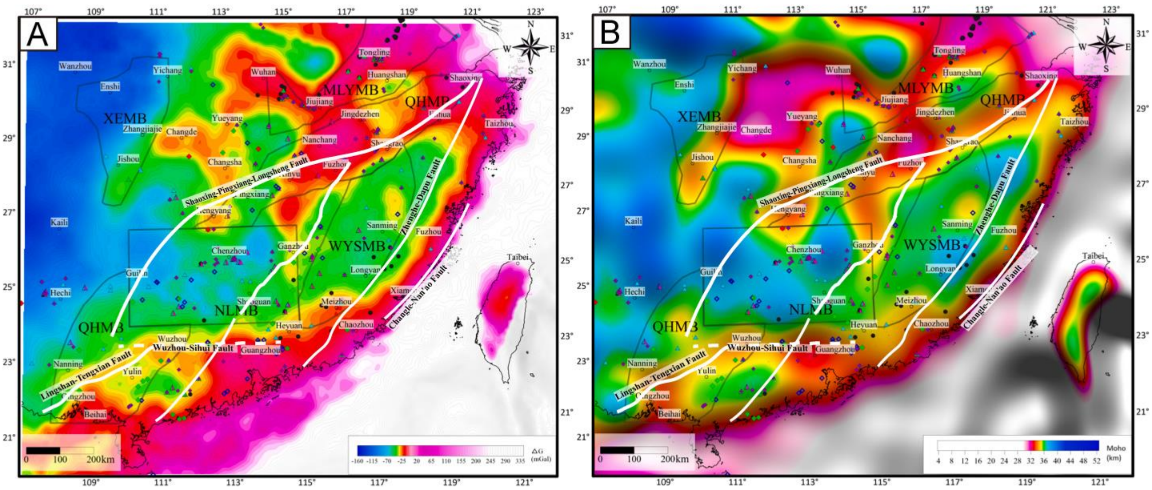

Figure 2.6. *Bouguer gravity anomalies and Moho depths of the South China Block (modified from Yan JY et al., 2021).*

2.3.4 Gravity field characteristics

The Cathaysia Block mainly exhibits a large area of the negative gravity anomaly with a few low positive anomalies, ranging from -100 mGal to 30 mGal (Fig. 2.6A;

Chisenga C and Yan JG, 2019; Yan JY et al., 2022; Li JH et al., 2023). It is characterized by the NE-trending gravity gradient belts with the values decreasing from southeast to northwest. Compared to the Wuyi and Yunkai massifs, the Nanling Massif exhibits a bit lower anomaly (Yan JY et al., 2022; Zhao FY et al., 2023). The Ganjiang Fault, Wuzhou-Sihui Fault and Lingshan-Tengxian Fault exhibit relatively higher gravity anomaly values (ca. -25 mGal; Deng P et al., 2003; Yan JY et al., 2021). Meanwhile, the Jiangshan-Shaoxing-Pingxiang Fault, Zhenghe-Dapu Fault and Wuchuan-Sihui-Yangchun Fault are the boundaries of the gradient belts (Fig. 2.6A; Nie TC and Zhu GL, 2004; Yan JY et al., 2021).

The Bouguer gravity anomaly in Cathaysia is controlled by the crustal thickness (Deng YF et al., 2021). The Cathaysia Block has a relatively thin crustal thickness of 32−42 km (Fig. 2.6B; Di QY et al., 2021; Yan JY et al., 2021). The major faults with higher gravity anomaly values show the thinner crustal thickness at ~32 km, while the thickest thickness of ~40 km is situated at the Nanling Massif (Deng P et al., 2003; Chisenga C and Yan JG, 2019; Yan JY et al., 2021). Additionally, the Yunkai Massif exhibits the thinnest crustal thickness of ~36 km (Chisenga C and Yan JG, 2019; Yan JY et al., 2021).

In summary, the lateral variation of the Bouguer gravity anomalies and crustal thickness indicated the heterogeneous crustal architecture across three massifs, showing a thinner crust in the Yunkai and Wuyi massifs, as well as revealing the major boundary faults within the Cathaysia Block.

2.3.5 Magnetotelluric and aeromagnetic characteristics

The published magnetic data are mainly in the northern part of the Cathaysia Block and show high variability without a specific regularity (Guo LH and Gao R, 2018; Bi BT et al., 2022). The magnetotelluric data show a relatively high resistivity (ca. >1000 Ωm), which is consistent with the dry and low-porosity crystallized basement (Zhang LT et al., 2015; Xu S et al., 2019; Zhang K et al., 2020; Di QY et al., 2021; Han S et al., 2025). The narrow strip of moderate resistivity occurred and probably represents the plutons and faults (Di QY et al., 2021). Beneath the Jiangshan-Shaoxing-Pingxiang Fault, Ganjiang Fault and Zhenghe-Dapu Fault, the significantly NE-trending high conduct (<15 Ωm) channels were identified, extending from the upper crust to the lithosphere (Xu S et al., 2019; Bi BT et al., 2022; Han S et al., 2025). These faults also show the negative aeromagnetic anomaly (Deng P et al., 2003; Han S et al., 2025). They may be the channel riched in fluid or melt.

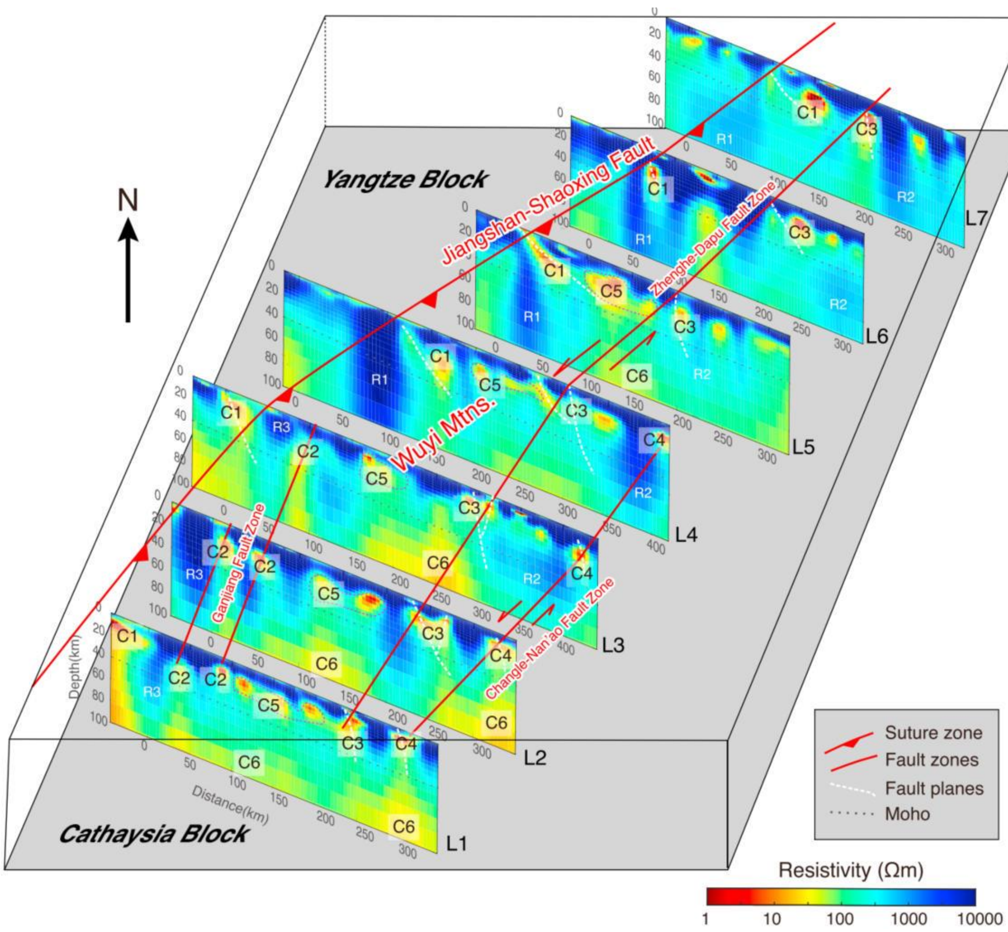

Figure 2.7. *Three-dimensional resistivity model of the Cathaysia Block (modified from Xu S et al., 2019).*

2.4 Deformation and metamorphism

2.4.1 Early Paleozoic

During the late Early Paleozoic, the Cathaysia block experienced a regional intracontinental tectonic event (Wang YJ et al., 2011, 2012; Shu LS et al., 2014, 2015;

Song MJ et al., 2015; Li SZ et al., 2016). The pre-Devonian rocks were strongly reworked and involved in the intense folding and ductile deformation (Shu LS, 2006; Shu LS et al., 2015; Song MJ et al., 2015). In the northern part of the Nanling and Wuyi massifs, plenty of folds are developed, which are represented by the NE-trending asymmetric and recumbent folds, and the maximum shortening was up to 40−67% (Shu LS, 2012; Shu LS et al., 2014). The NW-SE-directed regional positive flower structures are identified in the Wuyi and Nanling massifs, showing the top-to-the-SE thrust on the southeastern side of the Ganjiang Fault and the top-to-the-NW thrusting on the northwestern side (Charvet J et al., 2010, 2013; Shu LS, 2012). The ductile deformation is dominantly located in the Wuyi and Yunkai massifs, i.e., the NW-/SE- doubly vergent thrusting in the Wuyi Massif (Shu LS, 2006; Shu LS et al., 2015) and the NW-directed ductile shearing in the Yunkai Massif (Lin W et al., 2008). In addition, the syn-tectonic ductile deformation is developed along the margins of the batholiths, for example, the mylonitic or gneissic belts at Wugongshan, Ninghua and Lichuan (Shu LS, 2012).

Meanwhile, the Sinian to Early Paleozoic strata underwent the regional lower

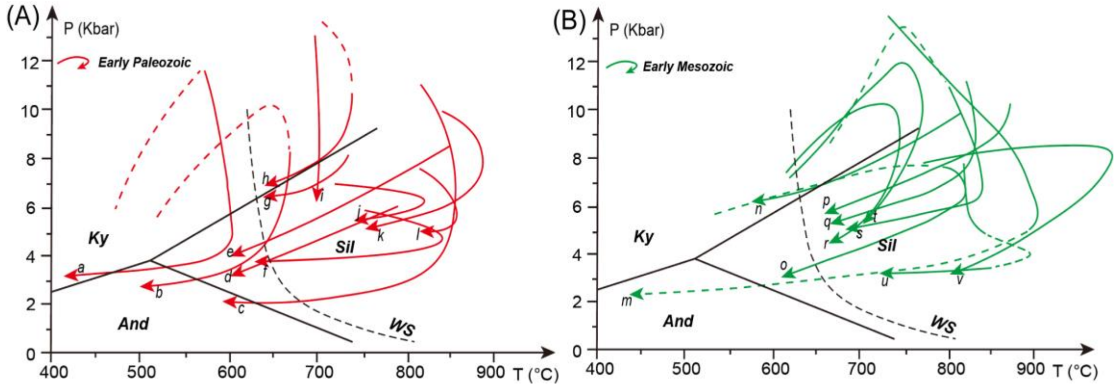

Figure 2.8. *The metamorphic P-T paths of the Early Paleozoic metamorphism (A) and the Early Mesozoic metamorphism (B). Data sources: a-Zhao GC and Cawood PA (1999); b-Li ZX et al. (2010); c-Yu JH et al. (2003); d, e-Zhao L et al. (2016); f, g, j, l-Li C (2020); h-Chen XY et al. (2015); i-Tong LX et al. (2021); k-Yu JH et al. (2014); m-Zhao L et al. (2017); n, p-Zhao L (2012); o-Zhao L and Zhou XW (2012); q-Zhou X (2018); r, t-Wang YJ et al. (2012); s-Dong YF et al. (2018); u-Jiao SJ et al. (2013); v-Zhao L et al. (2012).*

greenschist-facies metamorphism, represented by the silty-/muddy- slate and phyllite (Shu LS, 2006; Shu LS et al., 2020). From the margins of the Early Paleozoic batholiths to the country rocks, the magmatic granite, gneissic granite, two-mica shists and phyllite or slate were successively developed (Shu LS et al., 2015; Song MJ et al., 2015). In addition, the Early Paleozoic granulite, amphibolite and migmatites are locally exposed in the Wuyi and Yunkai massifs, such as Yiyang, Longyou, Taoxi and Gaozhou (Zhao GC and Cawood PA, 1999; Li ZX et al., 2010; Yu JH et al., 2014; Chen XY et al., 2015; Zhao L et al., 2016; Chen CH et al., 2018; Li C et al., 2020a, 2020b, 2025; Tong LX et al., 2021). Some of these rocks yield the near-isothermal decompression clockwise P-T paths (Fig. 2.8A; Zhao GC and Cawood PA, 1999; Yu JH et al., 2003, 2005, 2014; Charvet J et al., 2010; Li ZX et al., 2010; Chen XY et al., 2015; Zhao L et al., 2016; Tong LX et al., 2021).

2.4.2 Early Mesozoic

The Early Mesozoic tectonic event resulted in intense compressional deformation forming the widespread fold belts within the Cathaysia Block, and it almost totally reworked the Early Paleozoic fold-and-thrust structures (Wang YJ et al., 2007a, 2012; Shu LS et al., 2008a, 2009). Similar to the Early Paleozoic, the Early Mesozoic ductile deformation was mainly distributed at the Wuyi and Yunkai massifs, while the Nanling Massif was characterized by the folds and faults in the brittle domain. The Early Mesozoic deformation was represented by top-to-the-north dextral thrusting (~250−225 Ma) and NE-trending sinistral transpression shearing (~230−190 Ma; Wang YJ et al., 2007a, 2012, 2013). A large-scale regional positive-flower structure from Xuefengshan to the Yunkai Massif and further to the Wuyi Massif was proposed (Chu Y et al., 2012a; Wang YJ et al., 2021). Two superimposed fold-and-thrust systems with the E-W-trending and NE-trending strikes were developed in the Cathaysia Block, which resulted in a series of synclines and anticlines in the Nanling Massif (Zhang YQ et al., 2009). Several NE-trending ductile strike-slip shearing zones with Middle-Late Triassic mica $^{40}Ar/^{39}Ar$ ages (240−200 Ma) were reported, i.e., Shaoxing-Pingxiang fault, Yingyangguan shear zone, Qingliu shear zone, Badu shear zone, Hepu-Hetai shear zone and Yangchun-Sihui shear zone (Zhang KJ and Cai JX, 2009; Xu XB et al., 2011; Shu LS et al., 2015; Wang YJ et al., 2021; Li JH et al., 2022b; Xu XB, 2023).

The Early Mesozoic high-grade metamorphic rocks were mainly distributed at the Wuyi and Yunkai massifs, where ductile deformation is exposed. The amphibolite in the northern Wuyi Massif exhibits the isothermal decompression clockwise P-T path (Fig. 2.8B), which was dated at 246−243 Ma (Wang YJ et al., 2012). The garnet-bearing amphibolite and granulite enclaves in the charnockite in Yunkai Massif yielded the P-T conditions of the peak metamorphism at 7.5–8.0 kbar and 950–1000 °C, which was dated at 260−250 Ma (Peng SB et al., 2004; Zhao L et al., 2010, 2012; Chen CH et al., 2011). Additionally, some migmatites were reported in Zengcheng and Yangjiang with an age of 240−230 Ma (Yu JH et al., 2008, 2010; Zhang JH et al., 2017, 2023; Zhou DY and Xu XS, 2017; Cochelin B et al., 2022).

2.4.3 Late Mesozoic

The Late Mesozoic is characterized by brittle deformation. The lower and middle Jurassic strata developed the fold-and-thrust structures with a NW-SE shortening at the retro-arc setting, and some of these strata thrusted on the Paleozoic and Early Mesozoic sequences (Zhang YQ et al., 2009; Wang YJ et al., 2013; Li JH et al., 2018; Li CL et al., 2021, 2023). This compressional deformation was attributed to the westward-advancing subduction of the Paleo-Pacific Ocean at ca. 190-180 Ma, accompanied by the calc-alkaline magmatism (Li JH et al., 2018). Then, the retro-arc shortening was followed by the extension at ca. 170-150 Ma and ca. 136-118 Ma due to the extensional collapse of the overthickened crust in the continental back-arc setting (Li JH et al., 2018), characterized by the adakitic rock and bimodal gabbro-granite suites (Xia Y et al., 2016). Afterwards, a regional shortening occurred at 120-110 Ma coeval with the magmatism lull (Li JH et al., 2020). During the Late Cretaceous, numerous half-graben basins and magmatic ridges were developed in the Cathaysia Blocks, and formed the basin-and-range tectonics of South China (Shu LS et al., 2004), which was caused by the slab rollback of the Paleo-Pacific Ocean and was accompanied by the coastal magmatism (Li JH et al., 2024).

The Late Mesozoic metamorphic rocks are only exposed at the southeastern coast along the Changle-Nan'ao Fault Belts rather than the interior of the Cathaysia Block (Wang ZH and Lu HF, 2000; Liu Q et al., 2012; Cui JJ et al., 2013; Li Y et al., 2015; Wei W et al., 2015, 2023). It is beyond the scope of this thesis and will not be described in detail here.

2.5 Magmatism

The SCB developed large-scale magmatism during the Neoproterozoic to the Late Mesozoic and the total exposed area is more than 169,700 km^2, which was dominantly situated in the Jiangnan Orogenic Belt and the Cathaysia Block (Fig. 2.9; Sun T, 2006). Among them, the Neoproterozoic magmatism is only ~6% and dominantly occurred within the Jiangnan Orogenic Belt and only a few sporadic exposures in the Wuyi and Yunkai massifs. The Late Paleozoic magmatic activity was not strong except for the voluminous Permian Emeishan basalts (ca. 260 Ma; Xu YG et al., 2007). Thus, both Neoproterozoic and Late Paleozoic magmatism will not be described in the following.

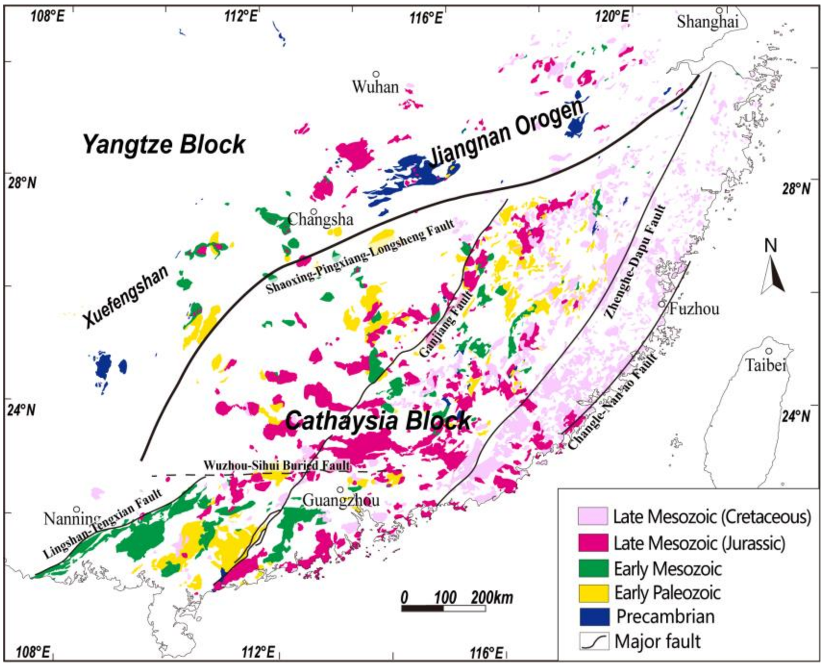

Figure 2.9. *The distribution of magmatism within South China (modified after Sun T, 2006).*

2.5.1 Early Paleozoic

The Early Paleozoic magmatism was characterized by the widespread felsic magmatism (~22,000 km^2) with a planar distribution, which was widespread in the Cathaysia Block (Fig. 2.9; Shu LS, 2006; Sun T, 2006). They are dominantly the massive or gneissic biotite granites, two-mica granites, cordierite-bearing granite and muscovite granites, which have an emplaced age at 464−390 Ma (Wang YJ et al., 2013; Shu LS et al., 2014, 2015, 2021; Song MJ et al., 2015; Song MJ, 2017). The deformed and undeformed granitoids have a similar age and did not exhibit any regularity in the spatio-temporal propagation distribution (Wang YJ et al., 2013; Song MJ et al., 2015). The coeval volcanic rocks were absent (Shu LS et al., 2008b). Most (>58.6%) of the Early Paleozoic granitoids exhibited peraluminous and high-K characteristics, and showed negative εHf(t) values (-3 to -12) and old Hf model ages (2.4−1.2 Ga), showing the features of the intraplate magmatism from the recycling of the Paleo-Mesoproterozoic crustal materials (Sun T, 2006; Shu LS et al., 2014, 2015, 2021). In addition, a few I-type granites, mafic rocks or enclaves were reported in some places with the age of 435−409 Ma (Yao WH et al., 2012; Wang YJ et al., 2013; Zhong YF et al., 2013). The deformation and high-grade metamorphism were observed along the margins of the plutons (Shu LS et al., 2015, 2021).

2.5.2 Early Mesozoic

The Early Mesozoic magmatism is mainly exposed in the Yunkai and Wuyi massifs (Fig. 2.9). Their area is more than 20,900 km^2 and exhibits the planar distribution without any spatio-temporal propagation regularity (Sun T, 2006; Zhou XM et al., 2006; Wang YJ et al., 2013; Song MJ et al., 2015; Liu JX et al., 2020). There are two age clusters of the Early Mesozoic magmatism, i.e., early stage at 244−228 Ma and late stage at 220−200 Ma (Peng BX et al., 2006; Wang YJ et al., 2007b, 2013; Song MJ et al., 2015). The felsic intrusive rocks are the majority and more than 90% of those are peraluminous (A/CNK>1.0), while the volcanic rocks are rarely exposed (Sun T, 2006; Zhou XM et al., 2006; Shu LS et al., 2021). The Early Mesozoic magmatism is represented by the muscovite granites, two-mica granites, cordierite-bearing granites, amphibole-bearing granites, and biotite granites (Sun T, 2006; Zhou XM et al., 2006; Wang YJ et al., 2013; Shu LS et al., 2015; Xia Y, 2015; Gao P et al., 2017; Song MJ, 2017; Liu JX et al., 2020). Three magmatic zones are discerned according to their distribution, i.e., northeast zone, middle zone and southwest zone (Gao P et al., 2017). These rocks are dominantly massive granitoids, and a small amount of those are gneissic granitoids, which are located at the center of the Yunkai Massif (Wang YJ et al., 2007a, 2013, 2021). They have the negative εHf(t) values (-2.0 to -20.2), εNd(t) values (-6.4 to -10.8), the old Hf and Nd model ages (2.3-1.4 Ga and 2.0-1.7 Ga, respectively), suggesting the reworking of the Proterozoic basement of the Cathaysia Block (Wang YJ et al., 2013; Shu LS et al., 2015, 2021; Liu JX et al., 2020). A few I-type granites represent the partial melting of the mafic lower crust (Song MJ et al., 2015). Additionally, some A-type granites were reported to the east of Cathaysia (Wang YJ et al., 2013; Gao P et al., 2017). Similar to the Early Paleozoic, the high-grade metamorphism is commonly developed close to the plutons and the rocks far away from the plutons were not subjected to the high-grade metamorphism (Shu LS et al., 2015, 2020).

2.5.3 Late Mesozoic

The Late Mesozoic magmatism accounts for the largest proportion (~67%) of the magmatism of South China, with the Jurassic being the most predominant among them (Sun T, 2006; Zhou XM et al., 2006). Take the Zhenghe-Dapu Fault as the boundary, the Cathaysia to the northwest is mainly Jurassic granites, which are exposed in Nanling and Wuyi massifs with a planar distribution. Meanwhile, the Cretaceous magmatism is exposed to the east of the Wuyi Massif and the Southeastern Coastal Belt (Sun T, 2006; Zhou XM et al., 2006; Liu JX et al., 2020). The Jurassic magmatism in the Nanling Massif consists of three east-west-trending magmatic belts, each of which is 30−50 km wide and 300−400 km long, i.e., Qitianling-Jiufengshan Belt, Dadongshan-Guidong Belt and Fogang-Xinfengjiang Belt (Shu LS et al., 2006; Zhou XM et al., 2006). They are represented by the metaluminous and calc-calc-alkaline series monzonite and granodiorite, accompanied by a few syenite and S-type granites (Sun T, 2006; Wang YJ et al., 2013; Liu JX et al., 2020). The Cretaceous magmatism shows the NNE-trending distribution, and developed a large volume of volcanic rocks, which is almost twice that of the synchronous intrusive rocks (Sun T, 2006). They are mainly the I-type and A-type granites with a small amount of alkaline rocks and mafic rocks (Zhou XM et al., 2006). Three age clusters of the Late Mesozoic magmatism were identified, i.e., 180–152 Ma, 145–120 and 110–80 Ma (Li ZX and Li XH, 2007; Li XH et al., 2009b; Wang YJ et al., 2013; Li JH et al., 2022a, 2024). The first period magmatism was developed in an intracontinental setting, coeval with the westward subduction of the Paleo-Pacific Ocean and crustal shortening of the South China (Li JH et al., 2018; Cao XZ et al., 2021). The other two periods of magmatism were developed in an extensional setting related to the slab rollback and breakoff of the Paleo-Pacific Plate (Li JH et al., 2018, 2020, 2024; Cao XZ et al., 2021). On the block scale, the Late Mesozoic magmatism exhibits a migration trend from inland to coastal areas over time (Sun T, 2006; Liu JX et al., 2020).

2.6 Geothermal characteristics

The current geothermal studies in South China focus on the modern heat flow measurements. A compiled heat flow dataset and its updated version have been published over the past twenty years (Hu SB et al., 2000; Yuan YS et al., 2006; Jiang GZ et al., 2019; Xiao ZC et al., 2020; Zhou ZM et al., 2020; Wang YB et al., 2024). The heat flow shows a good agreement with the tectonic units. The heat flow values higher than 60 mW/m^2 are almost in the Cathaysia Block and the lower ones are in the Yangtze Block (Fig. 2.10; Hu SB et al., 2000). The Cathaysia block exhibits a high mean heat flow of 73±5.7 mW/m^2 (Hu SB et al., 2000; Jiang GZ et al., 2019). Both the Yunkai and Wuyi massifs exhibit high heat flow, and the highest heat flow of the Cathaysia Block was located in the center of the Yunkai Massif (Hu SB et al., 2000; Yuan YS et al., 2006; Jiang GZ et al., 2019). The bead-like high anomaly belt with a maximum heat flow value >80 mW/m^2 is consistent with the Wuchuan-Yangchun-Sihui Fault and Ganjiang Fault (Yuan YS et al., 2006; Jiang GZ et al., 2019). The modern heat flow reflects the influences of the Late Mesozoic – Cenozoic events and has a good relationship with the crustal thickness (Fig. 2.6B), the location of the plate boundaries and the major faults (Yuan YS et al., 2006; Jiang GZ et al., 2019; Wang YB et al., 2024).

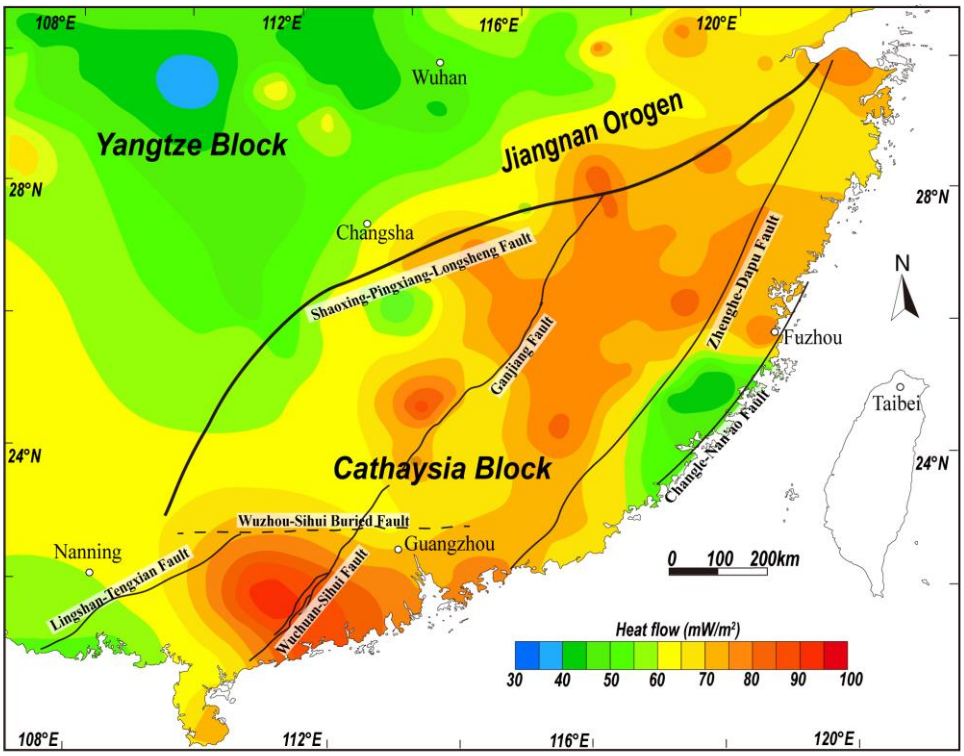

Figure 2.10. *The heat flow map of the South China Block (modified after Jiang GZ et al., 2019).*

However, the studies on the paleo-geothermal are still limited, constrained by the absence of tools or a thermometer for direct measurement and the resetting of the subsequent tectonic-thermal event. Based on the P-T-t data and the multi-mineral geochronology, some cooling paths of the metamorphic units in the geological history were reconstructed, i.e., the Wuyi Massif and Yunkai Massif, which exhibit a cooling from the >700 °C to ~300 °C during the Early Mesozoic (Chu Y et al., 2020; Li JH et al., 2022b).

Chapter 3. Research methods

3.1 Field investigation and structural analysis

Aiming to identify structural patterns, kinematics and decipher the tectonic evolution, the field investigation and structural analysis were performed. A total of six field investigations, spanning 107 days, were conducted across the Cathaysia Block, involving the provinces of Guangxi, Guangdong, Hunan, Jiangxi and Fujian. The objects of the investigation are the structures, deformations and metamorphism in three massifs in the Cathaysia Block and their boundaries.

Two regional-scale cross-sections were mainly focused on, i.e., the north-south-trending Yunkai-Nanling cross-section and the east-west-trending Nanling-Wuyi cross-section. Additionally, detailed mapping was conducted in the migmatitic region in Yangjiang, southeastern Yunkai Massif, where the outcrops are great and provide a continuous cross-section to study the middle-lower crustal rheology. The investigations were focused on the regional strata series and their lithology, deformation and metamorphism, as well as the regional unconformity. More than 4800 structural data are collected, involving bedding, schistosity, foliation, fault plane, striation and fold axis. More than 900 samples for the microtectonic analysis, Raman spectroscopy of carbonaceous material (RSCM) thermometer, petrological analysis and dating were collected. The RSCM samples were collected from the Neoproterozoic to Cretaceous strata far away from the plutons, particularly those with more carbonaceous material. The microtectonic samples were collected after a strict in-situ orientation, promising the correct reconstruction of their direction in the Laboratory.

Thin sections were prepared at Nanjing Hongchuang Co. Ltd. and Langfang Chenchang Co. Ltd.. They were cut to dimensions of 25 mm × 50 mm, with a thickness of 30 μm for microtectonic analysis and 50 μm for RSCM and petrological analysis. The microtectonic thin sections were prepared perpendicular to the schistosity and parallel to the lineation (XZ-plane). The microtectonic analyses were conducted at the State Key Laboratory of Critical Earth Material Cycling and Mineral Deposits (SKL-

CEMCMD), Nanjing University. Geological maps were created using *ArcGIS 10.5*, and the Schmidt lower hemisphere projection and the dip-pitch-plunge ternary diagrams of the structural data were plotted by *Stereonet 9.5* (Allmendinger RW et al., 2011) and ggtern-package in *R-language* (R Core Team, 2020), respectively. The sketches of the cross-sections were prepared by *Adobe Illustrator*.

3.2 Geochronological methods

3.2.1 U-Pb geochronology

Zircon U-Pb dating

Zircon U-Pb dating and trace elements analyses were conducted at SKL-CEMCMD of Nanjing University. The laser ablation inductively coupled plasma mass spectrometry (LA-ICP-MS) system consists of a Thermo Scientific iCAPQ ICP-MS coupled with a Coherent GeoLas Pro 193nm Laser ablation system. Analyses were carried out with a laser beam diameter of 32 μm, 5 Hz repetition rate and energy of 10 J/cm^2. After denudation, Helium was used as a carrier gas to enhance the transport efficiency of the ablated material, and then mixed with Argon gas before entering ICP-MS for analysis. The zircon standard sample GEMOC GJ-1 (^{207}Pb/^{206}Pb age of 608.5±1.5 Ma, Jackson SE et al., 2004) was used as the external standard to calibrate the U-Th-Pb ratios and absolute U abundances. The zircon standard sample MudTank (intercept age of 732±5 Ma, Black LP and Gulson BL, 1978) was used as the internal standard for quality control. The trace element analyses were performed at the same time as the U-Pb dating. The NIST610 glass standard from the National Institute of Standards and Technology (NIST, USA), as an external standard, was used to correct instrumental drift with ^{29}Si as the internal elemental standard. Both the raw U-Pb isotopic and trace elemental signal data were processed using the *GLITTER* software. Common Pb was corrected using the program *ComPbCorr#3* (Andersen T, 2002) embedded in *Microsoft Excel*®. The software *Isoplot* version 4.15 (Ludwig KR, 2012) was applied to calculate weighted mean ages and to plot U-Pb Concordia.

Monazite U-Pb dating

Monazite LA-ICP-MS U-Pb dating was carried out at SKL-CEMCMD of Nanjing University, utilizing a system consisting of ASI Resolution S-155 193nm ArF Excimer laser coupled to Thermo Scientific iCAP Qc quadrupole ICP-MS. U-Pb age data were collected by ablating with the laser beam diameter of 13 μm, the beam energy density of ~5 J/cm^2 and the repetition rate of 3 Hz, respectively. A full analytical session consists of eight standard analyses (two analyses on monazite standard sample Treblicock and KT-252, standard glass sample NIST610 and apatite standard sample Durango, respectively) followed by eight unknown samples. The U-Pb isotopic ratios were corrected by using the monazite standard sample Treblicock, which was an external standard (TIMS data at 272±2 Ma, Tomascak PB et al., 1996). KT-252 is dated at 252 Ma and was used as the internal standard for quality control. Monazite trace element analyses were simultaneously obtained during the U-Pb dating. The standard glass NIST610 as the external standard was used to calculate the trace element contents. Lanthanum (La) was selected as a standard to normalize each analysis. More details are outlined in Hu H et al. (2020). Data reduction was undertaken using *ICPMSDataCal* version 9.9 (Liu YS et al., 2008) and *Isoplot* version 4.15 (Ludwig KR, 2012) was used to make Concordia plots and calculate weighted averages.

Apatite U-Pb dating

Apatite LA-ICP-MS U-Pb dating was carried out in the same laboratory and under similar analytical conditions with the monazite dating. All the spot analyses were carried out using a 43 μm laser beam with a repetition rate of 5 Hz and laser energy of about 5 J/cm^2. The Madagascar apatite standard sample MAD1 (ID-TIMS age of 486.58±0.85Ma, Thomson SN et al., 2012) was treated as a primary standard to calibrate mass bias and instrument drift, which was measured twice every twelve unknown analyses. Qinghu ($^{206}Pb/^{238}U$ age of 159.5±0.2 Ma, Li XH et al., 2013) and Durango (reference age at 31.44±0.18 Ma, McDowell FW et al., 2005) were selected as unknown samples for quality monitoring. In addition, two NIST 610 and one NIST

612 standard glasses were analyzed in each analytical session for trace element analysis. Due to the existence of the high content of common Pb, the software *Iolite* version 4 (Paton C et al., 2011) was used to process the variable common Pb in external standards before the calibration of the unknown analyses (see details in Chew DM et al., 2014), and the ^{207}Pb-correction was applied here. The processed data were plotted on the Tera-Wasserburg Concordia using the software *Isoplot* version 4.15 (Ludwig KR, 2012), the lower intercept can be obtained by anchoring the inverse isochron to the ^{207}Pb/^{206}Pb ratio predicted by the Pb evolution model of Stacey JS and Kramers JD (1975). Besides, ^{206}Pb/^{238}U weighted mean age after the ^{207}Pb-correction was also calculated by *Isoplot* version 4.15 (Ludwig KR, 2012).

3.2.2 Sm-Nd geochronology

Sm-Nd geochronology of garnet was carried out at Nanjing FocuMS Technology Co. Ltd.. The first step is chemical leaching of the LREE mineral inclusion (e.g., apatite, monazite) inside the garnets, and it is necessary for improving the dating precision. About 300 mg garnet powder was mixed with 4ml 4mol/L hydrochloric acid in the Savillex baker, which was placed on the hotplate at 70°C for four hours. The hydrochloric acid was then centrifugated at 3000 rpm, and the supernate was considered as leaching of the LREE mineral inclusions while the residuals were pure garnet. Garnet residuals were mixed with 0.5 mL 60 wt% HNO_3 and 1.0 mL 40 wt% HF in high-pressure PTFE bombs. These bombs were steel-jacketed and placed in the oven at 195°C for one week to ensure complete digestion. Aliquots of supernate and residual digestion were spiked with a ^{149}Sm-^{150}Nd isotope tracer. Firstly, the BioRad AG50W-X8 cation exchange column was used to roughly separate Sr and REE. Matrix elements (Na, Mg, K, Ca) and Rb were separated by 2.0 N HCl; afterwards, Sr fractions were washed out by 2.5 N HCl; Finally, REE fractions were eluted by 6.0 N HCl and collected. Then, REE fractions were dried down, re-dissolved in 0.12 N HCl, and loaded into an LN-specific column (HDEHP-coated Teflon powder). LREE (La, Ce, Pr) were firstly washed out by 0.12 N HCl, then Nd was eluted by 0.18 N HCl, and Sm was washed out by 0.4 N HCl at last. The Sm and Nd-bearing elution was separately introduced into Nu Plasma II MC-ICP-MS for highly precise isotopic analysis. Sm and Nd concentrations were calculated from $^{149}Sm/^{147}Sm$ and $^{150}Nd/^{144}Nd$ ratios. External uncertainties of 1.0% and 0.0030% were applied to $^{147}Sm/^{144}Nd$ and $^{143}Nd/^{144}Nd$, respectively, according to the long-term reproducibility of rock standards. Sm-Nd dating was regressed using *Isoplot* version 4.15 (Ludwig KR, 2012) with ^{147}Sm decay constant of 6.54×10^{-12} (Lugmair GW and Marti K, 1978).

3.3 EPMA analysis of mineral compositions

Quantitative mineral major elements analyses were conducted using a JOEL JXA 8230 electron microprobe microanalysis (EPMA) at SKL-CEMCMD, Nanjing University. The instrument was operated in wavelength-dispersion mode, and its working conditions were a 15 kV accelerating voltage and a 20 nA beam current with a beam diameter of 1−5 μm. Element peaks and background signals were measured for all elements with counting times of 20s and 10s. Natural minerals and synthetic reference materials were used for element standardization before the quantitative analysis. The correction standard ZAF was applied to all the EPMA data. Detection limits were better than 0.02 wt% for the oxides of most elements. The compositional mapping was conducted in the same working conditions. The maps were acquired in a spot stage scan mode with a dwell time of 10ms and a step length of 1μm.

3.4 Phase equilibrium modelling

The P−T pseudo section was calculated in the system MnO-Na2O-CaO-K2O-FeO-MgO-Al2O3-SiO2-TiO2-H2O-O2 (MnNCKFMASTHO) using the *GeoPS* version 3.4 (Xiang H and Connolly JAD, 2022). The pseudo section was calculated using the thermodynamic dataset HP62.DS (Holland T and Powell R, 2011) and the fluid equation Pitzer94 (Pitzer KS and Sterner SM, 1994). The following solution models were used for the pseudo section calculation: garnet, biotite, cordierite, orthopyroxene, ilmenite, chlorite, chloritoid, staurolite, white mica and melt from White R et al. (2014), feldspar from Holland T and Powell R (2003), spinel from White R et al. (2002) and epidote from Holland T and Powell R (2011). Bulk rock compositions used for calculations were from the whole-rock powder analysis of the small block corresponding to the thin section. Assuming the P_2O_5 was sequestered in apatite and was used to correct the CaO content for calculation. O_2 content was calculated from the analyzed Fe^{3+} and Fe^{2+} contents.

3.5 Raman spectroscopy of carbonaceous material (RSCM)

The RSCM thermometer can record the highest temperature based on the degree of ordering of carbonaceous material (Beyssac O et al., 2002). The calibration is sensitive to 200−640 °C (Beyssac O et al., 2002; Lahfid A et al., 2010). The Raman spectra were carried out from polished petrographic thin sections with a thickness of 50 μm, and obtained using the Renishaw InVIA Qontor micro-spectrometer (CEMHTI, CNRS Orléans) equipped with a 514 nm argon laser and the Horiba LabRAM HR Evolution (SKL-CEMCMD, Nanjing University) equipped with a 532 nm laser. Meanwhile, the parallel analyses on the same thin section were performed in both laboratories, and the analytical results show that the difference of the middle/low-temperature samples is less than 15 °C, which is much less than the resolution of this method (~50 °C). Before each measurement session, the spectrometer was calibrated using the 520 cm^{-1} silicon standard. The laser power on the samples was set around 1−3 mW, focused by a Leica DM2500 microscope with a 100 times objective. The signal was dispersed using the 1800 lines/mm grating and analyzed by a CCD detector. The acquisition time of each measurement was set at 60 seconds and one accumulation. The Raman spectrum of the carbonaceous material can be divided into first order (1100−1800 cm^{-1}) and second order (2300−3500 cm^{-1}). All measurements were in the first order. As usual, 15−20 measurements were analyzed for each sample to check the data consistency. Given the effect of polishing, all the spectra were obtained by focusing the laser beam on the subsurface of the samples.

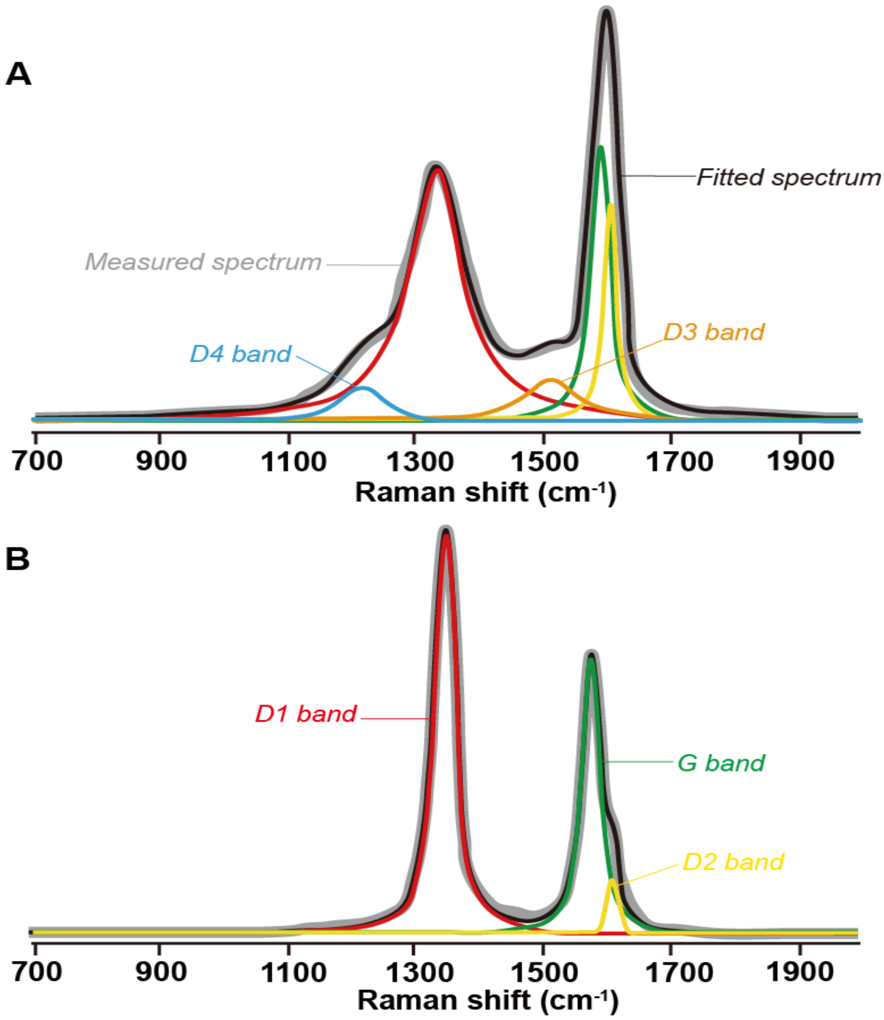

Figure 3.1. *Examples of the peak-fitting types (modified after Beyssac O and Lazzeri M, 2012). (A) Five-band peak-fitting with the Lorentzian function for the disordered graphite carbon in the high-temperature samples. (B) Three-band peak-fitting with the Voigt function for the highly ordered carbonaceous material in the high-temperature samples. The thick grey line is the measured spectrum, the black line is the fitted spectrum, the red line is the D1-band, the green line is the G-band, the yellow line is the D2-band, the orange line is the D3-band and the blue line is the D4-band.*

The acquired Raman spectra were processed using the software *PeakFit v4.06*. The spectra were corrected for the fluorescence background by subtracting the baseline, and then they were decomposed into different bands based on the crystallinity of carbonaceous material (Fig. 3.1). The choice of temperature equation is based on the shape of the Raman spectrum and the number of fitted bands. If the D3-band at 1500

cm^{-1} and D4-band at 1200 cm^{-1} were recognized, the spectrum would be processed using the five-band (G-band at 1580 cm^{-1}, D1-band at 1350 cm^{-1}, D2-band at 1620 cm^{-1}, D3-band and D4-band) fitting method with the Lorenzian function (Fig. 3.1A). In this case, the temperature equation proposed by Lahfid A et al. (2010) was used to calculate the temperature. The RA1 [=(D1 + D4)/(D1 + D2 + D3 + D4 + G)$_{area}$] parameter was calculated, and the final temperature was estimated following the equation: $T\ (°C) = 1250 \times RA1 - 469.75$. Conversely, if neither the D3 nor D4 bands were detected during peak fitting, it suggested a relatively ordered structure during the graphitization process. For such a spectrum, the three-band (D1, D2 and G bands) fitting method was applied with the Voigt function (Fig. 3.1B). The temperature equation proposed by Beyssac O et al. (2002) was applied to calculate the temperature. The parameter R2 [=D1/(G + D1 + D2)$_{area}$] was calculated and the temperature was estimated by $T\ (°C) = -445 \times R2 + 641$.

3.6 Geodynamic numerical modelling

3.6.1 Governing equations

(1) Continuity equation (mass conservation)

For many geological media, like the Earth's crust and mantle, if there are no too large changes in temperature and pressure, it would not lead to large changes in volume; thus, we can assume that they are incompressible. That means the density of the material point would not change in time. The 2-D incompressible continuity equation can be written as follows:

$$\frac{\partial v_x}{\partial x} + \frac{\partial v_y}{\partial y} = 0$$

where x and y are Cartesian coordinates, v_x and v_y are components of the velocity vector parallel to the respective coordinate axes.

(2) Stokes equation (momentum conservation)

Due to the rocks behaving as highly viscous fluids on a geological time scale, the inertial force $\rho\frac{Dv_i}{Dt}$ are far less than the gravitational force and the viscous resistance and can be negligible. Thus, the Stokes equation can be written as follows:

$$\frac{\partial\sigma'_{xx}}{\partial x}+\frac{\partial\sigma'_{xy}}{\partial y}-\frac{\partial P}{\partial x}=0$$

$$\frac{\partial\sigma'_{yy}}{\partial y}+\frac{\partial\sigma'_{yx}}{\partial x}-\frac{\partial P}{\partial y}+\rho g_y=0$$

where x and y are Cartesian coordinates, P is the dynamic pressure, g_y is the gravitational acceleration, ρ is the density which depends on the composition, melt fraction, temperature and pressure. σ'_{xx}, σ'_{xy} and σ'_{yy} are the deviatoric stress tensor components.

(3) Heat conservation equation (energy conservation)

The heat conservation equation, also called temperature equation, describes the heat balance in a continuum medium and the temperature changes due to heat generation, advection and conduction, which can be written as:

$$\rho C_p\frac{DT}{Dt}=\frac{\partial}{\partial x}\left(k\frac{\partial T}{\partial x}\right)+\frac{\partial}{\partial y}\left(k\frac{\partial T}{\partial y}\right)+H_r+H_s+H_a+H_L$$

where C_p is the heat capacity at constant pressure, T is the temperature, $\frac{DT}{Dt}$ is the substantive time derivative of temperature, k is the thermal conductivity, H_r, H_s, H_a and H_L are the radioactive, shear, adiabatic and latent heating, respectively.

3.6.2 Visco-plastic rheology

The viscosity of rocks ductile deforming can be expressed as follows:

$$\eta_{ductile}=A_D^{-\frac{1}{n}}\dot{\varepsilon}_{II}^{\frac{1-n}{n}}\exp\left(\frac{E_a+PV_a}{RT}\right)$$

where A_D is the material constant, n is the stress exponent (n = 1 in the case of diffusion creep and n > 1 in the case of dislocation creep), $\dot{\varepsilon}_{II}$ is the second invariant of the strain rate tensor, E_a is the activation energy, V_a is the activation volume, R is the gas constant.

The rock fails when the stress exceeds its plastic yield strength σ_{yield}, and the viscosity of the plastic rheology can be written as follows:

$$\sigma_{yield} = C_0 + P\sin(\Phi_{dry})\lambda$$

$$\eta_{plastic} = \frac{\sigma_{yield}}{2\dot{\varepsilon}_{II}}$$

where C_0 is the cohesion, Φ_{dry} is the internal frictional angle of dry rocks, λ is the pore fluid coefficient that controls the brittle strength of fluid-containing porous or fractured media.

The effective viscosity in the model was defined by the minimum value of the viscos or plastic viscosity:

$$\eta_{eff} = min(\eta_{ductile}, \eta_{plastic})$$

3.6.3 2D thermomechanical code structure

The continental lithosphere deformation and the temperature variation were simulated numerically by solving the partial differential equations using the 2D model code I2ELVIS operating on the finite difference and marker-in-cell methods in irregularly spaced staggered Eulerian grids (Fig. 3.2; Gerya TV and Yuen DA, 2003a, 2007). See Gerya T (2019) for more details about the 2D thermomechanical code structure.

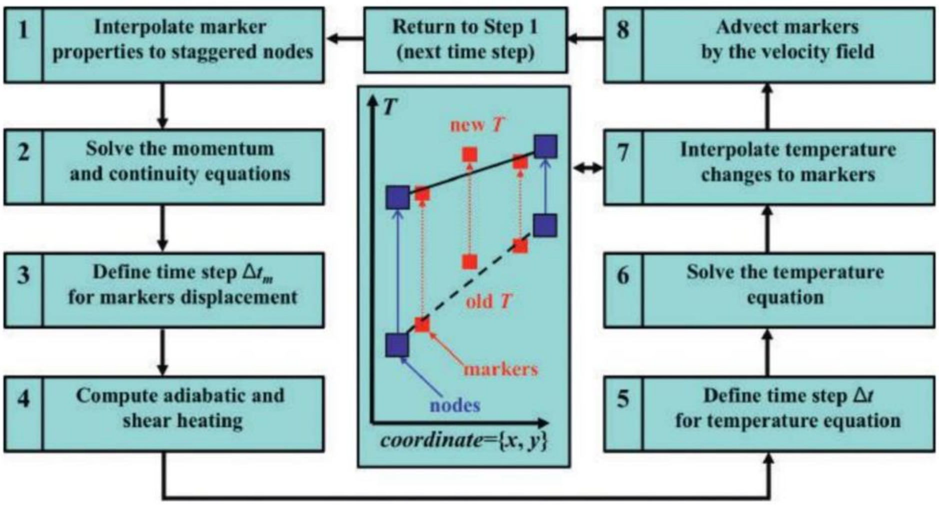

Figure 3.2. *The algorithm structure of the 2D thermomechanical code I2VIS (Gerya T, 2019).*

Chapter 4. Early Mesozoic deformation and high-temperature metamorphism in the Yunkai Massif

4.1 Introduction

The Yunkai Massif experienced the Early Paleozoic and the Early Mesozoic orogenic events (Fig. 4.1; Shu LS et al., 2006, 2015, 2021; Wang YJ et al., 2007a, 2012, 2013, 2021; Yu JH et al., 2007; Lin W et al., 2008; Chu Y et al., 2012a, 2012b; Faure M et al., 2014, 2016a, 2016b; Li JH et al., 2017, 2018, 2022b; Cochelin B et al., 2022). The latter one reworked the earlier records of the orogeny and led to a poor constraint on its tectonic evolution (Wang YJ et al., 2013; Shu LS et al., 2015; Li JH et al., 2017; Ke XZ et al., 2018; Wang XS et al., 2020; Cochelin B et al., 2022). Deciphering different tectono-metamorphic events entails performing precise structural-petrological-chronological studies.

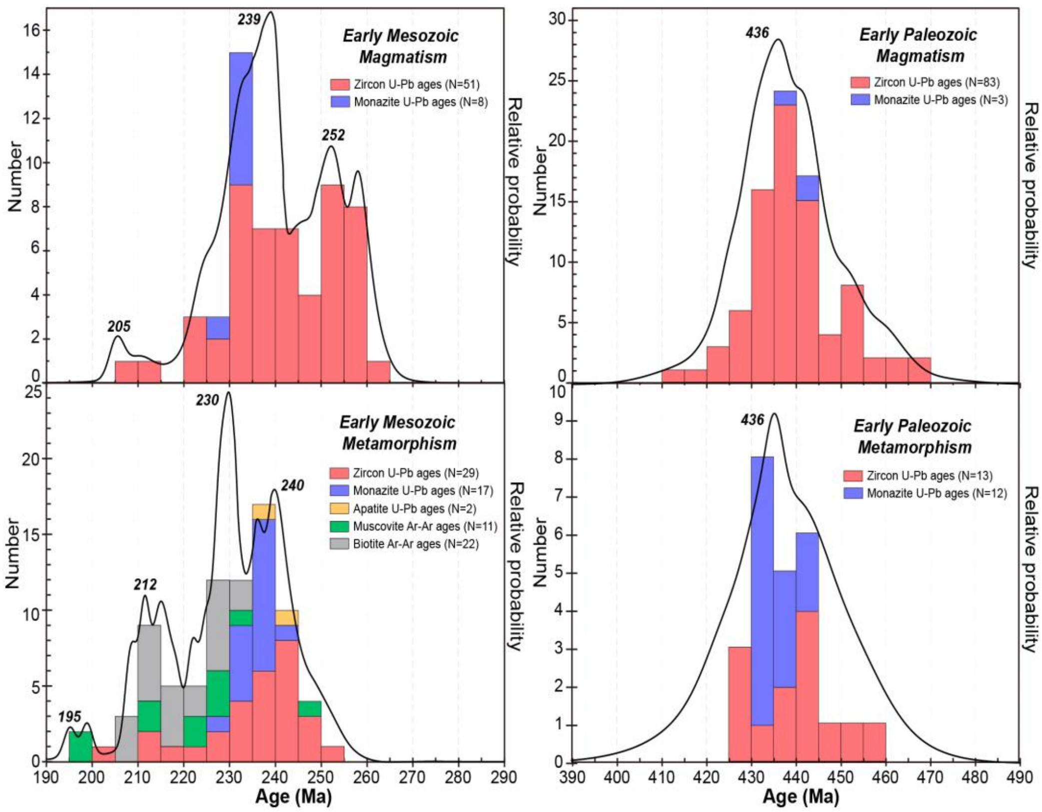

Figure 4.1. *Histograms and relative probability plots of multi-mineral chronology results of Early Mesozoic and Early Paleozoic magmatism and metamorphism within the Yunkai Massif, South China. Detailed data and sources are listed in Appendix Table S1.*

A compilation of the ages for the Early Paleozoic and Early Mesozoic magmatism and metamorphism within the Yunkai Massif is presented in Appendix Table S1. The peak of the Early Paleozoic magmatism occurred at 436 Ma (Fig. 4.1; Wang YJ et al., 2007c, 2013; Chen CH et al., 2017; Ke XZ et al., 2018; Wang XD et al., 2020). The metamorphism is overlapped with the magmatism (Fig. 4.1; Qin XF et al., 2006; Wan YS et al., 2010; Wang YJ et al., 2012; Zhang CL et al., 2015). Furthermore, the Early Mesozoic granitoids within the Yunkai massif are mainly peraluminous S-type granites and are exposed in the Shiwandashan-Darongshan, Wuzhou-Gaozhou and Yangchun (Fig. 4.2; Chen CH et al., 2011; Chen Z, 2017; Zhang JH et al., 2019; Qing L et al., 2020a, b; Wang YJ et al., 2021; Zhou D et al., 2021). The magmatism has a wide range of 265−205 Ma with peaks at 252 Ma, 239 Ma and 205 Ma, while the Early Mesozoic metamorphism ranges from 255 to 195 Ma (Fig. 4.1; Wang YJ et al., 2007a, 2013, 2021; Yu JH et al., 2007; Zhang KJ and Cai JX, 2009; Chen CH et al., 2012, 2017).

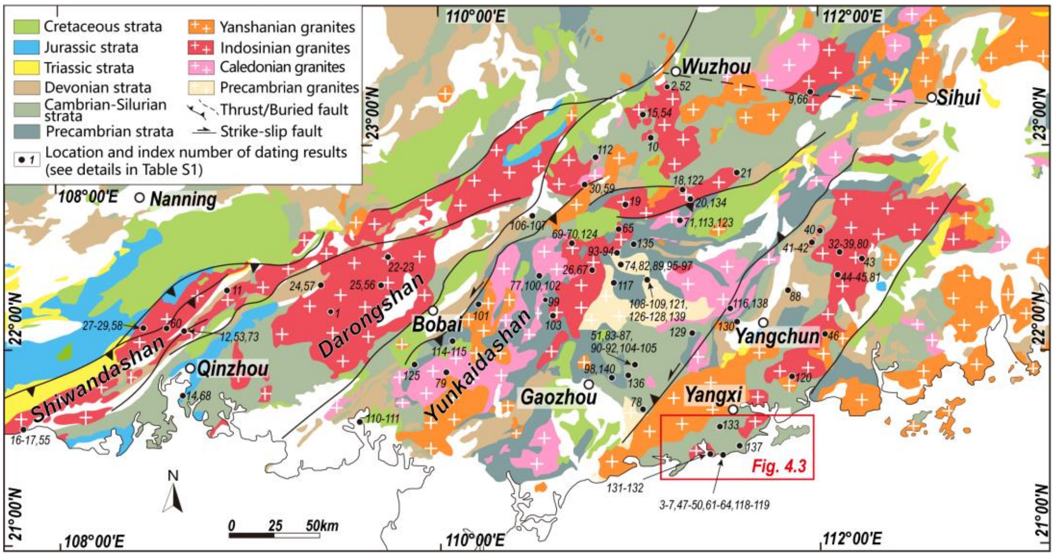

Figure 4.2. *Geological map of the Yunkai Massif with the locations of the published dating results.*

Numerous granites and migmatites are exposed within the Yunkai Massif. As transitional and endmember products of crustal melting, migmatites and granites are important records of deep crustal rheological behavior during orogeny (Foster DA et al., 2001; Wang SJ and Li SG, 2014; Jung S et al., 2022). It is of great significance to shed light on their protoliths, P-T conditions and mechanism of migmatization for discussing the orogenic processes. The protolith type controls the composition of the melts and eventually affects the partitioning behavior of the metallogenic elements (Wolf M et al., 2018). Furthermore, the estimation of the pressure and temperature can help us to reconstruct the thermal and pressure evolution within orogens, and thus their dynamics. The constraints of the ages and duration of the metamorphism and deformation during orogenesis are the key to quantitatively characterize different stages of the metamorphism and reconstruct the crustal evolution of the orogenic belts (Foster DA et al., 2001; Jung S et al., 2022).

In this chapter, we presented our new results from field investigations, petrological studies, zircon, monazite and apatite U-Pb dating and garnet Sm-Nd dating on the migmatites and granitoids in the Yangxi area, southeastern Yunkai Massif. The new results of this thesis, in combination with previously published data, provide more precise constraints on the timing and P-T conditions of the metamorphism and deformation.

4.2 Distribution of the magmatism, metamorphism and deformation

In order to better understand the mechanism of the migmatization and constrain the timing of the metamorphism, we conducted a detailed field investigation and systematic sampling in the Yangxi area, Yunkai Massif. The observations and sample collection are located in the Jiahai area, the Shapa-Fuhu Hill and the Hailing Island (Fig. 4.3). Three deformation phases, along with the magmatism and metamorphism associated with the D1-event, were identified and characterized along a regional NE-trending transect (Fig. 4.3).

In the field, the migmatites are well-exposed along the coast. The diatexite is dominantly exposed at the central Hailing Island, Fuhu Hill and western Jiahai area, while the metatexite is located at Shapa and eastern Hailing Island (Figs. 4.3 and 4.4). The meta-sedimentary rocks are observed to the eastmost of Hailing Island. The granites are dominantly exposed in the Jiahai area and Shapa-Fuhu Hill with scattered distribution in the Hailing Island (Figs. 4.3 and 4.4). On the regional scale, the extensive

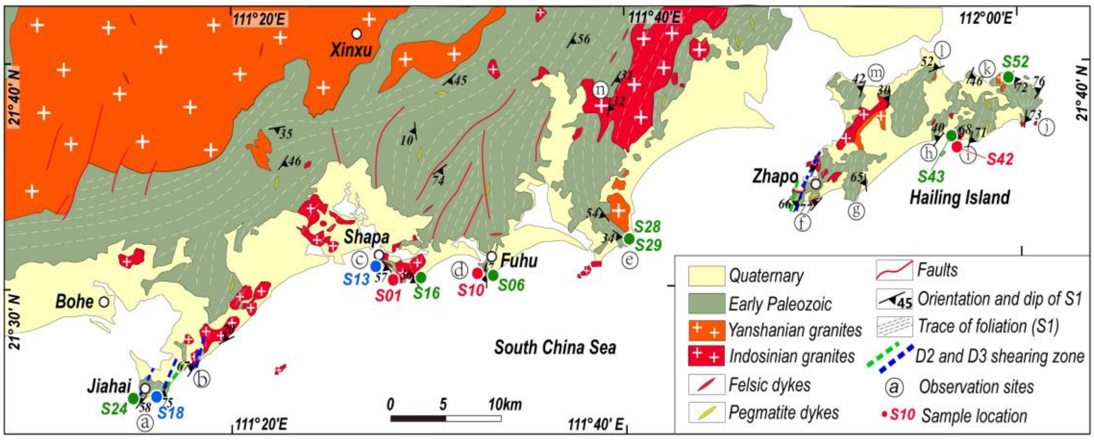

Figure 4.3. *Structural map of the study area showing the locations of the observation sites and samples, modified from the RGMRGD (1964). The non-deformed or syn-magmatic deformed granites samples are in red, the ductilely deformed granites samples are in blue and the metamorphic rocks samples are in green.*

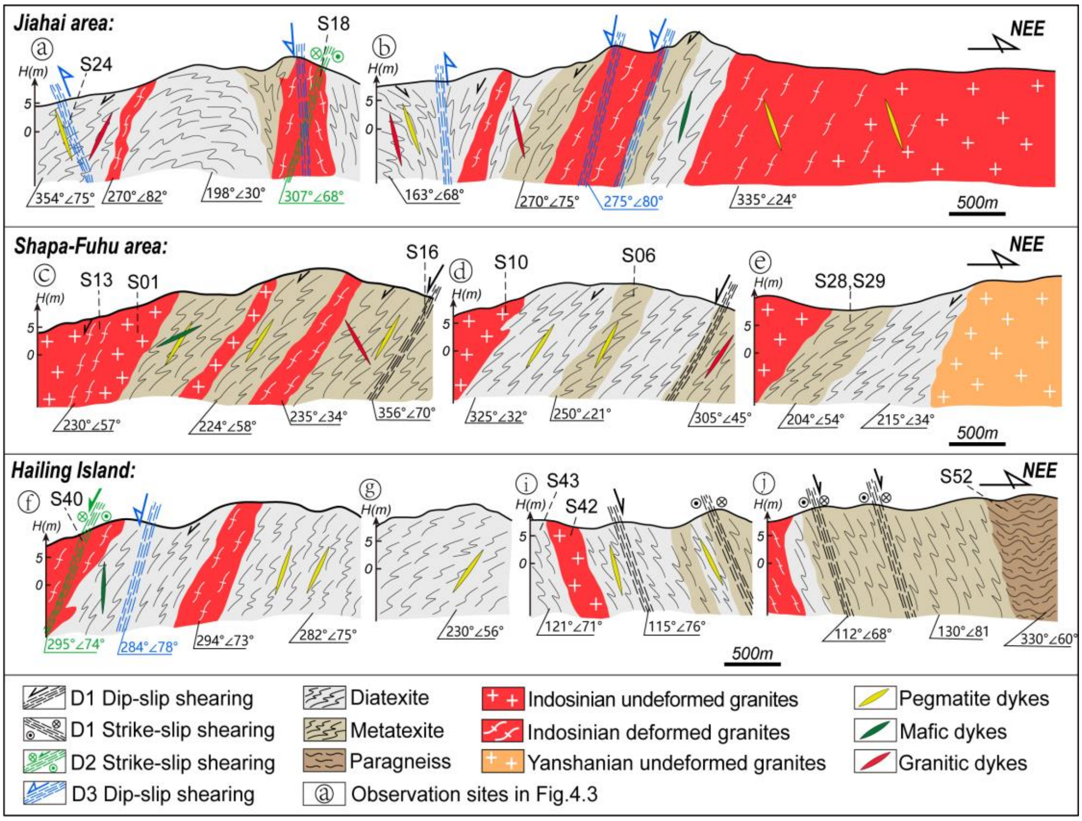

Figure 4.4. *The detailed cross-sections in the Jiahai area, the Shapa-Fuhu area and the Hailing Island, showing the lithologies, structures, contact relationships and sample locations. See the text for detailed descriptions of D1, D2 and D3.*

granites are planar distributed, the high-grade metamorphic rocks and migmatites are next to large granitic plutons (Fig. 4.2). Most of the granites along the study profile are ductile deformed, sometimes weakly deformed, showing a magmatic fabric (Fig. 4.5A), it is suggested that they were syn-tectonic. The weakly deformed granites are mainly porphyritic biotite granites with magmatic lineation characterized by the orientated

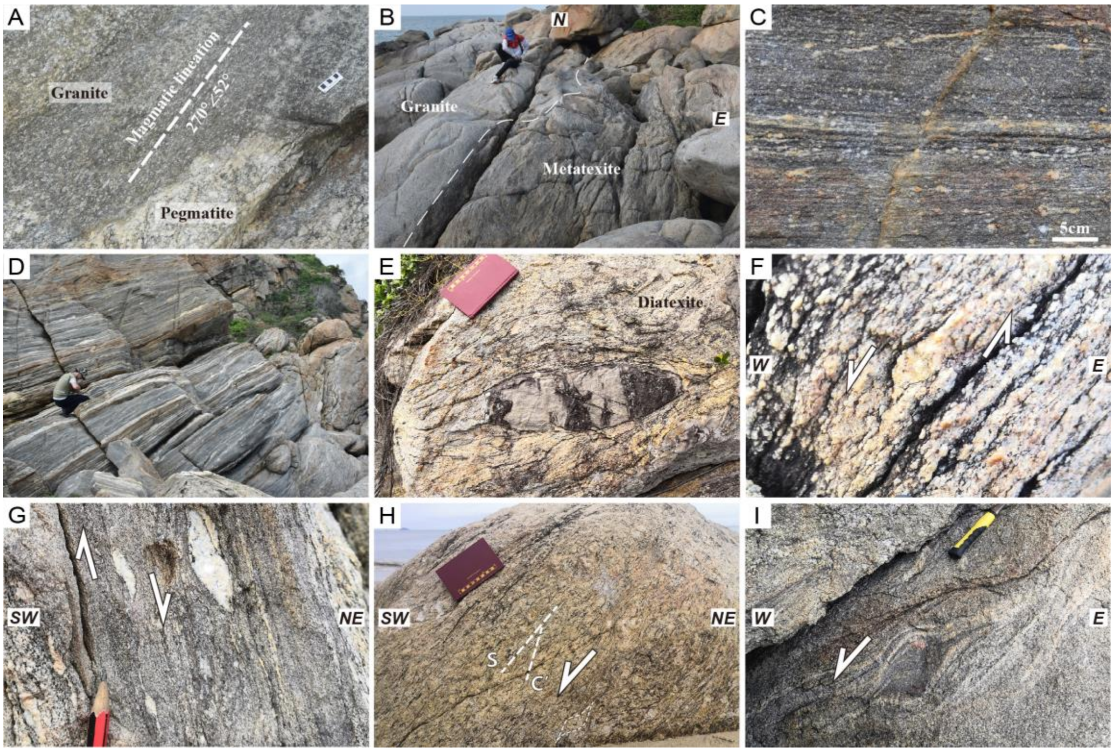

Figure 4.5. *Field photographs of granites, migmatites and D1 deformation in Hailing Island and Shapa-Fuhu area. (A) The weakly deformed porphyritic biotite granite shows magmatic lineation represented by the orientated plagioclases and biotites. (B) The contact between the weakly deformed biotite granite and metatexite in the Fuhu Hill. The magmatic foliation is consistent with the S1 foliation within metatexite. (C) Spotted metatexite was characterized by sporadic melts with a diameter <1cm and a discontinuous dotted distribution. (D) Banded metatexite displays continuous banded melts with a thickness of 1-10cm. (E) The diatexite developed with rootless folds and a dark paleosome block. (F-G) Asymmetric sigmoid quartz and leucosome in migmatites showing top-to-the SW and NE shearing in the western and eastern parts of Hailing Island, respectively. (H-I) The S-C' fabric and sigmoid feldspar phenocryst in orthogneiss and asymmetric melanosome in migmatite showing the top-to-the-west kinematics.*

plagioclases and biotites (Fig. 4.5A). The migmatites are in intrusive contact with the granites, rather than a progressive transition (Fig. 4.5B). They display significant heterogeneity based on the amount of the leucosomes (Figs. 4.4 and 4.5C-G). The country rocks of the migmatites are meta-sedimentary rocks, mainly quartz-mica shists and paragneiss. A typical profile was developed in the Fuhu Hill includes quartz-mica schist, spotted metatexite, stripped and banded metatexite and diatexite. The spotted metatexite is characterized by sporadic melts with a diameter <1cm and discontinuous dotted distribution (Fig. 4.5C), while the stripped and banded metatexite has a high leucosome proportion and gradually displays continuous banded distribution with a thickness of 1−10cm (Fig. 4.5D). The diatexite with the highest leucosome proportion has biotite-rich layers and some dark paleosome enclaves (Fig. 4.5E). The granitic dykes formed by the migrated melts and lots of pegmatite dykes are observed in the field, which are the precursors of the local magmatic granites.

The main deformation (D1) was characterized by the regional foliation (S1), which was well preserved in migmatites and deformed biotite granites. S1 foliation is well defined by the compositional layering and the banded-oriented leucosome layers in migmatites, and by the preferred orientation of biotite, feldspar ribbons and quartz in granites (Fig. 4.5). The S1 foliation and related lineation (L1) are variable in different locations and show a dome-like structure, e.g., Hailing Island and Jiahai area (Figs. 4.3 and 4.4). In the western Hailing Island, S1 foliation strikes in NE-SW and steeply dips (55−85°) to W/NW, and the stretching lineations steeply plunge (50−75°) to SW/NW (profile *f* in Figs. 4.3, 4.4 and 4.6). In contrast, the S1 foliation in the eastern part steeply dips (50−85°) into E/SE with NNE-striking. The L1 lineation moderately to steeply plunges (30−65°) into NW (profile *j* in Figs. 4.3, 4.4 and 4.6). In the central Hailing Island, the S1 foliation is flatter with moderate dips (mostly 40−60°) and the stretching lineations have gentle plunges (10−40°) (profiles *g*−*i* in Figs. 4.3, 4.4 and 4.6). The kinematics are characterized by the asymmetric sigmoid quartz in migmatites and S-C fabric in mylonites, showing top-to-the-SW/NE sense of shear in the western and

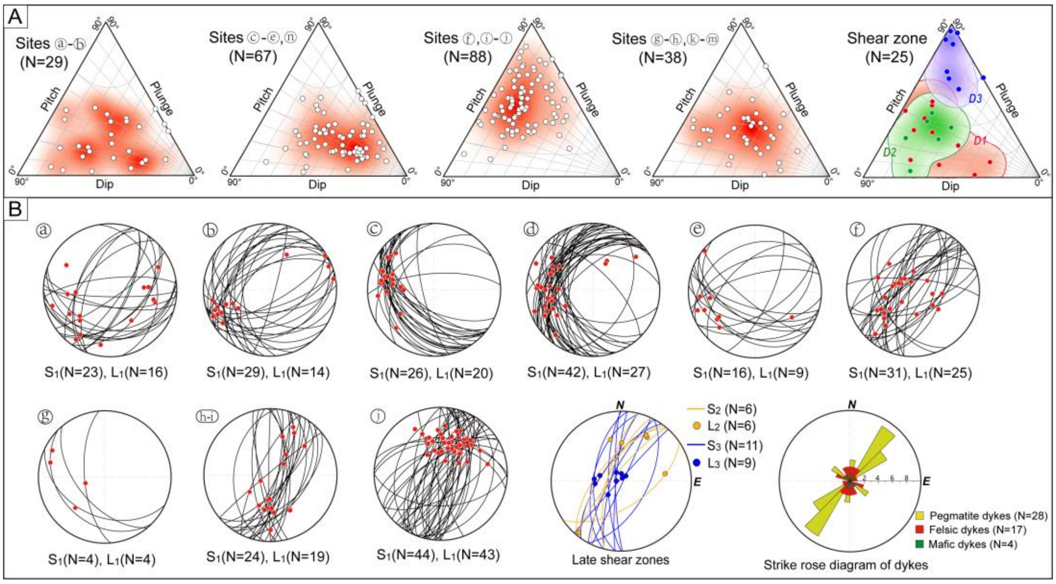

Figure 4.6. *The statistics of measurements in the field. (A) Dip-pitch-plunge ternary diagrams showing the crustal flow mode of different observation sites and shear zones. The D1, D2 and D3 deformations are represented by different colors in red, green and blue, respectively. Based on the quartz dynamic recrystallization, D1 and D2 were developed under the amphibolite-facies and greenschist-facies conditions, respectively. (B) Schmidt low-hemisphere plots of the foliations, lineations and the dykes at different observation sites in the Yunkai Massif. The observation sites are marked in Figure 4.3.*

eastern parts, respectively (Figs. 4.3, 4.4 and 4.5F-G).

Similarly, the Jiahai area also displays a dome-like structure. The S1 foliation dips moderately to steeply (40−80°) towards NW in the western part and towards SE in the eastern part. The L1 lineation steeply plunges (50−80°) to the SW or NE, respectively (profile *a* in Figs. 4.3 and 4.4). S1 foliation at the center dips more gently (~30°) than both sides (profile *a* in Figs. 4.3, 4.4 and 4.6). Continuing to the east, the S1 foliation and L1 lineation show similar features to those to the west. The S1 foliation strikes in NE-SW and dips moderately (30−70°) to the NW or SE (profile *b* in Figs. 4.3, 4.4 and 4.6). It is more likely the terminal of the western dome. The sigmoid melanosome, asymmetric folds of leucosome and the S-C fabrics in diatexite indicate top-to-the-NE/SW extension, respectively (profile *a*−*b* in Figs. 4.3, 4.4 and 4.7A).

The S1 foliation in the Fuhu Hill is consistent with each other. It strikes in N/NW with moderate dips (20−60°) to W/SW and the L1 lineation gently to moderately plunges (10−40°) to the west (profiles *c*−*e* in Figs. 4.3, 4.4 and 4.6). The S-C' fabric and sigmoid feldspar phenocryst in orthogneiss, as well as S-C fabric and asymmetric melanosome in migmatite, indicate the top-to-the-west sense of shear (Figs. 4.5H-I).

Several D1-related shearing bands were developed in the migmatites with diameters varying from decimeters to meters and the melts crosscut the S1 foliation in

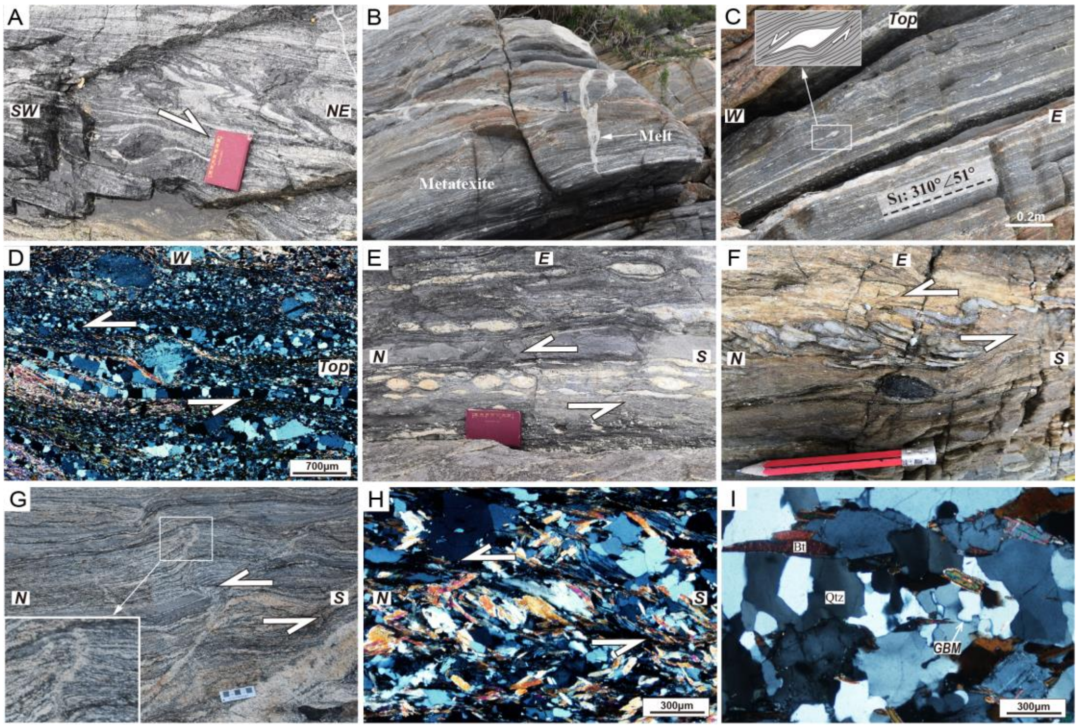

Figure 4.7. *Field and microscopic photographs of D1 deformation and local shear zones. (A) The sigmoid melanosome and asymmetric folds in diatexite show top-to-the-NE extension. (B) The S1 foliation in metatexite was crosscut by the melt. (C-D) Sigmoid leucosome in the field and sigmoid feldspar under the microscope both show the top-to-the-west shearing. (E-F) The strike-slip shear band with boudins and asymmetric folds of the leucosome shows sinistral shearing in the eastern Hailing Island. (G) The melts of the sinistral strike-slip shear band crosscut the main foliation in the migmatite. (H) The S-C fabric under the thin section shows sinistral shearing. (I) Grain boundary migration (GBM) recrystallization of quartz suggests the D1 deformation was under amphibolite facies (>500℃). Abbreviations: Bt-biotite, Qtz-quartz.*

migmatites (Figs. 4.7B-C). The asymmetric leucosome and sigmoid feldspar show the top-to-the-west shearing at the Fuhu Hill (Fig. 4.7C-D). Dextral shearing can be found in the northwest of Hailing Island, while more sinistral shearing developed in the east. The clear kinematics were shown by the boudins and asymmetric folds of the leucosome (Figs. 4.7E-H). The micro melts of the strike-slip deformation crosscut the S1 foliation, suggesting a D1 synchronous deformation (Fig. 4.7G). The GBM dynamic recrystallization of quartz (Fig. 4.7I) revealed the D1 deformation and its associated shear bands were developed under amphibolite facies (>500°C) conditions. In addition,

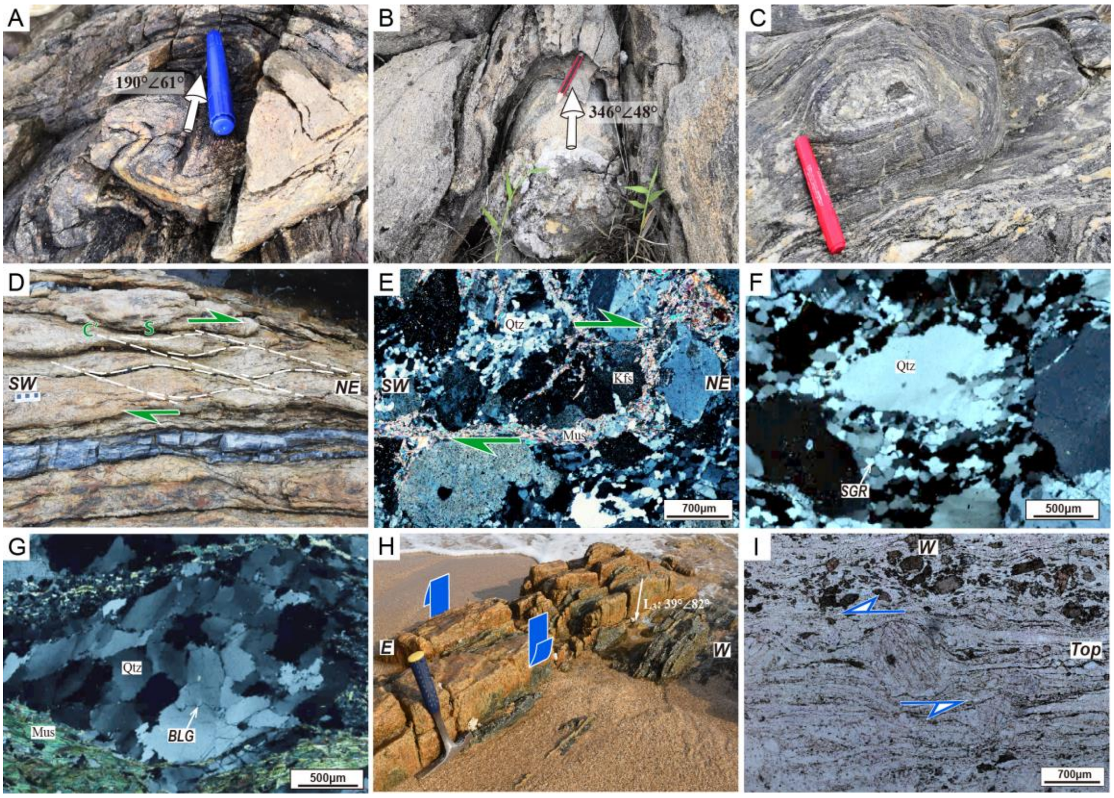

Figure 4.8. *Field and microscopic photographs of the three phases of deformation. (A-C) A-type folds and sheath folds (D1) show an extensional regime. (D-E) The S-C' fabric in the field and the domino-type porphyroblast of feldspar under the microscope, showing D2 dextral strike-slip shearing. (F-G) Subgrain rotation (SGR) and bulging (BLG) recrystallization of quartz suggest the D2-deformation was under greenschist-facies conditions. (H-I) The mylonite involved in the local D3 dip-slip deformation shows the western side going down. Abbreviations: Bt-biotite, Kfs-K-feldspar, Mus-muscovite, Qtz-quartz.*

a great number of A-type folds developed in the field with the axis striking N/NE (Figs. 4.8A-C), indicating the NE-SW stretching.

The D2 deformation was locally observed in the Jiahai area and western Hailing Island (profiles *a* and *f* in Fig. 4.4), characterized by the mylonitic granites and mylonites with the development of the dextral strike-slip shearing band (Figs. 4.8D-E). D2 shearing band strikes in NNE-SSW with steep dips (60−80°) towards NNW (Fig. 4.6). The stretching lineations (L2) gently plunge (5−40°) to NNE with the S-C, S-C' fabrics and domino-type fragmented feldspar phenocryst, showing dextral shearing (Figs. 4.8D-E). The bookshelf micro-fracturing in feldspar, BLG and SGR recrystallization of quartz suggest that the D2 deformation was developed under the greenschist-facies conditions with the temperature at ca. 400 °C (Figs. 4.8E-G), which was different from the D1 deformation. The D3 deformation was represented by the vertical shearing deformation. It was dominantly localized in the Jiahai area and western Hailing Island, with a width of 0.5−2m. Sometimes it reworked and overprinted the D2 deformed mylonitic granites. These vertical shearing band strikes in NNE-SSW and nearly vertical dip (60−90°) to NWW with the stretching lineation steeply plunging to the west (Fig. 4.8H). The sigmoid phenocryst indicates that the western side goes down (Fig. 4.8I).

4.3 Sample description

Considering that 1) petrological studies can decipher the pressure and temperature of the metamorphism, 2) multi-mineral geochronology based on the different closure temperatures can provide precise constraints on the timing of granite emplacement and migmatization, and unravel the exhumation process of the mid-lower crust, 3) combined petrological and geochronological data can provide critical constraints on the tectonic evolution of the orogenic belt, thus, three weakly deformed (syn-magmatic deformed) granites (S01, S10 and S42), two deformed granite (S13 and S18), five migmatites (S06, S16, S24, S28 and S29) and two meta-sedimentary rocks (S43 and S52) were collected for further petrological and chronological analyses (see locations in Fig. 4.3).

Granites

The granites located at the Fuhu Hill and the central Hailing Island exhibit a coarse-grained texture with grain sizes of 1-3 mm, while the others have a porphyritic texture, suggesting that the former experienced a slower crystallization. Granite S01 collected at Shapa town exhibits the syn-magmatic weak deformation in the field, including the magmatic foliations and lineations (Fig. 4.5A). It doesn't show significant orientation but a porphyritic texture, consisting of K-feldspar (~50%), plagioclase (~25%), quartz (~20%), muscovite (~5%) and a few ilmenite and magnetite (Fig. 4.9A). The phenocrysts are mainly the K-feldspar and plagioclase. The fine-grained quartz is distributed in the matrix. The muscovite occurred as bundled clusters and sometimes filled the fracture of the feldspar, which was like the secondary muscovite during the late alteration. Granite S10 at the Fuhu Hill doesn't show significant mineral orientation under the thin section, though there is a weak orientation of the biotite in the field (Figs. 4.9B-C). It mainly comprises quartz (~35%), plagioclase (~30%), biotite (~20%), K-feldspar (~10%) and a small amount of Fe-oxides and zircons (Fig. 4.9C). The K-feldspar shows slight weathering and a dirty surface, sometimes it contains subrounded quartz and biotite inclusions. The quartz displays an irregular shape and was recrystallized with GBM. Granite S42 was sampled at the southeastern Hailing Island. It has a porphyritic texture represented by the K-feldspar phenocrysts and the matrix with plagioclase and quartz (Figs. 4.9D-E). The oriented biotite and the quartz in the matrix define the S1 foliation under the thin section, and the preferred orientation of K-feldspar phenocrysts in the field defines the magmatic lineation (Figs. 4.9D-E). Garnet and tourmaline were also locally observed in other granite samples.

Granite S13 is a granitic augen gneiss collected from Shapa town (Figs. 4.3, 4.5H and 4.9F). It consists of plagioclase (~30%), alkali feldspar (~30%), quartz (~25%), biotite (~15%) and a small amount of accessory mineral (Fig. 4.9G). Myrmekites developed in the K-feldspar phenocrysts suggest high-temperature conditions. S-C

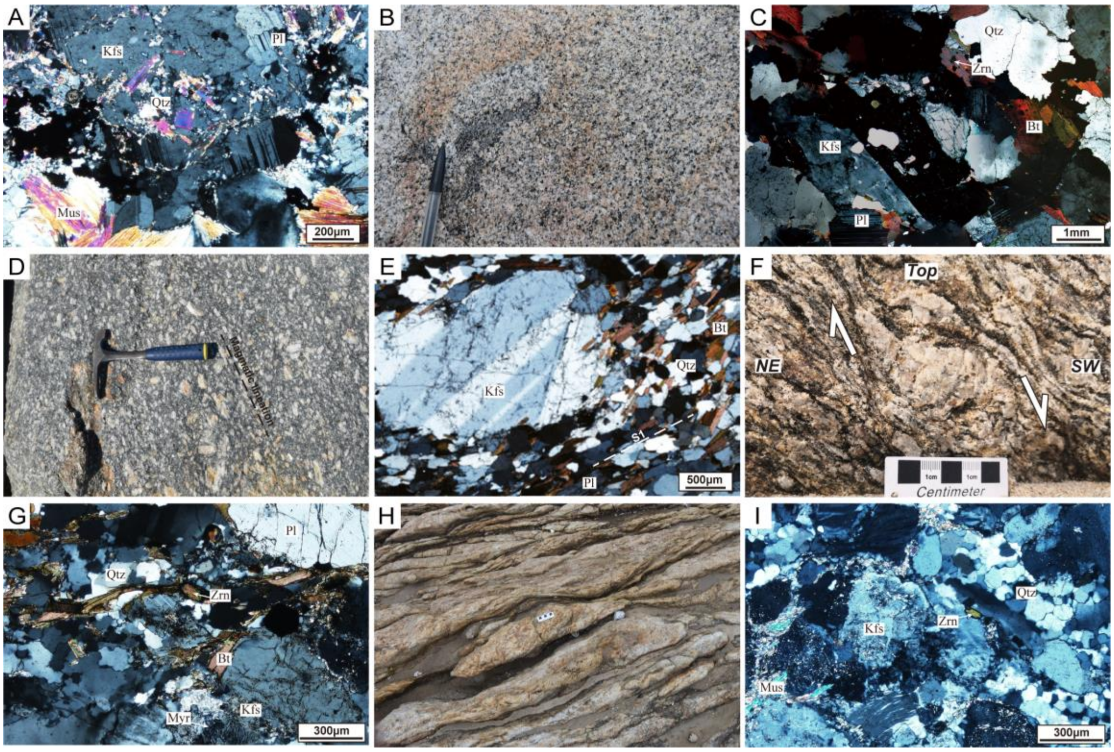

Figure 4.9. *Field and microscopic photographs of the granites. (A) K-feldspar phenocrysts and the secondary muscovite within weakly deformed granite S01. (B) The outcrop of the weakly deformed granite S10 with the preferred orientation of the biotite. (C) Granite S10 with coarse-grained granitic texture. (D) The magmatic lineation within the biotite porphyritic granite S42. (E) K-feldspar phenocrysts and the S1 foliation are defined by the oriented biotite and quartz. (F) Granitic augen gneiss showing the top-to-the-SW shearing at the outcrop of the sample S13. (G) K-feldspar and plagioclase phenocrysts, and the oriented band of the biotite within the sample S13. (H) The outcrop of the deformed granite where the sample S18 was collected. (I) Microscopic photo of the deformed granite S18. Abbreviations: Bt-biotite, Kfs-K-feldspar, Mus-muscovite, Myr-myrmekites, Pl-plagioclase, Qtz-quartz, Zrn-zircon.*

fabrics indicate top-to-the-SW kinematics involved in D1 deformation (Fig. 4.9F). Sample S18 is a mylonitic leucogranite sampled from the Jiahai area (Figs. 4.3, 4.8D and 4.9H), mainly consisting of quartz (~40%), K-feldspar (~40%), muscovite (~15%), garnet (~4%) and tourmaline (~1%; Fig. 4.9I). Well-defined S-C’ fabrics indicate dextral kinematics (Figs. 4.8D-E). The recrystallization of quartz was dominantly characterized by the BLG-SGR, suggesting greenschist-facies conditions (ca. 400 ℃;

Figs. 4.8F and 4.9I).

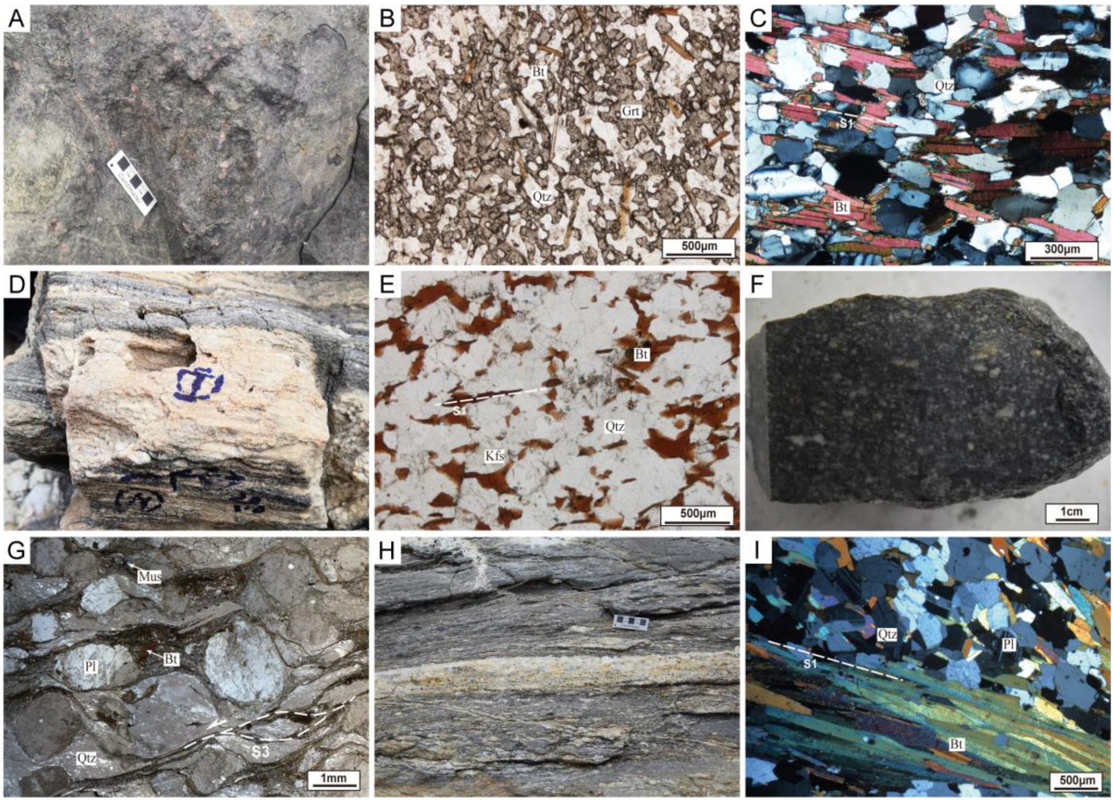

Figure 4.10. *Field and microscopic photographs of the migmatites. (A) Outcrop photo of the garnet-bearing melanosome (S06). (B) The embayed textures of the garnet within the sample S06. (C) S1 foliation was defined by the preferred oriented biotite and elongated quartz. (D) Outcrop photo of the mylonitic leucosome (S16). (E) S1 foliation defined by the preferred oriented biotite within the leucosome. (F) The specimen photo of the mylonitic melanosome sample S24. (G) Mylonitic melanosome (S24) showing the S-C fabric and kinematics related to D3 deformation. (H) Outcrop photo of the paleosome (S52). (I) The Biotite layer intercalated with the quartz-rich layer defined the S1 foliation in the paleosome. Abbreviations: Bt-biotite, Grt-garnet, Kfs-K-feldspar, Mus-muscovite, Pl-plagioclase, Qtz-quartz.*

Migmatites

Most of the migmatites exhibit a porphyritic texture with the K-feldspars or plagioclase porphyroblast. They comprise quartz, plagioclase, K-feldspar, biotite and muscovite. Sometimes they comprise a small amount of garnet, cordierite and sillimanite. The occurrence of garnet and sillimanite suggests an upper amphibolite facies metamorphism, in agreement with the estimated temperature from grain boundary migration recrystallization of quartz (>500°C).

Sample S06 is a garnet-bearing melanosome from the Fuhu Hill (Fig. 4.10A), consisting of quartz (~50%), plagioclase (~15%), biotite (~25%), garnet (~8%), Fe-Ti oxides (~1%) and minor other minerals (Figs. 4.10A-C). Garnet occurs as the porphyroblast in size of ~1cm, which shows embayed textures filled with quartz, biotite and Fe-Ti oxides (Fig. 4.10B), indicating resorption during the retrograde progress. Orientated biotite and elongated quartz define the S1 foliation (Fig. 4.10C). Sample S16 is a mylonitic metatexite collected from Shapa town (Fig. 4.10D), consisting of quartz (~45%), feldspar (~30%), biotite (~20%), minor muscovite and accessory minerals (Fig. 4.10E). The S1 foliation was defined by the preferred oriented biotite. Sample S24 was collected in the D3 vertical shear zone and exhibits as a mylonitic diatexite with augen-shaped plagioclase and quartz porphyroblast (Figs. 4.10F-G). The fine-grained quartz, biotite and muscovite are the mylonitic matrix and define the S3 foliation.

The melanosome (S28) for monazite dating and metamorphic P-T estimation exhibits a porphyritic texture (Figs. 4.11A-C). Relatively large (0.5–1.4 mm) garnet porphyroblasts occur in a schistose matrix. It is dominated by quartz (~40%) with a similar amount (~25%) of plagioclase and biotite, garnet (~5%), and rare accessory minerals (~5%). Aligned fine-grained (~100–400 μm) biotite together with quartz and plagioclase defined the foliation (Fig. 4.11B). The cracks were well-developed in garnets and showed an orientation. Garnet contains biotite, plagioclase and quartz inclusions, suggesting an earlier growth of the inclusion minerals predating the growth of the garnet, which probably preserves the prograde records. The straight boundary between the garnet and biotite suggests an equilibrium between them (Fig. 4.11B). Biotite was relatively developed near the garnet and around the garnet (Fig. 4.11C), suggesting a syn-deformation garnet growth. Both the biotite and plagioclase exhibit corroded flakes, suggesting they were present during the partial melting. The garnet porphyroblast was considered to have been in equilibrium with biotite, plagioclase,

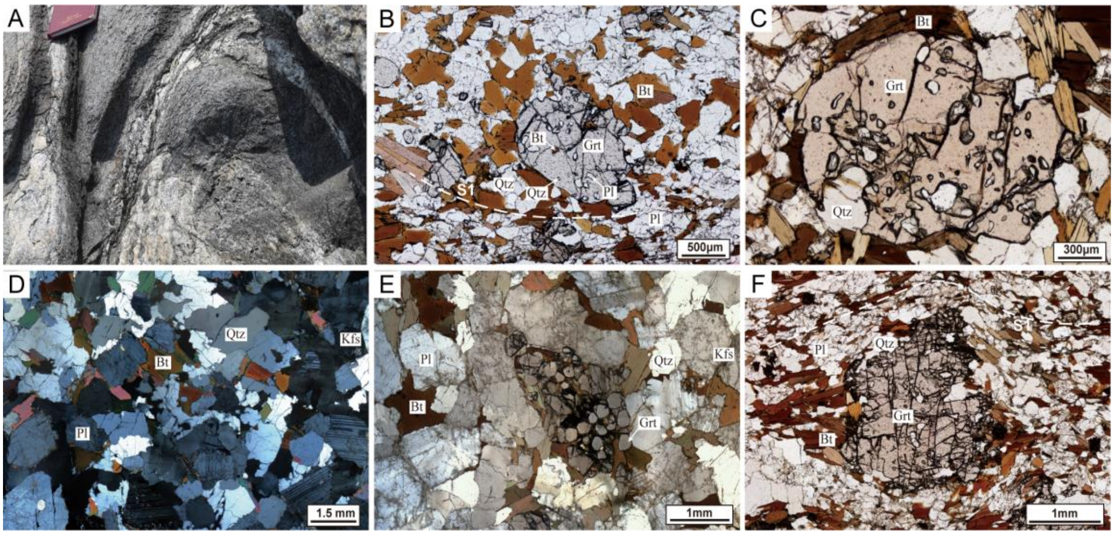

Figure 4.11. *Field and microscopic photographs of the migmatites. (A) Outcrop photo of the garnet-bearing melanosome S28 and leucosome S29. (B) Melanosome (S28) exhibits a porphyritic texture and the S1 foliation was defined by the aligned biotite together with quartz and plagioclase. Mineral inclusions of biotite, plagioclase and quartz were developed within the garnet. (C) The biotite around the garnet in the melanosome (S28). (D-E) The coarse-grained texture without orientation and the cluster of fine-grained garnets in the leucosome (S29). (F) Paragneiss S43 in Hailing Island exhibits a porphyritic texture. S1 foliation was defined by the oriented biotite, plagioclase and elongated quartz. The biotite and garnet porphyroblasts display pressure shadow. Abbreviations: Bt-biotite, Grt-garnet, Kfs-K-feldspar, Pl-plagioclase, Qtz-quartz.*

quartz and ilmenite in the matrix during the peak metamorphism. There is no significant representative retrograde mineral assemblage being observed under the thin section.

Different from the melanosome (S28), the leucosome (S29) collected from the same place doesn't have the orientation, but more like a coarse-grained granitic texture (Figs. 4.11D-E). It consists of quartz (~50%), plagioclase (~25%), biotite (~13%), K-feldspar (~7%), garnet (~3%) and cordierite (~2%). The biotite shows an irregular boundary and poor shape, which is probably a relic of the partial melting. The garnets in the leucosome (S29) are totally different from those in the melanosome (S28). They occurred as clusters of fine-grained garnets without the inclusions and replaced the biotite (Fig. 4.11E), suggesting the growth of the new garnets.

Meta-sedimentary rocks

The paragneiss (S43) is located to the east of the Hailing Island (Fig. 4.3). It is mainly composed of quartz (~35%), plagioclase (~25%), biotite (~30%), garnet (~8%) and rare chlorite and sericite (Fig. 4.11F). The S1 foliation was defined by the oriented biotite, plagioclase and elongated quartz. Large (ca. 1.0−1.5 mm) garnet porphyroblasts are rounded and most of them are broken and full of cracks (Fig. 4.11F). They exhibit a corroded shape. The biotites in contact with the garnets show characteristics of some reactions and display a pressure shadow, which were developed under the tectonic stress and suggested a syn-deformation growth of the garnet. Sample S52 is the paleosome in Hailing Island and mainly consists of quartz (~50%), biotite (~30%) and plagioclase (~20%) (Figs. 4.10H-I). The S1 foliation is defined by the biotite layer intercalated with the quartz-rich layer.

Figure 4.12. *Cathodoluminescence (CL) images of the zircons within the granites.*

4.4 Timing of the magmatism and deformation

Twelve zircon grains were analyzed for the weakly deformed porphyritic granite S01 at Shapa town. Most zircons predominantly exhibit euhedral, prismatic shape and some have an inherited core with oscillatory zoning or homogeneous structure. A few grains are small and nearly rounded. The inherited core behaves as the typical magmatic zircons (Fig. 4.12A), which yielded concordant $^{206}Pb/^{238}U$ with a weighted mean age of 426.4 ± 6.4 Ma (Fig. 4.13A). Additionally, two old Neoproterozoic ages at 834 Ma and 907 Ma were given by the inherited cores. Out of the inherited core is the oscillatory zoning crosscutting the internal structures, and outmost is the recrystallized CL-dark rim (Fig. 4.12A). The euhedral grains with no inherited cores yielded one concordant $^{206}Pb/^{238}U$ age of 237.1 ± 4.1 Ma (Fig. 4.13A). One analysis yielded a discordant age of 268 Ma. The ~237 Ma age was considered the crystallization age of the granite, while the ~426Ma age was the record of the Early Paleozoic event.

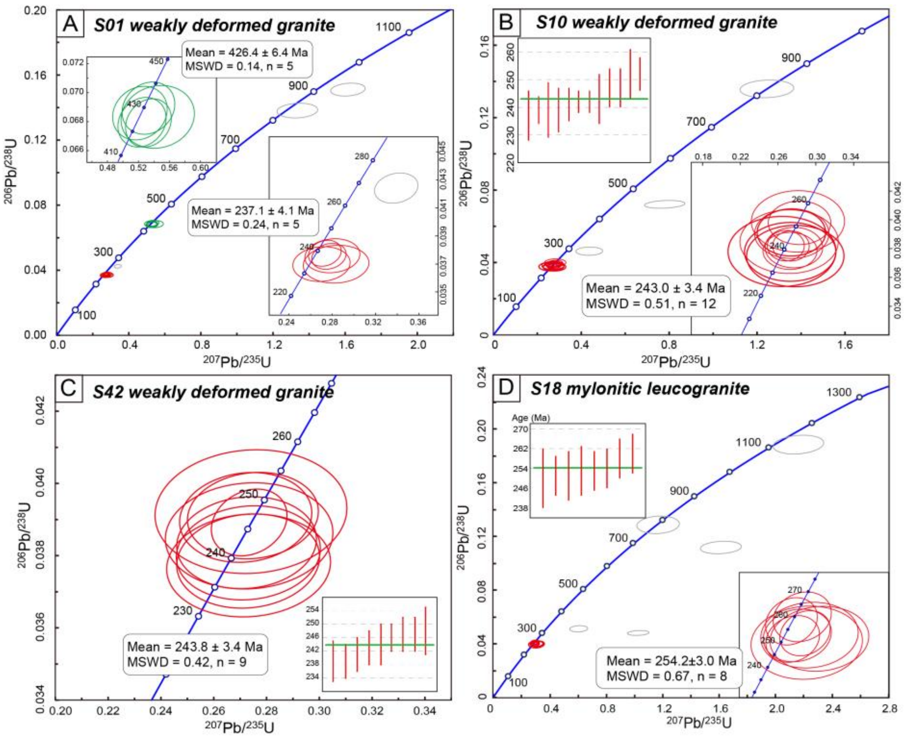

Figure 4.13. *Concordia diagrams of the zircon U-Pb dating of the granites.*

Zircon grains from the weakly deformed granite (S10) at the Fuhu Hill exhibit subhedral to euhedral prismatic shapes, ranging in length from 100 to 200 μm. They display variable length/width ratios from 1.5:1 to 3.5:1 (Fig. 4.12B). The Cathodoluminescence (CL) images reveal wide and quite dark concentric oscillatory zoning, indicating a magmatic origin. Additionally, some grains exhibit a core-rim structure showing a bright inherited core separated from the dark rim by clear boundaries. Fifteen zircons were analyzed and twelve analyses yielded a weighted mean $^{206}Pb/^{238}U$ age of 243.0 ± 3.4 Ma (Fig. 4.13B), which is interpreted as the crystallization age of this granite. Another three analyses gave an old inherited age

(~821Ma) from the core, and two discordant apparent ages (concordance < 75%), which were probably attributed to the mixture of core and rim.

Zircon grains from the weakly deformed porphyritic granite (S42) at Hailing Island are euhedral with a length/width ratio from 2:1 to 3.5:1 (Fig. 4.12C). They have the sharp concentric oscillatory zoning, suggesting magmatic origin. A few grains have inherited cores with a bright CL image. Outmost of these zircon grains have a CL-dark area due to the late overgrowth or recrystallization. One analysis on the inherited core yielded a concordant $^{206}Pb/^{238}U$ date at 1559 ± 37 Ma (Fig. 4.12C). The other nine analyses on the concentric oscillatory zoning and the overgrowth rims gave consistent $^{206}Pb/^{238}U$ ages, with a weighted mean age of 243.8 ± 3.4 Ma (Fig. 4.13C). It is interpreted as the crystallization age of the granite.

Twelve zircon grains selected from the mylonitic leucogranite S18 in the Jiahai area were analyzed. All the zircon grains exhibit obvious core-rim structures (Fig. 4.12D). They are subhedral to euhedral prismatic shape and have the length/width ratios from 2:1 to 3:1. The inherited cores have a high brightness in the CL image and most of those are homogeneous without any structure, only two inherited cores exhibit oscillatory zoning. The rims are dark and wide in the CL image and have vague oscillatory zoning, which have low Th/U ratios (~0.02) than the inherited cores. It suggests the zircon grains were crystallized from the anatectic melt. Two analyses on the inherited cores yielded the Proterozoic ages at 781Ma and 1113Ma. Eight analyses on the CL-dark rims gave a weighted mean $^{206}Pb/^{238}U$ age of 254.2 ± 3.0 Ma (Fig. 4.13D), which is interpreted as the crystallization age of the leucogranite. Additionally, two rims yielded the discordant ages at ~300Ma, which probably represents the partial resetting age.

Seventeen grains from granitic gneiss S13 at the Shapa town were analyzed. All the grains are euhedral and prismatic and exhibit concentric oscillatory zoning (Fig. 4.14A), suggesting the magmatic origins of these grains. A few grains have inherited cores that were crosscut by the oscillatory zoning. The thin rims due to the recrystallization can be observed in most grains. Eighteen analyses on the concentric oscillatory zoning yield concordant and consistent ages, with a weighted mean $^{206}Pb/^{238}U$ age of 439.4±3.1 Ma (Fig. 4.14B). Additionally, one analysis on the oscillatory zoning yielded a discordant age. Three analyses on the inherited cores gave the Proterozoic ages at 1108 Ma, 1451 Ma and 2037 Ma. Four analyses on the CL-bright recrystallized rim yielded younger ages at 342Ma, 386Ma and 416 Ma, suggesting an influence from the late tectonic-magmatic event. Thus, the age of ~439 Ma is interpreted as the crystallization age of the granite.

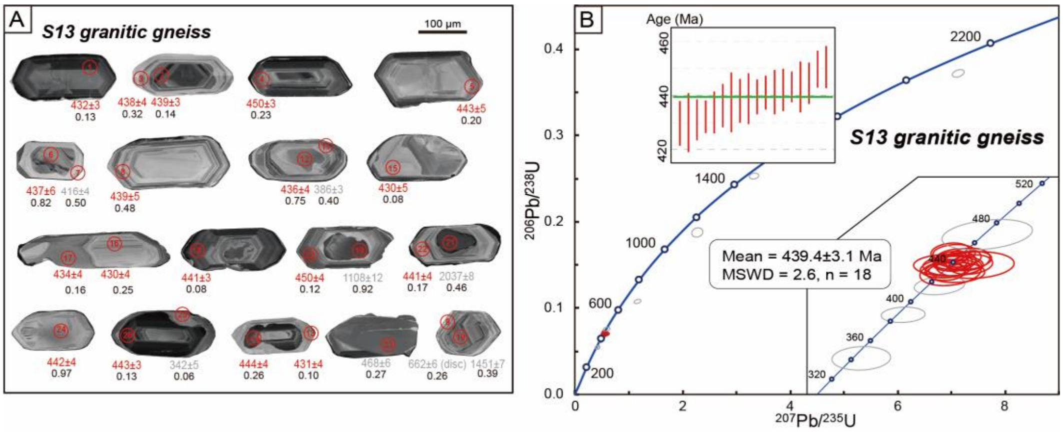

Figure 4.14. *Zircon U-Pb result of the S13 granitic gneiss. (A) Cathodoluminescence (CL) images of the zircons. (B) Concordia diagrams of the zircon U-Pb dating.*

The age and duration of the magma emplacement were constrained at 439 Ma and 254−237 Ma (Figs. 4.13 and 4.14). The D1 deformation lasted to at least 237 Ma constrained by the ages of the syn-tectonic granites at 244−237 Ma (Figs. 4.13A-C). The undeformed granitic dykes that crosscut the D2 strike-slip shear zone were dated at 225−210 Ma (Lu SH, 2025), suggesting the D2-deforamtion predates 225 Ma. Considering the ICB-SCB collision since ~250 Ma, the D1 and D2 deformation are interpreted to have occurred within this Indosinian geodynamic background. The age of D3-deformation is difficult to constrain due to the lack of geochronological data. However, the high-angle dip-slip ductile shearing is not common in Late Mesozoic deformation structures, which are characterized by the high-angle brittle normal faults, low-angle ductile shear zone in the Hengshan and Wuhua areas (Li JH et al., 2013, 2020), and ductile top-to-the-west thrusting along the Changle-Nan'ao Belt (Wei W et al., 2015, 2023).

4.5 Metamorphic P-T conditions

4.5.1 Mineral compositions

Garnet

Three garnet grains and the related plagioclases and biotites from the melanosome (S28) were analyzed. The representative major elements (Fe, Mg, Ca, and Mn) profiles and mapping images of the garnets are presented in Fig. 4.15. The garnets are pyrope-almandine solid solutions with minor grossular and spessartine endmembers. The typical core-rim structures were recognized in the major element profiles, displaying

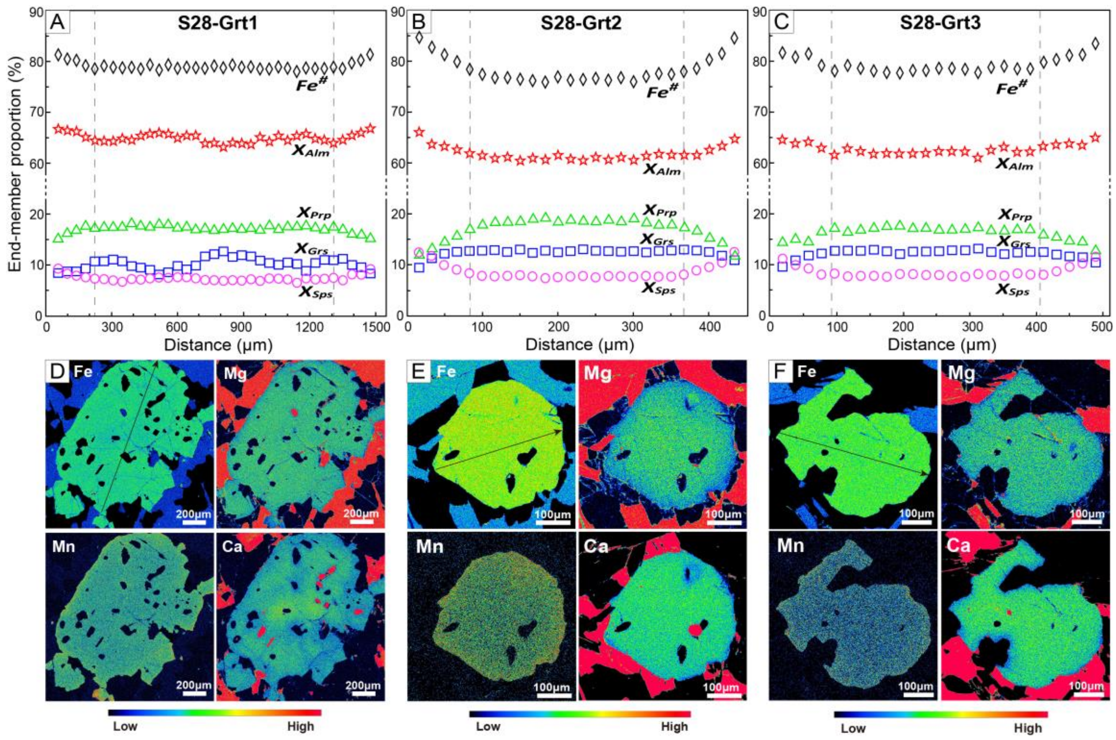

Figure 4.15. *(A-C) Major elements compositional zoning profiles of three garnets in the melanosome (S28) showing end-members proportions (X_{Alm}, X_{Grs}, X_{Prp}, X_{Sps} and $Fe^{\#}$). Abbreviations: Alm-almandine, Grs-grossular, Prp-pyrope, Sps-spessartine, $Fe^{\#}$=Fe/(Fe+Mg). (D-F) Composition maps for Fe, Mg, Mn and Ca in garnets. The black solid lines with arrows are the locations of the profiles in A-C, respectively.*

an obvious homogenous distribution in the core domain except for Grt-1 (Fig. 4.15). The smooth and consistent profiles of Grt-2 and Grt-3 revealed that almandine and spessartine increase from the core ($Alm_{61-63}Prp_{17-19}Grs_{12-13}Sps_{7-8}$) towards the rim ($Alm_{62-66}Prp_{12-17}Grs_{9-13}Sps_{8-12}$). In contrast, the pyrope and grossular decrease slightly towards the rim (Fig. 4.12).

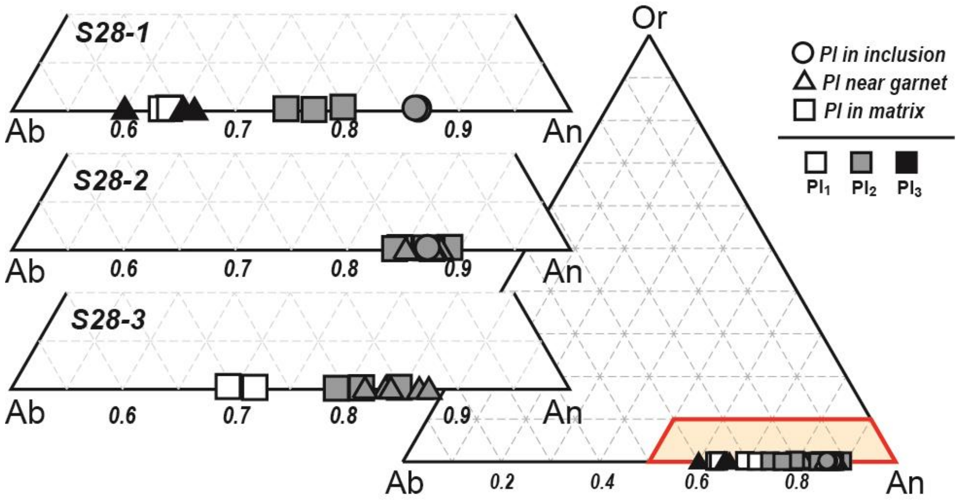

Figure 4.16. *Triplot for the plagioclase in the melanosome. Abbreviations: An-anorthite, Ab-Albite, Or-Orthoclase. Pl_1, Pl_2 and Pl_3 represent the plagioclase related to the prograde, peak and retrograde metamorphism.*

Plagioclase

The An-value (An_{84-89}) of the plagioclase in S28-2 is high and homogeneous, no matter where it developed (Fig. 4.16). It probably recorded the information of the peak metamorphism, because the regular and distinct boundary between the rim of the garnet and the surrounding plagioclase suggests no reaction during retrogression. Plagioclases in the matrix of S28-1 and S28-3 show core-rim structures on the compositional profile with an increase in An-value from the cores (An_{63-72}) to the rims (An_{74-85}), suggesting a growth from prograde to peak metamorphism. However, those near the garnet in S28-1 have a low An-value (An_{60-66}) and show harbor-like shapes, suggesting a reaction with the garnet during retrogression with a decrease in An-value. Meanwhile, the plagioclases near the garnet in S28-3 show regular boundaries and have a high and comparable An-value (An_{82-87}) with that of the rim of the matrix ones, suggesting a record of the peak metamorphism. Compared to the variable compositions ranging from An_{60} to An_{89} for the plagioclase in the matrix and near garnets, the plagioclase inclusion within the garnets has higher An values (An_{86-87}; Fig. 4.16).

Biotite

The biotites in the matrix have a high Ti-value of 0.114−0.191 and low $Mg^{\#}$ [$Mg/(Mg+Fe^{2+})$] of 0.528-0.559, while the Ti-value and $Mg^{\#}$ values of the biotites near the garnet are 0.107−0.178 and 0.534−0.569, respectively (Fig. 4.17). It suggests a higher temperature of the biotites in the matrix than those near the garnet (Fig. 4.17), which probably represents the peak of metamorphism. The biotite inclusions within the garnet have a higher $Mg^{\#}$ value ($Mg^{\#}$=0.603−0.620) than that in the matrix and near garnet ($Mg^{\#}$=0.528−0.569; Fig. 4.17). The Ti-value of the biotite inclusions is 0.141−0.149.

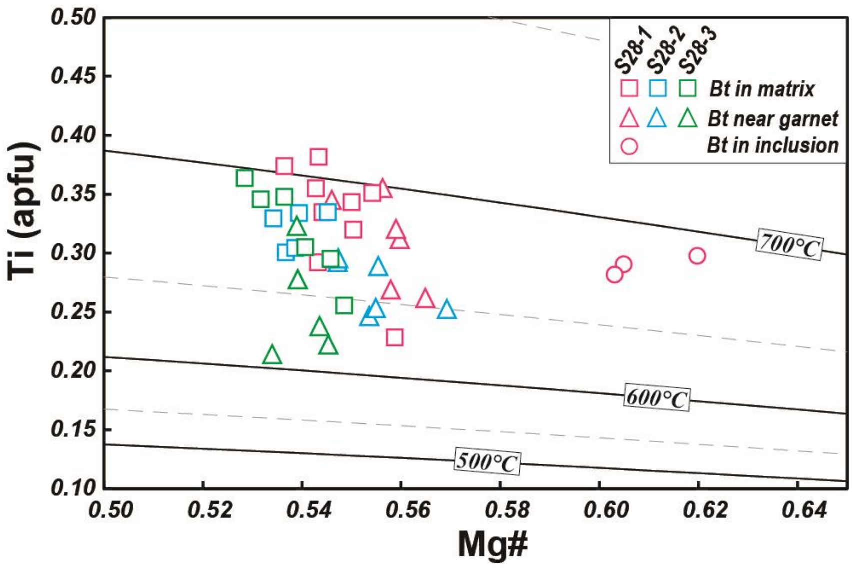

Figure 4.17. *Diagram of Ti (apfu) vs. $Mg^{\#}$ of the biotite in melanosome.*

4.5.2 GBPQ mineral thermobarometer

Three stages of metamorphism were identified based on petrologic observation and chemical composition. The mineral assemblage from the petrological observation revealed the prograde and peak metamorphism. The retrograde metamorphism was identified by the mineral composition profile. The major element profiles are almost flat in the cores and have slight changes in the rims (Fig. 4.15), indicating the two-stage history of the garnets. The content profiles are flat in the core, indicating that the garnets were homogenized during the growth at peak metamorphism without reabsorption. Following Taylor J and Stevens G (2010), this major element homogenization in the garnet core is associated with the anatexis. The characteristic of garnet cores suggests a peak metamorphic record that has overprinted the prograde information. However, the X_{Ca} and X_{Alm} in the core of garnet Grt-1 display the undulatory distribution (Figs. 4.15A and D), which is attributed to the entrapment of inclusions and slow diffusion during the garnet porphyroblast growth (Dempster TJ et al., 2020). Thus, the core of garnet Grt-1 is not suitable for quantifying the P-T conditions during the peak metamorphism, especially since the pressure will be misevaluated due to the Ca being sensitive to pressure.

Based on the mineral compositions and these rationales, the core of the garnet except for Grt-1, the rim of the plagioclase in the matrix and the biotites in the matrix were considered as the best to represent the composition of the peak metamorphism. Thus, they were used in the calculation of the conventional garnet-biotite-plagioclase-quartz (GBPQ) geothermobarometry. The GBPQ thermo-barometry constrained the pressure and temperature range of the peak metamorphism at 6.1–6.2 kbar and 665–692 °C. The temperature is in agreement with the temperature (688–707 °C) calculated by the Ti-in-Biotite thermometer proposed by Henry DJ et al. (2005) and the estimated temperature (650–740°C) based on the melt fraction (Zhang JH et al., 2017). Considering the activity of Ti might not be 1, which is the basic assumption of conventional mineral thermometry, the calculated temperatures correspond to minimum estimates.

Significant increases of X_{Mn}, $Fe^{\#}$ and a decrease of X_{Mg} in the rims (Fig. 4.15) suggest that the garnets have undergone a net transfer reaction during the low-temperature retrograde process (Kohn MJ and Spear F, 2000), although it was not observed by the microscope. The X_{Ca} also exhibits a slight decrease at the outer rims, suggesting a minor decompression process. It is almost impossible to reach thermodynamic equilibrium for the retrograde mineral assembly and garnet rims (Wu CM, 2018), most time there was no texture related to the reaction and lack of appropriate mineral phases under the thin section. Thus, the quantitative P-T conditions of the retrograde process were not determined by a conventional mineral thermobarometer.

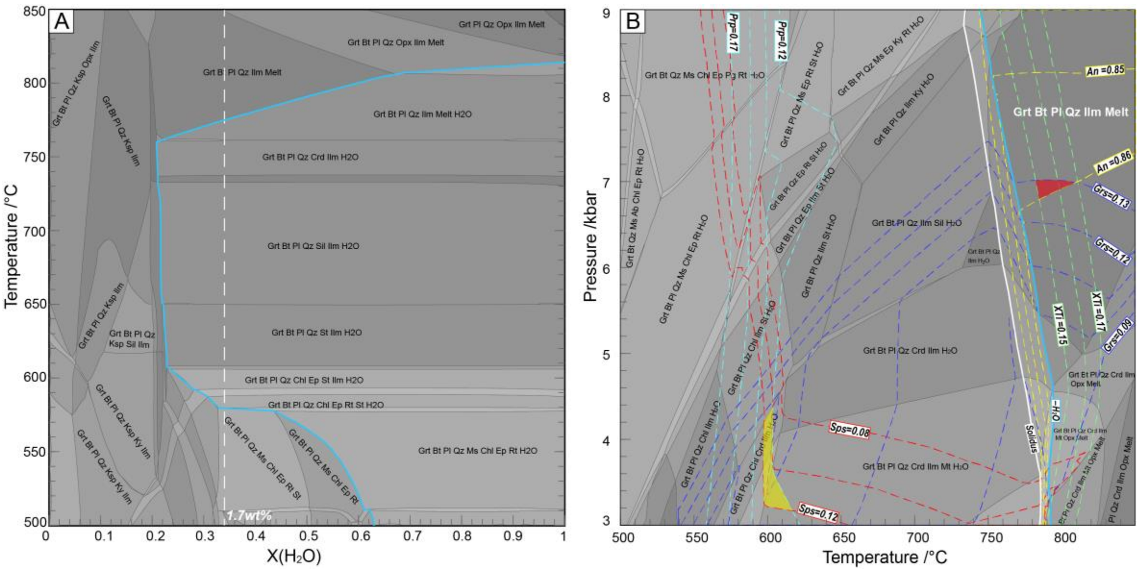

Figure 4.18. *Results of the P-T pseudosection calculation. (A) T-X (H2O) pseudosection at 6.0 kbar. The white dashed line is the selected water content at 1.7 wt%. The light blue solid line is the water-saturated line. (B) Calculated P–T pseudosection in the system MnO-Na2O-CaO-K2O-FeO-MgO-Al2O3-SiO2-TiO2-H2O-O2 [MnNCKFMASTHO]. The wet solidus is marked by a white solid line. The water-saturated line is marked by the light blue solid line. The red area represents the P-T conditions at the peak metamorphism, and the yellow area is the possible P-T conditions of the retrograde metamorphism. The mineral abbreviations used in the figures are those of Warr LN (2021).*

4.5.3 P-T pseudosection calculation

Bulk rock compositions used for P-T pseudosection calculations were from the melanosome sample S28. The T−X (H_2O) pseudosection was calculated at 6.0 kbar, aiming to determine the appropriate water content (Fig. 4.18A). The pressure calculated from the mineral thermobarometer was used as a reference for the T−X (H_2O) pseudosection settings. The changes of the X (H_2O) are from the anhydrous composition to 5 wt% water content. The H_2O content was set at 1.7 wt% based on the T−H_2O diagram so that the water-saturated line was close to the wet solidus (Fig. 4.18).

The P-T pseudosection of the melanosome displays that the solidus is at 730−790 °C (at 3−9 kbar), the observed mineral assemblage garnet, biotite, plagioclase, quartz, ilmenite and melt is stable in a large field at 750−850 °C and 5−9 kbar (Fig. 4.18B). The grossular component (X_{Grs}=0.12−0.13) in the garnet (Grt-2) core, Ti content (X_{Ti}=0.15−0.17) and An-value (An=0.84−0.86) of the biotite and plagioclase in the matrix define the P-T conditions of the peak metamorphism at 6.8−7.0 kbar and 780−810 °C within the stability field of the observed assemblage (Fig. 4.18B). The P-T conditions of the retrograde metamorphism were not constrained precisely in the P-T pseudosection, which yields a possible P-T range of 3.2−4.2 kbar and 595−615 °C, and reflects a cooling and decompression from the peak metamorphism (Fig. 4.18B). Since no retrograde mineral assemblages were observed under the thin sections, the retrograde P-T conditions cannot be robustly constrained. The value reported here is solely a preliminary estimate based on the compositional profile of the retrograde garnet rims.

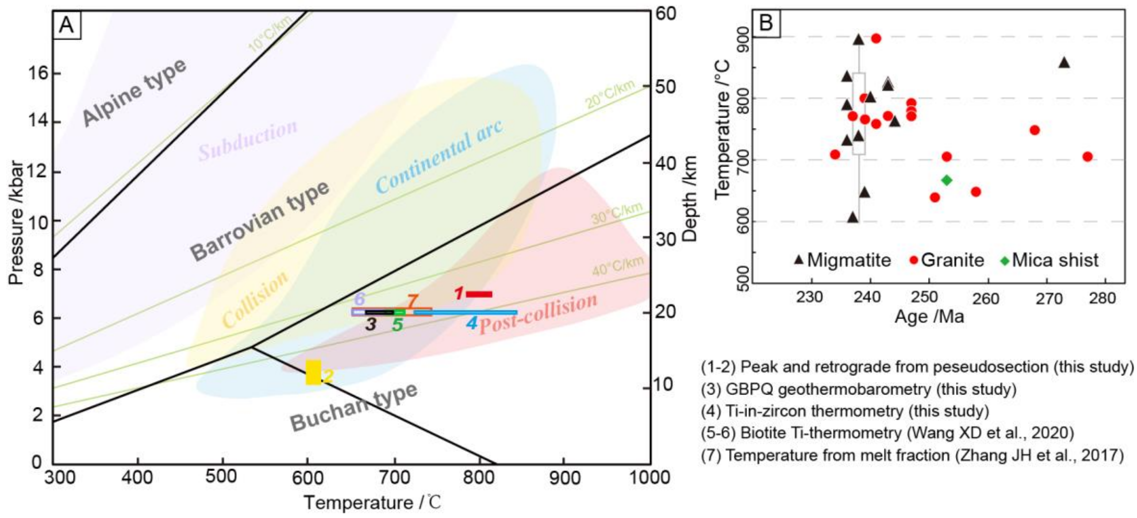

Figure 4.19. *Summary of the P–T estimation (A) and the results of Ti-in-zircon thermometry (B) of the Early Mesozoic high-grade metamorphic rocks in the Yunkai Massif, South China.*

Both the conventional mineral thermobarometer and the pseudosection calculation indicate a mid-crust upper-amphibolite-facies to granulite-facies high-temperature metamorphism. The estimated P-T conditions (Fig. 4.19) from the melanosome define a hot geothermal gradient of 35−40 °C/km.

4.6 Characteristics of the high-temperature metamorphism

4.6.1 Geochronological results

Zircon U-Pb dating

Most zircon grains in the melanosome S06 at the Shapa town are less than 100 μm and the main population exhibits a rounded and irregular shape (Fig. 4.20A). They don't have the typical core-rim structures and exhibit various internal textures. Some have oscillatory zoning and others are homogeneous. The above features suggest a detrital origin of the majority. Most zircons (33/38) yielded Proterozoic ages with an age peak at ca.1000 Ma (Figs. 4.20A and 4.21A). Among them, five ages are discordant. A few zircons (4/38) yielded Early Paleozoic ages at 391 Ma, 420 Ma, 439 Ma and 460 Ma. The ages of 439 Ma and 460 Ma come from the magmatic zircons, providing constraints on a lower limit of the sediment of the protolith. Additionally, there is another discordant age at 327 Ma.

Zircon grains within the mylonitic metatexite S16 at Shapa town are euhedral to subhedral with a size of ~100μm. They commonly show a core-mantle-rim structure under CL (Fig. 4.20B). Three grains exhibit obvious CL-bright inherited cores. All grains have a CL-dark mantle which is homogeneous and sometimes the vague oscillatory zoning can be observed. The outmost is the CL-grey recrystallized rim which is very narrow. Two analyses on the bright inherited core yielded two Neoproterozoic ages at 611 Ma and 790 Ma (Figs. 4.20B and 4.21B). Eight analyses on the dark mantle yielded an age cluster range from 442 Ma to 461 Ma. Seven of them gave a weighted mean $^{206}Pb/^{238}U$ age of 449.9 ± 4.7 Ma (Fig. 4.21B). The characteristics of quite low Th/U ratios (≤0.05) and the homogeneous mantle indicate

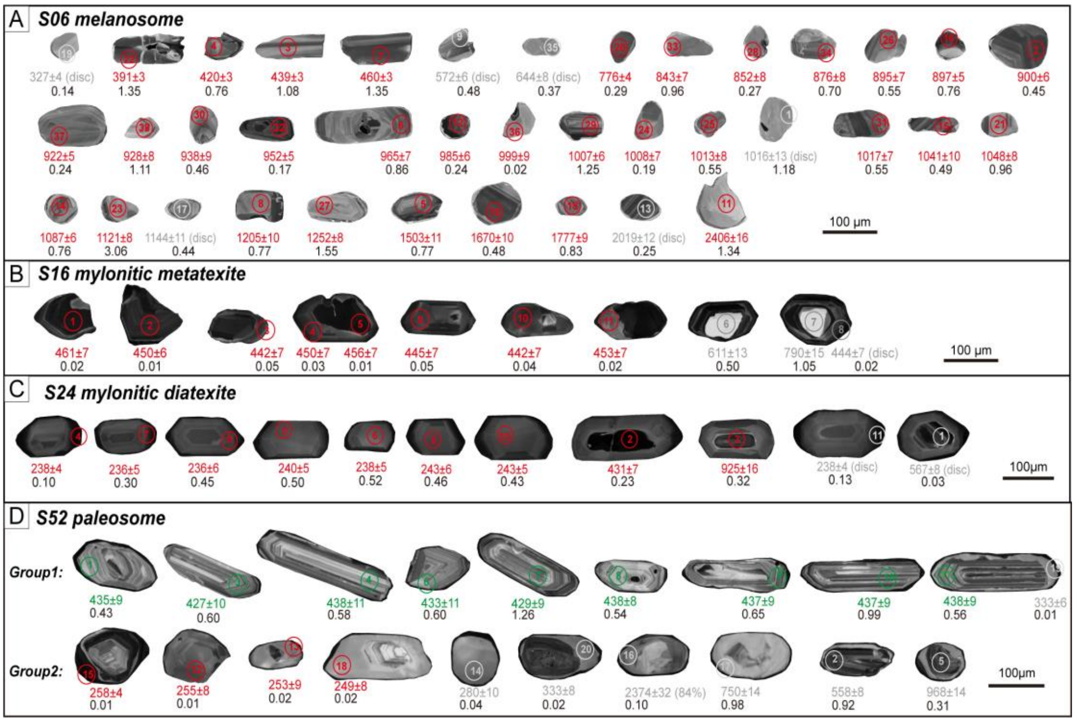

Figure 4.20. CL images of the zircons within the migmatites and meta-sedimentary rock.

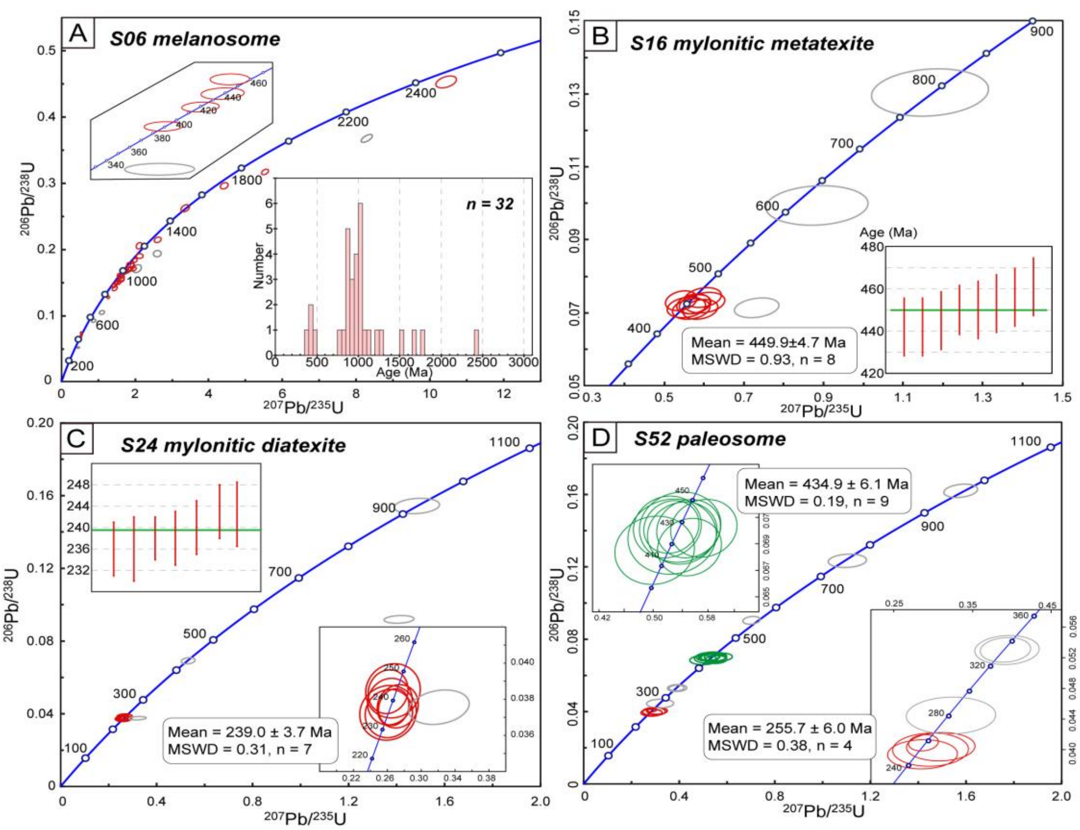

Figure 4.21. Concordia diagrams of the zircon U-Pb dating of the migmatites and meta-sedimentary rocks.

an anatectic genesis of these zircons. Thus, the age of 449.9 Ma is the time of the Early Paleozoic partial melting.

Zircon grains within the mylonitic diatexite S24 from the Jiahai Bay are euhedral and exhibit grey to dark polygonal sector zoning in the CL image (Fig. 4.20C). Only a few grains have inherited cores and are crosscut by the sector zoning. Three analyses on the inherited cores yielded apparent $^{206}Pb/^{238}U$ ages at 431 Ma, 935 Ma and a discordant age at 567 Ma (Fig. 4.21C). Eight analyses are on the polygonal sector zoning, and seven of them gave consistent $^{206}Pb/^{238}U$ ages. The weighted mean age was calculated at 239.0 ± 3.7 Ma (Fig. 4.21C), which is interpreted as the crystallization age of the newly formed zircons during regional partial melting.

Nineteen zircon grains were analyzed for the paleosome (S52) from the Hailing Island. The zircons can be classified into two distinct populations according to their morphology. Eleven zircons in Group-1 predominantly exhibit euhedral, prismatic and elongated in shape with lengths ranging from 100 to 250 μm and high length/width ratios from 1.5:1 to 5:1 (Fig. 4.20D). These zircons display well-developed bright to grey concentric oscillatory zoning, indicating a typical magmatic origin. Outside of the oscillatory zoning, narrow dark or bright rims can be recognized. It was attributed to the recrystallization or new growth during the late metamorphism (Fig. 4.20D). Nine analyses of Group-1 yielded a concordant weighted mean $^{206}Pb/^{238}U$ age at 434.9 ± 6.1 Ma (Fig. 4.21D), which is interpreted as the crystallization age of the zircons related to the Early Paleozoic orogenesis. Group-2 includes eight subrounded zircon grains displaying clear core-mantle-rim structures: inherited magmatic core, bright mantle and an outermost dark rim (Fig. 4.20D). Four analyses on the bright mantles and dark rims from Group-2 yielded a weighted mean $^{206}Pb/^{238}U$ age at 255.7 ± 6.0 Ma (Fig. 4.21D). Another five analyses (Nos. 14, 16, 17, 19 and 20) on the bright rims yielded older ages ranging from 280 to 2374 Ma, and two analyses on the inherited magmatic core (Nos. 2 and 5) yielded the ages at 558 Ma and 968 Ma. It reflected the information from the inherited ancient crustal materials. Due to the bright mantle and dark rims being very narrow in the CL images (Fig. 4.20D), the laser has probably penetrated these rims and resulted in a mixed age that was not totally reset. This is further supported by the continuous age distribution observed from 333 to 249 Ma on the U-Pb Concordia diagram (Fig. 4.21D). Therefore, the metamorphism was considered to postdate the mixed age of 249 Ma.

Monazite LA-ICP-MS U-Pb dating

Most monazite grains within granitic gneiss (S13) have a large size of ~200 μm, and show various internal structures including homogeneous, patchy and sector zoning (Fig. 4.22A). However, the ages of the different zones overlapped with each other and gave an age cluster from 229 Ma to 240 Ma. Thirty-one analyses yielded a weighted mean $^{206}Pb/^{238}U$ age of 233.6 ± 1.0 Ma (Fig. 4.23A), which is interpreted as the metamorphic age of the granitic protolith whose emplacement age is at 439 Ma (Fig. 4.14B).

Monazite grains from the mylonitic leucogranite S18 also exhibited a size mostly larger than 200 μm. The main population has a BSE-homogeneous internal structure, which is interpreted as the metamorphic monazite. A few grains exhibit the BSE-bright patchy zoning, and they have a sharp boundary with the BSE-dark domains, which represent the old core due to their slightly older age than the BSE-dark domains (Fig. 4.22B). Thirty analyses were conducted and twenty-three analyses yielded a concordant and consistent $^{206}Pb/^{238}U$ age cluster with the weighted mean age of 236.5 ± 1.4 Ma (Fig. 4.23B), which represents the age of metamorphism.

Monazite grains within melanosome S06 are smaller (<100 μm) than those in the above granitoid samples and mainly show dark to grey BSE zoning (Fig. 4.22C). The domains with different BSE brightness do not show a systematic difference in their ages. Thirty-one analyses on the monazite grains gave the overlapping ages and yielded a concordant age with a weighted mean $^{206}Pb/^{238}U$ age of 235.2 ± 1.1 Ma (Fig. 4.23C). Such an age represents the Early Mesozoic metamorphism, which is not recorded by zircons from the same sample.

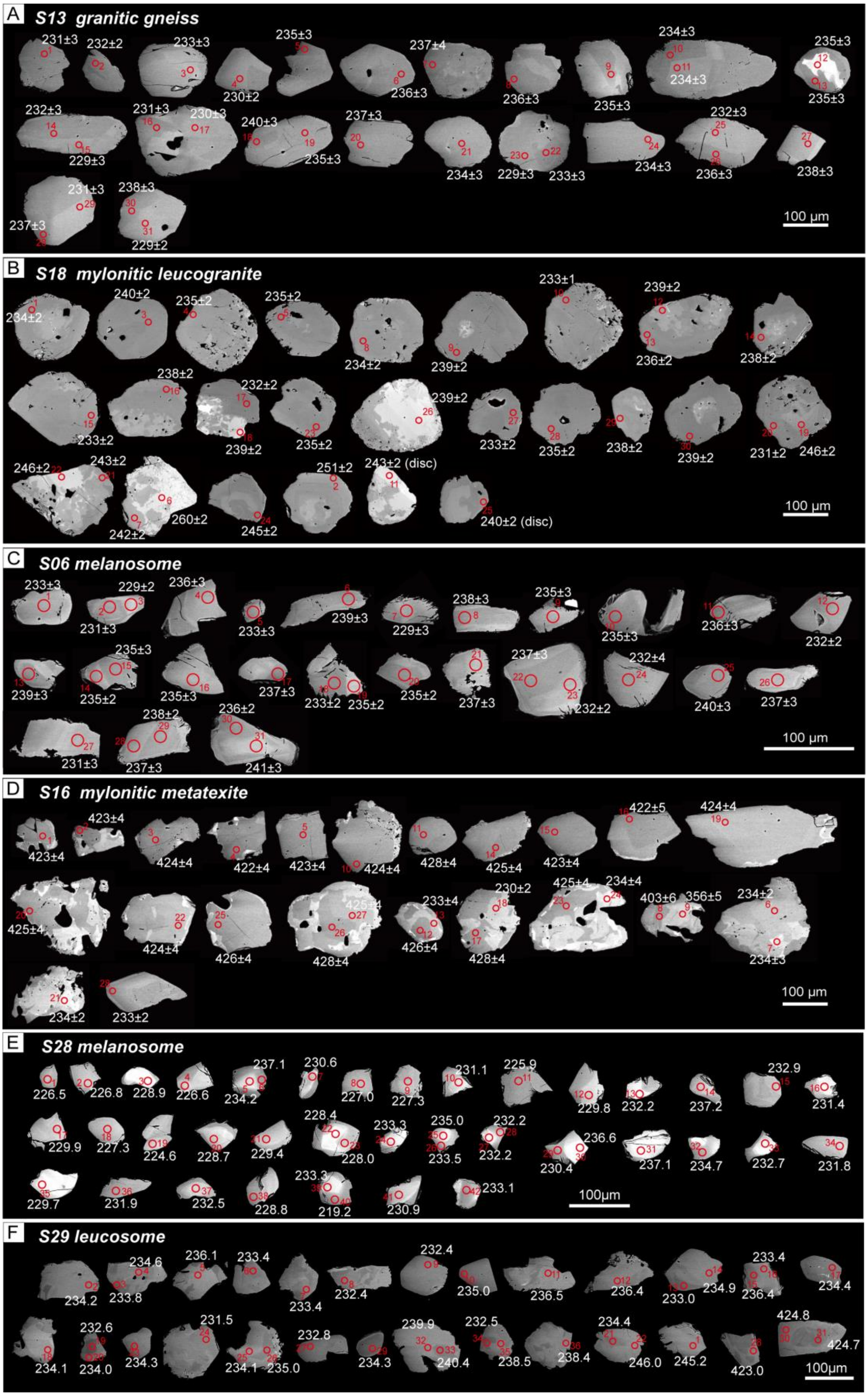

Figure 4.22. *Backscattered electron (BSE) images of the monazites.*

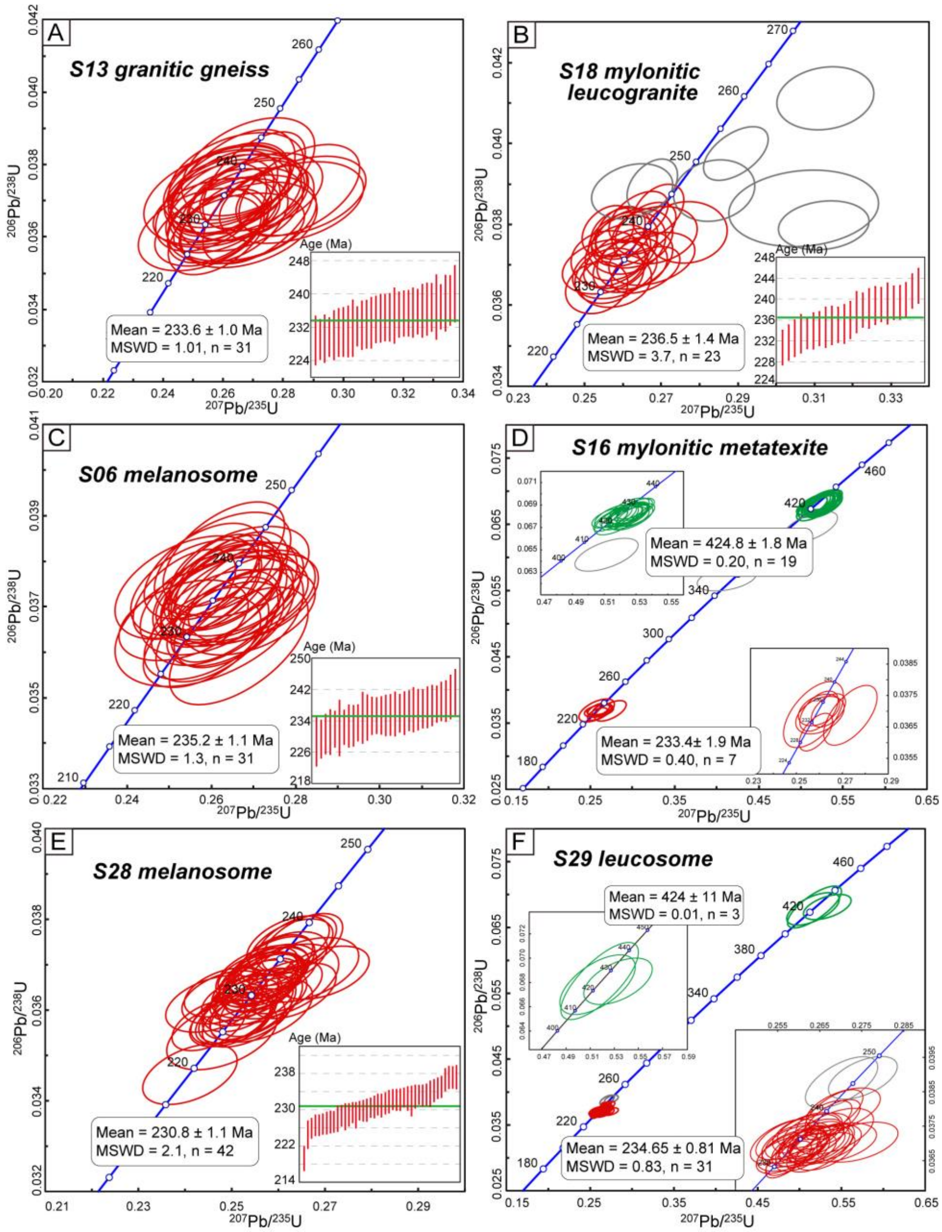

Figure 4.23. *Concordia diagrams of the monazite U-Pb dating.*

Most monazite grains within the mylonitic metatexite S16 show patchy zoning characterized by the BSE-dark metamorphic core and BSE-bright recrystallized domains as well as their sharp boundaries (Fig. 4.22D). Nineteen analyses on the BSE-dark core yielded the overlapping concordant age with weighted mean $^{206}Pb/^{238}U$ age of 424.8 ± 1.8 Ma, while seven analyses on the BSE-bright recrystallized domain yielded a weighted mean $^{206}Pb/^{238}U$ age of 233.4 ± 1.9 Ma (Fig. 4.23D). Additionally, two ages at 356 Ma and 403 Ma probably represent the partial resetting of age.

Forty-two analyses were done on thirty-six monazite grains from the melanosome S28 to the east of the Fuhu Hill. These monazite grains appear transparent with a slight yellow-green hue under transmission light. They are rounded or angular fragments in shape with length/width ratios close to 1:1 (Fig. 4.22E). The grains have similar sizes (50–80 μm). Most of them have a patchy or core-mantle-like internal texture. It is represented by two different responses in backscattered electron (BSE) images, a high BSE response core (generally Th/U>10) and a dark rim (generally Th/U<10), which is the result of dissolution-reprecipitation processes. Forty-two analyses are concordant and the ages from different BSE responses overlapped with each other. They displayed a tight cluster on U-Pb Concordia and yielded a weighted mean $^{206}Pb/^{238}U$ age at 230.8 ± 1.1 Ma (Fig. 4.23E).

Most monazite grains from the leucosome S29 have a size of 100–120 μm. They display a nearly homogeneous and gray pattern, sometimes lobate/embayment texture can be recognized with distinct boundaries (Fig. 4.22F). These features are characteristic of fluid-aided dissolution-reprecipitation reactions. Nevertheless, no differences were observed between the different BSE response domains due to their overlapping ages. Except for two grains yielding older ages at 245−246 Ma and another three grains preserving the Silurian (~424 Ma) information (Fig. 4.23F), thirty-one analyses formed a well-defined cluster and yielded a weighted mean $^{206}Pb/^{238}U$ age at 234.65 ± 0.81 Ma (Fig. 4.23F).

Apatite LA-ICP-MS U-Pb dating

Apatite grains in the granitic gneiss (S13) exhibit a rounded and irregular shape with a size of ~200 μm. There are no internal structures within the grains, but homogeneous in the CL images (Fig. 4.24A). Thirty-five spots were analyzed on the apatite grains, which are well scattered in the T-W diagram. They yielded a lower intercept age of 235.1 ± 4.6 Ma and the upper intercept was at a $^{207}Pb/^{206}Pb$ value of 0.907 (Fig. 4.25A).

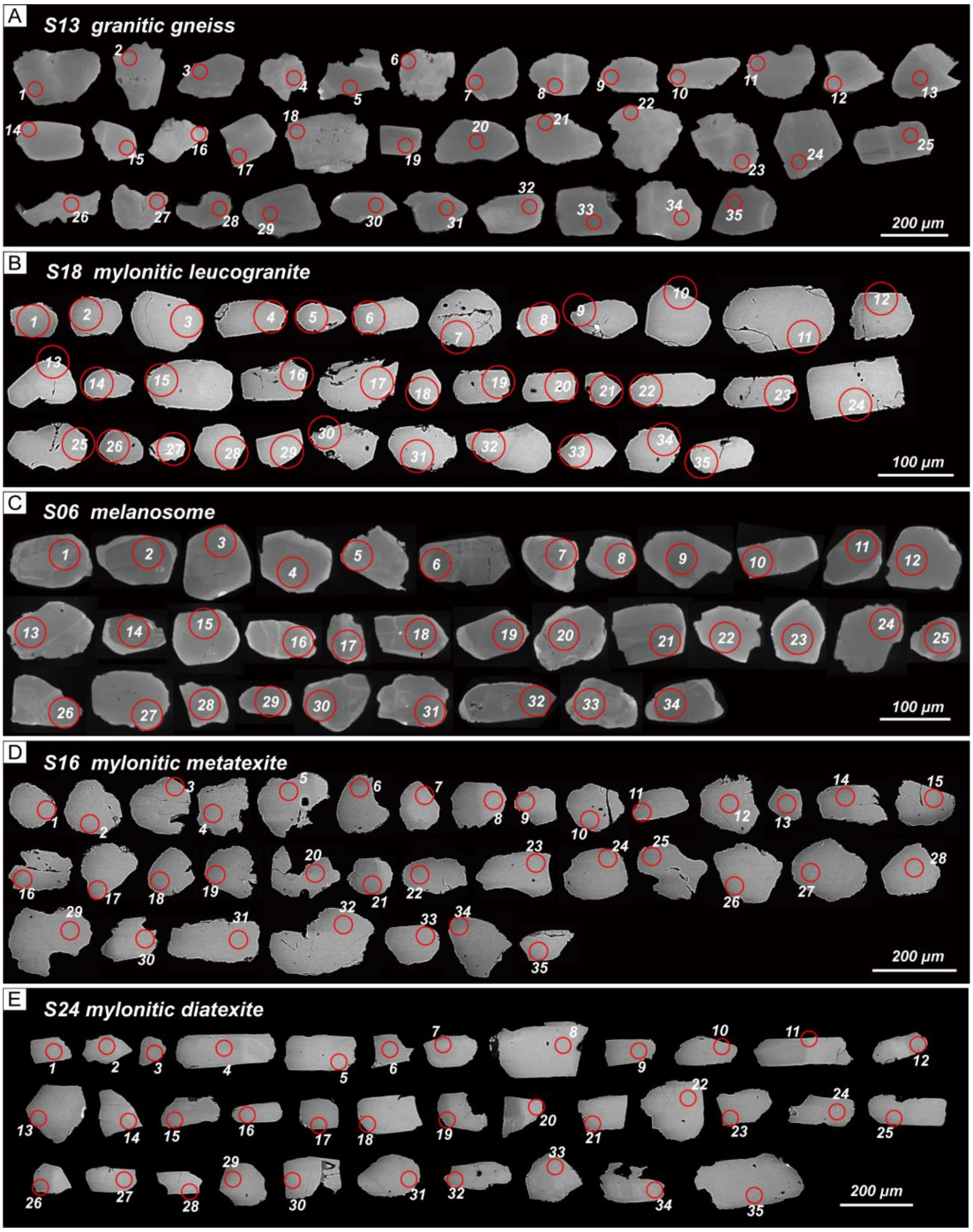

Figure 4.24. *CL (A and C) and BSE (B, D and E) images of the apatites.*

Apatite grains in mylonitic leucogranite S18 exhibit subhedral shape with a smaller size of ~100 μm and the length/width ratio is from 2:1−3:1. The BSE images are grey and homogeneous (Fig. 4.24B). Thirty-five analyses fall on a single discordia in the T-W diagram, yielding a lower intercept age of 239.2 ± 5.5 Ma and an upper intercept at 0.863 (Fig. 4.25B).

Apatite grains in melanosome S06 exhibit subhedral shape with a size of ~100 μm.

The CL images exhibit a core-rim structure characterized by the CL-dark homogeneous cores and narrow CL-bright rims (Fig. 4.24C). Sometimes, the dark core is divided into irregular areas by narrow bright zones inside. Thirty-four grains were analyzed and constrained the lower intercept ages at 231 ± 12 Ma with the upper intercept at 0.866 (Fig. 4.25C).

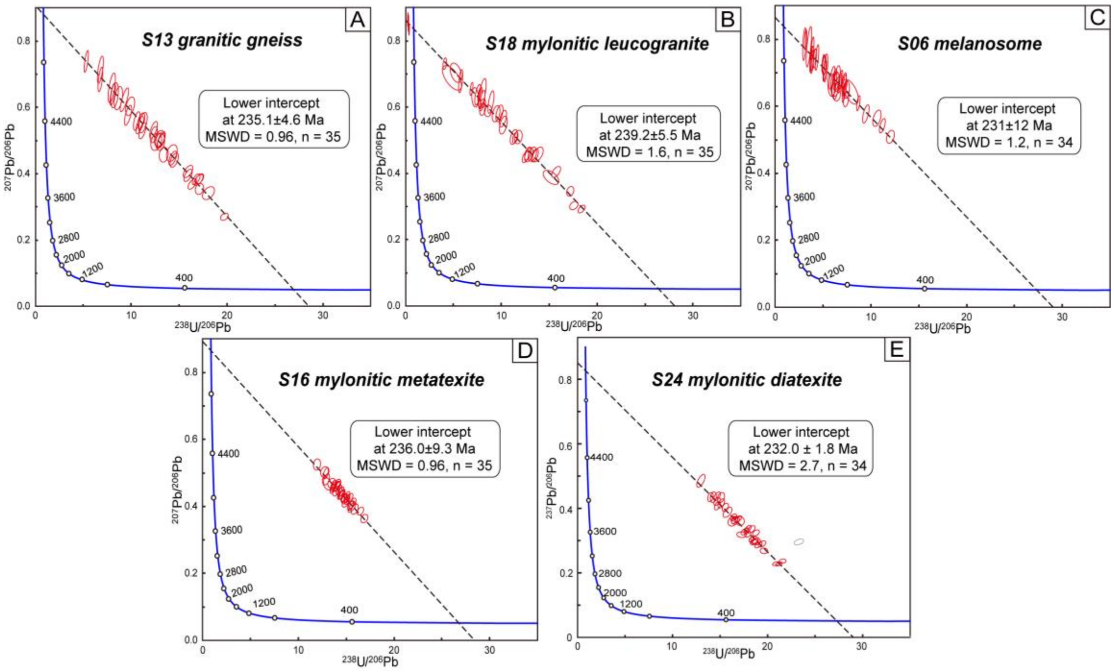

Figure 4.25. *Concordia diagrams of the apatite U-Pb dating.*

Thirty-five analyses were conducted on the apatite grains within mylonitic metatexite S16. These grains exhibit a rounded and irregular shape with a size of ~200 µm, and are homogenous in the BSE images without any internal structures (Fig. 4.24D). All analyses yielded a lower intercept age of 236.0 ± 9.3 Ma and an upper intercept at 0.894 (Fig. 4.25D).

Apatite grains in the mylonitic diatexite (S24) of the Jiahai area are colorless and transparent under transmission light. They are nearly prismatic to rounded in shape and have length/width ratios ranging from 3:1 to 1:1 with long axes ranging from 100 to 300 µm. Most apatites display homogeneous textures in the BSE images (Fig. 4.24E), suggesting a rapid crystallization without obvious compositional variations. Lower intercept age is calculated by anchoring the discordia at the $^{207}Pb/^{206}Pb$ initial ratio of

0.851, which is the calculated value at 230 Ma using the terrestrial Pb isotope evolution model. Thirty-four analyses yielded a well-constrained lower intercept age at 232.0 ± 1.8 Ma, except one outlier analysis (Fig. 4.25E).

Except for the apatites in melanosome S06 and three grains of the mylonitic leucogranite S18 were plotted in the low-grade metamorphic domain, the other samples, including the granitoids and the migmatites, exhibited the features of the high-grade metamorphic apatites (Fig. 4.26).

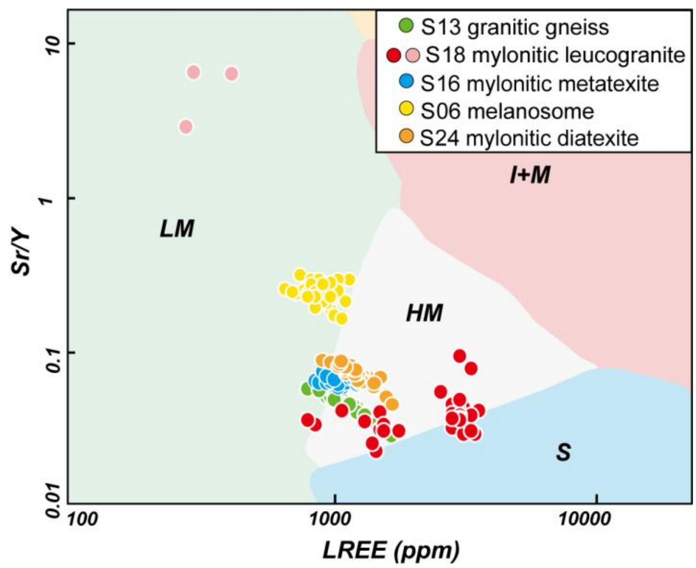

Figure 4.26. *Diagram of Sr/Y vs. LREE of the apatites.*

Sm-Nd geochronology of garnet

The garnets selected from the samples were randomly separated into different groups and analyzed. Hydrochloric acid leachate of garnet, plagioclase and apatite, which are present in the samples corresponding to the garnet, were also analyzed to constrain the left side of the isochron. In the Sm-Nd isochron diagrams, six points of garnet, apatite, plagioclase and leachate from the melanosome S06 defined a well-constrained regression line (Fig. 4.27A). It yielded an age of 208.6 ± 2.8 Ma with an intercept of $(^{143}Nd/^{144}Nd)_i$ at 0.512008. Five analyzed points from the melanosome S28, including garnet, apatite, plagioclase and leachate, defined the regression line (Fig. 4.27B). It yielded an age of 213.3 ± 2.1 Ma and the intercept of $(^{143}Nd/^{144}Nd)_i$ is 0.512008. Four analyzed points from the garnet, plagioclase and leachate of the paragneiss (S43) defined an isochron, yielding an age of 204.0 ± 2.0 Ma with an intercept of ($^{143}Nd/^{144}Nd)_i$ at 0.511843 (Fig. 4.27C).

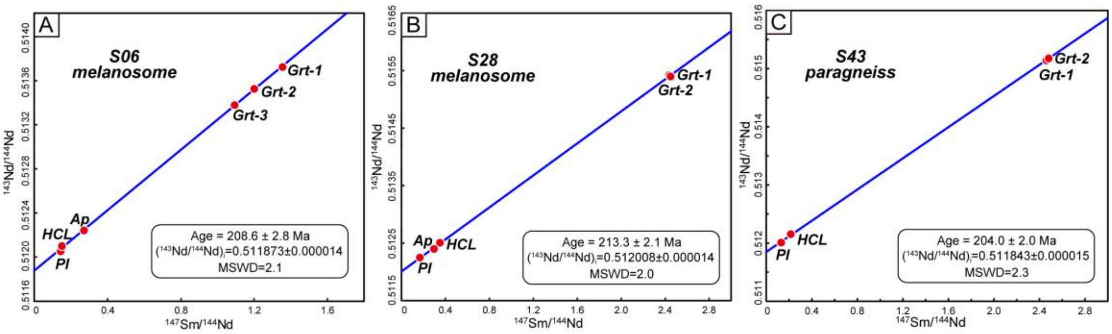

Figure 4.27. *Garnet Sm-Nd isochrons. Error bars are significantly smaller than the size of the symbols. Abbreviation: Grt-garnet, Ap-apatite, Pl-plagioclase, HCL-Hydrochloric acid leachate of garnet.*

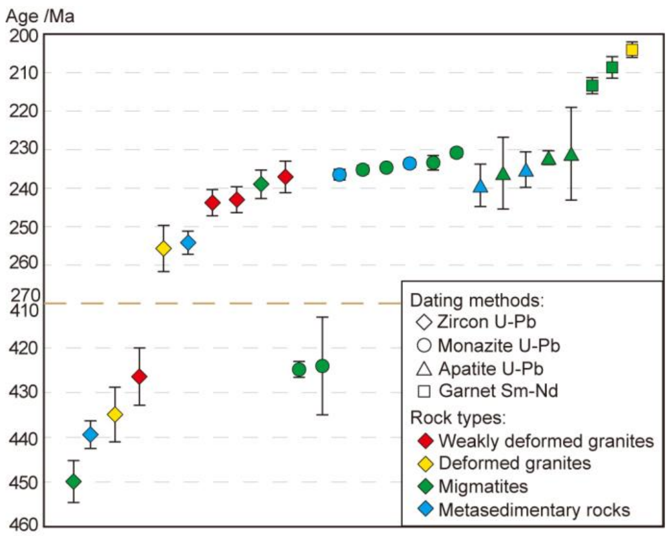

Figure 4.28. *The dating results of zircon, monazite and apatite U-Pb and garnet Sm-Nd.*

4.6.2 Timing of the high-temperature metamorphism and subsequent cooling processes

Multi-mineral geochronology with different closure temperatures was applied to unravel the precise timing of the metamorphic history (Fig. 4.28). The information at the high-temperature peak metamorphism can be well documented by the zircon and monazite U-Pb dating as well as garnet Sm-Nd dating. Meanwhile, the apatite U-Pb dating and published ^{40}Ar-^{39}Ar data provide more constraints on the subsequent cooling processes under the middle-lower temperatures.

The zircon U-Pb age at 239 Ma given by the mylonitic diatexite S24 provides a timing constraint on the migmatization (Fig. 4.21C). Group-2 zircons in paleosome (S52) show the characteristics of metamorphic zircons in texture and composition. They displayed irregular concentric zoning in the inherited core and were locally overprinted by the homogeneous domain of recrystallization and new growth (Fig. 4.20D; Hoskin PWO and Black LP, 2000; Corfu F et al., 2003), had low Th/U ratios (mostly <0.1) and displayed the REE pattern of metamorphic zircons equilibrated with garnet. The metamorphic zircons yielded an age of 256 Ma (Fig. 4.21D). However, as discussed before, it is probably a meaningless age due to the mixing of sampling from the dark and light domains, the timing of the high-temperature metamorphism should be later than this age (<256 Ma). Meanwhile, numerous metamorphic zircon ages were reported, predominantly from 244 Ma to 232 Ma (Table S1), suggesting a significant Triassic high-temperature metamorphism and migmatization. Among them, the age of diatexites and leucosomes at 241−238 Ma was considered as the timing of the peak metamorphism.

The monazites in the samples display patchy and lobate/embayment textures (Fig. 4.22) consistent with those developed in high-grade metamorphic rocks (Taylor RJM et al., 2014, 2016). The monazite U-Pb ages (237−231 Ma) are slightly younger than those of zircons. It may represent the early cooling stage of the crust because of the relatively lower closure temperature of monazites, which is considered at 530−750 °C (Black LP et al., 1984; Copeland P et al., 1988; Parrish RR, 1990; Oh CW, 2021). These monazite ages are coincident with those of the gneissic granites and gneiss, which underwent amphibolite-facies metamorphism in Gaozhou (237−230 Ma; Chen CH et al., 2012, 2017) and Wuyi Massif (239−237 Ma; Chen CH et al., 2018). The variation of the negative Eu anomalies and depletion of the HREE across time reflect the monazite growth during the plagioclase breakdown and garnet growth (Fig. 4.29).

The U-Pb dating on the high-grade metamorphic type apatites yielded the lower intercept ages ranging from 239−232 Ma (Figs. 4.25A-B, D-E and 4.26), indicating the time of cooling to approximately 350−550 ℃ after the peak metamorphism. In the chondrite-normalized REY+Sr plots (not shown), these apatites display a flatly distributed pattern, higher REE-abundances, and stronger depletion in Sr and Eu than that of the medium-low-grade metamorphism. The apatite grains within the melanosome S06 show characteristics of low-grade metamorphic ones, probably suffering from late hydrothermal alteration or metamorphism (Fig. 4.26).

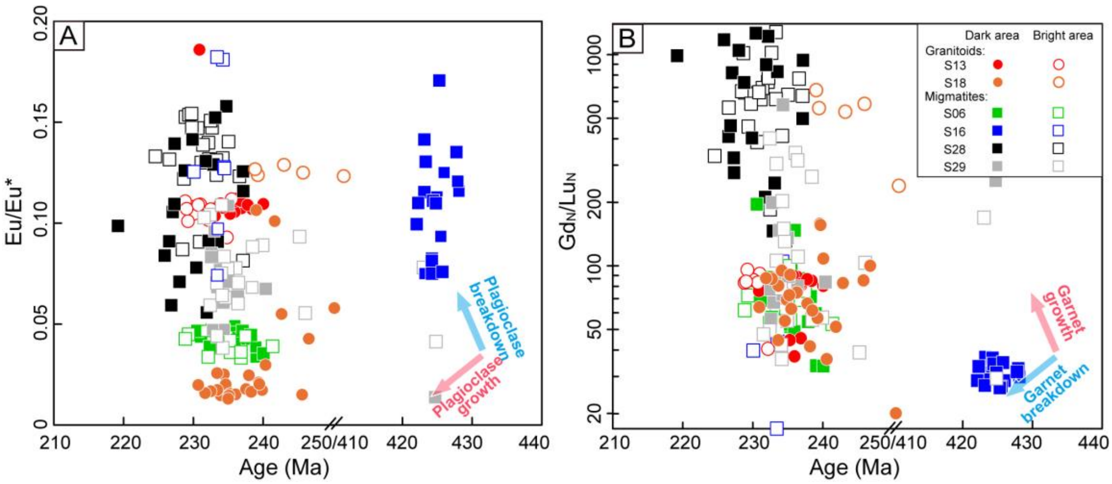

Figure 4.29. *Diagrams of Eu/Eu* and Gd_N/Lu_N versus age of the monazites.*

The Sm-Nd ages of garnets are well constrained at 213-204 Ma by the multi-point regression line (Fig. 4.27). However, they are slightly younger than the monazite U-Pb ages and the apatite U-Pb ages. Some major problems could influence the age of the garnet Sm-Nd dating: the presence of high-LREE inclusions (e.g., monazites, apatites), the uncertainty of the closure temperature of the Sm-Nd system, and the isotopic disequilibrium (Thöni M, 2002). Firstly, the presence of high-LREE inclusions can be precluded, because garnets were dated after acid leaching to remove the inclusions. Older age should be recorded by the garnet Sm-Nd system due to its high closure temperature at 600−750 ℃ (Mezger K et al., 1992; Hensen BJ and Zhou B, 1995; Dutch R and Hand M, 2010; Smit MA et al., 2013). Although some authors argued for a low closure temperature (560−600 ℃) and the recording of cooling ages (Mezger K et al., 1992; Smit MA et al., 2013), it still cannot explain the younger ages than the apatite U-Pb dating. Cheng H et al. (2019) proposed that there are similar effective diffusion radii

(~50 μm) for the garnets due to the widespread presence of fractures. It can cause partial resetting during the later thermal event and result in a younger age. In addition, the Nd-isotope ratio will be influenced by the monazite and apatite. The monazite dissolution and apatite retention will lead to melts with lower Sm/Nd (Ayres M and Harris N, 1997; Yakymchuk C and Brown M, 2014; Bea F et al., 2023). The garnet grew during this period, probably inherited this lower value and resulted in a younger age.

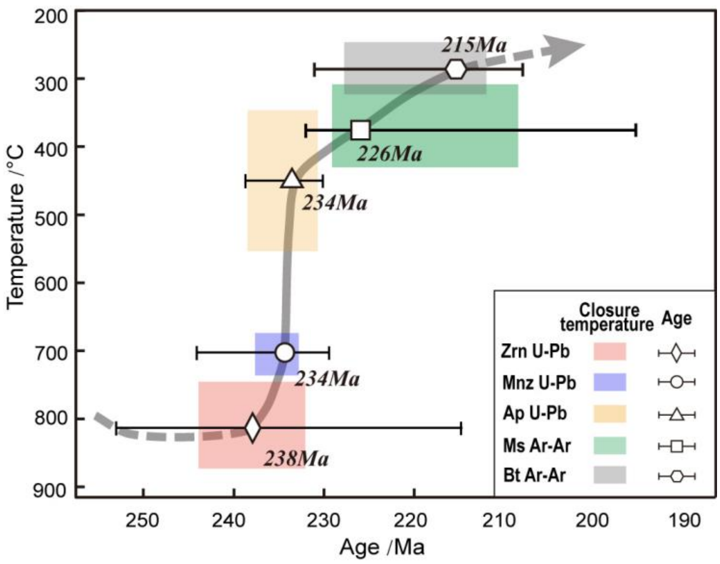

Figure 4.30. *Estimated thermal evolution based on the geochronological data from multi-mineral dating systems. The approximate closure temperatures of different minerals are from Chew DM and Spikings RA (2015).*

Previous geochronological studies on $^{40}Ar/^{39}Ar$ dating on muscovites and biotites provide constraints on the subsequent cooling processes of the metamorphism (Table S1). Taking such multi-mineral geochronological results into consideration, the peak metamorphism occurred at 241−238 Ma, followed by a cooling to ca. 300 °C within ca. 23 Ma (Fig. 4.30). In the previous studies, the metamorphism was interpreted as the Neoproterozoic or Early Paleozoic followed by the later Early Mesozoic low-temperature metamorphism (Zhou DY and Xu XS, 2017; Zhang JH et al., 2019, 2023; Chen Z et al., 2021). The new results suggest a strong Early Mesozoic reworking due to the high-temperature metamorphism, and it almost erased all the records of the Early Paleozoic with a few previous records preserved. It produced the migmatites and some crystallization of the new zircon, monazites and apatites during the Early Mesozoic. The intensity of Early Mesozoic metamorphism and its effect on the basement of the SCB were underestimated before.

4.6.3 Protoliths of the migmatites

The protoliths of the migmatites can be deciphered through field relationships, geochemical similarity and inherited zircons. The migmatites were surrounded by the Early Paleozoic metasedimentary rocks in the field, including paragneiss, mica-schist, phyllite and metasandstone (Figs. 4.2 and 4.3; RGMRGD, 1964). The meta-sedimentary rocks, such as paragneiss and mica-schist, are widely exposed to the east of the Hailing Island enveloping the granites, diatexites and metatexites (profile *j* in Fig. 4.4). Residual metasedimentary rocks were developed in migmatites, they were not involved in migmatization and still retain their earlier structures (Fig. 4.5E). The field relationship suggests that the protoliths of the migmatites are the adjacent exposed metasedimentary rocks. According to the geochemical analysis by Chen Z (2017) and Zhang JH et al. (2017), the migmatites have a composition close to the average composition of the greywacke and are plotted in the domain between argillaceous and sandstone fields in the (al+fm)-(c+alk) – Si discrimination diagram. The chemical similarity reveals that the protoliths probably belong to the greywacke. The existence of aluminum-rich minerals (e.g., garnet, muscovite, cordierite and sillimanite) supports the peraluminous protoliths.

The age of protoliths is still in discussion, as Late Neoproterozoic (<624 Ma; Zhou DY and Xu XS, 2017) and Late Mesoproterozoic ages (ca. 1000 Ma) were proposed (Zhang JH et al., 2019; Chen Z et al., 2021). Both of those come from the inherited zircons, the former was constrained by the youngest inherited zircon age, while the latter was given by the dominant age population of the zircon cores. Within the metatexite S16 and leucosome S29, the Early Paleozoic protolith information was not totally erased and recorded by the ~424 Ma inherited monazite (Figs. 4.23 D and F). That suggests the protolith is the Silurian metamorphic rocks, which probably sedimented during the Proterozoic as proposed by the previous work.

Furthermore, the granitic gneiss S13 exposed at the Shapa area was involved in the D1 deformation and the metamorphism (Fig. 4.5H), suggesting the protoliths also probably include earlier granites. Numerous inherited zircons with narrow and dark metamorphic rims are preserved within the paleosome (S52) and mylonitic metatexite (S16), displaying typical prismatic shape and oscillatory zoning (Figs. 4.20B and D). The age of 450−435 Ma given by the inherited zircons (Figs. 4.21B and D) was considered as the crystallized age of a denudated magmatic protolith. The magmatic zircons from the granitic gneiss yielded a similar age at 439 Ma (Fig. 4.14B). Thus, the magmatic protoliths can be constrained at 450−435 Ma, which is consistent with the timing of widespread magmatism and anatexis during the Early Paleozoic in the Yunkai Massif (Fig. 4.1). According to the youngest inherited magmatic zircon, the protoliths should be post-Silurian (<427 Ma) sediments in the Hailing Island.

On the basis of the field relationships, geochemical similarity and inherited zircons, the protoliths are the Silurian metamorphic greywacke and associated magmatic rocks, which experienced a strong Triassic reworking and only a few records were preserved by inherited zircons and monazites.

4.7 Effects of rock deformation-metamorphism on mineral age records

All the dating results obtained from the different methods were summarized in Table 4.1 and Fig. 4.28. The age series basically respects the closure temperature of the different minerals. The overlapping ages of the monazites and apatites were attributed to the rapid cooling of the high-temperature metamorphism (Figs. 4.28 and 4.30), whereas the anomalously young ages of garnet may be attributed to multiple potential factors (as discussed in Section 4.6.2).

The Early Paleozoic ages were mainly documented by zircons. The results show that zircons within the rocks exhibiting mylonitic deformation and high-grade migmatization (e.g., S18 and S24) are more prone to isotopic system resetting during the Early Mesozoic event, particularly those in meta-sedimentary rocks (e.g., S52) compared to those in granitic rocks. The Early Paleozoic records are prone to be preserved by the low-grade partial melting and weakly ductilely deformed rocks (e.g., S13, S06, S52). In addition, the monazite within the metatexite S16 also recorded the Early Paleozoic event, whereas the ~424 Ma ages recorded by three grains in the leucosome were considered as the capture age during the migration of the melt. Nearly all monazite, apatite and garnet samples yielded Early Mesozoic ages, regardless of lithology, indicating the influence of the Early Mesozoic high-temperature metamorphism.

Table 4.1 Summary of the dating results in the Yunkai Massif

	Sample	Lithology	Zrn U-Pb	Mnz U-Pb	Apt U-Pb	Grt Sm-Nd
weakly deformed granites	S01	porphyritic granite	237.1±4.1 & 426.4±6.4			
	S10	granite	243.0±3.4			
	S42	porphyritic granite	243.8±3.4			
deformed granites	S13	granitic gneiss	439.4±3.1	233.6±1.0	235.1±4.6	
	S18	mylonitic leucogranite	254.2±3.0	236.5±1.4	239.2±5.5	
mylonitic migmatites	S16	mylonitic metatexite	449.9±4.7	233.4±1.9 & 424.8±1.8	236.0±9.3	
	S24	mylonitic diatexite	239.0±3.7		232.0±1.8	
migmatites	S28	melanosome		230.8±1.1		213.3±2.1
	S29	leucosome		234.65±0.81 & 424±11		
	S06	melanosome	Peaks: ~450Ma, ~1000Ma	235.2±1.1	231.0±12	208.6±2.8
meta-sedimentary rocks	S43	paragneiss				204.0±2.0
	S52	paleosome	255.7±6.0 & 434.9±6.1			

The high-grade migmatization or partial melting resulted from elevated temperatures, which could reset zircon isotopic systems despite their high closure temperatures. Moreover, during the process of strong ductile deformation, the energy is not stored but dissipates diffusively while deforming. Most energy converts to heat, and the temperature gradually rises. If heat diffusion cannot keep up, the local temperatures continue to rise, resulting in viscosity decreases and strain further concentrates, and developing a narrow ductile shear zone. During this process, the temperatures of the deformed rocks are higher than the surrounding areas, ranging from tens to several hundreds of degrees, even causing a temperature surge of thousands of degrees under the thermal runaway regime (Spang A et al., 2024). That is the reason why the zircon isotopic system within strong mylonitic rocks is prone to being reset. Meanwhile, the meta-sedimentary rocks compared to the granitic rocks have less strength, which is easier to deform and produce heat to raise the temperature and reset the isotopic system.

4.8 Summary

The new results in this thesis revealed the strain partitioning of deformation in different locations and high-temperature metamorphism in the Early Mesozoic Yunkai Massif.

(1) Field and microscopic structural investigation revealed three phases of the deformation, namely, amphibolite-facies NE-SW flow (D1), greenschist-facies NE-SW dextral strike-slip shearing (D2) and vertical flow (D3). Therein, the D1 deformation is accompanied by the emplacement of the magma and migmatization.

(2) Petrological studies and P-T estimation revealed that the amphibolite-facies metamorphism experienced three stages, i.e., prograde, peak and retrograde stages. The peak metamorphic P-T conditions were at 6.8−7.0 kbar and 780−810 °C, followed by a cooling and decompression retrograde metamorphism probably at 3.2−4.2 kbar and 595−615 °C.

(3) The protoliths of the metamorphic rocks are the Silurian metamorphic greywacke and associated magmatic rocks.

(4) Multi-mineral geochronological data indicate the deformation lasted to at least 237 Ma, the magma emplaced and crystallized at 254−237 Ma and the high-temperature metamorphism occurred at 241−238 Ma, followed by rapid cooling.

Chapter 5. Early Mesozoic deformation, metamorphism and crustal thermal state of the Cathaysia Block

5.1 Introduction

Previous studies demonstrated that magmatism and deformation exhibited planar distribution characteristics within the Cathaysia Block. Meanwhile, the studies on metamorphism, geothermal and geophysical fields collectively revealed that the Cathaysia Block is vertically layered and horizontally block-divided (see details in Chapter 2). The differential phenomena across the massifs make the Cathaysia Block an ideal location to discuss their rheological properties of the lithosphere.

The Mesozoic period is focused in this chapter due to its strong reworking on the previous geological records (as discussed in Chapter 4). The Early Mesozoic deformation structures were identified as the top-to-the-north transpression (250−225 Ma; Wang YJ et al., 2021), characterized by the E/W-striking folds and thrust faults from the Yunkai to Nanling massifs with the intensity decreasing to the north (Wang YJ et al., 2007, 2021; Lin W et al., 2008; Faure M et al., 2014, 2016b). Additionally, Early Mesozoic NE-striking deformation structures developed in some places, i.e., top to the northwest thrust in Xuefengshan, Jiangnan Orogenic Belt (Chu Y et al., 2012), transpressional Yingyangguan shear zone in the Nanling Massif (Wang LZ et al., 2019), Yangchun shear zone in the Yunkai Massif (Wang YJ et al., 2007) and Changting and Badu shear zones in the Wuyi Massif (Xu XB et al., 2011; Wang YJ et al., 2013; Li JH et al., 2018). The Early Mesozoic high-grade metamorphism mostly developed in the southern Yunkai Massif (e.g., granulite in the Shiwandashan area and eclogite in the Hainan Island; Zhao L et al., 2011; Jiao SJ et al., 2013; Liu XC et al., 2020; Xia MM et al., 2022) and northern Wuyi Massif (e.g., amphibolite in the Longyou area and granulite in the Suichang-Longquan area; Wang YJ et al., 2013; Zhao L et al., 2015, 2017; Zhou X et al., 2018). These Early Mesozoic deformation and high-grade metamorphism in the Cathaysia Block were explained as the results of an oblique ICB-SCB collision and the Paleo-Pacific subduction (Wang YJ et al., 2007a, 2021; Li JH et al., 2017; Liu XC et al., 2020; Zhao L et al., 2022). Moreover, the pattern and distribution of the deformation and metamorphism, and geophysical fields are significantly controlled by the crustal thermal state (Fossen H et al., 2017; Vlaha DR et al., 2024), which is indispensable to shed light on lithospheric rheology. Previous studies attempted to explore the crustal thermal state by estimating the temperature from deformation and metamorphism (Xu XB et al., 2011; Chu Y et al., 2012b; Zhao L et al., 2012; Wang YJ et al., 2021; Cochelin B et al., 2022), which is limited to different local areas and sometimes is semiquantitative. Recent advancements in RSCM make it a new geothermometer to decipher the thermal state in ancient orogenic belts, which can record the highest temperature based on the degree of ordering of carbonaceous material (Beyssac O et al., 2002, 2004; Lahfid A et al., 2010). It provides a quick and quantitative tool and allows us to explore the crust in a block scale.

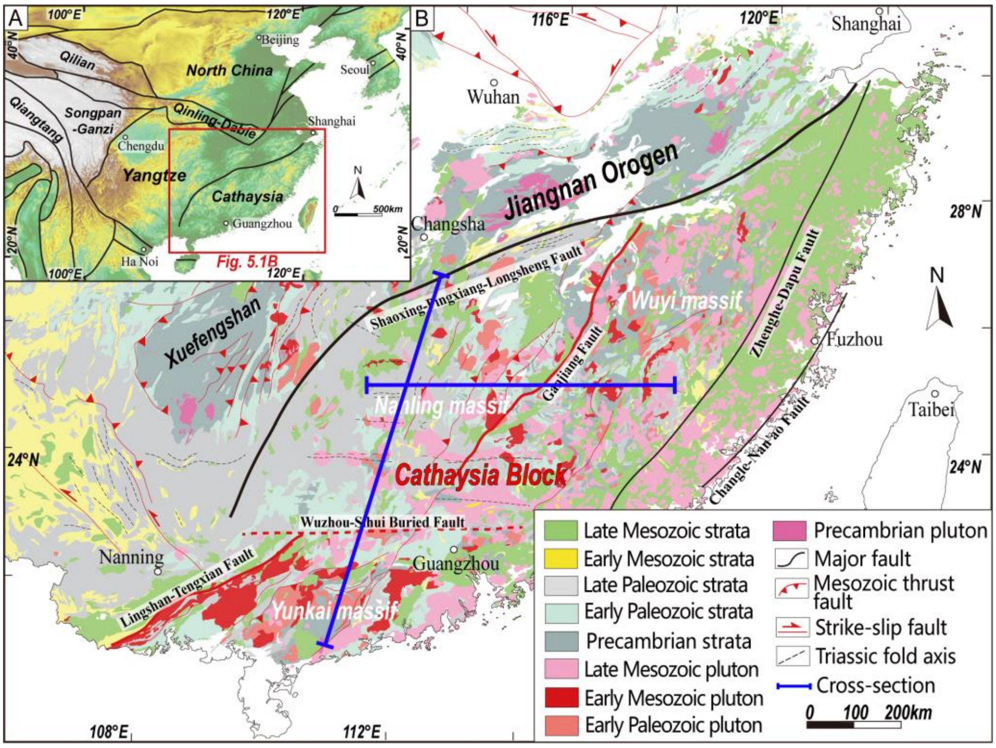

Figure 5.1. *(A) Topographic and tectonic sketch map of South China and its adjacent blocks. The black lines are the major suture boundaries (modified after Li JH et al., 2018). (B) The geological map of the Cathaysia Block (modified after China Geological Survey, 2020) shows the locations of the cross-section lines (in blue) of the field investigations.*

In this chapter, we conducted field investigations and RSCM thermometric analyses in the block scale of the Cathaysia Block, along two major cross-sections that are quasi perpendicular to each other (Fig. 5.1). To mitigate the impact of magmatism and decipher the regional metamorphic temperature, we specifically targeted the rocks situated far from the plutons. A total of 82 samples were collected from the Neoproterozoic to Early Triassic strata, including mudstone, siltstone, limestone, meta-sandstone, slate, phyllite, and schist.

The new results in this thesis decipher the spatial distribution and pattern of deformation and metamorphism. This first attempt of RSCM at this scale unravels the Early Mesozoic spatial distribution of the metamorphic temperature in the Cathaysia Block, highlighting the thermal heterogeneity among different massifs and the multi-block properties of the Cathaysia lithosphere. This work provides new insights to understand the orogenic evolution and lithospheric rheology.

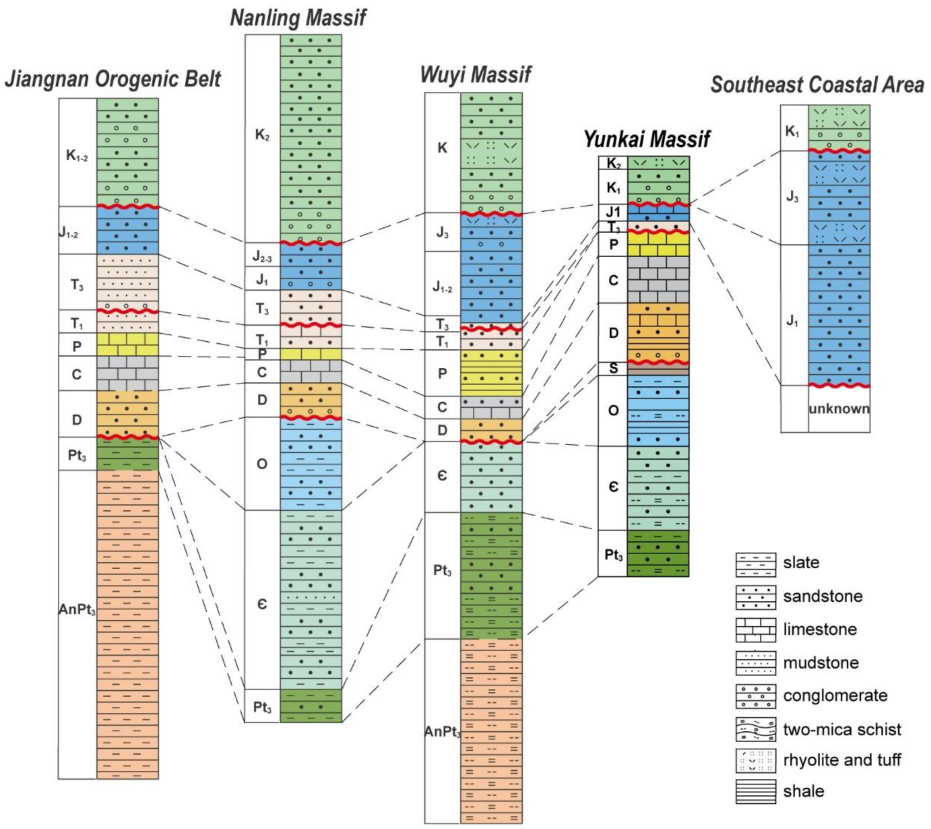

Figure 5.2. *The synthesized stratigraphical columns for the sections from the Jiangnan Orogenic Belt, Cathaysia Block (Yunkai, Wuyi, Nanling massifs) and Southeastern Coastal Area.*

5.2 Deformation and kinematic characteristics

The strata sequence from the Neoproterozoic to Cretaceous within the Cathaysia Block is subdivided into four units by three unconformities located below the Early Devonian, Upper Triassic and Lower Cretaceous (Fig. 5.2; Shu LS, 2012; Wang YJ et al., 2013; Zhang GW et al., 2013; Wang ZH et al., 2018; Shu LS et al., 2021). The intensity of the deformation is different between the different strata units and the different massifs.

5.2.1 Yunkai Massif

The Yunkai Massif exhibits more ductile deformation with respect to the other two massifs. The pre-Triassic rocks in the center of the Yunkai Massif exhibited intense ductile deformation (Fig. 5.3), characterized by the migmatization of Cambrian rocks, gneissification of Silurian granites and mylonitization of Devonian rocks (Figs. 4.5H and 5.4A-E). The foliation trajectory exhibits a dome-like structure at the center of the Yunkai Massif (Fig. 5.3). The foliation medium-steeply dips, and nearly E-W-trending dextral and NE-trending sinistral/dextral transpression were developed along the Fenjie and Yangchun faults, respectively (Figs. 5.3 and 5.5). To the north of the Fenjie Fault, the grade of the deformation decreases. The Neoproterozoic to Devonian rocks show the weak ductile deformation characterized by the schistosity and slate cleavage (Fig. 5.4F), whereas the Carboniferous-Permian rocks have no ductile deformation. To the southeast of the Yangchun Fault, a Late Paleozoic basin was developed and was characterized by undeformed Devonian siltstone and Carboniferous limestone (Fig. 5.4G). Numerous open pits and cement factories are in these limestone strata. The Neoproterozoic to Early Paleozoic rocks below the Yangchun Basin show the same low grade of ductile deformation as those in the north of the Fenjie Fault. The brittle domain deformation within the pre-Triassic rocks was mainly represented by the E/W-trending thrust-and-folds system, suggesting a crustal shortening in the approximately N-S direction (Fig. 5.5).

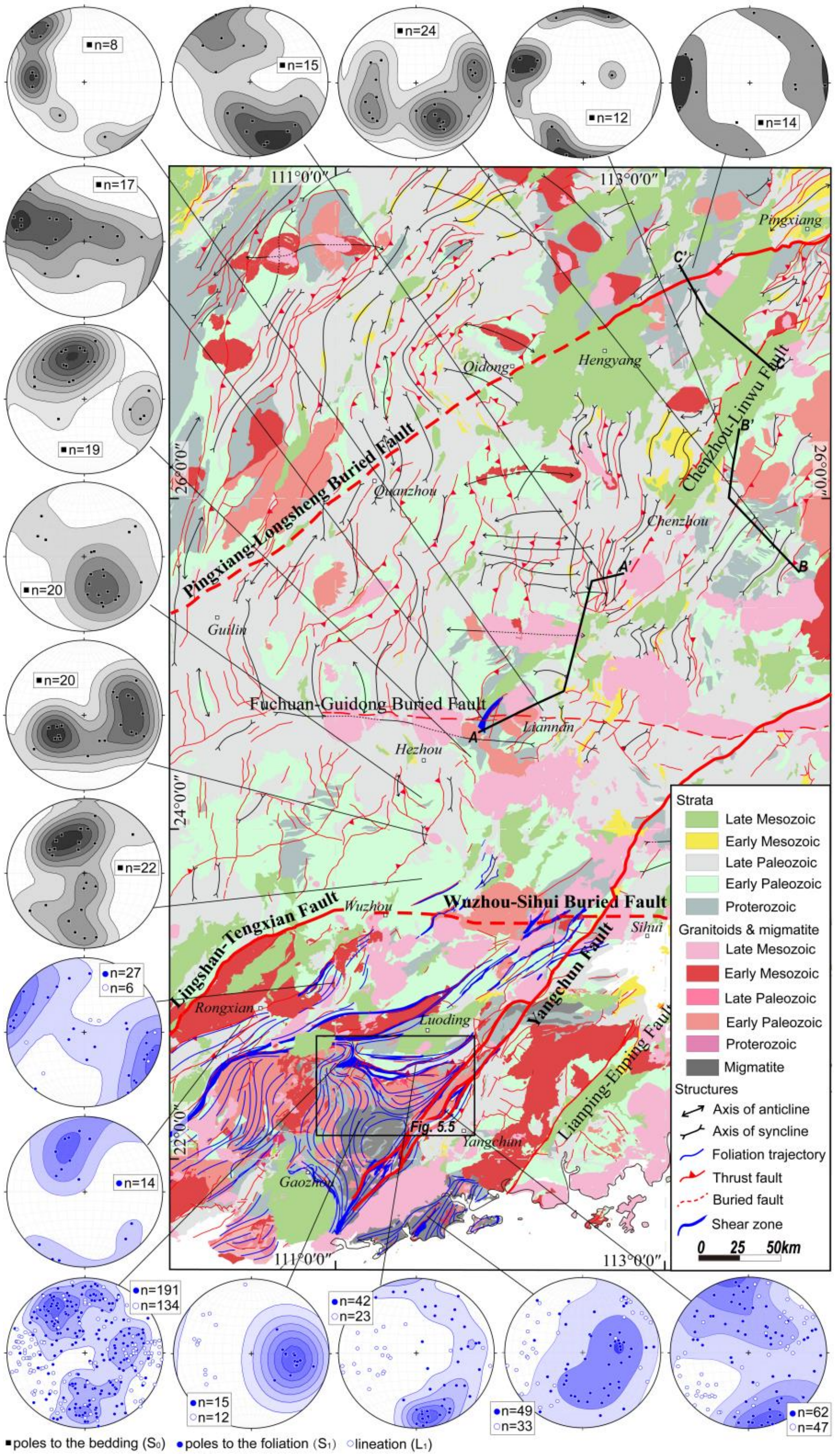

Figure 5.3. *(A) Structural geological map of the Yunkai-Nanling cross-section showing the foliation trajectories and shear zones in the Yunkai Massif, and the folds and faults in the Nanling Massif. (B) Stereonet projections (lower hemisphere, equal area) show the foliations of the Yunkai Massif (in blue) and the original beddings of the Nanling Massif (in black).*

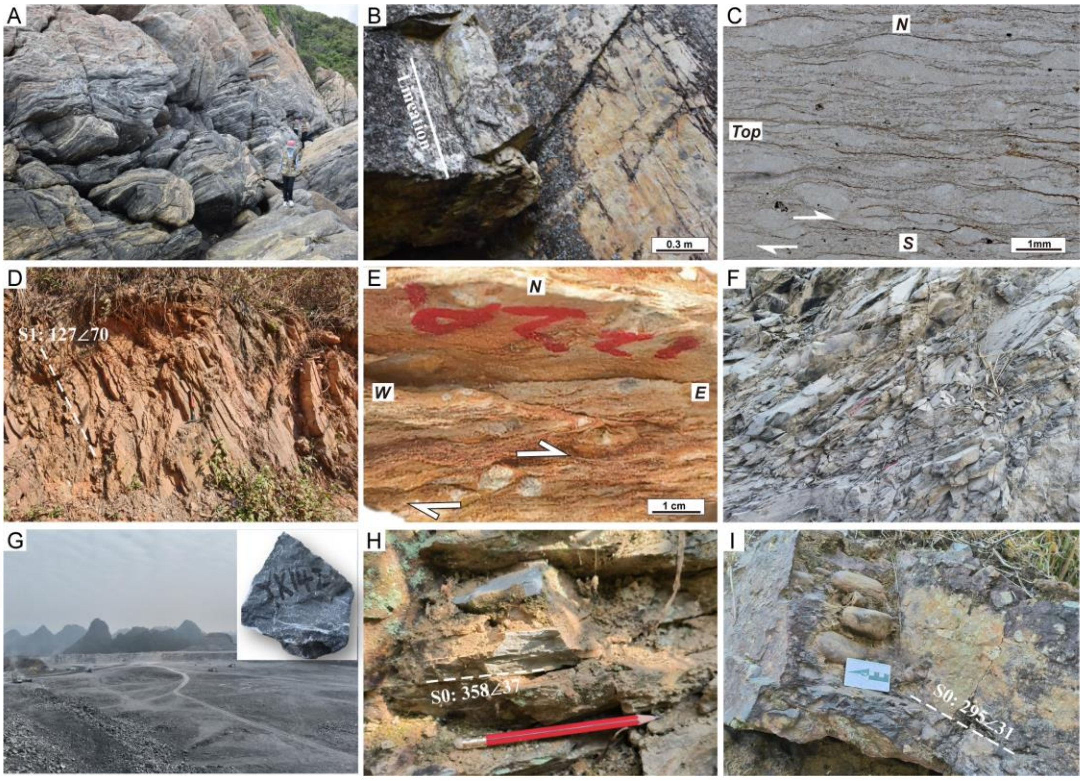

Figure 5.4. *Field and microscopic photographs showing the deformation intensity of rocks in the Yunkai Massif. (A) Migmatites with asymmetrical folds in Yangjiang. (B) Steeply dipping Devonian mylonites with nearly pure linear fabrics in Xinyi. (C) Microscopic photograph of the Devonian mylonites indicates the top-to-the-north thrusting. (D) The Devonian phyllite with strong ductile deformation in Luoding. (E) The Ordovician mylonite within the Shear zone in Luoding showing the EW-striking dextral shearing. (F) The schistosity developed within the Cambrian meta-siltstone in Wuzhou. (G) The open pit in the Carboniferous limestone in the Yangchun Basin. (H) The gentle beddings developed in T_3-J_1 non-ductile deformed siltstone in Luoding. (I) The beddings defined by the orientated array conglomerate in the Early Cretaceous in the Luoding Basin.*

The Late Mesozoic rocks are mainly distributed in the basins and their edges, such as the Luoding Basin (Fig. 5.3) which is located to the north of the Fenjie Fault (Fig. 5.5). The Late Triassic to Jurassic rocks and Cretaceous red beds are brittle deformed, characterized by the brittle faults and joints, which were not involved in the ductile deformation (Figs. 5.4H-I).

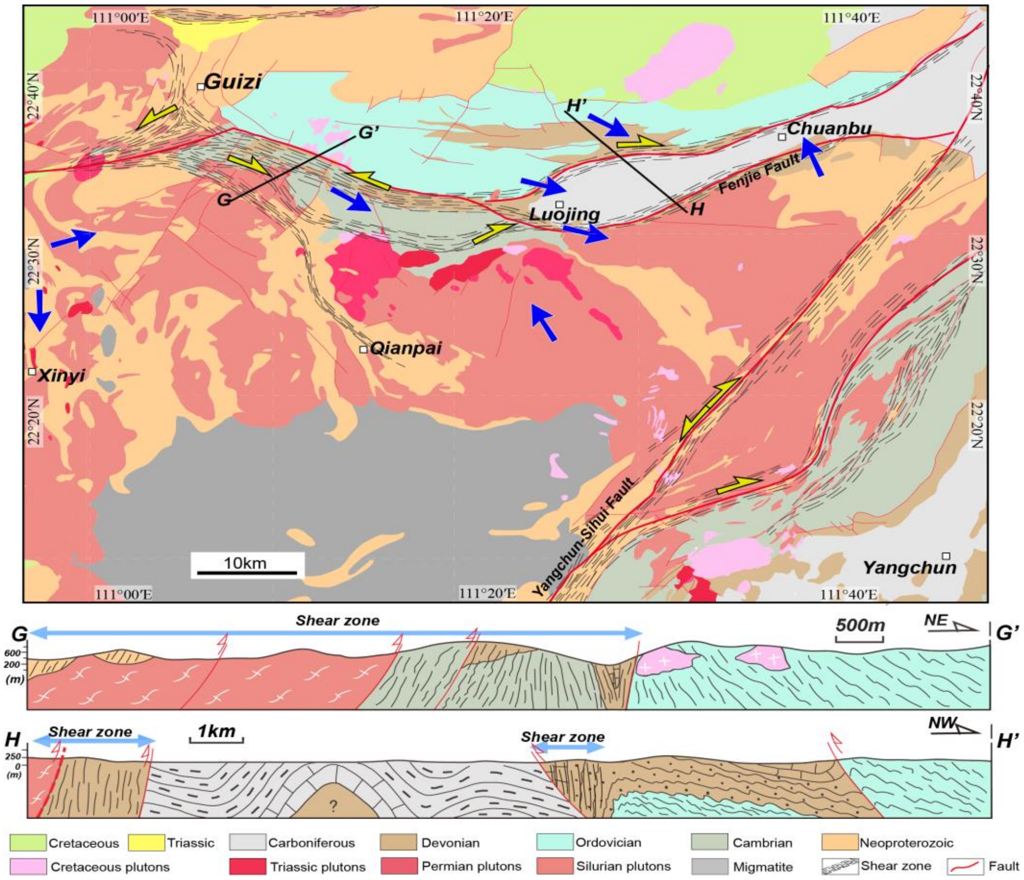

Figure 5.5. *Geological map and cross-section sketch of the Guizi-Yangchun area, displaying the structural pattern. The locations are shown in Figure 5.3. Locations of the geological cross-sections along the GG' and HH' are shown by the black solid lines. The yellow arrows represent strike-slip shearing. The blue arrows represent the direction of the thrust.*

5.2.2 Nanling Massif

Notable ductile deformation is absent in the Nanling Massif, only the Yingyangguan shear zone has a high strain showing a thrusting to the northwest (Fig. 5.3), which was dated by the mica $^{40}Ar/^{39}Ar$ and yielded the Triassic age (227−224 Ma; Wang LZ et al., 2019). Sometimes cleavage and schistosity are present within pre-Devonian rocks (Figs. 5.6A-C and 5.7). More often, the bedding of pre-Devonian rocks is obvious and is not replaced. Regionally, the pre-Devonian strata were folded and the fold-axis mostly strikes in a nearly East-West direction.

The Late Paleozoic strata were not involved in ductile deformation, and the predominant deformation patterns are the brittle folds and faults in different scales (Figs. 5.6D-G). The Late Paleozoic strata are folded along a nearly E-W striking direction, superimposed by NNE-trending folds (Figs. 5.3, 5.6F-G and 5.7), suggesting two shortening directions.

All the Neoproterozoic to Triassic strata are unconformably overlain by gently

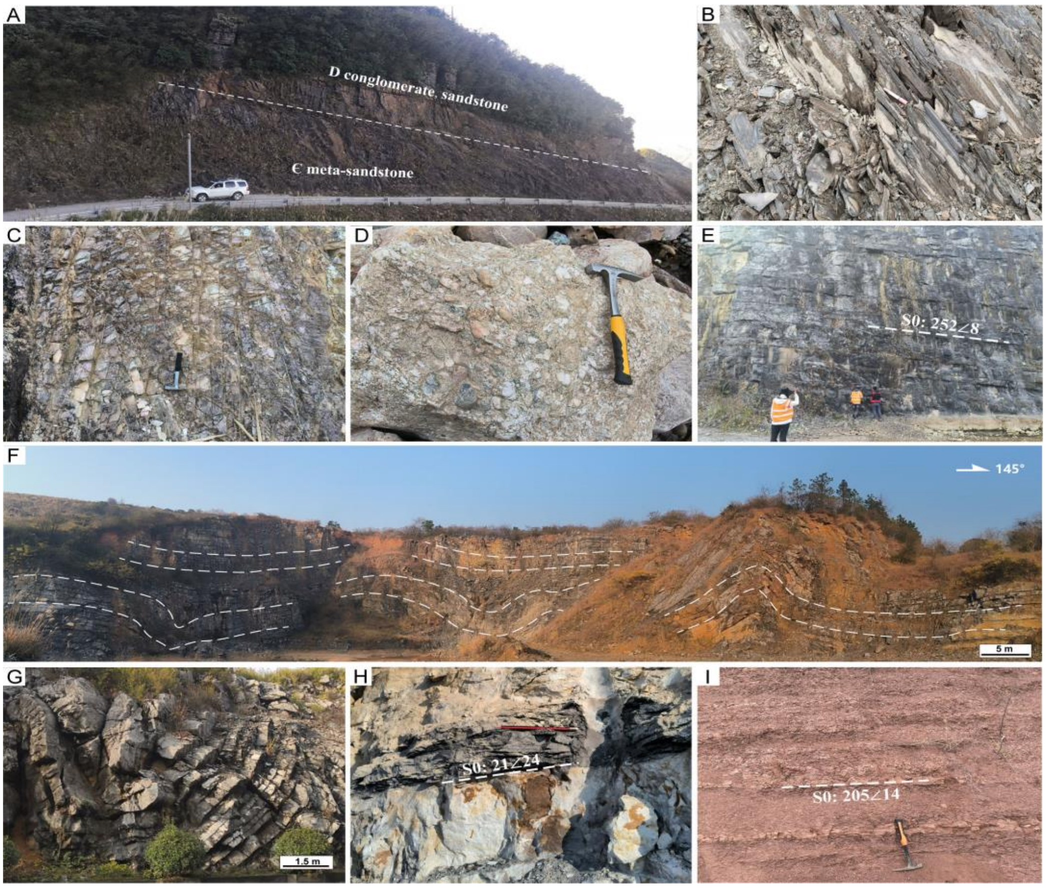

Figure 5.6. *Field photographs showing the deformation of rocks in the Nanling Massif. (A) The unconformity between the Cambrian meta-sandstone and Devonian sandstone in Hezhou. (B) Cambrian slate with slaty cleavage in Chenzhou. (C) The dense cleavages developed in the Cambrian slate in Cangwu County, Wuhou. (D) The conglomerate above the unconformity between the Cambrian and Devonian in Rucheng County, Chenzhou. (E) Stable and gentle bedding in Devonian limestone in Changning. (F) The folded Carboniferous limestone in Changning showing the NW-SE shortening. (G) Carboniferous folded thick-layered limestone in Chenzhou. (H) Gentle dipping Jurassic feldspathic sandstone with coal seams. (I) Cretaceous red beds in Hengyang Basin.*

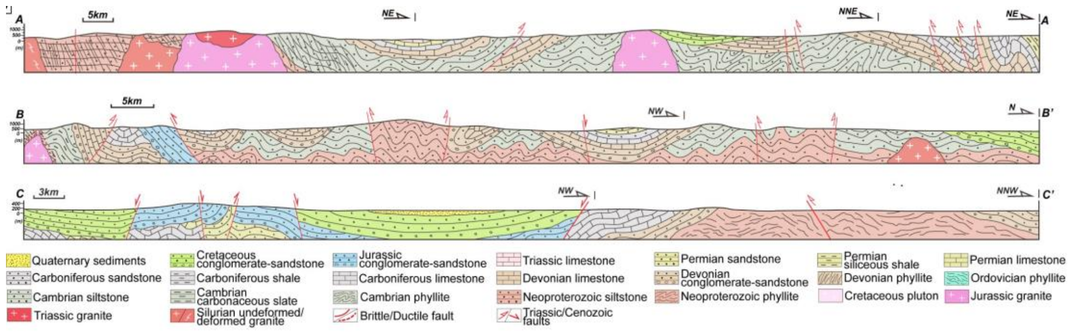

Figure 5.7. *The geological sketch shows the structural pattern of the Nanling Massif. The locations of the cross-sections are shown by the black lines AA', BB' and CC' in Figure 5.3.*

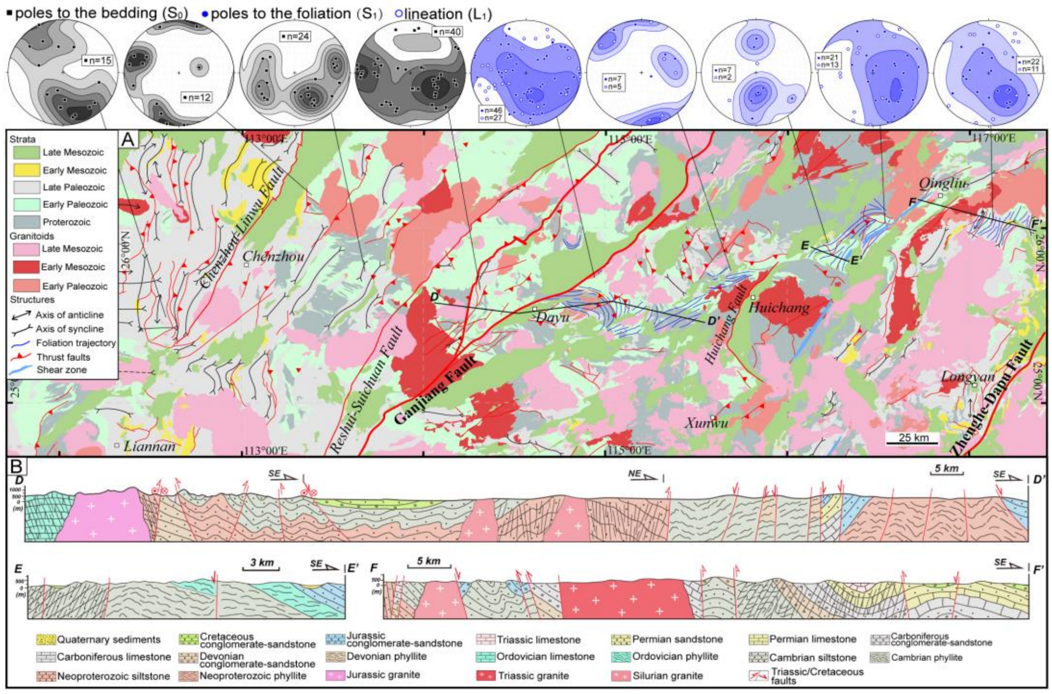

Figure 5.8. *(A) Structural geological map of the Nanling-Wuyi cross-section showing the faults and folds of the Nanling Massif, and the foliation trajectories of the Wuyi Massif. Stereonet projections (lower hemisphere, equal area) show the original beddings of the Nanling Massif (in black) and foliations of the Wuyi Massif (in blue). (B) The geological sketch shows the structural pattern of the Wuyi Massif. The locations of the cross-sections are shown by the black lines DD', EE' and FF' in Figure 5.8A.*

dipping Jurassic feldspathic sandstone with coal seams and are also intruded by the Jurassic granites (Fig. 5.6). Only the brittle deformation is developed. Above them is the nearly horizontal Cretaceous red bed with a few faults and joints (Fig. 5.6).

5.2.3 Wuyi Massif

The exposed rocks of the Wuyi Massif show some similarities with those in the Nanling Massif, but the basement is much more exposed (Figs. 5.3 and 5.8). Meanwhile, more cleavage and schistosity were observed within the Wuyi Massif, suggesting an intense deformation than the Nanling Massif.

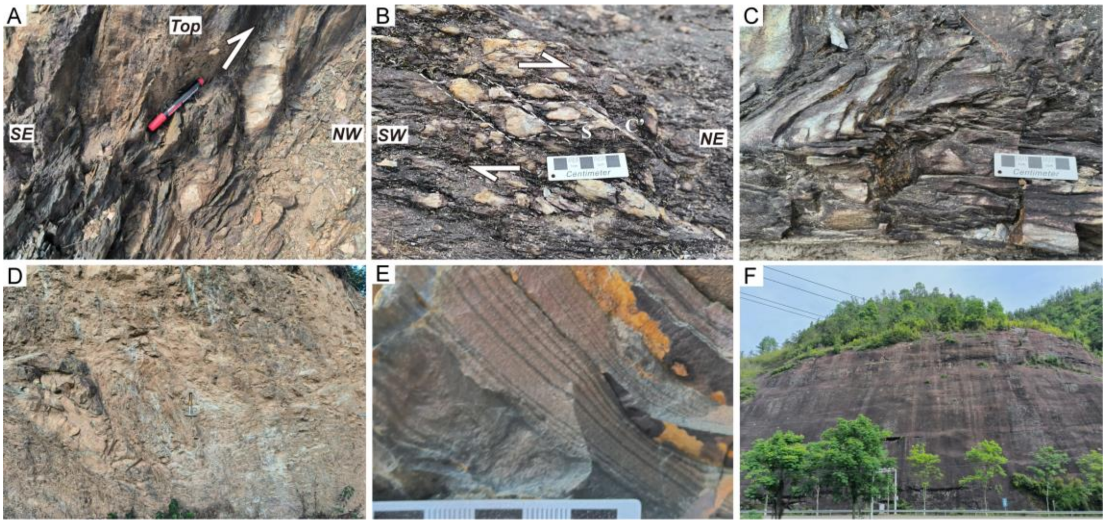

Figure 5.9. *Field photographs showing the deformation in the Wuyi Massif. (A) Sigmoid quartz in Neoproterozoic phyllite in Ganzhou, indicating the top-to-the-NW thrusting. (B) Sigmoid quartz within Carboniferous deformed quartz-sandstone in Yong'an, exhibiting the NE-trending dextral shearing. (C) A-type folds within the Devonian phyllite in Yong'an. (D) Schistosity in folded Cambrian phyllite in Changting. (E) Original beddings within the Cambrian meta-siltstone in Ruijin. (F) Undeformed Cretaceous red bed in Sanming.*

Generally, the Neoproterozoic to Early Paleozoic strata exhibit more ductile deformation, while the Late Paleozoic to Early Mesozoic rocks are mainly exposed in the basin without significant ductile deformation. However, the strata close to the boundary of the Wuyi Massif exhibit intense ductile deformation, including the Late Paleozoic strata. Along the Ganjiang Fault, which is the western edge of the Wuyi Massif, the sheared quartz boudins and asymmetric folds in Neoproterozoic phyllite imply the top-to-the-northwest sense of shear (Fig. 5.9A). Devonian−Carboniferous phyllite and quartz sandstone to the eastern boundary of the massif have undergone extensive ductile shearing, suggesting a NE-trending dextral shearing (Figs. 5.9B-C). In contrast, the Neoproterozoic to Early Paleozoic rocks in the central part of the Wuyi Massif exhibit relatively weaker ductile deformation. The schistosity is developed but often lacks lineation, and bedding planes are intermittently observable (Figs. 5.9D-E). The Late Paleozoic was characterized by folded sandstone and limestone with less ductile deformation, similar to that within the Nanling Massif. Additionally, broad and gentle NW-trending and NE-trending folds were developed in the massif (Fig. 5.8).

Brittle deformation, including faults, joints and folds, was widely developed in the Wuyi Massif, except for the Cretaceous red conglomerate and sandstone layers which are gently dipping like those exposed in the Yunkai and Wuyi massifs (Fig. 5.9F).

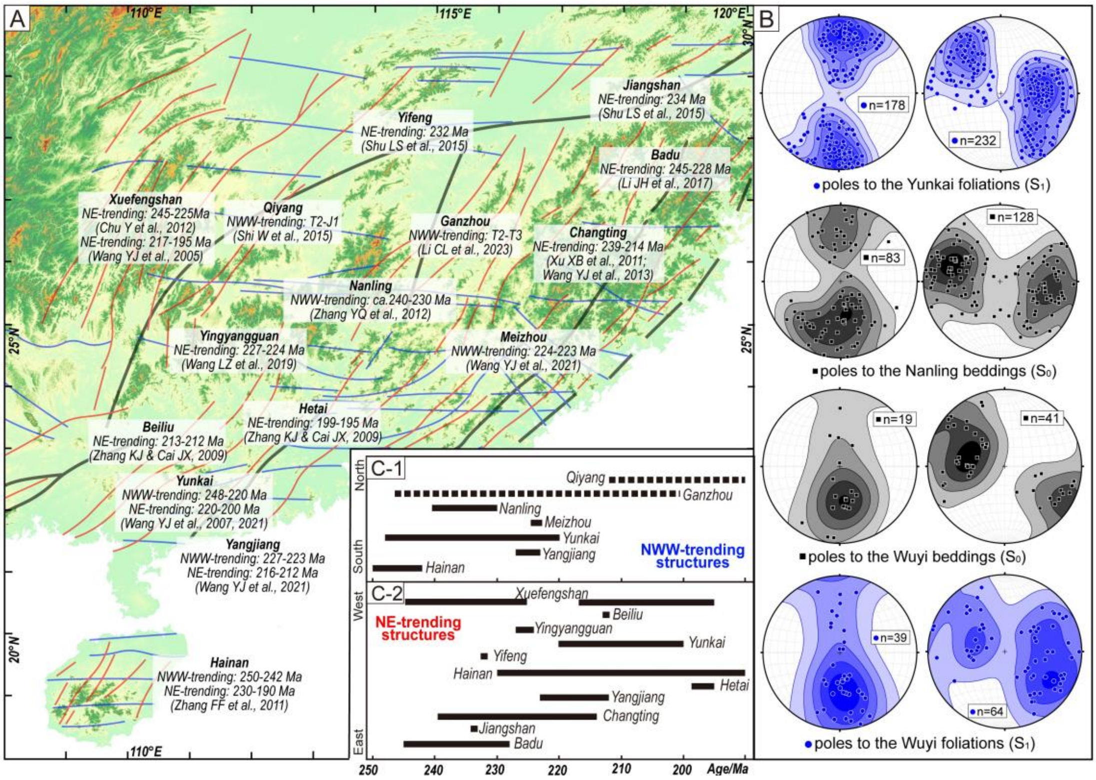

Figure 5.10. *Major groups of structures in the Cathaysia Block. (A) Summary of the Early Mesozoic structures in different directions. The structural basemap is modified from Wang YJ et al. (2021). (B) The statistics of the occurrences of the beddings (in black) and foliations (in blue) in different massifs. (C) The statistics of the E-W-trending and NE-trending structures based on their ages and locations.*

In summary, the field investigation reveals significant variations in deformation intensity across different massifs within the Cathaysia Block. In general, the Yunkai Massif exhibits more intense deformation, followed by the Wuyi Massif, while the Nanling Massif shows no ductile deformation. Additionally, the Early Paleozoic and Late Paleozoic rocks show the same deformation intensity in the center of the Yunkai Massif and the edge of the Wuyi Massif. In other places, the Late Paleozoic rocks above the unconformity were not ductilely deformed, while the Early Paleozoic rocks below the unconformity exhibit weak ductile deformation with slaty cleavage and schistosity. Meanwhile, two predominant structural orientations can be identified, including the E-W-trending and NNE-trending structures (Figs. 5.3, 5.8 and 5.10), suggesting two directions of shortening. A systematic trend emerges in the Cathaysia Block scale, in which the intensity of deformation decreases from south to north and increases from west to east. Moreover, the domains close to the major boundary faults display intense deformation (Fig. 5.11).

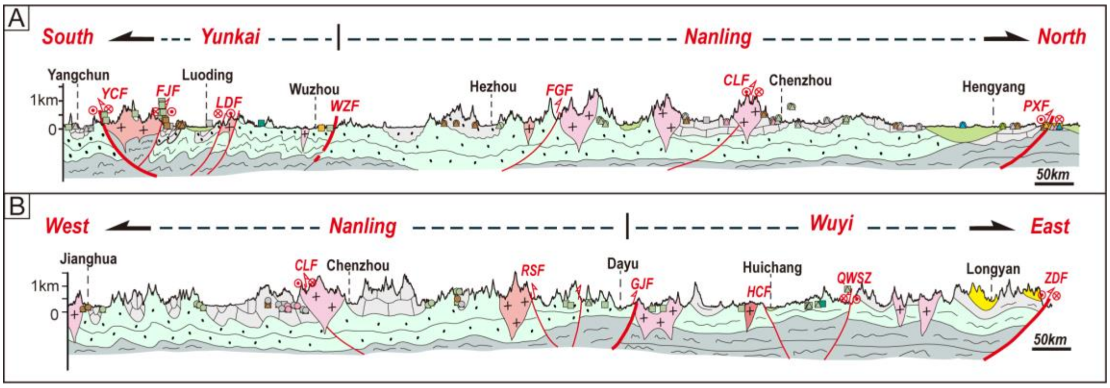

Figure 5.11. *Schematic sketches of the structural pattern from Yunkai to Nanling (A), and from Nanling to Wuyi (B). The locations of the cross-sections are shown in Figure 5.1.*

5.3 Distribution and characteristics of metamorphism

The grade of the metamorphism and the intensity of the deformation are closely related. Thus, the distribution and the characteristics are similar to the deformation across three massifs.

5.3.1 Yunkai Massif

The highest-grade regional metamorphism within the Yunkai Massif was situated at the central part (i.e., Xinyi and Gaozhou) and the southeastern coastal area (i.e., Yangjiang) (Figs. 5.3 and 5.5). It is represented by migmatites and granitic gneiss developed in the Neoproterozoic to Early Paleozoic rocks, as well as the Early Mesozoic (Figs. 5.4A and 5.12A). Metamorphism did not develop in some shallower Late Paleozoic basins, i.e., the Yangchun Basin and Luojing Basin, where the siltstone and limestone are exposed. Whereas the Neoproterozoic to Early Paleozoic basement of these basins exhibited low-grade regional metamorphism, characterized by slate and phyllite. Similar to the intensity of deformation, the grade of metamorphism decreases to the north, and the low-grade metamorphosed slate and meta-siltstone are the dominant rocks within the Neoproterozoic to Early Paleozoic strata (Fig. 5.4F). The Late Triassic to Cretaceous were not metamorphosed.

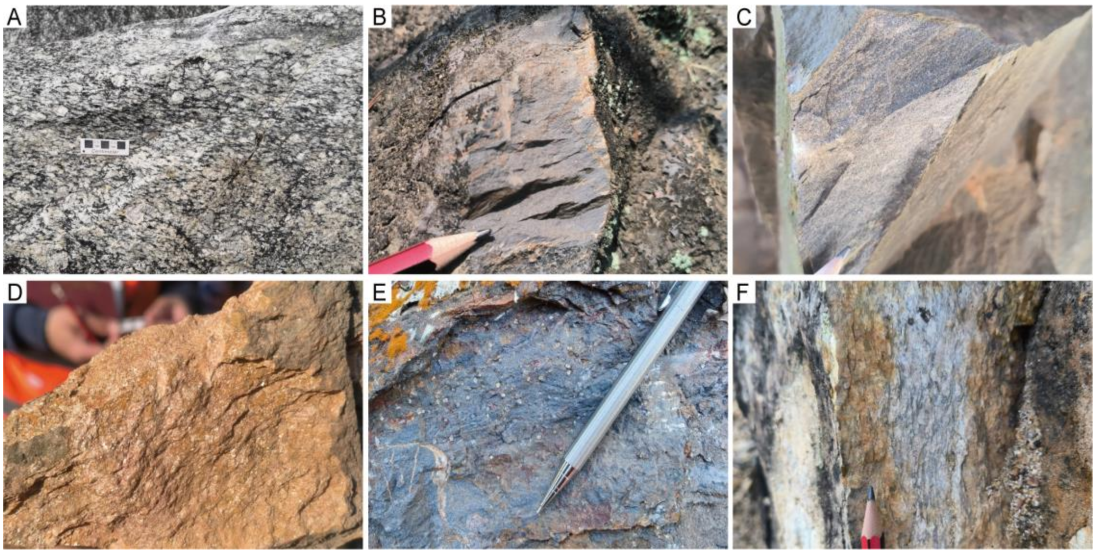

Figure 5.12. *Field photographs of metamorphic rocks in the Yunkai Massif. (A) Silurian granitic gneiss in Xinyi, which was metamorphosed during the Triassic. (B) Carbonaceous slate within the Cambrian strata to the east of Wuzhou. (C) Hornfelsic Cambrian sandstone in Fengkai. (D) Mica schist within the Cambrian country rocks of the Guangping pluton. (E) Andalusite hornfels in Yunan County. (F) Granitic gneiss within the northern part of the Yangchun shear zone.*

Additionally, metamorphism also occurred around the large plutons and within the shear zones due to heat generated by magmatic activity and shearing. For example, the carbonaceous slate, hornfelsic sandstone, mica schist and andalusite hornfels were observed around the Silurian Guangping pluton, while granitic gneiss and migmatite occurred in the Luoding shear zone and the country rocks adjacent to the Triassic Napeng pluton (Figs. 5.12B-F).

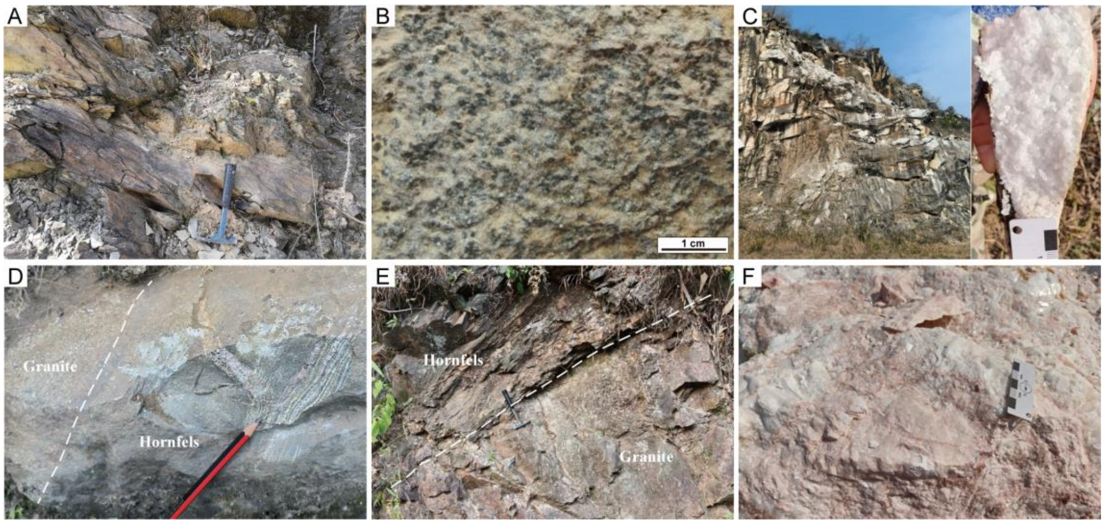

Figure 5.13. *Field photographs of metamorphic rocks in the Nanling Massif. (A) Regional low-grade metamorphosed silty slate within the Neoproterozoic strata in Hengshan County. (B) Hornfels within the country rocks of the Guandimiao pluton. (C) Coarse-grained marble within the country rocks of the Dayishan pluton. (D) The contact boundary between the Qitianling granite and its hornfelsic country rocks. (E) The contact boundary between the Dabang pluton and its hornfelsic country rocks. (F) Marblized limestone within the country rocks of the Huashan pluton.*

5.3.2 Nanling Massif

The Nanling Massif exhibits lower greenschist-facies metamorphism in Neoproterozoic to Early Paleozoic strata, dominantly characterized by muddy-sandy slate and meta-siltstone, which are unconformably overlain by unmetamorphosed Devonian to Early Triassic conglomerate, sandstone, and limestone (Fig. 5.6 and 5.13A). The uppermost layer consists of Late Mesozoic non-metamorphosed sedimentary rocks, which unconformably overlie the underlying strata. Contact metamorphism was often observed around plutons in the Nanling massif. It is characterized by the hornfelsic sandstone, hornfels, marble and migmatitic hornfels in the country rocks of the Triassic (i.e., Guandimiao) or Jurassic (i.e., Dayishan, Qitianling, Dabang and Huashan) plutons (Figs. 5.13B-F).

5.3.3 Wuyi Massif

The Wuyi Massif exhibits a higher grade of the regional metamorphism than the Nanling Massif, represented by more phyllite in comparison to slate. The Neoproterozoic to Early Paleozoic developed phyllite, slate and meta-sandstone, while the Late Paleozoic was dominantly the non-metamorphosed limestone and sandstone. However, the Devonian strata in the Yong'an Basin, which is located to the east of the Wuyi Massif, exhibit a higher grade of metamorphism with phyllite (Fig. 5.9C). Above the Late Paleozoic strata were the non-metamorphosed Jurassic-Cretaceous series, characterized by terrigenous clastic rock and volcanic rocks. In the northern part of Wuyi Massif (i.e., Chencai, Lichuan and Jianning), higher-grade metamorphism can be observed due to the exhumation of the basement rocks, which are represented by the migmatite, migmatitic granite, paragneiss and schist.

In summary, the Cathaysia Block exhibits variable grades of the regional metamorphism across different massifs. The Yunkai and Wuyi massifs have a high grade of regional metamorphism, followed by the Nanling Massif. The pre-Devonian rocks were involved in the regional metamorphism, while the Late Paleozoic regional metamorphism was predominantly developed in the Yunkai and eastern Wuyi massifs and absent in the Nanling Massif. Almost all the Mesozoic rocks were not involved in regional metamorphism. The grade of the metamorphism also exhibits the tendency that decreases from south to north and increases from west to east. Moreover, the rocks that were involved in the contact metamorphic aureole of the large plutons displayed a higher grade of metamorphism.

5.4 Timing of the deformation and metamorphism

Since the Neoproterozoic, the Cathaysia Block witnessed four orogenic/tectonic events: the Neoproterozoic amalgamation with the Yangtze Block to form the SCB and subsequent intracontinental rifting, the Early Paleozoic intracontinental orogeny, the Early Mesozoic reworking and the Late Mesozoic subduction of the Paleo-Pacific Plate (Wang YJ et al., 2007a; Shu LS et al., 2015; Xia Y et al., 2018; Dong SW et al., 2023; Li JH et al., 2024). Most of the magmatism, metamorphism, and deformation in the Cathaysia Block are attributed to these tectonic events. Due to the same deformation intensity and metamorphic grade between the Neoproterozoic and Cambrian strata in each massif, the deformation and metamorphism observed in the field were not attributed to the Neoproterozoic event.

The regional unconformity in the Nanling and Wuyi massifs separated the Early Paleozoic and Late Paleozoic sequences (Figs. 5.6A and D). The different dipping angles and metamorphic grades below and above the unconformity suggest that the Early Paleozoic Orogeny contributed to the regional greenschist-facies metamorphism developed in the Neoproterozoic – Ordovician rocks, as well as the E-W-striking folds in the Early Paleozoic strata. In addition, the high-grade metamorphic rocks of the basement located to the northern Wuyi and central Yunkai massifs resulted from the Early Paleozoic tectonic-magmatic event (Faure M et al., 2009; Yao JL et al., 2017; Li C et al., 2025).

The same deformed pattern and intensity in the Cambrian and Devonian in the Yunkai Massif (Fig. 5.5) suggest that the transpressional deformation occurred postdating the Early Paleozoic Orogeny, and the previous records had probably been reset. The top-to-the-north thrust and the northward decrease of the deformation intensity point to a driving force from the south, which is considered to be related to the Early Mesozoic Indosinian Orogeny (Wang YJ et al., 2007a, 2021; Lin W et al., 2008; Faure M et al., 2016b). In the block scale, the pre-Triassic strata were all involved in the E-W-trending and NE-trending superimposed fold-and-thrust system (Figs. 5.3, 5.7 and 5.8). They were covered by the gently dipping Late Mesozoic strata and intruded by the Jurassic pluton (e.g., Qitianling pluton), suggesting the superimposed folds were probably produced during the Early Mesozoic Orogeny. It is worth noting that the intense ductile deformation and low-grade metamorphism were developed in the Devonian quartz sandstone in the eastern Wuyi Massif (Figs. 5.9B-C), which is distinguished from the non-ductile deformed Late Mesozoic strata, and is supposed to have developed during the Early Mesozoic Orogeny. It is also supported by the same kinematics from the Early Mesozoic Qingliu and Badu shear zones in the Wuyi Massif (Xu XB et al., 2011; Li JH et al., 2017a).

Furthermore, an important number of geochronological data were published on the Cathaysia Block (Table S2), providing more constraints on the timing of the metamorphism and deformation. The new multi-mineral dating results in this thesis showed that the Yunkai Massif recorded an Early Mesozoic high-temperature metamorphism and migmatization at ca. 240Ma and its subsequent cooling, which P-T condition was up to 6.8–7.0 kbar and 780–810 ℃ (as discussed in Chapter 4). In previous studies, the Early Mesozoic amphibolite-facies transpression and NE-SW crustal flow were recognized (e.g., Wang YJ et al., 2007a, 2021; Lin W et al., 2008; Cochelin B et al., 2022). The Early Mesozoic high-temperature metamorphism and deformation were also reported in the northern Wuyi Massif (Wang YJ et al., 2012, 2013; Zhao L and Zhou XW, 2012; Zhao L et al., 2017; Dong YF et al., 2018; Zhou X et al., 2018). Moreover, numerous shear zones were developed in the Cathaysia Block. The mica $^{40}Ar/^{39}Ar$ dating reveals the mylonitic deformation in the Yunkai Massif and the shear zones in the Nanling and Wuyi massifs are of the Early Mesozoic (Fig. 5.10A; Table S2). The statistics based on the age and locations reveal that the E-W-trending structures predated the NE-trending ones, and the deformation propagated from south to north and from east to west (Figs. 5.10A, C and 5.11).

5.5 Crustal thermal state

Crustal thermal state serves as the primary driving force of geological processes, while simultaneously reflecting and recording the geological events. As the direct manifestation of the thermal state, temperature provides a critical window into understanding the thermal conditions and rheology of the Earth's crust.

5.5.1 RSCM temperature

The temperatures estimated from the laser Raman spectrum (Fig. 5.14) revealed the spatial temperature variation and differences among the Yunkai, Wuyi and Nanling massifs of the Cathaysia Block.

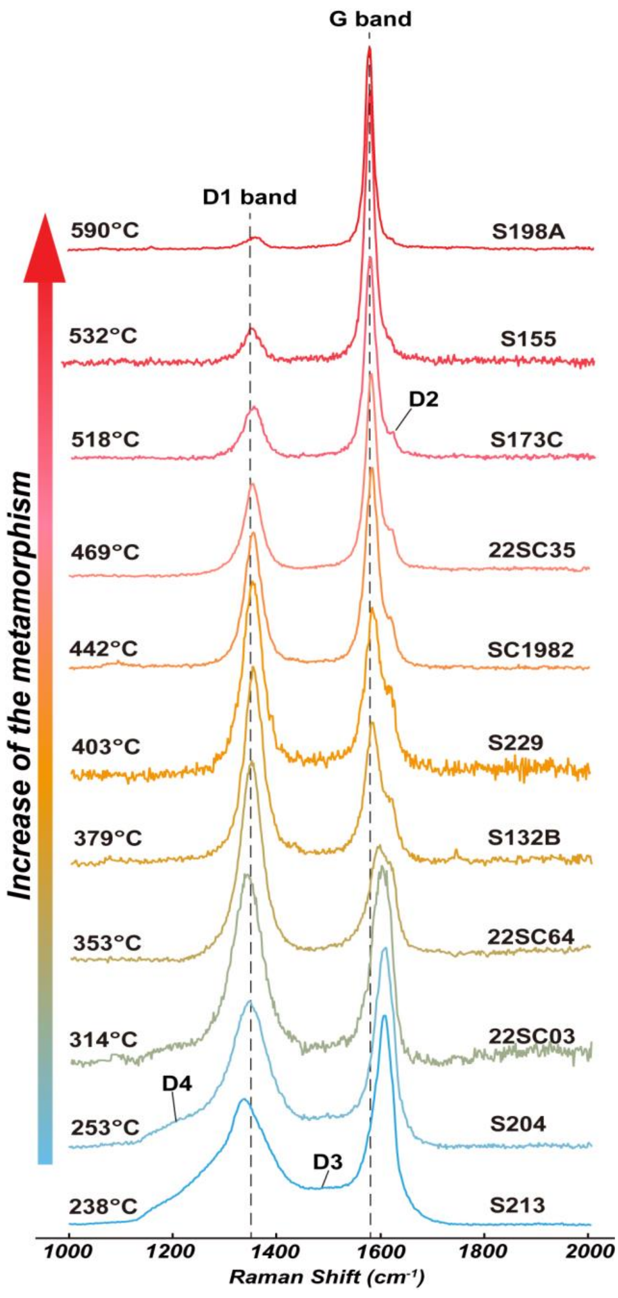

Figure 5.14. *The representative spectrum and its estimated temperature.*

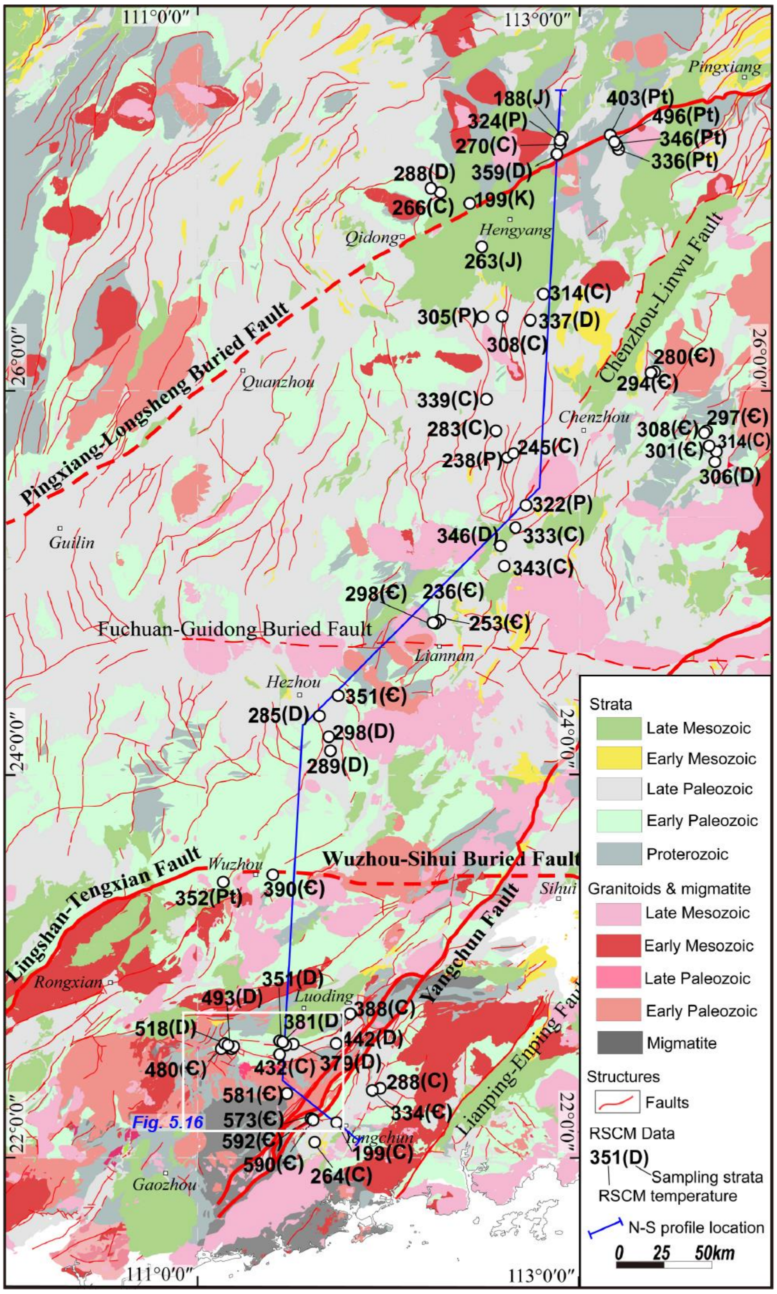

Figure 5.15. *The sampling sites and RSCM temperature of the Yunkai-Nanling cross-section. The blue solid line is the location of the profile mentioned in Figure 5.17A.*

In the Yunkai Massif, its center located to the south of the Fenjie Fault and to the northwest of the Yangchun Fault presents the highest RSCM temperature ranging from 432–592 °C with an average temperature of ~509±54 °C (Figs. 5.15, 5.16 and 5.17A). Crossing the Fenjie Fault into the northern Yunkai Massif, the temperature decreases to 351–393 °C with an average value of ~376±18 °C (Figs. 5.15 and 5.17A). The temperature did not show differences between the different sampling strata within the same sampling locality (Fig. 5.17A). To the southeast of the Yangchun Fault, there is a significant lower temperature at 199–334 °C, and the average temperature is at ~271±56 °C. Moreover, the Cambrian basement is at least 46±21 °C higher than the Late Paleozoic cover (Fig. 5.17A).

Different from the Yunkai Massif, the Nanling Massif reveals an almost consistent RSCM temperature within pre-Triassic strata ranging from 236 °C to 351 °C with an average of ~304±33 °C (Figs. 5.15 and 5.17). There is no significant regularity of the RSCM temperature across different sampling strata. To the northern Nanling Massif, the Late Mesozoic rocks present a much lower temperature, mostly lower than 200 °C (Figs. 5.15 and 5.17A). Notably, when coming into the Jiangnan Orogenic Belt, the temperature increases, especially up to 496 °C in the Neoproterozoic basement (Figs. 5.15 and 5.17A). Similarly, the temperature in the Ganjiang Fault that separates the Nanling massif from the Wuyi one increases significantly, ranging from 364–469 °C (Figs. 5.17B and 5.18).

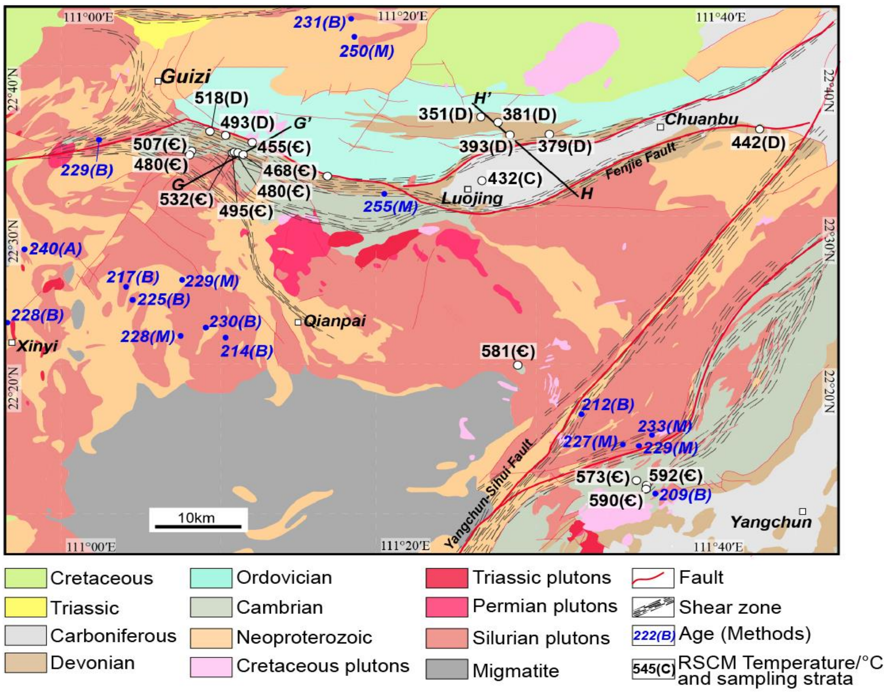

Figure 5.16. *The distribution of RSCM temperature results and compiled geochronological data. The data in black are the RSCM temperatures and their sampling strata, and those in blue are the geochronological data and dating methods (B-biotite* $^{40}Ar/^{39}Ar$*; M-muscovite* $^{40}Ar/^{39}Ar$*).*

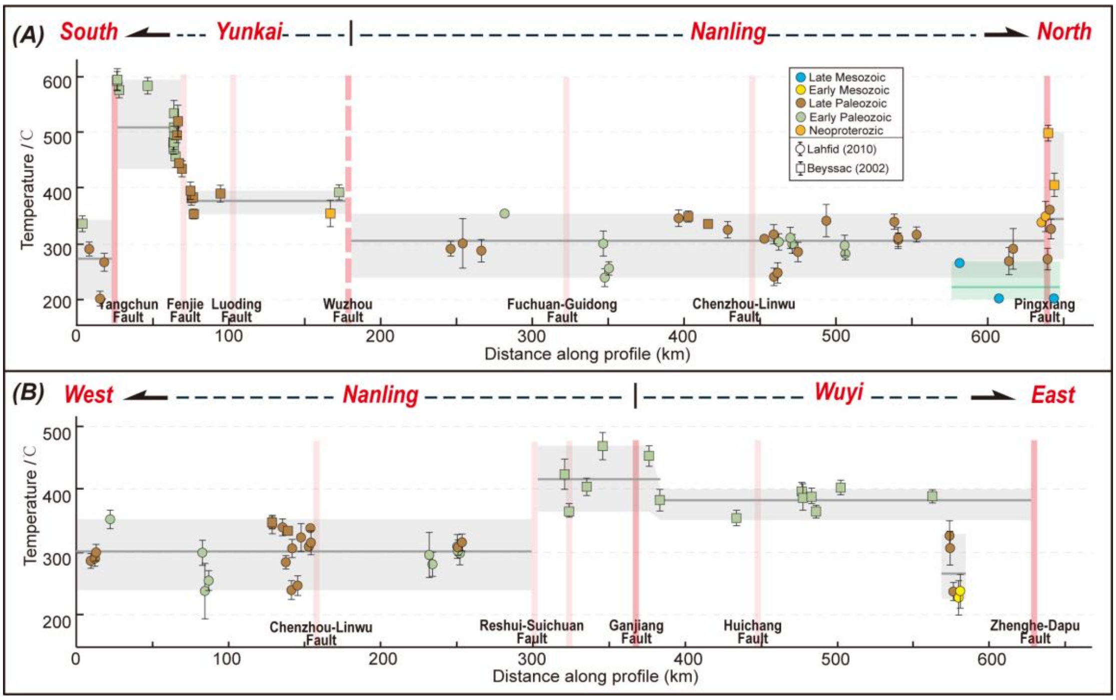

Figure 5.17. *The spatial variation of the RSCM temperatures along the profiles of Yunkai-Nanling (A) and Nanling-Wuyi (B). The grey domains and grey solid lines are the ranges and average temperatures within the pre-Triassic rocks, respectively. The green domain and green solid line are the range and average temperature within the Late Mesozoic rocks, respectively.*

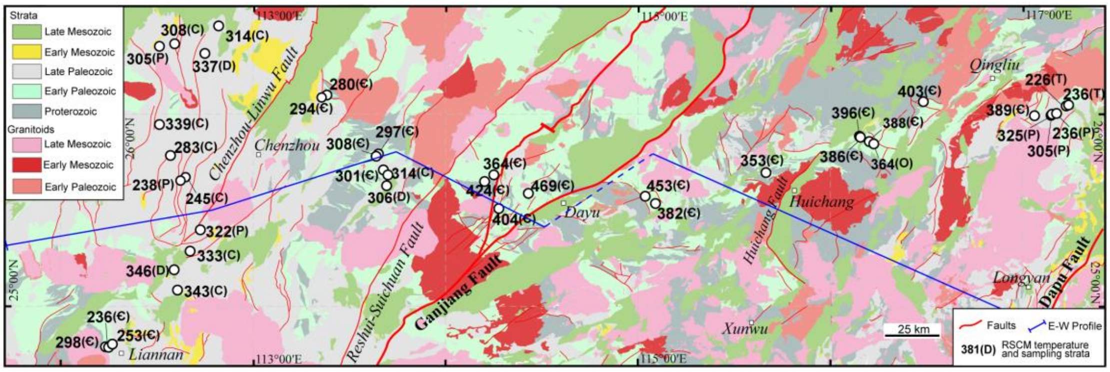

Figure 5.18. *The distribution of the sampling sites and RSCM temperature of the Nanling-Wuyi cross-section. The blue solid line is the location of the profile mentioned in Figure 5.17B.*

In the Wuyi Massif, the Early Paleozoic basement exhibits stabilized temperatures ranging from 353–403 °C, with an average temperature of ~383±18 °C (Figs. 5.17B and 5.18). The Late Paleozoic to Early Mesozoic basin in the eastern Wuyi Massif gives a low temperature of 226–325 °C, averaged at ~266±46 °C (Figs. 5.17B and 5.18).

Deformation and strain have been documented to significantly influence Raman spectra (Ross JV and Bustin RM, 1990; Henry DG et al., 2019; Schito A et al., 2023). The local heat from the ductile shear band or faults can lead to a ~60 ℃ temperature increase (Cottle et al., 2011; Mori et al., 2015). The deformed and undeformed samples from the Yunkai Massif do not reveal a significant temperature difference between them (Figs. 5.16 and 5.19).

In summary, the RSCM temperature reveals significant regional temperature differences among the three massifs of the Cathaysia Block. The Yunkai Massif has the highest average temperature of ~509±54 °C in the south and ~376±18 °C in the north. The Wuyi Massif has an average temperature of ~383±18 °C, while the Nanling Massif is only ~304±33 °C.

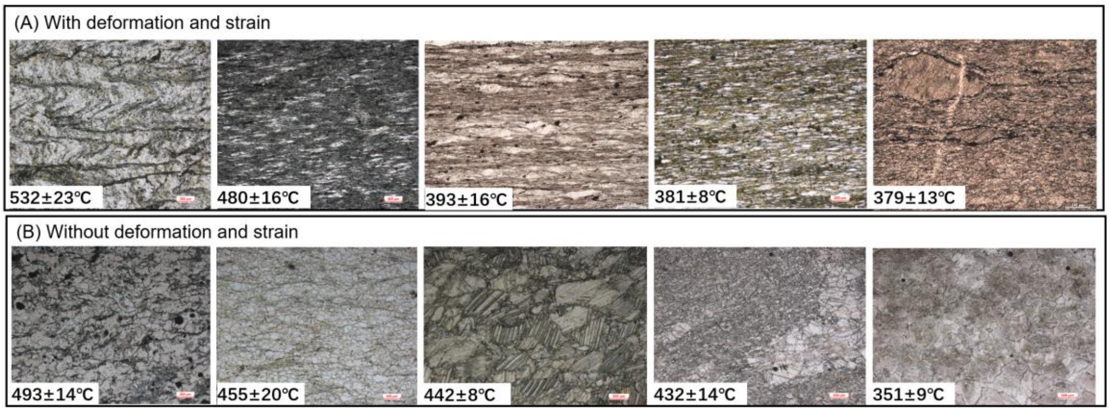

Figure 5.19 *The microscopic pictures of the deformed and undeformed samples in the Yunkai Massif and their RSCM temperatures.*

5.5.2 Temperature of quartz dynamic recrystallization

Quartz is one of the most common rock-forming minerals in the crust, and its deformation behavior is highly dependent on temperature (Tullis JA, 1979; Stipp M et al., 2002; Passchier CW and Trouw RA, 2005). With the increase of temperature, the dynamic recrystallization mechanism transitions from brittle fracturing and undulose extinction (<300 °C), bulging (~300−400 °C), subgrain rotation (~400–500 °C) to grain boundary migration (>500 °C). Temperature estimation based on the quartz dynamic recrystallization is qualitative due to this evaluation of the mechanism has an uncertainty. Nevertheless, it can still provide useful qualitative insights into the temperatures across different massifs and serve as a valuable cross-check for the RSCM temperature. The deformation temperature from the quartz dynamic recrystallization displays the differences between the different massifs and the different strata series (Figs. 5.20 and 5.21; Table S3).

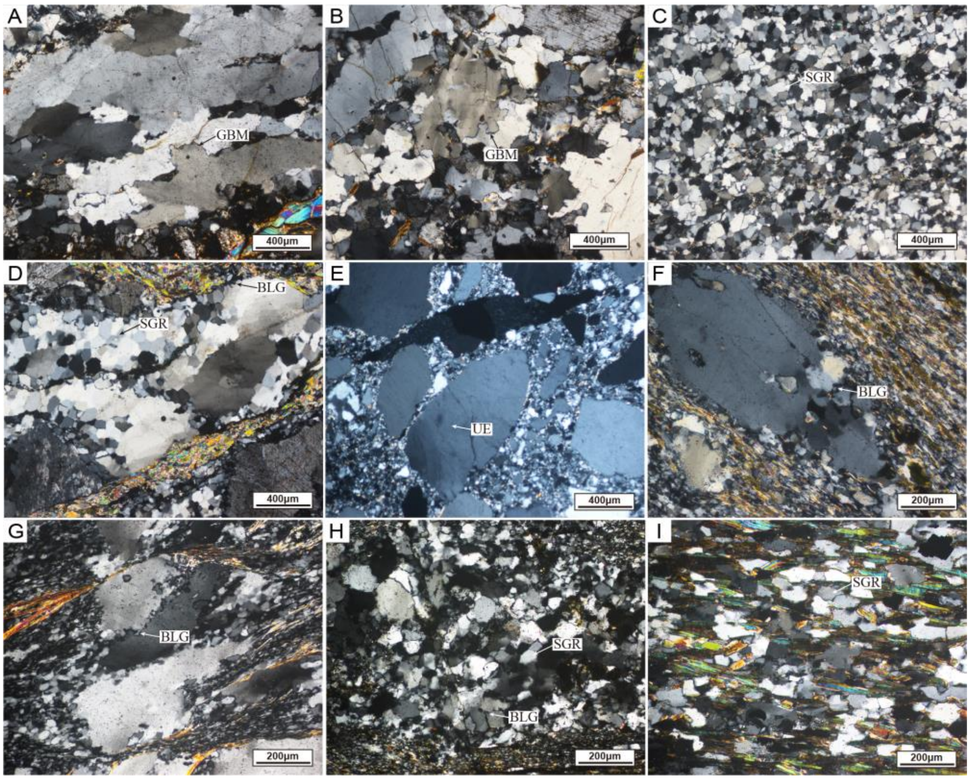

Figure 5.20. *The representative pictures of quartz dynamic recrystallization in the Yunkai (A-D), Nanling (E-F) and Wuyi (G-H) massifs, as well as the Ganjiang Fault (I).*

The dynamic recrystallization of quartz in the center of the Yunkai Massif is dominantly bulging to subgrain rotation and grain boundary migration (Figs. 5.20A-D), suggesting a highest temperature >500 °C. To the north of the Fenjie Fault, bulging is the dominant recrystallization mechanism, suggesting the metamorphic temperature decreased to ~300–400 °C (Fig. 5.21A). The Cambrian and Devonian strata within the Yunkai Massif display comparable deformation temperatures. In the Nanling Massif, it is dominantly characterized by brittle fracturing, undulose extinction and bulging (Figs. 5.20E-F), suggesting the low-temperature conditions at ~200–400 °C (Figs. 5.21A-B). Different from the Yunkai Massif, the strata in the Nanling Massif exhibit different temperatures. The deformation temperatures of Neoproterozoic to Cambrian strata are approximately at 200−500 °C, and those of Devonian strata are at ~200−300 °C (Fig. 5.21). The Wuyi Massif exhibits a consistent recrystallization mechanism, characterized by the bulging (Figs. 5.20G-H), which is mostly at ~300–400 °C, where the Neoproterozoic to Devonian exhibit comparable temperature (Fig. 5.21B). Additionally, the deformation temperature along the Ganjiang Fault (~115°E in Fig. 5.21B) exhibits a slight increase characterized by the subgrain rotation (Fig. 5.20I).

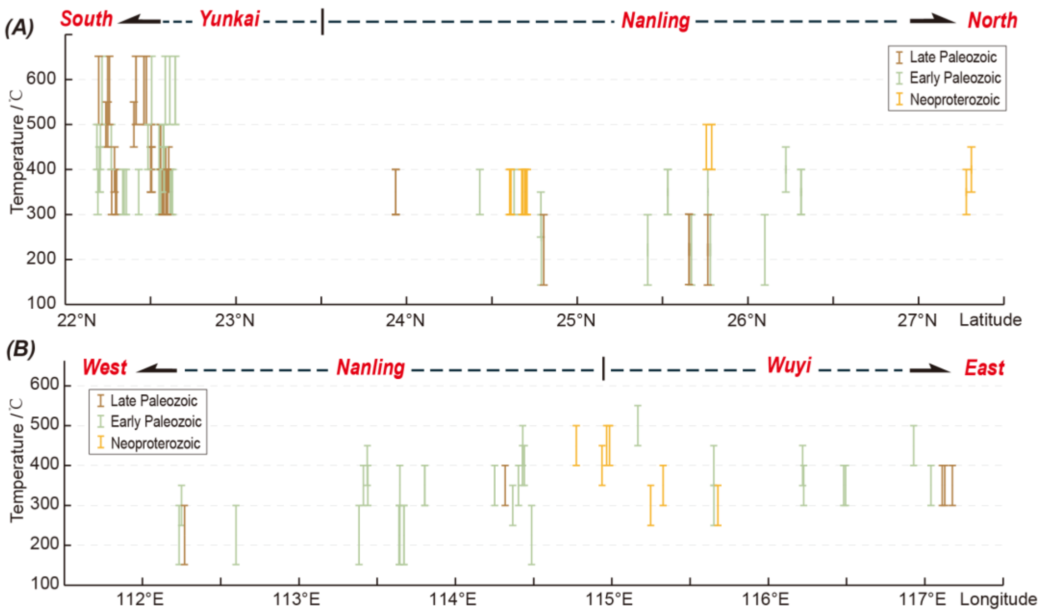

Figure 5.21. *The variation in deformation temperature along both latitudinal (A) and longitudinal (B) cross-sections, which was estimated from quartz dynamic recrystallization (Table S3).*

Both the temperatures estimated from the RSCM and quartz dynamic recrystallization indicate that the Yunkai Massif experienced higher temperatures than the Nanling and Wuyi massifs, as well as high temperatures along the Ganjiang Fault. The temperatures estimated from the quartz dynamic recrystallization do not clearly distinguish those of the Neoproterozoic-Early Paleozoic and the Late Paleozoic in Yunkai and Wuyi massifs, whereas the RSCM temperatures can effectively differentiate the Pre-Devonian basement from the Late Paleozoic basins. In the Nanling Massif, although recrystallization temperatures suggest lower temperatures during the Late Paleozoic, it remains difficult to fully separate the Early and Late Paleozoic thermal records, particularly using RSCM data.

5.5.3 Temperature based on the vitrinite reflectance of coal

Vitrinite reflectance is an important indicator of organic matter maturity, which is used to calibrate the thermal evolution of organic matter from early diagenesis to the deep metamorphic stage. It is based on the irreversible thermal maturity process of the organic matter and records the highest temperature during the basin evolution (Barker CE and Pawlewicz MJ, 1986; Barker CE, 1988). Previous studies comparing vitrinite reflectance (Ro) with temperature (T) have established a reliable regression relationship within the ranges of Ro = 0–4.5% and T = 0–300 °C (Barker CE and Pawlewicz MJ, 1986; Barker CE, 1988; Burnham AK and Sweeney JJ, 1989). The Easy%Ro model proposed by Sweeney JJ and Burnham AK (1990) suggests that vitrinite reflectance saturates at approximately 350 °C. This saturation is probably limited by conventional sedimentary and burial processes. However, plutonic activity leads to graphitization of organic matter and the development of a highly ordered structure, resulting in Ro values higher than those produced by the burial process alone (Li K et al., 2018). The published vitrinite reflectance data within Carboniferous to Triassic strata were compiled to estimate the paleotemperature, as detailed in the Appendix Table S4.

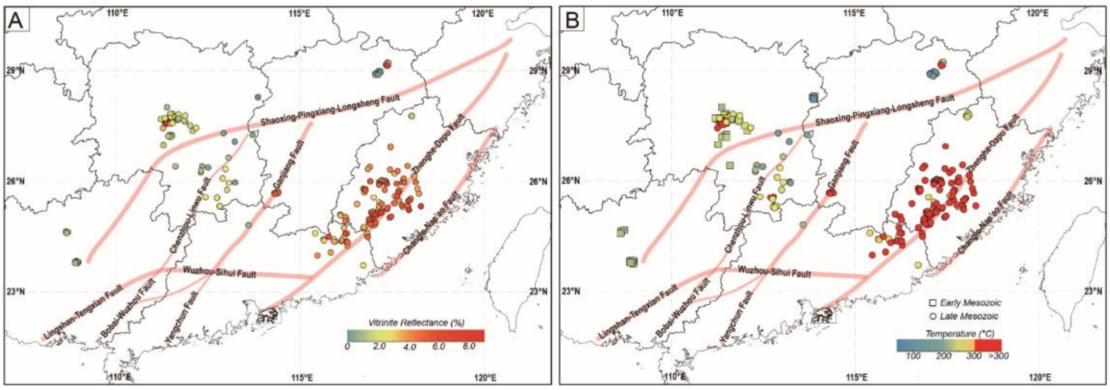

Figure 5.22. *The distribution of the vitrinite reflectance of the coal and estimated temperatures. The detailed data and their sources are presented in the Appendix Table S4. The squares and circles represent the temperatures recorded during the Early Mesozoic and the Late Mesozoic, respectively.*

The locations of the vitrinite reflectance data are dominant at the north of the Nanling Massif (i.e., Hengyang-Chenzhou), east of the Wuyi Massif (i.e., Sanming-

Meizhou) and the Jiangnan Orogenic Belt (i.e., Leping, Liuyang, and Shaoyang-Loudi, Laibin; Fig. 5.22). The temperatures (20/34) in the Nanling Massif exhibit a range from 187 to 280 °C, while the eastern part of the Wuyi Massif along the Zhenghe-Dapu Fault exhibits higher temperatures, most of which (135/154) is higher than 300 °C. Moreover, most of the estimations (96/120) of temperature within the Jiangnan Orogenic are 107−300 °C, and the temperature of the Youjiang Basin is 197−223 °C (Fig. 5.22). Other high temperatures over 300 °C were due to the emplacement of plutons.

5.5.4 Age of the temperature acquisition

The RSCM thermometer is based on the irreversible graphitization process, and it exclusively records the peak metamorphic temperature without time constraints (Beyssac O et al., 2002). Thus, it is crucial to constrain the age of the observed RSCM temperature. The depositional age of the sampled strata provides the lower limit of the time. There is no doubt that the age of the RSCM temperature should be younger than the depositional age of the sampling strata. The RSCM samples were collected from the Late Neoproterozoic to Early Triassic, suggesting that their temperature can probably be attributed to the orogenesis during the Early Paleozoic, Early Mesozoic or Late Mesozoic. However, the consistent and comparable temperatures between the Late Neoproterozoic − Early Paleozoic (~352−390 °C at the north and ~455−592 °C at the south) and Late Paleozoic (~351−393 °C at the north and ~432−518 °C at the south) sequence in the Yunkai Massif indicate that the temperature postdates the Early Paleozoic Orogeny (Fig. 5.17A). Especially, the Devonian strata in the Yunkai Massif exhibit the same metamorphic grades and deformation pattern as the Cambrian strata, produced by an Early Mesozoic tectonic event constrained by the zircon, monazite U-Pb ages and mica $^{40}Ar/^{39}Ar$ ages (Wang YJ et al., 2012, 2021; Wang D et al., 2013; Chen CH et al., 2017; Zhang JH et al., 2019; Jiao QQ et al., 2020; Cochelin B et al., 2022). Similar to the Yunkai Massif, the Neoproterozoic − Early Paleozoic (~236−351 °C) and Late Paleozoic (~238−358 °C) sequence in the Nanling Massif also exhibit consistent and comparable temperatures, arguing for an event that postdates the Early

Paleozoic (Fig. 5.17).

Additionally, three Late Mesozoic samples were analyzed to determine the temperature differences between the Pre-Triassic and Late Mesozoic rocks. These samples yielded a Late Mesozoic average temperature of ~220 °C, with two of them recording temperatures below 200 °C (Fig. 5.17A). It is significantly lower than the temperatures from the Late Neoproterozoic – Early Mesozoic strata (almost >250 °C). Meanwhile, the flat Late Mesozoic strata show weaker deformation and unconformably overlie the folded pre-Triassic strata (Figs. 5.4H-I, 5.6H-I and 5.9F). Thus, the RSCM

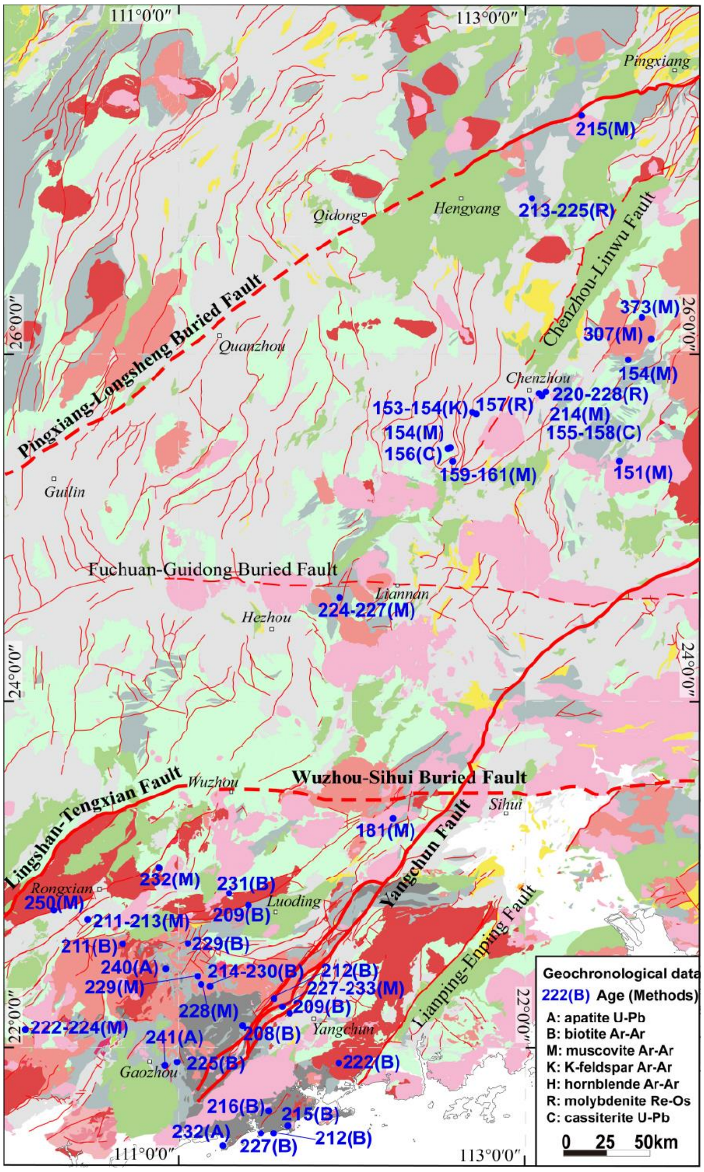

Figure 5.23. *The locations and ages of the compiled geochronological data in the Yunkai-Nanling cross-section.*

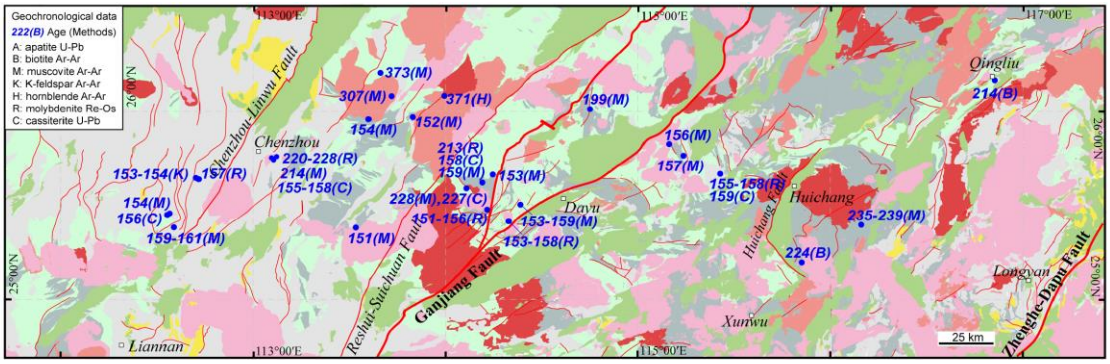

Figure 5.24. *The locations and ages of the compiled geochronological data in the Nanling-Wuyi cross-section.*

temperature, except for the three Late Mesozoic data, should predate the Late Mesozoic event.

Moreover, the geochronological data can provide more constraints on the age of the temperature. Thus, numerous geochronological data were collected and some of them were plotted on the geological maps (Figs. 5.23 and 5.24; Table S2).

It is worth noting that if the RSCM temperature is higher than the closure temperature of the dating minerals, the RSCM temperature should be obtained before the age, otherwise, the isotopic systems would be reset and record a younger age. Furthermore, if the RSCM temperature is equal to the closure temperature, the dating results can represent the age of the RSCM temperature. Even if the RSCM temperature is lower than the closure temperature, we can still make a maximum estimation for the previous RSCM temperature. Based on the above assumption, the RSCM temperature in the Yunkai and Wuyi massifs can be constrained to the Early Mesozoic (Fig. 5.25). However, the temperature in the Nanling Massif is not easy to constrain directly, because lots of the isotopic ages were reset by the large-scale tungsten-tin mineralization. Even so, we can make a maximum estimation for the Early Mesozoic temperature of the Nanling Massif, which will not exceed the RSCM temperature.

Based on the above discussion, we argue that the RSCM temperatures obtained in this study are essentially related to the Early Mesozoic orogenic event.

In addition, the ages of the vitrinite reflectance temperature were determined based

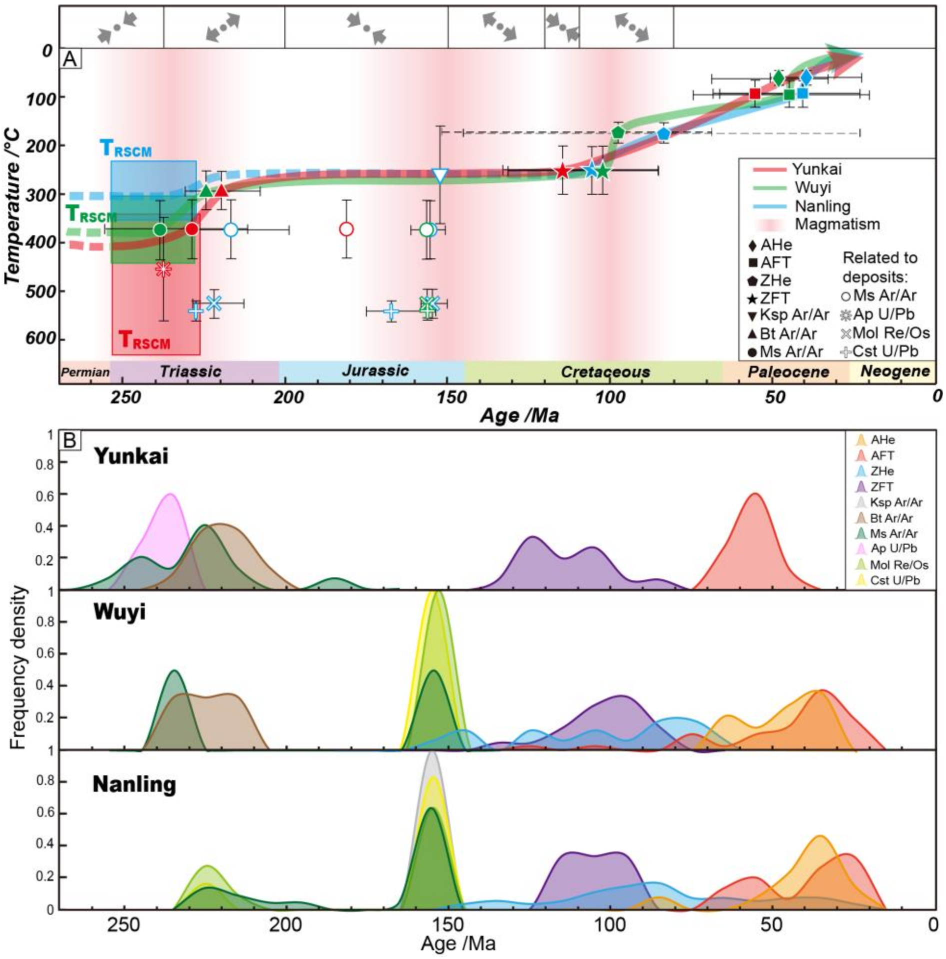

Figure 5.25. *(A) RSCM temperature ranges and the cooling paths of the regional metamorphism of the Yunkai, Wuyi and Nanling massifs. The compiled geochronological data can be found in Appendix Table S2. The magmatism is from Liu JX et al. (2020). The stress regime is from Li JH et al. (2020). The closure temperatures are from Chew DM and Spikings RA (2015). (B) Frequency density distribution of geochronological data for each dating method.*

on the reconstruction of the burial geothermal history of the well. The temperatures of Shaoyang-Loudi and Laibin in the Jiangnan Orogenic Belt were interpreted to reflect Early Mesozoic thermal events (Zhu W et al., 2015; Liu TL, 2018; Xi ZD et al., 2020; Hu ZF et al., 2023), while the temperatures recorded in the Nanling and Wuyi massifs were attributed to the Late Mesozoic burial and magmatic processes, especially the advective heat transfer along the Zhenghe-Dapu Fault (Fang HF et al., 2010; Yin ZS, 2015; Xu YJ et al., 2023). The elevated temperatures (Ro values at 4.32~9.5 with temperatures >300 °C) in the Jiangnan Orogenic Belt, Nanling Massif and Ganjiang

Fault (Fig. 5.22) were attributed to the emplacements of Mesozoic plutons (e.g., Tianlongshan, Qitianling, Jiulongnao plutons), which will not be in the discussions of the regional metamorphic thermal state. The high temperatures along the Zhenghe-Dapu Fault would have influenced the thermal records of earlier events. Due to the vitrinite reflectance recording the maximum temperatures, thus, the Early Mesozoic temperature would not exceed the Late Mesozoic lowest temperatures at approximately 300 °C, which is consistent with the thermal regimes documented in the Nanling Massif and the Jiangnan Orogenic Belt (Fig. 5.22). Otherwise, the vitrinite reflectance would not record these low temperatures. That is consistent with the Early Mesozoic RSCM result in the Nanling Massif (Fig. 5.17A).

According to the deformation temperature across the different strata series, the relative age can be determined. Considering the comparable deformation temperature within the Cambrian and Devonian strata in the Yunkai Massif (Fig. 5.21A), as well as the numerous Early Mesozoic $^{40}Ar/^{39}Ar$ ages constraints (Figs. 5.23 and 5.24), all the deformation temperatures (~300 to >500 °C) within the Yunkai Massif should be Early Mesozoic. The lower deformation temperatures in the Devonian strata with respect to those in Neoproterozoic to Cambrian strata suggest that the influence of the Early Paleozoic event, and the lower temperature are postdated that. The dating results reveal that the Devonian deformation temperatures (~200−300 °C) are Early Mesozoic (227−224Ma, Wang LZ et al., 2019). Additionally, the Devonian deformation temperature (~300−400 °C) in the Wuyi Massif is comparable with that of the Neoproterozoic and Cambrian strata, suggesting the Early Mesozoic and subsequent deformation temperatures do not exceed that value (Fig. 5.21B). The $^{40}Ar/^{39}Ar$ ages in the Wuyi Massif argue for an Early Mesozoic deformation temperature (Fig. 5.10; Xu XB et al., 2011; Wang YJ et al., 2013, 2021; Li JH et al., 2017a).

5.5.5 Early Mesozoic Paleo-geothermal gradient

A detailed analysis of temperature variation reveals that, in addition to the significant differences in the block scale, some overlooked differences persist within

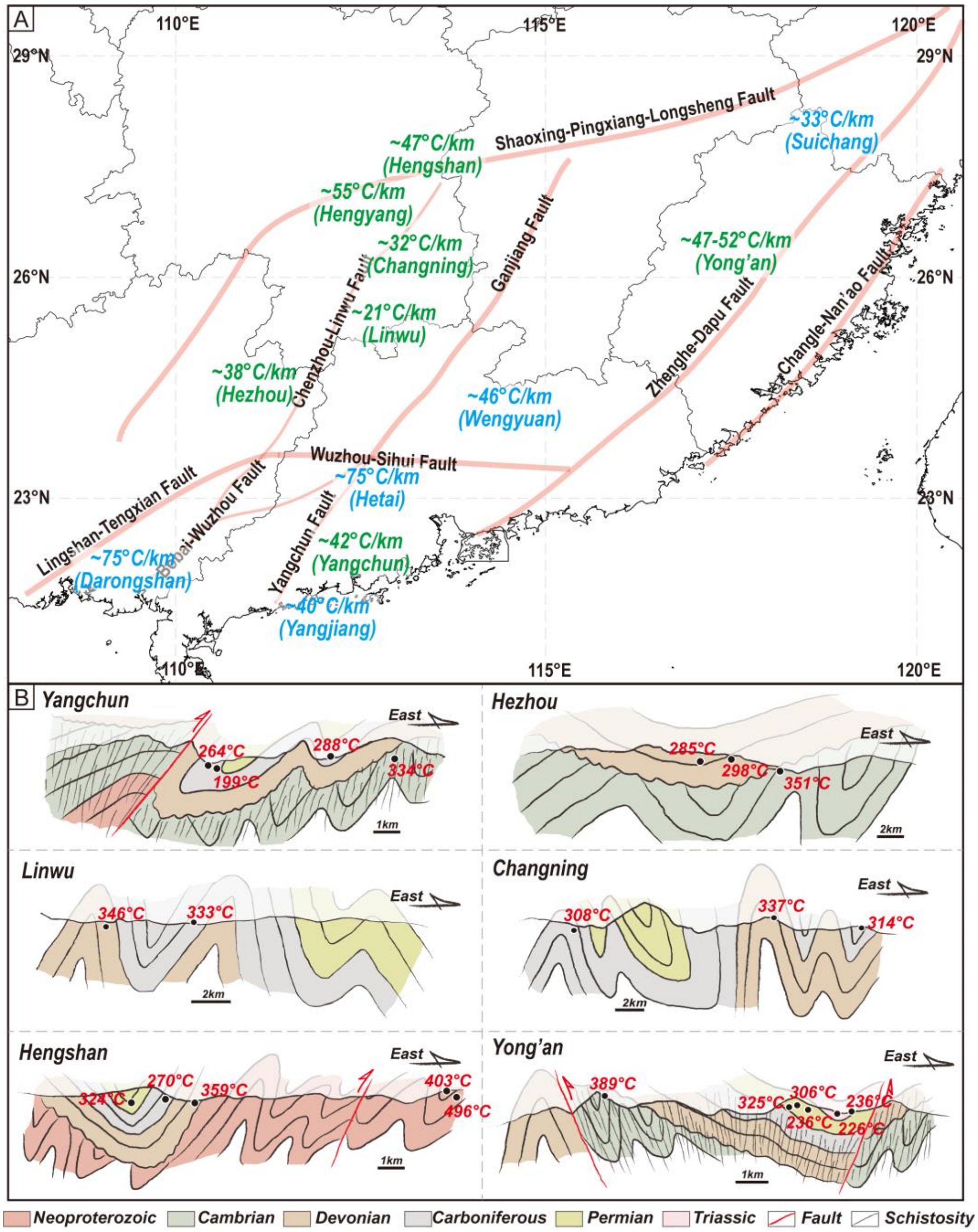

Figure. 5.26. *The results of the paleo-thermal gradient. (A) The distribution of the estimated paleo-thermal gradients within the Cathaysia Block. The data in blue are estimated from the metamorphic P-T data, and those in green are estimated from the RSCM temperature in Figure 5.26B. (B) The detailed cross-section of the unconformities and the Late Mesozoic basin at Yangchun, Hezhou, Linwu, Changning, Hengshan and Yong'an.*

the same massif (Fig. 5.17). These differences appear to be associated with unconformities, different structural levels, burial depth and late differential exhumation (Fig. 5.25). For example, the temperature differences across the Yangchun Fault and that in the Yong'an area. Although it is still preliminary, we attempt to use these differences to obtain the paleo-geothermal gradient (Fig. 5.26), which was calculated based on the thickness of the strata estimated from the geological map (scale 1:200,000) and the RSCM temperatures. We found that the highest thermal gradient is located at the Yunkai Massif (~40−75 °C/km) while relatively lower gradients characterize the Wuyi (~33−52 °C/km) and Nanling (~21−38 °C/km) massifs. The lowest gradient occurred in the center of the Nanling Massif. In contrast, the Jiangnan Orogenic Belt shows a higher gradient of ~47−55 °C/km.

5.6 Summary

The comprehensive study on the deformation, metamorphism and thermal state of the Cathaysia Block led to the following conclusions:

(1) The greenschist-facies regional metamorphism and E-W-trending folds developed in Neoproterozoic-Early Paleozoic strata, as well as some high-grade metamorphism exhumed in the central Yunkai and northern Wuyi massifs, were attributed to the Early Paleozoic orogenic event.

(2) The Early Mesozoic transpressional deformation of the Cathaysia Block was characterized by two distinct shortening structures, and the earlier E-W-trending structures were subsequently overprinted by those NE-trending ones. In addition, several shear belts were developed during the Early Mesozoic. The Early Mesozoic high-grade metamorphism was also recorded in the Yunkai and Wuyi massifs.

(3) Three massifs within the Cathaysia Block document significant variations in deformation intensity and metamorphic grade during the Early Mesozoic. The Yunkai Massif exhibits the highest grade, followed by Wuyi and Nanling. A pronounced south-to-north decrease and west-to-east increase in grade is observed across the region.

(4) The RSCM temperature and deformation temperature derived from quartz dynamic recrystallization indicate significant Early Mesozoic thermal heterogeneity among the three massifs. The Yunkai Massif records the highest temperature, followed by the Wuyi Massif, while the Nanling Massif exhibits the lowest temperature.

(5) The reconstruction of the paleo-thermal gradient of the Early Mesozoic Cathaysia Block reveals that the Yunkai Massif, which is close to the Early Mesozoic Indosinian Orogen, is hotter with respect to the Nanling and Wuyi massifs.

Chapter 6. Numerical modelling of tectonic evolution in the Early Mesozoic Cathaysia Block

6.1 Introduction

With the advancement of computer technology, particularly high-performance computing, numerical modelling has become an essential and widely used quantitative research method for understanding the dynamic evolution of the Earth. It has shifted the focus of geodynamic research from traditional observation and description (e.g., structural, magmatic, geophysical, and geochemical) of specific states within geological time slices to visualized deep dynamic and continuous processes over time (Gerya T, 2011, 2022; Li ZH et al., 2021). This paradigm shift enables scholars to go beyond purely descriptive or qualitative analysis and enter the realm of hypothesis testing and prediction (Weinberg RF and Hasalová P, 2015). By integrating geological, geophysical and geochemical observations into the numerical model, scholars can not only replicate and validate well-known events but also make predictions and provide inspiration for exploring future scenarios. Over the past fifty years, Earth's dynamic numerical modelling has made remarkable progress in understanding crustal deformation (Heron PJ and Pysklywec RN, 2016; Balázs A et al., 2017; Liu MX and Yang DH, 2022; Huangfu PP et al., 2023; Luo Y et al., 2024), magmatic activity (Rozel AB et al., 2017; Dong M et al., 2024; Ritter S et al., 2024), plate subduction (Capitanio FA et al., 2007; Mishin YA et al., 2008; Stern RJ and Gerya T, 2018), mantle convection (Jain C et al., 2019), as well as topographic evolution (Bahadori A et al., 2022; Wolf SG et al., 2022; Maiti G et al., 2024).

Up to now, most studies of the Cathaysia Block are based on observations from the ground surface, lacking information of the deep dynamic process. Although the geophysical investigation and mantle enclaves can provide information of the deep state in the Cathaysia Block (e.g., Gao WL et al., 2017; Zhao K et al., 2017; Xu S et al., 2019; Wei Y et al., 2020; Dong SW et al., 2023; Li JH et al., 2023; Li TZ et al., 2023; Zhang HJ et al., 2023), the continuous observation on a scale of geological time is absent. In this situation, dynamic numerical modelling is an indispensable approach to reveal the deep and continuous dynamic process of the Cathaysia Block.

In recent years, dynamic numerical modelling has been gradually applied in the study of tectonic evolution in South China. It provides new insights into understanding dynamic mechanisms and their responses on the surface (e.g., magmatism and crustal deformation) in the Cathaysia Block. Regarding the dynamic mechanism of the Mesozoic tectonic evolution, several studies focused on the flat subduction of the Paleo-Pacific Plate. Huangfu PP et al. (2016) and Jiang JW et al. (2022) proposed that thickened oceanic crust, young oceanic lithosphere, and a low initial subduction angle jointly facilitate the formation of flat subduction during the Mesozoic. The subsequent detachment and breakoff of slabs were induced by the reduction in convergence rate resulting from the northwestward movement of the SCB and the eclogitization of the oceanic crust, which led to the transition from flat to steep subduction and induced the surface tectonic shift from compression to extension (Dai LM et al., 2020; Jiang JW et al., 2022). Moreover, numerical modelling revealed connections between the deep dynamics process and shallow magmatism and structures. The flat plate subduction was considered as the main mechanism leading to the Early Mesozoic magmatic activity in the Cathaysia Block (Dai LM et al., 2020; Jiang JW et al., 2022). However, the flat subduction restricts the formation of mantle flow and probably inhibits the magmatism (Su JB, 2023). The slab roll-back and steepening of the subduction angle during the Late Mesozoic were proposed to trigger extensive magmatism and the extensional structures following the compression regime (Zuo XR et al., 2017; Su JB, 2023). Furthermore, Zhang Z et al. (2022) utilized a global mantle convection model and subduction-related dynamic tomography model to comprehensively explain the profound influence of the Paleo-Pacific subduction on the Late Mesozoic deformation and topography of South China.

However, a key controversy regarding the Paleo-Pacific subduction lies in the time when the Paleo-Pacific Ocean starts to subduct and significantly influences the geological responses within South China. Different opinions vary from Late Permian-Early Triassic (Li ZX and Li XH, 2007; Li ZX et al., 2012; Wang YN et al., 2017; Cochelin B et al., 2022), Early-Middle Jurassic (Zhou XM et al., 2006; Xu CH et al., 2017; Shu LS et al., 2021; Xu XS et al., 2024) to Early Cretaceous (Chen CH et al., 2008). Due to the lack of the significant Paleo-Pacific Ocean subducted-related magmatism and structures within the Cathaysia Block before the Early-Middle Jurassic (Zhou XM et al., 2006; Liu JX et al., 2020; Shu LS et al., 2021), most researchers proposed the driving force of the deformation, metamorphism and magmatism within in the South China was derived from the closure of the Paleo-Tethys Ocean and the ICB-SCB collision during the Late Permian to Triassic (Wang YJ et al., 2007a, 2021; Lin W et al., 2008, 2024; Faure M et al., 2014, 2016b). The current dynamic modelling of the Early Mesozoic evolution of South China predominantly relies on the flat subduction model of the Paleo-Pacific Ocean proposed by Li ZX and Li XH (2007). However, this model faces challenges from geological observations regarding the distribution of magmatism and structural pattern (e.g., Sun T, 2006; Zhou XM et al., 2006; Faure M et al., 2014; Gao P et al., 2017; Liu JX et al., 2020; Shu LS et al., 2021; Wang YJ et al., 2021). Thus, in contrast to the flat subduction model of the Paleo-Pacific Ocean during the Early Mesozoic, Liu HC et al. (2018) built a numerical model regarding the ICB-SCB collision which is based on the combination of geological observation of deformation, magmatism and geochemistry. Based on the Indosinian collision model, Wang YJ et al. (2002) and Liu HC et al. (2018) proposed that this collision led to lower crustal thickening and middle-lower crustal partial melting during 255–248 Ma, while a slab breakoff between 235–202 Ma induced asthenosphere upwelling and triggered middle-upper crustal partial melting. This provides a coherent explanation for Early Mesozoic I-type and S-type granites along the Jinshajiang–Ailaoshan–Song Ma suture zone.

Nevertheless, concerning the ICB-SCB collisional model during the Early Mesozoic, the subduction polarity of the Paleo-Tethys Ocean remains in debate. Several studies proposed that the eastern branch of the Paleo-Tethys Ocean southward subduction beneath the Indochina Block along the Jinshajiang – Ailaoshan – Song Ma – Song Chay – Hainan Indosinian suture zone (Faure M et al., 2014, 2016; Wang YJ et al., 2018; Zhang XC et al., 2019; Wang Y et al., 2022; Hung KT et al., 2023; Lin W et al., 2024), supported by (1) the northeastward distribution of magmatic arc, ophiolitic mélange zone, fold-and-thrust belt and Youjiang foreland basin (Wang YJ et al., 2018; Wang Y et al., 2022; Lin W et al., 2024), (2) top-to-the-northeast thrusting deformation (Faure M et al., 2014, 2016; Lin W et al., 2024), (3) magmatic arc northeastward migration induced by the steeping slab subduction angle (Lin W et al., 2024). Recently, some people proposed a bidirectional subduction based on the new findings of the Late Permian to Triassic magmatic rocks with continental arc affinity at Napo-Funing, Pingxiang, Nali and Danzhou to the northeast of the suture zone (Li YJ et al., 2016; Gao P et al., 2017; Xia XP et al., 2020; Xu J et al., 2020; Xiang ZJ et al., 2021, 2022; Huang WM et al., 2023; Shi WJ et al., 2023; Zhu X et al., 2025).

Moreover, in the ICB-SCB collisional numerical model, the SCB was represented by the Yangtze Block (Liu HC et al., 2018), which is a rigid craton, while the extensive magmatism and intense deformation predominantly documented within the Cathaysia Block (Sun T, 2006; Zhou XM et al., 2006; Lin W et al., 2008; Wang YJ et al., 2013, 2021; Gao P et al., 2017; Li JH et al., 2017a; Liu JX et al., 2020). The lithospheric rheology of the Cathaysia Block is probably weaker than that of the Yangtze Block. This weakness can be attributed to the Neoproterozoic and Early Paleozoic orogenic processes which produced numerous inherited structures within the Cathaysia Block (Shu LS et al., 2006, 2014, 2015, 2021; Wang YJ et al., 2013, 2021). Existing numerical models have primarily taken Early Mesozoic magmatism and deformation into consideration, but lack the evaluation of the inherited structure and its influences on the strain localization and paleo-thermal state.

To decipher the subduction polarity of the Paleo-Tethys Ocean, refine the Early Mesozoic dynamic model, and investigate the influence of ICB-SCB collision on the deformation, metamorphism and thermal state of the Cathaysia Block, as well as the role of inherited structures, this chapter employs high-resolution two-dimensional numerical modelling to test and validate the feasibility of the Indosinian collision model. Furthermore, we explore the effects of boundary faults and other pre-existing crustal structures on deformation patterns and thermal distribution.

6.2 Model design and boundary conditions

To study the deep dynamic process and surface responses within the Cathaysia Block, a regional two-dimensional thermal-mechanical dynamic model, defined by the I2VIS code based on the finite difference and mark-in-cell technology (Gerya TV and Yuen DA, 2003a, b), simulates the subduction of the Paleo-Tethys Ocean and the subsequent collision between the Indochina Block and Cathaysia Block.

The initial model has a length of 3000 km with a depth of 300 km, constructed with a nonuniform 1321 × 301 rectangular Euler grids and randomly distributed 9131760 Lagrangian markers. The grids provide the resolution varying from 10 km × 10 km at the Indochina Block and Paleo-Tethys Ocean to 1 km × 1 km at the Cathaysia Block.

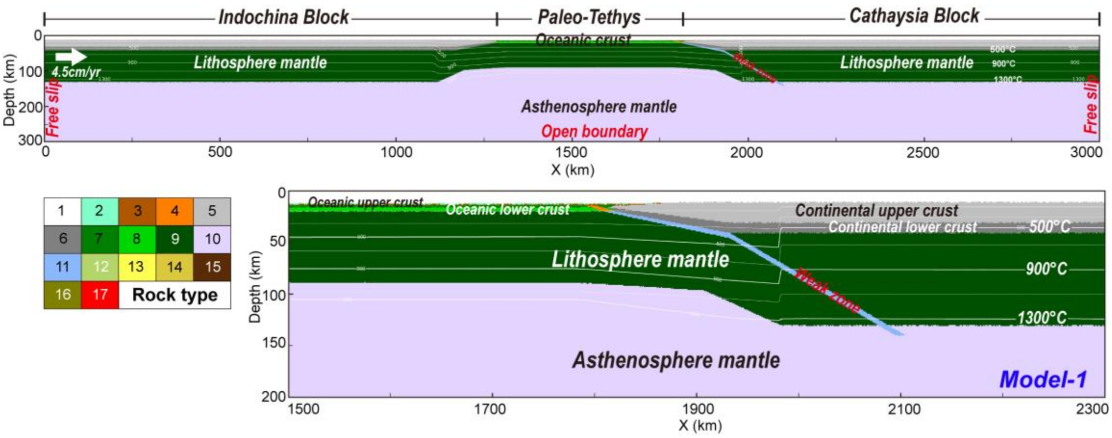

Figure. 6.1. Model setup for the reference model (model-1). The different lithologies were represented by different colors. 1-air; 2-water; 3,4-sediments; 5-continental upper crust; 6-continental lower crust; 7-oceanic upper crust; 8-oceanic lower crust; 9-lithosphere mantle; 10-asthenosphere mantle; 11-weak zone or hydrated mantle; 12-serpentinized mantle; 13-molten basalt; 14-quenched sediment; 15-quenched basalt; 16-molten peridotite; 17-motlen dry mantle.

In the initial configuration, the reference model (model-1) comprises three units, i.e., Cathaysia Block, Indochina Block and Paleo-Tethys Ocean (Fig. 6.1). Geophysical studies indicate that the Cathaysia and Indochina blocks have crustal thicknesses of approximately 32 km and 37 km, respectively (e.g., Yu YQ et al., 2017; Guo Z et al., 2018; Huang HB et al., 2020). The lithosphere thickness of the Cathaysia Block ranges from 85 to 150 km (Shan B et al., 2014, 2017; Dong YF et al., 2021), while that of the Indochina Block is between 80km and 110 km (Wu HH et al., 2004). For simplification and considering the lithosphere thinning during the Late Mesozoic, the continental lithosphere in this study is assumed to be 120-km thick, consisting of a 20-km-thick upper crust, a 10-km-thick lower crust and a 90-km-thick lithospheric mantle. The age of the oceanic lithosphere was set to 65 Ma, considering the Paleo-Tethys Ocean was an old oceanic lithosphere during the subduction. The oceanic lithosphere was set comprising 1-km-thick sediments, a 2-km-thick upper crust and a 4-km-thick lower crust, while the lower boundary of the lithosphere was set based on the half-space cooling model (Turcotte DL and Schubert G, 2002). A 10-km-thick sticky air layer with low density (1 kg/m^3) and viscosity (10^{18} Pa·s) was employed on the top of all blocks as a free internal surface to simulate the erosion/sedimentation processes and topography evolution. An inclined weak zone with wet olivine rheology was employed, aiming to initiate the subduction. The sediments, continental crust and oceanic upper crust employed the rheology of wet quartzite, the oceanic lower crust employed the rheology of plagioclase An_{75}, and the mantle employed the rheology of dry olivine (Ranalli G, 1995). The detailed properties of the rheology and rock types of different units in the model are described in Tables 6.1 and 6.2.

The top and side boundaries employed the free-slip boundary conditions, whereas the lower boundary was set to be the open permeable boundary condition, satisfying an external free slip below the 300 km depth of the model and avoiding the artificial effects (Burg JP and Gerya TV, 2005; Gorczyk W et al., 2007).

Table 6.1 Viscous flow laws used in the numerical model

Symbol	Flow laws	$1/A_D$ ($Pa^n \cdot s$)	Ea (J)	Va (J/bar)	n power
A	Air & Water	1.00×10^{18}	0	0	1
B	Wet quartzite	1.97×10^{17}	1.54×10^{5}	0.8	2.3
C	Plagioclase An_{75}	4.80×10^{22}	2.38×10^{5}	0.8	3.2
D	Dry olivine	3.98×10^{16}	5.32×10^{5}	0.8	3.5
E	Wet olivine	5.01×10^{20}	4.70×10^{5}	0.8	4

Note: $1/A_D$-material constant, Ea-activation energy, Va-activation volume, n-stress component.

Table 6.2 Material properties of the different units in the numerical model

Material	Rho (kg/m^3)	α (1/K)	β (1/kbar)	Cp (J/kg)	Kt (W/(m·K))	Tkt (W/m)	Pkt (1/bar)	Hr (W/kg)	Flow laws
Sticky air	1	0	0	3.33×10^{6}	200	0	0	0	A
water	1000	0	0	3.33×10^{6}	200	0	0	0	A
Sediment	2600	2.0×10^{-5}	7.5×10^{-4}	1.0×10^{3}	0.64	807	4.0×10^{-6}	2.0×10^{-6}	B
Continental upper crust	2750	2.0×10^{-5}	7.5×10^{-4}	1.0×10^{3}	0.64	807	4.0×10^{-6}	1.0×10^{-6}	B
Continental lower crust	3000	2.0×10^{-5}	7.5×10^{-4}	1.0×10^{3}	1.18	474	4.0×10^{-6}	2.5×10^{-7}	C
Oceanic upper crust	3000	2.0×10^{-5}	4.5×10^{-4}	1.0×10^{3}	1.18	474	4.0×10^{-6}	2.5×10^{-7}	C
Oceanic lower crust	3000	2.0×10^{-5}	4.5×10^{-4}	1.0×10^{3}	1.18	474	4.0×10^{-6}	2.5×10^{-7}	C
Lithospheric mantle	3300	2.0×10^{-5}	4.5×10^{-4}	1.0×10^{3}	0.73	1293	4.0×10^{-6}	2.2×10^{-8}	D
Asthenosphe re mantle	3300	2.0×10^{-5}	4.5×10^{-4}	1.0×10^{3}	0.73	1293	4.0×10^{-6}	2.2×10^{-8}	D
Weak zone	3250	2.0×10^{-5}	7.5×10^{-4}	1.0×10^{3}	0.73	1293	4.0×10^{-6}	2.2×10^{-8}	E

Note: Rho-density, α-thermal expansion coefficient, β-compressibility, Cp-heat capacity, Kt-thermal conductivity, Tkt-temperature dependency coefficient of conductivity, Pkt-pressure dependency coefficient of conductivity, Hr-radiogenic heat production, Flow laws - viscous flow laws presented in Table 6.1.

The initial temperature field of the oceanic lithosphere was derived from the half-space cooling model (Turcotte DL and Schubert G, 2002), which employed an initial temperature of 0°C and 1350°C at the top surface and the bottom of the oceanic lithospheric mantle, respectively. The initial temperatures of the top surface, Moho and lithosphere-asthenosphere boundary (LAB) were set at 0°C, 600°C and 1350°C, respectively. The initial temperature field within the continental lithosphere was linearly increasing. Meanwhile, an adiabatic thermal gradient of 0.5°C/km was employed for the asthenosphere mantle (Turcotte DL and Schubert G, 2002; Katsura T, 2022). The temperature of the upper boundary was fixed at 0°C, both the side boundaries were adiabatic boundaries without any heat flux, whereas the lower boundary was set as an open boundary assuming the fixed temperature was at 100km below the lower boundary of the model. All the initial temperature fields would evolve spontaneously during the running of the model.

The prescribed subduction velocity of oceanic lithosphere ensures horizontal compression and subduction. In the reference model, a right-lateral convergent rate of 4.5 cm/yr was adopted, which is estimated based on the paleomagnetic study (Yan YG et al., 2018).

Table 6.3 Setup of different models

Model name	Subduction direction	Pre-existing structures
Model-1 (reference model)	beneath Cathaysia Block	none
Model-2	beneath Cathaysia Block	50-km-wide boundary faults
Model-3	beneath Cathaysia Block	boundary faults and intra-crustal faults
Model-4	beneath Indochina Block	none
Model-5	beneath Indochina Block	50-km-wide boundary faults
Model-6	beneath Indochina Block	boundary faults and intra-crustal faults

For the purposes of testing the subduction direction of the Paleo-Tethys between the Indochina and Cathaysia blocks, as well as the influence of the pre-existing structures on the deformation behavior and thermal state within the Cathaysia Block, five other models were tested (Table 6.3). Model-1, 2 and 3 were employed to simulate the northward subduction of the Paleo-Tethys Ocean beneath the Cathaysia Block, while the Model-4, 5 and 6 simulated the southward subduction beneath the Indochina Block. Moreover, the boundary faults were added within the lithosphere of the Cathaysia Block in Model-2 and Model-5 (Fig. 6.2A), and both boundary faults and intra-crustal faults were added within the Cathaysia Block in Model-3 and Model-6 (Fig. 6.2B). Other parameters were the same as the Model-1 (reference model).

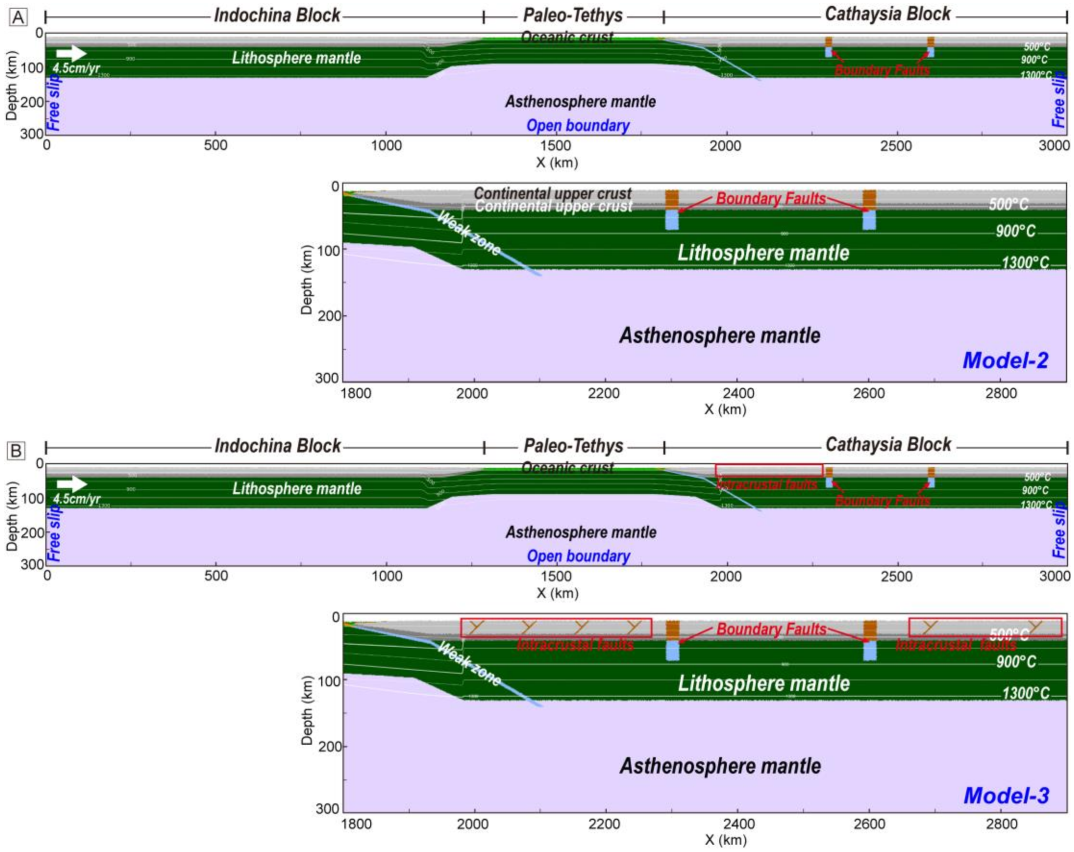

Figure. 6.2. Model setup for Model-1, Model-2 and Model-3. (A) The boundary faults within the Cathaysia Block were added in model-2. (B) The intra-crustal faults within the Cathaysia Block were added in model-3.

6.3 Modelling results

6.3.1 Reference model evolution

The reference model (Model-1), employing a uniform and homogeneous lithosphere for the Cathaysia Block, experienced the closure of the Paleo-Tethys Ocean

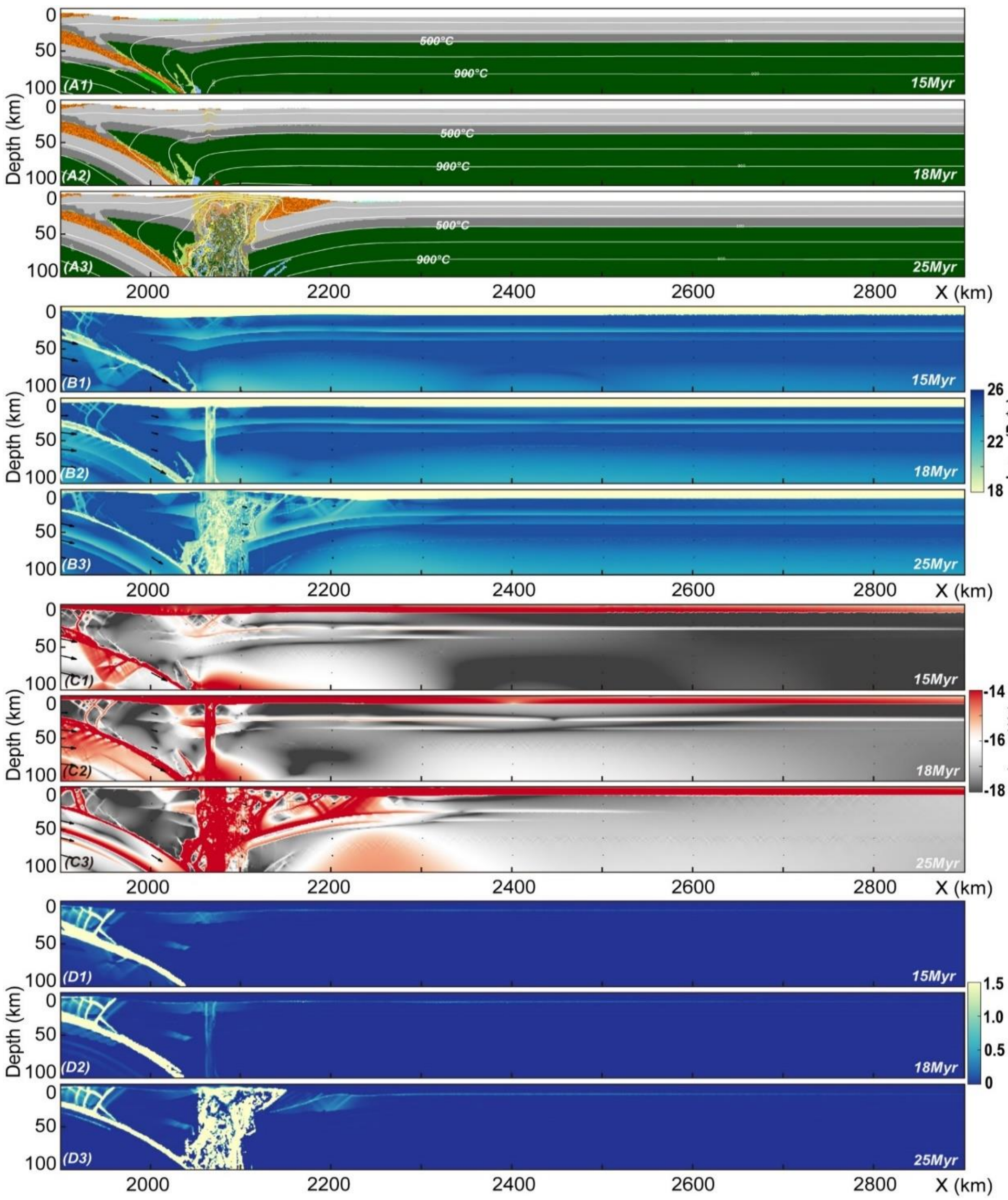

Figure 6.3. *Results of numerical experiments of the reference model (Model-1) showing the material fields (A), viscosity (B), second invariant of strain rate (C) and accumulated strain (D) within the Cathaysia Block at 15 Myr, 18 Myr and 25 Myr.*

after the 500-km northward subduction with 4.5 cm/yr convergent velocity and then produced a collision between the Indochina and Cathaysia blocks.

The oceanic subduction and subsequent continental collision induced the laterally heterogeneous responses within the overriding plate, affecting the crustal thickness, deformation, magmatism and thermal state. The evolution of the model can be divided into three stages (Fig. 6.3A). During the initial stage, the oceanic plate continuously subducted beneath the Cathaysia Block, leading to the formation of the accretionary edge and back-arc basin, along with a gradual increase in the subduction angle. A magmatic activity initiated at approximately 9 Myr after the onset of subduction. Then, the ocean closed, and the initial continental collision occurred around 15 Myr (Fig. 6.3A1), marking the transition to the collisional stage. At this stage, the continental plate continued to subduct driven by both the prescribed convergence rate and the gravitational pull of the oceanic slab. Concurrently, the compressive regime led to the closure of the back-arc basin by about 18 Myr and prompted a topographic uplift (Fig. 6.3A2). Subsequently, the continental crust experienced significant thickening, accompanied by widespread partial melting and extensive magmatism (Fig. 6.3A3).

The viscosity in the collisional belt (~2100 km in the model) significantly decreased due to the magmatism produced and upward migration (Fig. 6.3B). The strain rate and accumulated strain indicate that the deformation was predominantly concentrated in collisional zones of the orogen (Figs. 6.3B and C). During the subduction stage, deformation was localized in the arc and back-arc regions. After the continental collision, the stress propagated from the subduction zone into the interior of the overriding plate with the most intense deformation remaining close to the orogen. The degree of the melting (Fig. 6.3D) displayed a similar pattern to that of deformation, with the significant partial melting in the collisional zones. In contrast, the overriding plate far away from the collisional zones (>2150 km in the model) showed a few geological responses to the continental collision except for the influence of the stress field.

The degree of partial melting significantly increased after the continental collision and subduction of the continental plate (Fig. 6.4A). The partial melting was predominantly developed in the collisional zones with some spread laterally in shallow crust (Fig. 6.4A3), which is consistent with the domains of deformation. Compared to areas farther inland within the overriding plate where remain relatively unaffected by the orogenic thermal anomaly, a high temperature (approaching 800 °C) occurred in the collisional zones (Fig. 6.4B). The partial melting in the collisional zones also generated a 100-km-wide high-heat-flow zone in the shallow crust where has a high thermal gradient (Fig. 6.4C).

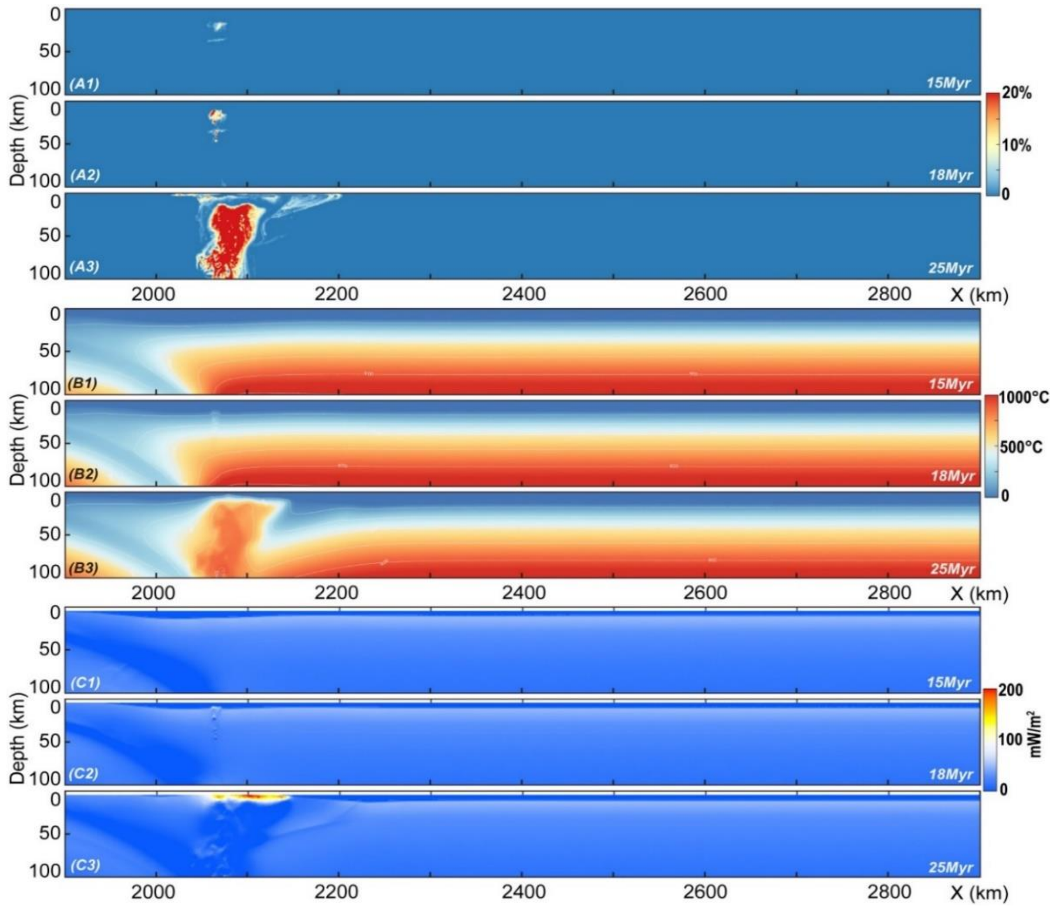

Figure 6.4. Results of numerical experiments of the reference model (model-1) showing the degree of melting (A), temperature (B) and heat flow (C) within the Cathaysia Block at 15 Myr, 18 Myr and 25 Myr.

6.3.2 Results of different models

The first set of numerical experiments (Model-1, 2, 3) simulated the northward subduction of the Paleo-Tethys Ocean beneath the Cathaysia Block, followed by the collision between the Indochina and Cathaysia blocks. In this group, all models adopted the same configuration as Model-1. The variable tested across these three models is the pre-existing structure within the overriding plate (i.e., Cathaysia Block; Fig. 6.2).

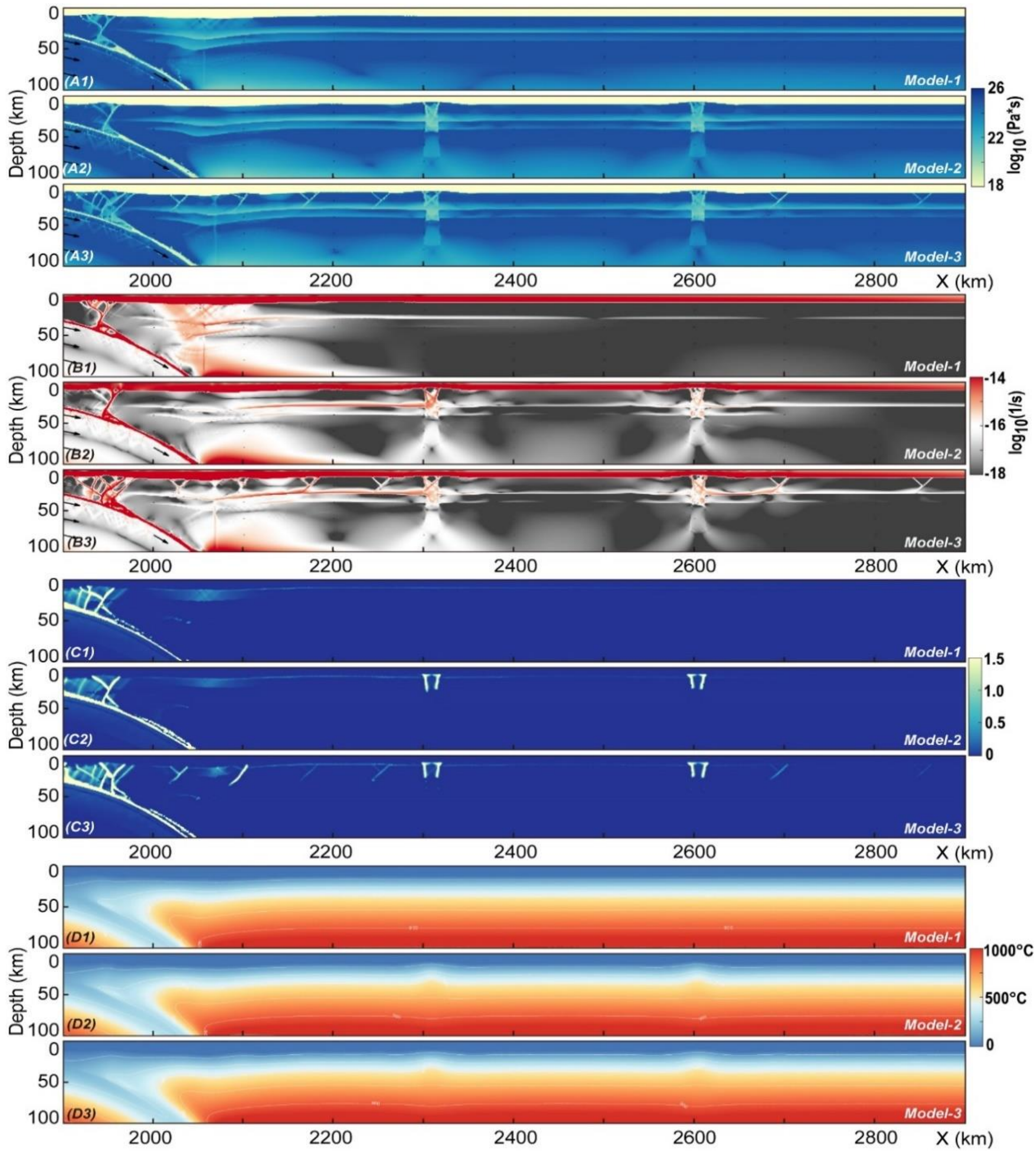

Figure 6.5. *Results of numerical experiments Model-1, Model-2 and Model-3, showing the viscosity (A), second invariant of strain rate (B), accumulated strain (C) and temperature (D) within the Cathaysia Block at 6.5 Myr since the northward subduction of the Paleo-Tethys Ocean.*

During the subduction stage (e.g., at 6.5Myr), the pre-existing structures have a significant influence on the distribution of the deformation and temperature within the overriding Cathaysia Block (Fig. 6.5). In Model-1, the Cathaysia Block was treated as homogeneous with no pre-existing structures. A region of low viscosity occurred in the arc and back-arc domains of the overriding plate. In contrast, the inland region far from the subduction zone exhibited laterally homogeneous properties, except for a localized low-viscosity anomaly at depths of ca. 70−100 km near the subducted slab which was attributed to deep mantle convection (Fig. 6.5A1). Influenced by viscosity, both the strain rate and accumulated strain exhibited similar distributions to the viscosity field, with the high values concentrated in the subduction zones but negligible deformation in the interior of the overriding plate. (Figs. 6.5B1 and C1). The temperature field also exhibited laterally homogeneous characteristics without any disturbance (Fig. 6.5D1). In contrast to Model-1, the pre-existing boundary and intra-crustal faults affected strain localization and led to heterogeneous distribution of both deformation and temperature.

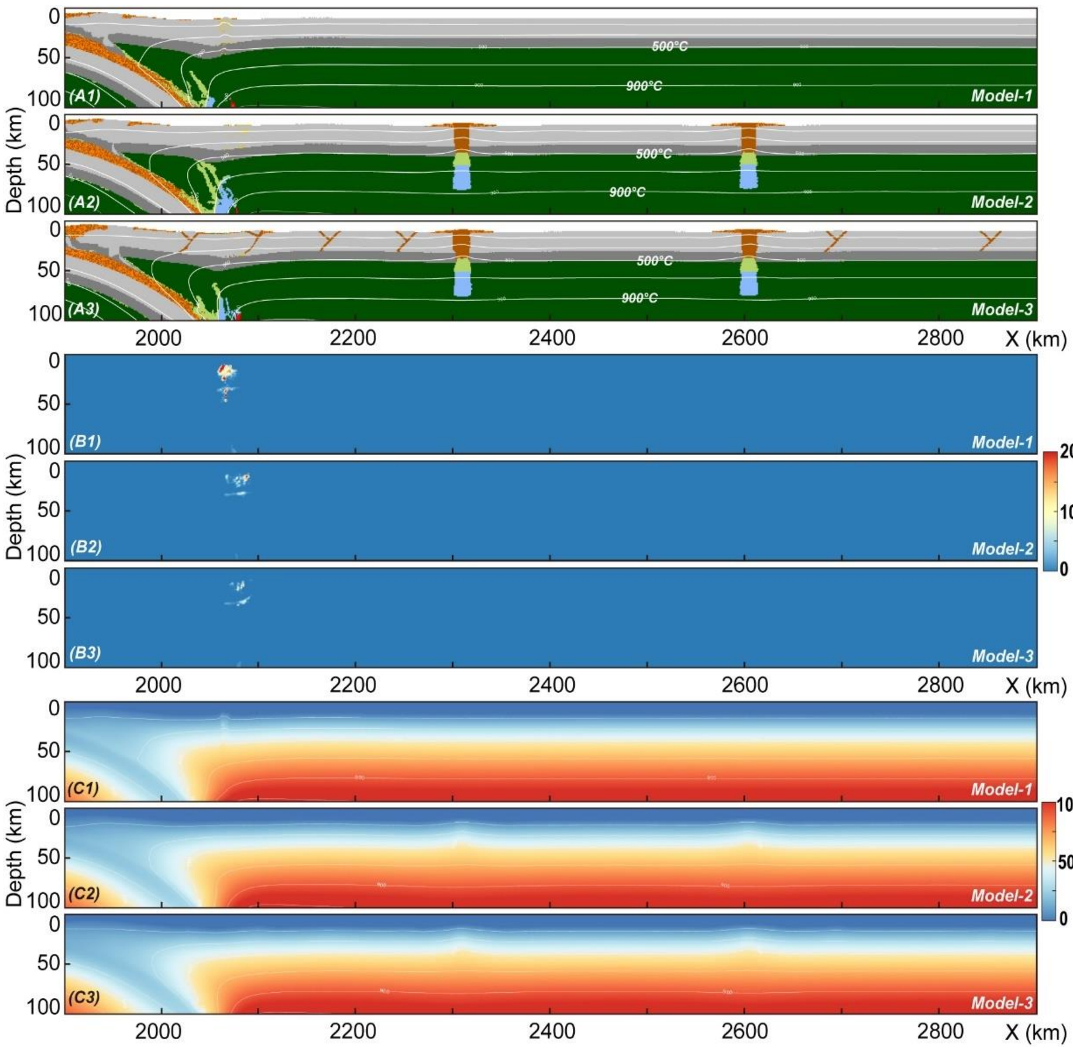

Figure 6.6. *Results of numerical experiments Model-1, Model-2 and Model-3, showing the material fields (A), degree of melting (B) and temperature (C) within the Cathaysia Block at 18 Myr since the northward subduction of the Paleo-Tethys Ocean.*

The pre-existing structures, particularly the large-scale boundary faults, exhibited low viscosity (Figs. 6.5A2 and A3). Consequently, the high strain rate and more strain were concentrated at these places (Figs. 6.5B2, B3, C2 and C3). Due to stress absorption by the boundary faults, a region of low strain rate developed adjacent to these pre-existing structures (Figs. 6.5B2 and B3). Furthermore, the accumulated strain field suggests an inland propagation of deformation (Fig. 6.5C3). Shortening along the pre-existing structures led to the formation of localized elevated topography. The temperature field exhibited localized high-temperature anomalies induced by the pre-existing structures (Figs. 6.5D2 and D3).

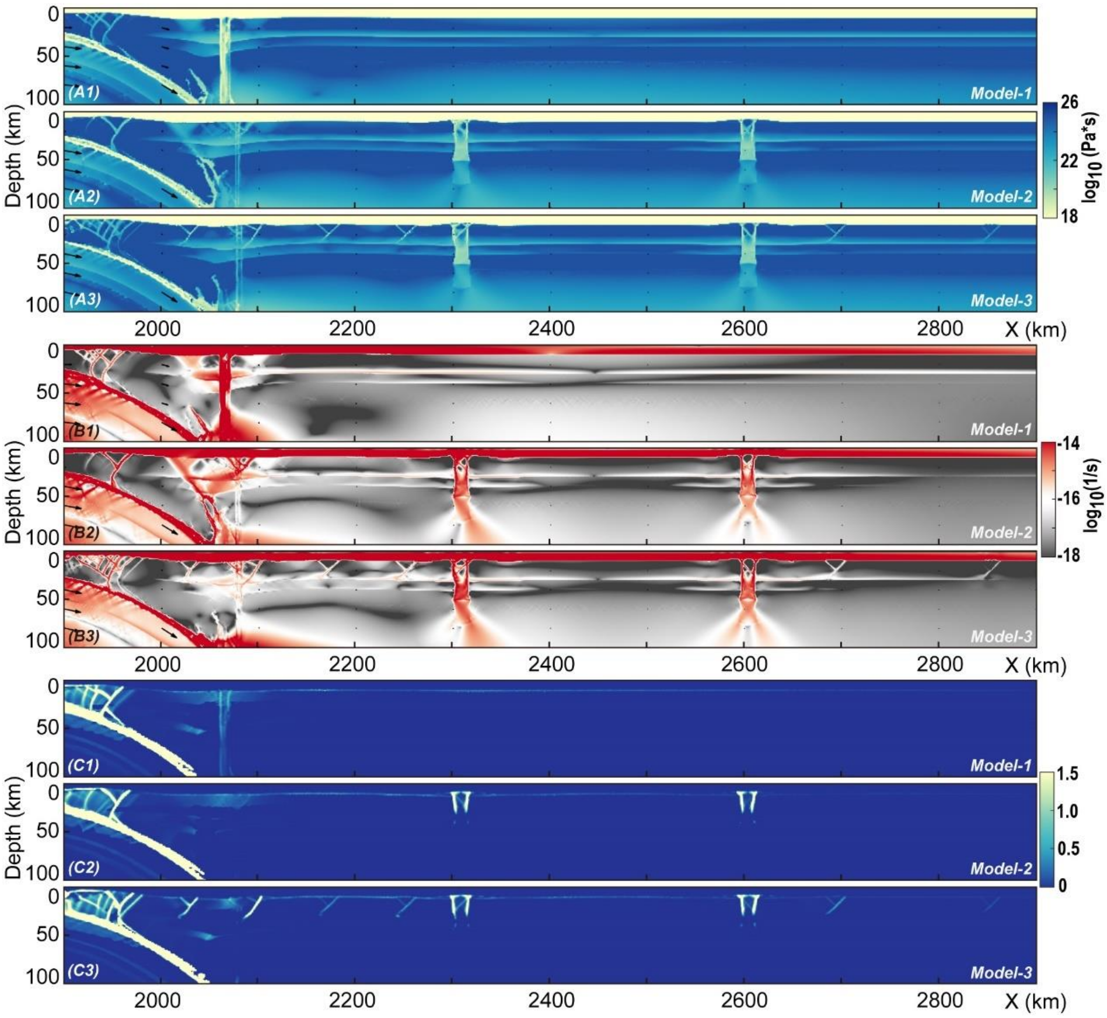

Figure 6.7. *Results of numerical experiments Model-1, Model-2 and Model-3, showing the viscosity (A), second invariant of strain rate (B) and accumulated strain (C) within the Cathaysia Block at 18Myr since the northward subduction of the Paleo-Tethys Ocean.*

As the models evolved, the ocean was closed and the continents collided. Throughout these processes, the distribution of temperature and deformation remained similar to the subduction stage (Figs. 6.6 and 6.7). The shortening and localized elevated topography developed along the pre-existing structures (Figs. 6.7B and C). Localized thermal anomalies were observed in the temperature field (Fig. 6.6C), resulting from partial melting in subduction zones and heat transport along the boundary faults. The presence of low-viscosity melts, in turn, facilitated localized deformation in the overriding plate, characterized by the high strain rate and more strain (Figs. 6.7B and C).

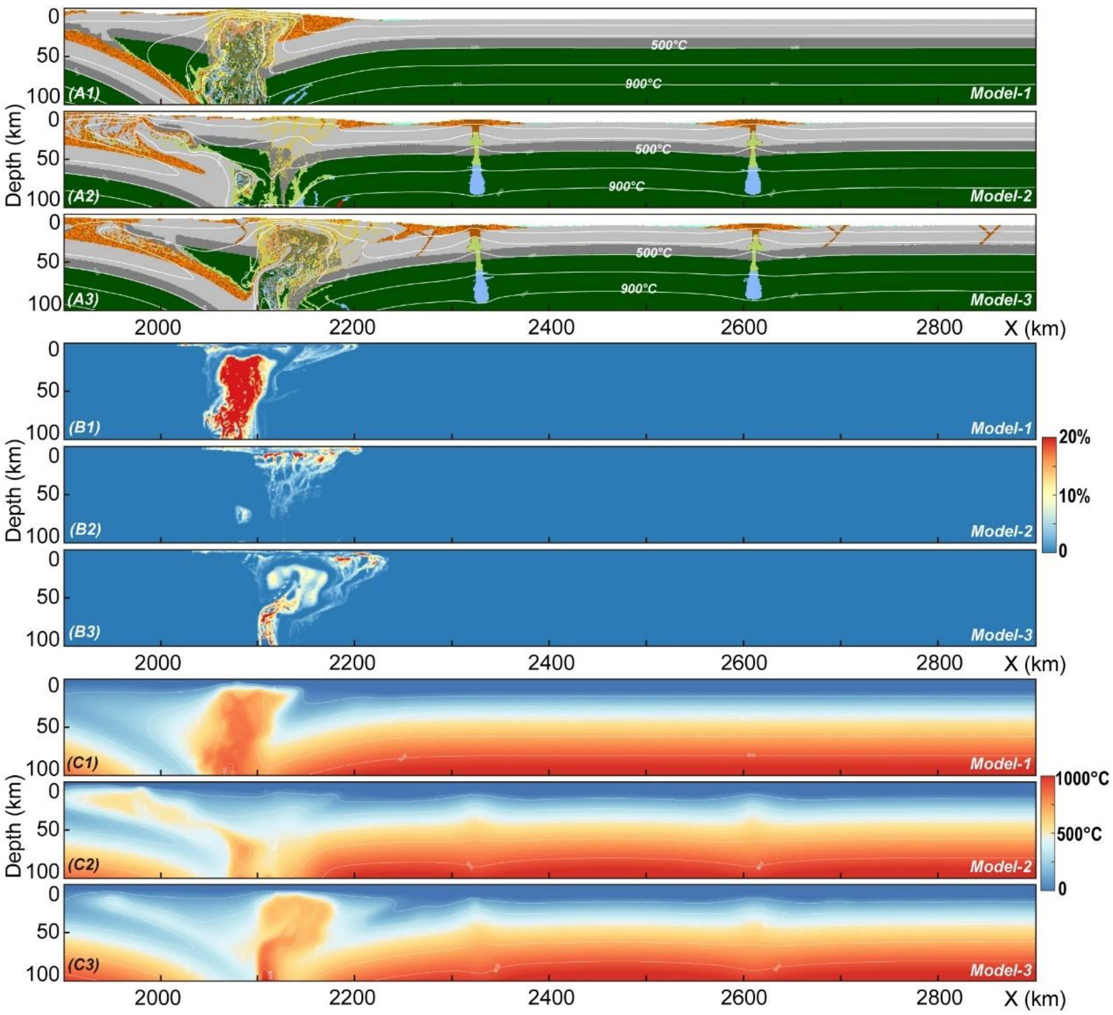

Figure 6.8. *Results of numerical experiments Model-1, Model-2 and Model-3, showing the material fields (A), degree of melting (B) and temperature (C) within the Cathaysia Block at 25Myr since the northward subduction of the Paleo-Tethys Ocean.*

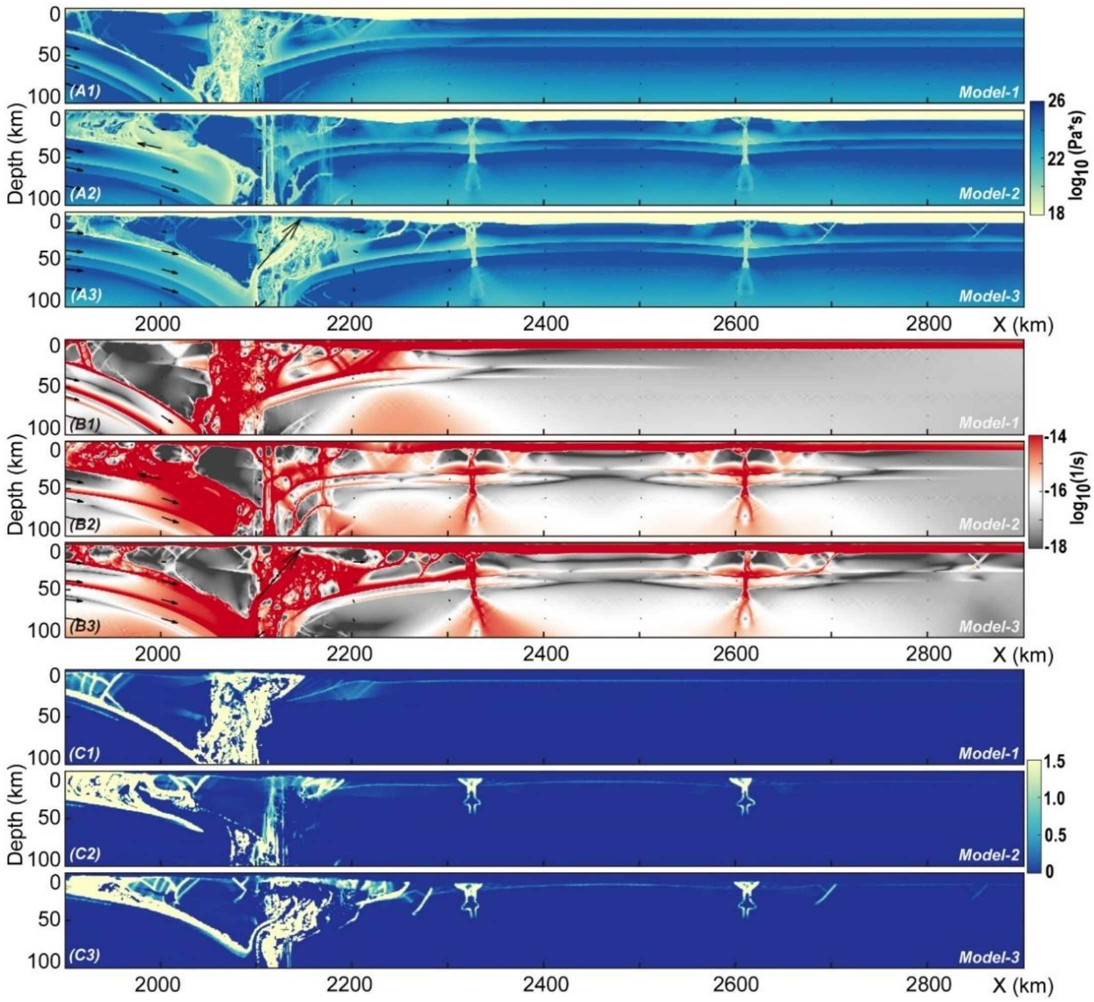

Figure 6.9. *Results of numerical experiments Model-1, Model-2 and Model-3, showing the viscosity (A), second invariant of strain rate (B) and accumulated strain (C) within the Cathaysia Block at 25Myr since the northward subduction of the Paleo-Tethys Ocean.*

Following 10 Myr of continental collision (at ~25 Myr), the overriding plate underwent significant deformation and thermal evolution. The distribution of these processes was strongly influenced by the pre-existing structures (Figs. 6.8 and 6.9). In contrast to Model-1, the Model-2 and Model-3 experienced significant crustal shortening in the overriding plate, which maximum up to ~500km. The crustal shortening was predominantly localized within pre-existing structures and exhibited the characteristics of elevated topography (Fig. 6.8A). The intra-crustal faults adjacent to the collisional zone facilitated the formation of the fold-and-thrust belt, resulting in the crustal thickening and the development of a wide orogenic plateau. Significant magma emplacement was observed along these intra-crustal faults, suggesting that the pre-existing faults served as crucial conduits that promoted the upward migration of melts (Fig. 6.8A3). The degree of melting and the temperature fields revealed a broad thermal disturbance associated with extensive magmatism (Figs. 6.8B and C). Although the partial melting was absent inland of the overriding plate (Fig. 6.8B), high temperature anomalies were observed along the pre-existing structures and the large-scale faults induced more significant thermal disturbance (Fig. 6.8C).

In addition, more significant deformation developed at ~25 Myr compared to the earlier subduction and initial collision stages (Fig. 6.9). The viscosity fields of Model-2 and Model-3 revealed pronounced heterogeneity within the overriding plate (Figs. 6.9A2 and A3), attributed to the occurrence of the pre-existing structures and extensive magmatism. The contrast in viscosity became more pronounced compared to earlier stages (Figs. 6.7A and 6.9A). Similarly, the strain localization within the overriding plate at ~25 Myr also became more pronounced than the earlier stage. It was characterized by higher strain rates concentrated along the pre-existing structures, because of this strain absorption, the other regions experienced correspondingly lower strain rates (Fig. 6.9B). Both the stain rate and accumulated strain fields exhibited a more pronounced inland propagation of the deformation (Fig. 6.9C), with a broad deformation belt up to 400-km wide (Fig. 6.9C3).

The temperature evolution of the Cathaysia Block at different depths was presented in Fig. 6.10. In Model-1, the temperature exhibited a high stability within the overriding plate without significant thermal disturbances, even at different crustal depths (Fig. 6.10A). The maximum temperature occurred adjacent to the orogenic belt reaching to ~800°C. In Model-2, boundary faults had a significant impact on the temperature distribution and produced temperature peaks (Fig. 6.10B). The thermal anomaly recorded by the maximum temperature was up to ~200°C, while the regions between the boundary faults exhibited relatively stable with low-temperature disturbances adjacent to the faults (Fig. 6.10B). Similar characteristics were observed in Model-3.

Besides the boundary faults, the intra-crustal also induced slight thermal disturbances (Fig. 6.10C). From the perspective of depth, the 15-km depth exhibited more heterogeneity with respect to the 10-km and 20-km depths. The highest temperatures in the three models were in the collisional zones induced by the voluminous partial melting and magma upward migration.

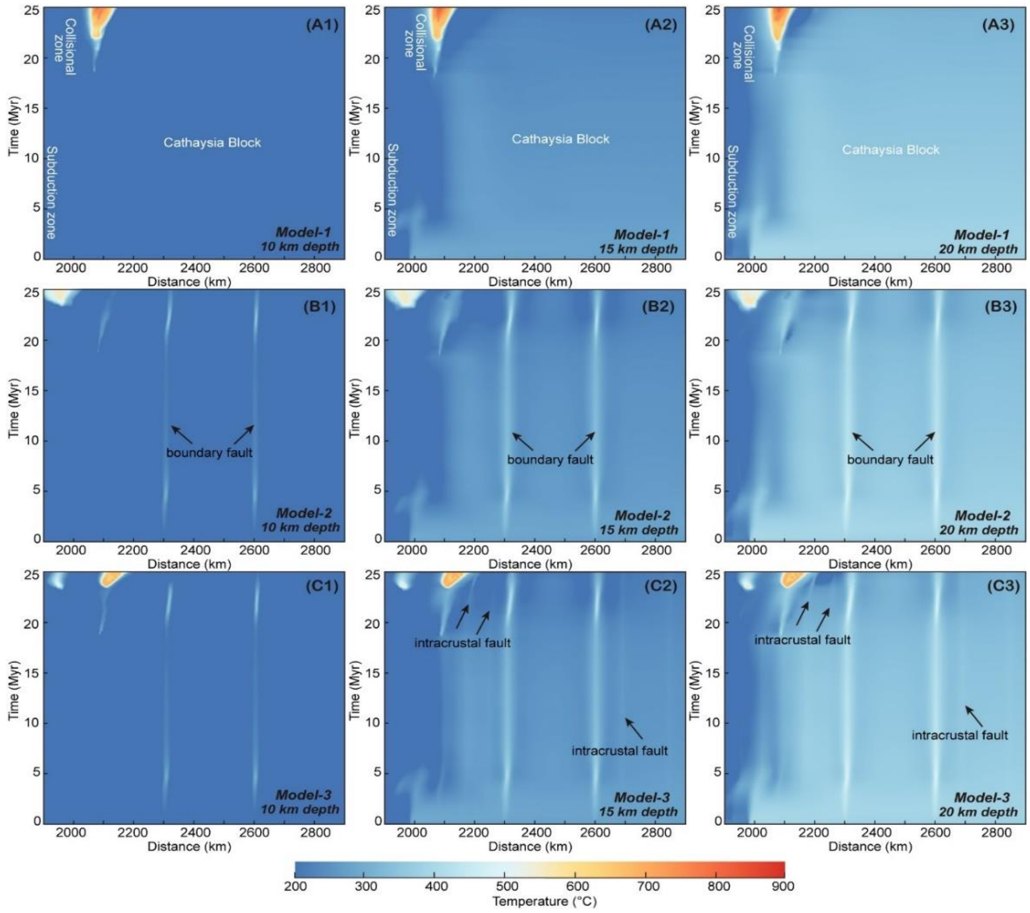

Figure 6.10. *The temperature evolutions of the Cathaysia Block at depths of 10km, 15km and 20km in numerical experiments Model-1, Model-2 and Model-3.*

In contrast to the simulated northward subduction of the Paleo-Tethys Ocean in the first set of experiments (Model-1, 2, 3), the second set (Model-4, 5, 6) simulated the southward subduction of the Paleo-Tethys Ocean beneath the Indochina Block and the subsequent continental collision (Fig. 6.11A). These models retained the same configuration as the first set, except for adjustments to the position and direction of prescribed convergent velocity to simulate opposing subduction polarity. The variable tested across the second set remained the pre-existing structure within Cathaysia Block.

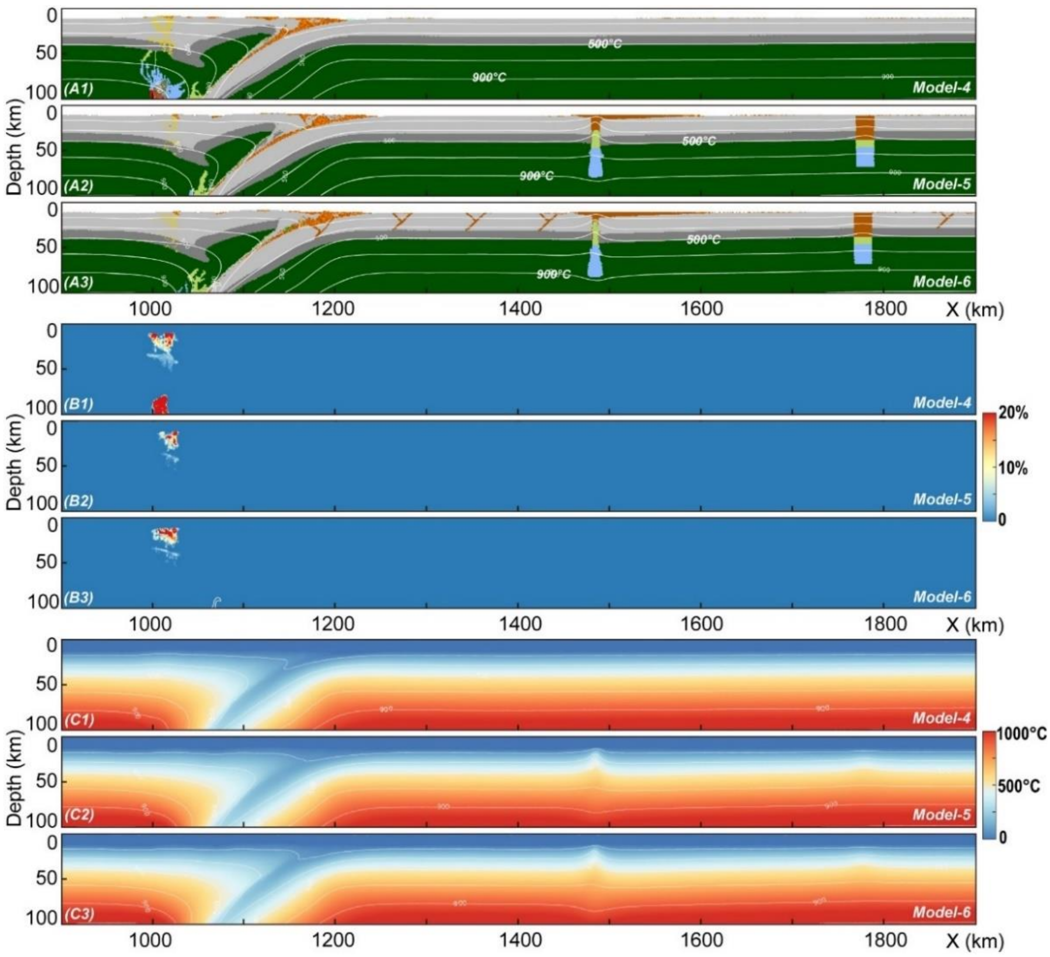

Figure 6.11. *Results of numerical experiments Model-4, Model-5 and Model-6, showing the material fields (A), degree of melting (B) and temperature (C) within the Cathaysia Block at 18Myr since the southward subduction of the Paleo-Tethys Ocean.*

As the model evolved to approximately 18 Myr, which is about 3 Myr after the initial continental collision, widespread partial melting occurred in the overriding Indochina Block, triggered by the dehydration of the subducted slab (Figs. 6.11A1 and B1). This was accompanied by the localized crustal shortening and thickening. In contrast, the subducted Cathaysia Block exhibited a few geological responses. However, with the incorporation of pre-existing structures, the slab dehydration and partial melting within the overriding plate diminished (Figs. 6.11A and B), while crustal compression and shortening became evident along the boundary faults in the Cathaysia Block (Figs. 6.11A2 and A3). The temperature field of Model-4, which lacked pre-existing structures, revealed a laterally homogeneous thermal structure within the subducted Cathaysia Block (Fig. 6.11C1). Similar to Model-2 and Model-3 with the pre-existing structures, Model-5 and Model-6 exhibited high-temperature anomalies despite having an opposite subducted polarity (Figs. 6.11C2 and C3). The enhanced thermal anomaly with respect to the first set of experiments was probably attributed to the position of the prescribed convergent velocity.

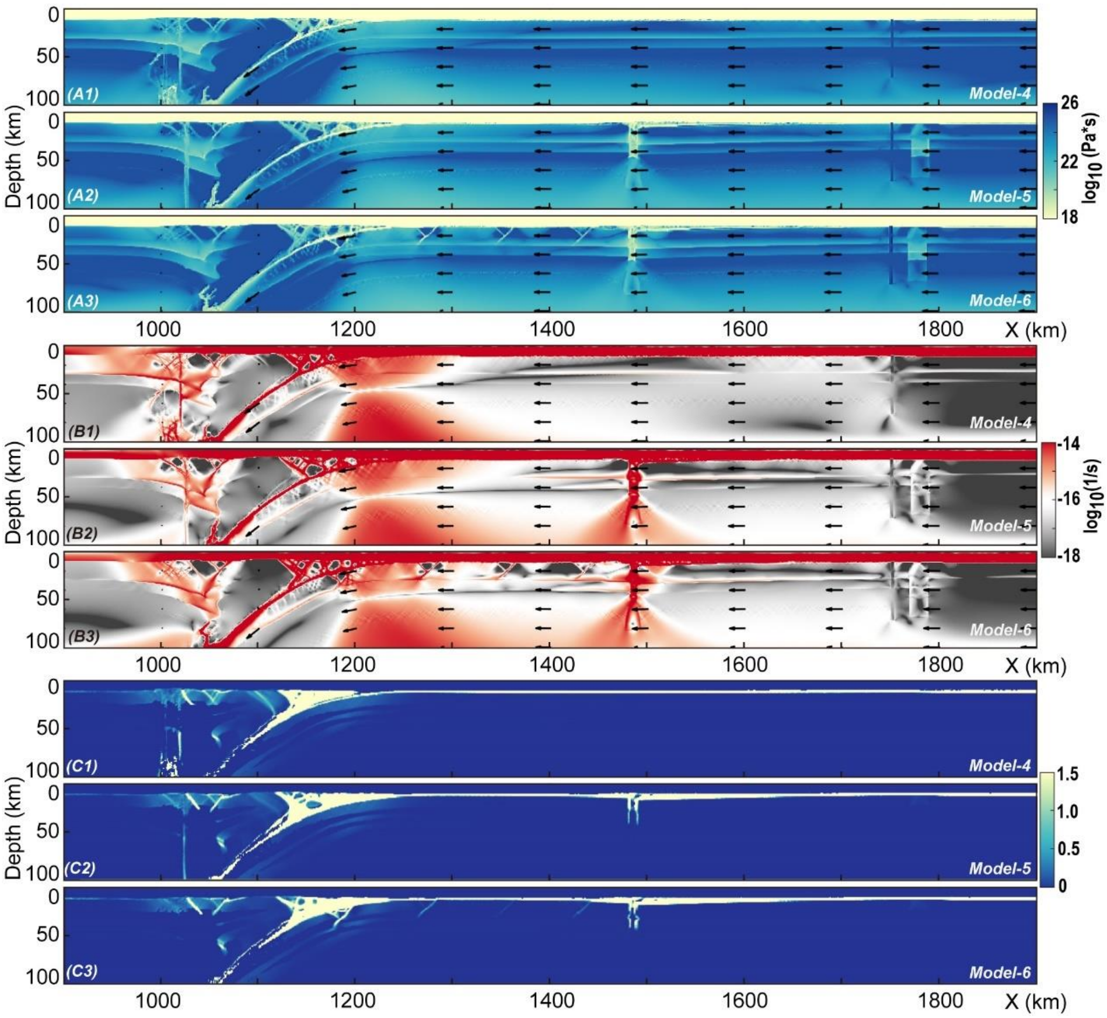

Figure 6.12. *Results of numerical experiments Model-4, Model-5 and Model-6, showing the viscosity (A), second invariant of strain rate (B) and accumulated strain (C) within the Cathaysia Block at 18Myr since the northward subduction of the Paleo-Tethys Ocean.*

The overriding Indochina Block adjacent to the subduction zone exhibited low viscosity, high strain rate and high accumulated strain (Fig. 6.12). The low viscosity regions within the Cathaysia Block were confined to the subducted zones and the pre-existing structures (Fig. 6.12A), which also coincided with domains of high strain rate (Fig. 6.12B). However, the strain was predominantly concentrated along the large-scale boundary, the intra-crustal faults exhibited a small amount of the strain accumulation, while the remaining regions of the Cathaysia Block showed negligible strain (Fig. 6.12C). Compared to the northward subduction models, these models exhibited more pronounced deformation at the neck of the subducted Cathaysia Block, due to the bending and extension. Moreover, the partial and associated magmatism were absent in the Cathaysia Block.

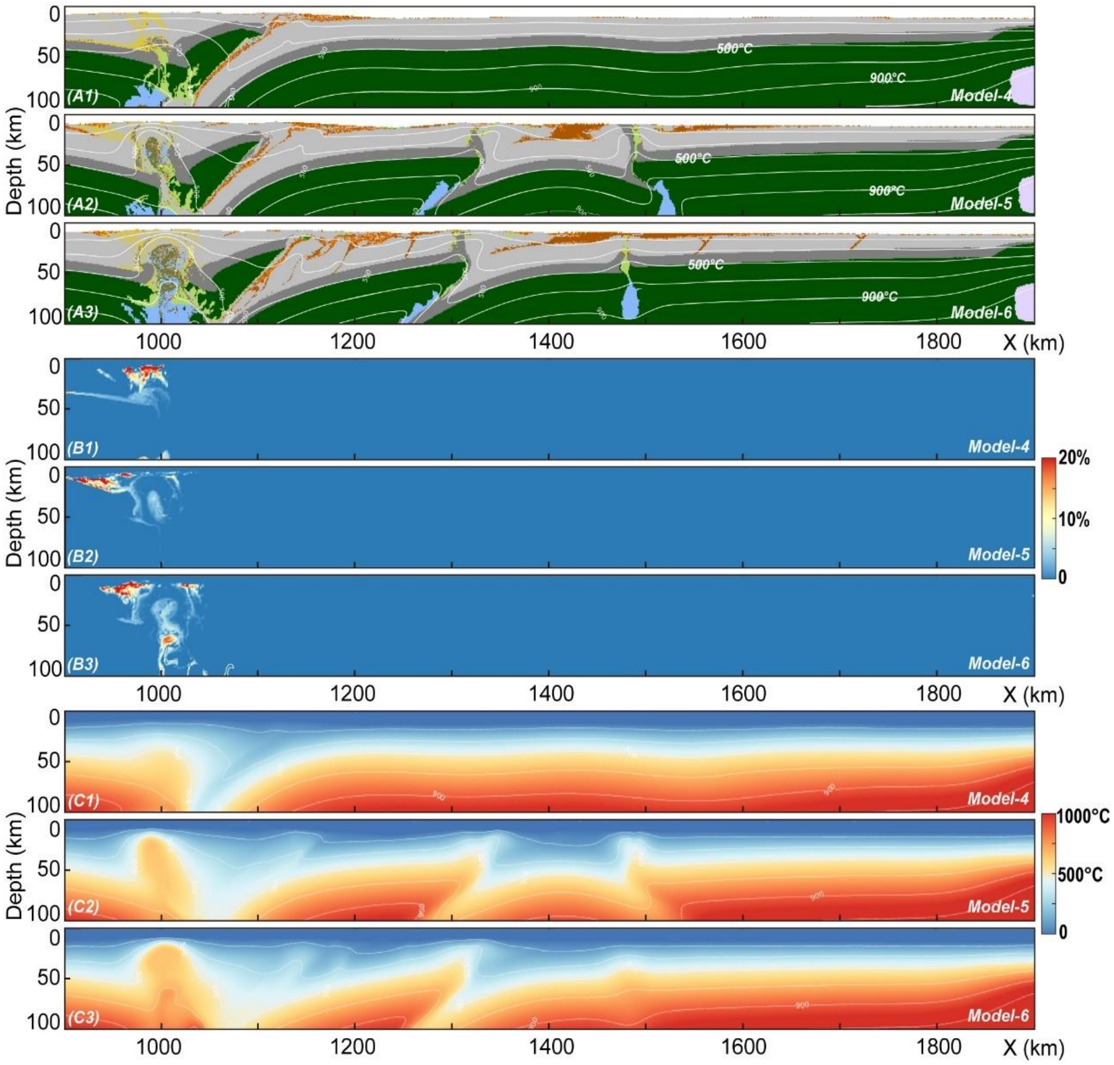

Figure 6.13. *Results of numerical experiments Model-4, Model-5 and Model-6, showing the material fields (A), degree of melting (B) and temperature (C) within the Cathaysia Block at 25Myr since the southward subduction of the Paleo-Tethys Ocean.*

At 25 Myr, extensive partial melting and associated magmatism developed within the overriding Indochina Block due to the subduction of the continental plate and the upwelling of the hydrated mantle (Figs. 6.13A and B). However, magmatism was absent in the subducted Cathaysia Block, and the exhumation of the subducted material along the subduction channel (Fig. 6.13A). It is noteworthy that the bending of the subducted Cathaysia Block developed in Model-4, while the large-scale intracontinental subduction occurred in Model-5 and Model-6 due to the presence of the boundary faults which represent weak zones with respect to the rigid plate (Figs. 6.13A2 and A3). In addition to high thermal anomalies within the overring Indochina Block, the temperature field showed slightly disturbances of the subducted Cathaysia Block, probably resulting from the bending of the rigid lithosphere (Fig. 6.13C1). Furthermore, the intracontinental subduction also exerted significant influence on the temperature distribution (Figs. 6.13C2 and C3).

Similar to magmatism, significant deformation was developed within the overriding Indochina Block, characterized by low viscosity, high strain rate and high strain accumulation (Fig. 6.14). Compared to Model-4, which employed a homogeneous lithosphere without pre-existing structures, Model-5 and Model-6 exhibited more extensive regions with low viscosity, high strain rate and high accumulated strain along these pre-existing structures (Fig. 6.14). Consequently, the Cathaysia Block displayed greater lateral heterogeneity. Compared to the first set experiments involving the northward subduction of the Paleo-Tethys Ocean, the southward subduction polarity and the subsequent intracontinental subduction produced more and widespread deformation in the Cathaysia Block, due to the occurrence of the intracontinental subduction. The strain rate and accumulated strain indicated that numerous compressive structures were developed in the collisional zones to the inland of the Cathaysia Block (Figs. 6.14B2 and C2). In addition to the boundary faults, the presence of more intra-crustal faults facilitated the deformation within the inland (Figs. 6.14B3 and C3).

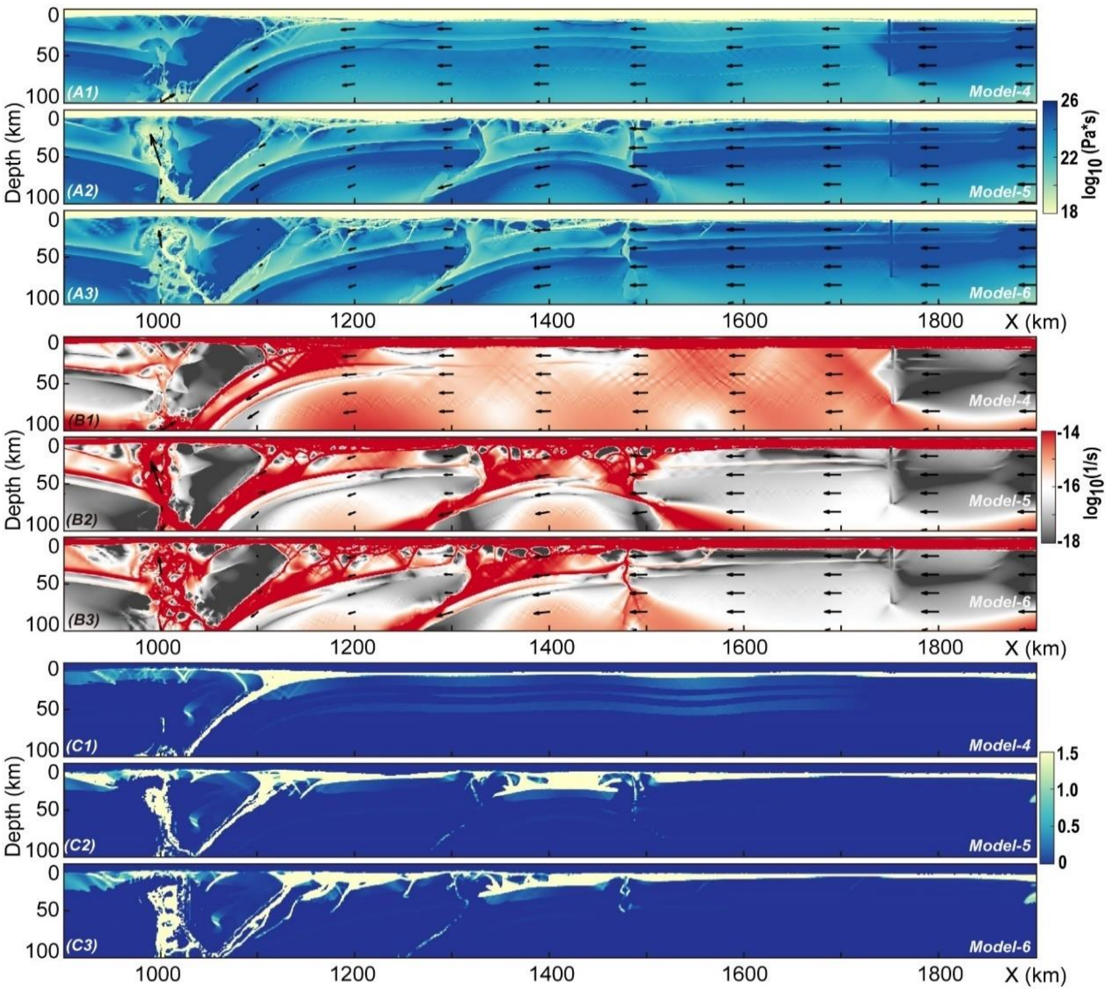

Figure 6.14. *Results of numerical experiments Model-4, Model-5 and Model-6, showing the viscosity (A), second invariant of strain rate (B) and accumulated strain (C) within the Cathaysia Block at 25Myr since the northward subduction of the Paleo-Tethys Ocean.*

The temperature evolution revealed a similar thermal structure of the Cathaysia Block with respect to the northward subduction polarity (Fig. 6.15). The Cathaysia Block exhibited a stable lateral thermal structure in Model-4, with no high-temperature regions near the collisional zone (Fig. 6.15A). In contrast, the temperature distribution in Model-5 and Model-6 at the same depth showed different characteristics. The presence of the boundary faults resulted in lateral discontinuities and generated high temperature anomalies, which became especially pronounced after continental collision (Figs. 6.15B and C). However, different from the northward subduction scenario, the intra-crustal faults caused negligible thermal disturbances within the Cathaysia Block

(Figs. 6.15B and C). The highest temperature occurred in the overriding plate rather than the Cathaysia Block.

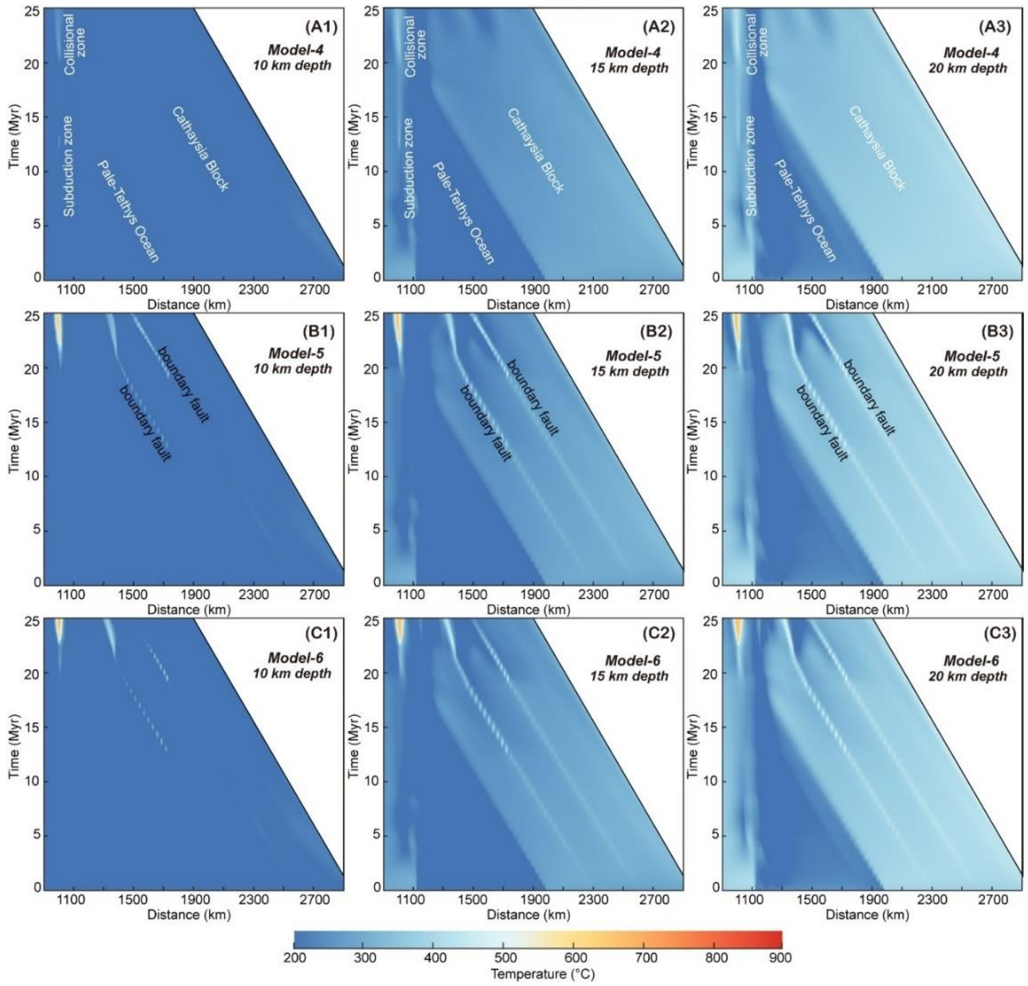

Figure 6.15. *The temperature evolutions of Cathaysia Block at the depths of 10km, 15km and 20km in numerical experiments Model-4, Model-5 and Model-6.*

6.4 Implications on the Early Mesozoic geodynamic setting of the Cathaysia Block

Numerical modelling demonstrates that the Paleo-Tethys subduction and the collision between the Indochina and Cathaysia blocks can lead to the northward heterogeneous response within the Cathaysia Block. This response is characterized by the high strain rate and significant strain accumulation adjacent to the collisional orogen, which decreased landward into the interior of the Cathaysia Block (Figs. 6.7, 6.9, 6.12 and 6.14). A similar lateral heterogeneity was observed in partial melting and thermal structures within the northward subduction models (Fig. 6.8). These geodynamic modelling results were consistent with the geological observations within the Cathaysia Block, including (1) a northward decrease deformation intensity and metamorphic grade from the Yunkai to Nanling massifs (as discussed in Sections 5.2 and 5.3), and (2) a northward decrease in temperature with the highest records in the Yunkai Massif (Fig. 5.17). These findings provided critical constraints on the geodynamic setting of the Cathaysia Block during the Early Mesozoic. They supported a driving force from the Indosinian collision rather than the subduction of the Paleo-Pacific Ocean, the latter would result in a nearly E-W-striking lateral heterogeneity which was homogenous parallel to the Paleo-Pacific subducted belt approximately in the N-S direction.

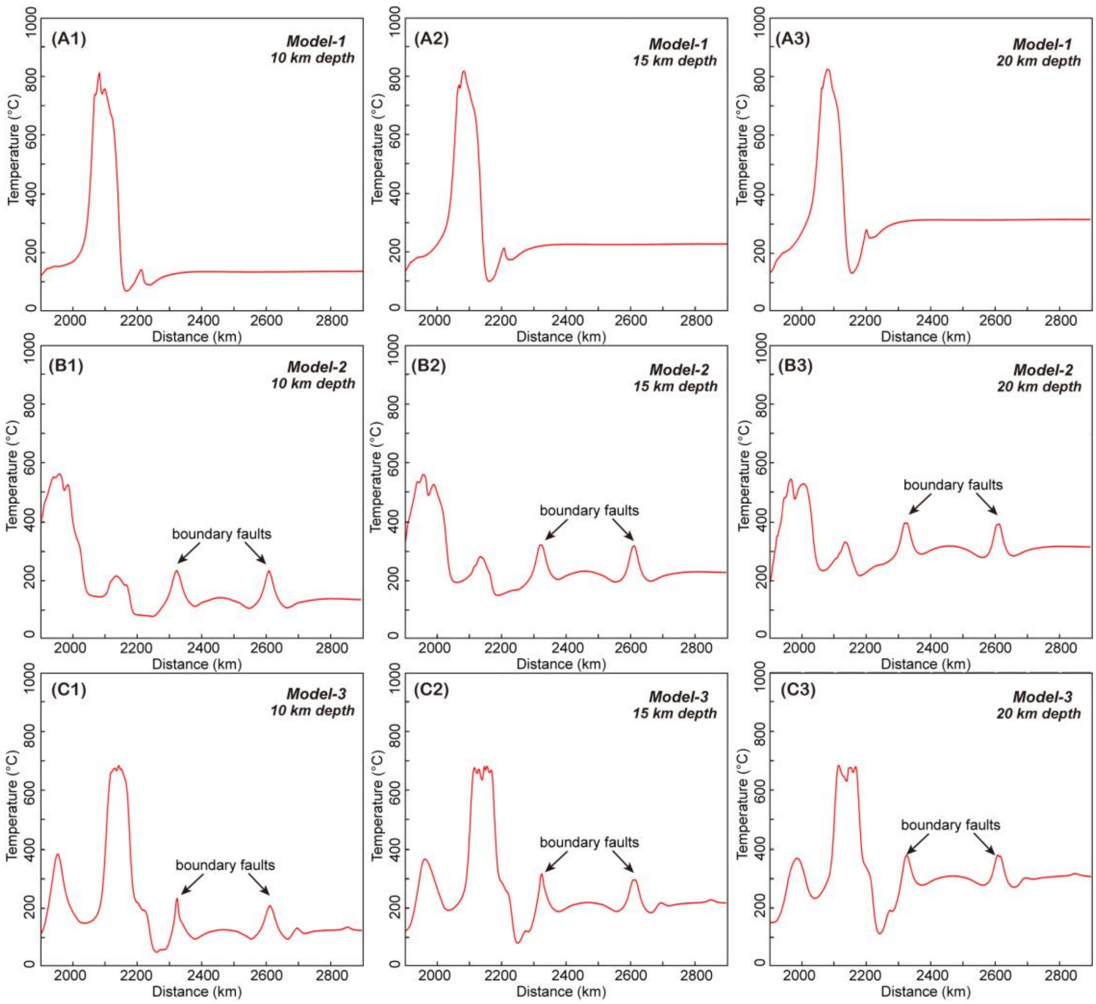

Figure 6.16. *Distribution of maximum temperature within the Cathaysia Block at 25 Myr from the numerical experiments Model-1, Model-2 and Model-3 simulating the northward subduction of the Paleo-Tethys Ocean.*

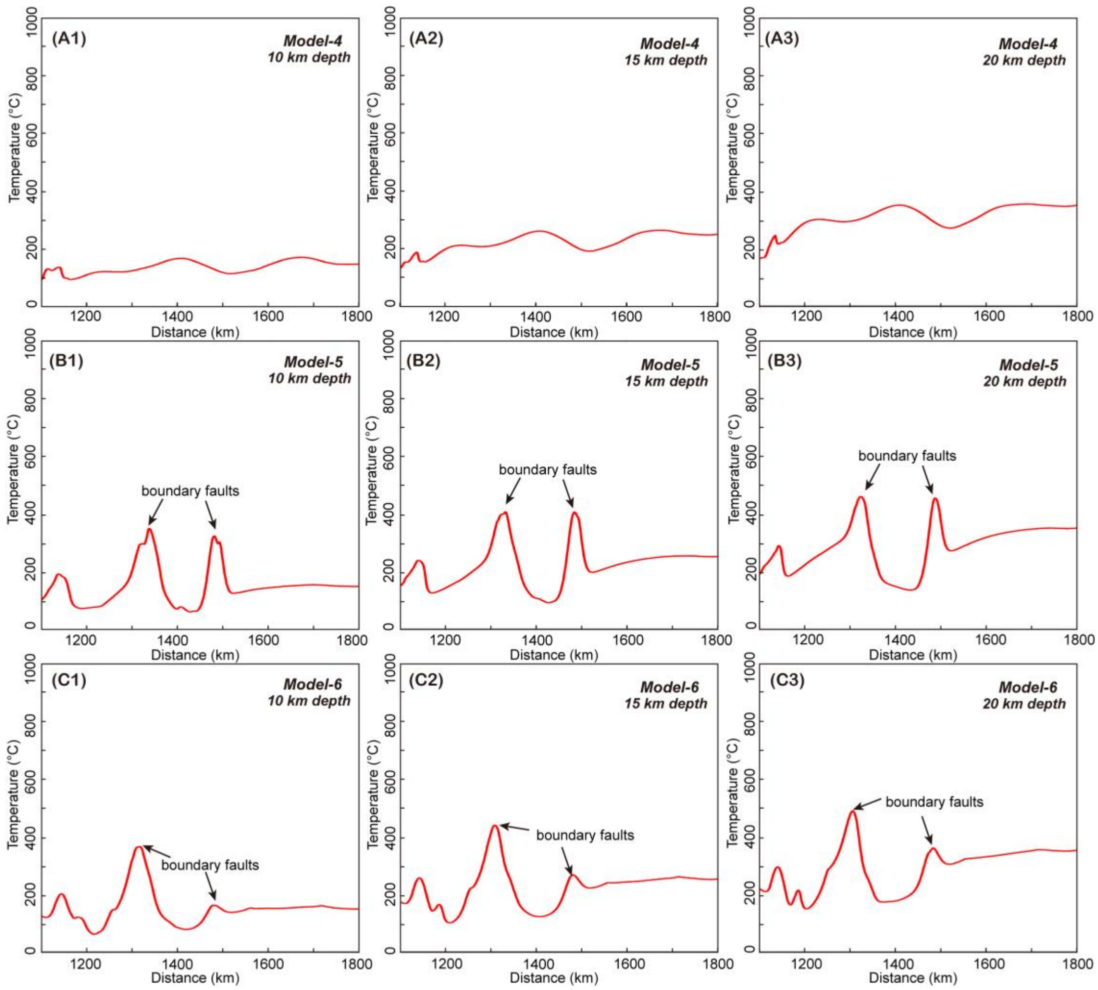

Figure 6.17. *Distribution of maximum temperature within the Cathaysia Block at 25 Myr from the numerical experiments Model-4, Model-5 and Model-6 simulating the southward subduction of the Paleo-Tethys Ocean.*

The numerical modelling revealed that the northward subduction could lead to the inland propagation of deformation within the Cathaysia Block, whereas southward subduction resulted in a broader deformation belt within the intracontinental subduction zone, without a significant inland propagation process (Fig. 6.14). However, the intracontinental subduction striking in East/West did not occur in the Cathaysia Block. In addition, the temperature field within the Cathaysia Block simulated by the northward subduction model was more consistent with the observed RSCM temperature results with respect to that from the southward subduction model (Figs. 6.16 and 6.17). The latter exhibited greater thermal disturbances within the interior of the Cathaysia Block and did not reproduce the high temperatures adjacent to the collisional orogen (Figs. 6.15 and 6.17). Furthermore, neither partial melting nor magmatism was observed within the Cathaysia Block in the southward subduction model, which failed to account for the magmatic activity observed northeast of the suture zone and those within the Cathaysia Block. Therefore, the northward subduction of the Paleo-Tethys Ocean appears to be a possibility. Nevertheless, the southward subduction cannot be ignored, as suggested by magmatic and structural evidence within the Indochina Block. It would be valuable to conduct further numerical experiments, such as bidirectional subduction, to better understand these processes and provide more constraint on the subduction of the Paleo-Tethys Ocean.

6.5 Effect of the pre-existing structures

Three distinct scenarios were designed in the numerical experiments to evaluate the influence of pre-existing structures, i.e., one homogeneous Cathaysia Block, one with boundary faults only and another one with both boundary and intra-crustal faults. The results revealed that these pre-existing structures significantly influenced the stress propagation, controlling strain localization and lateral thermal heterogeneity. Despite the deformation was predominantly concentrated in the subduction and collisional zones, the pre-existing structures modified the local viscosity of the lithosphere (Figs. 6.9A and 6.12A) and led to strain localization (Figs. 6.9B, 6.9C, 6.12B and 6.12C). This explains why strata close to the boundaries of the Wuyi Massif (e.g., east of the Ganjiang Fault and west of the Zhenghe-Dapu Fault) exhibited intense ductile deformation as discussed in Section 5.2.3. The reactivation of large-scale pre-existing boundary belts could accumulate more strain and lead to the intracontinental subduction (Fig. 6.13A). A representative example is the Xuefengshan structural belt (Chu Y et al., 2020), which is an intracontinental subduction belt in response to the closure of the Paleo-Tethys Ocean in the Songpan-Ganzi region. Meanwhile, pre-existing smaller-scale intra-crustal faults facilitated more widespread deformation (Figs. 6.9 and 6.12), as exemplified by the Yunkai Massif. In contrast, areas lacking pre-existing structures were characterized primarily by the bending of the rigid lithosphere.

The pre-existing structures also have a significant influence on magmatic activities. They acted as crucial conduits for upward and lateral melt migration (Figs. 6.8A and B), which widened magmatic distribution and further weakened the crust and facilitated deformation. This resulted in a high temperature adjacent to the collisional zone (Figs. 6.10 and 6.16). Moreover, strain localization along the boundary faults generated shear heating, while the pre-existing structures acted as conduits for the upward transporting of the deep heat. This resulted in the high temperature along the boundary faults (Figs. 6.10, 6.15, 6.16 and 6.17), which aligns with the high RSCM temperature observed along the Ganjiang Fault (Fig. 5.17).

In summary, the large-scale boundary faults defined the first-order tectonic framework and deformation pattern, whereas the numerous small-scale intra-crustal faults complicated the deformed pattern at the local regions. The geological responses of the Cathaysia Block were strongly influenced by the pre-existing structures, which were reactivated during the Indosinian collision. Furthermore, the high strain rate belts, high thermal anomaly and partial melting zones, particularly those at the intersections of different pre-existing structures, were the most favorable sites for the activation, migration and precipitation of metal elements, which were considered as the primary zones with high mineral potential.

6.6 Summary

The new modelling results in this thesis, integrated with geological observations, led to the following conclusions:

(1) The geological evolution of the Cathaysia Block was predominantly driven by the collision between the Indochina and Cathaysia blocks, which controlled the deformation pattern and thermal structure of the Cathaysia Block.

(2) The numerical experiments present a tentative possibility of the northward subduction of the Paleo-Tethys Ocean, which awaits additional experiments to verify.

(3) The pre-existing structure reactivated during the Indosinian Orogeny was the

key factor controlling strain localization and the development of thermal anomalies, having an important influence on the lateral heterogeneity within the Cathaysia Block.

Chapter 7. Discussion

The Early Mesozoic is a crucial period in the geological evolution of the SCB, characterized by extensive magmatic activity, deformation and metamorphism with significant tectonic reworking (as discussed in Chapters 2, 4 and 5). Aiming to address the relationship between magmatism and high-temperature metamorphism, clarify the lithospheric rheological behavior across the massifs in the Cathaysia Block, reconstruct the Early Mesozoic tectonic evolution and develop a more consistent tectonic model, this chapter will focus on discussing several key aspects:

7.1 Relationships between the Early Mesozoic magmatism and high-temperature metamorphism in the Yunkai Massif

The migmatites produced from high-temperature metamorphism and the granites serve as important records of the deep Earth's crust. It is crucial to clarify the mechanisms of partial melting and the relationship between migmatites and granites, in order to reveal the origin of migmatites and understand the crustal rheological behavior during this orogenic process.

Several mechanisms can cause the partial melting in an orogen by affecting the temperature, pressure and water activity: (1) accumulation of the heating produced by the radioactive elements (e.g., U, Th, K) in the thickened orogenic crust (Vanderhaeghe O and Teyssier C, 2001; Bea F, 2012; Chen L et al., 2019), (2) heating from the hot mantle due to the delamination of the lithospheric mantle or the roll-back of the subducted slab (Ueda K et al., 2012; Karsli O et al., 2018; Zhang HJ et al., 2023), (3) underplating of the hot basaltic magma such as mantle plume (Voshage H et al., 1990; Hao LL et al., 2016), (4) shear-heating during the rock deformation (Nabelek PI et al., 2010; Tumarkina E et al., 2011; Devès MH et al., 2014; Spang A et al., 2024), (5) decompression melting during the exhumation process (Harris N and Massey J, 1994; Carson CJ et al., 1997; Whitney DL et al., 2004), (6) influx of the water (Sawyer EW, 2010; Weinberg RF and Hasalová P, 2015; Collins WJ et al., 2016).

The migmatites in the Yunkai Massif were likely formed in a thickened orogenic crust. Firstly, there is no evidence to support the mechanism of underplating of the basaltic magma, due to no Triassic basaltic magma activities being traced up to now. Besides, the outer zone of the Permian Emeishan mantle plume (Xu YG et al., 2001, 2007; Lo CH et al., 2002) was more than 600 km far away to the west of the Yunkai Massif. Secondly, shearing heating can be precluded because the migmatites do not display significant localized distribution along the shear zone. The Paleo-Tethys Ocean was subducted southward beneath the Indochina Block at ~310−250 Ma (Cocks LRM and Torsvik TH, 2013; Faure M et al., 2016a; Li YJ et al., 2016; Wang HN et al., 2022; Wang Y et al., 2022; Zhang HC et al., 2023; Lin W et al., 2024). Despite the northward subduction being proposed in the recent studies, however, the ocean experienced scissor-like closure before approximately 240 Ma (Li YJ et al., 2016; Xia XP et al., 2020; Xiang ZJ et al., 2022; Huang WM et al., 2023; Shi WJ et al., 2023; Zhu X et al., 2025) and the collision occurred during ~258−240Ma (Carter et al., 2001; Faure M et al., 2016a; Li YJ et al., 2016; Wang YJ et al., 2018; Gao W et al., 2022; Wang HN et al., 2022; Wang Y et al., 2022; Lin W et al., 2024). Thus, the migmatites at 241−238Ma were unlikely to originate from the partial melting caused by the roll-back of the subducted slab of the Paleo-Tethys Ocean. Although the existence of the Paleo-Pacific Plate and its initial subduction beneath the SCB during the Early Mesozoic cannot be fully precluded, the roll-back of the subducted Paleo-Pacific slab was not supported by the following evidences: (1) The observation of the NE-SW stretching contradicts a trench-directed (i.e., NW-SE) extension associated with a hypothetical roll-back of the Paleo-Pacific slab; (2) Unlike the Jurassic higher Nd isotopes (mostly from -4 to 6), Triassic magmatism in the SCB has low Nd isotopes (mostly from -14 to -4; Gao P et al., 2017; Xu F et al., 2022), suggesting rare mantle component input; (3) The magmatic quiescence from 210 Ma to 180 Ma (Zhou XM et al., 2006; Wang YJ et al., 2013; Jiang XY et al., 2015; Liu JX et al., 2020) indicate a tectonic transition from the Paleo-Tethys regime to the Paleo-Pacific regime. The hypothesis of the delamination of the lithosphere and mantle upwelling was also not supported by the enriched Nd isotopes (Gao P et al., 2017; Xu F et al., 2022). The partial melting of the middle–lower crustal rocks can be induced by the fluid-absent dehydration reaction of the hydrous minerals (e.g., muscovite, biotite and hornblende) or the influx of aqueous fluid (Breton NL and Thompson AB, 1988; Brown M, 2013). They can be distinguished based on the existence of anhydrous peritectic minerals (e.g., garnet or pyroxene; Brown M, 2013). Petrological studies revealed that there are garnets in the migmatites in the Yunkai Massif and the mineral inclusions of biotite, plagioclase and quartz were developed in the garnet (Figs. 4.11B-C and E-F). Furthermore, the biotite shows harbor-like shapes, sometimes its inclusions were trapped in the plagioclase and quartz in the matrix of the leucosomes. According to the pseudosection, the migmatites were produced at a high temperature (~800 ℃) and the muscovite was absent (Fig. 4.18B), precluding the possibility of influx of the water. The presence of water would decrease the temperature of the solidus. The process was more likely that the hydrous minerals (e.g., muscovite, biotite) broke down and transformed into anhydrous peritectic minerals (e.g., garnet). Additionally, there is only limited fluid fluxed melting due to the low permeability and water content of the middle-lower crustal rocks (Yardley BWD, 2009). Thus, the migmatites in the Yunkai Massif were more likely related to crustal thickening during the Early Mesozoic.

Based on the field investigation, the migmatites show the characteristics of in-situ syn-deformational partial melting proposed by Calderón M et al. (2007) and Tibaldi AM et al. (2019). The low-grade metatexite had discontinuously dotted distributed melts (Fig. 4.5C) and they gradually exhibited continuous banded distribution with the increasing proportion of the melts (Fig. 4.5D). These melts were then extracted along the veins or dykes which crosscut the schistosity (Figs. 4.7B and G). These suggest an in-situ formation and aggregation of the melts. In addition, the extensively developed leucosomes are concordant with the schistosity showing similar deformation rates as the adjacent host rocks (Fig. 4.7A). The S1 foliation was developed in all observed migmatites, the layering of the migmatites is parallel to the S1 foliation at the same time (Figs. 4.5C-D and 4.6A-C). Thus, the migmatites were formed by the in-situ partial melting during the syn-deformation process.

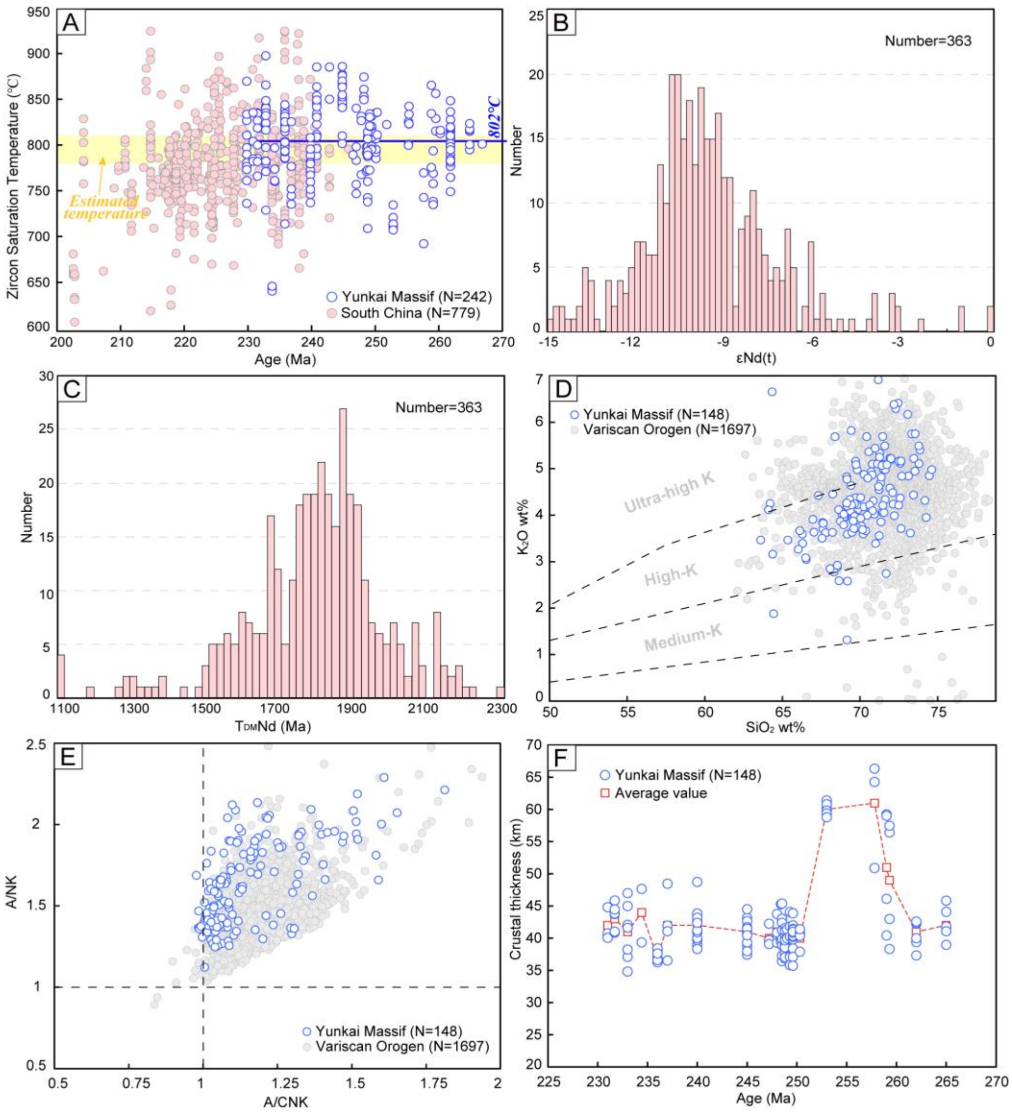

Figure 7.1. *(A) Zircon saturation temperature calculated from the granites in the Yunkai Massif and South China. The blue line is the average temperature from the granites of the Yunkai Massif. The light-yellow block represents the estimated temperature of the P-T pseudosection. (B-C) The Nd isotope and Nd model age of the granitoids in South China. (D-E) K_2O-SiO_2 and A/NCK-A/CNK diagrams of granitoids in the Yunkai Massif. The data of South China and Variscan Orogen are adopted from Gao P et al. (2017) and Jacob JB et al. (2021), respectively. (F) Calculated crustal thickness of the Yunkai Massif.*

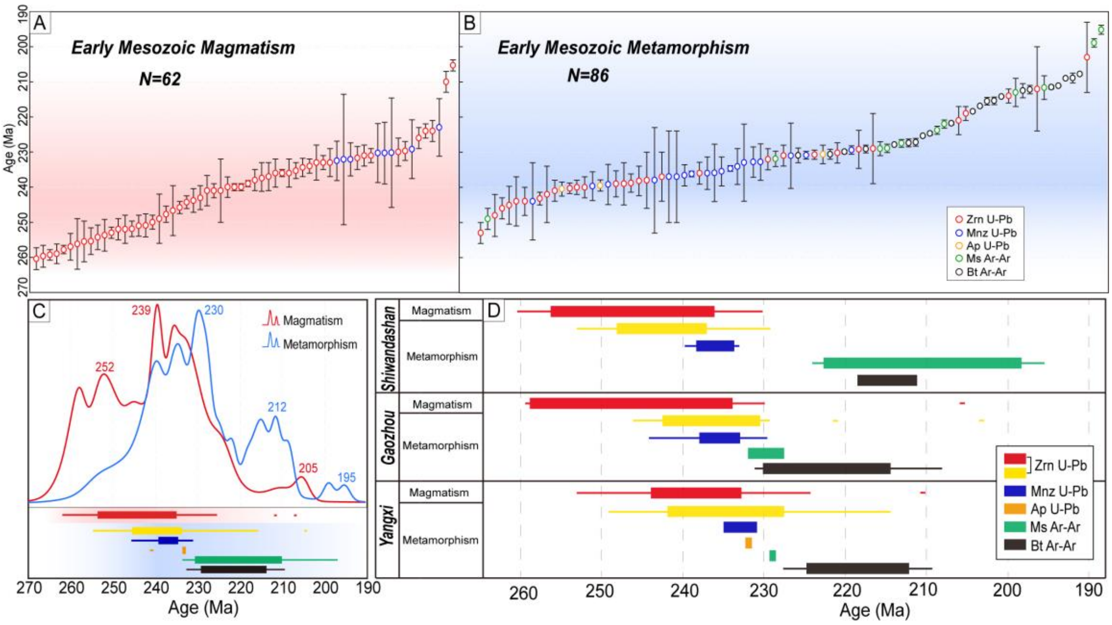

Figure 7.2. *(A-C) Relative probability plots and ages of Early Mesozoic magmatism and metamorphism in the Yunkai Massif. (D) The evolution of the Early Mesozoic magmatism and metamorphism at Shiwandashan, Gaozhou and Yangxi, respectively. Detailed data can be found in Appendix Table S1.*

It is commonly thought that the extracted granitic melts from the migmatite domes can migrate and accumulate, eventually forming larger granitic bodies intruding into surrounding rocks (Brown M, 1994; Moyen JF et al., 2021). This model is supported by the observations in the field: (1) melts extracted from the migmatites migrate upward and crosscut the S1 foliations (Fig. 4.7B) and (2) plenty of pegmatite dykes crosscut or parallel to the S1 foliation. It is undeniable that they formed the migmatitic granites related to the migmatite dome. However, the relationship between these migmatites and regional large number of peraluminous granites can help to decipher the origin of migmatites, rather than migmatitic granites. Considering that (1) granitic intrusions in Cathaysia volumetrically far exceed the high-grade metamorphic rocks and migmatites, however, the maximum melting fraction of migmatites will not exceed 70% (Chen Z et al., 2017), (2) granites, migmatites and high-grade metamorphic rocks were spatially associated distributed, and the high-grade metamorphic rocks and migmatites were always distributed next to the large granitic intrusions (Shu LS et al., 2015, 2021),

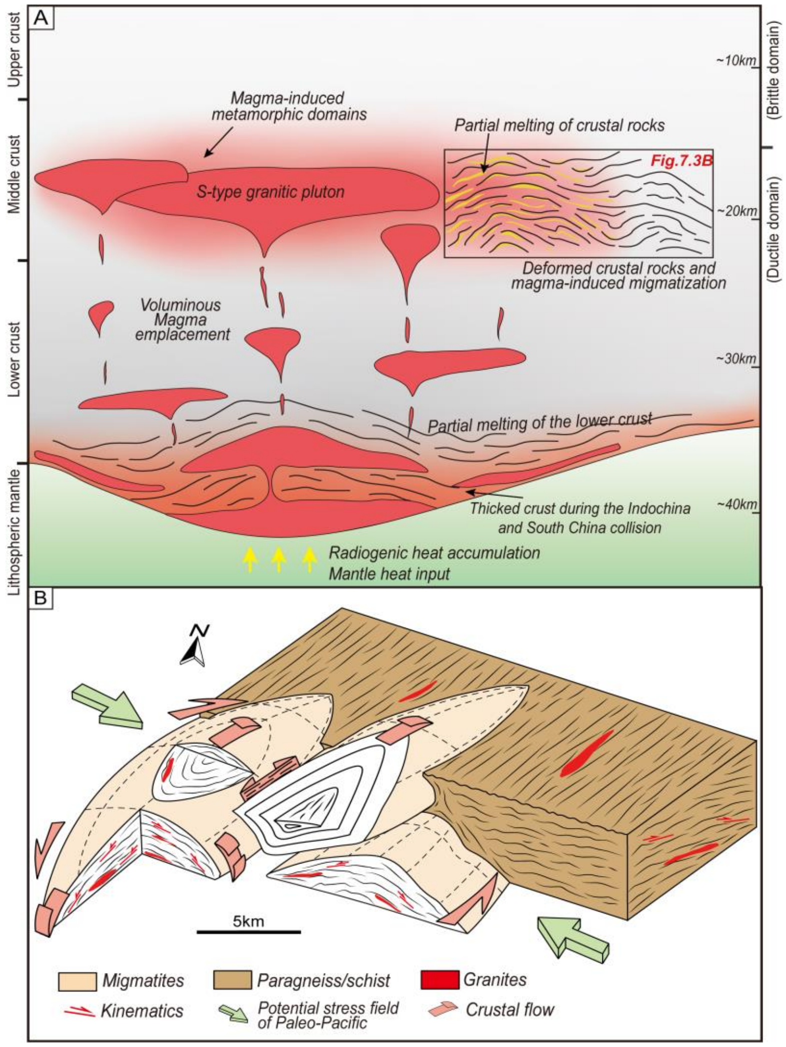

Figure 7.3. *Tentative model for the migmatization and strain partitioning of the dome.*

(3) the granites were intrusive contact with the migmatites rather than the successive transition (Fig. 4.5B), (4) besides S-type granite, there is a small amount of I-type and A-type granites which were not derived from the partial melting of the supracrustal rocks (Cai Y et al., 2015; Cai DW et al., 2017; Gao P et al., 2017; Qing L et al., 2020b; Xu J et al., 2020), (5) the temperature of the magmatism is ~800 °C closing to the upper limit of the migmatite temperature estimated from the P-T pseudosection (Fig. 7.1A), (6) the granites exhibit more complex sources based on the Nd isotope, Nd model age and O isotope (Figs. 7.1B-C; Gao P et al., 2017), (7) the granites have similar K_2O but relatively lower Al_2O_3 with respect to those in the Variscan belt produced from the gneiss dome (Fig. 7.1D-E), (8) the ~10 Ma differences revealed by the complied age data between the high-temperature magmatism (ca. 252−234 Ma) and the

metamorphism (ca. 244−232 Ma) in the Yunkai Massif (Fig. 7.2), thus we tentatively propose a new model (Fig. 7.3).

The large volumes of regional peraluminous granites are likely responsible for the local high-temperature metamorphism and migmatization. The partial melting that occurred in the thickened lower crust generated extensive peraluminous melts on a regional scale. The upward migration and emplacement of these melts at mid-crustal levels led to the formation of granitic plutons, triggering additional partial melting and high-temperature metamorphism. This magma-induced partial melting and high-temperature metamorphism significantly reduced crustal strength and facilitated strain localization. Ultimately, a NE–SW-trending mid-crustal flow developed in the weakened crust under the regional stress regime.

7.2 Relationships between the Early Mesozoic thermal state and deformation-metamorphism in the Cathaysia Block

The deformation and metamorphism records represent products of thermo-mechanical coupling within the continental crust. Although Early Mesozoic tectonic-thermal events have been extensively studied and are widely recognized (Xu XS et al., 2005; Li ZX and Li XH, 2007; Wang YJ et al., 2007a, 2013; Yu JH et al., 2007; Lin W et al., 2008; Zhang GW et al., 2013; Shu LS et al., 2015, 2021; Faure M et al., 2016b; Li JH et al., 2017a; Cochelin B et al., 2022), the mechanisms by which the crustal thermal state governed deformation and metamorphic responses within the Cathaysia Block were not addressed. Bridging the thermal parameters (e.g., paleotemperature and geothermal gradients) and mechanical behaviors (e.g., deformation and metamorphism) is essential to provide critical insights into the rheological properties of the lithosphere and to elucidate the driving mechanisms behind orogenic processes.

Taking the RSCM temperature as well as the metamorphic P-T data at the southmost of the Yunkai Massif into consideration, the temperature in the Yunkai Massif exhibits a northward decrease from >700 °C at the southmost coastal area to ~350 °C at the Wuzhou-Sihui Buried Fault at its northern part (Fig. 5.17A). The Nanling

Massif presents a relatively low and stable temperature of ~300 °C, while the Wuyi Massif shows a higher, but, also stable temperature close to ~400 °C (Fig. 5.17). The temperature variations among these three massifs are not strongly correlated with stratigraphic differences but are instead predominantly associated with their spatial locations, which exhibit strong correlation with the deformation and metamorphism.

In the southmost part of the Yunkai Massif, the migmatites yielded a temperature of 630–705 °C (Zhang JH et al., 2017), and even up to ~800 °C based on the P-T pseudosection calculations (as discussed in Section 4.5). Additionally, the Ti-in-biotite and monazite from gneiss revealed a temperature of 580–700 °C (Wang XD et al., 2020). The average RSCM temperature is ~509±54 °C, agreeing with the deformation temperature (>500 °C) given by quartz dynamic recrystallization (Figs. 5.17A and 7.4A-1) and quartz preferred orientation (Wang YJ et al., 2007a, 2021). Meanwhile, the intense deformation and high-temperature metamorphism are exposed in the same region, represented by the mylonites, migmatites and augen granitic gneiss (Figs. 5.4A-C and 5.12A). To the north of the Yunkai Massif, the RSCM temperature decreases to ~376 °C, consistent with the deformation temperature of quartz of 300–400 °C (Fig. 5.17A), where is characterized by the low-grade metamorphosed slate and meta-siltstone (Fig. 5.4F) and weak deformation with schistosity or slaty. The RSCM temperatures of the Nanling (~304 °C) and Wuyi (~383 °C) massifs are also consistent with the dynamic recrystallization temperatures of quartz, which are 200–400 °C in the Nanling Massif and 300–400 °C in the Wuyi Massif, respectively (Fig. 5.17). Accordingly, the Nanling and Wuyi massifs were dominated by the non-metamorphosed conglomerate, sandstone and limestone, and the low-grade metamorphic slate and meta-siltstone, along with the brittle-domain folds and faults (as discussed in Sections 5.2 and 5.3). It is noted that some regions with relatively low temperatures are coupled well with the unmetamorphosed Late Paleozoic basins (e.g., Yangchun Basin and Yong'an Basin) and depressions (e.g., Guiyang-Leiyang depression; Figs. 5.15 and 5.18). Similarly, the paleo-thermal gradients also consist

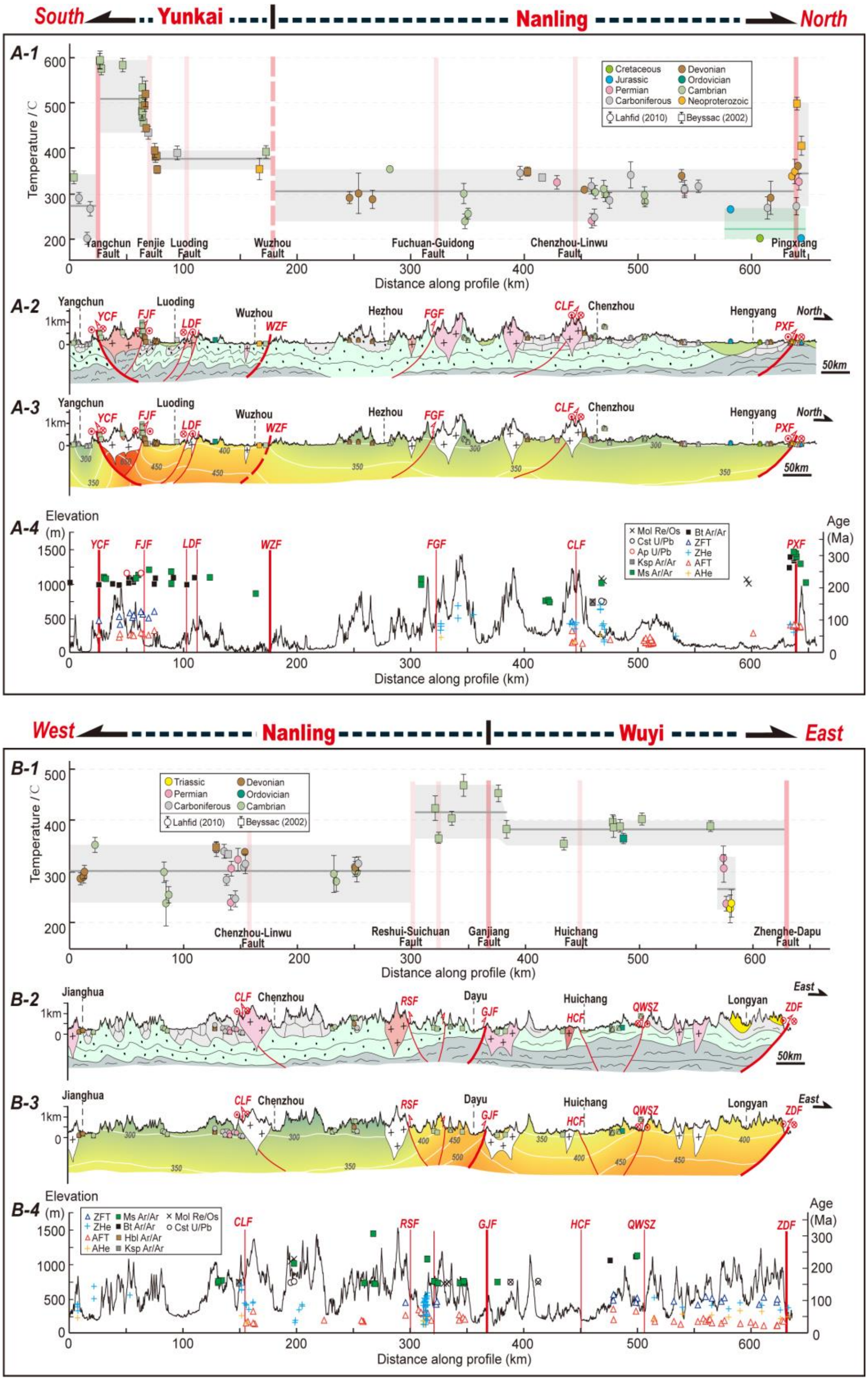

Figure 7.4. Comparative illustration of temperature spatial variation, structural style, thermal state, topographic and geochronological data of the Yunkai-Nanling cross-section (A) and the Nanling-Wuyi cross-section (B).

with deformation and metamorphism. The highest gradients occurred in the Yunkai Massif (~40−75 °C/km), and it decreased to the north with the lowest one in the center of the Nanling Massif (~21 °C/km). Then, there is an eastward increase from the Nanling Massif to Wuyi Massif (~47−52 °C/km; Figs. 5.26 and 7.4).

In summary, the temperatures and paleo-thermal gradients, which systematically decrease from the Yunkai to Nanling massifs and slightly increase from the Nanling to Wuyi massifs, fit well with the variation of deformation intensity and metamorphic grade observed in the field (Fig. 7.4). This consistency is attributed to the fact that the thermal state governs mechanical behavior. High thermal gradients and temperatures soften the rock and significantly reduce the strength of the continental crust by changing mineral deformation mechanisms, promoting ductile flow over brittle fracture, and inducing high-temperature metamorphism and partial melting (Lejeune A-M and Richet P, 1995; Rosenberg CL and Handy MR, 2005). As a result, the large-scale ductile shear bands and crustal flow were developed (Fig. 7.3). That is the reason why the Yunkai Massif with high paleo-thermal gradient and paleo-temperature is easier to develop high-temperature metamorphism, ductile deformation and mid-crustal flow (as discussed in Chapters 4, 5.2 and 5.3). In contrast, the Nanling Massif, which presents a low temperature, is characterized by the deformation in brittle domains and lower-greenschist-facies or non-metamorphosed rocks (as discussed in Sections 5.2 and 5.3).

Thus, the thermal state is coupled with the mechanical behavior in the Early Mesozoic Cathaysia Block, and the thermal state fundamentally controls the crustal rheological weakening, deformation, partial melting and high-temperature metamorphism. In turn, the deformation and high-temperature metamorphism reshaped the local thermal state.

7.3 Early Mesozoic crustal rheological characteristics of the Cathaysia Block

High temperature and partially molten rocks have made a significant contribution to the strength decrease of the crust. On the onset of partial melting, strength decrease can favor strain localization, while partial melting within the whole orogenic lower crust allows distributed crustal flow in the plate-scale (e.g., Rosenberg CL and Handy MR, 2005; Brown M, 2007; Groome WG et al., 2008). Though temperatures significantly decrease from the Yunkai to Nanling massifs, and slightly increase from the Nanling to Wuyi massifs, these three massifs exhibit significantly different temperature ranges from each other (Fig. 5.17). The crustal thermal and field structural investigations clearly identified three massifs with differential properties within the Cathaysia Block (Figs. 5.15, 5.17, 5.18 and 7.4). The Yunkai Massif is much hotter and more deformed with respect to the Wuyi and Nanling massifs, suggesting a rheological weakening and less rigidity (Fig. 7.5). Meanwhile, the Nanling Massif is characterized as a more rigid massif with a thin-skin structure, low paleo-temperature and low paleo-thermal gradient (Fig. 7.5).

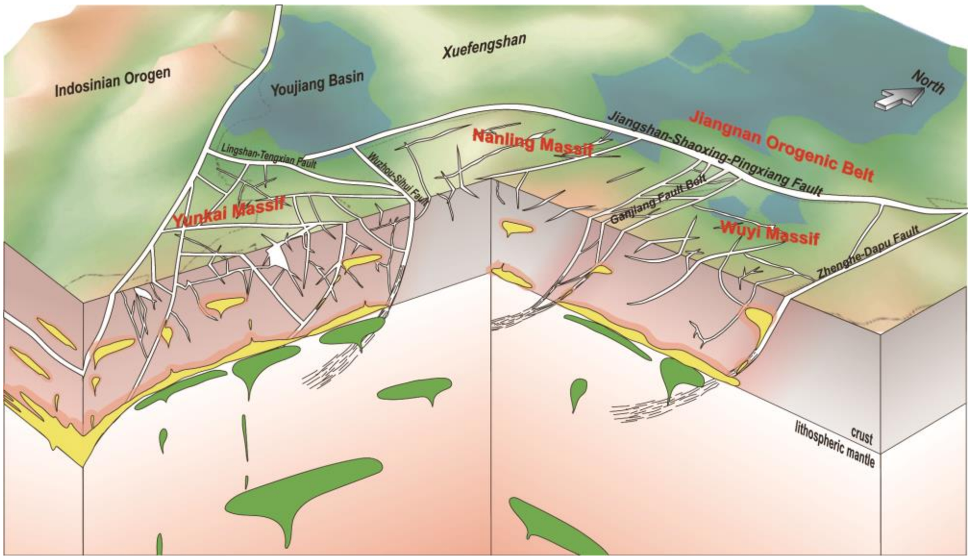

Figure 7.5. *The conceptual model illustrating multi-block properties of the Cathaysia Block and the heterogeneous thermal state and rigidity among the three massifs.*

Magmatic heat, derived from widespread magmatism within the Cathaysia Block, is an important heat source for maintaining and intensifying crustal thermal state (Annen C et al., 2006; Hilchie LJ and Jamieson RA, 2014). More Early Mesozoic intrusions in the Yunkai Massif with respect to the Wuyi and Nanling massifs, could be an important factor contributing to the thermal heterogeneity among them (Figs. 2.3 and 7.4). The properties of the multi-block in the Cathaysia Block can also be evidenced by the geophysical investigations on Lg attenuation (Shen L et al., 2023), ratio of Vp/Vs (Guo LH et al., 2019; He CS and Santosh M, 2021), and crustal anisotropy (Li MK et al., 2023; Li TZ et al., 2023), as well as the geochemical Hf isotopic mapping (Zhang ZY et al., 2023). All of them exhibit a different Yunkai Massif compared to the Wuyi and Nanling massifs. Although geophysical observations predominantly reflect the latest tectonic event, they are more or less influenced by tectonic inheritance. Lithospheric rheology and pre-existing structures are often reactivated during the subsequent tectonic events, which have a significant influence on later tectonic pattern. The similarity between the current and paleo-thermal regimes provides some evidence for this inheritance (Figs. 2.5, 5.15 and 5.18).

In addition, a pronounced temperature increase occurred near some boundary fault zones, particularly along the Ganjiang Fault Belt between the Nanling and Wuyi massifs (Figs. 5.17, 5.18 and 7.4B). This fault belt was identified as a trans-crustal fault in the magnetotelluric image (Xu S et al., 2019), hosting numerous second-order faults (Deng P et al., 2003). The extensive fault network represents the strain localization during the tectonic interaction between the relatively rigid Nanling and Wuyi massifs. They probably served as the potential conduits for the Early Mesozoic heat transfer in depth, promoting the upward migration of the heat and resulting the high thermal anomaly. In addition, multiple Jurassic tungsten-tin deposits were developed along the Ganjiang Fault Belt (Figs. 5.24 and 5.25; Yin YT et al., 2021; Zhang ZY et al., 2023). Therefore, the Ganjiang Fault Belt was probably reactivated multiple times, e.g., Early Mesozoic and Late Mesozoic. The secondary faulting network within the belt also provides conduits for the Jurassic mineralizing fluids, resulting in the clustered distribution of the Jurassic deposit in this region.

7.4 Tectonic setting of the Cathaysia Block during the Early Mesozoic

During the Early Mesozoic, the Cathaysia Block was surrounded by several blocks and involved in a tectonic transition from the Paleo-Tethys to Paleo-Pacific domains (Fig. 7.6; Wang YJ et al., 2013, 2021; Huang BC et al., 2018; Zhao GC et al., 2018; Li

CL et al., 2021; Shu LS et al., 2021; Xu XB, 2023). This complexity makes the debate on discussion of the tectonic regime of the Cathaysia Block still active.

As discussed in Section 7.1, the presence of migmatites implies in a crustal thickening setting. Considering the proposed geodynamics contexts of the Early Mesozoic Cathaysia Block, i.e., the Paleo-Pacific subduction (Li ZX and Li XH, 2007; Li ZX et al., 2012; Li CL et al., 2021; Cochelin B et al., 2022; Xu F et al., 2022), and Paleo-Tethys subduction and subsequent collision (Wang YJ et al., 2007a, 2013, 2021; Lin W et al., 2008, 2024; Faure M et al., 2014, 2016a; Shu LS et al., 2015, 2021; Li Y et al., 2016) , the migmatites can be formed in (1) thickened continental arc crust of the Andean-type orogenic plateau related to the advanced subduction of the Paleo-Pacific Ocean or (2) thickened crust of the collision orogen related to the ICB - SCB collision.

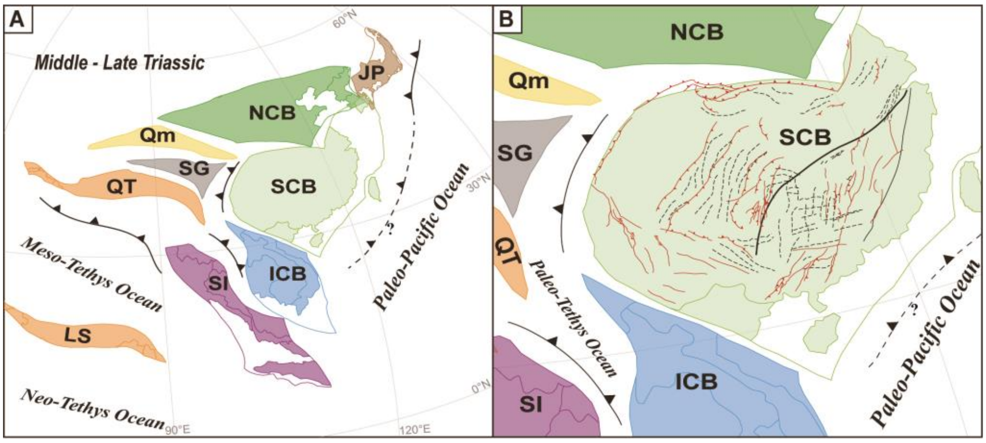

Figure 7.6. *(A) The Middle–Late Triassic construction maps of South China and its adjacent plates (modified after Scotese C, 2016). (B) The Middle–Late Triassic structures (faults and folds) within the South China Block respond to the interaction between the adjacent plates. Abbreviation: ICB-Indochina, JP-Japan, NCB-North China, Qm-Qaidam, QT-Qiangtang, SCB-South China, SG-Songpan-Ganzi, SI-Sibumasu.*

Some researchers proposed that the Early Mesozoic geodynamic driving force of magmatism, deformation and metamorphism in the Cathaysia Block is probably attributed to the subduction of the Paleo-Pacific Ocean. This opinion is argued by (1) the northwestward younging trend of the magmatism (Li ZX and Li XH, 2007) which was challenged by the latest dating results, (2) the Late Triassic (218–211 Ma) arc-type volcanic rocks found in the South China Sea (Wei W et al., 2022; Xu F et al., 2022), and (3) the deformation with the NE-SW-trending extension and NE-striking folds (Li CL et al., 2021; Cochelin B et al., 2022). Indeed, the subduction of the Paleo-Pacific Ocean can yield a NW-SE regional compressional stress field and result in the Andean-type crustal thickening. However, the Early Mesozoic advanced subduction of the Paleo-Pacific Ocean is not supported by the previous studies of that (1) the magmatism in the Cathaysia Block exhibits a planar distribution without any temporal-spatial variation and more than 90% of the magmatism is peraluminous (Sun T, 2006; Zhou XM et al., 2006; Wang YJ et al., 2013; Gao P et al., 2017; Liu JX et al., 2020), (2) lack of the Ealy Mesozoic arc-related magmatism and mantle component input in the Cathaysia Block, (3) the Suo and Akiyoshi high-pressure/low-temperature metamorphic belts in Japan occurred at the Late Triassic (ca. 200Ma; Wakita K, 2013) indicating an initial subduction of the Paleo-Pacific Ocean, (4) the earliest recorded magmatic activity related to the subduction of the Paleo-Pacific Ocean in the Cathaysia Block is in the Early – Middle Jurassic (Zhou XM et al., 2006), and (5) the northward subducted oceanic slab of Paleo-Tethys beneath the SCB and North China Block impeded the westward subduction of the Paleo-Pacific Ocean until the Late Triassic (Li SZ et al., 2025). The new RSCM results in Chapter 5 show that the Yunkai and Wuyi massifs have different temperatures and thermal gradients during the Early Mesozoic (Figs. 5.17, 5.26 and 7.4). This finding challenges the assumption of the Early Mesozoic subduction of the Paleo-Pacific Ocean as they have the same distance to the presumed subduction zone but exhibit distinct thermal states. Based on the comprehensive geochemical tracing, Mn-Zn and Pb-O-Hf isotopes and geophysical imaging, the westward subduction of the Paleo-Pacific Ocean beneath the Cathaysia Block was considered at the Early-Middle Jurassic (Xu XS et al., 2024), even later argued by the Early Cretaceous crustal shortening in both the North and South China blocks (Wei W et al., 2015, 2023; Qiu HB et al., 2023).

In contrast to the driving of the Paleo-Pacific subduction, the new findings in this thesis provide much stronger support for the Paleo-Tethys tectonic regime: (1) the deformation intensity and metamorphic grade decrease northwards from the Yunkai Massif to the Nanling Massif, (2) both the RSCM temperature and the recrystallization temperature of quartz show a northward decreasing tendency (Figs. 5.17 and 5.21), (3) the paleo-geothermal gradients decrease from the Yunkai Massif toward the center of the Nanling Massif (Fig. 5.26A), (4) NE-SW mid-crustal flow in the Yunkai Massif consistent with the Late Triassic post-collision extension in the previous studies, and (5) the crustal thickness from ~60 km to ~40 km during the Permian-Triassic supporting the collision and post-collision processes (Fig. 7.1F), (6) the numerical experiments provided evidence for the collision between the Indochina and Cathaysia blocks resulting in the lateral heterogeneity of the deformation, magmatism and thermal state from the collisional zone to the inland of the Cathaysia Block (Figs. 6.8 and 6.9).

In fact, numerous published data also suggest the Paleo-Tethys closure and the ICB-SCB collision during the Early Mesozoic: (1) the similarity of the Late Paleozoic − Early Triassic tropical Cathaysia-type floras and faunas from Eastern Peninsular Malaysia and SE Vietnam arguing for a Cathaysia-like affinities (Li XX and Wu XY, 1994; Metcalfe I, 1996; Wang YJ et al., 2024), (2) the northward transport of sediments into the hinterland of the SCB (Zhang XC et al., 2019), (3) the Early Mesozoic top-to-the-north thrust-and-fold system (Lin W et al., 2008; Faure M et al., 2016b) and WNW-trending dextral transpression deformation with the northward propagation and intensity decrease (Li JH et al., 2017a; Wang YJ et al., 2021), as well as the pull-apart basin at Shiwandashan (Ma SY et al., 2024), arguing for an oblique and diachronous collision of the SCB with the ICB, (4) an Early Mesozoic suture zone along the Ailaoshan-SongMa-SongChay-Hainan-Mindoro was identified by the arc-related, syn-collision and post-orogenic magmatism, ophiolitic mélange and related structures (Faure M et al., 2014, 2016b; Wang Y et al., 2022; Lin W et al., 2024), (5) the amphibolite-facie metamorphic complex in the northern Hainan island (Gao W et al., 2022; Hu J et al., 2022), (6) the Late Permian − Early Mesozoic large volume peraluminous granites arguing for the ICB-SCB collision and the subsequent orogenic collapse, and (7) the geochronology of the magmatism and deformation along the suture zone constrained that the collision occurred at the Early−Middle Triassic (~258−240 Ma) followed by the Late Triassic post-collision extension (e.g., Carter A et al., 2001; Wang YJ et al., 2018; Wang Y et al., 2022).

Integrating new results in this thesis and the published data, the thermal and tectonic history of the orogen can be reconstructed. During the Permian at the period of ~310−258 Ma (e.g., Carter A et al., 2001; Li YJ et al., 2016; Wang YJ et al., 2018; Wang Y et al., 2022; Lin W et al., 2024), the subduction of the Paleo-Tethys Ocean led to not only its scissor-like closure and also the collision between the ICB and the SCB at ~258−240 Ma (e.g., Faure M et al., 2014, 2016a; Li YJ et al., 2016; Wang YJ et al., 2018; Gao W et al., 2022), resulting in a crustal thickening in the Yunkai Massif up to ~60 km (Fig. 7.1F). During this process, supracrustal rocks were buried to depths deeper than 20 km, corresponding to pressures in excess of 7 kbar. Due to the accumulation of radioactive heat and mantle heat input, the thickened crust partially melted, and magma that produced by the partial melting moved up and formed granitic intrusions (Fig. 7.3A). The transition zone from ductile to brittle domain was the major mechanical barrier during the magma ascent (Vigneresse JL, 1995; Burchardt S, 2009) and made it stop at the mid-crustal depths. Both the heat accumulation of a large amount of the granitoids within the crust and the radioactive heat from the deep thickened crust, contributed to the relatively high temperature, which exceeds the solidus of deep-buried supracrustal rocks, and produced mid-crustal partial melting and dome-like migmatites at ~240 Ma (as discussed in Chapter 4).

Meanwhile, the collisions of the North China Block−SCB at ~246−220 Ma (e.g., Zhao XX and Coe RS, 1987; Rowley DB et al., 1997; Meng QR and Zhang GW, 1999; Liu DY et al., 2006; Liu FL and Liou JG, 2011) and Qiangtang Block−SCB at ~235-230 Ma (e.g., Yuan C et al., 2010; Li S et al., 2019) probably resulted in more responses within the lithosphere of the Cathaysia Block. For example, the reactivation of the

Neoproterozoic Jiangnan Orogenic Belt, and the increasing paleo-geothermal gradient from the center of the Nanling Massif to the Jiangnan Orogenic Belt (Fig. 5.26), as well as the reported high-temperature metamorphism in the northern Wuyi Massif and eastern Jiangnan Orogenic Belt (e.g., Li JH et al., 2017b). Concerning the NE-trending structures, they are probably attributed to the consumption and closure of the Paleo-Tethys Ocean located to the northwest of the SCB. The driving force propagated across the rigid Yangtze Carton and caused the NE-trending deformation at the intracontinental pre-existing weak zones, e.g., the Xuefengshan – Jiangnan Orogenic Belt and Badu areas (e.g., Wang YJ et al., 2005; Chu Y et al., 2012a, 2020; Li JH et al., 2022b; Gao WL and Wang ZX, 2024). Afterwards, the accumulated stress continues to extend into the interior of the Cathaysia Block.

The decompression from the post-collision collapse of the Indosinian Orogen at ~240−200Ma (e.g., Faure M et al., 2014; Wang Y et al., 2022; Lin W et al., 2024) facilitated the partial melting, resulting in a significant decrease of the crustal rheological strength. The presence of the Paleo-Pacific Plate to the southeast constrained the lateral extrusion of the crustal flow. Under the joint stress field, the low-viscosity middle-lower crust flowed horizontally in the NE-SW direction (Fig. 7.3B). The strain partitioning displayed different deformation patterns in different locations, that is, horizontal flow at the core of the dome and strike-slip and vertical flow at the edge (Fig. 7.3B). A rapid exhumation and cooling occurred in the southern Cathaysia Block during ~240−215 Ma (Figs. 4.30 and 5.25A). Afterwards, the evolution of the Cathaysia Block transitioned to the Paleo-Pacific tectonic regime during the period 205-180 Ma, evidenced by the magmatically inactive period (Zhou XM et al., 2006), increasing mantle input (Xu F et al., 2022), and crustal extension characterized by half-graben basin development (Shu LS et al., 2009). Influenced by the subduction of the Paleo-Pacific Ocean, the Cathaysia Block underwent three extension and exhumation processes at 150−110 Ma, 110−85 Ma and 66−38 Ma (Fig. 5.25; Wang Y et al., 2020; Wei W et al., 2023; Wu JH et al., 2023).

Chapter 8. Conclusions and Perspectives

8.1 Main conclusions

Through detailed studies on deformation, metamorphism, crustal thermal state of the Cathaysia Block during the Early Mesozoic as well as the dynamic numerical modelling, the results of this thesis reveal a significant rheological heterogeneity of the Cathaysia Block in the lithospheric scale and advance our understanding of the intracontinental tectonic responses to the deep lithospheric dynamic process. The main conclusions obtained in this thesis may be listed as follows:

(1) The Early Mesozoic widespread intracontinental magmatism within the Cathaysia induced the local high-temperature metamorphism and NE-SW mid-crustal flow. The P-T conditions of this high-temperature metamorphism in the Yunkai Massif are at 6.8−7.0 kbar and 780−810 °C, followed by a cooling and decompression retrograde stage probably at 3.2−4.2 kbar and 595−615 °C.

(2) A pronounced heterogeneity in deformation intensity and metamorphic grade was exhibited in the Cathaysia Block along both north-south and east-west directions. The Yunkai Massif exhibits the highest grade, followed by Wuyi and Nanling. The Early Mesozoic deformation was characterized by two distinct shortening directions, and the earlier E-W-trending structures were subsequently overprinted by those NE-trending structures.

(3) The Cathaysia Block cannot be considered as a rigid block during the Early Mesozoic; furthermore, it was characterized by a composite of sub-blocks with a heterogeneity in rheology. This heterogeneity is displayed in deformation, metamorphism and crustal thermal state, i.e., the Yunkai Massif exhibits a more intense deformation, a higher grade of metamorphism and a higher temperature with respect to the Wuyi and Nanling massifs.

(4) The pre-existing structural zones are important potential channels for heat transportation which exhibit thermal anomalies up to ~100 °C.

(5) The Early Mesozoic deformation, metamorphism and crustal thermal state of

the Cathaysia Block are the consequences of the geodynamic interaction among the multiple blocks during the closure of the Paleo-Tethys Ocean, and more specifically its collision with the Indochina Block along the Paleo-Tethys Belt.

8.2 Perspectives

Based on the evidence from deformation, metamorphism, RSCM temperature, geochronology and geodynamic modelling, this thesis studied Early Mesozoic magma-induced high-temperature and mid-crustal flow, crustal thermal heterogeneity and multi-block lithosphere of the Cathaysia Block. The results and findings help to understand the lithospheric rheology of the Cathaysia Block in a block scale and provide a basis for future research.

Despite these advances, some limitations and questions remain in this thesis: (1) although the new results on RSCM temperature show a good agreement with the field observation of the deformation and metamorphism, and provide a preliminary Early Mesozoic thermal architecture, it should still take cautions for their interpretations due to the absence of a homogeneous distribution of RSCM sampling in the whole Cathaysia Block preventing to propose a high-resolution profile or map; (2) the RSCM temperature will be significantly influenced by the deformation and strain, particular those samples in the faults belts or shear zones; (3) While the numerical experiments simulated both southward and northward subduction of the Paleo-Tethys Ocean, they do not constitute a verification of the bidirectional subduction model. Other important mechanisms, the breakoff of subducted slab, angle of subduction and the post-collisional orogenic collapse, were also not considered in the current models; (4) the geodynamic modelling employed a relatively simplified 2-D model and took only the subduction of the Paleo-Tethys Ocean into the consideration, that cannot reflect the lateral responses (e.g., deformation), and the complex structural overprinting of the Paleo-Tethys and Paleo-Pacific tectonic regimes, to reconstruct the Triassic – Cretaceous tectonic evolution of the Cathaysia Block which experienced the tectonic regime transition from the Paleo-Tethys to Paleo-Pacific.

Building upon the foundation of this thesis, future research can focus on the following aspects or questions:

(1) This first investigation of the paleo-thermal state in the Cathaysia Block deserves further effort to decipher its lithospheric rheology that will bring insights on structural architecture, deformation behavior, earthquake mechanism and tectonic evolution of the Cathaysia Block. The sampling needs to be homogenously distributed in the region, and the density of sampling needs to be enhanced, yielding a more precise Early Mesozoic regional thermal map of the Cathaysia Block and providing a key base for future studies. Moreover, the thermal map related to magmatism can also be restructured and the quantitative evaluation of this influence of deformation and strain is necessary in future research. All of these can help us to understand the true thermal state of the Early Mesozoic Cathaysia Block.

(2) The bidirectional subduction model for the Paleo-Tethys Ocean is supposed to be considered and verified. More factors should be taken into consideration and tested in the numerical model, e.g., subducted slab, angle of subduction, post-collisional orogenic collapse and heterogeneous rheological properties across the massifs. In addition, both the subductions of the Paleo-Tethys and Paleo-Pacific oceans are supposed to be considered in the future numerical models to verify the influence of the transition of the tectonic regime on the tectonic behaviors, and the Triassic–Cretaceous concessive evolution of the Cathaysia Block.

(3) Three-dimensional numerical modelling and analogue modelling are supposed to be applied in future studies, providing a lateral perspective to observe the distribution and propagation pattern of deformation and magmatism, as well as the major structural trajectory at the surface. It can also provide the model with the real spatial location of different blocks to check the interaction between the Cathaysia Block and adjacent blocks.

(4) The numerous mineral deposits discovered within the Cathaysia Block, including world-class W, Sn, Sb, and REE deposits, are closely linked to the thermal

state and geodynamic background. It is essential to study the relationship among the deposits, contemporary thermal architecture and dynamic background. This will provide critical insights for identifying potential target areas for mineral exploration.

Through these in-depth studies, it is expected to yield a transformative understanding of the lithospheric rheology and geodynamic evolution of the Cathaysia Block that can not only help to guide future mineral exploration, but more importantly to provide a critical example for deciphering the evolution of other intracontinental orogens worldwide and enhancing our fundamental knowledge of continental dynamics.

Reference

Afonso, J.C., Ranalli, G., 2004. Crustal and mantle strengths in continental lithosphere: is the jelly sandwich model obsolete? Tectonophysics 394, 221-232. https://doi.org/10.1016/j.tecto.2004.08.006

Aitken, A.R., Betts, P.G., Ailleres, L., 2009. The architecture, kinematics, and lithospheric processes of a compressional intraplate orogen occurring under Gondwana assembly: The Petermann orogeny, central Australia. Lithosphere 1, 343-357. https://doi.org/10.1130/L39.1

Allmendinger, R.W., Cardozo, N., Fisher, D.M., 2011. Structural geology algorithms: Vectors and tensors. Cambridge University Press.

Andersen, T., 2002. Correction of common lead in U–Pb analyses that do not report 204Pb. Chemical Geology 192, 59-79. https://doi.org/10.1016/S0009-2541(02)00195-X

Annen, C., Blundy, J.D., Sparks, R.S.J., 2006. The Genesis of Intermediate and Silicic Magmas in Deep Crustal Hot Zones. Journal of Petrology 47, 505-539. https://doi.org/10.1093/petrology/egi084

Artemieva, I.M., 2019. Lithosphere thermal thickness and geothermal heat flux in Greenland from a new thermal isostasy method. Earth-Science Reviews 188, 469-481. https://doi.org/10.1016/j.earscirev.2018.10.015

Ayres, M., Harris, N., 1997. REE fractionation and Nd-isotope disequilibrium during crustal anatexis: constraints from Himalayan leucogranites. Chemical Geology 139, 249-269. https://doi.org/10.1016/S0009-2541(97)00038-7

Bahadori, A., Holt, W.E., Feng, R., Austermann, J., Loughney, K.M., Salles, T., Moresi, L., Beucher, R., Lu, N., Flesch, L.M., Calvelage, C.M., Rasbury, E.T., Davis, D.M., Potochnik, A.R., Ward, W.B., Hatton, K., Haq, S.S.B., Smiley, T.M., Wooton, K.M., Badgley, C., 2022. Coupled influence of tectonics, climate, and surface processes on landscape evolution in southwestern North America. Nat Commun 13, 4437. https://doi.org/10.1038/s41467-022-31903-2

Balázs, A., Burov, E., Matenco, L., Vogt, K., Francois, T., Cloetingh, S., 2017. Symmetry during the syn- and post-rift evolution of extensional back-arc basins: The role of inherited orogenic structures. Earth and Planetary Science Letters 462, 86-98. https://doi.org/10.1016/j.epsl.2017.01.015

Barker, C.E., 1988. Geothermics of petroleum systems: Implications of the stabilization of kerogen thermal maturation after a geologically brief heating duration at peak temperature. Petroleum systems of the United States 1870, 26-29.

Barker, C.E., Pawlewicz, M.J., 1986. The correlation of vitrinite reflectance with maximum temperature in humic organic matter, In: Buntebarth, G., Stegena, L. (Eds.), Paleogeothermics: Evaluation of Geothermal Conditions in the Geological Past. Springer Berlin Heidelberg, Berlin, Heidelberg, pp. 79-93. https://doi.org/10.1007/BFb0012103

Burnham, A.K., Sweeney, J.J., 1989. A chemical kinetic model of vitrinite maturation and reflectance. Geochimica et Cosmochimica Acta 53, 2649-2657. https://doi.org/10.1016/0016-7037(89)90136-1

Bea, F., 2012. The sources of energy for crustal melting and the geochemistry of heat-producing elements. Lithos 153, 278-291. https://doi.org/10.1016/j.lithos.2012.01.017

Bea, F., Montero, P., Barcos, L., Cambeses, A., Molina, J.F., Morales, I., 2023. Understanding Nd model ages of granite rocks: The effects of the 147Sm/144Nd variability during partial melting and crystallization. Lithos 436, 106940. https://doi.org/10.1016/j.lithos.2022.106940

Beyssac, O., Bollinger, L., Avouac, J.-P., Goffé, B., 2004. Thermal metamorphism in the lesser Himalaya of Nepal determined from Raman spectroscopy of carbonaceous material. Earth and Planetary Science Letters 225, 233-241. https://doi.org/10.1016/j.epsl.2004.05.023

Beyssac, O., Goffé, B., Chopin, C., Rouzaud, J., 2002. Raman spectra of carbonaceous material in metasediments: a new geothermometer. Journal of Metamorphic

Geology 20, 859-871. https://doi.org/10.1046/j.1525-1314.2002.00408.x

Beyssac, O., Lazzeri, M., 2012. Application of Raman spectroscopy to the study of graphitic carbons in the Earth Sciences, Raman spectroscopy applied to Earth sciences and cultural heritage, pp. 415-454. https://doi.org/10.1180/EMU-notes.12.12

BGMRFJ, 1985. Regional Geology of Fujian Province, People's Republic of China. Geological Publishing House, Beijing.

BGMRGD, 1988. Regional Geology of Guangdong Province, People's Republic of China. Geological Publishing House, Beijing.

BGMRGX, 1985. Regional Geology of Guangxi Province, People's Republic of China. Geological Publishing House, Beijing.

BGMRHN, 1988. Regional Geology of Hunan Province, People's Republic of China. Geological Publishing House, Beijing.

BGMRJX, 1984. Regional Geology of Jiangxi Province, People's Republic of China. Geological Publishing House, Beijing.

BGMRZJ, 1989. Regional Geology of Zhejiang Province, People's Republic of China. Geological Publishing House, Beijing.

Bhowmick, S., Mondal, T.K., 2020. Control of pre-existing fabric in fracture formation, reactivation and vein emplacement under variable fluid pressure conditions: an example from Archean Greenstone belt, India. Solid Earth Discussions 2020, 1-48. https://doi.org/10.5194/se-11-1227-2020

Bi, B.T., Hu, X.Y., Li, J.W., Xu, S., 2022. Insights into deep metallogenic setting in SE China based on geophysical data. Geological Journal 58, 283-297. https://doi.org/10.1002/gj.4591

Black, L.P., Fitzgerald, J.D., Harley, S.L., 1984. Pb isotopic composition, colour, and microstructure of monazites from a polymetamorphic rock in Antarctica. Contributions to Mineralogy and Petrology 85, 141-148. https://doi.org/10.1007/BF00371704

Black, L.P., Gulson, B.L., 1978. The age of the mud tank carbonatite, strangways range, northern territory. Journal of Australian Geology and Geophysics 3, 227-232.

Boillot, G., Capdevila, R., 1977. The Pyrenees: subduction and collision? Earth and Planetary Science Letters 35, 151-160. https://doi.org/10.1016/0012-821X(77)90038-3

Bracène, R., Frizon de Lamotte, D., 2002. The origin of intraplate deformation in the Atlas system of western and central Algeria: from Jurassic rifting to Cenozoic–Quaternary inversion. Tectonophysics 357, 207-226. https://doi.org/10.1016/S0040-1951(02)00369-4

Breton, N.L., Thompson, A.B., 1988. Fluid-absent (dehydration) melting of biotite in metapelites in the early stages of crustal anatexis. Contributions to Mineralogy and Petrology 99, 226-237. https://doi.org/10.1007/BF00371463

Brown, M., 1994. The generation, segregation, ascent and emplacement of granite magma: the migmatite-to-crustally-derived granite connection in thickened orogens. Earth-Science Reviews 36, 83-130. https://doi.org/10.1016/0012-8252(94)90009-4

Brown, M., 2001. Orogeny, migmatites and leucogranites: A review. Journal of Earth System Science 110, 313-336. https://doi.org/10.1007/BF02702898

Brown, M., 2007. Crustal melting and melt extraction, ascent and emplacement in orogens: mechanisms and consequences. Journal of the Geological Society 164, 709-730. https://doi.org/10.1144/0016-76492006-171

Brown, M., 2013. Granite: From genesis to emplacement. Geological Society of America Bulletin 125, 1079-1113. https://doi.org/10.1130/B30877.1

Burchardt, S., 2009. Mechanisms of magma emplacement in the upper crust. Niedersächsische Staats-und Universitätsbibliothek Göttingen, Doctoral dissertation.

Burg, J.P., Gerya, T.V., 2005. The role of viscous heating in Barrovian metamorphism of collisional orogens: thermomechanical models and application to the Lepontine

Dome in the Central Alps. Journal of Metamorphic Geology 23, 75-95. https://doi.org/10.1111/j.1525-1314.2005.00563.x

Bürgmann, R., Dresen, G., 2008. Rheology of the Lower Crust and Upper Mantle: Evidence from Rock Mechanics, Geodesy, and Field Observations. Annual review of Earth and planetary sciences 36, 531-567. https://doi.org/10.1146/annurev.earth.36.031207.124326

Burov, E., Yamato, P., 2008. Continental plate collision, P–T–t–z conditions and unstable vs. stable plate dynamics: Insights from thermo-mechanical modelling. Lithos 103, 178-204. https://doi.org/10.1016/j.lithos.2007.09.014

Burov, E.B., Watts, A.B., 2006. The long-term strength of continental lithosphere: “jelly sandwich” or “crème brûlée”? GSA today 16. https://doi.org/10.1130/1052-5173(2006)016<4:Tltsoc>2.0.Co;2

Butler, R.W.H., Tavarnelli, E., Grasso, M., 2006. Structural inheritance in mountain belts: An Alpine–Apennine perspective. Journal of Structural Geology 28, 1893-1908. https://doi.org/10.1016/j.jsg.2006.09.006

Cagnard, F., Durrieu, N., Gapais, D., Brun, J.P., Ehlers, C., 2006. Crustal thickening and lateral flow during compression of hot lithospheres, with particular reference to Precambrian times. Terra Nova 18, 72-78. https://doi.org/10.1111/j.1365-3121.2005.00665.x

Cai, D.W., Zhao, J.Y., Tang, Y., Zhang, H., Liu, Y.L., Lv, Z.H., 2017. Geochemistry,petrogenesis and tectonic significance of the late Triassic A-type granite in Fujian,South China. Acta Geochimica 36, 166-180. https://doi.org/10.1007/s11631-017-0143-9

Cai, H.T., Hao, K.-C., Doo, W.-B., Chang, C.-P., Jin, X., Kuo, Y.-W., Wang, C.-Y., Chen, W.-S., Chang, W.-Y., 2021. Geophysical Evidence for the Ancient Suture Within the Cathaysia Block, In: Lo, C.-H., Xu, X., Chang, W.-Y., Ando, M. (Eds.), Earthquake Geology and Tectonophysics around Eastern Tibet and Taiwan. Springer Singapore, Singapore, pp. 127-140. https://doi.org/10.1007/978-981-15-

6210-5_8

Cai, Y., Lu, J.J., Ma, D.S., Huang, H., Zhang, H.F., Zhang, R.Q., 2015. The Late Triassic Dengfuxian A-type granite, Hunan Province: age, petrogenesis, and implications for understanding the late Indosinian tectonic transition in South China. International Geology Review 57, 428-445. https://doi.org/10.1080/00206814.2015.1012565

Calderón, M., Hervé, F., Massonne, H.J., Tassinari, C.G., Pankhurst, R.J., Godoy, E., Theye, T., 2007. Petrogenesis of the Puerto Edén Igneous and Metamorphic Complex, Magallanes, Chile: Late Jurassic syn-deformational anatexis of metapelites and granitoid magma genesis. Lithos 93, 17-38. https://doi.org/10.1016/j.lithos.2006.03.044

Canil, D., Russell, J.K., 2022. Xenoliths reveal a hot Moho and thin lithosphere at the Cordillera-craton boundary of western Canada. Geology 50, 1135-1139. https://doi.org/10.1130/g50151.1

Cao, X.Z., Flament, N., Li, S.Z., Müller, R.D., 2021. Spatio-temporal evolution and dynamic origin of Jurassic-Cretaceous magmatism in the South China Block. Earth-Science Reviews 217, 103605. https://doi.org/10.1016/j.earscirev.2021.103605

Capitanio, F.A., Morra, G., Goes, S., 2007. Dynamic models of downgoing plate-buoyancy driven subduction: Subduction motions and energy dissipation. Earth and Planetary Science Letters 262, 284-297. https://doi.org/10.1016/j.epsl.2007.07.039

Carson, C.J., Powell, R., Wilson, C.J.L., Dirks, P.H.G.M., 1997. Partial melting during tectonic exhumation of a granulite terrane: an example from the Larsemann Hills, East Antarctica. Journal of Metamorphic Geology 15, 105-126. https://doi.org/10.1111/j.1525-1314.1997.00059.x

Carter, A., Roques, D., Bristow, C., Kinny, P., 2001. Understanding Mesozoic accretion in Southeast Asia: significance of Triassic thermotectonism (Indosinian orogeny) in Vietnam. Geology 29, 211-214. https://doi.org/10.1130/0091-7613(2001)029<0211:UMAISA>2.0.CO;2

Cawood, P.A., Wang, W., Zhao, T.Y., Xu, Y.J., Mulder, J.A., Pisarevsky, S.A., Zhang, L.M., Gan, C.S., He, H.Y., Liu, H.C., Qi, L., Wang, Y.J., Yao, J.L., Zhao, G.C., Zhou, M.F., Zi, J.W., 2020. Deconstructing South China and consequences for reconstructing Nuna and Rodinia. Earth-Science Reviews 204, 103169. https://doi.org/10.1016/j.earscirev.2020.103169

Chardon, D., Gapais, D., Cagnard, F., 2009. Flow of ultra-hot orogens: A view from the Precambrian, clues for the Phanerozoic. Tectonophysics 477, 105-118. https://doi.org/10.1016/j.tecto.2009.03.008

Charvet, J., 2013. The Neoproterozoic–Early Paleozoic tectonic evolution of the South China Block: An overview. Journal of Asian Earth Sciences 74, 198-209. https://doi.org/10.1016/j.jseaes.2013.02.015

Charvet, J., Shu, L.S., Faure, M., Choulet, F., Wang, B., Lu, H.F., Breton, N.L., 2010. Structural development of the Lower Paleozoic belt of South China: Genesis of an intracontinental orogen. Journal of Asian Earth Sciences 39, 309-330. https://doi.org/10.1016/j.jseaes.2010.03.006

Chen, C.H., Hsieh, P.S., Lee, C.Y., Zhou, H.W., 2011. Two episodes of the Indosinian thermal event on the South China Block: Constraints from LA-ICPMS U–Pb zircon and electron microprobe monazite ages of the Darongshan S-type granitic suite. Gondwana Research 19, 1008-1023. https://doi.org/10.1016/j.gr.2010.10.009

Chen, C.H., Lee, C.Y., Liu, Y.H., Xiang, H., Zeng, W., Zhou, H.W., 2018. Precambrian protoliths and Phanerozoic overprinting on the Wuyishan terrain (South China): New evidence from a combination of LA-ICPMS zircon and EMP monazite geochronology. Precambrian Research 307, 229-254. https://doi.org/10.1016/j.precamres.2018.01.010

Chen, C.-H., Lee, C.-Y., Shinjo, R., 2008. Was there Jurassic paleo-Pacific subduction in South China?: Constraints from 40Ar/39Ar dating, elemental and Sr–Nd–Pb isotopic geochemistry of the Mesozoic basalts. Lithos 106, 83-92. https://doi.org/10.1016/j.lithos.2008.06.009

Chen, C.H., Liu, Y.H., Lee, C.Y., Sano, Y., Zhou, H.W., Xiang, H., Takahata, N., 2017. The Triassic reworking of the Yunkai massif (South China): EMP monazite and U-Pb zircon geochronologic evidence. Tectonophysics 694, 1-22. https://doi.org/10.1016/j.tecto.2016.11.022

Chen, C.H., Liu, Y.H., Lee, C.Y., Xiang, H., Zhou, H.W., 2012. Geochronology of granulite, charnockite and gneiss in the poly-metamorphosed Gaozhou Complex (Yunkai massif), South China: Emphasis on the in-situ EMP monazite dating. Lithos 144-145, 109-129. https://doi.org/10.1016/j.lithos.2012.04.009

Chen, H.L., Lin, X.B., Cheng, X.G., Gong, J.F., Bian, S., Wu, L., Jia, C.Z., Yang, S.F., Guo, Z.J., Jia, D., 2022. Two-phase intracontinental deformation mode in the context of India–Eurasia collision: insights from a structural analysis of the West Kunlun–Southern Junggar transect along the NW margin of the Tibetan Plateau. Journal of the Geological Society 179, jgs2021-2029. https://doi.org/10.1144/jgs2021-029

Chen, L., Song, X.D., Gerya, T.V., Xu, T., Chen, Y., 2019. Crustal melting beneath orogenic plateaus: Insights from 3-D thermo-mechanical modeling. Tectonophysics 761, 1-15. https://doi.org/10.1016/j.tecto.2019.03.014

Chen, X.Y., Tong, L.X., Zhang, C.L., Zhu, Q.B., Li, Y.N., 2015. Retrograde garnet amphibolite from eclogite of the Zhejiang Longyou area: New evidence of the Caledonian orogenic event in the Cathaysia block. Chinese Science Bulletin 60, 1207. (in Chinese with English abstract). https://doi.org/10.1360/N972015-00094

Chen, Z., 2017. Numerical Simulations of Crustal Melting and Rheology and theirs Geological Constraints. Doctoral dissertation, 1-141.

Chen, Z., Liu, Y.J., Chen, G.N., Peng, Z.L., 2017. Rheological transitions in progressive melting of rock and their geological constraints from the Fuhu metatexite-diatexite profile in Guangdong Province, SE China. Journal of Asian Earth Sciences 139, 192-201. https://doi.org/10.1016/j.jseaes.2017.02.009

Chen, Z., Liu, Y.J., Jin, W., Lou, F., Chen, G.N., 2021. A preliminary study of the siliceous and femic rock blocks in the Neoproterozoic diatexitic granite at Fuhu Hill in southwestern Guangdong, China. Geological Journal 56, 2888-2905. https://doi.org/10.1002/gj.4076

Cheng, H., Bloch, E.M., Moulas, E., Vervoort, J.D., 2019. Reconciliation of discrepant U–Pb, Lu–Hf, Sm–Nd, Ar–Ar and U–Th/He dates in an amphibolite from the Cathaysia Block in Southern China. Contributions to Mineralogy and Petrology 175, 1-17. https://doi.org/10.1007/s00410-019-1644-9

Chew, D.M., Petrus, J.A., Kamber, B.S., 2014. U–Pb LA–ICPMS dating using accessory mineral standards with variable common Pb. Chemical Geology 363, 185-199. https://doi.org/10.1016/j.chemgeo.2013.11.006

Chew, D.M., Spikings, R.A., 2015. Geochronology and Thermochronology Using Apatite: Time and Temperature, Lower Crust to Surface. Elements 11, 189-194. https://doi.org/10.2113/gselements.11.3.189

Chiaraluce, L., Barchi, M.R., Carannante, S., Collettini, C., Mirabella, F., Pauselli, C., Valoroso, L., 2017. The role of rheology, crustal structures and lithology in the seismicity distribution of the northern Apennines. Tectonophysics 694, 280-291. https://doi.org/10.1016/j.tecto.2016.11.011

China Geological Survey, 2020. Geological Map of the People's Republic of China. Geological Publishing House, Beijing, China. scale 1:1,500,000.

Chisenga, C., Yan, J.G., 2019. A new crustal thickness model for mainland China derived from EIGEN-6C4 gravity data. Journal of Asian Earth Sciences 179, 430-442. https://doi.org/10.1016/j.jseaes.2019.05.011

Chu, Y., Faure, M., Lin, W., Wang, Q.C., 2012a. Early Mesozoic tectonics of the South China block: Insights from the Xuefengshan intracontinental orogen. Journal of Asian Earth Sciences 61, 199-220. https://doi.org/10.1016/j.jseaes.2012.09.029

Chu, Y., Faure, M., Lin, W., Wang, Q.C., Ji, W.B., 2012b. Tectonics of the Middle Triassic intracontinental Xuefengshan Belt, South China: new insights from structural and chronological constraints on the basal décollement zone. International Journal of Earth Sciences 101, 2125-2150. https://doi.org/10.1007/s00531-012-0780-5

Chu, Y., Lin, W., Faure, M., Allen, M.B., Feng, Z.T., 2020. Cretaceous exhumation of the Triassic intracontinental Xuefengshan Belt: Delayed unroofing of an orogenic plateau across the South China Block? Tectonophysics 793, 228592. https://doi.org/10.1016/j.tecto.2020.228592

Cochelin, B., Wang, B., Liu, J.S., Lu, S.H., Shu, L.S., Gumiaux, C., Chen, Y., Song, F., 2022. Early Mesozoic Anatexis‐Induced Strain Partitioning and Gneiss Doming in the Yunkai Massif, South China: A Response to Contrasted Dynamics of Paleo‐Pacific and Paleo‐Tethys Subductions? Tectonics 41, e2022TC007457. https://doi.org/10.1029/2022tc007457

Cocks, L.R.M., Torsvik, T.H., 2013. The dynamic evolution of the Palaeozoic geography of eastern Asia. Earth-Science Reviews 117, 40-79. https://doi.org/10.1016/j.earscirev.2012.12.001

Collins, W.J., Huang, H.Q., Jiang, X.Y., 2016. Water-fluxed crustal melting produces Cordilleran batholiths. Geology 44, 143-146. https://doi.org/10.1130/G37398.1

Copeland, P., Parrish, R.R., Harrison, T.M., 1988. Identification of inherited radiogenic Pb in monazite and its implications for U–Pb systematics. Nature 333, 760-763. https://doi.org/10.1038/333760a0

Corfu, F., Hanchar, J.M., Hoskin, P.W.O., Kinny, P., 2003. Atlas of Zircon Textures. Reviews in Mineralogy & Geochemistry 53, 469-500. https://doi.org/10.2113/0530469

Cottle, J., Waters, D., Riley, D., Beyssac, O., Jessup, M., 2011. Metamorphic history of the South Tibetan Detachment System, Mt. Everest region, revealed by RSCM thermometry and phase equilibria modelling. Journal of Metamorphic Geology 29, 561-582.

Cui, J.J., Zhang, Y.Q., Dong, S.W., Jahn, B.-m., Xu, X.B., Ma, L.C., 2013. Zircon U–Pb geochronology of the Mesozoic metamorphic rocks and granitoids in the coastal tectonic zone of SE China: Constraints on the timing of Late Mesozoic orogeny. Journal of Asian Earth Sciences 62, 237-252. https://doi.org/10.1016/j.jseaes.2012.09.014

Cunningham, D., 2005. Active intracontinental transpressional mountain building in the Mongolian Altai: Defining a new class of orogen. Earth and Planetary Science Letters 240, 436-444. https://doi.org/10.1016/j.epsl.2005.09.013

Cunningham, D., Zhang, J., 2021. China | Mongolia: Mesozoic-Cenozoic, In: Alderton, D., Elias, S.A. (Eds.), Encyclopedia of Geology (Second Edition). Academic Press, Oxford, pp. 509-525. https://doi.org/10.1016/B978-0-08-102908-4.00164-8

Dai, L.M., Wang, L.L., Lou, D., Li, Z.H., Dong, H., Ma, F.F., Li, F.K., Li, S.Z., Yu, S.Y., 2020. Slab Rollback Versus Delamination: Contrasting Fates of Flat‐Slab Subduction and Implications for South China Evolution in the Mesozoic. Journal of Geophysical Research: Solid Earth 125, e2019JB019164. https://doi.org/10.1029/2019jb019164

Dempster, T.J., Coleman, S., Kennedy, R., Chung, P., Brown, R.W., 2020. Growth zoning of garnet porphyroblasts: Grain boundary and microtopographic controls. Journal of Metamorphic Geology 38, 1011-1027. https://doi.org/10.1111/jmg.12558

Deng, P., Shu, L.S., Xiao, D.H., 2002. A study on the tectonic basement of late Mesozoic igneous rocks in southeastern China. Geological Journal of China Universities 8, 169. (in Chinese with English abstract).

Deng, P., Shu, L.S., Yang, M.G., Guo, Y.J., Yu, X.Q., 2003. Geological features and dynamic evolution of the Ganjiang fault in Jiangxi Province. Geological review 49, 113-122. (in Chinese with English abstract).

Deng, Y.F., Xu, Y.G., Chen, Y., 2021. Formation mechanism of the North–South

Gravity Lineament in eastern China. Tectonophysics 818, 229074. https://doi.org/10.1016/j.tecto.2021.229074

Devès, M.H., Tait, S.R., King, G.C.P., Grandin, R., 2014. Strain heating in process zones; implications for metamorphism and partial melting in the lithosphere. Earth and Planetary Science Letters 394, 216-228. https://doi.org/10.1016/j.epsl.2014.03.002

Di, Q.Y., Tian, F., Suo, Y.H., Gao, R., Li, S.Z., Fu, C.M., Wang, G.Z., Li, F., Tan, Y.Y., 2021. Linkage of deep lithospheric structures to intraplate earthquakes: A perspective from multi-source and multi-scale geophysical data in the South China Block. Earth-Science Reviews 214, 103504. https://doi.org/10.1016/j.earscirev.2021.103504

Dong, M., Hao, T., Xu, L., Zhang, J., Zhang, J., Lü, C., He, Q., 2024. Subduction without volcanic arc magma: Insights from two young subduction zones in the western Pacific. Tectonophysics 874, 230231. https://doi.org/10.1016/j.tecto.2024.230231

Dong, S.W., Li, J.H., Cawood, P.A., Gao, R., Zhang, Y.Q., Xin, Y.J., 2020. Mantle influx compensates crustal thinning beneath the Cathaysia Block, South China: Evidence from SINOPROBE reflection profiling. Earth and Planetary Science Letters 544, 116360. https://doi.org/10.1016/j.epsl.2020.116360

Dong, S.W., Li, J.H., Gao, R., Cawood, P.A., Thybo, H., Johnston, S.T., Jiao, L.Q., Zhang, Y.Q., Wang, J.M., 2023. Intraplate lithospheric extension revealed by seismic reflection profiling of South China. Earth and Planetary Science Letters 609, 118100. https://doi.org/10.1016/j.epsl.2023.118100

Dong, Y.F., Zheng, C.Q., Zhou, X.W., Xu, J.L., Zhou, X., Wang, Z.Y., Zhong, D.D., 2018. Metamorphism and its tectonic implications of early Mesozoic pelitic granulites from Badu Complex of Southwestern Zhejiang Province, South China. Earth Science 43, 259-277. (in Chinese with English abstract).

Dong, Y.P., Zhang, G.W., Neubauer, F., Liu, X.M., Genser, J., Hauzenberger, C., 2011.

Tectonic evolution of the Qinling orogen, China: review and synthesis. Journal of Asian Earth Sciences 41, 213-237. https://doi.org/10.1016/j.jseaes.2011.03.002

Dutch, R., Hand, M., 2010. Retention of Sm–Nd isotopic ages in garnets subjected to high-grade thermal reworking: implications for diffusion rates of major and rare earth elements and the Sm–Nd closure temperature in garnet. Contributions to Mineralogy and Petrology 159, 93-112. https://doi.org/10.1007/s00410-009-0418-1

Fang, H.F., Yao, S.P., Jiao, K., Hu, W.X., Cao, J., Gao, Y.Q., 2010. Thermal Evolution and History of the Permian Coal Measures in Yongmei Depression. Geological Journal of China Universities 16, 255-264. (in Chinese with English abstract). https://doi.org/10.16108/j.issn1006-7493.2010.02.013

Faure, M., Lepvrier, C., Nguyen, V.V., Vu, T.V., Lin, W., Chen, Z.C., 2014. The South China block-Indochina collision: Where, when, and how? Journal of Asian Earth Sciences 79, 260-274. https://doi.org/10.1016/j.jseaes.2013.09.022

Faure, M., Lin, W., Chu, Y., Lepvrier, C., 2016a. Triassic tectonics of the Ailaoshan Belt (SW China): Early Triassic collision between the South China and Indochina Blocks, and Middle Triassic intracontinental shearing. Tectonophysics 683, 27-42. https://doi.org/10.1016/j.tecto.2016.06.015

Faure, M., Lin, W., Chu, Y., Lepvrier, C., 2016b. Triassic tectonics of the southern margin of the South China Block. Comptes Rendus Geoscience 348, 5-14. https://doi.org/10.1016/j.crte.2015.06.012

Faure, M., Lin, W., Le Breton, N., 2001. Where is the North China–South China block boundary in eastern China? Geology 29, 119-122. https://doi.org/10.1130/0091-7613(2001)029<0119:WITNCS>2.0.CO;2

Faure, M., Shu, L.S., Wang, B., Charvet, J., Choulet, F., Monie, P., 2009. Intracontinental subduction: a possible mechanism for the Early Palaeozoic Orogen of SE China. Terra Nova 21, 360-368. https://doi.org/10.1111/j.1365-3121.2009.00888.x

Feng, Z.H., Wang, C.Z., Liang, J.C., Li, J.C., Huang, Y.G., Liao, J.F., Wang, R., 2011. The emplacement mechanisms and growth styles of the Guposhan-Huashan batholith in western Nanling Range, South China. Sci China Earth Sci 41, 816-831. (in Chinese with English abstract).

Findlay, R.H., Trinh, P.T., 1997. The structural setting of the Song Ma region, Vietnam and the Indochina-South China plate boundary problem. Gondwana Research 1, 11-33. https://doi.org/10.1016/S1342-937X(05)70003-4

Ford, M., Vergés, J., 2021. Evolution of a salt-rich transtensional rifted margin, eastern North Pyrenees, France. Journal of the Geological Society 178, jgs2019-2157. https://doi.org/10.1144/jgs2019-157

Fossen, H., Cavalcante, G.C., de Almeida, R.P., 2017. Hot Versus Cold Orogenic Behavior: Comparing the Araçuaí-West Congo and the Caledonian Orogens. Tectonics 36, 2159-2178. https://doi.org/10.1002/2017tc004743

Foster, D.A., Schafer, C., Fanning, C.M., Hyndman, D.W., 2001. Relationships between crustal partial melting, plutonism, orogeny, and exhumation: Idaho–Bitterroot batholith. Tectonophysics 342, 313-350. https://doi.org/10.1016/S0040-1951(01)00169-X

Gao, P., Zheng, Y.F., Zhao, Z.F., 2017. Triassic granites in South China: A geochemical perspective on their characteristics, petrogenesis, and tectonic significance. Earth-Science Reviews 173, 266-294. https://doi.org/10.1016/j.earscirev.2017.07.016

Gao, W., Shi, J.R., Meng, Q.K., Shu, Q., Zhang, K.S., Wang, C.Y., Xu, G.J., 2022. Discovery and geological significance of the Indosinian granulites in Hainan Island: new evidence from U-Pb dating and trace element composition of zircons. Acta Geologica Sinica 96, 426-444. (in Chinese with English abstract). https://doi.org/10.19762/j.cnki.dizhixuebao.2022115

Gao, W.L., Wang, Z.X., 2024. Structural and chronological constraints for Longquan-Badu ductile shear zone: Implication for Triassic intraplate orogeny in South China Block. Geological Journal 59, 2883-2896. https://doi.org/10.1002/gj.5036

Gao, W.L., Wang, Z.X., Song, W.J., Li, C.L., 2017. The role of mafic microgranular enclaves in the generation of Early Cretaceous granitic rocks of SE China: evidence from zircon U–Pb geochronology, geochemistry, and Hf isotopic data for the Liangnong pluton, eastern Zhejiang Province. International Geology Review 59, 845-863. https://doi.org/10.1080/00206814.2016.1236297

Gapais, D., Cagnard, F., Gueydan, F., Barbey, P., Ballèvre, M., 2009. Mountain building and exhumation processes through time: inferences from nature and models. Terra Nova 21, 188-194. https://doi.org/10.1111/j.1365-3121.2009.00873.x

Gapais, D., Potrel, A., Machado, N., Hallot, E., 2005. Kinematics of long-lasting Paleoproterozoic transpression within the Thompson Nickel Belt, Manitoba, Canada. Tectonics 24, TC3002. https://doi.org/10.1029/2004TC001700

Gerya, T., 2011. Future directions in subduction modeling. Journal of Geodynamics 52, 344-378. https://doi.org/10.1016/j.jog.2011.06.005

Gerya, T., 2019. Introduction to Numerical Geodynamic Modelling, 2 ed. Cambridge University Press, Cambridge. https://doi.org/10.1017/9781316534243

Gerya, T., 2022. Numerical modeling of subduction: State of the art and future directions. Geosphere 18, 503-561. https://doi.org/10.1130/ges02416.1

Gerya, T.V., Yuen, D.A., 2003a. Characteristics-based marker-in-cell method with conservative finite-differences schemes for modeling geological flows with strongly variable transport properties. Physics of the Earth and Planetary Interiors 140, 293-318. https://doi.org/10.1016/j.pepi.2003.09.006

Gerya, T.V., Yuen, D.A., 2003b. Rayleigh–Taylor instabilities from hydration and melting propel 'cold plumes' at subduction zones. Earth and Planetary Science Letters 212, 47-62. https://doi.org/10.1016/S0012-821X(03)00265-6

Gerya, T.V., Yuen, D.A., 2007. Robust characteristics method for modelling multiphase visco-elasto-plastic thermo-mechanical problems. Physics of the Earth and Planetary Interiors 163, 83-105. https://doi.org/10.1016/j.pepi.2007.04.015

Goes, S., Hasterok, D., Schutt, D.L., Klöcking, M., 2020. Continental lithospheric temperatures: A review. Physics of the Earth and Planetary Interiors 306, 106509. https://doi.org/10.1016/j.pepi.2020.106509

Gomez, F., Barazangi, M., Bensaid, M., 1996. Active tectonism in the intracontinental Middle Atlas Mountains of Morocco: synchronous crustal shortening and extension. Journal of the Geological Society 153, 389-402. https://doi.org/10.1144/gsjgs.153.3.0389

Gomez, F., Beauchamp, W., Barazangi, M., 2000. Role of the Atlas Mountains (northwest Africa) within the African-Eurasian plate-boundary zone. Geology 28, 775-778. https://doi.org/10.1130/0091-7613(2000)28<775:Rotamn>2.0.Co;2

Gorczyk, W., Willner, A.P., Gerya, T.V., Connolly, J.A.D., Burg, J.-P., 2007. Physical controls of magmatic productivity at Pacific-type convergent margins: Numerical modelling. Physics of the Earth and Planetary Interiors 163, 209-232. https://doi.org/10.1016/j.pepi.2007.05.010

Groome, W.G., Koons, P.O., Johnson, S.E., 2008. Metamorphism, transient mid-crustal rheology, strain localization and the exhumation of high-grade metamorphic rocks. Tectonics 27, TC1001. https://doi.org/10.1029/2006tc001992

Groves, D.I., Santosh, M., Goldfarb, R.J., Zhang, L., 2018. Structural geometry of orogenic gold deposits: Implications for exploration of world-class and giant deposits. Geoscience Frontiers 9, 1163-1177. https://doi.org/10.1016/j.gsf.2018.01.006

Guo, L.H., Gao, R., 2018. Potential-field evidence for the tectonic boundaries of the central and western Jiangnan belt in South China. Precambrian Research 309, 45-55. https://doi.org/10.1016/j.precamres.2017.01.028

Guo, L.H., Gao, R., Shi, L., Huang, Z.R., Ma, Y.W., 2019. Crustal thickness and Poisson's ratios of South China revealed from joint inversion of receiver function and gravity data. Earth and Planetary Science Letters 510, 142-152. https://doi.org/10.1016/j.epsl.2018.12.039

Guo, L.Z., Shi, Y.S., Lu, H.F., Ma, R.S., Dong, H.G., Yang, S.F., 1989. The pre-

Devonian tectonic patterns and evolution of South China. Journal of Southeast Asian Earth Sciences 3, 87-93. https://doi.org/10.1016/0743-9547(89)90012-3

Guo, Z., Gao, X., Li, T., Wang, W., 2018. Crustal and uppermost mantle structures of the South China from joint analysis of receiver functions and Rayleigh wave dispersions. Physics of the Earth and Planetary Interiors 278, 16-25. https://doi.org/10.1016/j.pepi.2018.03.001

Han, S., Xu, L.Y., Shan, X.P., Xu, X., Kuang, X.T., Sun, Y.Y., Wang, B.D., 2025. Lithospheric electrical structure of Zhenghe-Dapu fault in South China determined by multi-geophysical observations: Implications for geothermal mechanism. Tectonophysics 906. https://doi.org/10.1016/j.tecto.2025.230723

Hao, L.L., Wang, Q., Wyman, D.A., Ou, Q., Dan, W., Jiang, Z.Q., Wu, F.Y., Yang, J.H., Long, X.P., Li, J., 2016. Underplating of basaltic magmas and crustal growth in a continental arc: Evidence from Late Mesozoic intermediate–felsic intrusive rocks in southern Qiangtang, central Tibet. Lithos 245, 223-242. https://doi.org/10.1016/j.lithos.2015.09.015

Harris, N., Massey, J., 1994. Decompression and anatexis of Himalayan metapelites. Tectonics 13, 1537-1546. https://doi.org/10.1029/94TC01611

He, C., Dong, S., Santosh, M., Chen, X., 2013. Seismic Evidence for a Geosuture between the Yangtze and Cathaysia Blocks, South China. Sci Rep 3, 2200. https://doi.org/10.1038/srep02200

He, C.S., Santosh, M., 2021. Mantle Upwelling Beneath the Cathaysia Block, South China. Tectonics 40. https://doi.org/10.1029/2020tc006447

He, J.R., Wang, A.G., Rui, X.J., Zeng, Y., Li, C.H., 2008. Middle Proterozoic submarine volcanic exhalative metallogenesis of Tieshajie, Yiyang, Jiangxi Province. Resources Survey & Environment 29, 261-269. (in Chinese with English abstract).

Henry, D.J., Guidotti, C.V., Thomson, J.A., 2005. The Ti-saturation surface for low-to-medium pressure metapelitic biotites: Implications for geothermometry and Ti-substitution mechanisms. American Mineralogist 90, 316-328.

https://doi.org/10.2138/am.2005.1498

Henry, D.G., Jarvis, I., Gillmore, G., Stephenson, M., 2019. Raman spectroscopy as a tool to determine the thermal maturity of organic matter: Application to sedimentary, metamorphic and structural geology. Earth-Science Reviews 198. https://doi.org/10.1016/j.earscirev.2019.102936

Hensen, B.J., Zhou, B., 1995. Retention of isotopic memory in garnets partially broken down during an overprinting granulite-facies metamorphism: Implications for the Sm-Nd closure temperature. Geology 23, 225-228. https://doi.org/10.1130/0091-7613(1995)023<0225:ROIMIG>2.3.CO;2

Heron, P.J., Pysklywec, R.N., 2016. Inherited structure and coupled crust - mantle lithosphere evolution: Numerical models of Central Australia. Geophysical Research Letters 43, 4962-4970. https://doi.org/10.1002/2016gl068562

Hilchie, L.J., Jamieson, R.A., 2014. Graphite thermometry in a low-pressure contact aureole, Halifax, Nova Scotia. Lithos 208-209, 21-33. https://doi.org/10.1016/j.lithos.2014.08.015

Holland, T., Powell, R., 2003. Activity–composition relations for phases in petrological calculations: an asymmetric multicomponent formulation. Contributions to Mineralogy and Petrology 145, 492-501. https://doi.org/10.1007/s00410-003-0464-z

Holland, T., Powell, R., 2011. An improved and extended internally consistent thermodynamic dataset for phases of petrological interest, involving a new equation of state for solids. Journal of Metamorphic Geology 29, 333-383. https://doi.org/10.1111/j.1525-1314.2010.00923.x

Hollister, L.S., Crawford, M.L., 1986. Melt-enhanced deformation: A major tectonic process. Geology 14, 558-561. https://doi.org/10.1130/0091-7613(1986)14<558:MDAMTP>2.0.CO;2

Hoskin, P.W.O., Black, L.P., 2000. Metamorphic zircon formation by solid-state recrystallization of protolith igneous zircon. Journal of Metamorphic Geology 18, 423-439. https://doi.org/10.1046/j.1525-1314.2000.00266.x

Hu, H., Wang, R.C., Shao, C.J., Xie, L., Tian, E.N., Che, X.D., Yang, Z.Y., 2020. In situ LA-ICP-MS U-Th-Pb isotopic dating of monazite based on the monazite standard Trebilcock. Journal of Nanjing University (Natural Sciences) 56, 763-773. (in Chinese with English abstract). https://doi.org/10.13232/j.cnki.jnju.2020.06.001

Hu, J., Liu, X.C., Xia, M.M., Chen, L.Y., Han, J.N., Hu, D.G., 2022. Triassic amphibolite-facies metamorphism in northeastern Hainan Island, South China. Journal of Asian Earth Sciences 240, 105446. https://doi.org/10.1016/j.jseaes.2022.105446

Hu, K.M., 2001. Initial discussion on the tectonic evolution of Jiangshan-Shaoxing fault zone. Geology of Zhejiang 17, 1-11. (in Chinese with English abstract).

Hu, S.B., He, L.J., Wang, J.Y., 2000. Heat flow in the continental area of China: a new data set. Earth and Planetary Science Letters 179, 407-419. https://doi.org/10.1016/S0012-821X(00)00126-6

Hu, X., Xu, J.K., Kang, H.N., Tong, C.X., Chen, C.H., Ye, G.G., 1991. Geological features of the lower Proterozoic Badu group of southwestern Zhejiang and its implications. Reg. Geol. China 3, 234-240. (in Chinese with English abstract).

Hu, Z.F., Wang, Y.F., Zhai, G.Y., Zhang, J.Z., Kang, H.X., Xue, Z.A., Li, J., Zhang, Y.X., Zhou, H., 2023. Reservoir Characteristics of High-Quality Shale of Carboniferour Luzhai Formation in Rongshui Area, Guangxi. Earth Science. (in Chinese with English abstract). https://doi.org/10.3799/dqkx.2022.437

Huang, B.C., Yan, Y.G., Piper, J.D.A., Zhang, D.H., Yi, Z.Y., Yu, S., Zhou, T.H., 2018. Paleomagnetic constraints on the paleogeography of the East Asian blocks during Late Paleozoic and Early Mesozoic times. Earth-Science Reviews 186, 8-36. https://doi.org/10.1016/j.earscirev.2018.02.004

Huang, H.B., Xiong, H., Qiu, X., Li, Y., 2020. Crustal structure and magmatic evolution in the Pearl River Delta of the Cathaysia Block: New constraints from receiver function modeling. Tectonophysics 778.

https://doi.org/10.1016/j.tecto.2020.228365

Huang, H.L., Zheng, J.Y., 2001. Research on Kinematic Characteristics of Wuchuang-Shihui Fault Zone. Uranium Geology 17, 34-43. (in Chinese with English abstract).

Huang, W.M., Liu, X.J., Liu, L., Li, Z.L., Liu, X., Wu, H., 2023. Early Triassic roll-back of subducted Paleo-Tethys oceanic lithosphere: Insights from A2-type silicic igneous rocks in the Pingxiang area, southwest China. Geosphere 19, 1372-1398. https://doi.org/10.1130/ges02617.1

Huangfu, P.P., Fan, W.M., Li, Z.H., Zhang, H., Zhao, J.M., Shi, Y.L., 2023. Linkage between the India–Asia collision and far-field reactivation of the Altai mountains. Palaeogeography, Palaeoclimatology, Palaeoecology 616. https://doi.org/10.1016/j.palaeo.2023.111478

Huangfu, P.P., Wang, Y.J., Cawood, P.A., Li, Z.H., Fan, W.M., Gerya, T.V., 2016. Thermo-mechanical controls of flat subduction: Insights from numerical modeling. Gondwana Research 40, 170-183. https://doi.org/10.1016/j.gr.2016.08.012

Hung, K.T., Golonka, J., Du, N.K., 2023. The Collision Between Indochina and South China Blocks in Northwestern Vietnam and its Controversy. Inżynieria Mineralna 1. https://doi.org/10.29227/im-2023-02-18

Jackson, J., 2002. Strength of the continental lithosphere: Time to abandon the jelly sandwich? GSA today 12, 4-9.

Jackson, S.E., Pearson, N.J., Griffin, W.L., Belousova, E.A., 2004. The application of laser ablation-inductively coupled plasma-mass spectrometry to in situ U–Pb zircon geochronology. Chemical Geology 211, 47-69. https://doi.org/10.1016/j.chemgeo.2004.06.017

Jacob, J.B., Moyen, J.F., Fiannacca, P., Laurent, O., Bachmann, O., Janoušek, V., Farina, F., Villaros, A., 2021. Crustal melting vs. fractionation of basaltic magmas: Part 2, Attempting to quantify mantle and crustal contributions in granitoids. Lithos 402-403, 106292. https://doi.org/10.1016/j.lithos.2021.106292

Jain, C., Rozel, A.B., Tackley, P.J., Sanan, P., Gerya, T.V., 2019. Growing primordial continental crust self-consistently in global mantle convection models. Gondwana Research 73, 96-122. https://doi.org/10.1016/j.gr.2019.03.015

Jian, X., Weislogel, A., Pullen, A., 2019. Triassic Sedimentary Filling and Closure of the Eastern Paleo - Tethys Ocean: New Insights From Detrital Zircon Geochronology of Songpan-Ganzi, Yidun, and West Qinling Flysch in Eastern Tibet. Tectonics 38, 767-787. https://doi.org/10.1029/2018tc005300

Jiang, G.M., Zhang, G.B., Zhao, D.P., Lü, Q.T., Shi, D.N., Li, H.Y., Li, X.F., 2021. Mantle flow and dynamics beneath central-east China: New insights from P-wave anisotropic tomography. Journal of Geophysical Research: Solid Earth 126, e2020JB020070.

Jiang, G.Z., Hu, S.B., Shi, Y.Z., Zhang, C., Wang, Z.T., Hu, D., 2019. Terrestrial heat flow of continental China: Updated dataset and tectonic implications. Tectonophysics 753, 36-48. https://doi.org/10.1016/j.tecto.2019.01.006

Jiang, J.W., Mao, Y.D., Hu, X.Y., 2022. Factors on the Mesozoic Transition From Flat to Steep Subduction of the Paleo-Pacific Plate Beneath South China: Thickened Oceanic Crust and Subduction Rate. Geochemistry, geophysics, geosystems 23. https://doi.org/10.1029/2022gc010523

Jiang, X.Y., Li, X.H., Collins, W.J., Huang, H.Q., 2015. U-Pb age and Hf-O isotopes of detrital zircons from Hainan Island: Implications for Mesozoic subduction models. Lithos 239, 60-70. https://doi.org/10.1016/j.lithos.2015.10.006

Jiao, Q.Q., He, C.K., Dong, Y.P., Xu, D.R., Chen, G.W., Chen, C., Shi, S., Gao, Y.W., 2020. The petrogenetic links of Indosinian granitoid and migmatite in the Hetai goldfiel., Guangdong Province of South China and the tectonic implication. Acta Petrologica Sinica 36, 893-912. (in Chinese with English abstract). https://doi.org/10.18654/1000-0569/2020.03.15

Jiao, S.J., Guo, J.H., Peng, S.B., 2013. Petrogenesis of garnet in the Darongshan-Shiwandashan granitic suite of the South China Block and the metamorphism of the granulite enclave. Acta Petrologica Sinica 29, 1740-1758. (in Chinese with

English abstract).

Jiao, S.J., Li, X.H., Huang, H.Q., Deng, X.G., 2015. Metasedimentary melting in the formation of charnockite: Petrological and zircon U-Pb-Hf-O isotope evidence from the Darongshan S-type granitic complex in southern China. Lithos 239, 217-233. https://doi.org/10.1016/j.lithos.2015.10.004

Jin, S., Sheng, Y., Comeau, M.J., Becken, M., Wei, W.B., Ye, G.F., Dong, H., Zhang, L.T., 2022. Relationship of the Crustal Structure, Rheology, and Tectonic Dynamics Beneath the Lhasa-Gangdese Terrane (Southern Tibet) Based on a 3-D Electrical Model. Journal of Geophysical Research: Solid Earth 127, e2022JB024318. https://doi.org/10.1029/2022JB024318

Jung, S., Pfänder, J.A., Mezger, K., Hellebrand, E., Brandt, S., 2022. Polyphase growth history of peritectic garnet from a granite: Trace-element zonation, Lu-Hf ages and their significance for the duration of granite-forming processes. Lithos 418-419, 106675. https://doi.org/10.1016/j.lithos.2022.106675

Karsli, O., Aydin, F., Uysal, I., Dokuz, A., Kumral, M., Kandemir, R., Budakoglu, M., Ketenci, M., 2018. Latest Cretaceous “A2-type” granites in the Sakarya Zone, NE Turkey: Partial melting of mafic lower crust in response to roll-back of Neo-Tethyan oceanic lithosphere. Lithos 302-303, 312-328. https://doi.org/10.1016/j.lithos.2017.12.025

Katsura, T., 2022. A Revised Adiabatic Temperature Profile for the Mantle. Journal of Geophysical Research: Solid Earth 127. https://doi.org/10.1029/2021jb023562

Ke, X.Z., Zhou, D., Long, W.G., Wang, J., Xu, D.M., Tian, Y., Jin, W., 2018. Indosinian metamorphism and anatexis in Yunkai Massif: evidences from zircon geochronology and Hf isotopes of migmatites and gneisses. Earth Science 43, 2249-2275. (in Chinese with English abstract). https://doi.org/10.3799/dqkx.2018.574

Kebede, H., Alemu, A., Kevin, M., 2022. Magnetic anomaly patterns and volcano-tectonic features associated with geothermal prospect areas in the Ziway-Shala

Lakes Basin, Central Main Ethiopian Rift. Geothermics 105, 102484.

Kohn, M.J., Spear, F., 2000. Retrograde net transfer reaction insurance for pressure-temperature estimates. Geology 28, 1127-1130. https://doi.org/10.1130/0091-7613(2000)28<1127:RNTRIF>2.0.CO;2

Kreemer, C., Holt, W.E., Haines, A.J., 2003. An integrated global model of present-day plate motions and plate boundary deformation. Geophysical Journal International 154, 8-34. https://doi.org/10.1046/j.1365-246X.2003.01917.x

Lahfid, A., Beyssac, O., Deville, E., Negro, F., Chopin, C., Goffé, B., 2010. Evolution of the Raman spectrum of carbonaceous material in low-grade metasediments of the Glarus Alps (Switzerland). Terra Nova 22, 354-360. https://doi.org/10.1111/j.1365-3121.2010.00956.x

Lambeck, K., 1983. Structure and evolution of the intracratonic basins of central Australia. Geophysical Journal International 74, 843-886. https://doi.org/10.1111/j.1365-246X.1983.tb01907.x

Le Pichon, X., 1968. Sea-floor spreading and continental drift. Journal of Geophysical Research (1896-1977) 73, 3661-3697. https://doi.org/10.1029/JB073i012p03661

Le Pichon, X., Francheteau, J., Bonnin, J., 1973. Plate Tectonics. Elsevier. https://doi.org/10.1016/B978-0-444-41094-8.50008-X

Lejeune, A.-M., Richet, P., 1995. Rheology of crystal-bearing silicate melts: An experimental study at high viscosities. Journal of Geophysical Research: Solid Earth 100, 4215-4229. https://doi.org/10.1029/94JB02985

Lewis, T.J., Hyndman, R.D., Flück, P., 2003. Heat flow, heat generation, and crustal temperatures in the northern Canadian Cordillera: Thermal control of tectonics. Journal of Geophysical Research: Solid Earth 108. https://doi.org/10.1029/2002jb002090

Li, C., 2020. Metamorphic evolution history of the Yunkai orogenic belt, South China: A case study of charnockites and granulite enclaves in the Gaozhou area. Guangzhou Institute of Geochemistry, Chinese Academy of Sciences, Doctoral dissertation, 209.

Li, C., Tong, L.X., Carvalho, B.B., Liu, Z., Dong, Y.P., Fan, J.J., Wang, X.S., 2025. Metamorphic evidence of the Kuunga orogeny in South China: High-pressure pelitic granulites and gneisses from the Gaozhou Complex. Geological Society of America Bulletin. https://doi.org/10.1130/b37768.1

Li, C., Tong, L.X., Huang, X.L., Liu, Z., Zhong, Z., 2020a. Metamorphic PT history of calc-silicate granulites at Gaozhou in the Yunkai massif, western Guangdong and its tectonic implications (in Chinese). Geotectonica et Metallogenia 44, 1172-1189. (in Chinese with English abstract). https://doi.org/10.16539/j.ddgzyckx.2020.06.010

Li, C., Tong, L.X., Liu, Z., Huang, X.L., 2020b. Genesis of the Gaozhou charnockite and its two types of garnets of Yunkai massif, South China: Evidence from petrology and zircon U-Pb geochronology. Acta Petrologica Sinica 36, 871-892. (in Chinese with English abstract). https://doi.org/10.18654/1000-0569/2020.03.14

Li, C.L., Wang, Z.X., Lü, Q.T., Tan, Y.L., Li, L.L., Tao, T., 2021. Mesozoic tectonic evolution of the eastern South China Block: A review on the synthesis of the regional deformation and magmatism. Ore Geology Reviews 131. https://doi.org/10.1016/j.oregeorev.2021.104028

Li, C.L., Wang, Z.X., Tan, Y.L., Li, L.L., 2023. Differential fold interference patterns in an intracontinental orogen: Insights from superposed buckle folding in southern Jiangxi Province, South China Block. Journal of Structural Geology 167. https://doi.org/10.1016/j.jsg.2023.104801

Li, J.H., Cawood, P.A., Ratschbacher, L., Zhang, Y.Q., Dong, S.W., Xin, Y.J., Yang, H., Zhang, P.X., 2020. Building Southeast China in the late Mesozoic: Insights from alternating episodes of shortening and extension along the Lianhuashan fault zone. Earth-Science Reviews 201, 103056. https://doi.org/10.1016/j.earscirev.2019.103056

Li, J.H., Dong, S.W., Cawood, P.A., Thybo, H., Clift, P.D., Johnston, S.T., Zhao, G.C., Zhang, Y.Q., 2023. Cretaceous long-distance lithospheric extension and surface response in South China. Earth-Science Reviews 243. https://doi.org/10.1016/j.earscirev.2023.104496

Li, J.H., Dong, S.W., Cawood, P.A., Zhao, G.C., Johnston, S.T., Zhang, Y.Q., Xin, Y.J., 2018. An Andean-type retro-arc foreland system beneath northwest South China revealed by SINOPROBE profiling. Earth and Planetary Science Letters 490, 170-179. https://doi.org/10.1016/j.epsl.2018.03.008

Li, J.H., Dong, S.W., Gao, R., Cawood, P.A., Zhang, Y.Q., Zhao, G.C., Li, Q.S., Xin, Y.J., Wang, J.M., Lü, F., 2022a. The Thinnest Crust in South China Associated With the Cretaceous Lithospheric Extension: Evidence From SINOPROBE Seismic Reflection Profiling. Tectonics 41. https://doi.org/10.1029/2022tc007240

Li, J.H., Dong, S.W., Zhao, G.C., Cawood, P.A., Johnston, S.T., Zhang, J., Xin, Y.J., Wang, J.M., 2024. Cretaceous coastal mountain building and potential impacts on climate change in East Asia. Science Advances 10, eads0587. https://doi.org/10.1126/sciadv.ads0587

Li, J.H., Zhang, Y.Q., Ratschbacher, L., Zhao, G.C., Dong, S.W., Xin, Y.J., Lü, F., 2022b. Polyphase deformation in the Badu complex: Insights into Triassic intraplate orogeny in South China. Journal of Structural Geology 154. https://doi.org/10.1016/j.jsg.2021.104475

Li, J.H., Zhang, Y.Q., Zhao, G.C., Johnston, S.T., Dong, S.W., Koppers, A., Miggins, D.P., Sun, H.S., Wang, W.B., Xin, Y.J., 2017a. New insights into Phanerozoic tectonics of South China: Early Paleozoic sinistral and Triassic dextral transpression in the east Wuyishan and Chencai domains, NE Cathaysia. Tectonics 36, 819-853. https://doi.org/10.1002/2016TC004461

Li, J.H., Zhao, G.C., Johnston, S.T., Dong, S.W., Zhang, Y.Q., Xin, Y.J., Wang, W.B., Sun, H.S., Yu, Y.Q., 2017b. Permo-Triassic structural evolution of the Shiwandashan and Youjiang structural belts, South China. Journal of Structural

Geology 100, 24-44. https://doi.org/10.1016/j.jsg.2017.05.004

Li, J.Y., Wang, X.L., Gu, Z.D., Huang, Y., Wang, G.G., 2024. Neoproterozoic Multi-Terrane Convergence in South China and Its Resource Implications. Acta Sedimentologica Sinica 42, 1876-1889. (in Chinese with English abstract).

Li, K., Rimmer, S.M., Liu, Q.F., 2018. Geochemical and petrographic analysis of graphitized coals from Central Hunan, China. International Journal of Coal Geology 195, 267-279. https://doi.org/10.1016/j.coal.2018.06.009

Li, M.K., Zhang, S.X., Wei, Y., Xu, C., 2023. Complex Crustal Deformation Beneath the Cathaysia Block in South China: Evidence From Receiver Function Analysis. Earth and Space Science 10. https://doi.org/10.1029/2022ea002235

Li, Q.W., Zhao, J.H., 2020. Amalgamation between the Yangtze and Cathaysia blocks in South China: Evidence from the ophiolite geochemistry. Precambrian Research 350, 105893. https://doi.org/10.1016/j.precamres.2020.105893

Li, S., Chung, S.L., Hou, Z., Chew, D., Wang, T., Wang, B., Wang, Y., 2019. Early Mesozoic Magmatism Within the Tibetan Plateau: Implications for the Paleo-Tethyan Tectonic Evolution and Continental Amalgamation. Tectonics 38, 3505-3543. https://doi.org/10.1029/2019tc005546

Li, S.L., Lai, J.Q., Xiao, W.Z., Belousova, E.A., Rushmer, T., Zhang, L.J., Ou, Q., Liu, C.Y., 2021. Crustal growth event in the Cathaysia Block at 2.5 Ga: evidence from chronology and geochemistry of captured zircons in Jurassic acidic dykes. Geological Magazine 158, 567-582. https://doi.org/10.1017/S0016756820000667

Li, S.Z., Li, X.Y., Zhao, S.J., Yang, Z., Liu, X., Guo, L.L., Wang, Y.M., Hao, Y., Zhang, J., Hu, M.Y., 2016. Global Early Paleozoic Orogens (Ⅲ): Intracontinental Orogen in South China. Journal of Jilin University (Earth Science Edition) 46, 1005-1025. (in Chinese with English abstract). http://dx.doi.org/10.13278/j.cnki.jjuese.201604103

Li, S.Z., Suo, Y.H., Li, X.Y., Zhou, J., Santosh, M., Wang, P.C., Wang, G.Z., Guo, L.L., Yu, S.Y., Lan, H.Y., Dai, L.M., Zhou, Z.Z., Cao, X.Z., Zhu, J.J., Liu, B., Jiang, S.H., Wang, G., Zhang, G.W., 2019. Mesozoic tectono-magmatic response in the East Asian ocean-continent connection zone to subduction of the Paleo-Pacific Plate. Earth-Science Reviews 192, 91-137. https://doi.org/10.1016/j.earscirev.2019.03.003

Li, S.Z., Zheng, Y.F., Suo, Y.H., 2025. Reconstructing the framework of the Paleo-Pacific Plate: A synthetic review. Journal of Structural Geology 199. https://doi.org/10.1016/j.jsg.2025.105505

Li, T.Z., Jiang, M.M., Zhao, L., Chu, Y., Yao, W.H., Wan, B., Chen, L., Ai, Y.S., Bodin, T., Yuan, H.Y., 2023. Continental Fragments in the South China Block: Constraints From Crustal Radial Anisotropy. Journal of Geophysical Research: Solid Earth 128. https://doi.org/10.1029/2023jb026998

Li, W., Chen, Y., Yuan, X.H., Xiao, W.J., Windley, B.F., 2022. Intracontinental deformation of the Tianshan Orogen in response to India-Asia collision. Nature communications 13, 3738. https://doi.org/10.1038/s41467-022-30795-6

Li, X.H., Li, W.X., Li, Z.X., Lo, C.H., Wang, J., Ye, M.F., Yang, Y.H., 2009a. Amalgamation between the Yangtze and Cathaysia Blocks in South China: Constraints from SHRIMP U–Pb zircon ages, geochemistry and Nd–Hf isotopes of the Shuangxiwu volcanic rocks. Precambrian Research 174, 117-128. https://doi.org/10.1016/j.precamres.2009.07.004

Li, X.H., Li, W.X., Wang, X.C., Li, Q.L., Liu, Y., Tang, G.Q., 2009b. Role of mantle-derived magma in genesis of early Yanshanian granites in the Nanling Range,South China:in situ zircon Hf-O isotopic constraints. SCIENCE IN CHINA(SERIES D) 39, 872-887. (in Chinese with English abstract).

Li, X.H., Li, Z.X., Li, W.X., 2014. Detrital zircon U–Pb age and Hf isotope constrains on the generation and reworking of Precambrian continental crust in the Cathaysia Block, South China: A synthesis. Gondwana Research 25, 1202-1215. https://doi.org/10.1016/j.gr.2014.01.003

Li, X.H., Tang, G.Q., Gong, B., Yang, Y.H., Hou, K.J., Hu, Z.C., Li, Q.L., Liu, Y., Li, W.X., 2013. Qinghu zircon: A working reference for microbeam analysis of U-Pb age and Hf and O isotopes. Chinese Science Bulletin 58, 4647-4654. https://doi.org/10.1007/s11434-013-5932-x

Li, X.H., Wang, Y.X., Zhao, Z.H., Chen, D.F., Zhang, H., 1998. SHRIMP U–Pb zircon geochronology for amphibolite from the Precambrian basement in SW Zhejiang and NW Fujian Provinces. Geochimica 27, 327-334. (in Chinese with English abstract).

Li, X.X., Wu, X.Y., 1994. The Cathaysian and Gondwana floras: their contribution to determining the boundary between eastern Gondwana and Laurasia. Journal of Southeast Asian Earth Sciences 9, 309-317. https://doi.org/10.1016/0743-9547(94)90041-8

Li, Y., Dong, S., Zhang, Y., Li, J., Su, J., Han, B., 2016. Episodic Mesozoic constructional events of central South China: constraints from lines of evidence of superimposed folds, fault kinematic analysis, and magma geochronology. International Geology Review 58, 1076-1107. https://doi.org/10.1080/00206814.2016.1146999

Li, Y., Ma, C.Q., Xing, G.F., Zhou, H.W., 2015. The Early Cretaceous evolution of SE China: Insights from the Changle–Nan'ao Metamorphic Belt. Lithos 230, 94-104. https://doi.org/10.1016/j.lithos.2015.05.014

Li, Y.J., Wei, J.H., Santosh, M., Tan, J., Fu, L.B., Zhao, S.Q., 2016. Geochronology and petrogenesis of Middle Permian S-type granitoid in southeastern Guangxi Province, South China: Implications for closure of the eastern Paleo-Tethys. Tectonophysics 682, 1-16. https://doi.org/10.1016/j.tecto.2016.05.048

Li, Z.H., Cui, Q.H., Zhong, X.Y., Liu, M.Q., Wang, Y., Huangfu, P., 2021. Numerical modeling of continental dynamics: questions, progress and perspectives. Acta Geologica Sinica 95, 238-258. (in Chinese with English abstract). https://doi.org/10.19762/j.cnki.dizhixuebao.2020276

Li, Z.X., Li, X.H., 2007. Formation of the 1300-km-wide intracontinental orogen and postorogenic magmatic province in Mesozoic South China: A flat-slab subduction model. Geology 35, 179-182. https://doi.org/10.1130/g23193a.1

Li, Z.X., Li, X.H., Chung, S.L., Lo, C.H., Xu, X.S., Li, W.X., 2012. Magmatic switch-on and switch-off along the South China continental margin since the Permian: Transition from an Andean-type to a Western Pacific-type plate boundary. Tectonophysics 532-535, 271-290. https://doi.org/10.1016/j.tecto.2012.02.011

Li, Z.X., Li, X.H., Wartho, J.A., Clark, C., Li, W.X., Zhang, C.L., Bao, C., 2010. Magmatic and metamorphic events during the early Paleozoic Wuyi-Yunkai orogeny, southeastern South China: New age constraints and pressure-temperature conditions. Geological Society of America Bulletin 122, 772-793. https://doi.org/10.1130/b30021.1

Li, Z.X., Wartho, J.A., Occhipinti, S., Zhang, C.L., Li, X.H., Wang, J., Bao, C.M., 2007. Early history of the eastern Sibao Orogen (South China) during the assembly of Rodinia: New mica 40Ar/39Ar dating and SHRIMP U–Pb detrital zircon provenance constraints. Precambrian Research 159, 79-94. https://doi.org/10.1016/j.precamres.2007.05.003

Liang, X., Wu, G.Y., 2006. Mesozoic evolution of the Ganjiang fault zone and related geodynamic settings. Chinese Journal of Geology 41, 64-80. (in Chinese with English abstract).

Lin, S.F., Beakhouse, G.P., 2013. Synchronous vertical and horizontal tectonism at late stages of Archean cratonization and genesis of Hemlo gold deposit, Superior craton, Ontario, Canada. Geology 41, 359-362. https://doi.org/10.1130/g33887.1

Lin, S.F., Wang, L.J., Xiao, W.J., Xing, G.F., Niu, Z.J., Zhao, X.L., Yin, C.Q., Zhang, S., Liu, H., 2024. The early Paleozoic Wuyi–Yunkai orogeny in South China: a collisional orogeny with a major lag in time between onset of collision and peak metamorphism in subducted continental crust, In: Nance, R.D., Strachan, R.A., Quesada, C., Lin, S. (Eds.), Supercontinents, Orogenesis and Magmatism. Geological Society of London, p. 0. https://doi.org/10.1144/sp542-2023-6

Lin, W., Liu, F., Wang, Y., Meng, L.T., Faure, M., Chu, Y., Nguyen, V.V., Wu, Q.Y., Wei, W., Thu, H.L.T., Vu, T.V., 2024. Temporal and spatial heterogeneity of the Ailaoshan–Song Ma–Song Chay ophiolitic mélange, and its significance on the evolution of Paleo-Tethys. Comptes Rendus. Géoscience 356, 115-136. https://doi.org/10.5802/crgeos.248

Lin, W., Wang, Q.C., Chen, K., 2008. Phanerozoic tectonics of south China block: New insights from the polyphase deformation in the Yunkai massif. Tectonics 27, TC6004. https://doi.org/10.1029/2007TC002207

Liu, D.Y., Jian, P., Kröner, A., Xu, S.T., 2006. Dating of prograde metamorphic events deciphered from episodic zircon growth in rocks of the Dabie–Sulu UHP complex, China. Earth and Planetary Science Letters 250, 650-666. https://doi.org/10.1016/j.epsl.2006.07.043

Liu, F.L., Liou, J.G., 2011. Zircon as the best mineral for P–T–time history of UHP metamorphism: A review on mineral inclusions and U–Pb SHRIMP ages of zircons from the Dabie–Sulu UHP rocks. Journal of Asian Earth Sciences 40, 1-39. https://doi.org/10.1016/j.jseaes.2010.08.007

Liu, H.C., Wang, Y.J., Li, Z.H., Zi, J.W., Huangfu, P.P., 2018. Geodynamics of the Indosinian orogeny between the South China and Indochina blocks: Insights from latest Permian–Triassic granitoids and numerical modeling. Bulletin 130, 1289-1306. https://doi.org/10.1130/B31904.1

Liu, H.S., Chen, Y., Wang, B., Faure, M., Erdmann, S., Martelet, G., Scaillet, B., Huang, F.F., 2020. Role of inherited structure on granite emplacement: An example from the Late Jurassic Shibei pluton in the Wuyishan area (South China) and its tectonic implications. Tectonophysics 779. https://doi.org/10.1016/j.tecto.2020.228394

Liu, J.X., Wang, S., Wang, X.L., Du, D.H., Xing, G.F., Fu, J.M., Chen, X., Sun, Z.M., 2020. Refining the spatio-temporal distributions of Mesozoic granitoids and volcanic rocks in SE China. Journal of Asian Earth Sciences 201, 104503. https://doi.org/10.1016/j.jseaes.2020.104503

Liu, M.X., Yang, D.H., 2022. How do pre-existing weak zones and rheological layering of the continental lithosphere influence the development and evolution of intra-continental subduction? Journal of Asian Earth Sciences 238. https://doi.org/10.1016/j.jseaes.2022.105385

Liu, Q., Yu, J.H., Wang, Q., Su, B., Zhou, M.F., Xu, H., Cui, X., 2012. Ages and geochemistry of granites in the Pingtan–Dongshan Metamorphic Belt, Coastal South China: New constraints on Late Mesozoic magmatic evolution. Lithos 150, 268-286. https://doi.org/10.1016/j.lithos.2012.06.031

Liu, S.F., Peng, S.B., Kusky, T., Polat, A., Han, Q.S., 2018. Origin and tectonic implications of an Early Paleozoic (460–440 Ma) subduction-accretion shear zone in the northwestern Yunkai Domain, South China. Lithos 322, 104-128. https://doi.org/10.1016/j.lithos.2018.10.006

Liu, S.W., Wang, L.S., Li, C., 2007. Rheology of continental lithosphere: An overview. PROGRESS IN GEOPHYSICS 22, 1209-1214. (in Chinese with English abstract).

Liu, T.L., 2018. Sedimentary and tectonic evolution of the Xiuwu Basin on thecontrol of the Lower Cambrian shale gas accumulation. China University of Petroleum, Master dissertation (in Chinese with English abstract). https://doi.org/10.27643/d.cnki.gsybu.2018.000517

Liu, X.C., Chen, Y., Wang, W.R., Xia, M.M., Hu, J., Li, Y.B., Hu, D.G., Song, B., 2020. Carboniferous eclogite and garnet–omphacite granulite from northeastern Hainan Island, South China: Implications for the evolution of the eastern Palaeo-Tethys. Journal of Metamorphic Geology 39, 101-132. https://doi.org/10.1111/jmg.12563

Liu, Y.S., Hu, Z.C., Gao, S., Günther, D., Xu, J., Gao, C.G., Chen, H.H., 2008. In situ analysis of major and trace elements of anhydrous minerals by LA-ICP-MS without applying an internal standard. Chemical Geology 257, 34-43. https://doi.org/10.1016/j.chemgeo.2008.08.004

Livaccari, R.F., Burke, K., Şengör, A.M.C., 1981. Was the Laramide orogeny related to subduction of an oceanic plateau? Nature 289, 276-278.

https://doi.org/10.1038/289276a0

Lo, C.H., Chung, S.L., Lee, T.Y., Wu, G.Y., 2002. Age of the Emeishan flood magmatism and relations to Permian–Triassic boundary events. Earth and Planetary Science Letters 198, 449-458. https://doi.org/10.1016/S0012-821X(02)00535-6

Lu S.H., 2025. Triassic magmatism, anatexis and gneiss dome structure in the southeastern Yunkai Massif, South China. Nanjing University, Master dissertation. pp 1-154.

Ludwig, K.R., 2012. User's manual for Isoplot 3.75, A geochronological toolkit for Microsoft Excel. BGC Special Publication 4: 2455 Ridge Road, Berkeley CA 94709, USA.

Lugmair, G.W., Marti, K., 1978. Lunar initial 143Nd/144Nd: differential evolution of the lunar crust and mantle. Earth and Planetary Science Letters 39, 349-357. https://doi.org/10.1016/0012-821X(78)90021-3

Luo, Y., Yang, J., Zhao, L., Zhao, P., 2025. Lithospheric Deformation of Far-Field Terranes in Response to the India–Asia Collision. Terra Nova 37, 119-128. https://doi.org/10.1111/ter.12756

Ma, S.Y., He, B., Xia, X.P., Li, P.F., Lai, C.K., Bartoli, O., 2025. The development of a pull-apart basin in response to collision of the irregular South China continental margin with Indochina. Geological Society of America Bulletin 137, 1687–1702. https://doi.org/10.1130/b37749.1

Maiti, G., Koptev, A., Baville, P., Gerya, T., Crosetto, S., Andrić-Tomašević, N., 2024. Topography Response to Horizontal Slab Tearing and Oblique Continental Collision: Insights From 3D Thermomechanical Modeling. Journal of Geophysical Research: Solid Earth 129, e2024JB029385. https://doi.org/10.1029/2024JB029385

Mareschal, J., Poirier, A., Rolandone, F., Bienfait, G., Gariépy, C., Lapointe, R., Jaupart, C., 2000. Low mantle heat flow at the edge of the North American continent, Voisey Bay, Labrador. Geophysical Research Letters 27, 823-826. https://doi.org/10.1029/1999GL011069

Marshak, S., Nelson, W.J., McBride, J.H., 2003. Phanerozoic strike-slip faulting in the continental interior platform of the United States: examples from the Laramide Orogen, Midcontinent, and Ancestral Rocky Mountains. Geological Society, London, Special Publications 210, 159-184. https://doi.org/10.1144/GSL.SP.2003.210.01.10

McDowell, F.W., McIntosh, W.C., Farley, K.A., 2005. A precise 40Ar–39Ar reference age for the Durango apatite (U–Th)/He and fission-track dating standard. Chemical Geology 214, 249-263. https://doi.org/10.1016/j.chemgeo.2004.10.002

McKenzie, D.P., Parker, R.L., 1967. The North Pacific: an Example of Tectonics on a Sphere. Nature 216, 1276-1280. https://doi.org/10.1038/2161276a0

McLaren, S., Sandiford, M., Dunlap, W.J., Scrimgeour, I., Close, D., Edgoose, C., 2009. Distribution of Palaeozoic reworking in the Western Arunta Region and northwestern Amadeus Basin from 40Ar/39Ar thermochronology: implications for the evolution of intracratonic basins. Basin Research 21, 315-334. https://doi.org/10.1111/j.1365-2117.2008.00385.x

Meng, Q.R., Zhang, G.W., 1999. Timing of collision of the North and South China blocks: Controversy and reconciliation. Geology 27, 123-126. https://doi.org/10.1130/0091-7613(1999)027<0123:TOCOTN>2.3.CO;2

Metcalfe, I., 1996. Gondwanaland dispersion, Asian accretion and evolution of eastern Tethys. Australian Journal of Earth Sciences 43, 605-623. https://doi.org/10.1080/08120099608728282

Mezger, K., Essene, E.J., Halliday, A.N., 1992. Closure temperatures of the Sm—Nd system in metamorphic garnets. Earth and Planetary Science Letters 113, 397-409. https://doi.org/10.1016/0012-821X(92)90141-H

Mishin, Y.A., Gerya, T.V., Burg, J.-P., Connolly, J.A.D., 2008. Dynamics of double subduction: Numerical modeling. Physics of the Earth and Planetary Interiors 171, 280-295. https://doi.org/10.1016/j.pepi.2008.06.012

Molnar, P., Tapponnier, P., 1975. Cenozoic Tectonics of Asia: Effects of a Continental Collision: Features of recent continental tectonics in Asia can be interpreted as results of the India-Eurasia collision. Science 189, 419-426. https://doi.org/10.1126/science.189.4201.419

Morgan, W.J., 1968. Rises, trenches, great faults, and crustal blocks. Journal of Geophysical Research 73, 1959-1982. https://doi.org/10.1029/JB073i006p01959

Mori, H., Wallis, S., Fujimoto, K., Shigematsu, N., 2015. Recognition of shear heating on a long-lived major fault using Raman carbonaceous material thermometry: implications for strength and displacement history of the MTL, SW Japan. Island Arc 24, 425-446. https://doi.org/10.1111/iar.12129

Moyen, J.F., Janoušek, V., Laurent, O., Bachmann, O., Jacob, J.B., Farina, F., Fiannacca, P., Villaros, A., 2021. Crustal melting vs. fractionation of basaltic magmas: Part 1, granites and paradigms. Lithos 402-403, 106291. https://doi.org/10.1016/j.lithos.2021.106291

Nabelek, P.I., Whittington, A.G., Hofmeister, A.M., 2010. Strain heating as a mechanism for partial melting and ultrahigh temperature metamorphism in convergent orogens: Implications of temperature-dependent thermal diffusivity and rheology. Journal of Geophysical Research: Solid Earth 115, B12417. https://doi.org/10.1029/2010jb007727

Nie, S.Y., Yin, A., Rowley, D.B., Jin, Y.G., 1994. Exhumation of the Dabie Shan ultra-high-pressure rocks and accumulation of the Songpan-Ganzi flysch sequence, central China. Geology 22, 999-1002.

Nie, T.C., Zhu, G.L., 2004. On the characteristics and evolution of geological structures in the intermediate section of the Zhenghe-Dapu deep faulted zone. Geology of Fujian 23, 186-194. (in Chinese with English abstract).

Oh, C.W., 2021. P-T-t Paths, Encyclopedia of Geology, pp. 597-611. https://doi.org/10.1016/b978-0-08-102908-4.00163-6

Parrish, R.R., 1990. U–Pb dating of monazite and its application to geological problems. Canadian Journal of Earth Sciences 27, 1431-1450. https://doi.org/10.1139/e90-152

Passchier, C.W., Trouw, R.A., 2005. Microtectonics. Springer Science & Business Media.

Paton, C., Hellstrom, J., Paul, B., Woodhead, J., Hergt, J., 2011. Iolite: Freeware for the visualisation and processing of mass spectrometric data. Journal of Analytical Atomic Spectrometry 26, 2508-2518. https://doi.org/10.1039/C1JA10172B

Peng, B.X., Wang, Y.J., Fan, W.M., Peng, T.P., Liang, X.Q., 2006. LA-ICPMS Zircon U-Pb Dating for Three Indosinian Granitic Plutons from Central Hunan and Western Guangdong Provinces and Its Petrogenetic Implications. Acta Geologica Sinica - English Edition 80, 660-669. https://doi.org/10.1111/j.1755-6724.2006.tb00290.x

Peng, N., Wang, Z.Y., Nie, B.F., Zhang, X.Y., Liu, Y.S., 2023. Correlation between fractal characteristics of fault structures and metallogenic density in the Nanling area, South China. Ore Geology Reviews 162. https://doi.org/10.1016/j.oregeorev.2023.105717

Peng, S.B., Fu, J.M., Liu, Y.H., 2004. The discovery and significance of A-type charnokite in southeast Guangxi Province, China. Science Technology and Engineering 4, 832-834. (in Chinese with English abstract).

Perchuk, A.L., Safonov, O.G., Smit, C.A., van Reenen, D.D., Zakharov, V.S., Gerya, T.V., 2018. Precambrian ultra-hot orogenic factory: Making and reworking of continental crust. Tectonophysics 746, 572-586. https://doi.org/10.1016/j.tecto.2016.11.041

Petroccia, A., Carosi, R., Montomoli, C., Iaccarino, S., Vitale Brovarone, A., 2022. Thermal variation across collisional orogens: Insights from the hinterland–foreland transition zone of the Sardinian Variscan belt. Terra Nova 35, 113-123. https://doi.org/10.1111/ter.12635

Pitzer, K.S., Sterner, S.M., 1994. Equations of state valid continuously from zero to extreme pressures for H2O and CO2. The Journal of chemical physics 101, 3111-3116. https://doi.org/10.1063/1.467624

Prasannakumar, V., McCaig, A., 2016. Reactivation and strain localisation in Bhavani shear zone, South India. Journal of the Geological Society of India 88, 421-432.

Qin, X.F., Pan, Y.M., Li, J., Li, R.S., Zhou, F.S., Hu, G.A., Zhong, F.Y., 2006. Zircon SHRIMP U–Pb geochronology of the Yunkai metamorphic complex in southeastern Guangxi, China. Geological Bulletin of China 25, 553-559. (in Chinese with English abstract).

Qin, X.F., Wang, Z.Q., Wang, T., Xiong, B., Feng, Z.H., Yang, W., Zhu, A., Song, J., Huang, J., 2015. The reconfirmation of age and tectonic setting of the volcanic rocks of Yingyangguan Group in the eastern Guangxi: Constraints on the structural pattern of the southwestern segment of Qinzhou-Hangzhou joint belt. Acta Geoscientica Sinica 36, 283-292. (in Chinese with English abstract).

Qing, L., Jiang, Y.H., Du, F.G., 2020a. Geodynamics of Late Paleozoic to Early Mesozoic Magmatism in South China: Insights from the Genesis of the Late Permian S-Type Granites in the Yunkai Massif. The Journal of Geology 128, 275-301. https://doi.org/10.1086/708465

Qing, L., Jiang, Y.H., Du, F.G., 2020b. Petrogenesis and tectonic significance of early Indosinian A-type granites in the Xinxing pluton, southern South China. Mineralogy and Petrology 114, 217-242. https://doi.org/10.1007/s00710-020-00701-3

Qiu, H.B., Lin, W., Chen, Y., Faure, M., 2023. Jurassic–Early Cretaceous tectonic evolution of the North China Craton and Yanshanian intracontinental orogeny in East Asia: New insights from a general review of stratigraphy, structures, and magmatism. Earth-Science Reviews 237, 104320. https://doi.org/10.1016/j.earscirev.2023.104320

R Core Team, 2020. R: A language and environment for statistical computing. Citeseer.

Raimondo, T., Hand, M., Collins, W.J., 2014. Compressional intracontinental orogens: Ancient and modern perspectives. Earth-Science Reviews 130, 128-153. https://doi.org/10.1016/j.earscirev.2013.11.009

Ranalli, G., 1995. Rheology of the Earth. Springer Science & Business Media.

Ranalli, G., 1997. Rheology of the lithosphere in space and time. Geological Society, London, Special Publications 121, 19-37. https://doi.org/10.1029/RG021i006p01458

Ranalli, G., Murphy, D.C., 1987. Rheological stratification of the lithosphere. Tectonophysics 132, 281-295. https://doi.org/10.1016/0040-1951(87)90348-9

Reiner, M., 1958. Rheology, Elasticity and Plasticity/Elastizität und Plastizität. Springer, pp. 434-550.

Ren, J.S., 1989. Some new ideas on tectonic evolution of eastern China and adjacent areas. Regional Geology of China 1, 289-300.

RGMRGD, 1964. Regional Geological Mapping and Report of Guangdong Province–Yangjiang Sheet. Institute of Geoscience, Ministry of Geology, Beijing, China, p. (In Chinese)

Ritter, S., Balázs, A., Ribeiro, J., Gerya, T., 2024. Magmatic fingerprints of subduction initiation and mature subduction: numerical modelling and observations from the Izu-Bonin-Mariana system. Frontiers in Earth Science 12. https://doi.org/10.3389/feart.2024.1286468

Rosenberg, C.L., Handy, M.R., 2005. Experimental deformation of partially melted granite revisited: implications for the continental crust. Journal of Metamorphic Geology 23, 19-28. https://doi.org/10.1111/j.1525-1314.2005.00555.x

Ross, J.V., Bustin, R.M., 1990. The role of strain energy in creep graphitization of anthracite. Nature 343, 58-60. https://doi.org/10.1038/343058a0

Rowley, D.B., Xue, F., Tucker, R.D., Peng, Z.X., Baker, J., Davis, A., 1997. Ages of ultrahigh pressure metamorphism and protolith orthogneisses from the eastern Dabie Shan: U/Pb zircon geochronology. Earth and Planetary Science Letters 151, 191-203. https://doi.org/10.1016/S0012-821X(97)81848-1

Rozel, A.B., Golabek, G.J., Jain, C., Tackley, P.J., Gerya, T., 2017. Continental crust formation on early Earth controlled by intrusive magmatism. Nature 545, 332-335. https://doi.org/10.1038/nature22042

Sánchez, M.A., García, H.P.A., Acosta, G., Gianni, G.M., Gonzalez, M.A., Ariza, J.P., Martinez, M.P., Folguera, A., 2019. Thermal and lithospheric structure of the Chilean-Pampean flat-slab from gravity and magnetic data, Andean Tectonics, pp. 487-507. https://doi.org/10.1016/b978-0-12-816009-1.00005-8

Sawyer, E.W., 2010. Migmatites formed by water-fluxed partial melting of a leucogranodiorite protolith: Microstructures in the residual rocks and source of the fluid. Lithos 116, 273-286. https://doi.org/10.1016/j.lithos.2009.07.003

Schito, A., Muirhead, D.K., Parnell, J., 2023. Towards a kerogen-to-graphite kinetic model by means of Raman spectroscopy. Earth-Science Reviews 237, 104292. https://doi.org/10.1016/j.earscirev.2022.104292

Scotese, C., 2016. PALEOMAP PaleoAtlas for GPlates and the PaleoData Plotter Program. https://doi.org/10.13140/RG.2.2.34367.00166

Scrimgeour, Close, 1999. Regional high-pressure metamorphism during intracratonic deformation: the Petermann Orogeny, central Australia. Journal of Metamorphic Geology 17, 557-572. https://doi.org/10.1046/j.1525-1314.1999.00217.x

Shan, B., Afonso, J.C., Yang, Y., Grose, C.J., Zheng, Y., Xiong, X., Zhou, L., 2014. The thermochemical structure of the lithosphere and upper mantle beneath south China: Results from multiobservable probabilistic inversion. Journal of Geophysical Research: Solid Earth 119, 8417-8441. https://doi.org/10.1002/2014jb011412

Shan, B., Xiong, X., Zhao, K.F., Xie, Z.J., Zheng, Y., Zhou, L., 2017. Crustal and upper mantle structure of South China from Rayleigh wave tomography. Geophysical Journal International, 1643-1654. https://doi.org/10.1093/gji/ggw477

Shao, J.G., Peng, S.M., Peng, S.B., 1995. 40Ar/36Ar-39Ar/36Ar isocharon dating for peripheral faults of Yunkai Massif. Guangdong Geology 10. (in Chinese with

English abstract).

She, Z.B., Ma, C.Q., Mason, R., Li, J.W., Wang, G.C., Lei, Y.H., 2006. Provenance of the Triassic Songpan–Ganzi flysch, west China. Chemical Geology 231, 159-175. https://doi.org/10.1016/j.chemgeo.2006.01.001

Shen, L., Zhao, L.F., Xie, X.B., Yang, G., Yao, Z.X., 2023. Extremely weak Lg attenuation reveals ancient continental relicts in the South China block. Earth and Planetary Science Letters 611. https://doi.org/10.1016/j.epsl.2023.118144

Shen, W.S., Wiens, D.A., Lloyd, A.J., Nyblade, A.A., 2020. A Geothermal Heat Flux Map of Antarctica Empirically Constrained by Seismic Structure. Geophysical Research Letters 47. https://doi.org/10.1029/2020gl086955

Shen, W.Z., Ling, H.F., Li, W.X., Wang, D.Z., 2000. Crust evolution in Southeast China: evidence from Nd model ages of granitoids. Science in China Series D: Earth Sciences 43, 36-49. https://doi.org/10.1007/BF02877829

Shi, W.J., Li, Y.J., Wei, J.H., 2023. Formation of the Middle Permian Danzhou monzogranite in northern Hainan Island (South China): Insight into the evolution of the eastern Paleo-Tethys. Lithos 446-447. https://doi.org/10.1016/j.lithos.2023.107140

Shu, L.S., 2006. Predevonian Tectonic Evolution of South China: from Cathaysian Block to Caledonian Period Folded Orogenic Belt. Geological Journal of China Universities 12, 418-431. (in Chinese with English abstract).

Shu, L.S., 2012. An analysis of principal features of tectonic evolution in South China Block. Geological Bulletin of China 31, 1035-1053. (in Chinese with English abstract).

Shu, L.S., Charvet, J., Shi, Y.S., Faure, M., Cluzel, D., Guo, L.Z., 1991. Structural analysis of the Nanchang-Wanzai sinistral ductile shear zone (Jiangnan region, South China). Journal of Southeast Asian Earth Sciences 6, 13-23. https://doi.org/10.1016/0743-9547(91)90091-B

Shu, L.S., Chen, X.Y., Lou, F.S., 2020. Pre-Jurassic tectonics of the South China. Acta

Geologica Sinica 94, 333-360. (in Chinese with English abstract). https://doi.org/10.19762/j.cnki.dizhixuebao.2020046

Shu, L.S., Faure, M., Wang, B., Zhou, X.M., Song, B., 2008a. Late Palaeozoic–Early Mesozoic geological features of South China: Response to the Indosinian collision events in Southeast Asia. Comptes Rendus Geoscience 340, 151-165. https://doi.org/10.1016/j.crte.2007.10.010

Shu, L.S., Jahn, B.M., Charvet, J., Santosh, M., Wang, B., Xu, X.S., Jiang, S.Y., 2014. Early Paleozoic depositional environment and intraplate tectono-magmatism in the Cathaysia Block (South China): Evidence from stratigraphic, structural, geochemical and geochronological investigations. American Journal of Science 314, 154-186.

Shu, L.S., Lu, H.F., Jia, D., 1999. Study of the 40Ar/39Ar Isotopic Age for the Early Paleozoic Tectonothermal Event in the Wuyishan Region, South China. Journal-Nanjing University Natural Sciences Edition 35, 668-674. (in Chinese with English abstract).

Shu, L.S., Wang, B., Cawood, P.A., Santosh, M., Xu, Z.Q., 2015. Early Paleozoic and Early Mesozoic intraplate tectonic and magmatic events in the Cathaysia Block, South China. Tectonics 34, 1600-1621. https://doi.org/10.1002/2015TC003835

Shu, L.S., Wang, J.Q., Yao, J.L., 2019. Tectonic evolution of the eastern Jiangnan region, South China: New findings and implications on the assembly of the Rodinia supercontinent. Precambrian Research 322, 42-65. https://doi.org/10.1016/j.precamres.2018.12.007

Shu, L.S., Yao, J.L., Wang, B., Faure, M., Charvet, J., Chen, Y., 2021. Neoproterozoic plate tectonic process and Phanerozoic geodynamic evolution of the South China Block. Earth-Science Reviews 216, 103596. https://doi.org/10.1016/j.earscirev.2021.103596

Shu, L.S., Yu, J.H., Jia, D., Wang, B., Shen, W.Z., Zhang, Y.Q., 2008b. Early Paleozoic orogenic belt in the eastern segment of South China. Geological Bulletin of China

27, 1581-1593.

Shu, L.S., Zhou, X.M., 2002. Late Cenozoic Tectonics of Southeast China. Geological review 48, 249-260. (in Chinese with English abstract).

Shu, L.S., Zhou, X.M., Deng, P., Wang, B., Jiang, S.Y., Yu, J.H., Zhao, X.X., 2009. Mesozoic tectonic evolution of the Southeast China Block: New insights from basin analysis. Journal of Asian Earth Sciences 34, 376-391. https://doi.org/10.1016/j.jseaes.2008.06.004

Shu, L.S., Zhou, X.M., Deng, P., Yu, X.Q., 2006. Principal geological features of Nanling tectonic belt, South China. Geological review 52, 251-265. (in Chinese with English abstract).

Shu, L.S., Zhou, X.M., Deng, P., Yu, X.Q., Wang, B., Zu, F.P., 2004. Geological features and tectonic evolution of Meso-Cenozoic basins in southeastern China. Geological Bulletin of China 23, 876-884. (in Chinese with English abstract).

Shui, T., Yan, J.Y., Shi, H.S., Pan, M.B., Wang, J.D., 1993. The elementary features and evolution models of Zhenghe-Dapu fault zone. Volcanology and Mineral Resources (in Chinese) 2, 53-62. (in Chinese with English abstract).

Smit, M.A., Scherer, E.E., Mezger, K., 2013. Lu–Hf and Sm–Nd garnet geochronology: Chronometric closure and implications for dating petrological processes. Earth and Planetary Science Letters 381, 222-233. https://doi.org/10.1016/j.epsl.2013.08.046

Song, M.J., 2017. Early Paleozoic and Early Mesozoicintracontinental tectonic evolution in South China. Nanjing University, Doctoral dissertation, 1-154.

Song, M.J., Shu, L.S., Santosh, M., 2017. Early Mesozoic intracontinental orogeny and stress transmission in South China: evidence from Triassic peraluminous granites. Journal of the Geological Society 174, 591-607. https://doi.org/10.1144/jgs2016-098

Song, M.J., Shu, L.S., Santosh, M., Li, J.Y., 2015. Late Early Paleozoic and Early Mesozoic intracontinental orogeny in the South China Craton: Geochronological and geochemical evidence. Lithos 232, 360-374. https://doi.org/10.1016/j.lithos.2015.06.019

Song, P.P., Ding, L., Lippert, P.C., Li, Z.Y., Zhang, L.Y., Xie, J., 2020. Paleomagnetism of Middle Triassic Lavas From Northern Qiangtang (Tibet): Constraints on the Closure of the Paleo-Tethys Ocean. Journal of Geophysical Research: Solid Earth 125. https://doi.org/10.1029/2019jb017804

Spang, A., Thielmann, M., Kiss, D., 2024. Rapid Ductile Strain Localization Due To Thermal Runaway. Journal of Geophysical Research: Solid Earth 129. https://doi.org/10.1029/2024jb028846

Stacey, J.S., Kramers, J.D., 1975. Approximation of terrestrial lead isotope evolution by a two-stage model. Earth and Planetary Science Letters 26, 207-221. https://doi.org/10.1016/0012-821X(75)90088-6

Stern, R.J., Gerya, T., 2018. Subduction initiation in nature and models: A review. Tectonophysics 746, 173-198. https://doi.org/10.1016/j.tecto.2017.10.014

Stipp, M., Stünitz, H., Heilbronner, R., Schmid, S.M., 2002. The eastern Tonale fault zone: a 'natural laboratory' for crystal plastic deformation of quartz over a temperature range from 250 to 700°C. Journal of Structural Geology 24, 1861-1884. https://doi.org/10.1016/S0191-8141(02)00035-4

Su, J.B., 2023. Accelerated subduction of the western Pacific Plate promotes the intracontinental uplift and magmatism in late Jurassic South China. Tectonophysics 869. https://doi.org/10.1016/j.tecto.2023.230136

Sun, H.S., Li, J.H., Zhang, Y.Q., Dong, S.W., Xin, Y.J., Yu, Y.Q., 2018. Early Paleozoic tectonic reactivation of the Shaoxing-Jiangshan fault zone: Structural and geochronological constraints from the Chencai domain, South China. Journal of Structural Geology 110, 116-130. https://doi.org/10.1016/j.jsg.2018.03.003

Sun, J.J., Shu, L.S., Santosh, M., Wang, L.S., 2018. Precambrian crustal evolution of the central Jiangnan Orogen (South China): Evidence from detrital zircon U-Pb ages and Hf isotopic compositions of Neoproterozoic metasedimentary rocks.

Precambrian Research 318, 1-24. https://doi.org/10.1016/j.precamres.2018.09.008

Sun, T., 2006. A new map showing the distribution of granites in South China and its explanatory notes. Geological Bulletin of China 25, 332-335. (in Chinese with English abstract).

Sun, Y.J., Dong, S.W., Liu, M., Zhang, H., Shi, Y.L., 2025. The rheological structure of East Asian continental lithosphere. Tectonophysics 895. https://doi.org/10.1016/j.tecto.2024.230575

Sun, Y.Y., Dong, S.W., Wang, X.Q., Liu, M., Zhang, H., Shi, Y.L., 2022. Three‐Dimensional Thermal Structure of East Asian Continental Lithosphere. Journal of Geophysical Research: Solid Earth 127. https://doi.org/10.1029/2021jb023432

Sweeney, J.J., Burnham, A.K., 1990. Evaluation of a Simple Model of Vitrinite Reflectance Based on Chemical Kinetics1. AAPG Bulletin 74, 1559-1570. https://doi.org/10.1306/0c9b251f-1710-11d7-8645000102c1865d

Tao, N., Li, Z.X., Danišík, M., Evans, N.J., Li, R.X., Pang, C.J., Li, W.X., Jourdan, F., Yu, Q., Liu, L.P., Batt, G.E., Xu, Y.G., 2019. Post-250 Ma thermal evolution of the central Cathaysia Block (SE China) in response to flat-slab subduction at the proto-Western Pacific margin. Gondwana Research 75, 1-15. https://doi.org/10.1016/j.gr.2019.03.019

Tarbuck, E.J., Lutgens, F.K., Tasa, D., 2017. An introduction to physical geology, 12th Edition ed. Pearson Education Limited.

Taylor, J., Stevens, G., 2010. Selective entrainment of peritectic garnet into S-type granitic magmas: Evidence from Archaean mid-crustal anatectites. Lithos 120, 277-292. https://doi.org/10.1016/j.lithos.2010.08.015

Taylor, R.J.M., Clark, C., Fitzsimons, I.C.W., Santosh, M., Hand, M., Evans, N., McDonald, B., 2014. Post-peak, fluid-mediated modification of granulite facies zircon and monazite in the Trivandrum Block, southern India. Contributions to Mineralogy and Petrology 168, 1044. https://doi.org/10.1007/s00410-014-1044-0

Taylor, R.J.M., Kirkland, C.L., Clark, C., 2016. Accessories after the facts: Constraining the timing, duration and conditions of high-temperature metamorphic processes. Lithos 264, 239-257. https://doi.org/10.1016/j.lithos.2016.09.004

Thomson, S.N., Gehrels, G.E., Ruiz, J., Buchwaldt, R., 2012. Routine low-damage apatite U-Pb dating using laser ablation-multicollector-ICPMS. Geochemistry, geophysics, geosystems 13, Q0AA21. https://doi.org/10.1029/2011gc003928

Thöni, M., 2002. Sm–Nd isotope systematics in garnet from different lithologies (Eastern Alps): age results, and an evaluation of potential problems for garnet Sm–Nd chronometry. Chemical Geology 185, 255-281. https://doi.org/10.1016/s0009-2541(01)00410-7

Tian, Y., Wang, W., Wang, L.Z., Li, X., Xie, G.G., Huang, S.F., 2020. Age and petrogenesis of the Yingyangguan volcanic rocks: Implications on constraining the boundary between Yangtze and Cathaysia blocks, South China. Lithos 376-377. https://doi.org/10.1016/j.lithos.2020.105775

Tibaldi, A.M., Barzola, M.G., Cristofolini, E.A., Otamendi, J.E., Demichelis, A.H., Leisen, M., Romero, R., Barra, F., Camilletti, G., Armas, P., 2019. Syn-deformational anatexis along the Santa Rosa river section, Argentina: Feedback relations between deformation, metamorphism and melt extraction. Journal of Structural Geology 124, 151-167. https://doi.org/10.1016/j.jsg.2019.04.011

Tomascak, P.B., Krogstad, E.J., Walker, R.J., 1996. U-Pb monazite geochronology of granitic rocks from Maine: implications for late Paleozoic tectonics in the Northern Appalachians. The Journal of Geology 104, 185-195. https://doi.org/10.1086/629813

Tong, L.X., Li, C., Liu, Z., Zhai, M.G., Li, W.X., 2021. First report of phengites in the Longyou paragneiss in the northern Early Paleozoic Wuyi-Yunkai orogen, South China: P-T conditions, zircon U-Pb ages and tectonic implications. Journal of Asian Earth Sciences 214. https://doi.org/10.1016/j.jseaes.2021.104754

Tullis, J.A., 1979. High temperature deformation of rocks and minerals. Reviews of Geophysics 17, 1137-1154. https://doi.org/10.1029/RG017i006p01137

Tumarkina, E., Misra, S., Burlini, L., Connolly, J.A.D., 2011. An experimental study of the role of shear deformation on partial melting of a synthetic metapelite. Tectonophysics 503, 92-99. https://doi.org/10.1016/j.tecto.2010.12.004

Turcotte, D.L., Schubert, G., 2002. Geodynamics. Cambridge university press.

Ueda, K., Gerya, T.V., Burg, J.P., 2012. Delamination in collisional orogens: Thermomechanical modeling. Journal of Geophysical Research: Solid Earth 117. https://doi.org/10.1029/2012JB009144

Vanderhaeghe, O., Teyssier, C., 2001. Partial melting and flow of orogens. Tectonophysics 342, 451-472. https://doi.org/10.1016/S0040-1951(01)00175-5

Vauchez, A., Tommasi, A., Barruol, G., 1998. Rheological heterogeneity, mechanical anisotropy and deformation of the continental lithosphere. Tectonophysics 296, 61-86. https://doi.org/10.1016/S0040-1951(98)00137-1

Vigneresse, J.L., 1995. Crustal regime of deformation and ascent of granitic magma. Tectonophysics 249, 187-202.

Vlaha, D.R., Zuza, A.V., Chen, L., Harlaux, M., 2024. Hot Cordilleran hinterland promoted lower crust mobility and decoupling of Laramide deformation. Nature communications 15, 3750. https://doi.org/10.1038/s41467-024-48182-8

Voshage, H., Hofmann, A., Mazzucchelli, M., Rivalenti, G., Sinigoi, S., Raczek, I., Demarchi, G., 1990. Isotopic evidence from the Ivrea Zone for a hybrid lower crust formed by magmatic underplating. Nature 347, 731-736. https://doi.org/10.1038/347731a0

Wakita, K., 2013. Geology and tectonics of Japanese islands: A review – The key to understanding the geology of Asia. Journal of Asian Earth Sciences 72, 75-87. https://doi.org/10.1016/j.jseaes.2012.04.014

Wan, Y.S., Liu, D.Y., Wilde, S.A., Cao, J.J., Chen, B., Dong, C.Y., Song, B., Du, L.L., 2010. Evolution of the Yunkai Terrane, South China: Evidence from SHRIMP zircon U–Pb dating, geochemistry and Nd isotope. Journal of Asian Earth Sciences 37, 140-153. https://doi.org/10.1016/j.jseaes.2009.08.002

Wang, D., Zheng, J.P., Ma, Q., Griffin, W.L., Zhao, H., Wong, J., 2013. Early Paleozoic crustal anatexis in the intraplate Wuyi–Yunkai orogen, South China. Lithos 175-176, 124-145. https://doi.org/10.1016/j.lithos.2013.04.024

Wang, E.C., Meng, Q.R., 2009. Mesozoic and Cenozoic tectonic evolution of the Longmenshan fault belt. Science in China Series D: Earth Sciences 52, 579-592. https://doi.org/10.1007/s11430-009-0053-8

Wang, H.N., Liu, F.L., Wang, F., Ji, L., Zhu, J.J., Thanh, N.X., 2022. Metamorphic Evolution and Orogenic Process Related to the Eastern Paleo-Tethyan Warm Subduction and Indochina–South China Collision. Journal of Petrology 63. https://doi.org/10.1093/petrology/egac114

Wang, L.S., Li, C., Liu, F.T., Li, H., Lu, H.F., Liu, S.W., 2000. Thermal-rheological structure of the lithosphere beneath two types of basins in eastern and western China. Science in China Series D: Earth Sciences 43, 200-207. https://doi.org/10.1007/BF02911945

Wang, L.Z., Tian, Y., Li, X., TU, B., TAN, J.J., XIE, G.G., ZHANG, Z.Y., ZHANG, J.Y., 2019. 40Ar/39Ar dating of Yingyangguan tectonic melange in the eastern Guangxi, China and its tectonic implications. Journal of Earth Sciences and Environment 41, 631-643. (in Chinese with English abstract).

Wang, L.Z., Tian, Y., Li, X., Xie, G.G., Tu, B., Zhang, Z.Y., Zhang, J.Y., Zeng, B.F., 2020. Composition and deformation of the Yingyangguan tectonic mélange in eastern Guangxi. Geotectonica et Metallogenia 44, 340-356. (in Chinese with English abstract).

Wang, S.J., Li, S.G., 2014. Migmatite and its geodynamic implications. Earth Science Frontiers 21, 21-31. (in Chinese with English abstract).

Wang, T.T., Zheng, J.P., Zhao, H., 2020. Unexposed Archean components and complex evolution beneath the Cathaysia Block: Evidence from zircon xenocrysts in the

Cenozoic basalts in Leizhou Peninsula, South China. Journal of Asian Earth Sciences 192, 104268. https://doi.org/10.1016/j.jseaes.2020.104268

Wang, X.D., Xu, D.M., Wang, L., Zhou, D., Hu, J., Ke, X.Z., 2020. Reworking of Indosinian tectono-thermal events in the Yunkai massif: Gneissic multi-mineral U-Pb geochronological evidence. Earth Science 45, 1653-1675. (in Chinese with English abstract). https://doi.org/10.3799/dqkx.2019.151

Wang, X.R., Li, Q.S., Zhang, H.S., Guo, C., 2018. Study of P-wave velocity structure in upper mantle in eastern South China. Global Geology 37, 620-626. (in Chinese with English abstract).

Wang, Y., Lin, W., Faure, M., Van Nguyen, V., Meng, L.T., Chu, Y., Wei, W., Thu, H.L.T., Lepvrier, C., Van Vu, T., Li, Q.L., Wang, H., Chen, Z.C., Wu, L., Wang, F., 2022. Correlation among the Ailaoshan–Song Ma–Song Chay orogenic belts and implications for the evolution of the eastern Paleo-Tethys Ocean. Tectonophysics 843, 229618. https://doi.org/10.1016/j.tecto.2022.229618

Wang, Y., Wang, Y.J., Li, S.B., Seagren, E., Zhang, Y.Z., Zhang, P.Z., Qian, X., 2020. Exhumation and landscape evolution in eastern South China since the Cretaceous: New insights from fission-track thermochronology. Journal of Asian Earth Sciences 191, 104239. https://doi.org/10.1016/j.jseaes.2020.104239

Wang, Y.B., Liu, S.W., Chen, C.Q., Jiang, G.Z., Wu, J.H., Guo, L.Y., Zhang, H.H., Wang, Z.T., Jiang, X.X., Zhu, C.Q., Zuo, Y.H., Hu, J., Zhang, C., He, L.J., Hu, S.B., Pang, Z.H., Wang, J.Y., 2024. Compilation of terrestrial heat flow data in continental China (5th edition). CHINESE JOURNAL OF GEOPHYSICS 67, 4233-4265. (in Chinese with English abstract). https://doi.org/10.6038/cjg2024S0284

Wang, Y.D., Yu, J.H., Li, X.L., Jiang, W., Xu, H., Li, M.Y., 2021. Western boundary between the Yangtze and Cathaysia blocks constrained by Neoproterozoic to Cambrian sedimentary rocks in the northern and eastern Guangxi Province, South China. Acta Geologica Sinica 95, 1712-1726.

Wang, Y.J., Fan, W.M., Cawood, P.A., Ji, S.C., Peng, T.P., Chen, X.Y., 2007a. Indosinian high-strain deformation for the Yunkaidashan tectonic belt, south China: Kinematics and 40Ar/39Ar geochronological constraints. Tectonics 26, TC6008. https://doi.org/10.1029/2007tc002099

Wang, Y.J., Fan, W.M., Guo, F., Peng, T.P., Li, C.W., 2003. Geochemistry of Mesozoic Mafic Rocks Adjacent to the Chenzhou-Linwu fault, South China: Implications for the Lithospheric Boundary between the Yangtze and Cathaysia Blocks. International Geology Review 2003, 263-286. https://doi.org/10.2747/0020-6814.45.3.263

Wang, Y.J., Fan, W.M., Sun, M., Liang, X.Q., Zhang, Y.H., Peng, T.P., 2007b. Geochronological, geochemical and geothermal constraints on petrogenesis of the Indosinian peraluminous granites in the South China Block: A case study in the Hunan Province. Lithos 96, 475-502. https://doi.org/10.1016/j.lithos.2006.11.010

Wang, Y.J., Fan, W.M., Zhang, G.W., Zhang, Y.H., 2013. Phanerozoic tectonics of the South China Block: Key observations and controversies. Gondwana Research 23, 1273-1305. https://doi.org/10.1016/j.gr.2012.02.019

Wang, Y.J., Fan, W.M., Zhao, G.C., Ji, S.C., Peng, T.P., 2007c. Zircon U–Pb geochronology of gneissic rocks in the Yunkai massif and its implications on the Caledonian event in the South China Block. Gondwana Research 12, 404-416. https://doi.org/10.1016/j.gr.2006.10.003

Wang, Y.J., Qian, X., Cawood, P.A., Gan, C.S., Zhang, Y.Z., Zhang, F.F., Asis, J.B., Yan, Y.G., Wang, C., 2024. Temporal-spatial patterns of Mesozoic Paleo-Pacific and Tethyan supra-subduction systems in SE Asia: Key observations and controversies in Borneo and its surroundings. Earth-Science Reviews 252, 104762. https://doi.org/10.1016/j.earscirev.2024.104762

Wang, Y.J., Qian, X., Cawood, P.A., Liu, H.C., Feng, Q.L., Zhao, G.C., Zhang, Y.H., He, H.Y., Zhang, P.Z., 2018. Closure of the East Paleotethyan Ocean and amalgamation of the Eastern Cimmerian and Southeast Asia continental fragments.

Earth-Science Reviews 186, 195-230. https://doi.org/10.1016/j.earscirev.2017.09.013

Wang, Y.J., Wang, Y., Zhang, Y.Z., Cawood, P.A., Qian, X., Gan, C.S., Zhang, F.F., Zhang, P.Z., 2021. Triassic two-stage intra-continental orogensis of the South China Block, driven by Paleotethyan closure and interactions with adjoining blocks. Journal of Asian Earth Sciences 206, 104648. https://doi.org/10.1016/j.jseaes.2020.104648

Wang, Y.J., Wu, C.M., Zhang, A.M., Fan, W.M., Zhang, Y.H., Zhang, Y.Z., Peng, T.P., Yin, C.Q., 2012. Kwangsian and Indosinian reworking of the eastern South China Block: Constraints on zircon U–Pb geochronology and metamorphism of amphibolites and granulites. Lithos 150, 227-242. https://doi.org/10.1016/j.lithos.2012.04.022

Wang, Y.J., Zhang, A.M., Fan, W.M., Zhao, G.C., Zhang, G.W., Zhang, Y.Z., Zhang, F.F., Li, S.Z., 2011. Kwangsian crustal anatexis within the eastern South China Block: Geochemical, zircon U–Pb geochronological and Hf isotopic fingerprints from the gneissoid granites of Wugong and Wuyi–Yunkai Domains. Lithos 127, 239-260. https://doi.org/10.1016/j.lithos.2011.07.027

Wang, Y.J., Zhang, Y., Fan, W.M., Xi, X.W., Guo, F., Lin, G., 2002. Numerical modeling of the formation of Indo-Sinian peraluminous granitoids in Hunan Province: Basaltic underplating versus tectonic thickening. Science in China Series D: Earth Sciences 45, 1042-1056. https://doi.org/10.1007/BF02911241

Wang, Y.J., Zhang, Y.H., Fan, W.M., Peng, T.P., 2005. Structural signatures and 40Ar/39Ar geochronology of the Indosinian Xuefengshan tectonic belt, South China Block. Journal of Structural Geology 27, 985-998. https://doi.org/10.1016/j.jsg.2005.04.004

Wang, Y.N., Wang, Q.F., Deng, J., Xue, S., Li, C., Ripley, E.M., 2021. Late Permian–Early Triassic mafic dikes in the southwestern margin of the South China block: Evidence for Paleo-Pacific subduction. Lithos 384-385.

https://doi.org/10.1016/j.lithos.2021.105994

Wang, Y.Y., Song, C.Z., Li, J.H., Lin, S.F., Li, Z.W., Yuan, F., Ren, S.L., 2022. Geochronology and structural deformation of Precambrian metamorphic basement in the eastern Jiangnan orogenic belt: constraints on the assembly time of the Yangtze and Cathaysia blocks. Earth Science Informatics 15, 1545-1562. https://doi.org/10.1007/s12145-022-00777-9

Wang, Z.H., Lu, H.F., 2000. Ductile deformation and 40Ar/39Ar dating of the Changle Nanao ductile shear zone, southeastern China. Journal of Structural Geology 22, 561-570.

Wang, Z.H., Yang, W.Q., Zhou, D., Niu, Z.J., He, Y.Y., Song, F., 2018. Detrital Zircon U-Pb Geochronological Records and Its Response of Provenance Transformation of Strata Surrounding Cambrian-Devonian Unconformity in Eastern Margin of Yunkai Massif. Earth Science 43, 4193-4203. (in Chinese with English abstract).

Warr, L.N., 2021. IMA–CNMNC approved mineral symbols. Mineralogical Magazine 85, 291-320. https://doi.org/10.1180/mgm.2021.43

Waszek, L., Tauzin, B., Schmerr, N.C., Ballmer, M.D., Afonso, J.C., 2021. A poorly mixed mantle transition zone and its thermal state inferred from seismic waves. Nature Geoscience 14, 949-955. https://doi.org/10.1038/s41561-021-00850-w

Wei, W., Faure, M., Chen, Y., Ji, W.B., Lin, W., Wang, Q.C., Yan, Q.R., Hou, Q.L., 2015. Back-thrusting response of continental collision: Early Cretaceous NW-directed thrusting in the Changle-Nan’ao belt (Southeast China). Journal of Asian Earth Sciences 100, 98-114. https://doi.org/10.1016/j.jseaes.2015.01.005

Wei, W., Lin, W., Chen, Y., Faure, M., Ji, W.B., Hou, Q.L., Yan, Q.R., Wang, Q.C., 2023. Tectonic Controls on Magmatic Tempo in an Active Continental Margin: Insights From the Early Cretaceous Syn‐Tectonic Magmatism in the Changle‐Nan’ao Belt, South China. Journal of Geophysical Research: Solid Earth 128, e2022JB025973. https://doi.org/10.1029/2022jb025973

Wei, W., Liu, C.Z., Hou, Y.F., Deng, C.L., Yan, W., Li, X.H., Chung, S.L., Mitchell, R.N., 2022. Discovery of a hidden Triassic Arc in the Southern South China Sea: Evidence for the breakaway of a ribbon continent with implications for the evolution of the Western Pacific margin. Terra Nova 34, 12-19. https://doi.org/10.1111/ter.12556

Wei, Y., Huang, X.L., Yu, Y., Wang, X., He, P.L., Ma, W.W., 2020. Phanerozoic magma underplating associated with remelting of the lower crust beneath the Cathaysia Block: Evidence from zircon UPb ages and HfO isotopes of granulite xenoliths from Daoxian, South China. Lithos 368-369, 105596. https://doi.org/10.1016/j.lithos.2020.105596

Wei, Y.H., Yang, H.Y., Li, W., Wang, G.C., 2025. Passive and active source imaging of the deep structure in the Pearl River Delta using a dense nodal array. Reviews of Geophysics and Planetary Physics 56, 193. (in Chinese with English abstract).

Weinberg, R.F., Hasalová, P., 2015. Water-fluxed melting of the continental crust: A review. Lithos 212-215, 158-188. https://doi.org/10.1016/j.lithos.2014.08.021

White, R., Powell, R., Clarke, G., 2002. The interpretation of reaction textures in Fe-rich metapelitic granulites of the Musgrave Block, central Australia: constraints from mineral equilibria calculations in the system K2O–FeO–MgO–Al2O3–SiO2–H2O–TiO2–Fe2O3. Journal of Metamorphic Geology 20, 41-55. https://doi.org/10.1046/j.0263-4929.2001.00349.x

White, R., Powell, R., Holland, T., Johnson, T., Green, E., 2014. New mineral activity–composition relations for thermodynamic calculations in metapelitic systems. Journal of Metamorphic Geology 32, 261-286. https://doi.org/10.1111/jmg.12071

Whitney, D.L., Teyssier, C., Fayon, A.K., 2004. Isothermal decompression, partial melting and exhumation of deep continental crust. Geological Society, London, Special Publications 227, 313-326. https://doi.org/10.1144/GSL.SP.2004.227.01.16

Wiemer, D., Hagemann, S.G., Hronsky, J., Kemp, A.I.S., Thébaud, N., Ireland, T., Villanes, C., 2022. Ancient structural inheritance explains gold deposit clustering in northern Perú. Geology 50, 1197-1201. https://doi.org/10.1130/g50208.1

Wolf, M., Romer, R.L., Franz, L., López-Moro, F.J., 2018. Tin in granitic melts: The role of melting temperature and protolith composition. Lithos 310-311, 20-30. https://doi.org/10.1016/j.lithos.2018.04.004

Wolf, S.G., Huismans, R.S., Braun, J., Yuan, X., 2022. Topography of mountain belts controlled by rheology and surface processes. Nature 606, 516-521. https://doi.org/10.1038/s41586-022-04700-6

Wu, C.M., 2018. Current Problems In Metamorphic Geology. Acta Petrologica Sinica 34, 873-894.

Wu, H.-H., Tsai, Y.-B., Lee, T.-Y., Lo, C.-H., Hsieh, C.-H., Toan, D.V., 2004. 3-D Shear Wave Velocity Structure of the Crust and Upper Mantle in South China Sea and its Surrounding Regions by Surface Wave Dispersion Analysis. Marine Geophysical Researches 25, 5-27. https://doi.org/10.1007/s11001-005-0730-8

Wu, H.L., Zhu, W.B., Ge, R.F., 2024. Garnet growth and diffusion zoning during the late Paleoproterozoic metamorphism, North Altyn area, SE Tarim Craton, NW China: Implications for a long-lived hot orogen. GSA Bulletin 136, 557–582. https://doi.org/10.1130/b36511.1

Wu, J.H., Li, H., Danišík, M., Yonezu, K., Zheng, H., Li, Z.H., 2023. Low‐Temperature Thermochronological Perspective on Geodynamic Evolution of the Cathaysia Block Since Early Mesozoic. Tectonics 42, e2022TC007662. https://doi.org/10.1029/2022tc007662

Wu, Y.B., Zheng, Y.F., 2013. Tectonic evolution of a composite collision orogen: An overview on the Qinling–Tongbai–Hong'an–Dabie–Sulu orogenic belt in central China. Gondwana Research 23, 1402-1428. https://doi.org/10.1016/j.gr.2012.09.007

Xi, Z.D., Tang, S.H., Zhang, S.H., 2020. Accumulation and combination characteristics of unconventional natural gas in Carboniferous coal-bearing strata: case study in the Central Hunan Province, South China. Energy Sources, Part A: Recovery, Utilization, and Environmental Effects 46, 6276-6288. https://doi.org/10.1080/15567036.2020.1745334

Xia, M.M., Liu, X.C., Chen, Y., Hu, J., Zheng, G.G., Chen, L.Y., Han, J.E., Hu, D.G., 2022. New U Pb zircon and geochemical constraints on Late Devonian Back-arc basin origin of eclogite protoliths from northeastern Hainan Island, South China. Lithos 418-419. https://doi.org/10.1016/j.lithos.2022.106677

Xia, X.P., Xu, J., Huang, C., Long, X.P., Zhou, M.L., 2020. Subduction polarity of the Ailaoshan Ocean (eastern Paleotethys): Constraints from detrital zircon U-Pb and Hf-O isotopes for the Longtan Formation. GSA Bulletin 132, 987-996. https://doi.org/10.1130/b35294.1

Xia, Y., 2015. Episodic Magmatism and continental crust growth and reworking in Cathaysia Block. Nanjing University, Doctoral dissertation, 1-344.

Xia, Y., Xu, X.S., Liu, L., 2016. Transition from adakitic to bimodal magmatism induced by the paleo-Pacific plate subduction and slab rollback beneath SE China: Evidence from petrogenesis and tectonic setting of the dike swarms. Lithos 244, 182-204. https://doi.org/10.1016/j.lithos.2015.12.006

Xia, Y., Xu, X.S., Niu, Y.L., Liu, L., 2018. Neoproterozoic amalgamation between Yangtze and Cathaysia blocks: The magmatism in various tectonic settings and continent-arc-continent collision. Precambrian Research 309, 56-87. https://doi.org/10.1016/j.precamres.2017.02.020

Xiang, H., Connolly, J.A.D., 2022. GeoPS: An interactive visual computing tool for thermodynamic modelling of phase equilibria. Journal of Metamorphic Geology 40, 243-255. https://doi.org/10.1111/jmg.12626

Xiang, Z.J., Yan, Q.R., Xia, L., Xia, W.J., 2021. The tectonic setting of the Early-Middle Triassic volcanic-sedimentary succession in Funing-Napo area, the south margin of Nanpanjiang Basin, South China. Geological Bulletin of China 40, 138-151. (in Chinese with English abstract). https://doi.org/10.12097/gbc.dztb-40-1-138

Xiang, Z.J., Yang, J.H., Yan, Q.R., Xia, L., Xia, W.J., White, J.D.L., 2022. Petrogenesis of the Early-Middle Triassic high-Mg andesitic rocks in the southern margin of the South China Block: Implications for the convergence between the South China and Indochina Blocks. Journal of Asian Earth Sciences 232. https://doi.org/10.1016/j.jseaes.2021.104994

Xiao, Z.C., Wang, S., Qi, S.H., Kuang, J., Zhang, M., Tian, F., Han, Y.J., 2020. Petrogenesis, Tectonic Evolution and Geothermal Implications of Mesozoic Granites in the Huangshadong Geothermal Field, South China. Journal of Earth Science 31, 141-158. https://doi.org/10.1007/s12583-019-1242-9

Xu, C.H., Zhang, L., Shi, H.S., Brix, M.R., Huhma, H., Chen, L.H., Zhang, M.Q., Zhou, Z.Y., 2017. Tracing an Early Jurassic magmatic arc from South to East China Seas. Tectonics 36, 466-492. https://doi.org/10.1002/2016TC004446

Xu, F., Zhang, G.L., Yan, W., Zhang, J., Yao, J.H., 2022. Subduction of the paleo-Pacific plate recorded by arc volcanism in the South China Sea margin. Gondwana Research 110, 58-72. https://doi.org/10.1016/j.gr.2022.05.018

Xu, J., Xia, X.-P., Cai, K., Lai, C.-K., Liu, X.-J., Yang, Q., Zhou, M.-L., Ma, P.-F., Zhang, L., 2020. Remnants of a Middle Triassic island arc on western margin of South China Block: Evidence for bipolar subduction of the Paleotethyan Ailaoshan Ocean. Lithos 360-361. https://doi.org/10.1016/j.lithos.2020.105447

Xu, J.S., Zeng, X.F., 2022. Tectonic Stress Redistribution Induced by Geothermal Gradient Difference: Numerical Modeling of Stress Around the Anninghe Seismic Gap in the Southeastern Tibetan Plateau. Pure and Applied Geophysics 179, 3713-3726. https://doi.org/10.1007/s00024-022-03162-1

Xu, S., Unsworth, M.J., Hu, X.Y., Mooney, W.D., 2019. Magnetotelluric Evidence for Asymmetric Simple Shear Extension and Lithospheric Thinning in South China. Journal of Geophysical Research: Solid Earth 124, 104-124. https://doi.org/10.1029/2018jb016505

Xu, X.B., 2023. Late Triassic to Middle Jurassic tectonic evolution of the South China Block: Geodynamic transition from the Paleo-Tethys to the Paleo-Pacific regimes.

Earth-Science Reviews 241. https://doi.org/10.1016/j.earscirev.2023.104404

Xu, X.B., Liang, C.H., Chen, J.J., Xu, Y.D., 2021. Fundamental geological features and metallogenic geological backgrounds of Nanling tectonic belt. Earth Science 46, 1133-1150. (in Chinese with English abstract).

Xu, X.B., Zhang, Y.Q., L.S., S., Jia, D., 2011. La-ICP-MS U–Pb and 40Ar/39Ar geochronology of the sheared metamorphic rocks in the Wuyishan: Constraints on the timing of Early Paleozoic and Early Mesozoic tectono-thermal events in SE China. Tectonophysics 501, 71-86. https://doi.org/10.1016/j.tecto.2011.01.014

Xu, X.S., Huang, Z.C., Jiang, D.S., Zeng, G., Dai, L.Q., 2024. Remnants and fragments of the subducted paleo-Pacific plate: Constraints from geochemistry and geophysics. Science China Earth Sciences 67, 3041-3061. https://doi.org/10.1007/s11430-024-1352-y

Xu, X.S., O'Reilly, S.Y., Griffin, W.L., Deng, P., Pearson, N.J., 2005. Relict Proterozoic basement in the Nanling Mountains (SE China) and its tectonothermal overprinting. Tectonics 24, TC2003. https://doi.org/10.1029/2004TC001652

Xu, Y.G., Chung, S.L., Jahn, B.M., Wu, G.Y., 2001. Petrologic and geochemical constraints on the petrogenesis of Permian–Triassic Emeishan flood basalts in southwestern China. Lithos 58, 145-168. https://doi.org/10.1016/S0024-4937(01)00055-X

Xu, Y.G., He, B., Huang, X.L., Luo, Z., Chung, S.L., Xiao, L., Zhu, D., Shao, H., Fan, W.M., Xu, J.F., Wang, Y.J., 2007. Identification of mantle plumes in the Emeishan Large Igneous Province. International Union of Geological Sciences 30, 32-42. https://doi.org/10.18814/epiiugs/2007/v30i1/005

Xu, Y.J., Li, Q.F., Ye, X., Lu, G.L., Jia, D., 2023. Geology and reservoir formation of coal measure gas in coastal swamp facies: a case study of the Longtan Formation in Chenzhou area Hunan Province. Science Technology and Engineering 23, 10764-10779. (in Chinese with English abstract).

Xue, L., Moucha, R., Kolawole, F., Muirhead, J.D., Scholz, C.A., 2024. The influence of the strength of pre-existing weak zones on rift geometry and strain localization. Tectonophysics 890. https://doi.org/10.1016/j.tecto.2024.230472

Yakymchuk, C., Brown, M., 2014. Behaviour of zircon and monazite during crustal melting. Journal of the Geological Society 171, 465-479. https://doi.org/10.1144/jgs2013-115

Yan, C.L., Shu, L.S., Faure, M., Chen, Y., Huang, R.B., 2019. Time constraints on the closure of the Paleo–South China Ocean and the Neoproterozoic assembly of the Yangtze and Cathaysia blocks: Insight from new detrital zircon analyses. Gondwana Research 73, 175-189. https://doi.org/10.1016/j.gr.2019.03.018

Yan, J.Y., Lü, Q.T., Luo, F., Cheng, S.B., Zhang, K., Zhang, Y.Q., Xu, Y., Zhang, C., Liu, Z.D., Ruan, S., Wang, X., 2021. A gravity and magnetic study of lithospheric architecture and structures of South China with implications for the distribution of plutons and mineral systems of the main metallogenic belts. Journal of Asian Earth Sciences 221, 104938. https://doi.org/10.1016/j.jseaes.2021.104938

Yan, J.Y., Zhang, K., Fu, G.M., Luo, F., Wang, H., Qi, G., 2019. Identification and determination of the boundary between the Cathaysian and Yangtze blocks: a preliminary understanding of gravity and magnetic fields. Acta Geologica Sinica - English Edition 93, 222-225. https://doi.org/10.1111/1755-6724.14052

Yan, J.Y., Zhang, Y.Q., Luo, F., She, J.J., Jiang, C.X., Liu, J.H., 2022. Isostatic gravity state in South China block and its geological implication. Acta Geoscientica Sinica 43, 744-754.

Yan, Y.G., Huang, B.C., Zhang, D.H., Charusiri, P.Y., Veeravinantanakul, A., 2018. Paleomagnetic Study on the Permian Rocks of the Indochina Block and Its Implications for Paleogeographic Configuration and Northward Drifting of Cathaysialand in the Paleo‐Tethys. Journal of Geophysical Research: Solid Earth 123, 4523-4538. https://doi.org/10.1029/2018jb015511

Yang, P., Liu, S.W., 2024. Heterogeneities of the lithospheric thermal structure and rheology control Cenozoic intracontinental deformation in southeast China.

Tectonophysics 870. https://doi.org/10.1016/j.tecto.2023.230153

Yao, J.L., Cawood, P.A., Shu, L.S., Santosh, M., Li, J.Y., 2016. An Early Neoproterozoic Accretionary Prism Ophiolitic Mélange from the Western Jiangnan Orogenic Belt, South China. The Journal of Geology 124, 587-601. https://doi.org/10.1086/687396

Yao, J.L., Shu, L.S., Cawood, P.A., Li, J.Y., 2017. Constraining timing and tectonic implications of Neoproterozoic metamorphic event in the Cathaysia Block, South China. Precambrian Research 293, 1-12. https://doi.org/10.1016/j.precamres.2017.01.032

Yao, J.L., Shu, L.S., Santosh, M., 2011. Detrital zircon U–Pb geochronology, Hf-isotopes and geochemistry—New clues for the Precambrian crustal evolution of Cathaysia Block, South China. Gondwana Research 20, 553-567. https://doi.org/10.1016/j.gr.2011.01.005

Yao, J.L., Shu, L.S., Santosh, M., Zhao, G.C., 2014. Neoproterozoic arc-related mafic–ultramafic rocks and syn-collision granite from the western segment of the Jiangnan Orogen, South China: Constraints on the Neoproterozoic assembly of the Yangtze and Cathaysia Blocks. Precambrian Research 243, 39-62. https://doi.org/10.1016/j.precamres.2013.12.027

Yao, W.H., Li, Z.X., Li, W.X., Wang, X.C., Li, X.H., Yang, J.H., 2012. Post-kinematic lithospheric delamination of the Wuyi–Yunkai orogen in South China: Evidence from ca. 435Ma high-Mg basalts. Lithos 154, 115-129. https://doi.org/10.1016/j.lithos.2012.06.033

Yardley, B.W.D., 2009. The role of water in the evolution of the continental crust. Journal of the Geological Society 166, 585-600. https://doi.org/10.1144/0016-76492008-101

Yin, A., 2010. Cenozoic tectonic evolution of Asia: A preliminary synthesis. Tectonophysics 488, 293-325. https://doi.org/10.1016/j.tecto.2009.06.002

Yin, Y.T., Jin, S., Wei, W.B., Lü, Q.T., Ye, G.F., Jing, J.E., Zhang, L.T., Dong, H., Xie, C.L., 2021. Lithosphere structure and its implications for the metallogenesis of the Nanling Range, South China: Constraints from 3-D magnetotelluric imaging. Ore Geology Reviews 131. https://doi.org/10.1016/j.oregeorev.2021.104064

Yin, Z.S., 2015. Tectonic and Burial History of Organic Matter Rich Shale Formations and Shale Gas Enrichment in Jiangxi Province. China University of Mining and Technology, Master dissertation (in Chinese with English abstract).

Yu, J.H., Lou, F.S., Wang, L.J., Shen, L.W., Zhou, X.Y., Zhang, C.H., Huang, Z.Z., 2014. The geological significance of a Paleozoic mafic granulite found in the Yiyang area of northeastern Jiangxi Province. Chinese Science Bulletin 59, 3508-3516. (in Chinese with English abstract). https://doi.org/10.1360/n972014-00395

Yu, J.H., O'Reilly, S.Y., Wang, L.J., Griffin, W.L., Zhang, M., Wang, R.C., Jiang, S.Y., Shu, L.S., 2008. Where was South China in the Rodinia supercontinent? Precambrian Research 164, 1-15. https://doi.org/10.1016/j.precamres.2008.03.002

Yu, J.H., O'Reilly, S.Y., Wang, L.J., Griffin, W.L., Zhou, M.F., Zhang, M., Shu, L.S., 2010. Components and episodic growth of Precambrian crust in the Cathaysia Block, South China: Evidence from U–Pb ages and Hf isotopes of zircons in Neoproterozoic sediments. Precambrian Research 181, 97-114. https://doi.org/10.1016/j.precamres.2010.05.016

Yu, J.H., O'Reilly, S.Y., Zhou, M.F., Griffin, W.L., Wang, L.J., 2012. U–Pb geochronology and Hf–Nd isotopic geochemistry of the Badu Complex, Southeastern China: Implications for the Precambrian crustal evolution and paleogeography of the Cathaysia Block. Precambrian Research 222-223, 424-449. https://doi.org/10.1016/j.precamres.2011.07.014

Yu, J.H., Wang, L.J., O'Reilly, S.Y., Griffin, W.L., Zhang, M., Li, C.Z., Shu, L.S., 2009. A Paleoproterozoic orogeny recorded in a long-lived cratonic remnant (Wuyishan terrane), eastern Cathaysia Block, China. Precambrian Research 174, 347-363. https://doi.org/10.1016/j.precamres.2009.08.009

Yu, J.H., Wang, L.J., Wei, Z.Y., Sun, T., Shu, L.S., 2007. Phanerozoic Metamorphic Episodes and Characteristics of Cathaysia Block. Geological Journal of China Universities 13, 474-483. (in Chinese with English abstract).

Yu, J.H., Wei, Z.Y., Wang, L.J., Shu, L.S., Sun, T., 2006. Cathaysia Block: A Young Continent Comprising Ancient Materials. Geological Journal of China Universities 12, 440. (in Chinese with English abstract).

Yu, J.H., Zhou, X.M., O'Reilly, Y.S., Zhao, L., Griffin, W.L., Wang, R.C., Wang, L.J., Chen, X.M., 2005. Formation history and protolith characteristics of granulite facies metamorphic rock in Central Cathaysia deduced from U-Pb and Lu-Hf isotopic studies of single zircon grains. Chinese Science Bulletin 50, 2080-2089. (in Chinese with English abstract). https://doi.org/10.1007/BF03322805

Yu, J.H., Zhou, X.M., Zhao, L., Chen, X.M., 2003. Discovery and implications of granulite facies metamorphic rocks in the eastern Nanling, China. Acta Petrologica Sinica 19, 461-467. (in Chinese with English abstract).

Yu, Y.Q., Hung, T.D., Yang, T., Xue, M., Liu, K.H., Gao, S.S., 2017. Lateral variations of crustal structure beneath the Indochina Peninsula. Tectonophysics 712-713, 193-199. https://doi.org/10.1016/j.tecto.2017.05.023

Yuan, C., Zhou, M.F., Sun, M., Zhao, Y., Wilde, S., Long, X., Yan, D., 2010. Triassic granitoids in the eastern Songpan Ganzi Fold Belt, SW China: Magmatic response to geodynamics of the deep lithosphere. Earth and Planetary Science Letters 290, 481-492. https://doi.org/10.1016/j.epsl.2010.01.005

Yuan, Y.S., Ma, Y.S., Hu, S.B., Guo, T.L., Fu, X.Y., 2006. Present-day geothermal characteristics in South China. CHINESE JOURNAL OF GEOPHYSICS 49, 9. (in Chinese with English abstract).

Zhang, B.T., Hum, G.R., 2006. The geochemical evidences for existence of Mesoproterozoic metamorphic basement in central Jiangxi Province. Geological Journal of China Universities 12, 466. (in Chinese with English abstract).

Zhang, C.L., Santosh, M., Zhu, Q.B., Chen, X.Y., Huang, W.C., 2015. The Gondwana connection of South China: Evidence from monazite and zircon geochronology in the Cathaysia Block. Gondwana Research 28, 1137-1151. https://doi.org/10.1016/j.gr.2014.09.007

Zhang, F.F., Wang, Y.J., Zhang, A.M., Fan, W.M., Zhang, Y.Z., Zi, J.W., 2012. Geochronological and geochemical constraints on the petrogenesis of Middle Paleozoic (Kwangsian) massive granites in the eastern South China Block. Lithos 150, 188-208. https://doi.org/10.1016/j.lithos.2012.03.011

Zhang, F.Q., Zhou, J.J., Dilek, Y., Zhu, K.Y., Wu, H.X., Sun, D.H., Deng, H.D., Sun, Y.H., Chen, H.L., Yang, S.F., 2025. Detrital zircon U-Pb geochronology of Ediacaran siliciclastic carbonate rocks in eastern South China: Insights into the Precambrian assembly of the Yangtze and Cathaysia blocks. Precambrian Research 424. https://doi.org/10.1016/j.precamres.2025.107814

Zhang, G.W., Guo, A.L., Wang, Y.J., Li, S.Z., Dong, Y.P., Liu, S.F., He, D.F., Cheng, S.Y., Lu, R.K., Yao, A.P., 2013. Tectonics of South China continent and its implications. Science China Earth Sciences 56, 1804-1828. https://doi.org/10.1007/s11430-013-4679-1

Zhang, H.C., Xu, Y.J., Cawood, P.A., Zi, J.W., Zhou, J.B., Du, Y.S., 2023. Linking the Paleozoic evolution of Hainan Island to Indochina and Australia: Implication for the paleogeography of the Eastern Tethys Ocean. Tectonophysics 858. https://doi.org/10.1016/j.tecto.2023.229882

Zhang, H.J., Lu, Q.T., Wang, X.L., Han, S.S., Liu, L.L., Gao, L., Wang, R., Hou, Z.Q., 2023. Seismically imaged lithospheric delamination and its controls on the Mesozoic Magmatic Province in South China. Nat Commun 14, 2718. https://doi.org/10.1038/s41467-023-37855-5

Zhang, J.H., Chen, Z., Chen, G.N., Ding, R.X., Peng, Z.L., 2017. Studies of formation temperature of Caledonian migmatite-granite at the Fuhuling area of the southern Qinzhou-Hangzhou zone, South China. Acta Petrologica Sinica 33, 887-895. (in Chinese with English abstract).

Zhang, J.H., Chen, Z., Yakymchuk, C., Sa, R., Huang, Q.T., Lou, F., Tu, S.C., Chen, T., 2023. Early Paleozoic crustal anatexis during Wuyi-Yunkai orogenesis: Insights from zircon of Fuhuling migmatites in the Yunkai region, South China. Geosphere 19, 1399-1420. https://doi.org/10.1130/ges02638.1

Zhang, J.H., Liu, W.L., Yakymchuk, C., Sa, R.N., Zeng, Z., Ding, R.X., Tang, G.J., Liu, H.Q., Xu, Q.Y., Wang, Y., 2019. Partial Melting and Crustal Deformation during the Early Paleozoic Wuyi–Yunkai Orogeny: Insights from Zircon U-Pb Geochronology and Structural Analysis of the Fuhuling Migmatites in the Yunkai Region, South China. Minerals 9, 621. https://doi.org/10.3390/min9100621

Zhang, J.J., Shang, S., Wei, C.J., Zhang, N., Zhang, G.W., Dong, Y.P., Jin, Z.M., Zhang, J.F., Cao, S.Y., Liu, J.L., 2019. Present status and development prospect of studies of rheology of continental lithosphere. Acta Geoscient Sin 40, 9-16. (in Chinese with English abstract). https://doi.org/10.3975/cagsb.2018.092901

Zhang, K., Lü, Q.T., Zhao, J.H., Yan, J.Y., Hu, H., Luo, F., Fu, G.M., Tao, X., 2020. Magnetotelluric evidence for the multi-microcontinental composition of eastern South China and its tectonic evolution. Scientific Reports 10, 13105.

Zhang, K.J., 1997. North and South China collision along the eastern and southern North China margins. Tectonophysics 270, 145-156. https://doi.org/10.1016/S0040-1951(96)00208-9

Zhang, K.J., Cai, J.X., 2009. NE–SW-trending Hepu–Hetai dextral shear zone in southern China: Penetration of the Yunkai Promontory of South China into Indochina. Journal of Structural Geology 31, 737-748. https://doi.org/10.1016/j.jsg.2009.04.012

Zhang, L.T., Jin, S., Wei, W.B., Ye, G.F., Jing, J.E., Dong, H., Xie, C.L., 2015. Lithospheric electrical structure of South China imaged by magnetotelluric data and its tectonic implications. Journal of Asian Earth Sciences 98, 178-187. https://doi.org/10.1016/j.jseaes.2014.10.034

Zhang, R.Y., Lo, C.H., Chung, S.L., Grove, M., Omori, S., Iizuka, Y., Liou, J.G., Tri, T.V., 2013. Origin and Tectonic Implication of Ophiolite and Eclogite in the Song Ma Suture Zone between the South China and Indochina Blocks. Journal of Metamorphic Geology 31, 49-62. https://doi.org/10.1111/jmg.12012

Zhang, S.B., Wu, R.X., Zheng, Y.F., 2012. Neoproterozoic continental accretion in South China: Geochemical evidence from the Fuchuan ophiolite in the Jiangnan orogen. Precambrian Research 220-221, 45-64. https://doi.org/10.1016/j.precamres.2012.07.010

Zhang, X.C., Wang, Y.J., Harris, R., Yan, Y., Zheng, Y., 2019. Discovery of Middle–Late Devonian and Early Permian magmatic events in East Asia and their implication for the Indosinian orogeny in South China: Insights from the sedimentary record. GSA Bulletin 131, 1519-1536. https://doi.org/10.1130/b35032.1

Zhang, Y.Q., Shi, D.N., Lü, Q.T., Xu, Y., Xu, Z.W., Gong, X.J., Yan, J.Y., Xu, T., 2021. A fine crustal structure and geodynamics revealed by receiver functions along the Guangchang-Putian line in the Cathaysia Block, South China. Tectonophysics 815. https://doi.org/10.1016/j.tecto.2021.229007

Zhang, Y.Q., Xu, X.B., Jia, D., Shu, L.S., 2009. Deformation record of the change from Indosinian collision-related tectonic system to Yanshanian subduction-related tectonic system in South China during the Early Mesozoic. Earth Science Frontiers 16, 234-247.

Zhang, Y.Z., Wang, Y.J., Zhang, Y.H., Zhang, A.M., 2015. Neoproterozoic assembly of the Yangtze and Cathaysia blocks: Evidence from the Cangshuipu Group and associated rocks along the Central Jiangnan Orogen, South China. Precambrian Research 269, 18-30. https://doi.org/10.1016/j.precamres.2015.08.003

Zhang, Z., Zheng, Q.F., Zhang, H., Wang, Q., Shi, Y.L., 2022. Late Mesozoic multi-plate convergence in East Asia: Insights from 3-D global mantle flow models. Tectonophysics 845. https://doi.org/10.1016/j.tecto.2022.229636

Zhang, Z.J., Xu, T., Zhao, B., Badal, J., 2013. Systematic variations in seismic velocity and reflection in the crust of Cathaysia: new constraints on intraplate orogeny in the South China continent. Gondwana Research 24, 902-917.

Zhang, Z.Y., Hou, Z.Q., Lü, Q.T., Zhang, X.W., Pan, X.F., Fan, X.K., Zhang, Y.Q., Wang, C.G., Lü, Y.J., 2023. Crustal architectural controls on critical metal ore systems in South China based on Hf isotopic mapping. Geology. https://doi.org/10.1130/g51203.1

Zhao, F.Y., Suo, Y.H., Liu, L.J., Cao, X.Z., Li, S.Z., Jiang, S.H., Deng, J.Z., Dai, M.X., Liu, Y., Hu, Y.P., Sheng, S.Z., Hu, B., 2023. Fine lithospheric structure controlling Meso-Cenozoic tectono-magmatism in the South China Block: Inference from a multidisciplinary analysis. Earth-Science Reviews 244. https://doi.org/10.1016/j.earscirev.2023.104524

Zhao, G.C., 2015a. Jiangnan Orogen in South China: Developing from divergent double subduction. Gondwana Research 27, 1173-1180. https://doi.org/10.1016/j.gr.2014.09.004

Zhao, G.C., 2015b. Jiangnan Orogen in South China: Developing from divergent double subduction. Gondwana Research 27, 1173-1180. https://doi.org/10.1016/j.gr.2014.09.004

Zhao, G.C., Cawood, P.A., 1999. Tectonothermal evolution of the Mayuan assemblage in the Cathaysia block: new evidence for Neoproterozoic collision-related assembly of the South China Craton. American Journal of Science 299, 309–339.

Zhao, G.C., Wang, Y.J., Huang, B.C., Dong, Y.P., Li, S.Z., Zhang, G.W., Yu, S., 2018. Geological reconstructions of the East Asian blocks: From the breakup of Rodinia to the assembly of Pangea. Earth-Science Reviews 186, 262-286. https://doi.org/10.1016/j.earscirev.2018.10.003

Zhao, J.H., Zhou, M.F., Yan, D.P., Zheng, J.P., Li, J.W., 2011. Reappraisal of the ages of Neoproterozoic strata in South China: No connection with the Grenvillian orogeny. Geology 39, 299-302. https://doi.org/10.1130/g31701.1

Zhao, K., Xu, X.S., Erdmann, S., Liu, L., Xia, Y., 2017. Rapid migration of a magma source from mid- to deep-crustal levels: Insights from restitic granulite enclaves and anatectic granite. GSA Bulletin 129, 1708-1725. https://doi.org/10.1130/B31462.1

Zhao, L., 2012. Study on the early precambrain metamorphic evolution and geochronology of the Badu group in southwestern Zhejiang province. Chinese Academy of Geological Sciences, Master degree, 1-111. (in Chinese with English abstract).

Zhao, L., Guo, F., Fan, W.M., Li, C.W., Qin, X.F., Li, H.X., 2010. Crustal evolution of the Shiwandashan area in South China: Zircon U-Pb-Hf isotopic records from granulite enclaves in Indo-Sinian granites. Chinese Science Bulletin 55, 2028-2038. https://doi.org/10.1007/s11434-010-3225-1

Zhao, L., Guo, F., Fan, W.M., Li, C.W., Qin, X.F., Li, H.X., 2012. Origin of the granulite enclaves in Indo-Sinian peraluminous granites, South China and its implication for crustal anatexis. Lithos 150, 209-226. https://doi.org/10.1016/j.lithos.2012.02.015

Zhao, L., Zhai, M.G., Santosh, M., Zhou, X.W., 2017. Early Mesozoic retrograded eclogite and mafic granulite from the Badu Complex of the Cathaysia Block, South China: Petrology and tectonic implications. Gondwana Research 42, 84-103. https://doi.org/10.1016/j.gr.2016.10.002

Zhao, L., Zhai, M.G., Zhou, X.W., Santosh, M., Ma, X.D., 2016. Thermal gradient and geochronology of a Paleozoic high-grade terrane in the northeastern Cathaysia block, South China. Tectonophysics 691, 311-327. https://doi.org/10.1016/j.tecto.2016.10.024

Zhao, L., Zhai, M., Zhou, X., 2022. Formation of an Intracontinental Orogen Above the Permo-Triassic Mantle Convection Cell in the Paleo-Tethys Tectonic Realm due to Far-Field Stress Derived From Continental Margins. Frontiers in Earth Science 10. https://doi.org/10.3389/feart.2022.892787

Zhao, L., Zhou, X.W., 2012. The metamorphic evolution and pT path of pelitic granulite from the Badu Group in southwestern Zhejiang Province. Acta Petrologica Et Mineralogica 31, 61-72. (in Chinese with English abstract).

Zhao, L., Zhou, X.W., Zhai, M.G., Santosh, M., Geng, Y.S., 2015. Zircon U–Th–Pb–Hf isotopes of the basement rocks in northeastern Cathaysia block, South China: Implications for Phanerozoic multiple metamorphic reworking of a Paleoproterozoic terrane. Gondwana Research 28, 246-261. https://doi.org/10.1016/j.gr.2014.03.019

Zhao, L., Zhou, X.W., Zhai, M.G., Santosh, M., Ma, X.D., Shan, H.X., Cui, X.H., 2014. Paleoproterozoic tectonic transition from collision to extension in the eastern Cathaysia Block, South China: Evidence from geochemistry, zircon U–Pb geochronology and Nd–Hf isotopes of a granite–charnockite suite in southwestern Zhejiang. Lithos 184-187, 259-280. https://doi.org/10.1016/j.lithos.2013.11.005

Zhao, X.X., Coe, R.S., 1987. Palaeomagnetic constraints on the collision and rotation of North and South China. Nature 327, 141-144. https://doi.org/10.1038/327141a0

Zheng, H.R., Hu, Z.Q., 2010. Atlas of Pre-Mesozoic tectonic lithofacies paleogeography in China. Geological Publishing House: Beijing, China.

Zheng, Y.F., 2021. Plate Tectonics, In: Alderton, D., Elias, S.A. (Eds.), Encyclopedia of Geology (Second Edition). Academic Press, Oxford, pp. 744-758. https://doi.org/10.1016/B978-0-08-102908-4.00058-8

Zhong, Y.F., Ma, C.Q., Zhang, C., Wang, S.M., She, Z.B., Liu, L., Xu, H.J., 2013. Zircon U–Pb age, Hf isotopic compositions and geochemistry of the Silurian Fengdingshan I-type granite Pluton and Taoyuan mafic–felsic Complex at the southeastern margin of the Yangtze Block. Journal of Asian Earth Sciences 74, 11-24. https://doi.org/10.1016/j.jseaes.2013.05.025

Zhong, Z.Q., You, Z.D., Zhou, H.W., Han, Y.J., 1996. The evolution and basic structural framework of the basement of the Yunkai uplift. Regional Geology of China 56, 36-43. (in Chinese with English abstract).

Zhou, D., Hu, J., Yang, W.Q., Chen, Q., Wang, X.D., Wang, L., Xu, D.M., 2021.

Formation age and petrogenesis of the Xinxing pluton in western Guangdong: Constraint on the closure of the East Paleo-Tethys Ocean. Geology in China 48, 1896-1923. (in Chinese with English abstract). https://doi.org/10.12029/gc20210618

Zhou, D.Y., Xu, X.S., 2017. Geochronology of Fuhuling migmatite and its protolith in western Guangdong. Acta Petrologica Et Mineralogica 36, 473-487. (in Chinese with English abstract). https://doi.org/10.3969/j.issn.1000-6524.2017.04.003

Zhou, H.W., You, Z.D., Zhong, Z.Q., Han, Y.J., 1997. Origin of thermal center type of migmatites in the Yunkai uplift. Earth Science - Journal of China University of Geosciences 22, 332-338. (in Chinese with English abstract).

Zhou, X., 2018. The Genesis and Metamorphic Evolution of Garnet Amphibolite Monzogneiss from the Suichang-Dazhe region in southwestern Zhejiang Province. Jilin University, Master degree, 1-67. (in Chinese with English abstract).

Zhou, X., Zheng, C., Dong, Y., Wang, Z., Song, Y., Han, X., 2018. Genesis and metamorphic evolution of garnet amphibolite monzogneiss from Suichang-Dazhe region in Southwestern Zhejiang Province. Earth Science 43, 199-219. (in Chinese with English abstract).

Zhou, X.M., Sun, T., Shen, W.Z., Shu, L.S., Niu, Y.L., 2006. Petrogenesis of Mesozoic granitoids and volcanic rocks in South China: a response to tectonic evolution. Episodes 29, 26-33. https://doi.org/10.18814/epiiugs/2006/v29i1/004

Zhou, Z.M., Ma, C.Q., Qi, S.H., Xi, Y.F., Liu, W., 2020. Late Mesozoic high-heat-producing (HHP) and high-temperature geothermal reservoir granitoids: The most significant geothermal mechanism in South China. Lithos 366-367, 105568. https://doi.org/10.1016/j.lithos.2020.105568

Zhu, W., Cao, Z.J., Li, C.W., 2015. Diagenetic evolution of reservoirs and reservoir forming stages in the Xiangzhong depression. Chinese Journal of Geology 50, 943-954. (in Chinese with English abstract). https://doi.org/10.3969/j.issn.0563-5020.2015.03.018

Zhu, X., Xia, X.P., Xu, J., Yang, Q., Cui, Z., Prasanth, M.P.M., 2025. Petrogenesis of early carboniferous and early Permian mafic intrusions in the Nanpanjiang Basin, SW China: Implications for northward subduction of the East Paleo-Tethys Ocean and back-arc basin formation. Journal of Asian Earth Sciences 287. https://doi.org/10.1016/j.jseaes.2025.106597

Zieman, L., Ibañez-Mejia, M., Rooney, A.D., Bloch, E., Pardo, N., Schoene, B., Szymanowski, D., 2023. To sink or not to sink: The thermal and density structure of the modern northern Andean arc constrained by xenolith petrology. Geology. https://doi.org/10.1130/g50973.1

Zuo, X.R., Chan, L.S., Gao, J.F., 2017. Compression-extension transition of continental crust in a subduction zone: A parametric numerical modeling study with implications on Mesozoic-Cenozoic tectonic evolution of the Cathaysia Block. PLoS One 12, e0171536. https://doi.org/10.1371/journal.pone.0171536

Appendix

Table S1. Compilations of ages of the magmatism and metamorphism within the Yunkai Massif

No.	Location	Long.(E)	Lat.(N)	Sample No.	Lithology	Age	error	Mineral	Method	Event	Reference
1. Early Mesozoic Ages											
1.1 Magmatism:											
1	Darongshan, Guangxi	109°23′22″	22°14′44″		Crd granite	233	5	Zircon	SHRIMP U-Pb	Magmatism	Deng X.G. et al., 2004
2	Darongshan, Guangxi	111°15′00″	23°25′00″	22GX-20	Crd-Bt granite	256.2	7.2	Zircon	LA-ICP-MS U-Pb	Magmatism	Chen C.H. et al., 2011
3	Fuhuling, Yangjiang	111°32′36″	21°30′42″	17FH-2D	Granitic dike	210	3	Zircon	LA-ICP-MS U-Pb	Magmatism	Wang Y.J. et al., 2021
4	Fuhuling, Yangjiang	111°32′30″	21°30′32.43″	DG2	Monzogranite	235.3	2.3	Zircon	LA-ICP-MS U-Pb	Magmatism	Zhang J.H. et al., 2019
5	Fuhuling, Yangjiang	111°32′27.26″	21°30′59.62″	MG-Zr	Granite	239	0.9	Zircon	LA-ICP-MS U-Pb	Magmatism	Chen Z. et al., 2021
6	Fuhuling, Yangjiang	111°32′29.75″	21°31′04.89″	DG-Zr	Granite	240	2.9	Zircon	LA-ICP-MS U-Pb	Magmatism	Chen Z. et al., 2021
7	Fuhuling, Yangjiang	111°32′23.73″	21°30′40.67″	DG3	Biotite monzogranite	241	4.3	Zircon	LA-ICP-MS U-Pb	Magmatism	Zhang J.H. et al., 2019
8	Guidong, Guangdong	113°51′48″	24°39′24″	2KSC6	Monzogranite	238	3	Zircon	SHRIMP U-Pb	Magmatism	Li Z.X. & Li X.H., 2007
9	Hetai, W. Sihui	112°02′00″	23°23′00″	5H031	Granodiorite	253	1.6	Zircon	LA-ICP-MS U-Pb	Magmatism	Jiao Q.Q. et al., 2020
10	Huilong pluton,	111°09′04.06″	23°09′15.12″	17HL-01	Hornblende gabbro	245.8	1.7	Zircon	LA-ICP-MS U-Pb	Magmatism	Li D.X. et al., 2020
11	Jiuzhou, Guangxi	108°48′54″	22°20′48″		Grt-Crd granite	230	4	Zircon	SHRIMP U-Pb	Magmatism	Deng X.G. et al., 2004
12	Jiuzhou, Guangxi	108°35′00″	22°08′00″	22GX-12	Crd-Bt monzogranite	259.7	3.1	Zircon	LA-ICP-MS U-Pb	Magmatism	Chen C.H. et al., 2011
13	Jiuzhou, Qinhou	108°35′00″	21°48′00″		Pelitic granulite enclaves	234	2	Zircon	LA-ICP-MS U-Pb	Magmatism	Zhao L. et al., 2010
14	Mengdong, Guangdong	114°02′20″	25°23′14″	04GD41	Ganodiorite	231	3	Zircon	SHRIMP U-Pb	Magmatism	Li Z.X. & Li X.H., 2007
15	N. Cenxi	111°06′06.1″	23°16′02.0″	28GX20	Undeformed granite	250.9	3.3	Zircon	LA-ICP-MS U-Pb	Magmatism	Chen C.H. et al., 2017

Table S1 (continued)

No.	Location	Long.(E)	Lat.(N)	Sample No.	Lithology	Age	error	Mineral	Method	Event	Reference
16	Nadong, Guangxi	107°42′00″	21°38′00″	22GX-07A	Biotite granite	254.3	3.5	Zircon	LA-ICP-MS U-Pb	Magmatism	Chen C.H. et al., 2011
17	Nadong, Guangxi	107°42′00″	21°38′00″	22GX-07	Biotite granite	257	3.8	Zircon	LA-ICP-MS U-Pb	Magmatism	Chen C.H. et al., 2011
18	Napeng pluton, Luoding	111°20′01″	22°52′46″	01YK-83	Mylonitic granite	205.3	1.6	Zircon	LA-ICP-MS U-Pb	Magmatism	Peng B.X. et al., 2006
19	Napeng pluton, W. Luoding	111°00′49″	22°48′26″	YK012	Bt monzogranite	257.8	1.2	Zircon	LA-ICP-MS U-Pb	Magmatism	Tian M.Y. et al., 2021
20	Napeng pluton, W. Luoding	111°22′00″	22°50′00″	NP-5	Grt biotite granite	259	2.8	Zircon	LA-ICP-MS U-Pb	Magmatism	Qing L.et al., 2020
21	Neihan, N. Luoding	111°41′01.7″	23°00′29.02″		Biotite monzogranite	246.7	7.1	Zircon	LA-ICP-MS U-Pb	Magmatism	Yan C.W. et al., 2014
22	Pubei, Guangxi	109°41′57.36″	22°31′48.20″	XH-14	Crd-Bt granite	244.3	1.8	Zircon	LA-ICP-MS U-Pb	Magmatism	Wang M.F. et al., 2015
23	Pubei, Guangxi	109°41′57.36″	22°31′48.20″	XH-5	Crd-Bt granite	251.9	2.2	Zircon	LA-ICP-MS U-Pb	Magmatism	Wang M.F. et al., 2015
24	Pubei, Guangxi	109°20′00″	22°23′00″	22GX-13	Crd-Bt granite	255.5	5.8	Zircon	LA-ICP-MS U-Pb	Magmatism	Chen C.H. et al., 2011
25	Pubei, Guangxi	109°40′00″	22°23′00″	22GX-16	Crd-Bt granite	260.4	3.1	Zircon	LA-ICP-MS U-Pb	Magmatism	Chen C.H. et al., 2011
26	Shicun pluton, W. Xinyi	110°50′00″	22°28′00″	SC-2-2	Two-mica granite	259.3	1.5	Zircon	LA-ICP-MS U-Pb	Magmatism	Qing L.et al., 2020
27	Taima, Guangxi	108°23′08″	22°09′29″		Hypersthene granite porphyry	236	4	Zircon	SHRIMP U-Pb	Magmatism	Deng X.G. et al., 2004
28	Taima, Guangxi	108°20′00″	22°08′00″	22GX-01A	Hypersthene granite porphyry	253.7	4.5	Zircon	LA-ICP-MS U-Pb	Magmatism	Chen C.H. et al., 2011
29	Taima, Guangxi	108°20′00″	22°08′00″	22GX-01	Hypersthene granite porphyry	255.4	3.8	Zircon	LA-ICP-MS U-Pb	Magmatism	Chen C.H. et al., 2011
30	W. Cenxi	110°47′10.5″	22°54′38.1″	28GX22	Undeformed granite	247.7	2.3	Zircon	LA-ICP-MS U-Pb	Magmatism	Chen C.H. et al., 2017
31	Xiazhuang, Guangdong	114°14′44″	24°34′47″		Biotite granite	236	1	Zircon	LA-ICP-MS U-Pb	Magmatism	Xu X.S. et al., 2005
32	Xinxing, Yangchun	112°12′10″	22°33′25″	D2268-1	Porphyritic granite	224	2	Zircon	LA-ICP-MS U-Pb	Magmatism	Zhou D. et al., 2021
33	Xinxing, Yangchun	112°11′37″	22°33′33″	D2264-5	Bt monzonite	226	3	Zircon	LA-ICP-MS U-Pb	Magmatism	Zhou D. et al., 2021

Table S1 (continued)

No.	Location	Long.(E)	Lat.(N)	Sample No.	Lithology	Age	error	Mineral	Method	Event	Reference
34	Xinxing, Yangchun	112°13′27″	22°31′18″	D3426	Porphyritic granite	231	2	Zircon	LA-ICP-MS U-Pb	Magmatism	Zhou D. et al., 2021
35	Xinxing, Yangchun	112°12′10″	22°33′25″	D2286-1	Monzonite	236	4	Zircon	LA-ICP-MS U-Pb	Magmatism	Zhou D. et al., 2021
36	Xinxing, Yangchun	112°09′57″	22°33′09″	PM11-39-1	Monzonite	237	4	Zircon	LA-ICP-MS U-Pb	Magmatism	Zhou D. et al., 2021
37	Xinxing, Yangchun	112°13′27″	22°32′27″	D6467-3	Mafic enclave	240	1	Zircon	LA-ICP-MS U-Pb	Magmatism	Zhou D. et al., 2021
38	Xinxing, Yangchun	112°13′27″	22°32′27″	D6467-3	Mafic enclave	250	2	Zircon	LA-ICP-MS U-Pb	Magmatism	Zhou D. et al., 2021
39	Xinxing, Yangchun	112°09′57″	22°33′09″	PM11-39-1	Monzonite	252	4	Zircon	LA-ICP-MS U-Pb	Magmatism	Zhou D. et al., 2021
40	Xinxing, Yangchun	112°05′28″	22°39′46″	D5784-1	Bt monzonite	241	2	Zircon	LA-ICP-MS U-Pb	Magmatism	Zhou D. et al., 2021
41	Xinxing, Yangchun	112°02′51″	22°36′21″	D7063	Gneissic granite	240	1	Zircon	LA-ICP-MS U-Pb	Magmatism	Zhou D. et al., 2021
42	Xinxing, Yangchun	112°02′51″	22°36′21″	D7063	Gneissic granite	251	3	Zircon	LA-ICP-MS U-Pb	Magmatism	Zhou D. et al., 2021
43	Xinxing, Yangchun	112°19′01″	22°31′17″	XX-5	Alkaline granite	231.7	3.3	Zircon	LA-ICP-MS U-Pb	Magmatism	Qing L.et al., 2020
44	Xinxing, Yangchun	112°11′11″	22°26′45″	D3406-1	Porphyritic granite	233	2	Zircon	LA-ICP-MS U-Pb	Magmatism	Zhou D. et al., 2021
45	Xinxing, Yangchun	112°11′11″	22°26′45″	D3406-1	Porphyritic granite	252	3	Zircon	LA-ICP-MS U-Pb	Magmatism	Zhou D. et al., 2021
46	Xinxing, Yangchun	112°07′07″	22°07′42″	XX-18	Monzonite	234.4	2.6	Zircon	LA-ICP-MS U-Pb	Magmatism	Qing L.et al., 2020, Mineral. Petrol.
47	Yangjiang	111°32′36″	21°30′42″	17FH-4A1	Deformed felsic dikes	224	3	Zircon	LA-ICP-MS U-Pb	Magmatism	Wang Y.J. et al., 2021
48	Yangjiang	111°32′36″	21°30′42″	17FH-2B1	Deformed felsic dikes	233	4	Zircon	LA-ICP-MS U-Pb	Magmatism	Wang Y.J. et al., 2021
51	Yunlu, Gaozhou	111°03′39″	21°58′25″	ID7-5	Granitic dykes	229.7	2.7	Zircon	LA-ICP-MS U-Pb	Magmatism	Ke X.Z. et al., 2018
52	Darongshan, Guangxi	111°15′00″	23°25′00″	22GX-20	Crd-Bt granite	232.1	18.6	Monazite	EMP U-Th-Pb	Magmatism	Chen C.H. et al., 2011
53	Jiuzhou, Guangxi	108°35′00″	22°08′00″	22GX-12	Crd-Bt monzogranite	223	8.2	Monazite	EMP U-Th-Pb	Magmatism	Chen C.H. et al., 2011

Table S1 (continued)

No.	Location	Long.(E)	Lat.(N)	Sample No.	Lithology	Age	error	Mineral	Method	Event	Reference
54	N. Cenxi	111°06′06.1″	23°16′02.0″	28GX20	Undeformed granite	232.1	4.7	Monazite	EMP U-Th-Pb	Magmatism	Chen C.H. et al., 2017
55	Nadong, Guangxi	107°42′00″	21°38′00″	22GX-07	Biotite granite	230.3	8.4	Monazite	EMP U-Th-Pb	Magmatism	Chen C.H. et al., 2011
56	Pubei, Guangxi	109°40′00″	22°23′00″	22GX-16	Crd-Bt granite	230.3	8.8	Monazite	EMP U-Th-Pb	Magmatism	Chen C.H. et al., 2011
57	Pubei, Guangxi	109°20′00″	22°23′00″	22GX-13	Crd-Bt granite	232.5	5.6	Monazite	EMP U-Th-Pb	Magmatism	Chen C.H. et al., 2011
58	Taima, Guangxi	108°20′00″	22°08′00″	22GX-01	Hypersthene granite porphyry	230.2	15.6	Monazite	EMP U-Th-Pb	Magmatism	Chen C.H. et al., 2011
59	W. Cenxi	110°47′10.5″	22°54′38.1″	28GX22	Undeformed granite	229.2	8.4	Monazite	EMP U-Th-Pb	Magmatism	Chen C.H. et al., 2017
-	Hailing island, Yangjiang	111°56′48.5″	21°36′20.9″	S42	Weakly deformed granite	243.8	3.4	Zircon	LA-ICP-MS U-Pb	Magmatism	Cochelin B. et al., 2022
-	Shapa, Yangjiang	111°28′18.1″	21°30′45.8″	S01	Weakly deformed granite	237.1	4.1	Zircon	LA-ICP-MS U-Pb	Magmatism	Cochelin B. et al., 2022
1.2 Metamorphism:											
49	Yangxi	111°32′36″	21°30′42″	17FH-9A1	Leucosomes	249	7	Zircon	LA-ICP-MS U-Pb	Magmatism	Wang Y.J. et al., 2021
50	Yangxi, Yangjiang	111°32′36″	21°30′42″	FH-11	Leucosomes in mylonitic gneiss	241	9	Zircon	SIMS U-Pb	Magmatism	Wang Y.J. et al., 2021
60	Dasi, Qinzhou	108°26′51.72″	22°08′02.22″	HG-132	Mafic granulite	244	7	Zircon	SHRIMP U-Pb	Metamorphism	Wang Y.J. et al., 2012
61	Fuhuling, Yangjiang	111°32′27.31″	21°30′35.25″	FHMG	Diatexite	238.8	2.6	Zircon	LA-ICP-MS U-Pb	Metamorphism	Zhang J.H. et al., 2019
62	Fuhuling, Yangjiang	111°32′50.77″	21°30′32.33″	SPM	Metatexite	240	2	Zircon	LA-ICP-MS U-Pb	Metamorphism	Zhang J.H. et al., 2019
63	Fuhuling, Yangjiang	111°32′50.77″	21°30′32.33″	SPMG	Diatexite	240	3	Zircon	LA-ICP-MS U-Pb	Metamorphism	Zhang J.H. et al., 2019,
64	Fuhuling, Yangjiang	111°32′50.77″	21°30′32.33″	SPM	Metatexite	244	4	Zircon	LA-ICP-MS U-Pb	Metamorphism	Zhang J.H. et al., 2019
65	Gaozhou complex, E. Xinyi	110°58′00″	22°40′00″	L114	Sill-Grt-Crd gneiss	242	8	Zircon	SHRIMP U-Pb	Metamorphism	Wan Y.S. et al., 2010
66	Hetai, W. Sihui	112°02′00″	23°23′00″	HT112	Migmatite	240.3	1.5	Zircon	LA-ICP-MS U-Pb	Metamorphism	Jiao Q.Q. et al., 2021
67	Jintong, Xinyi	110°46′48.88″	22°27′48.87″	YK-9A	Migmatized amphibolite	221	4	Zircon	LA-ICP-MS U-Pb	Metamorphism	Wang Y.J. et al., 2012

Table S1 (continued)

No.	Location	Long.(E)	Lat.(N)	Sample No.	Lithology	Age	error	Mineral	Method	Event	Reference
68	Jiuzhou, Qinzhou	108°35′00″	21°48′00″		Pelitic granulite enclaves	253	3	Zircon	LA-ICP-MS U-Pb	Metamorphism	Zhao L. et al., 2010
69	Licun, Rongxian	110°42′13.74″	22°35′59.88″	YK-13	Plagioclase amphibolite	248	6	Zircon	SHRIMP U-Pb	Metamorphism	Wang Y.J. et al., 2012
70	Licun, Rongxian	110°41′35.76″	22°36′09.18″	09YK-12a	Orthogneiss	239	6	Zircon	LA-ICP-MS U-Pb	Metamorphism	Wang Y.J. et al., 2011
71	Longwan, Luoding	111°17′12″	22°43′44″	D116-3	Migmatite	230.7	1.3	Zircon	LA-ICP-MS U-Pb	Metamorphism	Ke X.Z. et al., 2018
72	Maofengshan, NE. Guangzhou	113°22′30″	23°15′00″	BY004-1	Gneiss	212	12	Zircon	SHRIMP U-Pb	Metamorphism	Yang D.S. et al., 2010
73	Nameng, Qinzhou	108°34′16.02″	22°08′27.66″	HG-131	Pelitic granulite	238	8	Zircon	SHRIMP U-Pb	Metamorphism	Wang Y.J. et al., 2012
74	NE. Xinyi	110°56′13.2″	22°29′57.2″	11GD04	Biotite gneiss	245.1	5.4	Zircon	LA-ICP-MS U-Pb	Metamorphism	Chen C.H. et al., 2017
75	W. Boluo	113°49′11″	23°06′58″	ZC-12	Gneiss	231	3	Zircon	LA-ICP-MS U-Pb	Metamorphism	Yu J.H. et al., 2007
76	W. Boluo	113°49′11″	23°06′58″	ZC-8	Migmatite	232	3	Zircon	LA-ICP-MS U-Pb	Metamorphism	Yu J.H. et al., 2007
77	W. Xinyi	110°31′08.1″	22°25′44.6″	23GX04	Biotite gneiss	229	10	Zircon	LA-ICP-MS U-Pb	Metamorphism	Chen C.H. et al., 2017
78	Xiadong, Gaozhou	111°05′39″	21°44′18″	12GZ-30-1	Monzogranite	246	3	Zircon	LA-ICP-MS U-Pb	Metamorphism	Qin X.F. et al., 2016
79	Xieji, Gaozhou	110°00′31.02″	21°55′17.82″	GD-4	Grt amphibolite	237	7	Zircon	SHRIMP U-Pb	Metamorphism	Wang Y.J. et al., 2012
80	Xinxing, Yangchun	112°13′27″	22°31′18″	D3426	Porphyritic granite	214	2	Zircon	LA-ICP-MS U-Pb	Metamorphism	Zhou D. et al., 2021
81	Xinxing, Yangchun	112°11′11″	22°26′45″	D3406-1	Porphyritic granite	219	2	Zircon	LA-ICP-MS U-Pb	Metamorphism	Zhou D. et al., 2021
82	Yunlong, Xingyi	111°01′05.7″	22°30′09.42″	09YK-8B	Orthogneiss	203	10	Zircon	LA-ICP-MS U-Pb	Metamorphism	Wang Y.J. et al., 2011
83	Yunlu, Gaozhou	111°03′39″	21°58′25″	ID7-3	Migmatite	229.2	5.4	Zircon	LA-ICP-MS U-Pb	Metamorphism	Ke X.Z. et al., 2018
84	Yunlu, Gaozhou	111°03′39″	22°01′11″	GZ-08	Orthogneisses	238.2	4.2	Zircon	LA-ICP-MS U-Pb	Metamorphism	Chen C.H. et al., 2012
85	Yunlu, Gaozhou	111°04′43″	21°59′04″	GZ0307	Gneissic migmatite	241	3	Zircon	LA-ICP-MS U-Pb	Metamorphism	Wang D. et al., 2013

Table S1 (continued)

No.	Location	Long.(E)	Lat.(N)	Sample No.	Lithology	Age	error	Mineral	Method	Event	Reference
86	Yunlu, Gaozhou	111°04′43″	21°59′25″	GZ14-1	Grt Charnockite	243.2	1.8	Zircon	LA-ICP-MS U-Pb	Metamorphism	Li C. et al., 2020
87	Yuntan, Gaozhou	111°02′00″	21°55′00″	02YK-42	Biotite orthognesis	236	3.1	Zircon	LA-ICP-MS U-Pb	Metamorphism	Wang Y.J. et al., 2007
88	Zhiziling, N. Xinyi	111°54′20″	22°21′20″	1432-1	Migmatitic gneiss	230.2	2.9	Zircon	LA-ICP-MS U-Pb	Metamorphism	Ke X.Z. et al., 2018
-	Jiahai, Maoming	111°15′18.6″	21°25′01.5″	S24	Mylonitic migmatite	239	3.7	Zircon	LA-ICP-MS U-Pb	Metamorphism	Cochelin B. et al., 2022
89	Chidong, Xinyi	110°57′07.7″	22°27′45.2″	17YK19	Sill Bt monzogneiss	229.4	1.2	Monazite	LA-ICP-MS U-Pb	Metamorphism	Wang X.D. et al., 2020
90	NE. Gaozhou	111°03′04.0″	22°02′06.4″	11GD01	Gneissic granite	232.8	4.3	Monazite	EMP U-Th-Pb	Metamorphism	Chen C.H. et al., 2017
91	NE. Gaozhou	111°04′10.2″	22°00′36.2″	11GDGZA1	Gneissic granite	232.8	5.2	Monazite	EMP U-Th-Pb	Metamorphism	Chen C.H. et al., 2017
92	NE. Gaozhou	111°03′50.4″	22°00′31.3″	23GX11	Meta-sandstone	237	13	Monazite	EMP U-Th-Pb	Metamorphism	Chen C.H. et al., 2017
93	NE. Xinyi	110°56′46.5″	22°32′57.4″	23GX14	Grt schist	235.9	8.2	Monazite	EMP U-Th-Pb	Metamorphism	Chen C.H. et al., 2017
94	NE. Xinyi	110°56′45.8″	22°32′56.8″	11GD03	Grt schist	244	11	Monazite	EMP U-Th-Pb	Metamorphism	Chen C.H. et al., 2017
95	NE. Xinyi	110°56′13.2″	22°29′57.2″	11GD04	Biotite gneiss	236	4.6	Monazite	EMP U-Th-Pb	Metamorphism	Chen C.H. et al., 2017
96	NE. Xinyi	110°56′52.1″	22°27′54.0″	23GX13-2	Biotite gneiss	238	15	Monazite	EMP U-Th-Pb	Metamorphism	Chen C.H. et al., 2017
97	NE. Xinyi	110°57′08.3″	22°27′41.5″	11GD05	Biotite gneiss	239.2	5.7	Monazite	EMP U-Th-Pb	Metamorphism	Chen C.H. et al., 2017
98	Shikengtang, E. Gaozhou	110°55′19.8″	21°54′27.1″	17YK03	Bt granitic gneiss	236.2	0.8	Monazite	LA-ICP-MS U-Pb	Metamorphism	Wang X.D. et al., 2020
99	W. Xinyi	110°33′07.5″	22°18′26.4″	11GD07	Gneissic granite	233	11	Monazite	EMP U-Th-Pb	Metamorphism	Chen C.H. et al., 2017
100	W. Xinyi	110°31′08.1″	22°25′44.6″	23GX05-2	Biotite gneiss	234.1	5.1	Monazite	EMP U-Th-Pb	Metamorphism	Chen C.H. et al., 2017
101	W. Xinyi	110°10′43.7″	22°16′35.0″	23GX15	Two-mica gneiss	235.5	4.1	Monazite	EMP U-Th-Pb	Metamorphism	Chen C.H. et al., 2017
102	W. Xinyi	110°31′08.1″	22°25′44.6″	23GX04	Biotite gneiss	236.6	3	Monazite	EMP U-Th-Pb	Metamorphism	Chen C.H. et al., 2017

Table S1 (continued)

No.	Location	Long.(E)	Lat.(N)	Sample No.	Lithology	Age	error	Mineral	Method	Event	Reference
103	W. Xinyi	110°35′44.9″	22°13′19.1″	11GD06	Two-mica gneiss	239.7	4.1	Monazite	EMP U-Th-Pb	Metamorphism	Chen C.H. et al., 2017
104	Yunlu, Gaozhou	111°03′39″	22°01′11″	GZ-03	Charnockite	231	9.3	Monazite	EMP U-Th-Pb	Metamorphism	Chen C.H. et al., 2012
105	Yunlu, Gaozhou	111°03′17″	21°58′31″	23GX11	Paragneiss	237	13	Monazite	EMP U-Th-Pb	Metamorphism	Chen C.H. et al., 2012
106	E. Beiliu	110°29′00″	22°45′00″	Datong 2	Mylonite	211.64	3.39	Muscovite	Ar-Ar	Metamorphism	Zhang K.J. & Cai J.X., 2009
107	E. Beiliu	110°29′00″	22°45′00″	Datong 1	Mylonite	213	4	Muscovite	Ar-Ar	Metamorphism	Zhang K.J. & Cai J.X., 2009
108	Kengkou, Xinyi	111°07′33″	22°26′06″	10YK-42	Mylonitic gneiss	228.9	1.2	Muscovite	Ar-Ar	Metamorphism	Wang Y.J. et al., 2021
109	Liuyu, Xinyi	111°07′37″	22°22′07″	10YK-44	Mylonitic gneiss	227.5	1.1	Muscovite	Ar-Ar	Metamorphism	Wang Y.J. et al., 2021
110	NE. Hepu	109°32′00″	21°40′00″	Hetai 1	Mylonite	195.16	1.29	Muscovite	Ar-Ar	Metamorphism	Zhang K.J. & Cai J.X., 2009
111	NE. Hepu	109°32′00″	21°40′00″	Hetai 2	Mylonite	198.89	1.19	Muscovite	Ar-Ar	Metamorphism	Zhang K.J. & Cai J.X., 2009
112	Sanbao, NW. Cenxi	110°49′47″	23°02′12″	TW10-1017-1	Granitic mylonite	231.9	2.2	Muscovite	Ar-Ar	Metamorphism	Guo S.Y. et al., 2020
113	Silun, Luoding	111°18′50″	22°42′15″	G13Y1	Foliated schist	249	3	Muscovite	Ar-Ar	Metamorphism	Shao J.G. et al., 1995
114	Yingqiao, Bobai	110°02′16″	22°05′19″	ZMT-B1	Mylonite	221.98	1.16	Muscovite	Ar-Ar	Metamorphism	Ding R.X., et al., 2018
115	Yingqiao, Bobai	110°02′16″	22°05′19″	ZMT-B2	Mylonite	223.77	1.16	Muscovite	Ar-Ar	Metamorphism	Ding R.X., et al., 2018
116	Yongning, Yangchun	111°36′36″	22°15′04″	G03Y1	Gneissoid granite	229	2	Muscovite	Ar-Ar	Metamorphism	Shao J.G. et al., 1995
117	Chidong, Xinyi	110°56′31″	22°23′37″	02YK-74	Mylonitic paragneiss	227.9	0.3	Biotite	Ar-Ar	Metamorphism	Wang Y.J. et al., 2007
118	Fuhuling, Yangjiang	111°32′36″	21°30′42″	17FH-02	Mylonitic migmatite	212.2	1.2	Biotite	Ar-Ar	Metamorphism	Wang Y.J. et al., 2021
119	Fuhuling, Yangjiang	111°32′36″	21°30′42″	17FH-03	Mylonitic migmatite	212.5	2	Biotite	Ar-Ar	Metamorphism	Wang Y.J. et al., 2021
120	Gaoping,Gaozhou	111°55′11″	21°54′30″	02YK-38	Mylonitic gneiss	221.8	0.4	Biotite	Ar-Ar	Metamorphism	Wang Y.J. et al., 2007
121	Hebapu, Xinyi	111°09′15″	22°22′38″	02YK-27	Mylonitic granite	229.9	0.5	Biotite	Ar-Ar	Metamorphism	Wang Y.J. et al., 2007
122	Jinzhu, Luoding	111°17′43″	22°53′21″	10YK-55	Mylonite	230.9	2.1	Biotite	Ar-Ar	Metamorphism	Wang Y.J. et al., 2021
123	Liantang, Luoding	111°18′34″	22°43′20″	10YK-58	Mylonite	230.6	1.4	Biotite	Ar-Ar	Metamorphism	Wang Y.J. et al., 2021
124	Licun, Rongxian	110°42′00″	22°36′11″	02YK-64	Mylonite	211.1	0.2	Biotite	Ar-Ar	Metamorphism	Wang Y.J. et al., 2007

Table S1 (continued)

No.	Location	Long.(E)	Lat.(N)	Sample No.	Lithology	Age	error	Mineral	Method	Event	Reference
125	Lingwei, Bobai	109°50′24″	21°57′50″	02YK-56	Granitic mylonite	218.4	0.3	Biotite	Ar-Ar	Metamorphism	Wang Y.J. et al., 2007
126	N. Baishi, Xinyi	111°04′00″	22°25′04″	02YK-31	Mylonitic granite	216.9	0.3	Biotite	Ar-Ar	Metamorphism	Wang Y.J. et al., 2007
127	N. Baishi, Xinyi	111°04′39″	22°24′32″	02YK-30	Granitic mylonite	225.4	0.3	Biotite	Ar-Ar	Metamorphism	Wang Y.J. et al., 2007
128	Qianpai, Xinyi	111°10′33″	22°22′31″	02YK-26	Mylonitic gneiss	214.2	0.2	Biotite	Ar-Ar	Metamorphism	Wang Y.J. et al., 2007
129	Puzhou, Yangchun	111°21′57″	22°07′45″	02YK-09	Mylonitic gneiss	207.8	0.2	Biotite	Ar-Ar	Metamorphism	Wang Y.J. et al., 2007
130	Shaniutang,Yangchun	111°37′19″	22°11′36″	02YK-12	Mylonitic gneiss	209	0.2	Biotite	Ar-Ar	Metamorphism	Wang Y.J. et al., 2007
131	Shapa, Yangjiang	111°29′15″	21°30′43″	15YJ-14	Mylonitic gneiss	227.2	1.1	Biotite	Ar-Ar	Metamorphism	Wang Y.J. et al., 2021
132	Shapa, Yangjiang	111°28′26″	21°30′50″	15YJ-15	Mylonite	227.4	1.1	Biotite	Ar-Ar	Metamorphism	Wang Y.J. et al., 2021
133	Shimeng, Yangjiang	111°31′02″	21°38′47″	19YJ-03	Mylonite	215.5	1.1	Biotite	Ar-Ar	Metamorphism	Wang Y.J. et al., 2021
134	Tengbin, Luoding	111°23′32″	22°49′22″	02YK-80	Mylonitic granite	208.9	1.4	Biotite	Ar-Ar	Metamorphism	Wang Y.J. et al., 2007
135	Wenhua, Xinyi	111°02′53″	22°35′32″	10YK-43	Mylonitic gneiss	229.1	1.1	Biotite	Ar-Ar	Metamorphism	Wang Y.J. et al., 2021
136	Xieji, Gaozhou	111°00′31″	21°55′19″	02YK-39	Mylonitic migmatite	224.7	0.4	Biotite	Ar-Ar	Metamorphism	Wang Y.J. et al., 2007
137	Yangxi, Yangjiang	111°37′29″	21°33′08″	19YJ-01	Mylonite	215.4	1.1	Biotite	Ar-Ar	Metamorphism	Wang Y.J. et al., 2021
138	Yongning,Yangchun	111°32′39″	22°16′49″	02YK-15	Mylonite	211.5	0.5	Biotite	Ar-Ar	Metamorphism	Wang Y.J. et al., 2007
139	Chidong, Xinyi	110°57′07.7″	22°27′45.2″	17YK19	Sill Bt monzogneiss	239.5	1.6	Apatite	LA-ICP-MS U-Pb	Metamorphism	Wang X.D. et al., 2020
140	Shikengtang, E. Gaozhou	110°55′19.8″	21°54′27.1″	17YK03	Bt granitic gneiss	240.5	2	Apatite	LA-ICP-MS U-Pb	Metamorphism	Wang X.D. et al., 2020
2. Early Paleozoic Ages											
2.1 Magmatism:											
141	Beijie, Xinyi	110°48′04.02″	22°19′17.46″	1621	Muscovite granite	430	2.9	Zircon	LA-ICP-MS U-Pb	Magmatism	Yan C.L. et al., 2017
142	Bingrong, Beiliu	110°28′13″	22°35′43″	15BR04	Granitic gneiss	459.5	2.7	Zircon	LA-ICP-MS U-Pb	Magmatism	Ke X.Z. et al., 2018
143	Chidong, Xinyi	110°59′30″	22°30′00″	02YK-75	Biotite paragneiss	423	7	Zircon	LA-ICP-MS U-Pb	Magmatism	Wang Y.J. et al., 2007
144	Chidong, Xinyi	110°57′07.7″	22°27′45.2″	17YK19	Sill Bt monzogneiss	437	12	Zircon	LA-ICP-MS U-Pb	Magmatism	Wang X.D. et al., 2020
145	Dagu, Bobai	110°04′00″	21°57′00″	02YK-50	Granitic gneiss	421.9	9.8	Zircon	SHRIMP U-Pb	Magmatism	Wang Y.J. et al., 2007
146	Daning, Hezhou	111°52′31.14″	24°35′29.64″	1582	Monzonite	439	2.9	Zircon	LA-ICP-MS U-Pb	Magmatism	Yan C.L. et al., 2017

Table S1 (continued)

No.	Location	Long.(E)	Lat.(N)	Sample No.	Lithology	Age	error	Mineral	Method	Event	Reference
147	Dashuang	111°10′32″	23°06′20″	12DS05	Dacite dike	430	4	Zircon	LA-ICP-MS U-Pb	Magmatism	Liu S.F. et al., 2018
148	Dashuang	111°10′10″	23°06′05″	15DS10–4	Andesite	443	4	Zircon	LA-ICP-MS U-Pb	Magmatism	Liu S.F. et al., 2018
149	Dashuang	111°10′07″	23°06′06″	15DS11–4	Dolerite	452	7	Zircon	LA-ICP-MS U-Pb	Magmatism	Liu S.F. et al., 2018
150	Dashuang	111°10′19″	23°06′13″	15DS11–3	Basaltic andesite	460	6	Zircon	LA-ICP-MS U-Pb	Magmatism	Liu S.F. et al., 2018
151	Fangji island, Yanjiang	111°10′56″	21°22′49″	18YX17-1	Monzonite	427	5	Zircon	LA-ICP-MS U-Pb	Magmatism	Chen G.K. et al., 2021
152	Fangji island, Yanjiang	111°11′05″	21°22′27″	18YX11-1	Granitic gneiss	432	4	Zircon	LA-ICP-MS U-Pb	Magmatism	Chen G.K. et al., 2021
153	Fuhuling, Yangjiang	111°32′28.54″	21°30′56.90″	LFRB-Zr	Basalt	422	3.2	Zircon	LA-ICP-MS U-Pb	Magmatism	Chen Z. et al., 2021
154	Fuhuling, Yangjiang	111°32′27.26″	21°30′59.62″	MG-Zr	Granite	431	2.7	Zircon	LA-ICP-MS U-Pb	Magmatism	Chen Z. et al., 2021
155	Fuhuling, Yangjiang	111°32′30″	21°30′32.43″	DG2	Monzogranite	435.1	7	Zircon	LA-ICP-MS U-Pb	Magmatism	Zhang J.H. et al., 2019
156	Fuhuling, Yangjiang	111°32′50.77″	21°30′32.33″	SPMG	Diatexite	435.4	1.8	Zircon	LA-ICP-MS U-Pb	Magmatism	Zhang J.H. et al., 2019
157	Fuhuling, Yangjiang	111°32′27.31″	21°30′35.25″	FHMG	Diatexite	437.5	3	Zircon	LA-ICP-MS U-Pb	Magmatism	Zhang J.H. et al., 2019
158	Fuhuling, Yangjiang	111°32′50.77″	21°30′32.33″	SPM	Metatexite	443.3	2.7	Zircon	LA-ICP-MS U-Pb	Magmatism	Zhang J.H. et al., 2019
159	Fuhuling, Yangjiang	111°32′26.42″	21°30′54.80″	MFRB-Zr	Gabbro	452	3	Zircon	LA-ICP-MS U-Pb	Magmatism	Chen Z. et al., 2021
160	Gaozhang, Yunfu	111°52′30″	22°58′00″	gc-6-3	Granodiorite	450	4.5	Zircon	SHRIMP U-Pb	Magmatism	Yu X.G. et al., 2018
161	Gaozhang, Yunfu	111°52′30″	22°58′00″	gc-4	Granitic mylonite	451.5	2.8	Zircon	SHRIMP U-Pb	Magmatism	Yu X.G. et al., 2018
162	Gaozhang, Yunfu	111°52′30″	22°58′00″	V2-19	Biotite granite	463.3	3.3	Zircon	SHRIMP U-Pb	Magmatism	Yu X.G. et al., 2018
163	Gaozhou	110°51′20″	21°54′03″	HL-1	Grt biotite monzonitic granite	413	8	Zircon	SHRIMP U-Pb	Magmatism	Peng S.M. et al., 2006
162	Gaozhang, Yunfu	111°52′30″	22°58′00″	V2-19	Biotite granite	463.3	3.3	Zircon	SHRIMP U-Pb	Magmatism	Yu X.G. et al., 2018

Table S1 (continued)

No.	Location	Long.(E)	Lat.(N)	Sample No.	Lithology	Age	error	Mineral	Method	Event	Reference
163	Gaozhou	110°51′20″	21°54′03″	HL-1	Grt biotite monzonitic granite	413	8	Zircon	SHRIMP U-Pb	Magmatism	Peng S.M. et al., 2006
164	Gaozhou	110°51′20″	21°54′03″	HSW-1	Charnockite	435	11	Zircon	SHRIMP U-Pb	Magmatism	Peng S.B. et al., 2006
165	Gaozhou complex, E. Gaozhou	111°09′00″	22°04′00″	G0108-1	Gneissic granite	430	8	Zircon	SHRIMP U-Pb	Magmatism	Wan Y.S. et al., 2010
166	Gaozhou complex, E. Gaozhou	111°00′00″	22°04′00″	G0107-1	Gneissic granite	443	4	Zircon	SHRIMP U-Pb	Magmatism	Wan Y.S. et al., 2010
167	Gaozhou complex, E. Xinyi	111°12′00″	22°20′00″	G0102-1	Gneissic granite	437	5	Zircon	SHRIMP U-Pb	Magmatism	Wan Y.S. et al., 2010
168	Gaozhou complex, E. Xinyi	111°08′00″	22°20′00″	G0104-1	Two-mica gneiss	443	9	Zircon	SHRIMP U-Pb	Magmatism	Wan Y.S. et al., 2010
169	Hebapu, Xinyi	111°11′00″	22°37′00″	02YK-27	Granitic gneiss	429.6	5.2	Zircon	LA-ICP-MS U-Pb	Magmatism	Wang Y.J. et al., 2007
170	Huanglangen, Maoming	111°18′25.51″	21°58′11.91″	12GZ-24	Granodiorite	437	1.5	Zircon	LA-ICP-MS U-Pb	Magmatism	Qiu X.F. et al., 2018
171	Huangyajiao, Maoming	111°05′37.45″	21°47′42.65″	12GZ-29-1	Charnockite	435.2	2.2	Zircon	LA-ICP-MS U-Pb	Magmatism	Qiu X.F. et al., 2018
172	Jintong, Xinyi	110°46′00″	22°25′20.82″	09YK-10a	Gneissoid granite	449	5	Zircon	LA-ICP-MS U-Pb	Magmatism	Wang Y.J. et al., 2011
173	Licun, Rongxian	110°41′35.76″	22°36′09.18″	09YK-12a	Orthogneiss	443	7	Zircon	LA-ICP-MS U-Pb	Magmatism	Wang Y.J. et al., 2011
174	Lingshan, Rongxian	110°35′44.16″	22°36′40.32″	1633	Biotite gneissic granite	429	3.1	Zircon	LA-ICP-MS U-Pb	Magmatism	Yan C.L. et al., 2017
175	Lingshan, Rongxian	110°36′43.26″	22°35′53.28″	1630	Biotite gneissic granite	431	3.1	Zircon	LA-ICP-MS U-Pb	Magmatism	Yan C.L. et al., 2017
176	Lingshan, Rongxian	110°35′29.70″	22°36′50.40″	1628	Biotite mylonitic granite	435	3	Zircon	LA-ICP-MS U-Pb	Magmatism	Yan C.L. et al., 2017
177	Luchuan,	110°12′2.0″	22°16′7.4″	1009	Gneissic biotite monzogranite	443.3	2.6	Zircon	LA-ICP-MS U-Pb	Magmatism	Wang L. et al., 2013
178	Luchuan,	110°20′9.9″	22°14′11.8″	1010	Gneissic biotite monzogranite	445.7	2.3	Zircon	LA-ICP-MS U-Pb	Magmatism	Wang L. et al., 2013
179	Luofushan, NE. Dongguan	114°12′00″	23°19′30″	BY022-3	Gneiss	439	9	Zircon	SHRIMP U-Pb	Magmatism	Yang D.S. et al., 2010
180	Luogang, NE. Guangzhou	113°26′00″	23°14′00″	17GZ08-1	Biotite granodiorite	441.7	1.6	Zircon	LA-ICP-MS U-Pb	Magmatism	Liu X. et al., 2021

Table S1 (continued)

No.	Location	Long.(E)	Lat.(N)	Sample No.	Lithology	Age	error	Mineral	Method	Event	Reference
181	Maofengshan, NE. Guangzhou	113°22′30″	23°15′00″	BY004-1	Gneiss	446	7	Zircon	SHRIMP U-Pb	Magmatism	Yang D.S. et al., 2010
182	Maofengshan, NE. Guangzhou	113°28′00″	23°18′00″	BY005-1	Gneiss	453.5	7.8	Zircon	SHRIMP U-Pb	Magmatism	Yang D.S. et al., 2010
183	Nabu, Bobai	109°55′36.54″	21°50′57.84″	XD115	Gneissic monzonite	430	2	Zircon	LA-ICP-MS U-Pb	Magmatism	Xia J.L. et al., 2018
184	NE. Gaozhou	111°03′04.0″	22°02′06.4″	11GD01	Gneissic granite	437.4	5.5	Zircon	LA-ICP-MS U-Pb	Magmatism	Chen C.H. et al., 2017
185	NE. Gaozhou	111°07′18.7″	22°12′40.0″	11GD02	Gneissic granite	439.6	4.5	Zircon	LA-ICP-MS U-Pb	Magmatism	Chen C.H. et al., 2017
186	NE. Gaozhou	111°04′10.2″	22°00′36.2″	11GDGZA1	Gneissic granite	440.6	4.1	Zircon	LA-ICP-MS U-Pb	Magmatism	Chen C.H. et al., 2017
187	NE. Gaozhou	111°03′50.4″	22°00′31.3″	23GX11	Meta-sandstone	443.5	8.9	Zircon	LA-ICP-MS U-Pb	Magmatism	Chen C.H. et al., 2017
188	NE. Xinyi	110°57′08.3″	22°27′41.5″	11GD05	Biotite gneiss	431.3	5	Zircon	LA-ICP-MS U-Pb	Magmatism	Chen C.H. et al., 2017
189	Qingzhou island, Yanjiang	111°27′57″	21°28′48″	18YX09-1	Granitic gneiss	436	3	Zircon	LA-ICP-MS U-Pb	Magmatism	Chen G.K. et al., 2021
190	Shanping	110°25′11″	22°13′18″	15SW1–5	Amphibolite	455	6	Zircon	LA-ICP-MS U-Pb	Magmatism	Liu S.F. et al., 2018
191	Shikengtang, E. Gaozhou	110°55′19.8″	21°54′27.1″	17YK03	Bt granitic gneiss	433.9	5.7	Zircon	LA-ICP-MS U-Pb	Magmatism	Wang X.D. et al., 2020
192	Shikengtang, Maoming	110°55′30.85″	21°54′17.54″	12GZ-11	Gneissic monzonite	453.2	5.1	Zircon	LA-ICP-MS U-Pb	Magmatism	Qiu X.F. et al., 2018
193	Shiwo, Beiliu	110°25′23.16″	22°25′20.83″	09YK-15a	Gneissoid granite	415	7	Zircon	LA-ICP-MS U-Pb	Magmatism	Wang Y.J. et al., 2011
194	Songguangling, Cenxi	111°09′46.80″	22°44′15.72″	1601	Two-mica granite	443	3.2	Zircon	LA-ICP-MS U-Pb	Magmatism	Yan C.L. et al., 2017
195	Songwang, Bobai	109°45′35.64″	21°50′55.20″	XD116	Gneissic monzonite	426	4	Zircon	LA-ICP-MS U-Pb	Magmatism	Xia J.L. et al., 2018
196	Songwang, Bobai	109°50′00″	21°50′00″	02YK-60	Foliated granite	440.7	5.6	Zircon	LA-ICP-MS U-Pb	Magmatism	Wang Y.J. et al., 2007
197	W. Xinyi	110°35′44.9″	22°13′19.1″	11GD06	Two-mica gneiss	435	5.1	Zircon	LA-ICP-MS U-Pb	Magmatism	Chen C.H. et al., 2017
198	W. Xinyi	111°54′20″	22°21′20″	1431-1	Migmatitic gneiss	440.3	3.3	Zircon	LA-ICP-MS U-Pb	Magmatism	Ke X.Z. et al., 2018

Table S1 (continued)

No.	Location	Long.(E)	Lat.(N)	Sample No.	Lithology	Age	error	Mineral	Method	Event	Reference
199	Xieji, Gaozhou	111°01′00.12″	21°54′33.66″	09YK-16T	Leucosome in migmatite	435	8	Zircon	LA-ICP-MS U-Pb	Magmatism	Wang Y.J. et al., 2011
200	Xieji, Gaozhou	110°58′51.4″	21°55′17.2″	1012	Gneissic biotite monzogranite	441.1	2	Zircon	LA-ICP-MS U-Pb	Magmatism	Wang L. et al., 2013
201	Xindi, Wuzhou	111°11′13.98″	23°16′14.16″	1586	Granite	436	3	Zircon	LA-ICP-MS U-Pb	Magmatism	Yan C.L. et al., 2017
202	Xintong, Gaozhou	111°08′09.3″	21°52′22.14″	09YK-17	Orthogneiss	452	6	Zircon	LA-ICP-MS U-Pb	Magmatism	Wang Y.J. et al., 2011
203	Xinxing, Yangchun	112°05′28″	22°39′46″	D5784-1	Bt monzonite	444	3	Zircon	LA-ICP-MS U-Pb	Magmatism	Zhou D. et al., 2021
204	Xinyi	110°52′51″	22°21′32″	HXY-1	Biotite monzonitic granite	465	10	Zircon	SHRIMP U-Pb	Magmatism	Peng S.B. et al., 2006
205	Xinyi	110°52′51″	22°21′32″	HY-1	Charnockite	467	9.9	Zircon	SHRIMP U-Pb	Magmatism	Peng S.B. et al., 2006
206	Yingqiao, Bobai	110°01′51.00″	21°57′27.72″	XD119	Gneissic monzonite	433	2	Zircon	LA-ICP-MS U-Pb	Magmatism	Xia J.L. et al., 2018
207	Yonghe, Lianshan	112°02′47.04″	24°37′02.34″	1571	Two-mica granite	426	3.2	Zircon	LA-ICP-MS U-Pb	Magmatism	Yan C.L. et al., 2017
208	Youchalinchang, Nuodong	111°02′46″	23°04′53″	12ND05	Dolerite	437	5	Zircon	LA-ICP-MS U-Pb	Magmatism	Liu S.F. et al., 2018
209	Youchalinchang, Nuodong	111°02′32″	23°05′01″	12ND1–12	Dolerite	447	8	Zircon	LA-ICP-MS U-Pb	Magmatism	Liu S.F. et al., 2018
210	Yunlong, Xingyi	111°01′05.7″	22°30′09.42″	09YK-8B	Orthogneiss	450	8	Zircon	LA-ICP-MS U-Pb	Magmatism	Wang Y.J. et al., 2011
211	Yunlu, Gaozhou	111°04′43″	21°59′25″	GZ14-1	Grt Charnockite	431.4	4.1	Zircon	LA-ICP-MS U-Pb	Magmatism	Li C. et al., 2020
212	Yunlu, Gaozhou	111°03′39″	21°58′25″	ID7-3	Migmatite	431.5	4.3	Zircon	LA-ICP-MS U-Pb	Magmatism	Ke X.Z. et al., 2018
213	Yunlu, Gaozhou	111°03′39″	22°01′11″	GZ-03	Charnockite	432.5	3.2	Zircon	LA-ICP-MS U-Pb	Magmatism	Chen C.H. et al., 2012
214	Yunlu, Gaozhou	111°03′39″	22°01′11″	GZ-05	Orthogneisses	433.3	3.6	Zircon	LA-ICP-MS U-Pb	Magmatism	Chen C.H. et al., 2012
215	Yunlu, Gaozhou	111°03′39″	22°01′11″	GZ-07	Charnockite	433.7	3.5	Zircon	LA-ICP-MS U-Pb	Magmatism	Chen C.H. et al., 2012
216	Yunlu, Gaozhou	111°03′39″	22°01′11″	GZ-08	Orthogneisses	436.2	4.4	Zircon	LA-ICP-MS U-Pb	Magmatism	Chen C.H. et al., 2012

Table S1 (continued)

No.	Location	Long.(E)	Lat.(N)	Sample No.	Lithology	Age	error	Mineral	Method	Event	Reference
217	Yunlu, Gaozhou	111°04′43″	21°59′04″	GZ0307	Gneissic migmatite	437	4	Zircon	LA-ICP-MS U-Pb	Magmatism	Wang D. et al., 2013
218	Yunlu, Gaozhou	111°02′21″	22°01′20″	GZ0705	Gneissic migmatite	438	4	Zircon	LA-ICP-MS U-Pb	Magmatism	Wang D. et al., 2013
219	Yunlu, Gaozhou	111°04′43″	21°59′04″	GZ0301	Charnockite	439	2	Zircon	LA-ICP-MS U-Pb	Magmatism	Wang D. et al., 2013
220	Yunlu, Gaozhou	111°04′43″	21°59′04″	GZ0302	Charnockite	439	4	Zircon	LA-ICP-MS U-Pb	Magmatism	Wang D. et al., 2013
221	Yuntan, Gaozhou	111°02′00″	21°55′00″	02YK-42	Biotite orthognesis	427.1	4.2	Zircon	LA-ICP-MS U-Pb	Magmatism	Wang Y.J. et al., 2007
222	Zhusha, Xinyi	110°58′3.8″	22°33′55.9″	1018	Monzogranite	443.7	1.7	Zircon	LA-ICP-MS U-Pb	Magmatism	Wang L. et al., 2013
223	Zhuzhou island, Yanjiang	111°22′54″	21°26′22″	18YX18-2	Granitic gneiss	433	4	Zircon	LA-ICP-MS U-Pb	Magmatism	Chen G.K. et al., 2021
224	NE. Gaozhou	111°03′50.4″	22°00′31.3″	23GX11	Meta-sandstone	435	5.1	Monazite	EMP U-Th-Pb	Magmatism	Chen C.H. et al., 2017
225	NE. Xinyi	110°57′08.3″	22°27′41.5″	11GD05	Biotite gneiss	440.6	7.1	Monazite	EMP U-Th-Pb	Magmatism	Chen C.H. et al., 2017
226	W. Xinyi	110°31′08.1″	22°25′44.6″	23GX04	Biotite gneiss	440.7	10	Monazite	EMP U-Th-Pb	Magmatism	Chen C.H. et al., 2017
-	Shapa, Yangjiang	111°28′18.1″	21°30′45.8″	S01	Undeformed granite	426.4	6.4	Zircon	LA-ICP-MS U-Pb	Magmatism	Cochelin B. et al., 2022
2.2 Metamorphism:											
227	Fuhuling, Yangjiang	111°32′40.20″	21°30′27.40″	FHM	Metatexite	444	13	Zircon	LA-ICP-MS U-Pb	Metamorphism	Zhang J.H. et al., 2019
228	Gaozhou complex, E. Gaozhou	111°01′00″	21°57′00″	G0105-1	Biotite gneiss	438	8	Zircon	SHRIMP U-Pb	Metamorphism	Wan Y.S. et al., 2010
229	Qingshuikou, Beiliu	110°26′10″	22°36′58″	TW3062-1	Grt pyroxenite	439	8	Zircon	SHRIMP U-Pb	Metamorphism	Qin X.F. et al., 2006
230	Shiwo, Beiliu	110°26′15″	22°13′28″	TW3086-1	Plagioclase amphibolite	455	10	Zircon	SHRIMP U-Pb	Metamorphism	Qin X.F. et al., 2006
231	Xieji, Gaozhou	110°00′31.02″	21°55′17.82″	GD-4	Grt amphibolite	446	12	Zircon	SHRIMP U-Pb	Metamorphism	Wang Y.J. et al., 2012
232	Xinfeng, Beiliu	110°34′24″	22°29′13″	TW3102-1	Granitic gneiss	454	6	Zircon	SHRIMP	Metamorphism	Qin X.F. et al., 2006
233	Yunlu, Gaozhou	111°03′49″	21°57′24″	GZ0101	Bt-Pl gneiss	425	5	Zircon	LA-ICP-MS U-Pb	Metamorphism	Wang D. et al., 2013

Table S1 (continued)

No.	Location	Long.(E)	Lat.(N)	Sample No.	Lithology	Age	error	Mineral	Method	Event	Reference
234	Yunlu, Gaozhou	111°04′18.06″	22°00′38.40″	HG-153	Pelitic granulite	428	18	Zircon	SHRIMP U-Pb	Metamorphism	Wang Y.J. et al., 2012
235	Yunlu, Gaozhou	111°03′39″	22°01′11″	GZ-09	Granulites	428	16	Zircon	LA-ICP-MS U-Pb	Metamorphism	Chen C.H. et al., 2012
236	Yunlu, Gaozhou	111°03′49″	21°57′24″	GZ0102	Bt-Pl gneiss	432	3	Zircon	LA-ICP-MS U-Pb	Metamorphism	Wang D. et al., 2013
237	Yunlu, Gaozhou	111°03′39″	22°01′11″	GZ-13	Granulites	440.7	6.1	Zircon	LA-ICP-MS U-Pb	Metamorphism	Chen C.H. et al., 2012
238	Yunlu, Gaozhou	111°03′39″	22°01′11″	GZ-11	Granulites	442.2	5.2	Zircon	LA-ICP-MS U-Pb	Metamorphism	Chen C.H. et al., 2012
239	Yunlu, Gaozhou	111°03′17″	21°58′31″	23GX11	Paragneiss	443.6	9	Zircon	LA-ICP-MS U-Pb	Metamorphism	Chen C.H. et al., 2012
240	N. Gaozhou	110°56′03″	22°03′45″	2013YK25	Sill biotite schist	435.3	1.9	Monazite	LA-ICP-MS U-Pb	Metamorphism	Zhang C.L. et al., 2015
241	Yunlu, Gaozhou	111°03′39″	22°01′11″	GZ-09G	Granulites	432	12	Monazite	EMP U-Th-Pb	Metamorphism	Chen C.H. et al., 2012
242	Yunlu, Gaozhou	111°03′39″	22°01′11″	GZ-11	Granulites	432	12	Monazite	EMP U-Th-Pb	Metamorphism	Chen C.H. et al., 2012
243	Yunlu, Gaozhou	111°03′39″	22°01′11″	GZ-13-2	Granulites	432	21	Monazite	EMP U-Th-Pb	Metamorphism	Chen C.H. et al., 2012
244	Yunlu, Gaozhou	111°03′39″	22°01′11″	GZ-11G	Granulites	433	10	Monazite	EMP U-Th-Pb	Metamorphism	Chen C.H. et al., 2012
245	Yunlu, Gaozhou	111°03′39″	22°01′11″	GZ-15	Granulites	433	11	Monazite	EMP U-Th-Pb	Metamorphism	Chen C.H. et al., 2012
246	Yunlu, Gaozhou	111°03′39″	22°01′11″	GZ-07G	Charnockite	434	11	Monazite	EMP U-Th-Pb	Metamorphism	Chen C.H. et al., 2012
247	Yunlu, Gaozhou	111°03′17″	21°58′31″	23GX11	Paragneiss	434	18	Monazite	EMP U-Th-Pb	Metamorphism	Chen C.H. et al., 2012
248	Yunlu, Gaozhou	111°03′39″	22°01′11″	GZ-03	Charnockite	435.5	9.8	Monazite	EMP U-Th-Pb	Metamorphism	Chen C.H. et al., 2012
249	Yunlu, Gaozhou	111°03′39″	22°01′11″	GZ-13-1	Granulites	439	11	Monazite	EMP U-Th-Pb	Metamorphism	Chen C.H. et al., 2012
250	Yunlu, Gaozhou	111°03′39″	22°01′11″	GZ-15	Granulites	441	17	Monazite	EMP U-Th-Pb	Metamorphism	Chen C.H. et al., 2012
251	Yunlu, Gaozhou	111°03′39″	22°01′11″	GZ-11	Granulites	442	17	Monazite	EMP U-Th-Pb	Metamorphism	Chen C.H. et al., 2012

Notes: 1. The GPS estimated based on the geological map is marked with an underline. 2. The references in Chinese are marked with an underline.

Table S2. Compilations of the published middle-low-temperature geochronological data

No.	Massif	Location	Latitude	Longitude	Lithology	Sample	Age (Ma)	Error (Ma)	Method	References
1	Nanling	Piaotang, Dayu	25.51	114.39	Quartz vein	09PT12Ms	152.9	0.8	Muscovite Ar-Ar	Bai X.J. et al., 2013, Geochim. Cosmochim. Acta
2	Nanling	Piaotang, Dayu	25.51	114.39	Quartz vein	09PT31Ms	157.3	0.8	Muscovite Ar-Ar	Bai X.J. et al., 2013, Geochim. Cosmochim. Acta
3	Nanling	Piaotang, Dayu	25.51	114.39	Quartz vein	09PT37Ms	157.2	0.8	Muscovite Ar-Ar	Bai X.J. et al., 2013, Geochim. Cosmochim. Acta
4	Nanling	Piaotang, Dayu	25.51	114.39	Quartz vein	09PT01Ms	159.3	0.8	Muscovite Ar-Ar	Bai X.J. et al., 2013, Geochim. Cosmochim. Acta
5	Nanling	Taoxikeng, Chongyi	25.65	114.23	Ganite	FLK206-3	152.7	1.5	Muscovite Ar-Ar	Guo C.L. et al., 2011, Ore Geol. Rev.
6	Nanling	Taoxikeng, Chongyi	25.65	114.23	Ganite	FLK106-2	153.4	1.3	Muscovite Ar-Ar	Guo C.L. et al., 2011, Ore Geol. Rev.
7	Nanling	Xihuashan, Dayu	25.43	114.31	Granite	—	152.8	1.6	Muscovite Ar-Ar	Hu R.Z. et al., 2012, Lithos
8	Nanling	Aotou, Chongyi	25.59	114.10	Quartz vein	—	228.7	1.5	Muscovite Ar-Ar	Liu L. et al., 2023, Ore Geol. Rev.
9	Nanling	Keshuling, Chongyi	25.63	114.18	Quartz vein	—	158.9	1.4	Muscovite Ar-Ar	Liu S.B. et al., 2008, Acta Geol. Sinica
10	Nanling	Keshuling, Chongyi	25.63	114.18	Quartz vein	—	158.8	1.2	Muscovite Ar-Ar	Liu S.B. et al., 2008, Acta Geol. Sinica
11	Nanling	Dalingbei, Rucheng	25.37	113.53	Greisen	—	151	1	Muscovite Ar-Ar	Lu Y.Y. et al., 2018, J. Guilin Univ. Technology
12	Nanling	Mashuang, Ganzhou	26.01	114.75	Mylonitic granite	750	198.8	0.3	Muscovite Ar-Ar	Wang B. et al., 2014, J.Geol.
13	Nanling	Yajiangqiao, Zhuzhou	27.37	113.32	Quartz vein	—	215.1	2	Muscovite Ar-Ar	Yu Y.S. et al., 2022, Ore Geol. Rev.
14	Nanling	Xianghualing, Linwu	25.45	112.56	Ganite	TGP-24	154.4	1.1	Muscovite Ar-Ar	Yuan S.D. et al., 2007, Acta Geol. Sinica
15	Nanling	Xianghuapu, Linwu	25.40	112.60	Marble	XHP-65	161.3	1.1	Muscovite Ar-Ar	Yuan S.D. et al., 2007, Acta Geol. Sinica
16	Nanling	Jiangfengling, Linwu	25.39	112.58	Tin ore	JFL-2	158.7	1.2	Muscovite Ar-Ar	Yuan S.D. et al., 2007, Acta Geol. Sinica
17	Nanling	Zhangjialong, Zixing	25.97	113.62	Greisen	ZJL-2	153.5	1	Muscovite Ar-Ar	Yuan S.D. et al., 2018, Economic Geology
18	Nanling	Zhuyuanli, Zixing	25.97	113.82	Greisenized granite	ZYL-1	151.64	0.96	Muscovite Ar-Ar	Yuan Y.B. et al., 2018, Ore Geol. Rev.
19	Nanling	Wangxianling, Chenzhou	25.75	113.10	Tungsten deposit	WXL-2	214.3	1.1	Muscovite Ar-Ar	Zhang R.Q. et al., 2015, Ore Geol. Rev.
20	Nanling	Penggongmiao, Zixing	26.20	113.67	Pegmatite	PGM-07	372.7	2	Muscovite Ar-Ar	Zhang W.L. et al., 2014, Acta Geologica Sinica
21	Nanling	Penggongmiao, Zixing	26.08	113.73	Pegmatite	PGM-23	307	1.6	Muscovite Ar-Ar	Zhang W.L. et al., 2014, Acta Geologica Sinica
22	Nanling	Yingyangguan, Hezhou	24.60	111.91	Phyllite	PM009-26-1M	223.5	1.5	Sericite Ar-Ar	Wang L.Z. et al., 2019, J. Earth Science and Environment
23	Nanling	Yingyangguan, Hezhou	24.60	111.91	Phyllite	PM009-28-1M	227.4	1.5	Sericite Ar-Ar	Wang L.Z. et al., 2019, J. Earth Science and Environment
24	Nanling	Huangshaping, Guiyang	25.67	112.69	Granite porphyry	HSP-1	153.4	0.5	K-feldspar Ar-Ar	Li H. et al., 2017, Ore Geol. Rev.
25	Nanling	Huangshaping, Guiyang	25.67	112.69	Granite porphyry	HSP-2	153.2	0.5	K-feldspar Ar-Ar	Li H. et al., 2017, Ore Geol. Rev.
26	Nanling	Huangshaping, Guiyang	25.67	112.69	Quartz porphyry	HSP-3	154.3	0.6	K-feldspar Ar-Ar	Li H. et al., 2017, Ore Geol. Rev.
27	Nanling	Huangshaping, Guiyang	25.67	112.69	Granophyre	HSP-4	152.9	0.5	K-feldspar Ar-Ar	Li H. et al., 2017, Ore Geol. Rev.
28	Nanling	Guidong	26.08	114.00	Granodiorite	—	371.4	1.2	Hornblende Ar-Ar	Li X.H., 1994, Chemical Geol.
29	Nanling	Hongshuizhai, Dayu	25.48	114.24	Greisen	—	156.3	1.3	Molybdenite Re-Os	Feng C.Y. et al., 2011, China Tungsten Industry
30	Nanling	Jiulongnao, Dayu	25.48	114.20	Greisen	—	151.5	1.1	Molybdenite Re-Os	Feng C.Y. et al., 2011, China Tungsten Industry
31	Nanling	Zhangdongkeng, Dayu	25.46	114.21	Greisen	—	151.3	1.7	Molybdenite Re-Os	Feng C.Y. et al., 2011, China Tungsten Industry
32	Nanling	Taoxikeng, Chongyi	25.65	114.23	Quartz-veins	—	154.4	3.8	Molybdenite Re-Os	Guo C.L. et al., 2011, Ore Geol. Rev.

Table S2 (continued)

No.	Massif	Location	Latitude	Longitude	Lithology	Sample	Age (Ma)	Error (Ma)	Method	References
33	Nanling	Xihuashan, Dayu	25.43	114.31	Granite	—	157.8	0.9	Molybdenite Re-Os	Hu R.Z. et al., 2012, Lithos
34	Nanling	Chuankou, Hengyang	26.91	113.02	Quartz vein	CK211	212.5	7.3	Molybdenite Re-Os	Li W.S. et al., 2021, Ore Geol. Rev.
35	Nanling	Sanjiaotan, Hengyang	26.90	113.04	Quartz vein	—	224.9	1.3	Molybdenite Re-Os	Peng N.L., 2017, Mineral Deposits
36	Nanling	Huangshaping, Guiyang	25.67	112.69	Molybdenite	—	156.9	1.1	Molybdenite Re-Os	Yao J.M. et al., 2007, Science in China Series D: Earth Sciences
37	Nanling	Wangxianling, Chenzhou	25.75	113.10	Wolframite–quartz veins	—	228.1	2.6	Molybdenite Re-Os	Zhang R.Q. et al., 2015, Ore Geol. Rev.
38	Nanling	Wangxianling, Chenzhou	25.77	113.07	Wolframite–quartz veins	—	220.7	4.1	Molybdenite Re-Os	Zhang R.Q. et al., 2015, Ore Geol. Rev.
39	Nanling	Muziyuan, Dayu	25.47	114.36	Quartz vein	—	151.1	8.5	Molybdenite Re-Os	Zhang W.L et al., 2009, Acta Geol. Sin.
40	Nanling	Aotou, Chongyi	25.59	114.10	Quartz vein	—	227.4	6.9	Cassiterite U-Pb	Liu L. et al., 2023, Ore Geol. Rev.
41	Nanling	Xianghualing, Linwu	25.45	112.56	Tin ore	XF-51	156	4	Cassiterite U-Pb	Yuan S.D. et al., 2008, Miner Deposita
42	Nanling	Baxiannao, Dayu	25.67	115.43	Quartz vein	BXN	158.8	2.9	Cassiterite U-Pb	Zhang J. et al., 2021b, Ore Geol. Rev.
43	Nanling	Keshuling, Chongyi	25.63	114.18	Quartz vein	KSL	157.5	4.1	Cassiterite U-Pb	Zhang J. et al., 2021b, Ore Geol. Rev.
44	Nanling	Wangxianling, Chenzhou	25.77	113.07	Tin deposit	WXL-17	154.8	5.8	Cassiterite U-Pb	Zhang R.Q. et al., 2015, Ore Geol. Rev.
45	Nanling	Wangxianling, Chenzhou	25.75	113.10	Tin deposit	IV-1	157.8	4.1	Cassiterite U-Pb	Zhang R.Q. et al., 2015, Ore Geol. Rev.
46	Nanling	Qitianling	25.59	112.83	Granite	H63	26	3	Apatite fission track	Su J.B. et al., 2017, International Geol. Rev.
47	Nanling	Qitianling	25.51	112.84	Granite	H64	28.5	1.7	Apatite fission track	Su J.B. et al., 2017, International Geol. Rev.
48	Nanling	Dayishan	26.12	112.68	Granite	XN11	45.8	3	Apatite fission track	Su J.B. et al., 2017, International Geol. Rev.
49	Nanling	Dayishan	26.09	112.70	Granite	XN12	42.1	2.6	Apatite fission track	Su J.B. et al., 2017, International Geol. Rev.
50	Nanling	Rucheng	25.64	113.71	Sandstone	XN195	33.4	2.2	Apatite fission track	Su J.B. et al., 2017, International Geol. Rev.
51	Nanling	Rucheng	25.63	113.71	Sandstone	XN196	33.1	2.1	Apatite fission track	Su J.B. et al., 2017, International Geol. Rev.
52	Nanling	Rucheng	25.62	113.70	Sandstone	XN197	36.6	2.3	Apatite fission track	Su J.B. et al., 2017, International Geol. Rev.
53	Nanling	Qitianling north	25.83	113.33	Granite	XN228	37.4	2.5	Apatite fission track	Su J.B. et al., 2017, International Geol. Rev.
54	Nanling	Tashan	26.12	112.35	Granite	XN299	26.8	1.8	Apatite fission track	Su J.B. et al., 2017, International Geol. Rev.
55	Nanling	Tashan	26.12	112.34	Granite	XN300	36.3	2.1	Apatite fission track	Su J.B. et al., 2017, International Geol. Rev.
56	Nanling	Tashan	26.13	112.32	Granite	XN302	26.6	1.9	Apatite fission track	Su J.B. et al., 2017, International Geol. Rev.
57	Nanling	Tashan	26.14	112.37	Granite	XN303	29.7	1.5	Apatite fission track	Su J.B. et al., 2017, International Geol. Rev.
58	Nanling	Tashan	26.13	112.44	Granite	XN306	34.7	1.7	Apatite fission track	Su J.B. et al., 2017, International Geol. Rev.
59	Nanling	Tashan	26.12	112.44	Granite	XN307	24.9	1.3	Apatite fission track	Su J.B. et al., 2017, International Geol. Rev.
60	Nanling	Tashan	26.10	112.45	Granite	XN309	23.6	1.5	Apatite fission track	Su J.B. et al., 2017, International Geol. Rev.
61	Nanling	Dayishan	26.09	112.67	Granite	XN314	29.1	1.6	Apatite fission track	Su J.B. et al., 2017, International Geol. Rev.
62	Nanling	Dayishan	26.08	112.65	Granite	XN315	27.8	2.5	Apatite fission track	Su J.B. et al., 2017, International Geol. Rev.
63	Nanling	Dayishan	26.07	112.65	Granite	XN316	35	2	Apatite fission track	Su J.B. et al., 2017, International Geol. Rev.
64	Nanling	Qitianling	25.53	112.79	Granite	XN92	33	2.5	Apatite fission track	Su J.B. et al., 2017, International Geol. Rev.
65	Nanling	Qitianling	25.51	112.78	Granite	XN93	28.5	2	Apatite fission track	Su J.B. et al., 2017, International Geol. Rev.
66	Nanling	Zhuguangshan	25.31	113.97	Granite	YCJ01	59.4	2	Apatite fission track	Sun Y. et al., 2021, Ore Geol. Rev.
67	Nanling	Zhuguangshan	25.32	113.96	Granite	YCJ02	57.6	1.9	Apatite fission track	Sun Y. et al., 2021, Ore Geol. Rev.

Table S2 (continued)

No.	Massif	Location	Latitude	Longitude	Lithology	Sample	Age (Ma)	Error (Ma)	Method	References
68	Nanling	Zhuguangshan	25.31	113.95	Granite	YCJ05	62.8	1.5	Apatite fission track	Sun Y. et al., 2021, Ore Geol. Rev.
69	Nanling	Zhuguangshan	25.31	113.94	Granite	YCJ06	58.1	2.2	Apatite fission track	Sun Y. et al., 2021, Ore Geol. Rev.
70	Nanling	Zhuguangshan	25.29	113.94	Granite	YCJ08	57.5	2.5	Apatite fission track	Sun Y. et al., 2021, Ore Geol. Rev.
71	Nanling	Fuxi	25.22	113.84	Granite	12GH23	69	3.9	Apatite fission track	Tao N. et al., 2019, Gondwana Res.
72	Nanling	Fuxi	25.18	113.84	Granite	12GH24	62	3.3	Apatite fission track	Tao N. et al., 2019, Gondwana Res.
73	Nanling	Shitan, Hengyang	26.94	112.83	Granite	01GD-09	57.7	4.6	Apatite fission track	Wang Y. et al., 2020, J. Asian Earth Sci.
74	Nanling	Qitianling, Chenzhou	25.51	112.84	Granite	01QT-03	65.3	3.9	Apatite fission track	Wang Y. et al., 2020, J. Asian Earth Sci.
75	Nanling	Jiulongjiang, Rucheng	25.43	113.83	Granite	20YZH-30	52.9	5	Apatite fission track	Wang Y. et al., 2020, J. Asian Earth Sci.
76	Nanling	Zhuguangshan	25.32	113.96	Granite	YCJ03-1	43.3	2.7	Apatite (U-Th)/He	Sun Y. et al., 2021, Ore Geol. Rev.
77	Nanling	Zhuguangshan	25.32	113.96	Granite	YCJ03-2	33.5	2.1	Apatite (U-Th)/He	Sun Y. et al., 2021, Ore Geol. Rev.
78	Nanling	Zhuguangshan	25.32	113.96	Granite	YCJ03-3	46.4	2.9	Apatite (U-Th)/He	Sun Y. et al., 2021, Ore Geol. Rev.
79	Nanling	Zhuguangshan	25.32	113.94	Granite	YCJ04-1	22.9	1.4	Apatite (U-Th)/He	Sun Y. et al., 2021, Ore Geol. Rev.
80	Nanling	Zhuguangshan	25.32	113.94	Granite	YCJ04-2	25.6	1.6	Apatite (U-Th)/He	Sun Y. et al., 2021, Ore Geol. Rev.
81	Nanling	Zhuguangshan	25.31	113.93	Granite	YCJ10-1	34.8	2.2	Apatite (U-Th)/He	Sun Y. et al., 2021, Ore Geol. Rev.
82	Nanling	Zhuguangshan	25.31	113.93	Granite	YCJ10-2	36.2	2.2	Apatite (U-Th)/He	Sun Y. et al., 2021, Ore Geol. Rev.
83	Nanling	Fuxi	25.22	113.84	Granite	12GH23	34	2	Apatite (U-Th)/He	Tao N. et al., 2019, Gondwana Res.
84	Nanling	Fuxi	25.18	113.84	Granite	12GH24	37	3	Apatite (U-Th)/He	Tao N. et al., 2019, Gondwana Res.
85	Nanling	Baoshan, Guiyang	25.73	112.71	Granodioritic porphyry	BS-2	51.3	3.8	Apatite (U-Th)/He	Wu J.H. et al., 2023, Tectonics
86	Nanling	Qianlishan, Chenzhou	25.77	113.16	Granite	QLS-1	82	4.7	Apatite (U-Th)/He	Wu J.H. et al., 2023, Tectonics
87	Nanling	Qitianling, Chenzhou	25.53	112.78	Granite	QTL-2	30.6	1.9	Apatite (U-Th)/He	Wu J.H. et al., 2023, Tectonics
88	Nanling	Tongshanling, Jiaingyong	25.27	111.46	Granodiorite	TSL-3	44.7	3.3	Apatite (U-Th)/He	Wu J.H. et al., 2023, Tectonics
89	Nanling	Qunfeng, Zhuzhou	27.79	113.10	Granite	01JF-02	118.3	15	Zircon fission track	Wang Y. et al., 2020, J. Asian Earth Sci.
90	Nanling	Qitianling, Chenzhou	25.51	112.84	Granite	01QT-03	94.4	8.7	Zircon fission track	Wang Y. et al., 2020, J. Asian Earth Sci.
91	Nanling	Jiulongjiang, Rucheng	25.43	113.83	Granite	20YZH-30	106.6	7.9	Zircon fission track	Wang Y. et al., 2020, J. Asian Earth Sci.
92	Nanling	Zhuangguangshan	25.31	113.97	Granite	YCJ01-1	112.5	7	Zircon (U-Th)/He	Sun Y. et al., 2021, Ore Geol. Rev.
93	Nanling	Zhuangguangshan	25.31	113.97	Granite	YCJ01-2	85.4	5.3	Zircon (U-Th)/He	Sun Y. et al., 2021, Ore Geol. Rev.
94	Nanling	Zhuangguangshan	25.31	113.97	Granite	YCJ01-3	122.6	7.6	Zircon (U-Th)/He	Sun Y. et al., 2021, Ore Geol. Rev.
95	Nanling	Zhuangguangshan	25.32	113.96	Granite	YCJ02-1	38.1	2.4	Zircon (U-Th)/He	Sun Y. et al., 2021, Ore Geol. Rev.
96	Nanling	Zhuangguangshan	25.32	113.96	Granite	YCJ02-2	103.1	6.4	Zircon (U-Th)/He	Sun Y. et al., 2021, Ore Geol. Rev.
97	Nanling	Zhuangguangshan	25.32	113.96	Granite	YCJ02-3	107	6.6	Zircon (U-Th)/He	Sun Y. et al., 2021, Ore Geol. Rev.
98	Nanling	Zhuangguangshan	25.32	113.96	Granite	YCJ02-4	83.3	5.2	Zircon (U-Th)/He	Sun Y. et al., 2021, Ore Geol. Rev.
99	Nanling	Zhuangguangshan	25.32	113.96	Granite	YCJ03-1	23.6	1.5	Zircon (U-Th)/He	Sun Y. et al., 2021, Ore Geol. Rev.
100	Nanling	Zhuangguangshan	25.32	113.96	Granite	YCJ03-2	41	2.5	Zircon (U-Th)/He	Sun Y. et al., 2021, Ore Geol. Rev.
101	Nanling	Zhuangguangshan	25.32	113.96	Granite	YCJ03-3	55.1	3.4	Zircon (U-Th)/He	Sun Y. et al., 2021, Ore Geol. Rev.
102	Nanling	Zhuangguangshan	25.32	113.94	Granite	YCJ04-1	92.8	5.8	Zircon (U-Th)/He	Sun Y. et al., 2021, Ore Geol. Rev.
103	Nanling	Zhuangguangshan	25.32	113.94	Granite	YCJ04-2	93.7	5.8	Zircon (U-Th)/He	Sun Y. et al., 2021, Ore Geol. Rev.

Table S2 (continued)

No.	Massif	Location	Latitude	Longitude	Lithology	Sample	Age (Ma)	Error (Ma)	Method	References
104	Nanling	Zhuangguangshan	25.32	113.94	Granite	YCJ04-3	96.7	6	Zircon (U-Th)/He	Sun Y. et al., 2021, Ore Geol. Rev.
105	Nanling	Zhuangguangshan	25.32	113.94	Granite	YCJ04-4	106.3	6.6	Zircon (U-Th)/He	Sun Y. et al., 2021, Ore Geol. Rev.
106	Nanling	Zhuangguangshan	25.31	113.95	Granite	YCJ05-1	113.3	7	Zircon (U-Th)/He	Sun Y. et al., 2021, Ore Geol. Rev.
107	Nanling	Zhuangguangshan	25.31	113.95	Granite	YCJ05-2	96.2	6	Zircon (U-Th)/He	Sun Y. et al., 2021, Ore Geol. Rev.
108	Nanling	Zhuangguangshan	25.31	113.94	Granite	YCJ06-1	101.6	6.3	Zircon (U-Th)/He	Sun Y. et al., 2021, Ore Geol. Rev.
109	Nanling	Zhuangguangshan	25.31	113.94	Granite	YCJ06-2	105.1	6.5	Zircon (U-Th)/He	Sun Y. et al., 2021, Ore Geol. Rev.
110	Nanling	Zhuangguangshan	25.31	113.94	Granite	YCJ06-3	79.2	4.9	Zircon (U-Th)/He	Sun Y. et al., 2021, Ore Geol. Rev.
111	Nanling	Zhuangguangshan	25.28	113.95	Granite	YCJ07-1	51.5	3.2	Zircon (U-Th)/He	Sun Y. et al., 2021, Ore Geol. Rev.
112	Nanling	Zhuangguangshan	25.28	113.95	Granite	YCJ07-2	56.1	3.5	Zircon (U-Th)/He	Sun Y. et al., 2021, Ore Geol. Rev.
113	Nanling	Zhuangguangshan	25.28	113.95	Granite	YCJ07-3	49.9	3.1	Zircon (U-Th)/He	Sun Y. et al., 2021, Ore Geol. Rev.
114	Nanling	Zhuangguangshan	25.28	113.95	Granite	YCJ07-4	37.1	2.3	Zircon (U-Th)/He	Sun Y. et al., 2021, Ore Geol. Rev.
115	Nanling	Zhuangguangshan	25.29	113.94	Granite	YCJ08-1	63.9	4	Zircon (U-Th)/He	Sun Y. et al., 2021, Ore Geol. Rev.
116	Nanling	Zhuangguangshan	25.29	113.94	Granite	YCJ08-2	78.8	4.9	Zircon (U-Th)/He	Sun Y. et al., 2021, Ore Geol. Rev.
117	Nanling	Zhuangguangshan	25.29	113.94	Granite	YCJ08-3	68.4	4.2	Zircon (U-Th)/He	Sun Y. et al., 2021, Ore Geol. Rev.
118	Nanling	Zhuangguangshan	25.29	113.94	Granite	YCJ08-4	93.6	5.8	Zircon (U-Th)/He	Sun Y. et al., 2021, Ore Geol. Rev.
119	Nanling	Zhuangguangshan	25.31	113.93	Granite	YCJ10-1	92	5.7	Zircon (U-Th)/He	Sun Y. et al., 2021, Ore Geol. Rev.
120	Nanling	Zhuangguangshan	25.31	113.93	Granite	YCJ10-2	49.7	3.1	Zircon (U-Th)/He	Sun Y. et al., 2021, Ore Geol. Rev.
121	Nanling	Zhuangguangshan	25.31	113.93	Granite	YCJ10-3	24.3	1.5	Zircon (U-Th)/He	Sun Y. et al., 2021, Ore Geol. Rev.
122	Nanling	Zhuangguangshan	25.31	113.93	Granite	YCJ10-4	83.6	5.2	Zircon (U-Th)/He	Sun Y. et al., 2021, Ore Geol. Rev.
123	Nanling	Fuxi	25.22	113.84	Granite	12GH23	130	9	Zircon (U-Th)/He	Tao N. et al., 2019, Gondwana Res.
124	Nanling	Fuxi	25.18	113.84	Granite	12GH24	139	9	Zircon (U-Th)/He	Tao N. et al., 2019, Gondwana Res.
125	Nanling	Baoshan, Guiyang	25.73	112.71	Granodioritic porphyry	BS-1	132.9	4.5	Zircon (U-Th)/He	Wu J.H. et al., 2023, Tectonics
126	Nanling	Baoshan, Guiyang	25.73	112.71	Granodioritic porphyry	BS-2	146.2	4	Zircon (U-Th)/He	Wu J.H. et al., 2023, Tectonics
127	Nanling	Baoshan, Guiyang	25.73	112.71	Granodioritic porphyry	BS-3	131	7.4	Zircon (U-Th)/He	Wu J.H. et al., 2023, Tectonics
128	Nanling	Dayishan, Changning	26.32	112.54	Granite	DYS-1	48	3.1	Zircon (U-Th)/He	Wu J.H. et al., 2023, Tectonics
129	Nanling	Jiuyishan, Hongtangying	25.22	111.90	Granite	JYS-7	115.6	6.1	Zircon (U-Th)/He	Wu J.H. et al., 2023, Tectonics
130	Nanling	Qianlishan, Chenzhou	25.77	113.16	Granite	QLS-1	86.6	3.1	Zircon (U-Th)/He	Wu J.H. et al., 2023, Tectonics
131	Nanling	Qianlishan, Chenzhou	25.76	113.17	Granite	QLS-2	81.3	3.3	Zircon (U-Th)/He	Wu J.H. et al., 2023, Tectonics
132	Nanling	Qitianling, Chenzhou	25.54	112.76	Granite	QTL-1	90.2	3.5	Zircon (U-Th)/He	Wu J.H. et al., 2023, Tectonics
133	Nanling	Qitianling, Chenzhou	25.53	112.78	Granite	QTL-2	84.2	3.3	Zircon (U-Th)/He	Wu J.H. et al., 2023, Tectonics
134	Nanling	Qitianling, Chenzhou	25.53	112.80	Granite	QTL-5	71.2	3.5	Zircon (U-Th)/He	Wu J.H. et al., 2023, Tectonics
135	Nanling	Qitianling, Chenzhou	25.51	112.83	Granite	QTL-6	90.7	3.8	Zircon (U-Th)/He	Wu J.H. et al., 2023, Tectonics
136	Nanling	Qitianling, Chenzhou	25.46	112.80	Granite	QTL-7	87.4	4.6	Zircon (U-Th)/He	Wu J.H. et al., 2023, Tectonics
137	Nanling	Tongshanling, Jiaingyong	25.28	111.46	Granodiorite	TSL-1	86.6	3.4	Zircon (U-Th)/He	Wu J.H. et al., 2023, Tectonics
138	Nanling	Tongshanling, Jiaingyong	25.27	111.46	Granodiorite	TSL-3	79	4.8	Zircon (U-Th)/He	Wu J.H. et al., 2023, Tectonics
139	Nanling	Tongshanling, Jiaingyong	25.27	111.47	Granodiorite	TSL-4	87.5	2.5	Zircon (U-Th)/He	Wu J.H. et al., 2023, Tectonics

Table S2 (continued)

No.	Massif	Location	Latitude	Longitude	Lithology	Sample	Age (Ma)	Error (Ma)	Method	References
140	Nanling	Tongshanling, Jiaingyong	25.27	111.47	Granodiorite	TSL-6	67	4.1	Zircon (U-Th)/He	Wu J.H. et al., 2023, Tectonics
141	Nanling	Weijia, Jiangyong	25.36	111.58	Granite porphyry	WJ-1	142.9	6.2	Zircon (U-Th)/He	Wu J.H. et al., 2023, Tectonics
142	Nanling	Weijia, Jiangyong	25.36	111.58	Granite porphyry	WJ-3	104.3	10.1	Zircon (U-Th)/He	Wu J.H. et al., 2023, Tectonics
143	Nanling	Wangxianling, Chenzhou	25.77	113.13	Granite	WXL-1	69.8	3.9	Zircon (U-Th)/He	Wu J.H. et al., 2023, Tectonics
144	Nanling	Wangxianling, Chenzhou	25.77	113.10	Granite	WXL-5	37.1	3	Zircon (U-Th)/He	Wu J.H. et al., 2023, Tectonics
145	Nanling	Wangxianling, Chenzhou	25.77	113.10	Granite	WXL-6	30.6	1.1	Zircon (U-Th)/He	Wu J.H. et al., 2023, Tectonics
146	Wuyi	Taoxi, Wuping	25.38	116.16	Mylonite	JX-66	238.5	2.8	Muscovite Ar-Ar	Xu X.B. et al., 2011, Tectonophysics
147	Wuyi	Dabu, Ganzhou	25.83	115.15	Quartz vein	13D64	156.4	1	Sericite Ar-Ar	Li J.F. et al., 2022, Geol. J.
148	Wuyi	Junmenling, Xunwu	25.20	115.85	Porphyritic Granite	788	223.7	2.7	Biotite Ar-Ar	Wang B. et al., 2014, J.Geol.
149	Wuyi	Qingliu, Sanming	26.18	116.81	Mylonite	—	214	2	Biotite Ar-Ar	Wang Y.J. et al., 2013, Gondwana Res.
150	Wuyi	Taoxi, Wuping	25.38	116.15	Mylonite	JX-63	235.3	2.8	Biotite Ar-Ar	Xu X.B. et al., 2011, Tectonophysics
151	Wuyi	Pangushan, Yudu	25.67	115.43	Quartz vein	NKSD2	155.3	2.8	Molybdenite Re-Os	Fang G.C. et al., 2014, Acta Geosci. Sinica
152	Wuyi	Dabu, Ganzhou	25.83	115.15	Granite	13D63-1	156.3	2.7	Molybdenite Re-Os	Li J.F. et al., 2022, Geol. J.
153	Wuyi	Dabu, Ganzhou	25.83	115.15	Quartz vein	13D65-3-1	157	1.1	Molybdenite Re-Os	Li J.F. et al., 2022, Geol. J.
154	Wuyi	Dabu, Ganzhou	25.76	115.23	Quartz vein	CK-8	156.9	2	Molybdenite Re-Os	Zhang J. et al., 2021a, Ore Geol. Rev.
155	Wuyi	Dabu, Ganzhou	25.76	115.23	Quartz vein	CK-6	156.1	3.4	Cassiterite U-Pb	Zhang J. et al., 2021a, Ore Geol. Rev.
156	Wuyi	Longyuanba, Nanxiong	24.90	114.40	Granite	11GG10-1	51.1	5.6	Apatite fission track	Tao N. et al., 2017, Gondwana Res.
157	Wuyi	Mengdong	25.39	114.04	Granite	04GD43	37	3.3	Apatite fission track	Tao N. et al., 2019, Gondwana Res.
158	Wuyi	Shaoguan	25.00	113.52	Sandstone	09SC03-1	40	20	Apatite fission track	Tao N. et al., 2019, Gondwana Res.
159	Wuyi	Longnan	24.90	114.89	Sandstone	10JXLN04	72	5.2	Apatite fission track	Tao N. et al., 2019, Gondwana Res.
160	Wuyi	Shaoguan	25.00	113.52	Sandstone	12GH22-1	38	10	Apatite fission track	Tao N. et al., 2019, Gondwana Res.
161	Wuyi	Shaoguan	25.00	113.52	Sandstone	12GH22-1	109	20	Apatite fission track	Tao N. et al., 2019, Gondwana Res.
162	Wuyi	Shaoguan	25.00	113.52	Sandstone	12GH22-1	122	4.3	Apatite fission track	Tao N. et al., 2019, Gondwana Res.
163	Wuyi	Qiqicun, Anyuan	25.06	115.26	Granite	20GN-48	70.6	6	Apatite fission track	Wang Y. et al., 2020, J. Asian Earth Sci.
164	Wuyi	Zhengang, Anyuan	25.01	115.40	Gneiss	20GN-53	74.1	4.2	Apatite fission track	Wang Y. et al., 2020, J. Asian Earth Sci.
165	Wuyi	Fengshanxiang, Anyuan	25.06	115.39	Magmatite	20GN-58	55.8	1.9	Apatite fission track	Wang Y. et al., 2020, J. Asian Earth Sci.
166	Wuyi	Shangfeng, Wuping	25.04	116.01	Magmatite	20GN-87	65.6	7.5	Apatite fission track	Wang Y. et al., 2020, J. Asian Earth Sci.
167	Wuyi	Zhuziba, Huichang	25.45	115.99	Magmatite	20GN-96	71.7	6.5	Apatite fission track	Wang Y. et al., 2020, J. Asian Earth Sci.
168	Wuyi	Zhuziba, Huichang	25.48	116.00	Granite	20GN-98	38.8	3.6	Apatite fission track	Wang Y. et al., 2020, J. Asian Earth Sci.
169	Wuyi	Baishazhen, Longyan	25.22	116.71	Granodiorite	BSZ-01	38.5	2	Apatite fission track	Wang Y. et al., 2022, Tectonophysics
170	Wuyi	Baishazhen, Longyan	25.18	116.65	Granodiorite	BSZ-02	42.7	2.2	Apatite fission track	Wang Y. et al., 2022, Tectonophysics
171	Wuyi	Baishazhen, Longyan	25.12	116.57	Granodiorite	BSZ-03	33.1	2.6	Apatite fission track	Wang Y. et al., 2022, Tectonophysics
172	Wuyi	Caixi, Longyan	25.27	116.43	Monzogranite	CX-01	33.6	2.4	Apatite fission track	Wang Y. et al., 2022, Tectonophysics
173	Wuyi	Caixi, Longyan	25.22	116.47	Monzogranite	CX-02	24.7	1.4	Apatite fission track	Wang Y. et al., 2022, Tectonophysics
174	Wuyi	Yongfu, Longyan	25.03	117.26	Granite	EL-03	36.3	2.4	Apatite fission track	Wang Y. et al., 2022, Tectonophysics
175	Wuyi	Yongfu, Longyan	25.03	117.37	Granite	EL-05	48.6	3.1	Apatite fission track	Wang Y. et al., 2022, Tectonophysics

Table S2 (continued)

No.	Massif	Location	Latitude	Longitude	Lithology	Sample	Age (Ma)	Error (Ma)	Method	References
176	Wuyi	Yongfu, Longyan	25.02	117.43	Volcanic rokcs	EL-06	51.4	6.6	Apatite fission track	Wang Y. et al., 2022, Tectonophysics
177	Wuyi	Yongfu, Longyan	25.01	117.43	Granite	EL-07	45.6	3.9	Apatite fission track	Wang Y. et al., 2022, Tectonophysics
178	Wuyi	Gutianzhen, Longyan	25.22	116.82	Granodiorite	GT-04	27.7	2	Apatite fission track	Wang Y. et al., 2022, Tectonophysics
179	Wuyi	Gutianzhen, Longyan	25.21	116.84	Granodiorite	GT-05	36.3	2.8	Apatite fission track	Wang Y. et al., 2022, Tectonophysics
180	Wuyi	Longmen, Longyan	25.10	116.93	Granite	GY-01	26.6	0.8	Apatite fission track	Wang Y. et al., 2022, Tectonophysics
181	Wuyi	Hetian, Longyan	25.70	116.44	Syenite	HT-01	42.9	4	Apatite fission track	Wang Y. et al., 2022, Tectonophysics
182	Wuyi	Hetian, Longyan	25.68	116.44	Syenite	HT-02	33.2	2.1	Apatite fission track	Wang Y. et al., 2022, Tectonophysics
183	Wuyi	Dongxiao, Longyan	24.97	117.08	K-feldspar granite	JZ-05	20.2	1.5	Apatite fission track	Wang Y. et al., 2022, Tectonophysics
184	Wuyi	Yanshi, Longyan	25.25	117.13	Sandstone	TGS-01	23.4	1.2	Apatite fission track	Wang Y. et al., 2022, Tectonophysics
185	Wuyi	Yanshi, Longyan	25.27	117.09	granite	TGS-06	31.1	1.6	Apatite fission track	Wang Y. et al., 2022, Tectonophysics
186	Wuyi	Xikou, Longyan	25.07	116.66	Granite	XK-01	40.7	3.3	Apatite fission track	Wang Y. et al., 2022, Tectonophysics
187	Wuyi	Xikou, Longyan	25.09	116.68	Granodiorite	XK-02	28.8	2.4	Apatite fission track	Wang Y. et al., 2022, Tectonophysics
188	Wuyi	Yongfu, Longyan	25.08	117.23	K-feldspar granite	YF-01	20.1	2	Apatite fission track	Wang Y. et al., 2022, Tectonophysics
189	Wuyi	Yongfu, Longyan	24.97	117.25	Granite	YF-04	33.7	2.8	Apatite fission track	Wang Y. et al., 2022, Tectonophysics
190	Wuyi	Yongfu, Longyan	25.07	117.24	K-feldspar granite	YF-LC	20.7	2.7	Apatite fission track	Wang Y. et al., 2022, Tectonophysics
191	Wuyi	Miaoqian, Longyan	25.37	116.75	Granite porphyry	ZD-01	33.8	3.2	Apatite fission track	Wang Y. et al., 2022, Tectonophysics
192	Wuyi	Maozifeng, Nanxiong	25.21	114.25	Granite	Nx1-Ap	39.9	3	Apatite fission track	Yi Y. et al., 2009, Tectonophysics
193	Wuyi	Maozifeng, Nanxiong	25.22	114.24	Granite	Nx2-Ap	45.9	1.4	Apatite fission track	Yi Y. et al., 2009, Tectonophysics
194	Wuyi	Maozifeng, Nanxiong	25.26	114.22	Granodiorite	Nx3-Ap	37.3	2.3	Apatite fission track	Yi Y. et al., 2009, Tectonophysics
195	Wuyi	Maozifeng, Nanxiong	25.26	114.22	Granite	Nx4-Ap	54.2	1.6	Apatite fission track	Yi Y. et al., 2009, Tectonophysics
196	Wuyi	Xiaochi, Longyan	25.13	116.94	Granite	FJN10	67.3	9.9	Apatite (U-Th)/He	Ding R.X. et al., 2019, Gondwana Res.
197	Wuyi	Jiaoyang, Shanghang	25.27	116.76	Granite	FJN11	53.5	3.3	Apatite (U-Th)/He	Ding R.X. et al., 2019, Gondwana Res.
198	Wuyi	Nanlingcun, Shanghang	25.39	116.56	Granite	FJN13	56.1	10.1	Apatite (U-Th)/He	Ding R.X. et al., 2019, Gondwana Res.
199	Wuyi	Hetian, Changting	25.70	116.45	Granite	FJN15	40.1	6.8	Apatite (U-Th)/He	Ding R.X. et al., 2019, Gondwana Res.
200	Wuyi	Gutianzhen, Longyan	25.29	116.91	Granite	FJN19	46.7	10	Apatite (U-Th)/He	Ding R.X. et al., 2019, Gondwana Res.
201	Wuyi	Longshan, Zhangzhou	24.67	117.38	Sandstone	FJN4	68.5	5.2	Apatite (U-Th)/He	Ding R.X. et al., 2019, Gondwana Res.
202	Wuyi	Hexi, Zhangzhou	24.84	117.24	Granite	FJN7	48	6.7	Apatite (U-Th)/He	Ding R.X. et al., 2019, Gondwana Res.
203	Wuyi	Hexi, Zhangzhou	24.91	117.20	Granite	FJN8	42.3	1.7	Apatite (U-Th)/He	Ding R.X. et al., 2019, Gondwana Res.
204	Wuyi	Dongxiao, Longyan	24.96	117.06	Granite	FJN9	64.6	20.2	Apatite (U-Th)/He	Ding R.X. et al., 2019, Gondwana Res.
205	Wuyi	Mengdong	25.39	114.04	Granite	04GD43	37	7	Apatite (U-Th)/He	Tao N. et al., 2019, Gondwana Res.
206	Wuyi	Shaoguan	25.00	113.52	Sandstone	09SC03-1	36	4	Apatite (U-Th)/He	Tao N. et al., 2019, Gondwana Res.
207	Wuyi	Liyuan	24.59	114.76	Granite	12GH15	38	3	Apatite (U-Th)/He	Tao N. et al., 2019, Gondwana Res.
208	Wuyi	Shaoguan	25.00	113.52	Sandstone	12GH22-1	35	11	Apatite (U-Th)/He	Tao N. et al., 2019, Gondwana Res.
209	Wuyi	Keshubei	25.14	115.27	Granite	2KGN38-1	33	5	Apatite (U-Th)/He	Tao N. et al., 2019, Gondwana Res.
210	Wuyi	Dazhuyuan, Dingnan	24.92	115.12	Mylonite	20GN-29	131.1	6.9	Zircon fission track	Wang Y. et al., 2020, J. Asian Earth Sci.
211	Wuyi	Qiqicun, Anyuan	25.06	115.26	Granite	20GN-48	128	7.9	Zircon fission track	Wang Y. et al., 2020, J. Asian Earth Sci.

Table S2 (continued)

No.	Massif	Location	Latitude	Longitude	Lithology	Sample	Age (Ma)	Error (Ma)	Method	References
212	Wuyi	Zhengang, Anyuan	25.01	115.40	Gneiss	20GN-53	109.3	10	Zircon fission track	Wang Y. et al., 2020, J. Asian Earth Sci.
213	Wuyi	Fengshanxiang, Anyuan	25.06	115.39	Magmatite	20GN-58	110.4	5	Zircon fission track	Wang Y. et al., 2020, J. Asian Earth Sci.
214	Wuyi	Shangfeng, Wuping	25.04	116.01	Magmatite	20GN-87	117.6	5.9	Zircon fission track	Wang Y. et al., 2020, J. Asian Earth Sci.
215	Wuyi	Zhuziba, Huichang	25.45	115.99	Magmatite	20GN-96	95.9	7.7	Zircon fission track	Wang Y. et al., 2020, J. Asian Earth Sci.
216	Wuyi	Zhuziba, Huichang	25.48	116.00	Granite	20GN-98	99.6	6.6	Zircon fission track	Wang Y. et al., 2020, J. Asian Earth Sci.
217	Wuyi	Baishazhen, Longyan	25.12	116.57	Granodiorite	BSZ-03	96.4	5.5	Zircon fission track	Wang Y. et al., 2022, Tectonophysics
218	Wuyi	Caixi, Longyan	25.27	116.43	Monzogranite	CX-01	93.2	4.2	Zircon fission track	Wang Y. et al., 2022, Tectonophysics
219	Wuyi	Dongxiao, Longyan	25.00	117.05	K-feldspar granite	DY-05	107.2	4.4	Zircon fission track	Wang Y. et al., 2022, Tectonophysics
220	Wuyi	Gutianzhen, Longyan	25.22	116.82	Granodiorite	GT-04	106.2	4	Zircon fission track	Wang Y. et al., 2022, Tectonophysics
221	Wuyi	Gutianzhen, Longyan	25.21	116.84	Granodiorite	GT-05	96.3	4.5	Zircon fission track	Wang Y. et al., 2022, Tectonophysics
222	Wuyi	Dongxiao, Longyan	24.97	117.08	K-feldspar granite	JZ-05	86.5	3.6	Zircon fission track	Wang Y. et al., 2022, Tectonophysics
223	Wuyi	Luoxi, Longyan	25.25	117.59	Granite	LY-G	102.7	4.4	Zircon fission track	Wang Y. et al., 2022, Tectonophysics
224	Wuyi	Xikou, Longyan	25.09	116.68	Granodiorite	XK-02	111.2	5.8	Zircon fission track	Wang Y. et al., 2022, Tectonophysics
225	Wuyi	Yongfu, Longyan	25.08	117.23	K-feldspar granite	YF-01	109	5.3	Zircon fission track	Wang Y. et al., 2022, Tectonophysics
226	Wuyi	Yongfu, Longyan	24.97	117.25	Granite	YF-04	103.3	4.5	Zircon fission track	Wang Y. et al., 2022, Tectonophysics
227	Wuyi	Yongfu, Longyan	25.07	117.24	K-feldspar granite	YF-LC	93.6	6	Zircon fission track	Wang Y. et al., 2022, Tectonophysics
228	Wuyi	Miaoqian, Longyan	25.37	116.75	Granite porphyry	ZD-01	85.1	3.3	Zircon fission track	Wang Y. et al., 2022, Tectonophysics
229	Wuyi	Maozifeng, Nanxiong	25.21	114.00	Granite	Nx1-Zr	87.3	4	Zircon fission track	Yi Y. et al., 2009, Tectonophysics
230	Wuyi	Maozifeng, Nanxiong	25.22	114.00	Granite	Nx2-Zr	92.8	4.9	Zircon fission track	Yi Y. et al., 2009, Tectonophysics
231	Wuyi	Xiaochi, Longyan	25.13	116.94	Granite	FJN10	92	14.7	Zircon (U-Th)/He	Ding R.X. et al., 2019, Gondwana Res.
232	Wuyi	Jiaoyang, Shanghang	25.27	116.76	Granite	FJN11	83.9	2.8	Zircon (U-Th)/He	Ding R.X. et al., 2019, Gondwana Res.
233	Wuyi	Nanlingcun, Shanghang	25.39	116.56	Granite	FJN13	77.8	9.2	Zircon (U-Th)/He	Ding R.X. et al., 2019, Gondwana Res.
234	Wuyi	Hetian, Changting	25.70	116.45	Granite	FJN15	107.7	31.2	Zircon (U-Th)/He	Ding R.X. et al., 2019, Gondwana Res.
235	Wuyi	Gutianzhen, Longyan	25.29	116.91	Granite	FJN19	72.9	3.9	Zircon (U-Th)/He	Ding R.X. et al., 2019, Gondwana Res.
236	Wuyi	Longshan, Zhangzhou	24.67	117.38	Sandstone	FJN4	85.5	19.9	Zircon (U-Th)/He	Ding R.X. et al., 2019, Gondwana Res.
237	Wuyi	Hexi, Zhangzhou	24.84	117.24	Granite	FJN7	76.5	5	Zircon (U-Th)/He	Ding R.X. et al., 2019, Gondwana Res.
238	Wuyi	Hexi, Zhangzhou	24.91	117.20	Granite	FJN8	69	9	Zircon (U-Th)/He	Ding R.X. et al., 2019, Gondwana Res.
239	Wuyi	Dongxiao, Longyan	24.96	117.06	Granite	FJN9	83.7	7.9	Zircon (U-Th)/He	Ding R.X. et al., 2019, Gondwana Res.
240	Wuyi	Longyuanba, Nanxiong	24.90	114.40	Granite	11GG10-1	103.1	6.8	Zircon (U-Th)/He	Tao N. et al., 2017, Gondwana Res.
241	Wuyi	Mengdong	25.39	114.04	Granite	04GD43	124	9	Zircon (U-Th)/He	Tao N. et al., 2019, Gondwana Res.
242	Wuyi	Shaoguan	25.00	113.52	Sandstone	09SC03-1	142	15	Zircon (U-Th)/He	Tao N. et al., 2019, Gondwana Res.
243	Wuyi	Mengdong	24.90	114.89	Sandstone	10JXLN04	152	10	Zircon (U-Th)/He	Tao N. et al., 2019, Gondwana Res.
244	Wuyi	Liyuan	24.59	114.76	Granite	12GH15	126	9	Zircon (U-Th)/He	Tao N. et al., 2019, Gondwana Res.
245	Wuyi	Shaoguan	25.00	113.52	Sandstone	12GH22-1	148	12	Zircon (U-Th)/He	Tao N. et al., 2019, Gondwana Res.
246	Wuyi	Keshubei	25.14	115.27	Granite	2KGN38-1	115	9	Zircon (U-Th)/He	Tao N. et al., 2019, Gondwana Res.
247	Yunkai	Yingqiao, Bobai	22.09	110.04	Mylonite	ZMT-B1	221.98	1.16	Muscovite Ar-Ar	Ding R.X., et al., 2018, Earth Sci.

Table S2 (continued)

No.	Massif	Location	Latitude	Longitude	Lithology	Sample	Age (Ma)	Error (Ma)	Method	References
248	Yunkai	Yingqiao, Bobai	22.09	110.04	Mylonite	ZMT-B2	223.77	1.16	Muscovite Ar-Ar	Ding R.X., et al., 2018, Earth Sci.
249	Yunkai	Sanbao, NW. Cenxi	23.04	110.83	Granitic mylonite	TW10-1017-1	231.9	2.2	Muscovite Ar-Ar	Guo S.Y. et al., 2020, Geotectonica et Metallogenia
250	Yunkai	Rongxian	22.82	110.36	Granitic mylonite	G21002-N3	249.6	2.4	Muscovite Ar-Ar	Huang W.Q. et al., 2024, Acta Geol. Sinica
251	Yunkai	Rongxian	22.82	110.36	Granitic mylonite	G21008-N1	246.9	2.3	Muscovite Ar-Ar	Huang W.Q. et al., 2024, Acta Geol. Sinica
252	Yunkai	Yongning, Yangchun	22.25	111.59	Mylonitic granite	YC-15	227.38	2.23	Muscovite Ar-Ar	Li C.A. et al., 2022, South China Geology
253	Yunkai	Yongning, Yangchun	22.25	111.62	Mylonitic granite	YC-16	232.77	4.27	Muscovite Ar-Ar	Li C.A. et al., 2022, South China Geology
254	Yunkai	Hetai goldfield	23.32	112.29	Mylonite gneiss	YX07	181.16	0.81	Muscovite Ar-Ar	Ni J.L. et al., 2019, Geol. J.
255	Yunkai	Silun, Luoding	22.70	111.31	Foliated schist	G13Y1	249.72	2.61	Muscovite Ar-Ar	Shao J.G. et al., 1995, Guangdong Geology
256	Yunkai	Yongning, Yangchun	22.25	111.61	Foliated gneissoid granite	G03Y1	229.35	2.5	Muscovite Ar-Ar	Shao J.G. et al., 1995, Guangdong Geology
257	Yunkai	Fenjie, Xinyi	22.53	111.34	Mylonite	G12Y2	255.33	3.03	Muscovite Ar-Ar	Shao J.G. et al., 1995, Guangdong Geology
258	Yunkai	Kengkou, Xinyi	22.44	111.13	Mylonitic gneiss	10YK-42	228.9	1.2	Muscovite Ar-Ar	Wang Y.J. et al., 2021, J. Asian Earth Sci.
259	Yunkai	Liuyu, Xinyi	22.37	111.13	Mylonitic gneiss	10YK-44	227.5	1.1	Muscovite Ar-Ar	Wang Y.J. et al., 2021, J. Asian Earth Sci.
260	Yunkai	E. Beiliu	22.75	110.48	Mylonite	Datong 2	211.64	3.39	Muscovite Ar-Ar	Zhang K.J. & Cai J.X., 2009, J. Structural Geol.
261	Yunkai	E. Beiliu	22.75	110.48	Mylonite	Datong 1	213	4	Muscovite Ar-Ar	Zhang K.J. & Cai J.X., 2009, J. Structural Geol.
262	Yunkai	Chidong, Xinyi	22.39	110.94	Mylonitic paragneiss	02YK-74	227.9	0.3	Biotite Ar-Ar	Wang Y.J. et al., 2007, Tectonics
263	Yunkai	Gaoping,Gaozhou	21.91	111.92	Mylonitic gneiss	02YK-38	221.8	0.4	Biotite Ar-Ar	Wang Y.J. et al., 2007, Tectonics
264	Yunkai	Hebapu, Xinyi	22.38	111.15	Mylonitic granite	02YK-27	229.9	0.5	Biotite Ar-Ar	Wang Y.J. et al., 2007, Tectonics
265	Yunkai	Licun, Rongxian	22.60	110.70	Mylonite	02YK-64	211.1	0.2	Biotite Ar-Ar	Wang Y.J. et al., 2007, Tectonics
266	Yunkai	N. Baishi, Xinyi	22.42	111.07	Mylonitic granite	02YK-31	216.9	0.3	Biotite Ar-Ar	Wang Y.J. et al., 2007, Tectonics
267	Yunkai	N. Baishi, Xinyi	22.41	111.08	Granitic mylonite	02YK-30	225.4	0.3	Biotite Ar-Ar	Wang Y.J. et al., 2007, Tectonics
268	Yunkai	Qianpai, Xinyi	22.38	111.18	Mylonitic gneiss	02YK-26	214.2	0.2	Biotite Ar-Ar	Wang Y.J. et al., 2007, Tectonics
269	Yunkai	Puzhou, Yangchun	22.13	111.37	Mylonitic gneiss	02YK-09	207.8	0.2	Biotite Ar-Ar	Wang Y.J. et al., 2007, Tectonics
270	Yunkai	Shaniutang,Yangchun	22.19	111.62	Mylonitic gneiss	02YK-12	209	0.2	Biotite Ar-Ar	Wang Y.J. et al., 2007, Tectonics
271	Yunkai	Tengbin, Luoding	22.82	111.39	Mylonitic granite	02YK-80	208.9	1.4	Biotite Ar-Ar	Wang Y.J. et al., 2007, Tectonics
272	Yunkai	Xieji, Gaozhou	21.92	111.01	Mylonitic migmatite	02YK-39	224.7	0.4	Biotite Ar-Ar	Wang Y.J. et al., 2007, Tectonics
273	Yunkai	Yongning,Yangchun	22.28	111.54	Mylonite	02YK-15	211.5	0.5	Biotite Ar-Ar	Wang Y.J. et al., 2007, Tectonics
274	Yunkai	Fuhuling, Yangjiang	21.51	111.54	Mylonitic migmatite	17FH-02	212.2	1.2	Biotite Ar-Ar	Wang Y.J. et al., 2021, J. Asian Earth Sci.
275	Yunkai	Fuhuling, Yangjiang	21.51	111.54	Mylonitic migmatite	17FH-03	212.5	2	Biotite Ar-Ar	Wang Y.J. et al., 2021, J. Asian Earth Sci.
276	Yunkai	Jinzhu, Luoding	22.89	111.30	Mylonite	10YK-55	230.9	2.1	Biotite Ar-Ar	Wang Y.J. et al., 2021, J. Asian Earth Sci.
277	Yunkai	Liantang, Luoding	22.72	111.31	Mylonite	10YK-58	230.6	1.4	Biotite Ar-Ar	Wang Y.J. et al., 2021, J. Asian Earth Sci.
278	Yunkai	Shapa, Yangjiang	21.51	111.49	Mylonitic gneiss	15YJ-14	227.2	1.1	Biotite Ar-Ar	Wang Y.J. et al., 2021, J. Asian Earth Sci.
279	Yunkai	Shapa, Yangjiang	21.51	111.47	Mylonite	15YJ-15	227.4	1.1	Biotite Ar-Ar	Wang Y.J. et al., 2021, J. Asian Earth Sci.
280	Yunkai	Shimeng, Yangjiang	21.65	111.52	Mylonite	19YJ-03	215.5	1.1	Biotite Ar-Ar	Wang Y.J. et al., 2021, J. Asian Earth Sci.
281	Yunkai	Wenhua, Xinyi	22.59	111.05	Mylonitic gneiss	10YK-43	229.1	1.1	Biotite Ar-Ar	Wang Y.J. et al., 2021, J. Asian Earth Sci.
282	Yunkai	Yangxi, Yangjiang	21.55	111.62	Mylonite	19YJ-01	215.4	1.1	Biotite Ar-Ar	Wang Y.J. et al., 2021, J. Asian Earth Sci.

Table S2 (continued)

No.	Massif	Location	Latitude	Longitude	Lithology	Sample	Age (Ma)	Error (Ma)	Method	References
283	Yunkai	Chidong, Xinyi	22.46	110.95	Sill Bt monzogneiss	17YK19	239.5	1.6	Apatite U-Pb	Wang X.D. et al., 2020, Earth Sci.
284	Yunkai	Shikengtang, E. Gaozhou	21.91	110.92	Bt granitic gneiss	17YK03	240.5	2	Apatite U-Pb	Wang X.D. et al., 2020, Earth Sci.
285	Yunkai	Shilu, Yangchun	22.19	111.62	Migmatite	YK12	53.4	3.7	Apatite fission track	Li X.M. et al., 2005, Chin. Sci. Bull.
286	Yunkai	Heshui, Xinyi	22.37	111.42	Granitic mylonite	YK21	53.3	2.2	Apatite fission track	Li X.M. et al., 2005, Chin. Sci. Bull.
287	Yunkai	Hebapu, Xinyi	22.52	111.40	Granitic mylonite	YK27	51.9	2.1	Apatite fission track	Li X.M. et al., 2005, Chin. Sci. Bull.
288	Yunkai	Baishi, Xinyi	22.41	111.08	Mylonite	YK30	52.1	3.1	Apatite fission track	Li X.M. et al., 2005, Chin. Sci. Bull.
289	Yunkai	Xieji, Gaozhou	21.92	111.01	Migmatite	YK39	60.8	3	Apatite fission track	Li X.M. et al., 2005, Chin. Sci. Bull.
290	Yunkai	Yuntan, Gaozhou	21.88	111.17	Plagiogneiss	YK42	55.1	2.4	Apatite fission track	Li X.M. et al., 2005, Chin. Sci. Bull.
291	Yunkai	Xin’an, Lianjiang	21.65	110.43	Granite	YK46	65.5	2.7	Apatite fission track	Li X.M. et al., 2005, Chin. Sci. Bull.
292	Yunkai	Danqiao, Huazhou	21.46	110.64	Plagiogneiss	YK47	60.8	2.2	Apatite fission track	Li X.M. et al., 2005, Chin. Sci. Bull.
293	Yunkai	Dagu, Bobai	21.90	110.14	Mylonite	YK50	47.5	3	Apatite fission track	Li X.M. et al., 2005, Chin. Sci. Bull.
294	Yunkai	Wendi, Bobai	21.94	110.21	Plagiogneiss	YK54	50.4	2.5	Apatite fission track	Li X.M. et al., 2005, Chin. Sci. Bull.
295	Yunkai	Lingshan, Rongxian	22.60	110.70	Plagiogneiss	YK64	65.9	3.2	Apatite fission track	Li X.M. et al., 2005, Chin. Sci. Bull.
296	Yunkai	Longsheng, Beiliu	22.52	110.46	Granodiorite	YK70	55.9	4.2	Apatite fission track	Li X.M. et al., 2005, Chin. Sci. Bull.
297	Yunkai	Chitong, Xinyi	22.43	110.95	Gneiss	YK75	50.1	1.7	Apatite fission track	Li X.M. et al., 2005, Chin. Sci. Bull.
298	Yunkai	Hongguan, Xinyi	22.47	111.12	Plagiogneiss	YK76	59.3	2.4	Apatite fission track	Li X.M. et al., 2005, Chin. Sci. Bull.
299	Yunkai	Puzhu, Yangchun	22.13	111.37	Migmatite	YK9	45	1.9	Apatite fission track	Li X.M. et al., 2005, Chin. Sci. Bull.
300	Yunkai	Shilu, Yangchun	22.19	111.62	Migmatite	YK12	97.4	5.5	Zircon fission track	Li X.M. et al., 2005, Chin. Sci. Bull.
301	Yunkai	Heshui, Xinyi	22.37	111.42	Granitic mylonite	YK21	121.6	4.9	Zircon fission track	Li X.M. et al., 2005, Chin. Sci. Bull.
302	Yunkai	Hebapu, Xinyi	22.52	111.40	Granitic mylonite	YK27	105.4	10.2	Zircon fission track	Li X.M. et al., 2005, Chin. Sci. Bull.
303	Yunkai	Baishi, Xinyi	22.41	111.08	Mylonite	YK30	107.2	10.7	Zircon fission track	Li X.M. et al., 2005, Chin. Sci. Bull.
304	Yunkai	Xieji, Gaozhou	21.92	111.01	Migmatite	YK39	106.6	6	Zircon fission track	Li X.M. et al., 2005, Chin. Sci. Bull.
305	Yunkai	Yuntan, Gaozhou	21.88	111.17	Plagiogneiss	YK42	85	4.6	Zircon fission track	Li X.M. et al., 2005, Chin. Sci. Bull.
306	Yunkai	Xin’an, Lianjiang	21.65	110.43	Granite	YK46	124.4	6.3	Zircon fission track	Li X.M. et al., 2005, Chin. Sci. Bull.
307	Yunkai	Danqiao, Huazhou	21.46	110.64	Plagiogneiss	YK47	133	5.9	Zircon fission track	Li X.M. et al., 2005, Chin. Sci. Bull.
308	Yunkai	Dagu, Bobai	21.90	110.14	Mylonite	YK50	127.3	6.6	Zircon fission track	Li X.M. et al., 2005, Chin. Sci. Bull.
309	Yunkai	Wendi, Bobai	21.94	110.21	Plagiogneiss	YK54	118.9	6.3	Zircon fission track	Li X.M. et al., 2005, Chin. Sci. Bull.
310	Yunkai	Lingshan, Rongxian	22.60	110.70	Plagiogneiss	YK64	125.7	9	Zircon fission track	Li X.M. et al., 2005, Chin. Sci. Bull.
311	Yunkai	Longsheng, Beiliu	22.52	110.46	Granodiorite	YK70	117.5	6.9	Zircon fission track	Li X.M. et al., 2005, Chin. Sci. Bull.
312	Yunkai	Chitong, Xinyi	22.43	110.95	Gneiss	YK75	114.3	6.1	Zircon fission track	Li X.M. et al., 2005, Chin. Sci. Bull.
313	Yunkai	Hongguan, Xinyi	22.47	111.12	Plagiogneiss	YK76	125.3	6.7	Zircon fission track	Li X.M. et al., 2005, Chin. Sci. Bull.
314	Yunkai	Puzhu, Yangchun	22.13	111.37	Migmatite	YK9	109.2	7.9	Zircon fission track	Li X.M. et al., 2005, Chin. Sci. Bull.

Note: 1.The GPS estimated based on the geological map is marked with underline. 2. Nos. 1-45, 146-155, 247-284 are plotted in the Figures 5.23 and 5.24.

Table S3. Estimates of deformation temperatures by the quartz dynamic recrystallization

No.	Sample No.	Locality	Massif	Latitude	Longitude	Rock Type	Mineral Assemblage	Quartz re-crystallization	Temperature (℃)
1	22SC06	Rucheng	Nanling	25.78	113.64	Є1 silty slate	Phenocryst (10%): Qz. Matrix (90%): Ser, Qz, Ms	UE	<300
2	22SC07	Rucheng	Nanling	25.77	113.65	Є2 slate	Fine-grained, Ser (95%), Qz (5%）	BLG	300-400
3	22SC08	Rucheng	Nanling	25.77	113.65	D1 siltstone	Fine-grained, Qz (60%), Ser (40%）	UE	<300
4	22SC10	Rucheng	Nanling	25.67	113.67	Є slate	Phenocryst (25%): Qz. Matrix (75%): Qz, Ser, Ms	UE	<300
5	22SC11	Rucheng	Nanling	25.67	113.67	D sandstone	Fine-grained, Qz (60%), Ser (40%）	UE	<300
6	22SC17	Chongyi	Nanling	25.68	114.25	Є1 slate	Fine-grained, Qz (5%), Ser (95%)	BLG	300-400
7	22SC18	Chongyi	Nanling	25.72	114.32	D3 siltstone	Fine-grained, Qz (75%), Ser (25%)	BLG	300-400
8	22SC28	SE. Chongyi	Nanling	25.66	114.37	Є2 slate	Phenocryst (2%): Qz. Matrix (98%): Ser, Qz	UE-BLG	~300
9	22SC29	SE. Chongyi	Nanling	25.65	114.40	Є2 slate	Fine-grained, Ser (96%), Qz (3%), Ms (1%)	BLG	300-400
10	22SC33	SE. Chongyi	Nanling	25.64	114.49	Є1 siltstone	Phenocryst (10%): Qz. Matrix (90%): Ser, Qz	UE	<300
11	22SC35	SE. Chongyi	Nanling	25.59	114.43	Є1 phyllite	Fine-grained, Qz (5%), Ser (95%)	BLG-SGR	~400
12	22SC37	SE. Chongyi	Nanling	25.52	114.43	Є1 slate	Fine-grained, Qz (5%), Ser (93%), Ms (2%)	SGR	400-500
13	22SC38	SE. Chongyi	Nanling	25.49	114.44	Є1 siltstone	Phenocryst (40%): Qz. Matrix (60%): Ser, Qz, Ms	BLG-SGR	~400
14	S80	NE. Hezhou	Nanling	24.67	111.91	Z silty phyllite	Phenocryst (1%): Qz. Matrix (99%): Qz, Ser	BLG	300-400
15	S81	NE. Hezhou	Nanling	24.68	111.90	Z siliceous phyllite	Fine-grained, Qz, (60%), Ser (40%)	BLG	300-400
16	S82	NE. Hezhou	Nanling	24.63	111.89	Є phyllite	Phenocryst (3%): Qz. Matrix (97%): Qz, Ser	BLG	300-400
17	S83	NE. Hezhou	Nanling	24.69	111.91	Z sandy slate	Fine-grained, Qz, (60%), Ser (40%)	BLG	300-400
18	S84	NE. Hezhou	Nanling	24.70	111.91	Z mylonitic phyllite	Phenocryst (5%) Qz, Fsp. Matrix (95%): Qz, Bt, Fsp, Ser	BLG	300-400
19	S88B	NE. Hezhou	Nanling	24.61	111.93	Z mudstone	Fine-grained, Qz (50%), Ser (50%)	BLG	300-400
20	S89	NE. Hezhou	Nanling	24.70	111.94	Z mylonitic pelitic phyllite	Fine-grained, Qz (70%), Ser (20%), Mag (10%)	BLG	300-400
21	S90	NE. Hezhou	Nanling	24.71	111.95	Z pelitic phyllite	Fine-grained, Qz (50%), Ms (50%)	BLG	300-400
22	S92	E. Hezhou	Nanling	24.43	111.93	Є sandy slate	Phenocryst (5%): Qz. Matrix (95%): Qz, Fsp, Ser	BLG	300-400
23	S206	Lianzhou	Nanling	24.79	112.25	Є silty phyllite	Phenocryst (10%): Qz. Matrix (90%): Qz, Ser	UE-BLG	~300
24	S207	Lianzhou	Nanling	24.79	112.23	Є siltstone	Phenocryst (10%): Qz. Matrix (90%): Qz, Ser	UE	<300
25	S209B	Lianzhou	Nanling	24.80	112.27	D sandstone	Phenocryst (45%): Qz. Matrix (55%): Ser	UE	<300
26	S211	Linwu-Zixing	Nanling	25.41	112.60	Є siltstone	Phenocryst (5%): Qz. Matrix (95%): Qz, Ser	UE	<300

Table S3 (continued)

No.	Sample No.	Locality	Massif	Latitude	Longitude	Rock Type	Mineral Assemblage	Quartz re-crystallization	Temperature (°C)
27	S216	Zixing-Yongxing	Nanling	26.10	113.38	Є muddy slate	Phenocryst (5%): Qz, Matrix (95%) Qz, Ser	UE-BLG	~300
28	S226	Zhuzhou	Nanling	27.28	113.19	Pt slate	Fine-grained, Qz (15%), Ser (85%)	BLG	300-400
29	S228	Zhuzhou	Nanling	27.31	113.16	Pt mudstone	Fine-grained, Qz (10%), Ser (90%)	BLG-SGR	~400
30	22SC12	Rucheng	Nanling	25.53	113.80	Є2 slate	Phenocryst (10%): Qtz. Matrix (90%): Qz, Ser, Ms	BLG	300-400
31	22SC13	Rucheng	Nanling	25.53	113.80	Є2 hornfels	Phenocryst (40%): Qz. Matrix (60%): Qz, Ser, Ms	BLG	300-400
32	22SC39	SE. Ganzhou	Nanling	25.76	114.97	Z meta-siltstone	Fine-grained, Qz (60%), Ms (30%), Ser (10%)	SGR	400-500
33	22SC40A	SE. Ganzhou	Nanling	25.79	114.99	Z1 phyllite	Fine-grained, Qz (50%), Ms (50%)	SGR	400-500
34	22SC40B	SE. Ganzhou	Nanling	25.79	114.99	Z1 schist	Fine-grained, Qz (70%), Ms (30%)	SGR	400-500
35	S220A	Zixing-Yongxing	Nanling	26.22	113.44	Є phyllite-mica schist	Qz (50%), Ms (50%)	BLG-SGR	~400
36	S221	Zixing-Yongxing	Nanling	26.31	113.44	Є slate/ mudstone	Fine-grained, Qz (10%), Ser (90%)	BLG	300-400
37	S223B	Zixing-Yongxing	Nanling	26.31	113.41	Є slate/ mudstone	Fine-grained, Qz (10%), Ser (90%)	BLG	300-400
38	S85	NE. Hezhou	Nanling	24.61	111.90	Z phyllite	Fine-grained, Qz, (30%), Ser (60%), Mag (10%)	BLG	300-400
39	S86	NE. Hezhou	Nanling	24.61	111.90	Z phyllite	Fine-grained, Qz (50%), Ser (50%)	BLG	300-400
40	S87	NE. Hezhou	Nanling	24.60	111.91	Pt pelitic phyllite	Fine-grained, Qz (40%), Ser (60%)	BLG	300-400
41	S96	Dabang village	Nanling	23.94	111.56	D1 siltstone	Fine-grained, Qz (70%), Ser (30%)	BLG	300-400
42	S97	Dabang village	Nanling	23.94	111.56	D1 siltstone	Qz (50%), Ms (50%)	BLG	300-400
43	S99	Dabang village	Nanling	23.94	111.56	D1 siltstone	Qz (60%), Ms (40%)	BLG	300-400
44	22SC47	Nankang	Wuyi	25.60	114.77	Z1 Grt-schist	Fine-grained, Qz (45%), Ms (50%), Grt (5%)	SGR	400-500
45	22SC53	Nankang	Wuyi	25.63	114.94	Z1 phyllite	Fine-grained, Qz (5%), Ser (94%), Ms (1%)	BLG-SGR	~400
46	22SC57	NE. Xinfeng	Wuyi	25.53	115.17	Є3 phyllite	Coarse-grained, Qz (50%), Pl (30%), Ser (15%), Ms (5%)	SGR-GBM	~500

Table S3 (continued)

No.	Sample No.	Locality	Massif	Latitude	Longitude	Rock Type	Mineral Assemblage	Quartz re-crystallization	Temperature (°C)
47	22SC58	NE. Xinfeng	Wuyi	25.50	115.25	Z standstone	Phenocryst (10%): Qz. Matrix (90%): Ser, Qz, Ms	UE-BLG	~300
48	22SC59	NE. Xinfeng	Wuyi	25.49	115.33	Z1 silty phyllite	Phenocryst (40%): Qz. Matrix (60%): Ser, Qz, Pl	BLG	300-400
49	22SC64	NW. Huichang	Wuyi	25.70	115.65	Є1 meta-sandstone	Phenocryst (30%): Qz, Ksp. Matrix (70%): Ser, Qz, Ms	UE-BLG	~300
50	22SC65	NW. Huichang	Wuyi	25.72	115.65	Є1 meta-sandstone	Phenocryst (40%): Qz. Matrix (60%): Qz, Ser, Ms	BLG-SGR	~400
51	22SC70	W. Changting	Wuyi	25.85	116.22	Є1 phyllite	Phenocryst (5%): Qz. Matrix (95%): Ser, Ms	BLG	300-400
52	22SC71	W. Changting	Wuyi	25.84	116.23	O phyllite	Fine-grained, Qz (5%), Ser (95%)	BLG-SGR	~400
53	22SC76	E. Changting	Wuyi	25.96	116.49	Є1 meta-sandstone	Phenocryst (50%): Qz. Matrix (50%): Qz, Ms, Ser	BLG	300-400
54	22SC78	E. Changting	Wuyi	26.07	116.48	Є1 phyllite	Phenocryst (3%): Qz. Matrix (97%): Ser, Qz, Ms	BLG	300-400
55	22SC82	Qingliu-Yong'an	Wuyi	26.00	117.04	Є1 phyllite	Phenocryst (25%): Qz. Matrix (75%): Qz, Ms, Ser	BLG	300-400
56	22SC87	Qingliu-Yong'an	Wuyi	25.99	117.11	D2 phyllite	Phenocryst (10%): Qz. Matrix (90%): Ser, Qz, Ms	BLG	300-400
57	22SC88	Qingliu-Yong'an	Wuyi	26.00	117.13	C1 sandy phyllite	Fine-grained, Qz (90%), Ser (10%)	BLG	300-400
58	22SC91	Qingliu-Yong'an	Wuyi	25.99	117.18	P2 siltstone	Fine-grained, Qz (90%), Ser (10%)	BLG	300-400
59	22SC62	NW. Huichang	Wuyi	25.65	115.68	Z1 phyllite	Fine-grained, Qz (5%), Ms (2%), Ser (93%)	UE-BLG	~300
60	22SC81	Qingliu-Yong'an	Wuyi	26.09	116.93	Є1 silt-phyllite	Fine-grained, Qz (50%), Sil (25%), Ser (20%), Ms (5%)	SGR	400-500
61	S108	Guizi, NE. Xinyi	Yunkai	22.56	111.23	Є siliceous phyllite	Fine-grained, Qz (70%), Ms (30%)	BLG	300-400
62	S109B	Guizi, NE. Xinyi	Yunkai	22.55	111.23	Є phyllite	Fine-grained, Qz (20%), Ser (80%)	BLG	300-400
63	S111	Guizi, NE. Xinyi	Yunkai	22.59	111.01	Є mica schist	Coarse-grained, Qz (70%), Ms (30%)	GBM	500-700

Table S3 (continued)

No.	Sample No.	Locality	Massif	Latitude	Longitude	Rock Type	Mineral Assemblage	Quartz re-crystallization	Temperature (℃)
64	S112	Guizi, NE. Xinyi	Yunkai	22.61	111.07	Є mica schist	Coarse-grained, Qz (50%), Pl (25%), Ms (25%)	GBM	500-700
65	S113	Guizi, NE. Xinyi	Yunkai	22.55	111.22	rhyolite porphyry	Fine-grained, Qz (95%), Ms (5%)	SGR	400-500
66	S114A	Guizi, NE. Xinyi	Yunkai	22.55	111.22	rhyolite porphyry	Phenocryst (40%): Qz. Matrix (60%): Qz, Ser	SGR	400-500
67	S115A	Guizi, NE. Xinyi	Yunkai	22.46	110.95	deformed granitic porphyry	Phenocryst (30%): Fsp, Qz. Matrix (70%): Qz, Bt, Fsp	GBM	500-700
68	S116	Guizi, NE. Xinyi	Yunkai	22.46	110.95	deformed granitic porphyry	Phenocryst (25%): Fsp, Qz. Matrix (75%): Qz, Bt, Fsp	GBM	500-700
69	S117	Guizi, NE. Xinyi	Yunkai	22.64	111.09	Є mica schist	Coarse-grained, Qz (75%), Bt (25%)	GBM	500-700
70	S118	Guizi, NE. Xinyi	Yunkai	22.64	111.09	Є mica schist	Coarse-grained, Qz (80%), Bt (15%), Ms (5%)	GBM	500-700
71	S121	Guizi, NE. Xinyi	Yunkai	22.51	111.01	Є granitic gneiss	Coarse-grained, Qz (50%), Fsp (25%), Bt (15%), Ms (10%)	GBM	500-700
72	S123	Guizi, NE. Xinyi	Yunkai	22.56	111.13	Є phyllite	Fine-grained, Qz (60%), Ms (40%)	BLG	300-400
73	S124A	S. Luojing	Yunkai	22.50	111.46	D1 conglomerate	Phenocryst (30%): Qz. Matrix (70%): Qz, Ms	SGR	400-500
74	S125	S. Luojing	Yunkai	22.50	111.46	D1 conglomerate	Phenocryst (30%): Qz. Matrix (70%): Qz, Ms	SGR	400-500
75	S127A	S. Luojing	Yunkai	22.50	111.46	deformed Kf-granite	Phenocryst (30%): Qz, Fsp. Matrix (70%): Qz, Ms	BLG-SGR	~400
76	S128	S. Luojing	Yunkai	22.50	111.46	D1 quartz sandstone	Phenocryst (20%): Qz. Matrix (80%): Qz, Ms	BLG-SGR	~400
77	S129	S. Luojing	Yunkai	22.51	111.46	D1 conglomerate	Phenocryst (40%): Qz. Matrix (60%): Qz, Ms	BLG-SGR	~400
78	S130	S. Luojing	Yunkai	22.51	111.46	D1 quartz sandstone	Fine-grained, Qz (50%), Ms (50%)	BLG-SGR	~400
79	S133	N. Taiping	Yunkai	22.59	111.47	D1 quartz sandstone	Phenocryst (40%): Qz. Matrix (60%): Qz, Ser	BLG	300-400
80	S134	N. Taiping	Yunkai	22.59	111.47	D1 silty phyllite	Phenocryst (40%): Qz. Matrix (60%): Qz, Ser	BLG-SGR	~400
81	S135	N. Taiping	Yunkai	22.62	111.43	O phyllite	Fine-grained, Qz (20%), Ms (80%)	BLG	300-400
82	S137	N. Taiping	Yunkai	22.56	111.42	O phyllite	Phenocryst (40%) Qz. Matrix (60%): Qz, Ser	BLG	300-400

Table S3 (continued)

No.	Sample No.	Locality	Massif	Latitude	Longitude	Rock Type	Mineral Assemblage	Quartz re-crystallization	Temperature (°C)
83	S138	N. Taiping	Yunkai	22.56	111.42	D1 quartz sandstone	Fine-grained, Qz (90%), Ms (10%)	SGR	400-500
84	S140A	N. Luojing	Yunkai	22.59	111.47	D1 sandy slate	Fine-grained, Qz (20%), Ms (80%)	BLG	300-400
85	S140B	N. Luojing	Yunkai	22.59	111.47	D1 quartz sandstone	Phenocryst (70%): Qz. Matrix (30%): Qz, Ser	BLG	300-400
86	S141	N. Luojing	Yunkai	22.59	111.47	D1 siltstone	Phenocryst (25%): Qz. Matrix (75%): Qz, Ser	BLG	300-400
87	S143	N. Luojing	Yunkai	22.61	111.46	D1 sandstone	Phenocryst (50%): Qz. Matrix (50%): Qz, Ser	BLG-SGR	~400
88	S147	N. Luojing	Yunkai	22.62	111.39	Oc phyllite	Fine-grained, Qz (20%), Ser (80%)	BLG	300-400
89	S148A	N. Luojing	Yunkai	22.63	111.40	Ob phyllite	Fine-grained, Qz (30%), Ser (70%)	BLG	300-400
90	S150	N. Luojing	Yunkai	22.61	111.44	D1 phyllite	Phenocryst (20%): Qz. Matrix (80%): Qz, Ms	BLG	300-400
91	S151	N. Luojing	Yunkai	22.62	111.43	D1 phyllite	Phenocryst (30%): Qz. Matrix (80%): Qz, Ser	BLG	300-400
92	S155	Guizi, NE. Xinyi	Yunkai	22.57	111.18	Є silty phyllite	Fine-grained, Qz (60%), Ser (40%)	BLG	300-400
93	S157A	Guizi, NE. Xinyi	Yunkai	22.57	111.18	D deformed quartz sandstone	Phenocryst (30%): Qz, Fsp. Matrix (80%): Qz, Fsp, Ser	BLG	300-400
94	S161B	Guizi, NE. Xinyi	Yunkai	22.57	111.20	D quartz sandstone	Phenocryst (25%): Qz. Matrix (75%): Qz, Ser	BLG	300-400
95	S162A	Guizi, NE. Xinyi	Yunkai	22.57	111.20	D deformed conglomerate	Phenocryst (15%): Qz. Matrix (85%): Qz, Ser	BLG	300-400
96	S163	Guizi, NE. Xinyi	Yunkai	22.57	111.20	Є pelitic phyllite	Fine-grained, Qz (30%), Ser (70%)	BLG	300-400
97	S164	Guizi, NE. Xinyi	Yunkai	22.57	111.20	Є phyllite	Fine-grained, Qz (25%), Ser (75%)	BLG	300-400
98	S166	Guizi, NE. Xinyi	Yunkai	22.58	111.20	Є phyllite	Fine-grained, Qz (20%), Ser (85%)	BLG	300-400
99	S167	Guizi, NE. Xinyi	Yunkai	22.58	111.20	Є mylonitic sandstone	Fine-grained, Qz (90%), Ser (10%)	BLG-SGR	~400
100	S168	Guizi, NE. Xinyi	Yunkai	22.58	111.20	Є mylonitic sandstone	Fine-grained, Qz (90%), Ser (10%)	BLG-SGR	~400
101	S169	Guizi, NE. Xinyi	Yunkai	22.58	111.14	D quartzite	Fine-grained, Qz (90%), Ser (10%)	BLG-SGR	~400

Table S3 (continued)

No.	Sample No.	Locality	Massif	Latitude	Longitude	Rock Type	Mineral Assemblage	Quartz re-crystallization	Temperature (℃)
102	S170	Guizi, NE. Xinyi	Yunkai	22.58	111.14	Є phyllite	Fine-grained, Qz (60%), Ser (40%)	SGR	400-500
103	S171A	Guizi, NE. Xinyi	Yunkai	22.57	111.14	Є phyllite	Fine-grained, Qz (25%), Ser (75%)	SGR	400-500
104	S171B	Guizi, NE. Xinyi	Yunkai	22.57	111.14	Є phyllite	Phenocryst (15%): Qz. Matrix (85%): Qz, Ser	SGR	400-500
105	S173A	Guizi, NE. Xinyi	Yunkai	22.60	111.16	Є metasandstone	Fine-grained, Qz (40%), Ms (60%)	BLG	300-400
106	S173B	Guizi, NE. Xinyi	Yunkai	22.60	111.16	Є metasandstone	Fine-grained, Qz (90%), Ser (10%)	BLG	300-400
107	S173D	Guizi, NE. Xinyi	Yunkai	22.60	111.16	Є metasandstone	Phenocryst (15%): Qz. Matrix (85%): Qz, Ser	BLG	300-400
108	S177A	Xinyi-Yangchun	Yunkai	22.41	111.26	biotite granitic gneiss	Phenocryst (40%): Fsp. Matrix (60%): Qz, Bt, Fsp	GBM	500-700
109	S178	Xinyi-Yangchun	Yunkai	22.43	111.30	Є phyllite	Phenocryst (5%): Fsp. Matrix (95%): Qz, Ms, Fsp	BLG	300-400
110	S181	Xinyi-Yangchun	Yunkai	22.40	111.38	Bt-granitic gneiss	Phenocryst (30%): Qz, Fsp. Matrix (70%): Qz, Fsp, Bt,	SGR-GBM	~500
111	S182	Xinyi-Yangchun	Yunkai	22.36	111.38	Є schist	Coarse-grained, Qz (50%), Ms (50%)	BLG	300-400
112	S183	Xinyi-Yangchun	Yunkai	22.34	111.47	Є schist	Coarse-grained, Qz (40%), Ms (60%)	BLG	300-400
113	S185	Xinyi-Yangchun	Yunkai	22.30	111.50	biotite granitic gneiss	Coarse-grained, Qz (50%), Fsp (30%), Bt (10%), Ms (10%)	BLG	300-400
114	S186	Xinyi-Yangchun	Yunkai	22.29	111.53	biotite granitic gneiss	Phenocryst (30%): Qz, Fsp. Matrix (70%): Qz, Fsp, Ms	BLG	300-400
115	S187A	Xinyi-Yangchun	Yunkai	22.29	111.53	mylonitic granite	Phenocryst (30%): Qz, Fsp. Matrix (70%): Qz, Fsp, Ms	BLG-SGR	~400
116	S188	Xinyi-Yangchun	Yunkai	22.27	111.56	mylonitic granite	Phenocryst (10%): Qz, Fsp. Matrix (90%): Qz, Fsp, Ms	BLG	300-400
117	S189A	Xinyi-Yangchun	Yunkai	22.27	111.58	Є sandy phyllite	Coarse-grained, Qz (30%), Ms (70%)	SGR	400-500

Table S3 (continued)

No.	Sample No.	Locality	Massif	Latitude	Longitude	Rock Type	Mineral Assemblage	Quartz re-crystallization	Temperature (℃)
118	S190A	Xinyi-Yangchun	Yunkai	22.26	111.60	biotite granitic gneiss	Phenocryst (30%) Fsp. Matrix (70%): Qz, Fsp, Ms, Bt	GBM	500-700
119	S191	Xinyi-Yangchun	Yunkai	22.25	111.61	mylonitic granite	Phenocryst (20%): Qz, Fsp. Matrix (80%): Qz, Fsp, Ms Bt	SGR-GBM	~500
120	S192A	Xinyi-Yangchun	Yunkai	22.25	111.61	mylonitic granite	Phenocryst (30%): Qz, Fsp. Matrix (70%): Qz, Fsp, Ms, Bt	GBM	500-700
121	S193	Xinyi-Yangchun	Yunkai	22.24	111.62	mylonitic granite	Phenocryst (30%): Qz, Fsp. Matrix (70%): Qz, Fsp, Ms, Bt	SGR-GBM	~500
122	S194	Xinyi-Yangchun	Yunkai	22.21	111.60	Є mica schist	Qz (50%), Ms (50%)	GBM	500-700
123	S196	Xinyi-Yangchun	Yunkai	22.21	111.61	Є metasandstone	Coarse-grained, Qz (80%), Bt (20%)	SGR	400-500
124	S199	Xinyi-Yangchun	Yunkai	22.20	111.62	deformed Ms-granite	Phenocryst (30%): Fsp. Matrix (70%): Fsp, Qz, Ms	GBM	500-700
125	S200	Xinyi-Yangchun	Yunkai	22.19	111.62	mylonitic granite	Phenocryst (30%): Fsp. Matrix (70%): Qz, Fsp, Ms	BLG	300-400
126	S202	Xinyi-Yangchun	Yunkai	22.19	111.63	Є metasandstone	Fine-grained, Qz (50%), Ser (50%)	BLG	300-400
127	S203	Xinyi-Yangchun	Yunkai	22.19	111.63	Є sandy phyllite	Fine-grained, Qz (60%), Ser (30%), Ms (10%)	SGR	400-500
128	S177A	Xinyi-Yangchun	Yunkai	22.41	111.26	biotite granitic gneiss	Phenocryst (40%): Fsp. Matrix (60%): Qz, Bt, Fsp	GBM	500-700
129	S179	Xinyi-Yangchun	Yunkai	22.47	111.34	deformed Kf granite	Phenocryst (25%): Qz, Fsp. Matrix (95%): Qz, Fsp, Ms	GBM	500-700
130	S180-1	Xinyi-Yangchun	Yunkai	22.48	111.36	Є hornfel	Fine-grained, Qz (70%), Ms (30%)	SGR	400-500
131	S184	Xinyi-Yangchun	Yunkai	22.34	111.48	Є schist-paragneiss	Coarse-grained, Qz (50%), Ms (30%), Fsp (20%)	BLG	300-400
132	S197B	Xinyi-Yangchun	Yunkai	22.20	111.62	Є metasandstone	Coarse-grained, Qz (80%), Ms (20%)	BLG-SGR	~400
133	S198B	Xinyi-Yangchun	Yunkai	22.20	111.61	Є hornfel sandstone	Phenocryst (20%): Qz, Fsp. Matrix (80%): Qz, Fsp, Ms	BLG-SGR	~400

Table S4. Compilations of the vitrinite reflectance of the coal and estimation of temperatures

No.	Massif	Location	CoalMine / Section	Latitude	Longitude	Period	Formation	Lithology	Sample No.	Ro (%)	Temperature (°C)	References
1	JNOB	Leping, Jiangxi		28.98	117.15	P3	Longtan Fm.	Coal	84-L-ab	0.677	107	Yang Z.Q. & Xu J.W., 1987
2	JNOB	Leping, Jiangxi		28.98	117.15	P3	Longtan Fm.	Coal		0.71	112	Sun X.G., 2002
3	JNOB	Leping, Jiangxi		28.98	117.15	P3	Longtan Fm.	Coal		0.73	115	Sun X.G., 2002
4	JNOB	Leping, Jiangxi	Mingshan (鸣山)	28.93	117.05	P3	Longtan Fm.	Coal	sample-1	0.73	115	Yu H.Y. & Sun X.G., 2007
5	JNOB	Leping, Jiangxi	Mingshan (鸣山)	28.93	117.05	P3	Longtan Fm.	Coal	sample-3	0.73	115	Yu H.Y. & Sun X.G., 2007
6	JNOB	Leping, Jiangxi	Mingshan (鸣山)	28.93	117.05	P3	Longtan Fm.	Coal	sample-2	0.75	118	Yu H.Y. & Sun X.G., 2007
7	JNOB	Leping, Jiangxi	Qiaotouqiu (桥头丘)	28.87	117.13	P	Leping Fm.	Coal	C13(2)	0.87	134	Querol, X.et al.,, 2001
8	JNOB	Leping, Jiangxi	Yangou (沿沟)	29.17	117.35	P	Leping Fm.	Coal	B4(3)	2.42	240	Querol, X.et al.,, 2001
9	JNOB	Leping, Jiangxi	Yangou (沿沟)	29.17	117.35	P	Leping Fm.	Coal	B4(5)	2.43	240	Querol, X.et al.,, 2001
10	JNOB	Leping, Jiangxi	Yangou (沿沟)	29.17	117.35	P	Leping Fm.	Coal	B4(1)	2.44	241	Querol, X.et al.,, 2001
11	JNOB	Leping, Jiangxi	Yangou (沿沟)	29.17	117.35	P	Leping Fm.	Coal	B4(2)	2.49	243	Querol, X.et al.,, 2001
12	JNOB	Leping, Jiangxi	Yangou (沿沟)	29.17	117.35	P	Leping Fm.	Coal	B4(4)	2.54	245	Querol, X.et al.,, 2001
13	JNOB	Liuyang, Hunan	Yonghe (永和)	28.29	113.86	P1	Qixia Fm.	Coal	84-Y-15	0.406	54	Yang Z.Q. & Xu J.W., 1987
14	JNOB	Liuyang, Hunan	Yonghe (永和)	28.29	113.86	P1	Qixia Fm.	Coal	84-Y-12	0.515	79	Yang Z.Q. & Xu J.W., 1987
15	JNOB	Liuyang, Hunan	Yonghe (永和)	28.29	113.86	P3	Longtan Fm.	Coal	84-Y-27	0.517	79	Yang Z.Q. & Xu J.W., 1987
16	JNOB	Lianyuan, Hunan	Lian-shao (涟-邵)	27.69	111.66	C1	Ceshui Fm.	Coal		0.78	122	Sun X.G., 2002
17	JNOB	Xinhua, Hunan	Youxi (油溪)	28.01	111.38	C1	Ceshui Fm.	Shale		1.95	217	Wang S.B., 2013
18	JNOB	Xinhua, Hunan	Ketouxiang (科头乡)	27.68	111.27	C1	Ceshui Fm.	Shale		2.05	223	Wang S.B., 2013
19	JNOB	Xinhua, Hunan	Manzhu (满竹)	27.72	111.40	C1	Ceshui Fm.	Shale		2.15	228	Wang S.B., 2013
20	JNOB	Lengshuijiang, Hunan	Lianhe (联合)	27.84	111.51	C1	Ceshui Fm.	Shale		2.16	228	Wang S.B., 2013
21	JNOB	Lengshuijiang, Hunan	Kuangshanxiang (矿山乡)	27.78	111.50	C1	Ceshui Fm.	Shale		2.17	229	Wang S.B., 2013
22	JNOB	Xinhua, Hunan	Chaoshuixiang (潮水乡)	27.63	111.35	C1	Ceshui Fm.	Shale		2.27	233	Wang S.B., 2013
23	JNOB	Lianyuan, Hunan	Jinzhushan (金竹山)	27.61	111.51	C1	Ceshui Fm.	Shale		2.29	234	Wang S.B., 2013

Table S4 (continued)

No.	Massif	Location	CoalMine / Section	Latitude	Longitude	Period	Formation	Lithology	Sample No.	Ro (%)	Temperature (°C)	References
24	JNOB	Lengshuijiang, Hunan	Kuangshanxiang (矿山乡)	27.78	111.50	C1	Ceshui Fm.	Shale		2.36	237	Wang S.B., 2013
25	JNOB	Lianyuan, Hunan	Sanjia (三甲)	27.66	111.64	C1	Ceshui Fm.	Shale		2.37	238	Wang S.B., 2013
26	JNOB	Lianyuan, Hunan	Jiangjiang (浆江)	27.78	111.66	C1	Ceshui Fm.	Shale		2.45	241	Wang S.B., 2013
27	JNOB	Lengshuijiang, Hunan	Kuangshanxiang (矿山乡)	27.78	111.50	C1	Ceshui Fm.	Shale		2.46	242	Wang S.B., 2013
28	JNOB	Lianyuan, Hunan	Jinzhushan (金竹山)	27.61	111.51	C1	Ceshui Fm.	Shale		2.47	242	Wang S.B., 2013
29	JNOB	Shuangfeng, Hunan	Guanghui (光辉)	27.37	112.08	C1	Ceshui Fm.	Shale		2.47	242	Wang S.B., 2013
30	JNOB	Lengshuijiang, Hunan	Huaxi (化溪)	27.67	111.38	C1	Ceshui Fm.	Shale		2.49	243	Wang S.B., 2013
31	JNOB	Loudi, Hunan	Jinpenwan (金盆湾)	27.62	111.87	C1	Ceshui Fm.	Shale		2.54	245	Wang S.B., 2013
32	JNOB	Lengshuijiang, Hunan	Nangong (南宫)	27.68	111.40	C1	Ceshui Fm.	Shale		2.69	251	Wang S.B., 2013
33	JNOB	Lianyuan, Hunan	Furongxiang (芙蓉乡)	27.72	111.63	C1	Ceshui Fm.	Shale		2.7	251	Wang S.B., 2013
34	JNOB	Xinhua, Hunan	Baitang (白塘)	27.69	111.21	C1	Ceshui Fm.	Shale		2.7	251	Wang S.B., 2013
35	JNOB	Lianyuan, Hunan	Jiangjiang (浆江)	27.78	111.66	C1	Ceshui Fm.	Shale		2.72	252	Wang S.B., 2013
36	JNOB	Lianyuan, Hunan	Daqiaoxiang (大桥乡)	27.52	112.01	C1	Ceshui Fm.	Shale		2.75	253	Wang S.B., 2013
37	JNOB	Xinhua, Hunan	Huanxin (焕新)	27.83	111.50	C1	Ceshui Fm.	Shale		2.77	254	Wang S.B., 2013
38	JNOB	Lianyuan, Hunan	Shaoping (沙坪)	27.67	111.85	C1	Ceshui Fm.	Shale		2.78	254	Wang S.B., 2013
39	JNOB	Lianyuan, Hunan	Limin (利民)	27.75	111.60	C1	Ceshui Fm.	Shale		2.97	261	Wang S.B., 2013
40	JNOB	Lianyuan, Hunan	Xinping (新坪)	27.79	111.88	C1	Ceshui Fm.	Shale		3.12	266	Wang S.B., 2013
41	JNOB	Lianyuan, Hunan	Anping (安平)	27.82	111.69	C1	Ceshui Fm.	Shale		3.15	267	Wang S.B., 2013
42	JNOB	Lianyuan, Hunan	Jinzhushan (金竹山)	27.61	111.51	C1	Ceshui Fm.	Shale		3.24	270	Wang S.B., 2013
43	JNOB	Lianyuan, Hunan	Jinzhushan (金竹山)	27.61	111.51	C1	Ceshui Fm.	Shale		3.26	271	Wang S.B., 2013
44	JNOB	Lengshuijiang, Hunan	Minzhu (民主)	27.71	111.46	C1	Ceshui Fm.	Shale		3.27	271	Wang S.B., 2013
45	JNOB	Lianyuan, Hunan	Jinzhushan (金竹山)	27.61	111.51	C1	Ceshui Fm.	Shale		3.31	272	Wang S.B., 2013
46	JNOB	Xinhua, Hunan	Zijiang (资江)	27.72	111.33	C1	Ceshui Fm.	Shale		3.39	275	Wang S.B., 2013
47	JNOB	Lianyuan, Hunan	Jinzhushan (金竹山)	27.61	111.51	C1	Ceshui Fm.	Shale		3.56	280	Wang S.B., 2013
48	JNOB	Shuangfeng, Hunan	Shuangfeng (双峰)	27.46	112.17	C1	Ceshui Fm.	Shale		3.61	282	Wang S.B., 2013
49	JNOB	Lianyuan, Hunan	Jinzhushan (金竹山)	27.61	111.51	C1	Ceshui Fm.	Shale		3.75	285	Wang S.B., 2013
50	JNOB	Lianyuan, Hunan	Jinzhushan (金竹山)	27.61	111.51	C1	Ceshui Fm.	Coal	JZS-3	4.36	301	Li K., 2019

Table S4 (continued)

No.	Massif	Location	CoalMine / Section	Latitude	Longitude	Period	Formation	Lithology	Sample No.	Ro (%)	Temperature (°C)	References
51	JNOB	Xinshao, Hunan	Longxipu (龙溪铺)	27.45	111.28	C1	Ceshui Fm.	Shale		4.63	307	Wang S.B., 2013
52	JNOB	Lianyuan, Hunan	Lianxin (联新)	27.67	111.37	C1	Ceshui Fm.	Coal	LX-3	4.7	309	Li K., 2019
53	JNOB	Lianyuan, Hunan	Lianxin (联新)	27.67	111.37	C1	Ceshui Fm.	Coal	SHL-3	4.84	312	Li K., 2019
54	JNOB	Lianyuan, Hunan	Lianxin (联新)	27.67	111.37	C1	Ceshui Fm.	Coal	SHL-5	5.01	316	Li K., 2019
55	JNOB	Lianyuan, Hunan	Jinzhushan (金竹山)	27.61	111.51	C1	Ceshui Fm.	Coal	JZS-3	5.34	322	Tang Y.G. et al., 2022
56	JNOB	Lianyuan, Hunan	Lianxin (联新)	27.67	111.37	C1	Ceshui Fm.	Coal	CM-3	5.91	333	Li K., 2019
57	JNOB	Lianyuan, Hunan	Choumu (稠木)	27.62	111.35	C1	Ceshui Fm.	Mudstone		6.02	335	Li H.T. et al., 2022
58	JNOB	Lianyuan, Hunan	Lianxin (联新)	27.67	111.37	C1	Ceshui Fm.	Coal	SL-3	6.09	336	Li K., 2019
59	JNOB	Lianyuan, Hunan	Shengli (胜利)	27.61	111.35	C1	Ceshui Fm.	Mudstone		6.59	344	Li H.T. et al., 2022
60	JNOB	Lianyuan, Hunan	Lianxin (联新)	27.67	111.37	C1	Ceshui Fm.	Coal	BC-3	6.62	345	Li K., 2019
61	JNOB	Lianyuan, Hunan	Baichong (稗冲)	27.58	111.35	C1	Ceshui Fm.	Mudstone		6.71	346	Li H.T. et al., 2022
62	JNOB	Xinhua, Hunan	Tianlongshan (天龙山)	27.59	111.35	C1	Ceshui Fm.	Shale		7.27	354	Wang S.B., 2013
63	JNOB	Lianyuan, Hunan	Lianxin (联新)	27.67	111.37	C1	Ceshui Fm.	Coal	BC-5	7.48	357	Li K., 2019
64	JNOB	Lianyuan, Hunan	Choumu (稠木)	27.62	111.35	C1	Ceshui Fm.	Mudstone	CM-5	7.49	357	Tang Y.G. et al., 2022
65	JNOB	Lianyuan, Hunan	Lianxin (联新)	27.67	111.37	C1	Ceshui Fm.	Coal	CM-5	7.67	360	Li K., 2019
66	JNOB	Lianyuan, Hunan	Shixiangli (石巷里)	27.58	111.35	C1	Ceshui Fm.	Mudstone		7.73	361	Li H.T. et al., 2022
67	JNOB	Lianyuan, Hunan	Lianxin (联新)	27.67	111.37	C1	Ceshui Fm.	Coal	SL-5	8.23	367	Li K., 2019
68	JNOB	Lianyuan, Hunan	Shengli (胜利)	27.61	111.35	C1	Ceshui Fm.	Mudstone	SL-5	8.31	368	Tang Y.G. et al., 2022
69	JNOB	Lianyuan, Hunan	Baichong (稗冲)	27.58	111.35	C1	Ceshui Fm.	Mudstone	BC-5	9.14	378	Tang Y.G. et al., 2022
70	JNOB	Xinhua, Hunan	Tianlongshan (天龙山)	27.59	111.35	C1	Ceshui Fm.	Shale		9.5	382	Wang S.B., 2013
71	JNOB	Lianyuan, Hunan		27.69	111.66	C1	Ceshui Fm.	Coal	JZS-3	1.85	212	Xi Z.D. et al., 2024
72	JNOB	Lianyuan, Hunan		27.69	111.66	C1	Ceshui Fm.	Coal	LSJ-3	1.91	215	Xi Z.D. et al., 2024
73	JNOB	Lianyuan, Hunan		27.69	111.66	C1	Ceshui Fm.	Coal	JZS-2	1.95	217	Xi Z.D. et al., 2024
74	JNOB	Lianyuan, Hunan		27.69	111.66	C1	Ceshui Fm.	Coal	LSJ-2	1.97	219	Xi Z.D. et al., 2024
75	JNOB	Lianyuan, Hunan		27.69	111.66	C1	Ceshui Fm.	Coal	JZS-1	2.01	221	Xi Z.D. et al., 2024
76	JNOB	Lianyuan, Hunan		27.69	111.66	C1	Ceshui Fm.	Coal	LSJ5	2.13	227	Xi Z.D. et al., 2024
77	JNOB	Shaoyang, Hunan		27.24	111.47	C1	Ceshui Fm.	Shale	JZS07	1.6	197	Xiao Z.H. et al., 2018
78	JNOB	Shaoyang, Hunan		27.24	111.47	C1	Ceshui Fm.	Shale	LMJ02	1.6	197	Xiao Z.H. et al., 2018
79	JNOB	Shaoyang, Hunan		27.24	111.47	C1	Ceshui Fm.	Shale	XD06	1.7	203	Xiao Z.H. et al., 2018
80	JNOB	Shaoyang, Hunan		27.24	111.47	C1	Ceshui Fm.	Shale	JZS09	1.7	203	Xiao Z.H. et al., 2018
81	JNOB	Shaoyang, Hunan		27.24	111.47	C1	Ceshui Fm.	Shale	LMJ06	1.7	203	Xiao Z.H. et al., 2018
82	JNOB	Shaoyang, Hunan		27.24	111.47	C1	Ceshui Fm.	Shale	XD01	1.8	209	Xiao Z.H. et al., 2018

Table S4 (continued)

No.	Massif	Location	CoalMine / Section	Latitude	Longitude	Period	Formation	Lithology	Sample No.	Ro (%)	Temperature (°C)	References
83	JNOB	Shaoyang, Hunan		27.24	111.47	C1	Ceshui Fm.	Shale	ZY04	2	220	Xiao Z.H. et al., 2018
84	JNOB	Shaoyang, Hunan		27.24	111.47	C1	Ceshui Fm.	Shale	LSJ01	2	220	Xiao Z.H. et al., 2018
85	JNOB	Shaoyang, Hunan		27.24	111.47	C1	Ceshui Fm.	Shale	ZY08	2.1	225	Xiao Z.H. et al., 2018
86	JNOB	Shaoyang, Hunan		27.24	111.47	C1	Ceshui Fm.	Shale	LSJ04	2.1	225	Xiao Z.H. et al., 2018
87	JNOB	Yongzhou, Hunan		26.42	111.61	C1	Ceshui Fm.	Shale		2.2	230	Wang S.B., 2013
88	JNOB	Shaoyang, Hunan		27.24	111.47	C1	Ceshui Fm.	Shale	JZS05	2.4	239	Xiao Z.H. et al., 2018
89	JNOB	Shaoyang, Hunan		27.24	111.47	C1	Ceshui Fm.	Shale	LSJ05	2.4	239	Xiao Z.H. et al., 2018
90	JNOB	Shaoyang, Hunan		26.99	111.29	C1	Ceshui Fm.	Shale		2.43	240	Wang S.B., 2013
91	JNOB	Shaoyang, Hunan		27.24	111.47	P3	Dalong Fm.	Shale	QXJ05	1.2	167	Xiao Z.H. et al., 2018
92	JNOB	Shaoyang, Hunan		27.24	111.47	P3	Dalong Fm.	Shale	QXJ08	1.2	167	Xiao Z.H. et al., 2018
93	JNOB	Shaoyang, Hunan		27.24	111.47	P3	Dalong Fm.	Shale	DQ09	1.3	175	Xiao Z.H. et al., 2018
94	JNOB	Shaoyang, Hunan		27.24	111.47	P3	Longtan Fm.	Shale	DLS02	1.4	183	Xiao Z.H. et al., 2018
95	JNOB	Shaoyang, Hunan		27.24	111.47	P3	Longtan Fm.	Shale	QXJ14	1.4	183	Xiao Z.H. et al., 2018
96	JNOB	Shaoyang, Hunan		27.24	111.47	P3	Dalong Fm.	Shale	DPQ06	1.5	190	Xiao Z.H. et al., 2018
97	JNOB	Shaoyang, Hunan		27.24	111.47	P3	Longtan Fm.	Shale	DLS05	1.5	190	Xiao Z.H. et al., 2018
98	JNOB	Shaoyang, Hunan		27.24	111.47	P3	Longtan Fm.	Shale	NT03	1.5	190	Xiao Z.H. et al., 2018
99	JNOB	Shaoyang, Hunan		27.24	111.47	P3	Longtan Fm.	Shale	NT02	1.6	197	Xiao Z.H. et al., 2018
100	JNOB	Shaoyang, Hunan		27.24	111.47	P3	Dalong Fm.	Shale	QXJ02	1.7	203	Xiao Z.H. et al., 2018
101	JNOB	Shaoyang, Hunan		27.24	111.47	P3	Dalong Fm.	Shale	DPQ03	1.8	209	Xiao Z.H. et al., 2018
102	JNOB	Shaoyang, Hunan		27.24	111.47	P3	Longtan Fm.	Shale	QXJ10	1.8	209	Xiao Z.H. et al., 2018
103	JNOB	Shaoyang, Hunan		27.24	111.47	P3	Dalong Fm.	Shale	DPQ02	2	220	Xiao Z.H. et al., 2018
104	JNOB	Leping, Jiangxi	Yangou (沿沟)	29.17	117.35	T	Anyuan Fm.	Coal	A2	1.7	203	Querol, X. et al., 2001
105	JNOB	Leping, Jiangxi	Yangou (沿沟)	29.17	117.35	T	Anyuan Fm.	Coal	B	1.75	206	Querol, X. et al., 2001
106	JNOB	Leping, Jiangxi	Yangou (沿沟)	29.17	117.35	T	Anyuan Fm.	Coal	D	1.82	210	Querol, X. et al., 2001
107	JNOB	Leping, Jiangxi	Yangou (沿沟)	29.17	117.35	T	Anyuan Fm.	Coal	Q	1.84	211	Querol, X. et al., 2001
108	JNOB	Leping, Jiangxi	Yangou (沿沟)	29.17	117.35	T	Anyuan Fm.	Coal	F	1.87	213	Querol, X. et al., 2001
109	JNOB	Leping, Jiangxi	Yangou (沿沟)	29.17	117.35	T	Anyuan Fm.	Coal	G	1.89	214	Querol, X. et al., 2001
110	JNOB	Leping, Jiangxi	Yangou (沿沟)	29.17	117.35	T	Anyuan Fm.	Coal	E	1.94	217	Querol, X. et al., 2001
111	JNOB	Leping, Jiangxi	Yangou (沿沟)	29.17	117.35	T	Anyuan Fm.	Coal	A1	1.96	218	Querol, X. et al., 2001
112	JNOB	Leping, Jiangxi	Yangou (沿沟)	29.17	117.35	T	Anyuan Fm.	Coal	H	1.96	218	Querol, X. et al., 2001
113	JNOB	Leping, Jiangxi	Yangou (沿沟)	29.17	117.35	T	Anyuan Fm.	Coal	R	1.98	219	Querol, X. et al., 2001
114	JNOB	Leping, Jiangxi	Yangou (沿沟)	29.17	117.35	T	Anyuan Fm.	Coal	8-1-2A	2.02	221	Querol, X. et al., 2001
115	JNOB	Leping, Jiangxi	Yangou (沿沟)	29.17	117.35	T	Anyuan Fm.	Coal	M	2.02	221	Querol, X. et al., 2001

Table S4 (continued)

No.	Massif	Location	CoalMine / Section	Latitude	Longitude	Period	Formation	Lithology	Sample No.	Ro (%)	Temperature (°C)	References
116	JNOB	Leping, Jiangxi	Yangou (沿沟)	29.17	117.35	T	Anyuan Fm.	Coal	P	2.04	222	Querol, X. et al., 2001
117	JNOB	Leping, Jiangxi	Yangou (沿沟)	29.17	117.35	T	Anyuan Fm.	Coal	6-2-3	2.05	223	Querol, X. et al., 2001
118	JNOB	Leping, Jiangxi	Yangou (沿沟)	29.17	117.35	T	Anyuan Fm.	Coal	K	2.05	223	Querol, X. et al., 2001
119	JNOB	Leping, Jiangxi	Yangou (沿沟)	29.17	117.35	T	Anyuan Fm.	Coal	C	2.15	228	Querol, X. et al., 2001
120	JNOB	Leping, Jiangxi	Yangou (沿沟)	29.17	117.35	T	Anyuan Fm.	Coal	A1	8.27	368	Querol, X. et al., 2001
121	Nanling	Yizhang, Hunan	Meitian (梅田)	25.32	112.82	P3	Longtan Fm.	Coal	12U-1	2.64	249	Xiao Z.H. et al., 2018, Minerals
122	Nanling	Yizhang, Hunan	Meitian (梅田)	25.32	112.82	P3	Longtan Fm.	Coal	Av	2.8	255	Xiao Z.H. et al., 2018, Minerals
123	Nanling	Yizhang, Hunan	Meitian (梅田)	25.32	112.82	P3	Longtan Fm.	Shale		2.81	255	Xu Y.J. et al., 2023
124	Nanling	Chenzhou, Hunan		25.77	113.02	P3	Longtan Fm.	Shale		2.85	257	Xun Y.J. et al., 2023
125	Nanling	Yizhang, Hunan	Meitian (梅田)	25.32	112.82	P3	Longtan Fm.	Coal	12L-1	2.89	258	Xiao Z.H. et al., 2018, Minerals
126	Nanling	Yizhang, Hunan	Meitian (梅田)	25.32	112.82	P3	Longtan Fm.	Coal	12U-2	2.96	261	Xiao Z.H. et al., 2018, Minerals
127	Nanling	Jiahe, Hunan	Yuanjia (袁家)	25.57	112.43	P3	Longtan Fm.	Shale		3.13	267	Xu Y.J. et al., 2023
128	Nanling	Yizhang, Hunan	Meitian (梅田)	25.32	112.82	P3	Longtan Fm.	Coal	Av	3.17	268	Xiao Z.H. et al., 2018, Minerals
129	Nanling	Chenzhou, Hunan	Jiedong (街洞)	25.97	113.07	P3	Longtan Fm.	Shale		3.35	274	Xu Y.J. et al., 2023
130	Nanling	Yizhang, Hunan	Meitian (梅田)	25.32	112.82	P3	Longtan Fm.	Coal	12L-2	3.45	277	Xiao Z.H. et al., 2018, Minerals
131	Nanling	Yongxing, Hunan	Matian (马田)	26.09	112.90	P3	Longtan Fm.	Shale		3.56	280	Xu Y.J. et al., 2023
132	Nanling	Chenzhou, Hunan	Lutang (鲁塘)	25.56	112.74	P3	Longtan Fm.	Shale		3.37	274	Xun Y.J. et al., 2023
133	Nanling	Chenzhou, Hunan	Lutang (鲁塘)	25.56	112.74	P3	Longtan Fm.	Coal	HN-9	6.48	342	Wang L., 2020
134	Nanling	Chenzhou, Hunan	Lutang (鲁塘)	25.56	112.74	P3	Longtan Fm.	Coal	HN-11	7.34	355	Wang L., 2020
135	Nanling	Chongyi, Jiangxi	Chongyi (崇义)	25.68	114.31	P3	Leping Fm.	Coal		3.09	265	Mi Z.H. et al., 2021
136	Nanling	Chongyi, Jiangxi	Chongyi (崇义)	25.68	114.31	P3	Longtan Fm.	Coal	JX	4.04	293	Wang L., 2020
137	Nanling	Chongyi, Jiangxi	Dumuqiao (独木桥)	25.71	114.39	P3	Longtan Fm.	Coal	CYSM-2	4.04	293	Li Y. et al., 2019
138	Nanling	Chongyi, Jiangxi	Dumuqiao (独木桥)	25.71	114.39	P3	Longtan Fm.	Coal	CYSM-4	4.6	307	Li Y. et al., 2019
139	Nanling	Chongyi, Jiangxi	Dumuqiao (独木桥)	25.71	114.39	P3	Longtan Fm.	Coal	CYSM-3	4.68	309	Li Y. et al., 2019
140	Nanling	Chongyi, Jiangxi	Dumuqiao (独木桥)	25.71	114.39	P3	Longtan Fm.	Coal	CYSM-6	4.89	313	Li Y. et al., 2019
141	Nanling	Chongyi, Jiangxi	Dumuqiao (独木桥)	25.71	114.39	P3	Longtan Fm.	Coal	CYSM-1	5.35	322	Li Y. et al., 2019

Table S4 (continued)

No.	Massif	Location	CoalMine / Section	Latitude	Longitude	Period	Formation	Lithology	Sample No.	Ro (%)	Temperature (°C)	References
142	Nanling	Chongyi, Jiangxi	Dumuqiao (独木桥)	25.71	114.39	P3	Longtan Fm.	Coal	CYSM-5	5.52	326	Li Y. et al., 2019
143	Nanling	Chongyi, Jiangxi	Chongyi (崇义)	25.68	114.31	P3	Longtan Fm.	Coal	JX	6.04	335	Wang L., 2020
144	Nanling	Chongyi, Jiangxi	Dumuqiao (独木桥)	25.71	114.39	P3	Longtan Fm.	Coal	CYSM-7	6.04	335	Li Y. et al., 2019
145	Nanling	Chongyi, Jiangxi	Chongyi (崇义)	25.68	114.31	P3	Leping Fm.	Coal		6.58	344	Mi Z.H. et al., 2021
146	Nanling	Hengshan, Hunan	Xialiuchong (霞流冲)	27.31	112.92	P3	Longtan Fm.	Shale		1.45	187	Xu Y.J. et al., 2023
147	Nanling	Youxian, Hunan	Taoshui (桃水)	27.08	113.22	P3	Longtan Fm.	Shale		1.54	193	Xu Y.J. et al., 2023
148	Nanling	Youxian, Hunan	Huangfengqiao (黄丰桥)	27.26	113.71	P3	Longtan Fm.	Shale		1.62	198	Xu Y.J. et al., 2023
149	Nanling	Changning, Hunan	Yanhu (盐湖)	26.39	112.50	P3	Longtan Fm.	Shale		1.63	199	Xu Y.J. et al., 2023
150	Nanling	Changning, Hunan	Douling (斗岭)	26.26	112.30	P3	Longtan Fm.	Shale		1.65	200	Xun Y.J. et al., 2023
151	Nanling	Changning, Hunan	Zhengtong (正同)	26.43	112.34	P3	Longtan Fm.	Shale		1.8	209	Xu Y.J. et al., 2023
152	Nanling	Changning, Hunan	Shihuichong (石灰冲)	26.30	112.31	P3	Longtan Fm.	Shale		2.1	225	Xu Y.J. et al., 2023
153	Nanling	Leiyang, Hunan	Mashui (马水)	26.66	113.06	P3	Longtan Fm.	Shale		2.2	230	Xu Y.J. et al., 2023
154	Nanling	Leiyang, Hunan	Qianjin (前进)	26.35	112.97	P3	Longtan Fm.	Shale		3.51	279	Xu Y.J. et al., 2023
155	Nanling	Zixing, Hunan		25.98	113.24	T		Coal	(min)	0.914	139	Chen H.Z. & Chen W.M., 2000
156	Nanling	Zixing, Hunan		25.98	113.24	T		Coal	(max)	1.417	184	Chen H.Z. & Chen W.M., 2000
157	Wuyi	Longyan, Fujian	Kengbing (坑柄)	25.15	116.94	P2	Tongziyan Fm.	Coal		3.44	276	Fang H.F. et al., 2010
158	Wuyi	Longyan, Fujian	Fengshanqi (凤山岐)	25.22	117.14	P2	Tongziyan Fm.	Coal		3.59	281	Fang H.F. et al., 2010
159	Wuyi	Liancheng, Fujian	Laiyuan (赖源)	25.56	117.01	P2	Tongziyan Fm.	Coal		3.8	287	Fang H.F. et al., 2010
160	Wuyi	Longyan, Fujian	Xihushan (西湖山)	25.07	116.98	P2	Tongziyan Fm.	Coal		4.02	293	Fang H.F. et al., 2010
161	Wuyi	Anxi, Fujian	Pantian (潘田)	25.31	117.80	P2	Tongziyan Fm.	Coal		4.07	294	Fang H.F. et al., 2010
162	Wuyi	Longyan, Fujian	Niukeng (牛坑)	25.42	117.16	P2	Tongziyan Fm.	Coal		4.17	297	Fang H.F. et al., 2010
163	Wuyi	Anxi, Fujian	Jiandou (剑斗)	25.32	117.94	P2	Tongziyan Fm.	Coal		4.34	301	Fang H.F. et al., 2010
164	Wuyi	Longyan, Fujian	Renpan (仁盘)	25.25	117.14	P2	Tongziyan Fm.	Mudstone		4.35	301	Fang H.F. et al., 2010
165	Wuyi	Longyan, Fujian	Dingfengshan (顶峰山)	25.00	116.94	P2	Tongziyan Fm.	Coal		4.37	301	Fang H.F. et al., 2010
166	Wuyi	Longyan-Yongding, Fujian		24.73	116.74	P2	Tongziyan Fm.	Shale	(average)	4.4	302	Chen Q.L., 2020
167	Wuyi	Longyan, Fujian	Subangbei (苏邦北)	25.32	117.17	P2	Tongziyan Fm.	Mudstone		4.42	303	Fang H.F. et al., 2010
168	Wuyi	Wuping, Fujian	Jianliaokeng (剪寮坑)	25.10	116.10	P2	Tongziyan Fm.	Coal	JLK	4.47	304	Wang L., 2020
169	Wuyi	Wuping, Fujian	Jianliaokeng (剪寮坑)	25.10	116.10	P2	Tongziyan Fm.	Coal	JLK-3	4.47	304	Deng R.J., 2020
170	Wuyi	Longyan, Fujian	Longtanxi (龙潭西)	24.84	116.99	P2	Tongziyan Fm.	Coal		4.49	304	Fang H.F. et al., 2010

Table S4 (continued)

No.	Massif	Location	CoalMine / Section	Latitude	Longitude	Period	Formation	Lithology	Sample No.	Ro (%)	Temperature (°C)	References
171	Wuyi	Liancheng, Fujian	Beituan (北团)	25.80	116.72	P2	Tongziyan Fm.	Coal		4.59	306	Fang H.F. et al., 2010
172	Wuyi	Longyan-Yongding, Fujian		24.73	116.74	P2	Tongziyan Fm.	Shale	(average)	4.59	306	Chen Q.L., 2020
173	Wuyi	Longyan, Fujian	Subang (苏邦)	25.32	117.17	P2	Tongziyan Fm.	Coal		4.6	307	Fang H.F. et al., 2010
174	Wuyi	Liancheng-Wuping, Fujian		25.38	116.56	P2	Tongziyan Fm.	Shale	(average)	4.61	307	Chen Q.L., 2020
175	Wuyi	Longyan-Yongding, Fujian		24.73	116.74	P2	Tongziyan Fm.	Shale	(average)	4.62	307	Chen Q.L., 2020
176	Wuyi	Wuping, Fujian	Ningyang (宁洋)	24.94	116.27	P2	Tongziyan Fm.	Coal		4.65	308	Fang H.F. et al., 2010
177	Wuyi	Longyan, Fujian	Xiejiabang (谢家邦)	25.11	117.11	P2	Tongziyan Fm.	Coal		4.72	309	Fang H.F. et al., 2010
178	Wuyi	Longyan, Fujian	Changta (长塔)	25.48	117.69	P2	Tongziyan Fm.	Coal		4.83	312	Fang H.F. et al., 2010
179	Wuyi	Longyan, Fujian	Hukengshan (虎坑山)	25.08	116.98	P2	Tongziyan Fm.	Coal		5	315	Fang H.F. et al., 2010
180	Wuyi	Liancheng, Fujian	Huangkeng (黄坑)	25.79	116.78	P2	Tongziyan Fm.	Coal		5.05	316	Fang H.F. et al., 2010
181	Wuyi	Liancheng, Fujian	Miaoqian (庙前)	25.70	116.75	P2	Tongziyan Fm.	Coal		5.06	317	Fang H.F. et al., 2010
182	Wuyi	Longyan, Fujian	Longtanzhong (龙潭中)	24.82	117.04	P2	Tongziyan Fm.	Coal		5.13	318	Fang H.F. et al., 2010
183	Wuyi	Liancheng, Fujian	Wenfeng (文峰)	25.78	116.75	P2	Tongziyan Fm.	Coal	WF-3	5.38	323	Deng R.J., 2020
184	Wuyi	Longyan, Fujian	Neiluoqiao (内罗桥)	25.12	117.13	P2	Tongziyan Fm.	Coal		5.46	325	Fang H.F. et al., 2010
185	Wuyi	Anxi, Fujian	Dongyang (东阳)	25.30	117.95	P2	Tongziyan Fm.	Coal		5.62	328	Fang H.F. et al., 2010
186	Wuyi	Wuping, Fujian	Ningyang (宁洋)	24.94	116.27	P2	Tongziyan Fm.	Coal		5.62	328	Fang H.F. et al., 2010
187	Wuyi	Anxi, Fujian	Houjing (后井)	25.33	117.93	P2	Tongziyan Fm.	Coal		5.63	328	Fang H.F. et al., 2010
188	Wuyi	Longyan, Fujian	Cuipingshan (翠屏山)	25.10	117.04	P2	Tongziyan Fm.	Coal		5.64	328	Fang H.F. et al., 2010
189	Wuyi	Longyan, Fujian	Baisha (白沙)	25.38	117.23	P2	Tongziyan Fm.	Coal		5.74	330	Fang H.F. et al., 2010
190	Wuyi	Longyan, Fujian	Kengbing (坑柄)	25.15	116.94	P2	Tongziyan Fm.	Coal		5.8	331	Fang H.F. et al., 2010
191	Wuyi	Longyan, Fujian	Jiangshan (江山)	25.17	116.98	P2	Tongziyan Fm.	Coal		5.83	331	Fang H.F. et al., 2010
192	Wuyi	Longyan, Fujian	Shizishan (十字山)	25.40	117.58	P2	Tongziyan Fm.	Coal		5.87	332	Fang H.F. et al., 2010
193	Wuyi	Longyan, Fujian	Wangzhuang (王庄)	25.04	117.06	P2	Tongziyan Fm.	Coal		5.89	332	Fang H.F. et al., 2010
194	Wuyi	Longyan, Fujian	Hongtanshan (红炭山)	25.08	116.98	P2	Tongziyan Fm.	Coal		6.06	335	Fang H.F. et al., 2010
195	Wuyi	Longyan, Fujian	Tianluoxing (田螺形)	25.00	116.97	P2	Tongziyan Fm.	Coal		6.16	337	Fang H.F. et al., 2010
196	Wuyi	Liancheng, Fujian	Huangkeng (黄坑)	25.79	116.78	P2	Tongziyan Fm.	Coal		6.2	338	Fang H.F. et al., 2010
197	Wuyi	Longyan, Fujian	Longtandong (龙潭东)	24.87	117.07	P2	Tongziyan Fm.	Coal		6.48	342	Fang H.F. et al., 2010
198	Wuyi	Liancheng, Fujian	Huangfang (黄坊)	25.76	116.79	P2	Tongziyan Fm.	Coal		6.55	343	Fang H.F. et al., 2010
199	Wuyi	Longyan, Fujian	Beishan (北山)	25.20	117.23	P2	Tongziyan Fm.	Coal		6.71	346	Fang H.F. et al., 2010

Table S4 (continued)

No.	Massif	Location	CoalMine / Section	Latitude	Longitude	Period	Formation	Lithology	Sample No.	Ro (%)	Temperature (°C)	References
200	Wuyi	Longyan, Fujian	Lujiadi (陆家地)	25.13	117.10	P2	Tongziyan Fm.	Coal		6.74	346	Fang H.F. et al., 2010
201	Wuyi	Longyan, Fujian	Cuipingshan (翠屏山)	25.10	117.04	P2	Tongziyan Fm.	Coal	CPS-3	7.74	361	Deng R.J., 2020
202	Wuyi	Anxi, Fujian	Qingyang (青洋)	25.22	117.96	P2	Tongziyan Fm.	Coal	QY	8.38	369	Wang L., 2020
203	Wuyi	Anxi, Fujian	Qingyang (青洋)	25.22	117.96	P2	Tongziyan Fm.	Coal	QY-1	8.38	369	Deng R.J., 2020
204	Wuyi	Wuping, Fujian	Shifangzhen (十方镇)	25.03	116.24	P3	Dalong Fm.	Mudstone		5.07	317	Fang H.F. et al., 2010
205	Wuyi	Longyan, Fujian		25.08	117.02	P3		Coal	(average)	5.64	328	Chen H.Z. & Chen W.M., 2000
206	Wuyi	Meizhou, Guangdong	Wenfuzhen (文福镇)	24.74	116.20	P1	Qixia Fm.	Limestone		4.41	302	Fang H.F. et al., 2010
207	Wuyi	Meizhou, Guangdong	Luogangzhen (罗岗镇)	24.42	115.64	P2	Tongziyan Fm.	Coal		2.68	251	Fang H.F. et al., 2010
208	Wuyi	Meizhou, Guangdong	Bingcunzhen (丙村镇)	24.36	116.28	P2	Tongziyan Fm.	Mudstone		3.03	263	Fang H.F. et al., 2010
209	Wuyi	Meizhou, Guangdong	Daping (大坪)	24.36	115.96	P2	Tongziyan Fm.	Mudstone		3.53	279	Fang H.F. et al., 2010
210	Wuyi	Meizhou, Guangdong	Baidu (白渡)	24.50	116.20	P2	Tongziyan Fm.	Coal		3.54	279	Fang H.F. et al., 2010
211	Wuyi	Meizhou, Guangdong	Guikeng (桂坑)	23.72	116.72	P2	Tongziyan Fm.	Coal		3.56	280	Fang H.F. et al., 2010
212	Wuyi	Heyuan, Guangdong	Mabugang (麻布岗)	24.59	115.42	P2	Tongziyan Fm.	Mudstone		3.85	288	Fang H.F. et al., 2010
213	Wuyi	Meizhou, Guangdong	Zhukeng (柱坑)	24.43	115.92	P2	Tongziyan Fm.	Mudstone		4.06	294	Fang H.F. et al., 2010
214	Wuyi	Meizhou, Guangdong	Luogangzhen (罗岗镇)	24.42	115.64	P2	Tongziyan Fm.	Mudstone		4.19	297	Fang H.F. et al., 2010
215	Wuyi	Meizhou, Guangdong	Bingcunzhen (丙村镇)	24.36	116.28	P2	Tongziyan Fm.	Mudstone		4.44	303	Fang H.F. et al., 2010
216	Wuyi	Meizhou, Guangdong	Daping (大坪)	24.36	115.96	P2	Tongziyan Fm.	Coal		4.69	309	Fang H.F. et al., 2010
217	Wuyi	Meizhou, Guangdong	Bingcunzhen (丙村镇)	24.36	116.28	P2	Tongziyan Fm.	Mudstone		4.71	309	Fang H.F. et al., 2010
218	Wuyi	Meizhou, Guangdong	Dongxing (东兴)	24.07	115.84	P2	Tongziyan Fm.	Mudstone		4.8	311	Fang H.F. et al., 2010

Table S4 (continued)

No.	Massif	Location	CoalMine / Section	Latitude	Longitude	Period	Formation	Lithology	Sample No.	Ro (%)	Temperature (°C)	References
219	Wuyi	Meixian, Guangdong	Xietian (谢田)	24.37	116.14	P2	Tongziyan Fm.	Coal		4.81	311	Fang H.F. et al., 2010
220	Wuyi	Meizhou, Guangdong	Bingcunzhen (丙村镇)	24.36	116.28	P2	Tongziyan Fm.	Coal		4.82	312	Fang H.F. et al., 2010
221	Wuyi	Meizhou, Guangdong	Bingcunzhen (丙村镇)	24.36	116.28	P2	Tongziyan Fm.	Coal		4.84	312	Fang H.F. et al., 2010
222	Wuyi	Meizhou, Guangdong	Bingcunzhen (丙村镇)	24.36	116.28	P2	Tongziyan Fm.	Coal		5.07	317	Fang H.F. et al., 2010
223	Wuyi	Wuhua, Guangdong	Huangta (黄塔)	23.98	115.48	P2	Tongziyan Fm.	Coal		5.08	317	Fang H.F. et al., 2010
224	Wuyi	Meizhou, Guangdong	Chengdongzhen (城东镇)	24.38	116.14	P2	Tongziyan Fm.	Mudstone		5.1	317	Fang H.F. et al., 2010
225	Wuyi	Meizhou, Guangdong	Mingshan (明山)	24.25	116.29	P2	Tongziyan Fm.	Coal		5.11	318	Fang H.F. et al., 2010
226	Wuyi	Meizhou, Guangdong	Gaosizhen (高斯镇)	24.58	116.28	P2	Tongziyan Fm.	Coal		5.21	320	Fang H.F. et al., 2010
227	Wuyi	Meizhou, Guangdong	Bingcunzhen (丙村镇)	24.36	116.28	P2	Tongziyan Fm.	Coal		5.54	326	Fang H.F. et al., 2010
228	Wuyi	Meizhou, Guangdong	Bingcunzhen (丙村镇)	24.36	116.28	P2	Tongziyan Fm.	Coal		5.64	328	Fang H.F. et al., 2010
229	Wuyi	Meizhou, Guangdong	Bingcunzhen (丙村镇)	24.36	116.28	P2	Tongziyan Fm.	Coal		6.01	335	Fang H.F. et al., 2010
230	Wuyi	Meizhou, Guangdong	Siwangzhang (四望璋)	24.49	115.79	P2	Tongziyan Fm.	Mudstone		6.85	348	Fang H.F. et al., 2010
231	Wuyi	Jiaoling, Guangdong	Dadi (大地)	24.59	116.23	P2	Tongziyan Fm.	Coal		7.41	356	Fang H.F. et al., 2010
232	Wuyi	Sanming, Fujian	Taijiang (台江)	26.23	117.58	P2	Tongziyan Fm.	Coal		4.4	302	Fang H.F. et al., 2010
233	Wuyi	Youxi-Yongchun, Fujian		25.67	118.24	P2	Tongziyan Fm.	Shale	(average)	4.64	308	Chen Q.L., 2020
234	Wuyi	Youxi-Yongchun, Fujian		25.67	118.24	P2	Tongziyan Fm.	Shale	(average)	4.7	309	Chen Q.L., 2020
235	Wuyi	Youxi-Yongchun, Fujian		25.67	118.24	P2	Tongziyan Fm.	Shale	(average)	4.73	310	Chen Q.L., 2020
236	Wuyi	Jiangle, Fujian	Linkeng (林坑)	26.94	117.47	P2	Tongziyan Fm.	Coal		5.17	319	Fang H.F. et al., 2010
237	Wuyi	Mingxi, Fujian	Niujiaokeng (牛角坑)	26.33	117.45	P2	Tongziyan Fm.	Coal		5.18	319	Fang H.F. et al., 2010

Table S4 (continued)

No.	Massif	Location	CoalMine / Section	Latitude	Longitude	Period	Formation	Lithology	Sample No.	Ro (%)	Temperature (°C)	References
238	Wuyi	Shaxian, Fujian	Duanxi (端溪)	26.43	117.94	P2	Tongziyan Fm.	Coal		5.28	321	Fang H.F. et al., 2010
239	Wuyi	Sanming, Fujian	Bikou (碧口)	26.29	117.66	P2	Tongziyan Fm.	Coal		5.63	328	Fang H.F. et al., 2010
240	Wuyi	Youxi, Fujian	Gujicun (古迹村)	25.98	118.15	P2	Tongziyan Fm.	Coal		5.9	333	Fang H.F. et al., 2010
241	Wuyi	Yong'an, Fujian	Suqiao (苏桥)	26.05	117.82	P1	Qixia Fm.	Mudstone		4.44	303	Fang H.F. et al., 2010
242	Wuyi	Yong'an, Fujian	Caoyuanzhen (曹远镇)	26.02	117.34	P1	Qixia Fm.	Limestone		4.47	304	Fang H.F. et al., 2010
243	Wuyi	Yongding, Fujian	Peifeng (培丰)	24.91	116.95	P2	Tongziyan Fm.	Coal		4.18	297	Fang H.F. et al., 2010
244	Wuyi	Yong'an-Datian, Fujian		26.15	118.12	P2	Tongziyan Fm.	Shale	(average)	4.3	300	Chen Q.L., 2020
245	Wuyi	Yongding, Fujian	Niulanshan (牛栏山)	24.72	116.73	P2	Tongziyan Fm.	Coal		4.41	302	Fang H.F. et al., 2010
246	Wuyi	Yongding, Fujian	Hongxi (红溪)	24.57	116.83	P2	Tongziyan Fm.	Coal		4.48	304	Fang H.F. et al., 2010
247	Wuyi	Yong'an-Datian, Fujian		26.15	118.12	P2	Tongziyan Fm.	Shale	(average)	4.55	306	Chen Q.L., 2020
248	Wuyi	Yong'an, Fujian	Shuinan (水南)	25.99	117.15	P2	Tongziyan Fm.	Coal		4.58	306	Fang H.F. et al., 2010
249	Wuyi	Yong'an, Fujian	Xikou (溪口)	26.04	117.23	P2	Tongziyan Fm.	Coal		4.63	307	Fang H.F. et al., 2010
250	Wuyi	Yong'an-Datian, Fujian		26.15	118.12	P2	Tongziyan Fm.	Shale	(average)	4.75	310	Chen Q.L., 2020
251	Wuyi	Yongding, Fujian	Fuling (富岭)	24.97	116.91	P2	Tongziyan Fm.	Coal		4.75	310	Fang H.F. et al., 2010
252	Wuyi	Yong'an, Fujian	Banzhukeng (斑竹坑)	26.02	117.23	P2	Tongziyan Fm.	Coal		4.77	310	Fang H.F. et al., 2010
253	Wuyi	Dehua, Fujian	Zengban (曾坂)	25.80	118.20	P2	Tongziyan Fm.	Coal		4.79	311	Fang H.F. et al., 2010
254	Wuyi	Yong'an, Fujian	Xiaha (虾蛤)	25.99	117.33	P2	Tongziyan Fm.	Coal		4.83	312	Fang H.F. et al., 2010
255	Wuyi	Ninghua, Fujian	Ganmutan (甘木潭)	26.41	116.90	P2	Tongziyan Fm.	Coal		4.9	313	Fang H.F. et al., 2010
256	Wuyi	Ninghua, Fujian	Hucun (湖村)	26.35	116.85	P2	Tongziyan Fm.	Coal		4.96	315	Fang H.F. et al., 2010
257	Wuyi	Yong'an, Fujian	Fenghai (丰海)	26.02	117.21	P2	Tongziyan Fm.	Mudstone		4.96	315	Fang H.F. et al., 2010
258	Wuyi	Yong'an, Fujian	Xiaohua (小华）	25.76	117.71	P2	Tongziyan Fm.	Coal	XH-3	5	315	Deng R.J., 2020
259	Wuyi	Yongding, Fujian	Changfushan (昌福山)	24.81	116.99	P2	Tongziyan Fm.	Coal		5.04	316	Fang H.F. et al., 2010
260	Wuyi	Yong'an, Fujian	Suqiao (苏桥)	26.05	117.82	P2	Tongziyan Fm.	Coal		5.15	318	Fang H.F. et al., 2010
261	Wuyi	Yong'an, Fujian	Jiafu (加福)	25.99	117.18	P2	Tongziyan Fm.	Coal		5.22	320	Fang H.F. et al., 2010
262	Wuyi	Yongding, Fujian	Wayaoping (瓦窑坪)	24.88	116.88	P2	Tongziyan Fm.	Coal		5.25	320	Fang H.F. et al., 2010
263	Wuyi	Yong'an, Fujian	Jingdong (京东)	25.71	117.69	P2	Tongziyan Fm.	Coal	JD-1	5.27	321	Deng R.J., 2020
264	Wuyi	Yong'an, Fujian	Dongkengzai (东坑仔)	25.94	117.17	P2	Tongziyan Fm.	Coal		5.28	321	Fang H.F. et al., 2010
265	Wuyi	Yong'an, Fujian	Yong'an (永安)	25.94	117.37	P2	Tongziyan Fm.	Coal	TXY2	5.33	322	Li J.Q. et al., 2022

Table S4 (continued)

No.	Massif	Location	CoalMine / Section	Latitude	Longitude	Period	Formation	Lithology	Sample No.	Ro (%)	Temperature (°C)	References
266	Wuyi	Datian, Fujian	Guangping (广平)	26.09	117.83	P2	Tongziyan Fm.	Coal		5.37	323	Fang H.F. et al., 2010
267	Wuyi	Yongding, Fujian	Dongzhong (东中)	24.90	116.98	P2	Tongziyan Fm.	Coal		5.5	325	Fang H.F. et al., 2010
268	Wuyi	Yongding, Fujian	Kanshi (坎市)	24.92	116.89	P2	Tongziyan Fm.	Coal		5.51	325	Fang H.F. et al., 2010
269	Wuyi	Qingliu, Fujian	Luokou (罗口)	26.01	116.91	P2	Tongziyan Fm.	Coal		5.53	326	Fang H.F. et al., 2010
270	Wuyi	Datian, Fujian	Jianshe (建设)	25.98	117.79	P2	Tongziyan Fm.	Coal		5.54	326	Fang H.F. et al., 2010
271	Wuyi	Yong'an, Fujian	Houpu (后埔)	25.77	117.31	P2	Tongziyan Fm.	Coal	HP-1	5.59	327	Deng R.J., 2020
272	Wuyi	Yongding, Fujian	Qiaxi (洽溪)	24.49	116.85	P2	Tongziyan Fm.	Coal		6.13	337	Fang H.F. et al., 2010
273	Wuyi	Yongding, Fujian	Wenxi (文溪)	24.93	116.94	P2	Tongziyan Fm.	Coal		6.15	337	Fang H.F. et al., 2010
274	Wuyi	Yong'an, Fujian	Pingxiao (坪笑)	25.92	117.16	P2	Tongziyan Fm.	Coal	PX1	6.2	338	Deng R.J., 2020
275	Wuyi	Yongding, Fujian	Fuling (富岭)	24.97	116.91	P2	Tongziyan Fm.	Coal		6.31	340	Fang H.F. et al., 2010
276	Wuyi	Yongding, Fujian	Fushi (抚市)	24.83	116.93	P2	Tongziyan Fm.	Coal		6.34	340	Fang H.F. et al., 2010
277	Wuyi	Datian, Fujian	Qiongkou (琼口)	25.97	117.84	P2	Tongziyan Fm.	Coal	QK-1	6.43	342	Deng R.J., 2020
278	Wuyi	Yong'an, Fujian	Xiagaizhu (下盖竹)	25.94	117.63	P2	Tongziyan Fm.	Coal	XG1	6.43	342	Deng R.J., 2020
279	Wuyi	Yong'an, Fujian	Chang'ao (长坳)	25.91	117.16	P2	Tongziyan Fm.	Coal	CO3	6.47	342	Deng R.J., 2020
280	Wuyi	Qingliu, Fujian	Luokou (罗口)	26.01	116.91	P2	Tongziyan Fm.	Coal	LK	6.51	343	Wang L., 2020
281	Wuyi	Yong'an, Fujian	Yong'an (永安)	25.94	117.37	P2	Tongziyan Fm.	Coal	JK	7.01	351	Li J.Q. et al., 2022
282	Wuyi	Datian, Fujian	Xiyang (溪洋)	25.35	117.78	P2	Tongziyan Fm.	Coal	XY4	7.13	352	Deng R.J., 2020
283	Wuyi	Yong'an, Fujian	Yong'an (永安)	25.94	117.37	P2	Tongziyan Fm.	Coal	CA3	7.17	353	Li J.Q. et al., 2022
284	Wuyi	Yongding, Fujian	Gaobei (高陂)	24.97	116.88	P2	Tongziyan Fm.	Coal		7.17	353	Fang H.F. et al., 2010
285	Wuyi	Datian, Fujian	Shangjing (上京)	25.72	117.67	P2	Tongziyan Fm.	Coal		7.21	353	Fang H.F. et al., 2010
286	Wuyi	Yong'an, Fujian	Yong'an (永安)	25.94	117.37	P2	Tongziyan Fm.	Coal	TXY1	7.25	354	Li J.Q. et al., 2022
287	Wuyi	Yong'an, Fujian	Yong'an (永安)	25.94	117.37	P2	Tongziyan Fm.	Coal	PK	7.32	355	Li J.Q. et al., 2022
288	Wuyi	Yong'an, Fujian	Yong'an (永安)	25.94	117.37	P2	Tongziyan Fm.	Coal	CA1	7.94	363	Li J.Q. et al., 2022
289	Wuyi	Yong'an, Fujian	Yong'an (永安)	25.94	117.37	P2	Tongziyan Fm.	Coal	QK	8.95	376	Li J.Q. et al., 2022
290	Wuyi	Yong'an, Fujian	Caoyuanzhen (曹远镇)	26.02	117.34	P3	Cuipingshan Fm.	Mudstone		4.68	309	Fang H.F. et al., 2010
291	Wuyi	Zhangping,Fujian	Lingdicun (灵地村)	25.61	117.59	P2	Tongziyan Fm.	Coal		3.42	276	Fang H.F. et al., 2010
292	Wuyi	Zhangping,Fujian	Lingdicun (灵地村)	25.61	117.59	P2	Tongziyan Fm.	Mudstone		3.68	284	Fang H.F. et al., 2010
293	Wuyi	Yongchun, Fujian	Shangyao (上姚)	25.53	118.02	P2	Tongziyan Fm.	Mudstone		3.88	289	Fang H.F. et al., 2010
294	Wuyi	Zhangping,Fujian	Lingdicun (灵地村)	25.61	117.59	P2	Tongziyan Fm.	Coal		4.32	300	Fang H.F. et al., 2010
295	Wuyi	Yongchun, Fujian	Shangyao (上姚)	25.53	118.02	P2	Tongziyan Fm.	Coal		4.68	309	Fang H.F. et al., 2010

Table S4 (continued)

No.	Massif	Location	CoalMine / Section	Latitude	Longitude	Period	Formation	Lithology	Sample No.	Ro (%)	Temperature (°C)	References
296	Wuyi	Zhangping,Fujian	Wushige (乌石隔)	25.25	117.38	P2	Tongziyan Fm.	Coal	WSG-1	4.94	314	Deng R.J., 2020
297	Wuyi	Yongchun, Fujian	Tianhushan (天湖山)	25.48	117.99	P2	Tongziyan Fm.	Coal		5.6	327	Fang H.F. et al., 2010
298	Wuyi	Yongchun, Fujian	Tianhushan (天湖山)	25.48	117.99	P2	Tongziyan Fm.	Coal		5.63	328	Fang H.F. et al., 2010
299	Wuyi	Yongchun, Fujian	Hanchun (含春)	25.46	117.95	P2	Tongziyan Fm.	Coal	HC6	5.74	330	Wang L., 2020
300	Wuyi	Yongchun, Fujian	Hanchun (含春)	25.46	117.95	P2	Tongziyan Fm.	Coal	HC-6	5.74	330	Deng R.J., 2020
301	Wuyi	Zhangping,Fujian	Wukeng (乌坑)	25.02	117.45	P2	Tongziyan Fm.	Coal	WK	6.2	338	Wang L., 2020
302	Wuyi	Zhangping,Fujian	Wukeng (乌坑)	25.02	117.45	P2	Tongziyan Fm.	Coal	WK-3	6.2	338	Deng R.J., 2020
303	Wuyi	Zhangping,Fujian	Kekeng (可坑)	25.15	117.21	P2	Tongziyan Fm.	Coal	KK	6.26	339	Wang L., 2020
304	Wuyi	Zhangping,Fujian	Kekeng (可坑)	25.15	117.21	P2	Tongziyan Fm.	Coal	KK-1	6.26	339	Deng R.J., 2020
305	Wuyi	Zhangping,Fujian	Shisunkeng (石笋坑)	25.28	117.38	P2	Tongziyan Fm.	Coal	SSK-1	6.34	340	Deng R.J., 2020
306	Wuyi	Zhangping,Fujian	Wusi (吾祠)	25.59	117.65	P2	Tongziyan Fm.	Coal		6.71	346	Fang H.F. et al., 2010
307	Wuyi	Zhangping,Fujian	Guantian (官田)	25.04	117.49	P2	Tongziyan Fm.	Coal	GT	6.96	350	Deng R.J., 2020
308	Wuyi	Yongchun, Fujian	Tianhushan (天湖山)	25.48	117.99	P2	Tongziyan Fm.	Coal		7.37	356	Fang H.F. et al., 2010
309	Wuyi	Zhangping,Fujian	Kekeng (可坑)	25.15	117.21	P2	Tongziyan Fm.	Coal	KK-3	7.98	364	Deng R.J., 2020
310	Wuyi	Yongchun, Fujian	Yangshan (阳山)	25.32	118.29	P2	Tongziyan Fm.	Coal		8.17	366	Fang H.F. et al., 2010
311	YJB	Laibin, Guangxi	Heshan (合山)	23.81	108.89	P3	Heshan Fm.	Coal	SCG-2	1.608	197	Niu Y.J. et al., 2020
312	YJB	Laibin, Guangxi	Heshan (合山)	23.81	108.89	P3	Heshan Fm.	Coal	SCG-3	1.613	198	Niu Y.J. et al., 2020
313	YJB	Laibin, Guangxi	Heshan (合山)	23.81	108.89	P3	Heshan Fm.	Coal	SCG-1	1.624	198	Niu Y.J. et al., 2020
314	YJB	Laibin, Guangxi	Heshan (合山)	23.81	108.89	P3	Heshan Fm.	Coal	HS-3	1.68	202	Li X. 2022
315	YJB	Laibin, Guangxi	Heshan (合山)	23.81	108.89	P3	Heshan Fm.	Coal	SC-3	1.682	202	Niu Y.J. et al., 2020
316	YJB	Laibin, Guangxi	Shicun (石村)	23.83	108.91	P3	Heshan Fm.	Coal	SK-4-M2	1.682	202	Xie Z.Z., 2019
317	YJB	Yizhou, Guangxi	Yishan (宜山)	24.63	108.64	P3	Heshan Fm.	Coal	CG1-K7	1.7	203	Dai S.F. et al., 2017
318	YJB	Laibin, Guangxi	Heshan (合山)	23.81	108.89	P3	Heshan Fm.	Coal	HS-1	1.72	204	Li X. 2022
319	YJB	Laibin, Guangxi	Heshan (合山)	23.81	108.89	P3	Heshan Fm.	Coal	SC-1	1.721	204	Niu Y.J. et al., 2020
320	YJB	Laibin, Guangxi	Heshan (合山)	23.81	108.89	P3	Heshan Fm.	Coal	HS-5	1.73	205	Li X. 2022
321	YJB	Laibin, Guangxi	Heshan (合山)	23.81	108.89	P3	Heshan Fm.	Coal	SC-5	1.73	205	Niu Y.J. et al., 2020
322	YJB	Laibin, Guangxi	Shicun (石村)	23.83	108.91	P3	Heshan Fm.	Coal	SK-4-M4	1.73	205	Xie Z.Z., 2019
323	YJB	Laibin, Guangxi	luoshan (洛山)	23.81	108.97	P3	Heshan Fm.	Coal	HLLS-4-M4	1.731	205	Xie Z.Z., 2019
324	YJB	Laibin, Guangxi	Heshan (合山)	23.81	108.89	P3	Heshan Fm.	Coal	4L-C	1.74	206	Dai S.F. et al., 2013
325	YJB	Laibin, Guangxi	luoshan (洛山)	23.81	108.97	P3	Heshan Fm.	Coal	HLLS-4-M3	1.742	206	Xie Z.Z., 2019
326	YJB	Laibin, Guangxi	luoshan (洛山)	23.81	108.97	P3	Heshan Fm.	Coal	HLLS-4-M5	1.775	208	Xie Z.Z., 2019

Table S4 (continued)

No.	Massif	Location	CoalMine / Section	Latitude	Longitude	Period	Formation	Lithology	Sample No.	Ro (%)	Temperature (°C)	References
327	YJB	Laibin, Guangxi	Heshan (合山)	23.81	108.89	P3	Heshan Fm.	Coal	HS-2	1.78	208	Li X. 2022
328	YJB	Laibin, Guangxi	Heshan (合山)	23.81	108.89	P3	Heshan Fm.	Coal	SC-2	1.781	208	Niu Y.J. et al., 2020
329	YJB	Laibin, Guangxi	Shicun (石村)	23.83	108.91	P3	Heshan Fm.	Coal	SK-4-M1	1.781	208	Xie Z.Z., 2019
330	YJB	Laibin, Guangxi	Shicun (石村)	23.83	108.91	P3	Heshan Fm.	Coal	SK-4-M9	1.786	208	Xie Z.Z., 2019
331	YJB	Laibin, Guangxi	luoshan (洛山)	23.81	108.97	P3	Heshan Fm.	Coal	HLLS-4-M2	1.795	209	Xie Z.Z., 2019
332	YJB	Yizhou, Guangxi	Yishan (宜山)	24.63	108.64	P3	Heshan Fm.	Coal	CG3-K6	1.8	209	Dai S.F. et al., 2017
333	YJB	Laibin, Guangxi	luoshan (洛山)	23.81	108.97	P3	Heshan Fm.	Coal	HLLS-4-M1	1.832	211	Xie Z.Z., 2019
334	YJB	Laibin, Guangxi	Heshan (合山)	23.81	108.89	P3	Heshan Fm.	Coal	SC-4	1.838	211	Niu Y.J. et al., 2020
335	YJB	Laibin, Guangxi	Shicun (石村)	23.83	108.91	P3	Heshan Fm.	Coal	SK-4-M3	1.838	211	Xie Z.Z., 2019
336	YJB	Laibin, Guangxi	Heshan (合山)	23.81	108.89	P3	Heshan Fm.	Coal	HS-4	1.84	211	Li X. 2022
337	YJB	Laibin, Guangxi	Heshan (合山)	23.81	108.89	P3	Heshan Fm.	Coal	SC-8	1.86	213	Niu Y.J. et al., 2020
338	YJB	Laibin, Guangxi	Shicun (石村)	23.83	108.91	P3	Heshan Fm.	Coal	SK-4-M7	1.86	213	Xie Z.Z., 2019
339	YJB	Laibin, Guangxi	Heshan (合山)	23.81	108.89	P3	Heshan Fm.	Coal	4U-C1	1.88	214	Dai S.F. et al., 2013
340	YJB	Laibin, Guangxi	Heshan (合山)	23.81	108.89	P3	Heshan Fm.	Coal	SC-7	1.887	214	Niu Y.J. et al., 2020
341	YJB	Laibin, Guangxi	Shicun (石村)	23.83	108.91	P3	Heshan Fm.	Coal	SK-4-M6	1.887	214	Xie Z.Z., 2019
342	YJB	Laibin, Guangxi	Heshan (合山)	23.81	108.89	P3	Heshan Fm.	Coal	HS-6	1.89	214	Li X., 2022
343	YJB	Laibin, Guangxi	Heshan (合山)	23.81	108.89	P3	Heshan Fm.	Coal	SC-6	1.891	214	Niu Y.J. et al., 2020
344	YJB	Laibin, Guangxi	Shicun (石村)	23.83	108.91	P3	Heshan Fm.	Coal	SK-4-M5	1.891	214	Xie Z.Z., 2019
345	YJB	Laibin, Guangxi	Heshan (合山)	23.81	108.89	P3	Heshan Fm.	Coal	3L-C	1.9	215	Dai S.F. et al., 2013
346	YJB	Laibin, Guangxi	Heshan (合山)	23.81	108.89	P3	Heshan Fm.	Coal	4U-C2	1.9	215	Dai S.F. et al., 2013
347	YJB	Laibin, Guangxi	Heshan (合山)	23.81	108.89	P3	Heshan Fm.	Coal	SC-9	1.919	216	Niu Y.J. et al., 2020
348	YJB	Laibin, Guangxi	Heshan (合山)	23.81	108.89	P3	Heshan Fm.	Coal	3U-C	1.92	216	Dai S.F. et al., 2013
349	YJB	Yizhou, Guangxi	Yishan (宜山)	24.63	108.64	P3	Heshan Fm.	Coal	LL5-K3	2.05	223	Dai S.F. et al., 2017

Note: The temperatures were esitimated based on the Barker C.E. (1988). The Ro and Temperature with underline, as well as those in the Wuyi Massif are related to the emplacement of magmatism. JNOB-Jiangnan Orogenic Belt; YJB-Youjiang Basin.

Publications

[1] **Liu, J.S.**, Wang, B., Ni, X.H., Song, F., Sun, Z.C., Deng, J., Li, Y.Y., 2022. Late Devonian transition from advancing to retreating subduction in the SW Central Asian Orogenic Belt: Insights from multiple deformation and magmatic events in the southern Yili Block, NW China. *Gondwana Research* 105, 468-487.

[2] **Liu, J.S.**, Wang, B., Cochelin, B., Shu, L., Lu, S.H., Gumiaux, C., Chen, Y., Raimbourg, H., Augier, R., Faure, M., Ni, X.H., 2025. Early Mesozoic magma-induced mid-crustal flow and high-temperature metamorphism in the Yunkai Massif, South China. *Journal of Geophysical Research: Solid Earth*, **in preparation**.

[3] **Liu, J.S.**, Wang, B., Cochelin, B., Shu, L.S., Augier, R., Raimbourg, H., Chen, Y., Canizarés, A., Liu, H.S., Cao, T.T., Chen, Y.Y., 2025. Multi-block Lithosphere of the Early Mesozoic Cathaysia Block (South China): Insights from its Crustal Thermal Heterogeneity. *Earth and Planetary Science Letters*, **in preparation**.

[4] Cochelin, B., Wang, B., **Liu, J.S.**, Lu, S.H., Shu, L.S., Gumiaux, C., Chen, Y., Song, F., 2022. Early Mesozoic Anatexis-Induced Strain Partitioning and Gneiss Doming in the Yunkai Massif, South China: A Response to Contrasted Dynamics of Paleo-Pacific and Paleo-Tethys Subductions? *Tectonics* 41, e2022TC007457.

[5] Sun, Z.C., Wang, B., **Liu, J.S.**, Ni, X.H., Song, F., 2021. Age and tectonic setting of Neoproterozoic gneissic granites in the southern Yili Block (NW China) and implications for the origins of the continental blocks in SW Central Asian Orogenic Belt. *Geological Journal* 56, 5027–5045.

[6] Ni, X.H., Wang, B., Cluzel, D., **Liu, J.S.**, He, Z.Y., 2021. Late Paleozoic tectonic evolution of the North Tianshan Belt: New structural and geochronological constraints from meta-sedimentary rocks and migmatites in the Harlik Range (NW China). *Journal of Asian Earth Sciences* 210, 104711.

[7] Zhu, X.Y., Wang, B., Sun, Z.C., **Liu, J.S.**, He, Z.Y., Zhong, L.L., 2020. Detrital zircon ages of the Mesoproterozoic metasedimentary rocks in the southern Yili Block: Implications for tectonic affinities of the microcontinents in SW Central Asian

Orogenic Belt. *Precambrian Research* 350, 105926.

[8] He, Z.Y., Wang, B., Su, W.B., Glorie, S., Ni, X.H., **Liu, J.S.**, Cai, D.X., Zhong, L.L., De Grave, J., 2022. Meso-Cenozoic thermo-tectonic evolution of the Yili block within the Central Asian Orogenic Belt (NW China): Insights from apatite fission track thermochronology. *Tectonophysics* 823, 229194.

[9] He, Z.Y., Wang, B., Glorie, S., Su, W.B., Ni, X.H., Jepson, G., **Liu, J.S.**, Zhong, L.L., Gillespie, J., De Grave, J., 2022. Mesozoic building of the Eastern Tianshan and East Junggar (NW China) revealed by low-temperature thermochronology. *Gondwana Research* 103, 37-53.

[10] He, Z.Y., Wang, B., Ni, X.H., De Grave, J., Scaillet, S., Chen, Y., **Liu, J.S.**, Zhu, X., 2021. Structural and kinematic evolution of strike-slip shear zones around and in the Central Tianshan: Insights for eastward tectonic wedging in the southwest Central Asian Orogenic Belt. *Journal of Structural Geology* 144, 104279.

[11] He, Z.Y., Wang, B., Nachtergaele, S., Glorie, S., Ni, X.H., Su, W.B., Cai, D.X., **Liu, J.S.**, De Grave, J., 2021. Long-term topographic evolution of the Central Tianshan (NW China) constrained by low-temperature thermochronology. *Tectonophysics* 817, 229066.

Conferences

[1] EGU General Assembly 2024, April 2024, Vienna, Austria.

[2] Academic Forum on Structural Geology and Geodynamics 2025, April 2025, Chengdu, China.

[3] Workshop 2025 of the 10th National Metamorphic Petrology Committee, April 2025, Zhuhai, China.

[4] International Workshop on Lithospheric Evolution and Earth's Habitability, July 2025, Beijing, China.

[5] Annual Meeting of the Chinese Geoscience Union (CGU-2025), October 2025, Chengdu, China.

Jiashuo LIU

Rhéologie lithosphérique du bloc Cathaysia (Chine du Sud) au Mésozoïque précoce: Perspectives issues de la déformation, du métamorphisme, du magmatisme et de la modélisation géodynamique

L'une des prémisses fondamentales de la tectonique des plaques est celle des plaques lithosphériques rigides. Cependant, les plaques lithosphériques sont des corps visco-élastiques plutôt que parfaitement rigides, composés de multiples sous-blocs mécaniquement hétérogènes. La rhéologie lithosphérique est la clé pour décrypter l'évolution et les processus géodynamiques de la lithosphère continentale. Depuis le Méso-/Néo-Protérozoïque, l'évolution du Bloc de la Chine du Sud (SCB) est le produit de l'assemblage et la fragmentation des supercontinents. En tant que composante principale du SCB, le Bloc de Cathaysia (CB) joue un rôle clé dans la compréhension de l'évolution tectonique du SCB et du continent est-asiatique. Cependant, des controverses persistent concernant ses propriétés rhéologiques et son évolution géodynamique. La déformation omniprésente et le magmatisme distribué de manière plane au sein du CB en font un laboratoire idéal pour examiner la rhéologie et la rigidité de la plaque lithosphérique. Cette thèse présente une étude à l'échelle des blocs et multidisciplinaire sur la déformation, le métamorphisme, l'état thermique crustal et le contexte dynamique du CB, incluant la géologie structurale, la géochronologie, la thermobarométrie métamorphique, les investigations thermiques et la modélisation dynamique. Les principales conclusions sont : (1) Le magmatisme intracontinental du Mésozoïque précoce au sein du CB a induit un métamorphisme de haute température et un écoulement de la croûte moyenne, atteignant 6,8-7,0 kbar et 780-810℃. (2) Le CB présente une hétérogénéité de déformation, de métamorphisme et d'état thermique crustal durant le Mésozoïque précoce. Le Massif de Yunkai présente notamment une déformation plus intense, un grade de métamorphisme plus élevé et une température plus haute. (3) Le CB était composé de sous-blocs présentant une hétérogénéité rhéologique durant le Mésozoïque précoce. (4) Les zones structurelles préexistantes constituent des canaux importants pour le transport de chaleur. (5) Les comportements du CB au Mésozoïque précoce résultent de l'interaction entre les multiples blocs, particulièrement le long de la ceinture de la Téthys paléozoïque. La force motrice principale provient de la collision avec le Bloc indochinois.

Mots clés: Rhéologie lithosphérique, État thermique crustal, Déformation et métamorphisme, Modélisation géodynamique, Mésozoïque inférieur, Chine du Sud

Early Mesozoic lithospheric rheology of the Cathaysia Block, South China: Insights from deformation, metamorphism, magmatism and geodynamic modelling

One of the fundamental premises of plate tectonics is that of rigid lithospheric plates. However, the lithospheric plates are visco-elastic rather than perfectly rigid bodies. This implies a rheologically heterogeneous lithosphere comprising multiple sub-blocks. The lithospheric rheology is the key to deciphering the evolution and geodynamic processes of the continental lithosphere. Since the Meso-/Neo-Proterozoic, the evolution the South China Block (SCB) has been influenced by the assembly and break-up of the supercontinents. As the main component of the SCB, the Cathaysia Block (CB) plays a key role in understanding the tectonic evolution of the SCB and the East Asian Continent. However, there are still controversies about rheological properties and the dynamic background. The pervasive deformation and planar distributed magmatism within the CB make it an ideal laboratory for examining the rheology and rigidity of the lithosphere plate. This thesis presents a block-scale and multi-disciplinary study on deformation, metamorphism, crustal thermal state and the dynamic background of the CB, including the structural geology, geochronology, P-T estimation, thermal investigations and dynamic modelling. The main conclusions are: (1) The Early Mesozoic intracontinental magmatism within the CB induced the high-temperature metamorphism and mid-crustal flow, which reached 6.8-7.0 kbar and 780-810 ℃. (2) The CB exhibits a heterogeneity of deformation, metamorphism and crustal thermal state during the Early Mesozoic. The Yunkai Massif exhibits a more intense deformation, a higher grade of metamorphism and a higher temperature. (3) The CB was composed of sub-blocks with rheological heterogeneity during the Early Mesozoic. (4) The pre-existing structural zones are an important potential channel for heat transportation. (5) The Early Mesozoic behaviors of the CB are the results of the interaction between the multiple blocks, especially along the Paleo-Tethys Belt. The main driving force is from the collision with the Indochina Block.

Keywords : Lithospheric rheology, Crustal thermal state, Deformation and metamorphism, Geodynamic modelling, Early Mesozoic, South China

Université d'ORLÉANS

Institut des Sciences de la Terre d'Orléans

Univ Orléans, CNRS, BRGM, OSUC, F-45071 Orléans, France

NANJING UNIVERSITY 1902